

HYDRODYNAMICS, MASS TRANSFER AND MODELING OF THE TOLUENE OXIDATION PROCESS

by

Romain Lemoine

B.S. in Chemical Engineering and Chemistry, ENSCL Lille, France, 1998

Submitted to the Graduate Faculty of

the School of Engineering in partial fulfillment

of the requirements for the degree of

Doctor of Philosophy

University of Pittsburgh

2005

UNIVERSITY OF PITTSBURGH

SCHOOL OF ENGINEERING

This dissertation was presented by

by

Romain Lemoine

It was defended on

March 10, 2005

and approved by

Shiao-Hung Chiang, Professor Emeritus, Chemical and Petroleum Engineering Department

Robert Enick, Professor, Chemical and Petroleum Engineering Department

Badie I. Morsi, Professor, Chemical and Petroleum Engineering Department

Rachid Oukaci, Associate Professor, Chemical and Petroleum Engineering Department

Patrick Smolinski, Associate Professor, Mechanical Engineering Department

Dissertation Director: Badie I. Morsi, Professor, Chemical and Petroleum Engineering Department

ABSTRACT

HYDRODYNAMICS, MASS TRANSFER AND MODELING OF THE TOLUENE OXIDATION PROCESS

Romain Lemoine, Ph.D.

University of Pittsburgh, 2005

The equilibrium solubility (C^*), Critical mixing speed (N_{CRE}) and (N_{CRI}), Induced gas flow rate (Q_{GI}), volumetric liquid-side mass transfer coefficient ($k_L a$), liquid-side mass transfer (k_L), gas-liquid interfacial area (a), gas holdup (ε_G), Sauter mean bubble diameter (d_S), and the bubble size distribution of N_2 , O_2 and air in liquid toluene and three mixtures of toluene, benzaldehyde and benzoic acid, aimed at simulating the continuous liquid phase toluene oxidation (LPTO), were measured in a 4-liter ZipperClave surface aeration (SAR), gas inducing (GIR) and gas sparging (GSR) reactors operating under wide ranges of mixing speed (N) (800-1200 rpm), liquid height (H) (0.171-0.268 m in the SAR and GIR), superficial gas velocities (U_G) (0.000-0.004 m/s in the GSR), temperature (T) (300-453 K) and pressure (P) (1-15 bar). These parameters were also measured in a 1-ft diameter, 10-ft high bubble column reactor (BCR) under various pressures (P) (2-8 bar), gas velocities (U_G) (0.06-0.15 m/s).

The solubility values of N_2 , O_2 and air in liquid toluene and the three mixtures were calculated using a modified Peng-Robinson equation of state. ($k_L a$) data were determined using the transient physical absorption technique. The bubble size distributions as well as the Sauter mean bubble diameters were obtained from the photographic method and the gas disengagement technique in the agitated reactors and bubble column reactor, respectively. In the agitated reactor, the gas holdup values were measured through the dispersion height measurement technique, and the manometric method using two differential pressure (dP) cells was employed in the bubble column reactor. From the gas holdup, Sauter mean bubble diameter and $k_L a$ experimental values, a and k_L were calculated under various operating conditions. N_{CRE} and N_{CRI} as well as a_{Wave} were estimated by analyzing the videos taken with an on-line high-speed Phantom camera through the reactor's Jerguson windows. In the GIR, Q_{GI} was determined using a highly sensitive Coriolis mass flow meter. The Central Composite Statistical Design and analysis technique was used to study the effect of operating conditions on these hydrodynamic parameters.

At constant temperature, the equilibrium solubilities (C^*) of the three gases in all liquids used appeared to increase linearly with pressure and obey Henry's Law, however, the values exhibited minima with increasing temperature. The C^* values were found to increase with increasing gas molecular weight, and decrease with the addition of benzaldehyde and benzoic acid to pure toluene. A dimensionless form of Arrhenius-type equation, in which the activation energy was dependent of temperature, was developed to predict Henry's law constant for the three gases in toluene and mixtures with a regression coefficient > 99%.

In the SAR, increasing N , T or decreasing H increased a_{Wave} , ε_G , a , k_L and $k_L a$, and decreased d_S and N_{CRE} , whereas increasing P , decreased a_{Wave} , ε_G , a , k_L and $k_L a$ and had no effect on d_S and N_{CRE} . In the GIR, increasing N or

decreasing H increased Q_{GI} , ε_G , a , k_L , $k_L a$ and d_S and decreased N_{CRI} . Also, increasing T increased and then decreased Q_{GI} , ε_G and a ; increased k_L and $k_L a$; and decreased d_S and N_{CRI} . In addition, increasing P decreased slightly Q_{GI} and ε_G but did not affect a , k_L , $k_L a$, d_S and N_{CRI} under the operating conditions used. In the GSR, increasing N , T and U_G increased ε_G , a , k_L and $k_L a$. Also, increasing N and T , or decreasing U_G decreased d_S .

The addition of benzaldehyde and benzoic acid to pure toluene was found to significantly affect the hydrodynamic parameters (d_S and ε_G), in the GSR and GIR, especially at low temperature due to formation of froth, which led to the enhancement of $k_L a$. The hydrodynamic and mass transfer parameters obtained indicated that the behavior of the SAR was mainly dependent on k_L , whereas those of the GSR and GIR were strongly affected not only by k_L , but also by a . In the bubble column reactor, under the operating conditions used, $k_L a$, a and ε_G values were found to increase with increasing gas superficial velocity and pressure, whereas d_S and k_L values appeared to decrease with pressure and increase with superficial gas velocity. The effect of gas nature on the hydrodynamic and mass transfer parameters was found to be insignificant, whereas the effect of addition of benzaldehyde and benzoic acid to pure toluene, aimed at mimicking the actual continuous liquid-phase toluene oxidation process, appeared to have a strong impact on both parameters due to froth formation.

Empirical, statistical and Back-Propagation Neural Network (BPNN) correlations were also developed to predict the hydrodynamic and mass transfer parameters obtained in this study in the agitated reactors (ARs) and bubble column reactor (BCR) along with a large data bank of literature data (7374 data points in ARS and 3881 data points in BCRs). These correlations were then incorporated in calculation algorithms for predicting both hydrodynamic and mass transfer parameters in ARs and BCRs.

Using these algorithms, two comprehensive models, including the effects of mass and heat transfer, hydrodynamics, and kinetics were developed for bubble column reactors (BCRs) and series of gas sparging reactors (GSRs) to simulate the commercial Liquid-Phase Toluene Oxidation (LPTO) process. An intrinsic kinetic rate equation for the toluene oxidation was also developed using literature data. The effects of the reactor diameter (D_C), reactor height (H), and superficial gas velocity (U_G) or mixing speed (N) on the LPTO process performances (toluene conversion, benzaldehyde selectivity and yield) were investigated in a BCR and a cascade of GSRs. The pressure and temperature at the inlet of the reactors were set at 1.0 MPa and 420 K; the feed gas to the reactors was a mixture (50/50 by mole) of oxygen and nitrogen; and the liquid feed was toluene containing Co catalyst and a NaBr promoter at concentrations of 0.22 wt% and 1.76 wt%, respectively. The heat of reaction was removed from both reactor types using water in cooling pipes, representing 2% of the reactor volume; and the gas was sparged into the reactors through a multi-orifices gas distributor with an open area, representing 10% of the reactor cross-sectional area.

The model predictions showed that under the operating conditions used, toluene conversion of about 12%, a benzaldehyde selectivity of 40% and a benzaldehyde production in the range of about 1500 tons/year could be achieved using a superficial gas velocity of 0.1 m/s in the BCR (10-m height, 2-m Inside diameter) and 0.002 m/s in the series of 5 GSRs (2-m inside diameter, and 2-m liquid height). The BCR selected was found to operate in the kinetically-controlled regime whereas the 5-GSRs appeared to operate in a regime controlled by both gas-liquid

mass transfer and reaction kinetics. Thus, due to its attractive economics in addition to the mechanical constraints of GSRs, the BCR seems to be the reactor of choice for the commercial-scale LPTO process.

DESCRIPTORS

Absorption	Mass Transfer Coefficient
Bubble Column Reactor	Neural Networks
Entrainment	Sauter Mean Bubble Diameter
Gas-Inducing Reactor	Solubility
Gas Holdup	Statistical Experimental Design
Gas-Liquid Interfacial Area	Surface Aeration Reactor
Gas-Sparging Reactor	Toluene Oxidation Process
Hydrodynamics	Volumetric Mass transfer Coefficient

TABLE OF CONTENTS

	Page
ABSTRACT	iii
DESCRIPTORS.....	vi
TABLE OF CONTENTS	vii
LIST OF TABLES.....	xi
LIST OF FIGURES.....	xv
NOTATION	xix
ACKNOWLEDGMENT	xxviii
1.0 INTRODUCTION AND BACKGROUND.....	1
1.1 Industrial Liquid-Phase Oxidation Processes	5
1.2 Gas-Liquid Transport in the Liquid Phase Toluene Oxidation.....	7
2.0 LITERATURE REVIEW	10
2.1 Gas Solubility in Liquids, C^*	10
2.2 Kinetics of Toluene Oxidation	12
2.2.1 Toluene Oxidation Reactions.....	12
2.3 Reactors Utilized.....	21
2.3.1 Stirred Reactors	21
2.3.2 Bubble Column Reactors.....	22
2.4 Hydrodynamic Parameters.....	24
2.4.1 Hydrodynamic Regimes in Agitated reactors	24
2.4.2 Critical Mixing speeds and Gas Flow Rates in Agitated Reactors	26
2.4.3 Hydrodynamic Parameters in Bubble Column Reactors (BCR).....	36
2.4.4 Gas Bubbles in Agitated Reactors	41
2.4.5 Gas Bubbles in Bubble Column Reactors.....	42
2.4.6 Bubble Size Measurement Techniques in gas-Liquid Contactors.	43
2.4.7 Gas Holdup in Agitated Reactors	43
2.4.8 Gas Holdup in Bubble Column Reactors.....	44

2.4.9 Gas Holdup Measurement Techniques in gas-Liquid Contactors.....	45
2.5 Mass Transfer Characteristics.....	47
2.5.1 Mass Transfer Measurement Techniques in Gas-Liquid Contactors	47
2.5.2 Gas-liquid Interfacial Area in Gas-Liquid Contactors, a	48
2.5.3 Volumetric Mass Transfer Coefficient, kLa	49
2.5.4 Mass Transfer Coefficient, k_L	57
3.0 Objectives	59
4.0 Experimental.....	60
4.1 Gas-Liquid systems and Operating Variables.....	60
4.2 Properties of the Gas-Liquid Systems used	60
4.2.1 Vapor Pressure of Toluene	61
4.2.2 Density of Toluene	62
4.2.3 Viscosity of Toluene.....	70
4.2.4 Surface Tension of Toluene.....	70
4.2.5 Gas Diffusivity in Toluene	72
4.2.6 Gas viscosity in Toluene.....	73
4.3 Experimental Set-up.....	76
4.3.1 Agitated Reactors.....	76
4.3.2 Bubble Column Reactor (BCR).....	84
4.4 Experimental Procedures.....	89
4.4.1 Mass Transfer and Thermodynamic Parameters in the Agitated Reactors	89
4.4.2 Mass Transfer and Thermodynamic Parameters in the BCR.....	90
4.4.3 Hydrodynamic Parameters in the Agitated Reactors	91
4.4.4 Hydrodynamic Parameters in the BCR.....	93
4.5 Safety Issues	95
4.6 Oxidation Issues.....	95
5.0 CALCULATIONS.....	99
5.1 Thermodynamic Parameters	99
5.1.1 Calculation of C^* in the SAR and GIR.....	99
5.1.2 Calculation of C^* in the GSR	105
5.1.3 Calculation of C^* in the Bubble Column Reactor	105
5.2 Hydrodynamic Parameters.....	109
5.2.1 Critical Mixing Speed Measurement, N_{CR} , in the Agitated Reactors	109
5.2.2 Calculation of the Gas Flow Rate, Q_{GI} , in the Agitated Reactors	109
5.2.3 Calculation of the Gas Flow Rate, Q_G , in the BCR.....	109

5.2.4	Calculation of the Superficial Gas Velocity, U_G , in both Contactors	110
5.2.5	Gas Holdup in the Agitated Reactors, ε_G	110
5.2.6	Gas Holdup in the BCR, ε_G	111
5.2.7	Bubble Size Distribution and Sauter Mean Bubble Diameter in the Agitated Reactors, d_s	112
5.2.8	Bubble Size Distribution and Sauter Mean Bubble Diameter in the BCR, d_s	114
5.3	Mass Transfer Parameters.....	119
5.3.1	Calculation of the Gas-Liquid Interfacial Areas, a , in the Agitated Reactors.....	119
5.3.2	Calculation of the Gas-Liquid Interfacial Areas, a , in the BCR	120
5.3.3	Calculation of the Volumetric Mass Transfer Coefficient, $k_L a$, in the Agitated Reactors	120
5.3.4	Calculation of the Volumetric Mass Transfer Coefficient, $k_L a$, in the BCR.....	125
5.3.5	Calculation of the Gas-Liquid Mass Transfer Coefficient, k_L , in the Agitated Reactors	126
5.3.6	Calculation of the Gas-Liquid Mass Transfer Coefficient, k_L , in the BCR.....	127
6.0	RESULTS AND DISCUSSION	128
6.1	Thermodynamic Parameters	131
6.1.1	Gas Solubility in the Liquids Studied	131
6.1.2	Activation Energy, Heat and Entropy of Solution of N_2 and O_2 in Toluene.....	137
6.2	Hydrodynamic and Mass Transfer Parameters in Agitated Reactors.....	141
6.2.1	Effect of Mixing Speed on the Hydrodynamic and Mass Transfer Parameters	141
6.2.2	Effect of Liquid Height on the Hydrodynamic and Mass Transfer Parameters	142
6.2.3	Effect of Superficial Gas Velocity on the Hydrodynamic and Mass Transfer Parameters	151
6.2.4	Effect of Temperature on the Hydrodynamic and Mass Transfer Parameters	151
6.2.5	Effect of Pressure on the Hydrodynamic and Mass Transfer Parameters	161
6.2.6	Effect of Gas Nature on the Hydrodynamic and Mass Transfer Parameters	162
6.2.7	Effect of Froth, Liquid Nature on the Hydrodynamic and Mass Transfer Parameters	166
6.2.8	Effect of Reactor Mode on the Hydrodynamic and Mass Transfer Parameters.....	170
6.3	Hydrodynamic and Mass Transfer Parameters in the BCR.....	172
6.3.1	Effect of Pressure on the Hydrodynamic and Mass Transfer Parameters	172
6.3.2	Effect of Superficial Gas Velocity on the Hydrodynamic and Mass Transfer Parameters	183
6.3.3	Effect of Gas Nature on the Hydrodynamic and Mass Transfer Parameters	184
6.3.4	Effect of Liquid Nature on the Hydrodynamic and Mass Transfer Parameters	184
6.4	Correlations and Calculation Algorithm in the Agitated Reactors.....	186
6.4.1	Empirical Correlations of the Hydrodynamic and Mass transfer Parameters in the Agitated Reactors... 186	
6.4.2	Statistical Correlations of the Hydrodynamic and Mass transfer Parameters in the Agitated Reactors... 198	
6.4.3	BPNN Correlations of the Hydrodynamic and Mass transfer Parameters in the Agitated Reactors..... 206	
6.4.4	Calculation Algorithm of the Hydrodynamic and Mass transfer Parameters in the Agitated Reactors ... 215	
6.5	Correlations and Calculation Algorithm in the BCR.....	217

6.5.1 Empirical Correlations of the Hydrodynamic and Mass Transfer Parameters in the BCR.....	217
6.5.2 Statistical Correlations of the Hydrodynamic and Mass Transfer Parameters in the BCR.....	227
6.5.3 BPNN Correlations of the Hydrodynamic and Mass Transfer Parameters in the BCR.....	231
6.5.4 Calculation Algorithm of the Hydrodynamic and Mass Transfer Parameters in the BCR	231
6.6 Simulation.....	242
6.6.1 Modeling of LPTO Process in a BCR.....	242
6.6.2 Modeling of LPTO Process in a Cascade of GSRs.....	247
6.6.3 Kinetic Model and parameters	249
6.6.4 Hydrodynamic and Mass transfer Parameters	251
6.6.5 Liquid and Gas-Phase Mixing Parameters.....	251
6.6.6 Heat Transfer Parameters.....	252
6.6.7 Gas-Liquid thermodynamic and Physicochemical Properties	254
6.6.8 Simulation Results on the BCR	255
6.6.9 The Cascade of GSRs and Comparison with the BCR	261
CONCLUDING REMARKS	266
APPENDIX A: Literature Survey on the Hydrodynamic and Mass transfer Correlations	268
APPENDIX B: Chemical Analysis.....	298
APPENDIX C: Error Analysis.....	300
APPENDIX D: Experimental Procedure	311
APPENDIX E: Experimental Design and Analysis Techniques.....	315
REFERENCES	324

LIST OF TABLES

	Page
Table 1: Toluene Producers and Plant Capacities in US in 2000 ⁽²⁾	2
Table 2: Comparison between Gas and liquid-Phase Selectivity	3
Table 3: Comparison between Gas and liquid-Phase Operating Conditions.....	3
Table 4: Literature Survey on Solubility of N ₂ and O ₂ in Toluene.....	11
Table 5: Literature Survey on the Kinetic Mechanisms of the Toluene Oxidation	14
Table 6: Geometrical Ratios of Agitated reactors	21
Table 7: Hydrodynamic Studies in Surface Aeration Reactors	27
Table 8: Hydrodynamic Studies in Gas Inducing Reactors	29
Table 9: Hydrodynamic Studies in Gas Sparging Reactors	33
Table 10: Hydrodynamic Studies Using Bubble Columns Larger than 0.15 m	39
Table 11: Comparison of Small and Large Bubble Diameters in the BCR.....	46
Table 12: Literature Survey on Mass Transfer in Surface Aeration Reactors.....	51
Table 13: Literature Survey on Mass Transfer in Gas Inducing Reactor.....	52
Table 14: Literature Survey on Mass Transfer in Gas-Sparged Reactors.....	53
Table 15: Literature Survey on Mass Transfer in Bubble Column Reactors	55
Table 16: Thermodynamics properties of toluene, benzoic acid, benzaldehyde, nitrogen and oxygen ⁽³²⁸⁾	61
Table 17: Composition of the Different Liquid Mixtures Used	61
Table 18: Physical Properties of the Liquid Systems Used	65
Table 19: Phase molar fraction for O ₂ and N ₂ in toluene.....	72
Table 20: Ignition temperature for air-toluene mixture ^(334, 335, 336)	95
Table 21: Flammability limits of air and O ₂ -toluene mixtures in the vapor phase	96
Table 22: Constants in Equations (5-19) and (5-20)	101

Table 23: Operating variables and their ranges for the agitated reactors	129
Table 24: Operating, Coded variables and their Ranges for the BCR	130
Table 25: Experimental conditions and coded variables for the agitated reactors.....	130
Table 26: Henry's law constant and apparent activation energy of absorption	138
Table 27: Parameters for the General Solubility Correlation Equation (6-5).....	138
Table 28: Geometrical and Operating Parameters Used by Fillion ⁽³⁴⁹⁾	154
Table 29: Quantitative Effect of Benzaldehyde and Benzoic Acid Addition to Toluene on d_s , ε_G , and k_La in the GIR	168
Table 30: Quantitative Effect of Benzaldehyde and Benzoic Acid Addition to Toluene on d_s , ε_G , and k_La in the GSR	169
Table 31: Quantitative Effect of Benzaldehyde and Benzoic Acid Addition to Toluene on d_s , ε_G , and k_La in the BCR	185
Table 32: Data Base on ARs used in this Study.....	190
Table 33: Upper and Lower limits of the variables used in Equations (6-19) through (6-54).....	195
Table 34: Coefficients of the Statistical Correlations for N_{CR} , a_{Wave} and Q_{GI}	199
Table 35: Coefficients of the Statistical Correlations for d_s	201
Table 36: Coefficients of the Statistical Correlations for ε_G	201
Table 37: Coefficients of the Statistical Correlations for k_La	202
Table 38: Coefficients of the Statistical Correlations for a	203
Table 39: Coefficients of the Statistical Correlations for k_L	204
Table 40: Architecture and Input Variables of the N_{CR} , Q_{GI} , ε_G , d_s , a_{Wave} and k_La BPNN Correlations.....	207
Table 41: Statistical Analysis of the Empirical and BPNN Correlations.....	208
Table 42: Input Variables for Gas distribution and Reactor Type used in the BPNN Correlations.....	208
Table 43: Architecture, Weights of the N_{CR} BPNN Correlation.....	209
Table 44: Architecture, Weights of the Q_{GI} BPNN Correlation	209
Table 45: Architecture, Weights of the ε_G BPNN Correlation	210
Table 46: Architecture, Weights of the d_s BPNN Correlation	210
Table 47: Architecture, Weights of the k_La BPNN Correlation	211

Table 48: Architecture, Weights of the a_{Wave} BPNN Correlation	212
Table 49: Database used in this study on BCRs and SBCRs	219
Table 50: Value of α used in Equation (6-67).....	224
Table 51: Upper and Lower limits of the variables in Equations (6-64) through (6-71).....	224
Table 52: Coefficients of the Statistical Correlations for the Hydrodynamic and Mass Transfer Parameters	228
Table 53: Statistical Analysis of the Empirical and BPNN Correlations.....	233
Table 54: Architecture, Weights of the d_S , $d_{S-Large}$ and k_La BPNN Correlations.....	233
Table 55: Architecture, Weights of the ε_G BPNN Correlation	234
Table 56: Architecture, Weights of the $\varepsilon_{G-Large}$ BPNN Correlation	235
Table 57: Architecture, Weights of the d_S BPNN Correlation	236
Table 58: Architecture, Weights of the $d_{S-Large}$ BPNN Correlation	237
Table 59: Architecture, Weights of the k_La BPNN Correlation	238
Table 60: Geometrical Ratios of Bubble Column Reactors	243
Table 61: Kinetics Parameters	251
Table 62: Operating Variables for the BCRs	257
Table 63: Operating Variables for the GSRs	262
Table A-1: Literature Correlations of Critical Mixing Speeds in the SAR.....	269
Table A-2: Literature Correlations of Critical Mixing Speeds in the GIR.....	271
Table A-3: Literature Correlations of Critical Mixing Speeds in the GSR.....	272
Table A-4: Literature Correlations of the Induced and Entrainment Gas Flow Rate.....	273
Table A-5: Literature Correlations of the Sauter Mean Bubble Diameter in Agitated Reactors	276
Table A-6: Literature Correlations of the Sauter Mean Bubble Diameter in the BCR	277
Table A-7: Literature Correlations for the Bubble Rise Velocity in the BCR	278
Table A-8: Literature Correlations of the Gas Holdup in Agitated Reactors	279
Table A-9: Literature Correlations of Gas Holdup in Bubble Column Reactors.....	282
Table A-10: Literature Correlations of the Gas-Liquid Interfacial Area	284
Table A-11: Literature Correlations of k_La in the SAR	287

Table A-12: Literature Correlations of $k_L a$ in the GIR	288
Table A-13: Literature Correlations of $k_L a$ in the GSR	290
Table A-14: Literature Correlations of $k_L a$ in the BCR	292
Table A-15: Literature Correlations of the Mass Transfer Coefficient in Agitated Reactors.....	294
Table A-16: Literature Correlations for the Mass Transfer Coefficient in the BCR	296
Table E-1: Distribution and spatial settings of the experiments according to the central composite statistical design	317

LIST OF FIGURES

	Page
Figure 1: Toluene Oxidation Products Tree ⁽³⁾	4
Figure 2: The Dow Toluene Oxidation Process ⁽¹⁾	6
Figure 3: Gas Concentration Profile in the Toluene Oxidation Process	9
Figure 4: Operation Modes of Agitated Reactors	23
Figure 5: Effect of Temperature on Toluene and Toluene Mixtures Vapor Pressure	64
Figure 6: Effect of Temperature on Toluene and the three Mixtures Density	66
Figure 7: Effect of Temperature on Toluene and the three Mixtures Viscosity.....	67
Figure 8: Effect of Temperature on Toluene and the three Mixtures Surface Tension.....	68
Figure 9: Effect of Pressure and Temperature on Toluene Surface Tension	69
Figure 10: Effect of Temperature on Gas Diffusivity in Toluene and the three Mixtures	74
Figure 11: Effect of Temperature and Pressure on Gas Viscosity ⁽³²⁸⁾	75
Figure 12: Schematic of the Experimental Setup for Mass Transfer Measurements	78
Figure 13: Schematic of the Experimental Setup for Hydrodynamic Measurements	79
Figure 14: Details of the Agitated Reactors Dimensions.....	80
Figure 15: Impeller and Shaft Design in the Agitated Reactors	81
Figure 16: Design of the Jerguson Windows and Position of the Impeller.....	82
Figure 17: Bottom View of the Gas Distributor in The GSR	83
Figure 18: Schematic of the Bubble Column Reactor	86
Figure 19: Spider Type Sparger Design ⁽⁵⁶⁾	87
Figure 20: dP Legs Position along the BCR ⁽⁵⁶⁾	88
Figure 21: Schematic of the Multi-Step Procedure at Constant Temperature, Mixing Speed and Liquid Height.....	92
Figure 22: Typical Image of Gas Bubbles before and after Processing in Agitated Reactors	94

Figure 23: Flammability Limits of O ₂ in Toluene as Function of % V/V Toluene and O ₂ Partial Pressure	98
Figure 24: Validation of the Modified PR-EOS by Density Calculation.....	103
Figure 25: Flow Diagram of the re-circulation Path in the GSR.....	106
Figure 26: Algorithm for C* Calculation in the Agitated Reactors ⁽²⁴⁹⁾	108
Figure 27: Comparison Between k_La Values Obtained in the Two Agitated Reactors Used	113
Figure 28: Dynamic Gas Disengagement Technique and dP Cells Position for the Bubble Size Measurement in the BCR	116
Figure 29: Effect of the dP Cells Position and Gas Velocity on Axial Distribution of the Gas Holdup	117
Figure 30: Bubble Size Distribution for N ₂ in Toluene in the Agitated Reactors.....	118
Figure 31: Algorithm for C _L and V _L Calculation in the Agitated Reactors ⁽²⁴⁹⁾	124
Figure 32: Comparison Between the C* Values Obtained in the Bubble Column and the Agitated Reactors.....	132
Figure 33: Reproducibility and Effect of Pressure, Temperature, and Gas and Liquid Nature on C* Values	133
Figure 34: Effect of Temperature on Henry Constants for N ₂ and O ₂ in Toluene.....	134
Figure 35: Turn Around Temperature Effect on C* Values in Water ⁽³⁵⁰⁾ and Toluene	139
Figure 36: Comparison Between Experimental and Predicted Henry Constants from Equation (6-5).....	140
Figure 37: Effect of Mixing Speed, Pressure and Liquid Nature on k_La values in the SAR, GIR and GSR	143
Figure 38: Effect of Mixing Speed, Pressure and Liquid Nature on d_s and ε_G values in the SAR, GIR and GSR	144
Figure 39: Effect of Mixing Speed, Pressure and Liquid Nature on Q_{GI} and a_{Wave} values in the SAR, GIR and GSR	145
Figure 40: Effect of Mixing Speed, Pressure and Liquid Nature on a and k_L values in the SAR, GIR and GSR.....	146
Figure 41: Effect of Liquid Height, Pressure and Liquid Nature on k_La values in the SAR and GIR	147
Figure 42: Effect of Liquid Height, Pressure and Liquid Nature on N_{CRE} , N_{CRB} , Q_{GI} and a_{Wave} values in the SAR and GIR	148
Figure 43: Effect of Liquid Height, Pressure and Liquid Nature on d_s and ε_G values in the SAR and GIR.....	149
Figure 44: Effect of Liquid Height, Pressure and Liquid Nature on a and k_L values in the SAR and GIR.....	150
Figure 45: Effect of Superficial Gas Velocity, Pressure and Liquid Nature on k_La , d_s , ε_G , a and k_L in the GSR	155
Figure 46: Effect of Temperature, Pressure and Gas Nature on k_La in the SAR, GIR and GSR.....	156
Figure 47: Effect of Temperature, Pressure, Gas and Liquid Nature on N_{CRE} , N_{CRB} , Q_{GI} and a_{Wave} in the SAR, GIR and GSR	157

Figure 48: Effect of Viscosity and Density on N_{CRI} and Q_{GI} in the GIR.....	158
Figure 49: Effect of Temperature and Pressure on d_S and ε_G in the SAR, GIR and GSR.....	159
Figure 50: Effect of Temperature and Pressure on a and k_L in the SAR, GIR and GSR.....	160
Figure 51: Effect of Liquid, Gas Nature and Pressure on k_La , d_S and ε_G in the GIR.....	164
Figure 52: Effect of Liquid, Gas Nature and Pressure on a and k_L in the GIR.....	165
Figure 53: Comparison of the Hydrodynamic and Mass Transfer Parameters in the SAR, GIR and GSR.....	171
Figure 54: Effect of Pressure and Superficial Gas velocity on d_S of N_2 and Air in the Liquids Studied.....	173
Figure 55: Effect of Pressure and Superficial Gas Velocity on the Bubble Size Distribution.....	174
Figure 56: Effect of Pressure and Superficial Gas Velocity on d_S and $d_{S-Small}$ of N_2 and Air in the Liquids Studied	175
Figure 57: Effect of Pressure and Superficial Gas velocity on ε_G of N_2 and Air in the Liquids Studied	176
Figure 58: Effect of Pressure and Superficial Gas velocity on $\varepsilon_{G-Small}$ of N_2 and Air in the Liquids Studied.....	177
Figure 59: Effect of Pressure and Superficial Gas Velocity on ε_G and $\varepsilon_{G-Small}$ of N_2 and Air in the Liquids Studied	178
Figure 60: Effect of Pressure and Superficial Gas velocity on a of N_2 and Air in the Liquids Studied.....	179
Figure 61: Effect of Pressure and Superficial Gas Velocity on a and a_{Small} of N_2 and Air in the Liquids Studied	180
Figure 62: Effect of Pressure and Superficial Gas velocity on k_La of N_2 and Air in the Liquids Studied.....	181
Figure 63: Effect of Pressure and Superficial Gas velocity on k_L of N_2 and Air in the Liquids Studied.....	182
Figure 64: Comparison between Experimental and Predicted N_{CR} , Q_{GI} , ε_G and d_S Values using Empirical Correlations	196
Figure 65: Comparison between Experimental and Predicted k_La and a_{Wave} Values using Empirical Correlations...	197
Figure 66: Comparison between Experimental and Predicted N_{CRE} , N_{CRb} , Q_{GI} and a_{Wave} Values Using the Statistical Correlations	200
Figure 67: Comparison between Experimental and Predicted d_S , ε_G , a , k_La and k_L Values Using the Statistical Correlations	205
Figure 68: Comparison between Experimental and Predicted N_{CR} , Q_{GI} , ε_G and d_S Values using BPNN Correlations	213
Figure 69: Comparison between Experimental and Predicted k_La and a_{Wave} Values using BPNN Correlations	214
Figure 70: Calculation Algorithm for the Hydrodynamic and Mass Transfer Parameters Using the Empirical and BPNN Correlations	216

Figure 71: Comparison between ε_G , $\varepsilon_{G-Large}$, d_S and $d_{S-Large}$ Experimental and Predicted values using Empirical Correlations	225
Figure 72: Comparison between $k_L a$ Experimental and Predicted values using Empirical Correlations	226
Figure 73: Comparison between Experimental and Predicted d_S , $d_{S-Small}$, ε_G and $\varepsilon_{G-Large}$ Values Using the Statistical Correlations	229
Figure 74: Comparison between Experimental and Predicted a , a_{Small} , $k_L a$ and k_L Values Using the Statistical Correlations	230
Figure 75: Comparison between ε_G , $\varepsilon_{G-Large}$, d_S and $d_{S-Large}$ Experimental and Predicted values using BPNN Correlations	239
Figure 76: Comparison between $k_L a$ Experimental and Predicted values using BPNN Correlations	240
Figure 77: Algorithm for Calculating the Hydrodynamic and Mass Transfer Parameters in BCRs and SBCRs	241
Figure 78: Geometry of the BCRs used	244
Figure 79: Arrangement of n-GSRs in Series	248
Figure 80: Prediction of Literature Experimental Data using the Kinetic Model Developed	253
Figure 81: Typical Concentration and Temperature profiles in BCRs	258
Figure 82: Effect of Column Height and Height to Diameter ratio on the Performances of BCRs	259
Figure 83: Effect of Superficial Gas Velocity on the Performances of the BCR	260
Figure 84: Effect of U_G on the on the Performances of the 3-GSRs	263
Figure 85: Effect of Height to Diameter Ratio and Mixing Speed on the Performances of the 5-GSRs	264
Figure 86: Comparison between the Performances of BCRs and GSRs	265
Figure B-1: Gas Chromatography of Run OTS5321	298
Figure B-2: Gas Chromatography and Mass Spectroscopy of Run OTS5329	299
Figure D-1: Typical Experimental P(t)-t Curve For the Transient Gas-Absorption	312
Figure D-2: Plot of F(t) vs. t	313
Figure D-3: Comparison Between Experimental and Back-Calculated P(t) vs. t Curve	314
Figure E-1: Schematic of a Simple Artificial Neural Network	319
Figure E-2: Basic Architecture of the Neural Networks Employed	322
Figure E-3: Training Algorithm of Back-Propagation Neural Networks	323

NOTATION

A	numerical constants,-
a	Gas-liquid interfacial area per unit liquid volume, m^{-1}
a_B	Gas-liquid interfacial area of the gas bubbles per unit liquid volume, m^{-1}
$a_{Entrained}$	Gas-liquid interfacial area of the entrained bubbles per unit liquid volume, m^{-1}
$a_{Induced}$	Gas-liquid interfacial area of the induced bubbles per unit liquid volume, m^{-1}
a_{pipes}	Cooling tube specific external area referred to the total reactor volume, m^{-1}
$a_{Sparged}$	Gas-liquid interfacial area of the sparged bubbles per unit liquid volume, m^{-1}
a_{wall}	Wall specific area referred to the total reactor volume, m^{-1}
B	numerical constants,-
C	numerical constants,-
C^*	Equilibrium gas solubility in the liquid, kmol.m^{-3}
$C_{i,G, Large}$	Concentration of component i in the large bubbles, mol.m^{-3}
$C_{i,G, Small}$	Concentration of component i in the small bubbles, mol.m^{-3}
$C_{i,L}$	Concentration of component i in the liquid phase, mol.m^{-3}
C_G	Gas concentration, mol/m^3
$C_{P,L}$	Heat capacity of the liquid phase, J/kg/K
D_{AB}	Diffusivity of the gases in toluene, $\text{m}^2.\text{s}^{-1}$
d_B	Bubble diameter, m or mm (when specified)
D_C	Diameter of the column, m
$D_{C,in}$	Inside column diameter, m
$D_{C,out}$	Outside column diameter, m
D_G	Gas dispersion coefficient, m^2s^{-1}
$D_{G,W}$	Gas dispersion coefficient of water in the vapor phase, m^2s^{-1}
D_{Isol}	Diameter of the isolation, m

$d_{imp.}$	Diameter of the impeller, m
D_L	Liquid dispersion coefficient, m^2s^{-1}
$D_{L,w}$	Liquid water dispersion coefficient, m^2s^{-1}
d_o	Orifice diameter, m
$D_{pipes,out}$	Outside diameter of the cooling pipes, m
$D_{pipes,in}$	Inside diameter of the cooling pipes, m
d_R	Reactor diameter, m
d_S	Sauter mean bubble diameter, m or mm (when specified)
d_T	Diameter of the tank, m
d_W	Width of the impeller blade, m
E_i	Value of the i^{th} variable in Equation (E-10), Unit of the variable
ΔE_i	Energy of activation, J/mol
E_T	Total power input from agitation, and bubble rise, W
f	Fugacity, bar
f	Fanning factor, -
G	Numerical parameter in the Grunberg and Nissan equation , -
g	Acceleration due to gravity, $m\ s^{-2}$
H	Liquid height above the bottom of the reactor, m
H	Column Height, m
H_C	Height of liquid circulation eddies , m
H_D	Dispersion height, m
He	Henry's constant, $kJ.kmol^{-1}$
He'	Modified Henry's constant, atm/mole fraction
H_L	Liquid height above the impeller of the reactor, m
h_L	Heat transfer coefficient of the Liquid, $W.m^{-2}.K^{-1}$
H_o	Pre-exponential constant in Equation (6-2), $kJ.kmol^{-1}$
He_i	Henry's Law constant of gas component i, $Pa.m^3.mol^{-1}$
He^*	Reduced Henry's Law constant, -
He_{MAX}	Henry's Law constant at turn around point of solubility data, $Pa.m^3.mol^{-1}$

$\Delta H_{R,i}$	Heat of reaction, J/mol
K	Pseudo kinetic constant, s ⁻¹
k_i	Rate constant of the oxidation reactions, -
$k_{i,Ref.}$	Constants in the rate of the oxidation reactions, -
k_L	Liquid-side mass transfer coefficient, m.s ⁻¹
$k_L a$	Volumetric liquid-side mass transfer coefficient, s ⁻¹
k_{L-B}	Liquid-side mass transfer coefficient of the induced gas bubbles, m.s ⁻¹
m_i	Constant in the reaction rate equations, -
M_w	Molecular weight of toluene, kg.kmol ⁻¹
$M^*_{Measured}$	Total Induced gas flow rate of N ₂ , kg.s ⁻¹
N	Mixing speed, rpm or Hz (when specified)
n	Numerical parameter, -
N_{CR}	Critical mixing speed, rpm or Hz (when specified)
N_0	Number of Orifices in the gas distributor, -
N_P	Power Number
n_{pipes}	Number of cooling tubes, -
P^*	Total power input, W
P_G^*	Gassed power input, W
P	Pressure, bar
P_C	Critical pressure, bar
$P_{I,F}$	Equilibrium partial pressure of gas, bar
P_F	Equilibrium pressure, bar
P_m	Mean partial pressure of gas, bar
P^S	Vapor Pressure, bar
P_T	Total Pressure, bar
P_W	Water Pressure, bar
Q_G	Gas volumetric flow rate, m ³ .s ⁻¹
Q_{GI}	Induced gas flow rate of N ₂ , m ³ .s ⁻¹ and cm ³ .s ⁻¹ in Equation (5-48)
R	Universal gas constant, kJ.kmol ⁻¹ .K ⁻¹

r_i	Reaction rate, mol/m ³ /s
T	Temperature, K
T'	Temperature, C
T^*	Reduced Temperature, -
T_C	Critical temperature, K
T_L	Liquid Temperature, K
T_{MAX}	Temperature at turn around point of solubility data, K
$T_{outside}$	Outside Temperature, K
$T_{Ref.}$	Constant in Equation (6-117), K
T_S	Saturation temperature of water, K
T_W	Water Temperature, K
$u_{0,i}$	Bias of the i th hidden node
$u_{i,j}$	Weight of the connection between the i th input and the j th hidden node
U_G	Superficial gas velocity, m.s ⁻¹
$U_{G,Large}$	Superficial gas velocity of large bubbles, m.s ⁻¹
$U_{G,Small}$	Superficial gas velocity of small bubbles, m.s ⁻¹
U_L	Superficial liquid velocity, m.s ⁻¹
U_{pipes}	Heat transfer conductance for the cooling pipes, J/m ² /s/K
U_S	Superficial gas velocity, m.s ⁻¹
U_t	Bubble rising velocity m.s ⁻¹
U_T	Terminal gas velocity, m.s ⁻¹
U_W	Superficial Water velocity, m.s ⁻¹
U_{wall}	Heat transfer conductance for the wall, J/m ² /s/K
V	Volume, m ³
v	Phase molar volume, m ³ .kmol ⁻¹
V_B	Gas bubble volume in the liquid, m ³
V_C	Critical molar volume, m ³ .kmol ⁻¹
$v_{C,Loc}$	Local liquid velocity, m/s
V_L	Liquid phase volume, m ³

v_L	Molar volume, mol/m ³
$V_L(0)$	Center-line liquid velocity, m/s
V_R	Reactor volume, m ³
V_T	Total liquid volume, m ³
W	Baffle width, m
w_0	Bias of the output node
w_i	Weight fraction , -
w_i	Weight of the connection between the i th hidden node and the output node
x_i	Mole fraction of component i, -
x_1	Coded variable for T(Stirred Tank), -; for P (Bubble column), -
x_2	Coded variable for N(Stirred Tank), -; for U _G (Bubble column), -
x_3	Coded variable for P, -
x_4	Coded variable for H, -
$x_{i,n}$	Normalized input values of the n th observation
z	Axial coordinates (reactor length), m
Z_{RA}	Numerical parameters defined in the Rackett Equation,
y	Steam mole fraction, -
y_{pred}	Net input of the output node
Y_{pred}	Output signal of the output node
Z	Compressibility factor, -
$z_{pred\ i}$	Net input of the i th hidden node
$Z_{pred\ i}$	Output signal of the i th hidden node
% V/V	Toluene % in volume, Vol. %

Greek Letters

α	Intensity, - (Q_I/Q_I)
δ	Film thickness, m
δ	Solubility parameter, MPa ^{1/2}
ΔE	Apparent activation energy of absorption, kJ.kmol ⁻¹

ε	Agitation power per unit mass, W.kg^{-1}
ε_G	Gas holdup, %
ε_S	Volumetric fraction of the pipes with respect to reactor volume, -
γ_a	Average shear rate, s^{-1}
η	Intensity (Q_I/Q_{TOTAL})
Φ_K	Reactant concentration function
Φ	Volume fraction of the liquid, -
Ψ	Energy dissipation function, -
ψ	Associate factor in Equation (4-28), -
λ	Wavelength, m
$\lambda_{\text{isol.}}$	Heat conductivity of the isolation, W/m/K
λ_{pipes}	Heat conductivity of the cooling pipes, W/m/K
λ_R	Heat conductivity of reactor wall, W/m/K
μ	Viscosity, $\text{kg.m}^{-1}.\text{s}^{-1}$ or Pa.s
μ_{eff}	Effective viscosity, $\text{kg.m}^{-1}.\text{s}^{-1}$ or Pa.s
μ_w^0	Water viscosity at 298 K, $\text{kg.m}^{-1}.\text{s}^{-1}$ or Pa.s
$\bar{\mu}$	Geometric mean bubble diameter, mm
ν	Normal velocity, m.s^{-1}
ρ	Density, kg.m^{-3}
σ	Surface tension, N.m^{-1}
σ	Standard deviation,
τ	Shear stress, $\text{N.m}^{-1}.\text{s}^{-2}$
ω	Wave frequency of the gravity waves, s^{-1}
ω	Accentric factor, -
ξ	Parameter for the effect of waves sweeping high concentration layer, -
ξ	Parameter describing the energy distribution, -
ζ	Open area of the gas distributor, - $\zeta = N_o \left(\frac{d_o}{D_c} \right)^2$
ζ	Vertical displacement of the surface, m

Subscripts

<i>C</i>	Critical condition
<i>CR</i>	Critical
<i>E</i>	Entrainment
<i>F</i>	Final condition
<i>G</i>	Gas phase
<i>i</i>	Component i
<i>IE</i>	Intensification of the entrainment phenomena
<i>In</i>	Inlet
<i>L</i>	Liquid phase
<i>Large</i>	Large gas bubbles
<i>Mix</i>	Mixture
<i>Out</i>	Outlet
<i>Ri</i>	i th reactor in the series of CSTRs
<i>T</i>	Total
<i>Small</i>	Small gas bubbles
<i>W</i>	Water
<i>*</i>	Reduced
<i>1</i>	Component 1: Gas
<i>2</i>	Component 2: Liquid

Acronyms

AARE	Average absolute relative error , -
ANN	Artificial neural network
AR	Agitated reactors
BCR	Bubble column reactor
BZC	Benzoic acid
BZL	Benzaldehyde
GIR	Gas-inducing reactor
GSR	Gas sparging reactor

LFL	Lower flammability limit, Vol. %
MAX	Maximum
MOC	Minimum oxygen concentration, Vol. %
RT	Ripple tank
SAR	Surface Aeration Reactor
SBCR	Slurry bubble column reactor
Tol.	Toluene
UFL	Upper flammability limit, Vol. %
WT	Wetted Column

Dimensionless Numbers

Aeration Number:
$$Ae = \frac{Q_{Gl}}{N \times d_{imp.}^3}$$

Scale Number:
$$Bs = d_{imp.} \times \left(\frac{\rho_L g}{\sigma_L} \right)^{1/2}$$

Bond Number:
$$Bo = \frac{\rho_L g D_C^2}{\sigma_L}$$

Critical Froude Number:
$$Fr_C = \frac{d_{imp.}^2 \times N_{CR}^2}{g \times H_L}$$

Euler Number:
$$Eu = \frac{P_m}{d_{imp.}^2 \times \rho_L \times N^2}$$

Froude Number:
$$Fr = \frac{d_{imp.}^2 \times N^2}{g \times H_L}$$

Modified Froude Number:
$$Fr^* = \frac{d_{imp.} \times N^2}{g}$$

Froude Number (Bubble column):
$$Fr = \frac{U_G}{(g D_C)^{0.5}}$$

Galileo Number:
$$Ga = \frac{\rho_L^2 g D_C^3}{\mu_L^2}$$

Morton Number:
$$Mo = \frac{\mu_L^4 g}{\rho_L \sigma_L^3}$$

Modified Aeration Number:
$$Na = \frac{d_{imp.} N}{U_s}$$

Re-circulation Number:
$$N_{cir} = d_{imp.} N \times \left(\frac{\rho_L}{g \sigma_L (\rho_L - \rho_G)} \right)^{1/4}$$

Power Number
$$N_p = \frac{P^*}{\rho_L N^3 d_{imp.}^5}$$

Peclet Number of the Gas
$$Pe_G = \frac{u_G H}{\varepsilon_G D_G}$$

Peclet Number of the Liquid
$$Pe_L = \frac{u_L H}{D_L}$$

Reynolds Number (Bubble column):
$$Re = \frac{\rho_L d_s U_G}{\mu_L}$$

Reynolds Number (Stirred tank):
$$Re = \frac{d_{imp.}^2 \times \rho_L \times N}{\mu_L}$$

Viscosity Number:
$$Rp = \left(\frac{\sigma_L^3 \rho_L}{g \mu_L^4} \right)^{1/4}$$

Schmidt Number:
$$Sc = \frac{\mu_L}{\rho_L \times D_A}$$

Sherwood Number (Stirred tank):
$$Sh = \frac{k_L a \times d_{imp.}^2}{D_A}$$

Sherwood Number (Bubble column):
$$Sh = \frac{k_L a \times D_C^2}{D_A}$$

Weber Number (Stirred tank):
$$We = \frac{d_{imp.}^3 \times \rho_L \times N^2}{\sigma_L}$$

Weber Number (Bubble column):
$$We = \frac{\rho_L U_G^2 d_s}{\sigma_L}$$

ACKNOWLEDGMENT

I would like to express my sincere gratitude to my advisor and mentor Professor Badie I. Morsi for his valuable guidance and support throughout this study. I am grateful to Professor Shiao-Hung Chiang, Professor Robert Enick, Professor Rachid Oukaci and Professor Patrick Smolinski for serving at my committee.

I would like to acknowledge the financial support of the Chemical and Petroleum Engineering Department. I extend my thanks to Micro Motion Inc. and Mr. Tom Kuny for providing the Coriolis mass flow meter. The technical support of the Chemical and Petroleum Engineering faculty, Mr. Ron Bartlett, Mr. Bob Maniet and the School of Engineering Machine Shop is greatly appreciated.

I am thankful to the member of my research group: Dr. Arsam Behkish, Dr. Benoit Fillion, Mr. Yannick Heintz, Mr. Abdul Karim Alghamdi, Mr. Laurent Sehabiague, Mr. Jean-Philippe Soriano, for their valuable contribution, help, and constructive criticism during this research project.

I am eternally indebted to my parents, brother, family, and friends for their support and encouragement throughout this endeavor.

I dedicate this thesis to my parents.

1.0 INTRODUCTION AND BACKGROUND

Toluene, also known as methylbenzene, is mainly produced by catalytic reforming of naphtha and by gasoline pyrolysis during ethylene and propylene production ⁽¹⁾. As shown in Table 1, 90% of the 1940 millions of gallons of toluene produced per year by the US are recovered from catalytic reforming, while the remaining of the toluene production is either obtained by gasoline pyrolysis (7%) or as a by-product of the styrene process from ethylbenzene (3%). The US demand for toluene is growing at an annual rate of 2.5% as of today, however, the toluene demand is decreasing due to its environmental and health issues, which explain why no new toluene plants are being built and why the toluene current prices on the market is relatively stable at about \$1.00 per gallon ⁽²⁾. While the major uses for toluene are for substitution to benzene, either as an additive to motor oil for better octane rate, or as a solvent, or as a chemical intermediate, toluene is the raw material for wide applications, including resins, polymers, explosive, fine chemicals and saccharin ⁽³⁾.

The toluene oxidation process is primarily used to produce benzoic acid, benzaldehyde, benzoate salts and benzyl alcohols, which are widely employed in diverse industrial applications as can be seen in Figure 1. For instance, benzoic acid is used as a prime raw material to produce phenol ^(1,4,5,6,7,8), caprolactam ⁽⁴⁾, glycol dibenzoates ^(4, 9) and, benzoates salts ^(8,9,10), which are utilized in the food industry because of their flavoring characteristic ^(8, 10), and in the pharmaceutical industry to produce various aldehydes ^(1, 8, 10). In 1994, caprolactam, benzoic acid and benzaldehyde were among the most produced chemicals in the United States ⁽¹¹⁾. Moreover, in 1997, the worldwide leader in benzoic acid (over 30%), DSM had its annual sales of fine chemicals reaching \$700 millions, where the toluene phenol production process (TOLOX) represented a substantial part ⁽³⁾. Currently, however, the manufacturers of benzoic acid through the liquid-phase toluene oxidation are starting to shift the production to the high value by-products, benzyl alcohols and benzaldehydes due to the following reasons: (1) the environmental problems are making phenol production through benzoic acid uneconomical ⁽⁵⁵⁾; (2) the overproduction of benzoic acid and the inability of finding attractive markets are steadily decreasing the price of benzoic acid ^(12,55); and (3) the relatively high operating costs and environmental problems are affecting the production of benzyl alcohols and benzaldehydes via the toluene chlorination/hydrolysis process ⁽¹³⁾. For these reasons, the toluene oxidation process is of great challenges through its unique multi-functionality.

The toluene oxidation process can be carried out either in the liquid-phase ^(7,8,10) or in the gas-phase ^(1,6,7). Liquid-phase oxidation, however, appeared to be more advantageous than the gas-phase due to the following reasons:

1. The reaction takes place more easily in the liquid-phase (393-453 K) than in the gas-phase (673-800 K) ^(8,10) due to better temperature control and energy savings.
2. The selectivity of valuable products in the liquid-phase is higher than in the gas-phase, as can be seen from Table 2 due to the formation of more by-products in the latter process ^(7,10).

Table 1: Toluene Producers and Plant Capacities in US in 2000 ⁽²⁾

Company	Site	Capacity 10 ⁶ Gal./y.
BP Chemicals	Alliance, Louisiana; Lima, Ohio; Texas City, Texas.	365
Chevron	Port Arthur, Texas.	50
Citgo	Corpus Christi, Texas; Lake Charles, Louisiana; Lemont, Illinois.	105
Coastal	Corpus Christi, Texas; Westville, New Jersey.	65
Dow	Plaquemine, Louisiana.	40
Equilon,	El Dorado, Kansas.	10
Equistar Chemicals	Alvin, Texas; Channelview, Texas.	85
Exxon Mobil	Baton Rouge, Louisiana; Chalmette, Louisiana; Baytown, Texas, Beaumont, Texas.	330
Fina Oil and Chemical	Port Arthur, Texas.	100
Hovensa	St. Croix, Virgin Islands.	120
Koch Industries	Corpus Christi, Texas.	150
Lyondell-Citgo	Houston, Texas.	35
Marathon Ashland Petroleum	Catlettsburg, Kentucky; Texas City, Texas.	60
Phillips Petroleum	Sweeny, Texas; Guayama, Puerto Rico.	120
Shell Chemical	Deer Park, Texas.	45
Sunoco	Marcus Hook, Pennsylvania; Philadelphia, Pennsylvania; Toledo, Ohio	145
Ultramar Diamond Shamrock	Three Rivers, Texas.	45
Valero Energy	Houston, Texas.	15

Table 2: Comparison between Gas and liquid-Phase Selectivity

Reaction Phase	Conversion of Toluene, %	Yield to Benzoic Acid, %	Yield to Benzaldehyde, %
Gas	Low ⁽¹⁾ ≤ 15 ⁽¹⁰⁾	50-60 ⁽¹⁾	85 ⁽¹⁾
Liquid	10-15 ⁽⁵⁵⁾ -30-40 ⁽¹⁾	10-40 ⁽⁵⁵⁾ , 90 ⁽¹⁾	40-70 ⁽¹⁰⁾ , 10-30 ⁽⁵⁵⁾

Table 3: Comparison between Gas and liquid-Phase Operating Conditions

Reaction Phase	Temperature range, K	Pressure range, bar	Catalyst wt % of toluene, %
Gas	670-800 ⁽¹⁾	300 ⁽¹⁾	-
Liquid	350-440 ⁽¹⁾	1-20 ⁽¹⁾	0.02-5.0 ⁽¹⁾

The industrial liquid-phase toluene oxidation is a continuous process in which a mixture of toluene, homogeneous cobalt-based catalyst and air (or oxygen) is fed to a vessel under pressures of 0.1-2.0 MPa and temperatures of 350-440 K ^(10,13,14,55) as shown in Table 3. Typically, this process is carried out either in modified cascade of agitated reactors ^(15,16,17,18,19) or in a bubble column reactor ^(13,14,20) (BCR). The two desirable products of the oxidation are benzoic acid and benzaldehyde; however, since these are highly reactive intermediates in the free radical chain reaction, numerous undesirable by-products are also formed ^(7,8,10,21). Thus, controlling the oxygen/toluene ratio in the feed to the reactor will affect the kinetics, hydrodynamics, and heat as well as mass transfer, which in turn will impact the selectivity, yield of the desirable products, i.e., the performance of the oxidation process ^(8,9).

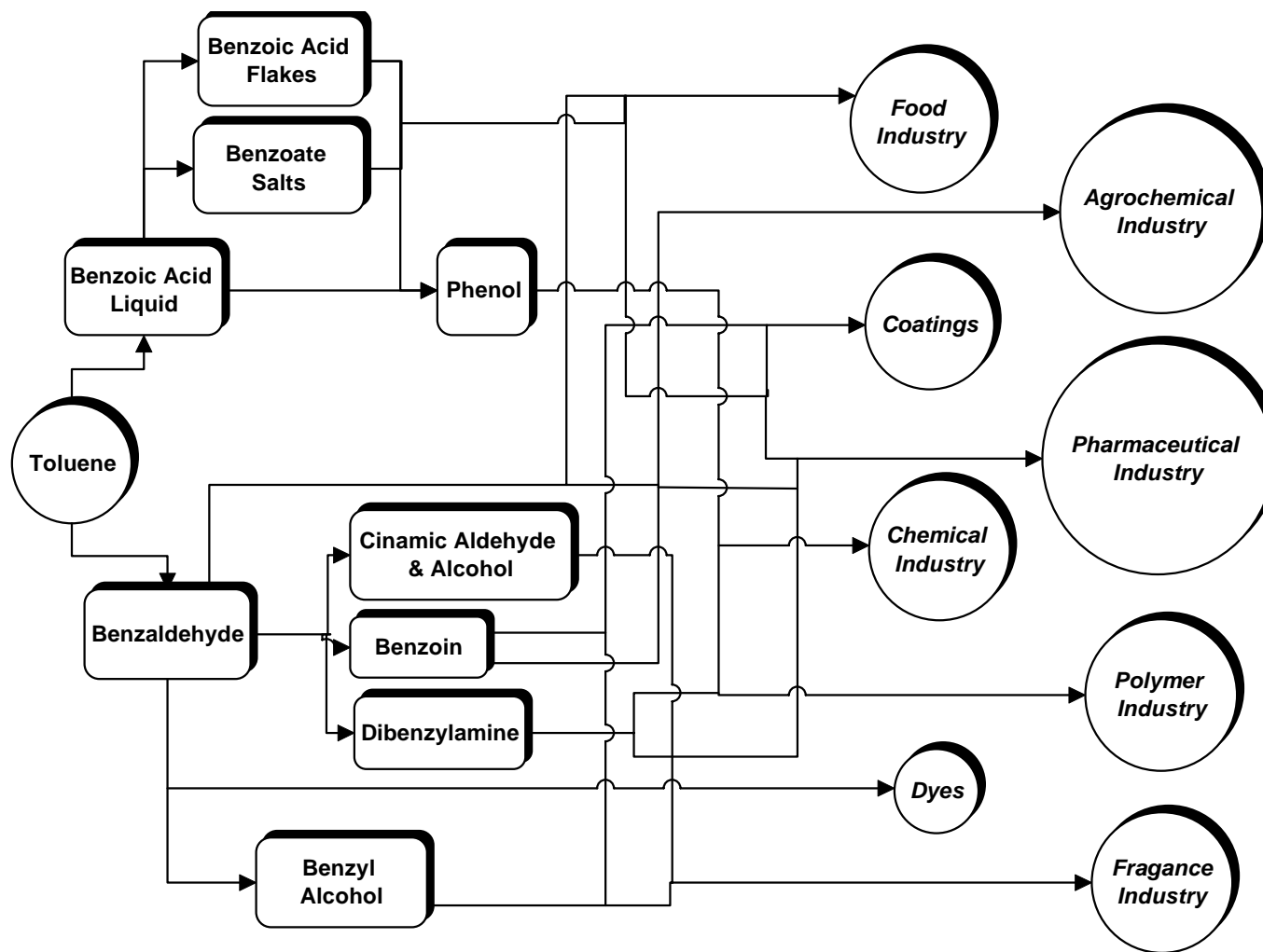


Figure 1: Toluene Oxidation Products Tree ⁽³⁾

1.1 INDUSTRIAL LIQUID-PHASE OXIDATION PROCESSES

Several liquid-phase processes have been developed and modified since its first commercial introduction in the 1950s. Different routes can be employed during liquid-phase toluene oxidation process, in order to obtain a good selectivity of the desirable products. The oldest process, i.e. Dow process, uses metal catalyst ⁽¹⁾, which is either cobalt acetate in aqueous solution or cobalt heptanoate. No promoter is added and the operation is performed continuously, by recycling the major by-products, toluene, and chain initiators, assuring an optimum reaction rate without any induction period. The oxidation reactors operate at temperatures between 410-420 K and pressures between 6-8 bars. The air is usually fed through a sparger and the reactor's oxidizing medium is circulating through an external heat exchanger as shown in Figure 2. The reactor effluent produces benzoic acid with an average conversion of 35 %. This effluent is then stripped of toluene and other light compounds or simply distilled fractionally.

In another process, promoters are added such as:

- Sodium Bromide
- AIBN (2-2'-azo-bis-isobutyronitrile)
- Aldehydes

This promoted oxidation process is essentially used to increase the yield towards benzaldehyde ^(1, 21). The promoters are used to protect benzaldehyde from further oxidation. However, the separation stage caused by the addition of the promoter appears obviously as a disadvantage in this process. The high peroxide oxidation process is also used in order to increase considerably the chain propagation ^(1, 4, 38). Benzyl-hydro-peroxides, which are the first intermediates produced, can enhance the reaction towards benzyl alcohol or acetate at lower temperature with catalyst such as Co, Cr or Fe.

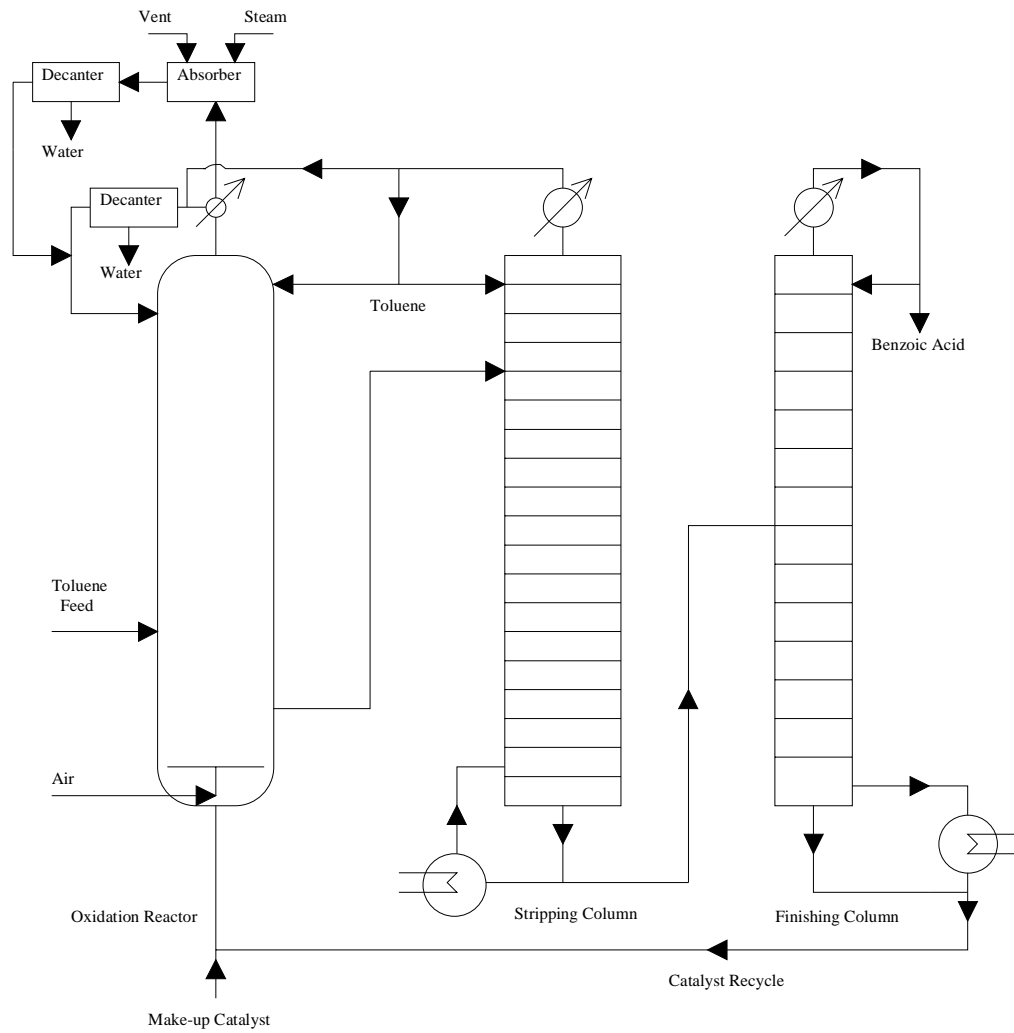


Figure 2: The Dow Toluene Oxidation Process ⁽¹⁾

1.2 GAS-LIQUID TRANSPORT IN THE LIQUID PHASE TOLUENE OXIDATION

From the gas absorption viewpoint, toluene oxidation in the liquid-phase is a typical example for an industrial process employing gas absorption with a chemical reaction, despite the lack of literature cited for this process. Hence, the mass and heat transfer parameters, hydrodynamics, and reaction kinetics can affect the course of the reaction, since the process involves the following steps^(22,23):

Step 1: Transport of oxygen from the gas phase bulk to the gas-liquid interface.

Step 2: Transport of oxygen from the interface to the bulk liquid (toluene) through the liquid film.

Step 3: Chemical reaction between the dissolved oxygen and liquid toluene.

For steps 1 and 2 according to the two-film theory, a steady state mass transfer across a stagnant gas-liquid interface can be described for the gas-side and the liquid-side, as shown schematically in Figure 3, by the following equations:

$$R_s = k_G a (P - P^*) = k_G a H e \left(\frac{P}{H e} - \frac{P^*}{H e} \right) = k_G a H e (C_G - C^*) \quad (1-1)$$

$$R_s = k_L a (C^* - C_L) \quad (1-2)$$

$$R_s = k_{Kinetics} C_L^{m_1} C_{TOL}^{m_2} C_{Catalyst}^{m_3} = K \Phi_K C_L \quad (1-3)$$

with K the pseudo kinetic constant and Φ_K is function of the oxygen concentration.

The overall rate of mass transfer in terms of the bulk gas and liquid concentrations of oxygen or nitrogen can thus be expressed as:

$$R_s = \frac{C_G}{\frac{1}{k_G a H e} + \frac{1}{k_L a} + \frac{1}{K \Phi_K}} \quad (1-4)$$

Generally, the partial pressure of toluene in the gas phase is so small that the gas phase resistance can be neglected. This assumption suggests that Equation (1-4) can be reduced to Equation (1-2) and accordingly, the knowledge of the solubility (C^*) and the volumetric liquid-side mass transfer coefficient ($k_L a$) is essential in order to determine the rate of mass transfer in the oxidation process. Besides, if both mass transfer and kinetic parameters control the process, the knowledge of the mass transfer coefficient (k_L) and the gas-liquid interfacial area (a) in addition to the kinetic model and its constants are needed in order to elucidate their effects on the products composition and yield.

For step 3, there are several kinetic models in the literature, as described in Table 5, in order to describe the catalyzed toluene auto-oxidation process. Despite the different number of steps suggested by the reaction mechanism reported in the literature^(5-10,22,38-50), all models indicate the nature of free radical autocatalytic chain reaction in such a process, and the existence of an induction period, representing the time required to form a benzyl radical. This, also called lag time, is often reduced by the addition of a promoter⁽¹⁾. Thus, depending on how fast or

slow the chemical reaction involved is, the overall rate of the process may be controlled by liquid-side mass transfer, kinetics or both.

The mass and heat transfer, hydrodynamics, and reaction kinetics can affect the course of the reaction, and subsequently the selection and design of the reactor for any oxidation processes is essential. Stirred tanks, such as gas sparging reactors (GSR), are commonly used in chemical and petroleum industries, and often preferred over bubble column reactors (BCRs). This is generally attributed to the better knowledge of the design constraints such as mass transfer and hydrodynamic parameters in the case of stirred tanks. Nevertheless, depending on the gas-liquid process, BCRs could be a viable alternative to stirred tank reactors for both economic and operating reasons. The design and scale-up of both gas-liquid contactors require, among others, precise knowledge of the kinetics, hydrodynamics, and heat as well as mass transfer characteristics.

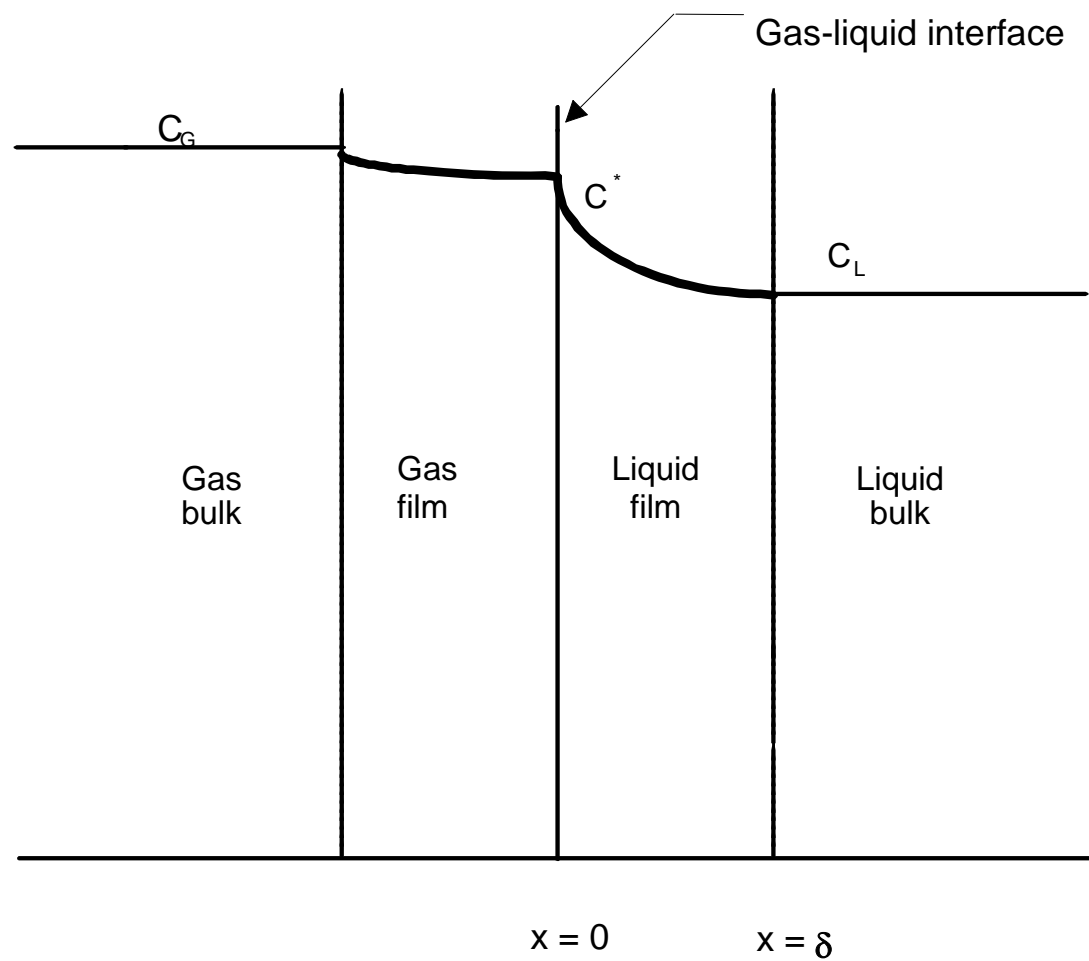


Figure 3: Gas Concentration Profile in the Toluene Oxidation Process

2.0 LITERATURE REVIEW

The knowledge of thermodynamic, mass transfer, heat transfer and hydrodynamic characteristics, as well as the reaction kinetics involved is of crucial importance in the design and modeling of gas-liquid processes^(8, 24). In fact, the selectivity and productivity of the process are affected by the reactor type, configuration and operating mode through these parameters. Hence, the main thermodynamic, mass transfer and hydrodynamic as well as kinetic characteristics of the liquid-phase toluene oxidation process are discussed below.

2.1 GAS SOLUBILITY IN LIQUIDS, C^*

The gas equilibrium solubility C^* in liquids is required as shown in Equations (1-2) and (1-4) to design and determine the process rates in gas-liquid reactors. The equilibrium solubility C^* of N_2 and O_2 in toluene is scarcely reported in the literature, as shown in Table 4. Also, available studies were usually limited by the operating conditions at which they were carried out, since several of them were conducted under atmospheric pressure and ambient temperature. This raises serious concerns for the industrial uses of such experimental data and correlations.

Table 4: Literature Survey on Solubility of N₂ and O₂ in Toluene

References	P, bar	T, K	Remarks
Merck Handbook ⁽²⁵⁾	1	290-300	Solubility data
Lachowicz et al. ⁽²⁶⁾	1	298	Molar fractions of N ₂ are measured in liquid phase.
Prausnitz et al. ⁽²⁷⁾	20-50	323, 348	Molar fractions of N ₂ , H ₂ and CO ₂ are measured in gas phase.
Stephen et al. ⁽²⁸⁾	1	293	Solubility of O ₂ is reported.
Wilhem and Battino ⁽²⁹⁾	1	298	Molar fractions of N ₂ and O ₂ are measured in liquid phase.
Field et al. ⁽³⁰⁾	1	280-315	Molar fractions, Ostwald and Bunsen coefficients, partial molar Gibbs energy of solution of N ₂ and O ₂ are measured.
Battino et al. ⁽³¹⁾	15-400	480-550	Molar fractions of toluene in N ₂ and O ₂ gas phase are obtained.
Battino et al. ⁽³²⁾	15-400	480-550	Molar fractions of N ₂ in toluene are reported.
Liave et al. ⁽³³⁾	35-355	320-350	Molar fractions of toluene in liquid phase are measured as function of temperature and pressure (N ₂).
Richon et al. ⁽³⁴⁾	100-1000	310-475	Molar fractions of N ₂ are measured in gas and liquid phase.
Schlichting et al. ⁽³⁵⁾	15-105	240-285	Molar fractions of toluene in N ₂ gas phase are obtained.
Lin et al. ⁽³⁶⁾	50-155	423-545	Molar fractions of N ₂ and He are measured in both phases, as well as equilibrium constants.
Ashcroft and Ben Isa ⁽³⁷⁾	1.013	298	Mole fraction of N ₂ and O ₂ are reported.

2.2 KINETICS OF TOLUENE OXIDATION

Currently, air oxidation of toluene is the main source of most of the world's synthetic benzaldehyde, benzyl alcohol, benzoic acid, benzoic salts and phenol as reviewed in Section 1.0. Both vapor- and liquid-phase air oxidation processes have been used. The vapor-phase oxidation was the dominant process in the 1950s and early 1960s, but due to its high cost, the liquid-phase process had emerged. The process was introduced and developed in the late 1950s by Dow Chemicals Company^(5,6) and DSM⁽⁵⁾.

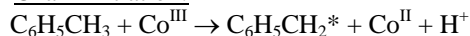
2.2.1 Toluene Oxidation Reactions

Despite several studies over the years on the kinetics of toluene oxidation, few data are available. Nevertheless, toluene oxidation is usually described as a free radical autocatalytic chain reaction mechanism involving three different steps:

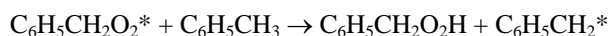
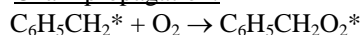
- Chain initiation
- Chain propagation
- Chain termination

According to Sheldon et al.⁽²¹⁾, the three steps involved take place as follow:

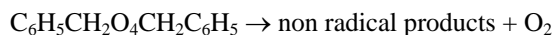
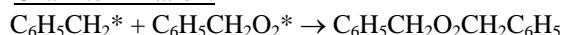
Chain initiation:



Chain propagation:

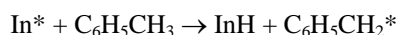
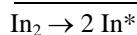


Chain termination:



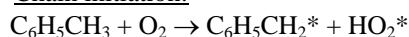
Sheldon et al.⁽²¹⁾ described also a mechanism based on promoter decomposition in the chain initiation as follow:

Chain initiation:

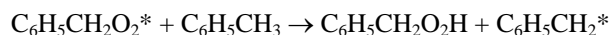
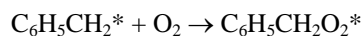


In addition, a mechanism of non-catalytic oxidation of toluene was proposed by Emmanuel et al.⁽³⁸⁾ and Sheldon et al.⁽²¹⁾:

Chain initiation:



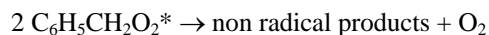
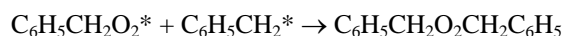
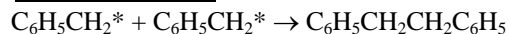
Chain propagation:



Degenerate Chain-Branching:



Chain termination:



During all these mechanisms, the oxidation process starts with a chain initiation, which generates free radicals. After the formation of the free radicals, the process propagates via hydro-peroxide formations. This chain propagation process is relatively rapid due to low activation energy of reaction ⁽²¹⁾ ($E=85\text{kcal/mol}$). Finally, the chain terminates as a result of reactions between free radicals.

Several authors' proposed diverse mechanisms for the liquid-phase toluene oxidation and the result of their studies are listed in Table 5. Sheldon et al. ⁽⁷⁾, Borgaonkar et al. ⁽¹⁰⁾, as well as Vasvari and Gal ⁽³⁹⁾ and Quiroga et al. ⁽⁴⁰⁾ noted the existence of an induction period also called lag time. This period is usually defined as the time required to produce the benzyl radicals. This finding is of great importance in order to perform the measurement of the reaction-free mass transfer parameters during the process. According to these authors, the induction period could range between 20 minutes to 6 hours, depending on the temperature, catalyst and promoter used.

Table 5: Literature Survey on the Kinetic Mechanisms of the Toluene Oxidation

Reference	Scheme	Remarks
Dewar ⁽⁴¹⁾	$\text{Pb}(\text{OAc})_4 \rightarrow \text{Pb}(\text{OAc})_2 + 2 \text{OAc}^*$	Free chain auto-catalytic
Cavill et al. ⁽⁴²⁾	$\text{OAc}^* + \text{Ph-CH}_3 \rightarrow \text{AcOH} + \text{Ph-CH}_2^*$ $\text{OAc}^* \rightarrow \text{CH}_3^* + \text{CO}_2$ $\text{CH}_3^* + \text{Ph-CH}_3 \rightarrow \text{Ph-CH}_2^* + \text{CH}_4$ $\text{Ph-CH}_2^* + \text{Pb}(\text{OAc})_4 \rightarrow \text{Ph-CH}_2 \text{OAc} + \text{OAc}^* + \text{Pb}(\text{OAc})_2$ $\text{Ph-CH}_2^* + \text{OAc}^* \rightarrow \text{Ph-CH}_2 \text{OAc}$	Mechanism with lead tetra-acetate. (1 st mechanism proposed for this process)
Bacon et al ⁽⁴³⁾	$\text{Mn}^{\text{IV}}, \text{Mn}^{\text{III}}, \text{Ce}^{\text{IV}}$ $\text{Ph-CH}_3 \rightarrow \text{Ph-CHO} + \text{H}_2\text{O}$ $\text{S}_2\text{O}_8^{2-} \text{---Ag}^+$	Direct free chain catalytic oxidation pathway (mechanism not described)
Kaeding ⁽⁵⁾ , Kaeding et al. ⁽⁶⁾	<p style="text-align: center;">Cu salt</p> $\text{Ph-CH}_3 + 3/2 \text{O}_2 \rightarrow \text{Ph-CO}_2\text{H} + \text{H}_2\text{O}$ $\text{Ph-CO}_2\text{H} + \text{O}_2 \rightarrow \text{by-products: dimmers, phenol}$	Overall chemical reaction, addition of benzoic acid enhances phenol production
Howard et al. ⁽⁴⁴⁾	$\text{Ph-CH}_2\text{O}_2^* + \text{Ph-CH}_3 \rightarrow \text{Ph-CO}_2\text{H} + \text{Ph-CH}_2^*$ $\text{Ph-CH}_2\text{O}_2^* + \text{Ph-CH}_2\text{O}_2^* \rightarrow \text{inactive products}$	Rate of termination and propagation at 303 K
Morimoto et al. ⁽⁹⁾	$\text{Ph-CH}_3 + \text{Co}^{3+} \rightarrow \text{Ph-CH}_2^* + \text{Co}^{2+} + \text{H}^+$ $\text{Ph-CH}_2^* + \text{O}_2 \rightarrow \text{Ph-CH}_2\text{O}_2^*$ $\text{Ph-CH}_2\text{O}_2^* + \text{Co}^{2+} \rightarrow \text{Ph-CHO} + \text{Co}^{3+} + \text{OH}^-$ $\text{Ph-CHO} + \text{Co}^{3+} \rightarrow \text{Ph-CO}^* + \text{Co}^{2+} + \text{H}^+$ $\text{Ph-CO}^* + \text{O}_2 \rightarrow \text{Ph-CO}_3^*$ $\text{Ph-CO}_3^* + \text{Ph-CH}_3 \rightarrow \text{Ph-CH}_2^* + \text{Ph-CO}_3\text{H}$ $\text{Ph-CO}_3^* + \text{Ph-CHO} \rightarrow \text{Ph-CO}_3\text{H} + \text{Ph-CO}^*$ $\text{Ph-CO}_3\text{H} + \text{Co}^{2+} \rightarrow \text{Ph-CO}_2^* + \text{OH}^- + \text{Co}^{3+}$ $\text{Ph-CO}_2^* + \text{Ph-CH}_3 \rightarrow \text{Ph-CH}_2^* + \text{Ph-CO}_2\text{H}$ $\text{Ph-CO}_2^* + \text{Ph-CHO} \rightarrow \text{Ph-CO}^* + \text{Ph-CO}_2\text{H}$	Rate constants and induction times are given at 360 K for the autocatalytic oxidation of toluene in soluble cobaltic salt. The effect of promoter was also studied in the same conditions: benzaldehyde

Table 5 (Cont'd)

Reference	Scheme	Remarks
Gadelle et al. ⁽⁴⁵⁾	$\text{Promoter} \rightarrow \text{r}^*$ $\text{r}^* + \text{O}_2 \rightarrow \text{rO}_2^*$ $\text{rO}_2^* + \text{Ph-CH}_3 \rightarrow \text{rO}_2\text{H} + \text{Ph-CH}_2^*$ $\text{Ph-CH}_2^* + \text{O}_2 \rightarrow \text{Ph-CH}_2\text{O}_2^*$ $\text{Ph-CH}_2\text{O}_2^* + \text{Ph-CH}_3 \rightarrow \text{Ph-CH}_2\text{O}_2\text{H} + \text{Ph-CH}_2^*$ $\text{Ph-CH}_2\text{O}_2^* + \text{Ph-CH}_2\text{O}_2^* \rightarrow$ $\text{Ph-CH}_2\text{O}_2^* + \text{rO}_2^* \rightarrow \text{inactive products} + \text{O}_2$ $\text{rO}_2^* + \text{rO}_2^* \rightarrow$	Rate constants for initiation propagation and termination are provided as well as the activation energies for the auto-oxidation of toluene
Sakota et al. ⁽⁴⁶⁾	$\text{Ph-CH}_3 + \text{Co}^{(\text{III})}\text{Br} \xrightarrow{k_1'} \text{Ph-CH}_2\text{OO}^* + \text{Co}^{(\text{II})}\text{BrH}$ $\text{Ph-CH}_2\text{OO}^* + \text{Co}^{(\text{II})}\text{BrH} \xrightarrow{k_3} \text{Ph-CHO} + \text{Co}^{(\text{III})}\text{Br} + \text{H}_2\text{O}$ $\text{Ph-CH}_2\text{OO}^* + \text{Ph-CH}_3 \xrightarrow{k_4} \text{Ph-CH}_2\text{OOH} + \text{Ph-CH}_2^*$ $\text{Ph-CH}_2\text{OO}^* + \text{Ph-CHO} \xrightarrow{k_5} \text{Ph-CH}_2\text{OOH} + \text{Ph-CO}^*$ $\text{Ph-CHO} + \text{Co}^{(\text{III})}\text{Br} \xrightarrow{k_6'} \text{Ph-CO}_3^* + \text{Co}^{(\text{II})}\text{BrH}$ $\text{Ph-CO}_3^* + \text{Co}^{(\text{II})}\text{BrH} \xrightarrow{k_8} \text{Ph-COOOH} + \text{Co}^{(\text{III})}\text{Br}$ $\text{Ph-CO}_3^* + \text{Ph-CH}_3 \xrightarrow{k_9} \text{Ph-COOOH} + \text{Ph-CH}_2^*$ $\text{Ph-CO}_3^* + \text{Ph-CHO} \xrightarrow{k_{10}} \text{Ph-COOOH} + \text{Ph-CO}^*$ $\text{Ph-CO}_3\text{H} + \text{Co}_2 \xrightarrow{k_{12}} \text{Radical} \rightarrow 2 \text{Co}^{(\text{III})}\text{Br}$ $\text{Ph-CO}_3\text{H} + \text{Ph-CHO} \xrightarrow{k_{13}} 2 \text{Ph-CO}_2\text{H}$ $2 \text{Ph-CH}_2\text{OO}^* \xrightarrow{k_{14}} \text{Ph-CHO} + \text{Ph-CH}_2\text{OH}$ $2 \text{Ph-CO}_3^* \xrightarrow{k_{15}} (\text{Ph-COO})_2 + \text{O}_2$ $\text{Ph-CO}_3^* + \text{Ph-CH}_2\text{OO}^* \xrightarrow{k_{16}} \text{Ph-CHO} + \text{Ph-CO}_2\text{H} + \text{O}_2$	Determination of the mechanism of the autoxidation of toluene catalyzed with cobalt monobromide. Apparent zero and first-order in toluene concentration for long duration and initial conditions respectively. Second-order in cobalt ion concentration.

Table 5 (Cont'd)

Reference	Scheme	Remarks
Scott et al. ⁽⁴⁷⁾	$\text{Ph-CH}_3 + \text{O}_2 \xrightarrow{\text{Co}^{\text{III}}} \text{Ph-CO}_2\text{H}$	Overall rate for the auto-catalytic oxidation of toluene by cobalt acetate
Bhattacharya et al. ⁽⁴⁸⁾	$\begin{aligned} &\text{HBr} + \text{O}_2 \rightarrow \text{Br}^* + \text{HO}_2^* \\ &\text{Ph-CH}_3 + \text{Br}^* \rightarrow \text{Ph-CH}_2^* + \text{HBr} \\ &\text{Ph-CH}_2^* + \text{O}_2 \rightarrow \text{Ph-CH}_2\text{O}_2^* \\ &\text{Ph-CH}_2\text{O}_2^* + \text{Ph-CH}_3 \rightarrow \text{Ph-CH}_2\text{O}_2\text{H} + \text{Ph-CH}_2^* \\ &\text{Ph-CH}_2\text{O}_2\text{H} + \text{Co}^{2+} \rightarrow \text{Ph-CH}_2\text{O}^* + \text{OH}^- + \text{Co}^{3+} \\ &2 \text{ Ph-CH}_2\text{O}^* \rightarrow \text{Ph-CHO} + \text{Ph-CH}_2\text{OH} \\ &\text{Co}^{3+} + \text{HBr} \rightarrow \text{Co}^{2+} + \text{H}^+ + \text{Br}^* \\ &2 \text{ Ph-CH}_2\text{O}_2^* \rightarrow \text{chain termination products} \end{aligned}$	Free radical chain reaction mechanism is proposed. An overall rate is given for the process at 415 K
Ivanov et al. ⁽⁴⁹⁾	$\begin{aligned} &\text{Co(Oac)}_2 + \text{Br}_2 \rightarrow \text{Co(Oac)}_2\text{Br}^- + \text{Br}^+ \\ &\text{Co(Oac)}_2\text{Br}^- + \text{Ph-CH}_3 \rightarrow \text{Co(Oac)}_2\text{HBr} + \text{Ph-CH}_2^* \\ &\text{Ph-CH}_2^* + \text{O}_2 \rightarrow \text{Ph-CH}_2\text{OO}^* \\ &\text{Ph-CH}_2\text{OO}^* + \text{Co(Oac)}_2\text{HBr} \rightarrow \text{Ph-CH}_2\text{OOH} + \text{Co(Oac)}_2\text{Br}^- \\ &\text{Ph-CH}_2\text{OOH} \rightarrow \text{Ph-CHO} + \text{H}_2\text{O} \\ &\text{Ph-CHO} + \text{O}_2 \rightarrow \text{Ph-CO}_2\text{H} + \frac{1}{2} \text{O}_2 \end{aligned}$	3 steps mechanism of free chain catalytic reaction in presence of bromine as promoter in methanol. Overall rate and kinetic constants are given between 403-423 K
Panneerselvam et al. ⁽²⁴⁰⁾	<p>Catalyst, Promoter</p> $\begin{aligned} &\text{Ph-CH}_3 + \frac{1}{2} \text{O}_2 \rightarrow \text{Ph-CHO} + \text{H}_2\text{O} \\ &\text{Ph-CHO} + \frac{1}{2} \text{O}_2 \rightarrow \text{Ph-CO}_2\text{H} \end{aligned}$	Provide 2 kinetics rates including mass transfer resistance.
Quiroga et al. ⁽⁴⁰⁾	$\begin{array}{c} \text{Ph-CH}_3 \rightarrow \text{Ph-CHO} \rightarrow \text{Ph-COOH} \\ \uparrow \\ \text{Ph-CH}_2\text{OH} \end{array}$	An auto-catalytic scheme for the toluene oxidation and a kinetic model
Borgaonkar et al. ⁽¹⁰⁾	$\begin{array}{ccccc} \text{Ph-CH}_3 & \rightarrow & \text{Ph-CHO} & \rightarrow & \text{Ph-COOH} \\ & & \downarrow & & \downarrow \\ & & \text{by-product formation} & & \end{array}$	The effect of T, P and promoter on product yields and induction period

Table 5 (Cont'd)

Reference	Scheme	Remarks
Emmanuel et al. (38)	$\text{Ph-CH}_3 + \text{O}_2 \rightarrow \text{Ph-CH}_2\text{O}_2\text{H}$ $\text{Ph-CH}_2\text{O}_2\text{H} + \text{Co}^{2+} \rightarrow \text{Ph-CH}_2\text{O}^* + \text{Co}^{3+} + \text{OH}^-$ $\text{Ph-CH}_2\text{O}_2\text{H} + \text{Co}^{3+} \rightarrow \text{Ph-CH}_2\text{O}_2^* + \text{Co}^{2+} + \text{H}^+$ $\text{Ph-CH}_2\text{O}_2^* + \text{Ph-CH}_3 \rightarrow \text{Ph-CH}_2\text{O}_2\text{H} + \text{Ph-CH}_2^*$ $\text{Ph-CH}_2^* + \text{O}_2 \rightarrow \text{Ph-CH}_2\text{O}_2^*$ $\text{Ph-CH}_2\text{O}_2\text{H} + \text{Co}^{2+} \rightarrow \text{Ph-CH}_2\text{O}^* + \text{Co}^{3+} + \text{OH}^-$ $\text{Ph-CH}_2\text{O}^* + \text{OH}^- \rightarrow \text{Ph-CHO} + \text{H}_2\text{O}$ $\text{Ph-CHO} + \text{Co}^{3+} \rightarrow \text{Ph-CO}^* + \text{Co}^{2+} + \text{H}^+$ $\text{Ph-CO}^* + \text{O}_2 \rightarrow \text{Ph-CO}_3^*$ $\text{Ph-CO}_3^* + \text{Ph-CHO} \rightarrow \text{Ph-CO}_3\text{H} + \text{Ph-CO}^*$ $\text{Ph-CO}_3\text{H} + \text{Ph-CHO} \rightarrow \text{Ph-CO}_2\text{H}$ $\text{Ph-CH}_2\text{O}^* + \text{Ph-CH}_3 \rightarrow \text{Ph-CH}_2\text{OH} + \text{Ph-CH}_2^*$	Mechanism of the hydro-peroxide route. The hydro-peroxide are believed to have a slow decomposition due the energy required to break O-O bond
Taqi Khan et al. (50)	$\text{Ph-CH}_3 \rightarrow \text{Ph-CHO}$ \downarrow $\text{Ph-CH}_2\text{OH}$	Rate and activation parameter of toluene oxidation. Catalyst: Ru^{III} -EDTA complex
Vasvari et al. (39)	AIBN $\text{O}_2 \rightarrow 2\text{rO}_2^* + \text{N}_2^*$ 2rO_2^* $\text{Ph-CH}_3 + \text{O}_2 \rightarrow \text{rOOH} + \text{Ph-CH}_2\text{O}^*_2$ $\text{Ph-CH}_2\text{O}^*_2 + \text{Ph-CH}_3 \rightarrow \text{Ph-CH}_2\text{OOH} + \text{Ph-CH}_2\text{O}^*_2$ $2 \text{Ph-CH}_2\text{O}^*_2 \rightarrow \text{Ph-CHO} + \text{Ph-CH}_2\text{OH} + \text{O}_2$ $2 \text{Ph-CH}_2\text{O}^*_2 \rightarrow 2 \text{Ph-CH}_2\text{O}^* + \text{O}_2$ $2 \text{Ph-CH}_2\text{O}^*_2 \rightarrow 2 \text{Ph-C}^*\text{HOOH}$ $2 \text{Ph-CH}_2\text{O}^*_2 \rightarrow 2 \text{Ph-CHO} + \text{H}_2\text{O}_2$ $\text{Ph-CH}_2\text{O}^* + \text{Ph-CH}_3 \rightarrow \text{Ph-CH}_2\text{OH} + \text{Ph-CH}_2\text{O}^*_2$ $\text{Ph-C}^*\text{HOOH} \rightarrow \text{Ph-CHO} + \text{OH}^*$ $\text{OH}^* + \text{Ph-CH}_3 \rightarrow \text{Ph-CH}_2\text{O}^*_2 + \text{H}_2\text{O}$ $2 \text{Ph-CHO} + \text{H}_2\text{O}_2 \rightarrow \text{Ph-CHO} + \text{Ph-COOH} + \text{H}_2\text{O}$ $\text{Ph-CH}_2\text{O}_2\text{H} + \text{Ph-COOH} \rightarrow \text{Ph-COOH} + \text{Ph-CHO} + \text{H}_2\text{O}$	Rate constants for the liquid phase toluene oxidation are given between 350-365 K. The free chain reaction was initiated by AIBN. This study stressed out the importance of radicals for the mechanism proposed.

Table 5 (Cont'd)

Reference	Scheme	Remarks
Gardner et al. ⁽⁵¹⁾	KMnO_4 in water $\text{Ph-CH}_3 + \text{MnO}_4^- \rightarrow \text{Ph-CH}_2\text{H}_2\text{O}^+ + \text{HOMnO}_3^{2-}$ $\text{nBu}_4\text{NMnO}_4$ in neat toluene $\text{Ph-CH}_3 + \text{MnO}_4^- \rightarrow \text{Ph-CH}_2^* + \text{HOMnO}_3^-$	Kinetic data for the toluene oxidation by permanganate. Initiation chain mechanism for two different solvents.
Lee et al. ⁽⁵²⁾	$\text{Ph-CH}_3 + \text{Ag}^{++} \rightarrow \text{Ph-CH}_2^* + \text{Ag}^+$ $\text{Ph-CH}_2^* + \text{Ag}^{++} \rightarrow \text{Ph-CH}_2^+ + \text{Ag}^+$ $\text{Ph-CH}_2^+ + \text{H}_2\text{O} \rightarrow \text{Ph-CH}_2\text{OH}_2^+$ $\text{Ph-CH}_2\text{OH}_2^+ + 2 \text{Ag}^{++} \rightarrow \text{Ph-CHOH}^+ + 2 \text{Ag}^+ + 2 \text{H}^+$ $\text{Ph-CHOH}^+ \rightarrow \text{Ph-CHO} + 2 \text{H}^+$	Mechanism and rate constant are provided for the anodic oxidation of toluene catalyzed by $\text{Ag}^{\text{I}}/\text{Ag}^{\text{II}}$
Fereydoon et al. ⁽⁵³⁾	$\text{Ph-CH}_3 + \text{O}_2 \rightarrow \text{Ph-CO}_2\text{H}$ Co(Oac)_2	Overall reaction rate function of the toluene, catalyst concentrations and P_{O_2} . Diffusion control the reaction
Bejan et al. ⁽²⁴¹⁾	$\text{Ph-CH}_3 + \text{Co}^{3+} \rightarrow [\text{Ph-CH}_3]^{+*} + \text{Co}^{2+}$ $[\text{Ph-CH}_3]^{+*} \rightarrow \text{Ph-CH}_2^* + \text{H}^+$ $\text{Ph-CH}_2^* + \text{O}_2 \rightarrow \text{Ph-CH}_2\text{O}_2^*$ $\text{Ph-CH}_2\text{O}_2^* + \text{Co}^{2+} \rightarrow \text{Ph-CHO} + [\text{HOCO}]^{2+}$ $\text{Ph-CHO} + \text{O}_2 \rightarrow \text{Ph-CO}_2\text{H}$	Mechanism of the electro-chemical assistance of catalytic oxidation. Conversion and yields
Bahranowski et al. ⁽⁵⁴⁾	H_2O_2 , catalyst $\text{Ph-CH}_3 \rightarrow \text{Ph-CHO} + \text{OH-Ph-CH}_3$	Study of Cu-doped alumina-pillared as catalyst

Table 5 (Cont'd)

Reference	Scheme	Remarks
Mills et al. ⁽⁸⁾	<p>Free Radical Chain Mechanism:</p> $\text{Ph-CH}_3 \rightarrow \text{Ph-CH}_2^*$ $\text{Ph-CH}_2^* + \text{O}_2 \rightarrow \text{Ph-CH}_2\text{O}_2^*$ $\text{Ph-CH}_2\text{O}_2^* + \text{Ph-CH}_3 \rightarrow \text{Ph-CH}_2^* + \text{Ph-CH}_2\text{O}_2\text{H}$ $\text{Ph-CH}_2\text{O}_2\text{H} + \text{M}^{n+} \rightarrow \text{Ph-CH}_2\text{O}_2^* + \text{M}^{(n-1)+} + \text{H}^+$ $\text{Ph-CH}_2\text{O}_2\text{H} + \text{M}^{(n-1)+} \rightarrow \text{Ph-CH}_2\text{O}^* + \text{M}^{(n-1)+}\text{OH}$ $\text{Ph-CH}_2\text{O}^* + \text{Ph-CH}_3 \rightarrow \text{Ph-CH}_2^* + \text{Ph-CH}_2\text{OH}$ $\text{Ph-CH}_2\text{O}^* + \text{Ph-CH}_2\text{O}_2\text{H} \rightarrow \text{Ph-CH}_2^* + \text{Ph-CH}_2\text{OH}$ $\text{Ph-CH}_2\text{O}_2^* \rightarrow \text{Ph-CH}_2\text{O}^* + \text{O}_2$ $2 \text{ Ph-CH}_2\text{O}_2^* \rightarrow \text{Ph-CH}_2\text{OH}^* + \text{Ph-CHO}^* \mid \text{O}_2$ $2 \text{ Ph-CH}_2^* \rightarrow \text{Ph-CH}_2\text{-CH}_2\text{-Ph}$ <p>Catalytic Oxygen transfer:</p> <p style="padding-left: 40px;">M: Metal Catalyst</p> $\text{Ph-CH}_2\text{O}_2\text{H} + \text{S} \rightarrow \text{Ph-CH}_2\text{OH} + \text{SO}$ <p>Mars-van Krevelen Mechanism:</p> $\text{MO} + \text{S} \rightarrow \text{M} + \text{SO}$ $2 \text{ M} + \text{O}_2 \rightarrow 2 \text{ MO}$	General study of hydrocarbon oxidation process and modeling

Kantam et al. (55)

Study on the reaction mechanism of toluene oxidation with manganese acetate as initiator to improve conversion and yields

2.3 REACTORS UTILIZED

As pointed out in Section 1.0, agitated reactors^(8, 15-19) and bubble column reactors^(1, 4, 13, 14, 20, 56) have been used in the liquid-phase toluene oxidation processes. Despite obvious geometrical dissimilarities between agitated reactors and bubble column reactors, the critical operating difference is the mean of mixing. While in agitated reactors, mixing can easily be controlled by one or several agitators, in bubble column reactors, mixing is provided through gas sparging. Due to these fundamental differences, each reactor has a specific range of application. In the following, reactor modes, configuration, characteristic and applicability will be briefly discussed.

2.3.1 Stirred Reactors

Stirred reactors are commonly used in gas-liquid processes as their low initial cost, flexibility and simple mixing control offer great advantages. Their use in large throughput processes, however, is limited due to geometrical restrictions. Stirred tank or series of stirred tanks are employed in several commercial gas-liquid processes, such as cyclohexane and benzoic acid oxidations^(11,23), vegetable oil hydrogenations⁽³⁴⁹⁾. While the basic geometrical ratios of agitated reactors, summarized in Table 6 have been accepted as the standard geometry, the design of the impeller, sparger, baffles, cooling coil, sampling and feeding ports are critical, and particular attention should be paid to these design criteria during the scale-up of the reactor. The stirred tank reactors are flexible, hence different and multiple modes of dispersion can be successfully used depending on the gas-liquid process. The three modes depicted in Figure 4, in which the stirred reactor can be operated, are:

1. Gas-sparging reactor (GSR)
2. Gas-inducing reactor (GIR)
3. Surface-aeration reactor (SAR)

Table 6: Geometrical Ratios of Agitated reactors

Ratios	Ranges ⁽⁵⁷⁾
H/d_T	1
d_{imp}/d_T	1/4-1/2
H_I/d_T	1/2-5/6
$d_w/d_{imp.}$	1/4-1/6
W/d_T	1/10-1/12

In gas-sparging reactor, the gas is bubbled through the liquid at a given superficial velocity from a distributor located at the bottom of the reactor underneath the impeller, which is used to mix the gas and liquid. In gas-inducing

reactor, holes, located in the gas and liquid phases, are machined in the hollow shaft of the impeller. The angular velocity of the impeller creates a pressure drop between the top and bottom of the shaft, which induces the gas into the liquid phase. In surface-aeration reactor, the mixing is provided by the impeller and the only contact between the two phases is the flat surface, where the gas is absorbed. The volumetric rate of mass transfer and the hydrodynamic parameters are expected to be different for each of these three reactors. Obviously, the rate of absorption in the SAR is much lower than in the GIR and GSR, but this mode of operation has the advantage of being simple. The GIR has higher rate of absorption and higher gas holdup without any additional costs to the SAR, providing commercial advantages. In the GSR, the increase of gas-holdup and interfacial area through higher power consumption causes, however, the highest rate of absorption, but economically adds substantial costs to the process as a compressor is often required to sparge the gas into the reactor.

2.3.2 Bubble Column Reactors

The mode of operation in bubble column reactors is rather simple as the gas is sparged through the liquid using a compressor at high superficial gas velocity from a distributor located at the bottom of the reactor and thus liquid mixing is achieved by the turbulent hydrodynamic regime developed in the reactor. Due to lack of knowledge on the scale-up methodologies in bubble column reactors, chemical processes⁽⁵⁶⁾ are often carried out in agitated reactors. Bubble column reactors, however, offer several advantages, such as high reaction rate, high gas-liquid mass transfer and gas holdup, high volume of reactors, temperature control and flexibility of operations. Nevertheless, inherent back-mixing, causing low conversion is usually seen as a major disadvantage for scale-up. While the standard geometrical ratios in bubble column reactors, $H/D_C \approx 4-6$ and the minimum $D_C = 0.15-0.30\text{m}$, have been accepted^(56, 190, 217), the design of the sparger, internals, cooling coil, sampling and feeding ports can have a critical impact on the design and scale-up of the reactor.

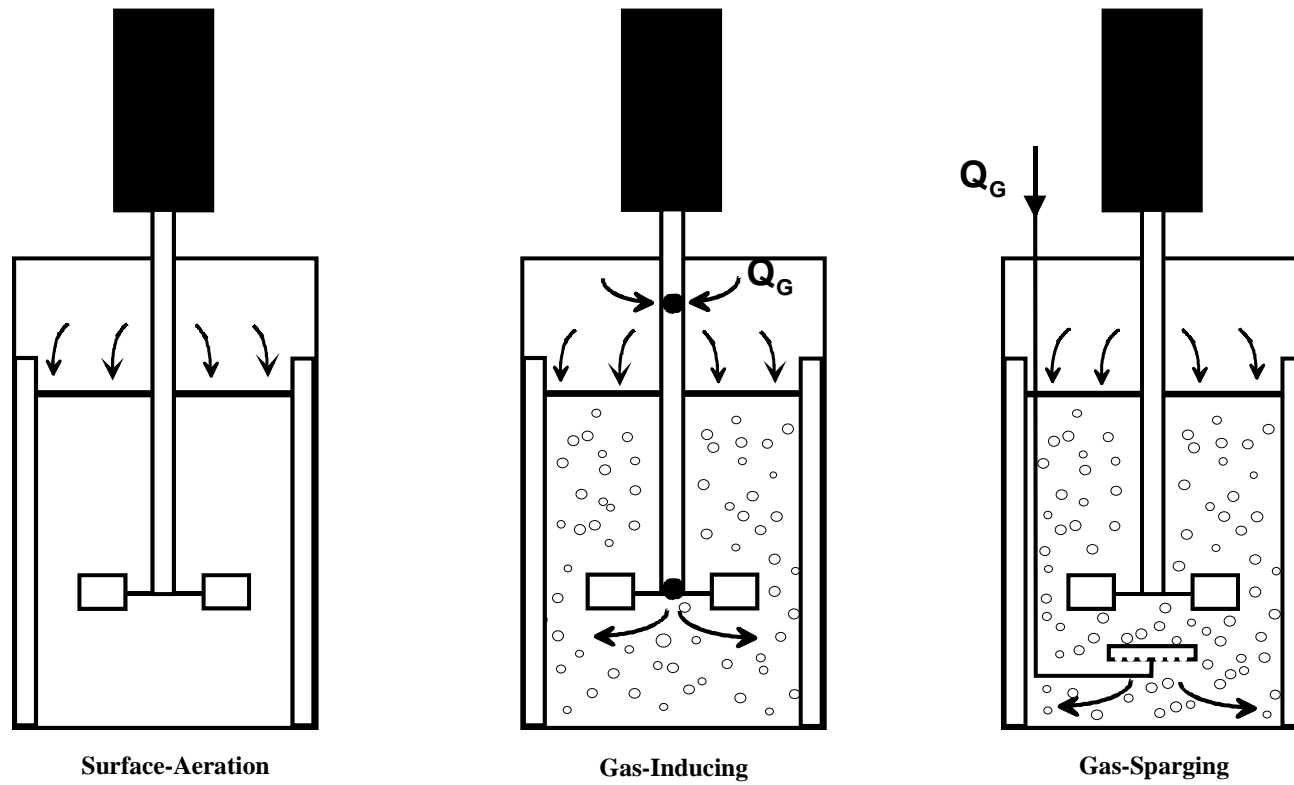


Figure 4: Operation Modes of Agitated Reactors

2.4 HYDRODYNAMIC PARAMETERS

Valuable studies on the hydrodynamic parameters have been reported in the literature as shown in Tables 7 and 10. As pointed out by these studies, the hydrodynamic parameters in BCR and agitated reactors are affected by different factors. For instance in the BCR, the gas and liquid properties, gas and liquid superficial velocities, gas distributor design, reactor internals, geometry, and size have been reported to influence the hydrodynamic parameters^(56,176,181,186,190,194). In agitated reactors, the impeller type and design, cooling coil, number of baffles, gas distributor, position of the impeller and liquid height have been known to impact the hydrodynamic^(60,64,69,73-80,92,106,108,113,120,122,125,126,130). It is also critical to mention that some of these factors could affect the rate-limiting step of the process⁽⁵⁶⁾. Most of the literature studies, however, were conducted with air and aqueous media, or used small diameter columns or tanks under atmospheric conditions. This raises concerns and controversy on their applicability for the scale-up of industrial processes often carried out under high pressures and temperatures in large scale reactors. Hence, the main hydrodynamic parameters, i.e., the flow regimes, the bubbles sizes and the gas holdup will be reviewed for each type of reactors in the following.

2.4.1 Hydrodynamic Regimes in Agitated reactors

As described in Section 2.3.1, agitated stirred reactors can be operated as SAR, GIR or GSR. The hydrodynamic regimes existing in each of these reactors will be described in the following.

In the SAR, different hydrodynamic regimes can occur depending on the mixing speed, relative position of the impeller to the gas-liquid surface, impeller and reactor sizes and baffles height and width^(60, 63-65, 67-78, 80-83). At low mixing speed, the gas is absorbed at the gas-liquid interface and is distributed throughout the tank due to the radial-downward flow created by the impeller. When the mixing speed is sufficiently increased, gas bubbles start to be entrained from the free surface of the liquid whether or not the stirred vessel is equipped with baffles as reported by Albal et al.⁽⁶⁷⁾, Tanaka and Izumi⁽⁷⁷⁾ and Patwardhan et al.⁽⁸⁴⁾. In the absence of baffles, a vortex, which was studied by Nagata⁽⁴⁸⁰⁾, Tanaka and Izumi⁽⁷⁷⁾, Smit and During⁽⁴⁸¹⁾, and Ciofano et al.⁽⁸²⁾, is formed around the shaft at the liquid surface due to the circulatory motion of the liquid created by the impeller. Further increase in the mixing speed increases the depth of the vortex until it reaches the impeller, where gas bubbles entrapment occurs. In the presence of baffles, however, the circular motion of the liquid is disturbed, which causes turbulences at the surface and creates a wavy gas-liquid surface, observed by Boerma and Lankester⁽⁶³⁾, Van Dierendonck et al.⁽⁶⁵⁾, Miller⁽¹²⁶⁾, Nagata⁽⁴⁸⁰⁾, Matsumura et al.⁽⁴⁵⁷⁾, Albal et al.⁽⁶⁷⁾, Greaves and Kobbacy⁽⁶⁸⁾, Heywood et al.⁽⁷³⁾, Tanaka and Izumi⁽⁷⁴⁾ and Patwardhan et al.⁽⁸⁴⁾. Under sufficient mixing, Clark and Verneulen⁽⁶⁰⁾ and Greaves and Kobbacy⁽⁶⁸⁾ observed that surface vortices entrapped gas bubbles in the liquid phase, due to the oscillatory random waves generated at the gas-liquid surface by the agitation. As the mixing speed increases, more gas bubbles are entrained

and dispersed throughout the liquid ^(67, 77, 84), leading to an increase of the gas holdup near the surface, which could eliminate the need for a compressor to recycle the gas. A sudden drop in the power input was reported to characterize this region ⁽⁶⁰⁾, where the gas bubbles are entrained in the liquid. The surface entrainment can therefore be summarized as a two-step mechanism ⁽⁸⁴⁾:

- Entrapment of the gas bubbles at the liquid surface due to turbulences; and
- Dispersion of the gas bubbles throughout the vessel

In the GIR, different hydrodynamic regimes could occur depending on the mixing speed, relative position of the impeller to the gas-liquid surface, impeller and reactor sizes and design ^(89, 92-94, 103, 106, 108, 109, 112). At low mixing speed, gas-inducing reactors behave as surface aeration reactors, since no gas is induced into the liquid. As the mixing speed increases the pressure near the impeller decreases until at a critical mixing speed, the pressure around the impeller becomes so small that gas bubbles are induced into the reactor. Further increase of the mixing speed increases the pumping capacity of the impeller, which results in an increase of the induced gas flow rate. Thus, more gas bubbles are induced and dispersed throughout the liquid. Under these conditions, Aldrich and van Deventer ⁽¹⁰¹⁾ and Patwardhan et al. ⁽¹¹⁴⁾ reported that the circular motion of the impeller creates a flow separation, which forms a wake region below the impeller. Consequently, gas cavities appear behind the impeller, which reduce subsequently the average density of the mixture and decrease the power input. These cavities can also be perceived as a local gas holdup in the vicinity of the impeller. In fact, when such cavities are observed behind the blades, the impeller is considered flooded. Thus, the gas inducing regimes can be summarized as follow:

- Surface aeration regime until the critical mixing speed for gas induction
- At the critical mixing speed, bubbling ⁽¹¹¹⁾ commences
- Continuous bubbling ⁽¹¹¹⁾ occurs as the mixing speed is increased
- Gas jet ⁽¹¹¹⁾ or flooding at very high mixing speeds, i.e. high gas induction rate

In the GSR, Several hydrodynamic regimes ^(64, 81, 120-122, 125, 130, 135-138, 148) were observed depending on the mixing speed, gas flow rate, relative position and type of the impeller, gas distributor and reactor size. The control of the superficial gas flow rate is the most important difference and advantage of the GSR over the SAR and GIR, although it can complicate the understanding of the hydrodynamic regime. At low mixing speed regardless of the gas flow rate, the gas is not well dispersed as it moves upward due to the poor mixing achieved under those conditions ^(131, 135, 136, 58). Increasing mixing speed causes better dispersion of the gas bubbles, which occurs first in the upper part of the reactor in the loading regime and then as the agitation is further increased, the gas bubbles disperse throughout the tank ^(131, 135, 136, 148, 58). Under higher mixing, the reactor reaches a fully dispersed regime where re-circulation loops are created in the upper and lower part of the vessel. It is also important to mention that under high agitation, surface entrainment takes place in small-scale GSR reactors ^(118, 119, 125, 126, 129-131, 141, 143), and is negligible in pilot and industrial scale reactors ^(125, 126, 130). Under constant mixing, when the gas flow rate is further increased, impeller flooding can occur ^(122, 135, 136, 140, 148, 58), where ragged or clinging cavities ^(131, 136) are observed behind the blades of the impeller. Thus, the GSR regimes are as follow:

- Loading regime with no gas re-circulation

- Fully dispersed regime with gas re-circulation
- Under intensive mixing, surface entrainment takes place.
- Flooding regime

2.4.2 Critical Mixing speeds and Gas Flow Rates in Agitated Reactors

Since mixing speeds and gas flow rates influence the different hydrodynamic regimes in agitated reactors, it is essential to investigate the effect of process variables on these parameters as well as their measuring techniques.

In the SAR, gas bubbles can be entrapped at the liquid surface due to the turbulences created by the impeller. Patwardhan and Joshi⁽⁸⁴⁾ divided the surface entrainment mechanism into an entrapment of gas bubbles followed by the dispersion of the entrapped gas bubbles throughout the vessel. Therefore, two critical mixing speeds can be defined:

- N_{CRE} : corresponding to the mixing speed at which the first bubble is being entrapped

- N_{CRIE} : corresponding to the mixing speed at which bubbles start to be dispersed in the liquid

As can be seen in Tables A-1 and A-3, various studies have reported empirical correlations for predicting the critical mixing speed of gas entrainment in the SAR^(60, 63, 65, 68-71, 73-77, 83) and in the GSR^(120, 126, 143). In the SAR, while Tanaka et al.⁽⁷⁴⁾ and Wichterle and Sverak⁽⁸³⁾ reported a decrease of the critical mixing speed of entrainment with liquid surface tension, Tanaka and Izumi⁽⁷⁷⁾ found an opposite effect. Controversial effect of liquid viscosity and liquid density were also reported as can be seen in Table A-1. The effects of impeller and reactor diameters as well as liquid height on the critical mixing speed, however, are unanimous. As shown in Table A-1, N_{CR} generally increases with both the reactor diameter^(60, 63, 65, 68, 70, 71, 73-77) and the liquid height^(60, 65, 68, 71, 73-77) and decreases with the impeller diameter^(60, 63, 65, 68, 70, 71, 73-77). In the GSR, however, liquid surface tension^(120, 126) was found to increase the critical mixing speed of gas entrainment while liquid density^(120, 126) and viscosity⁽¹²⁶⁾ were found to decrease N_{CR} . Also, the effect of impeller and reactor dimensions^(120, 126, 143) appears to be similar to the one reported for the SAR.

Table 7: Hydrodynamic Studies in Surface Aeration Reactors

Authors	Reactor	Gas/Liquid	Reactor characteristics	Remarks
Chandrasekhar ⁽⁵⁹⁾	SAR	-	-	“Kelvin-Helmoltz” instability at the G-L interface
Clark and Verneulen ⁽⁶⁰⁾	SAR	Water, CCl ₄	d_T : 0.254/4 Baffles 4-B Pa: 0.051-0.153	Effect of $d_{Imp.}$ on P^* and N_{CRE}
Muenz and Marchello ⁽⁶¹⁾	RT	O ₂ , He, CO ₂ , C ₃ H ₆ /Water	d_T : 0.15x0.51 Wave damper	Wave amplitude attenuation
Muenz and Marchello ⁽⁶²⁾	RT	O ₂ , He, CO ₂ , C ₃ H ₆ /Water	d_T : 0.15x0.51 Wave damper	Effect ripples frequency on the effective diffusivity
Boerma and Lankester ⁽⁶³⁾	SAR	CO ₂ /Sodium carbonate	d_T : 0.194/4 Baffles 6-B RT: 0.04-0.10	Effect of impeller diameter on N_{CRE}
Mehta and Sharma ⁽⁶⁴⁾	GSR SAR	Air, CO ₂ , O ₂ /H ₂ O+MEA, +DIPA +DEG, +NaOH, +Na ₂ S ₂ O ₄ , CuCl+HCl, +NaCl, +CuCl ₂	d_T : 0.125-0.700/4-Baffles 6-B DT: 0.04-0.33 4-B, 6-B curved T, 5-B DT	Effect of reactor mode, impeller type, d_T , $d_{Imp.}$, H , viscosity, surface tension, ionic strength, N and U_G on a .
van Dierendonck et al. ⁽⁶⁵⁾	SAR	-	d_T : 0.165, 2.6 6-B RT: 0.13-0.7 d_T	Effect of liquid properties and reactor geometry on N_{CRE}
Bossier et al. ⁽⁶⁶⁾	SAR	O ₂ /alkyl+p-xylene, nujol, tetradecane	d_T : 0.1016/4 Baffles 6-B DT: 0.0508	Determination of a
Albal et al. ⁽⁶⁷⁾	SAR	He, O ₂ /Water, CMC, glycerin	d_T : 0.10/4 Baffles 6-B RT: 0.45-0.57 d_T	Flow regimes in the SAR
Greaves and Kobbacy ⁽⁶⁸⁾	SAR	Water, electrolytic solution	d_T : 0.20	Bubble size and N_{CRE} as a function of N and H
Sverak and Hruby ⁽⁶⁹⁾	SAR	H ₂ O, glycerin, CCl ₄ , tenside, ethylsioide	d_T : 0.06-1.00/4-B DT 4 Baffles	Effect of d_T and liquid density on N_{CRE}
Joshi et al. ⁽⁷⁰⁾	SAR	-	-	Review on agitated gas-liquid contactors
Matsumura et al. ⁽⁷¹⁾	SAR	Water+sodium alginate	d_T : 0.242 6-B DT+6-B DT: 0.2-0.57 d_T	Effect of liquid properties on N_{CRE} and P^*
Matsumura et al. ⁽⁷²⁾	SAR	Water+sodium alginate	d_T : 0.19, 0.242, 0.316 6-B DT+6-B DT: 0.2-0.57 d_T	Effect of liquid properties on N_{CRE} , a and ε_G
Heywood et al. ⁽⁷³⁾	SAR	Aqu. polyvinyl alcohol	d_T : 0.21-0.54/Baffles 6-B RT, PT, P: 0.13-0.40	Effect of impeller and reactor design in order to minimize gas entrainment

Table 7 (Cont'd)

Authors	Reactor	Gas/Liquid	Reactor characteristics	Remarks
Tanaka et al. ⁽⁷⁴⁾	SAR	Aqu. polyvinyl alcohol	d_T : 0.10, 0.15, 0.20/4 Baffles 6-B DT: 0.05, 0.075, 0.10	Effect of d_T , $d_{Imp.}$, H_L on N_{CRE}
Ram Mohan ⁽⁷⁵⁾ and Kobbe ⁽⁷⁶⁾	SAR	Water, sodium chloride, CMC, isopropanol	d_T : 0.57/ $d_{Imp.}/d_i$: 0.3-0.5/Baffles Vaned DT, Conical Impeller	Effect of impeller design on ε_G
Tanaka and Izumi ⁽⁷⁷⁾	SAR	H ₂ O	d_T : 0.12-0.20/Baffles, draught tubes 6-B RT/4-B PT/3-B P: 0.05	Effect of impeller type, d_T and H_L on N_{CRE}
Bittins and Zehner ⁽⁷⁸⁾	SAR	-	DT, Pa/4 Baffles	Effect of $d_{Imp.}$, d_T , H and baffles height on P^*
Kamen et al. ⁽⁷⁹⁾	SAR	O ₂ /Water + sulfite	-(3.5, 16 liters)/3 Baffles	Effect of N on a_{SAR} , k_{L-SAR} and $k_L a_{SAR}$
Wichterle ⁽⁸⁰⁾	SAR	H ₂ O, glycerin, CCl ₄ , tenside, ethylsioide	d_T : 0.06-1.00/4 Baffles 4-B DT	Effect of d_T , $d_{Imp.}$, baffles, liquid viscosity and density on P^* and ε_G
Wu ⁽⁸¹⁾	SAR, GSR	Air/H ₂ O	d_T : 0.202, 0.305/4 Baffles 6-B DT: 0.6 d_T	Effect of H_L/d_T on $k_L a$ in surface aeration and N_{CRE}
Ciofao et al. ⁽⁸²⁾	SAR	-	d_T : 0.19/4-B RT: 0.095	Prediction of vortex amplitude
Wichterle and Sverak ⁽⁸³⁾	SAR	H ₂ O, glycerin, CCl ₄ , tenside, ethylsioide	d_T : 0.06- 1.00/4 Baffles 4-B DT	Effect of d_T , $d_{Imp.}$, baffles, liquid viscosity and density on N_{CRE} and P^*
Patwardhan and Joshi ⁽⁸⁴⁾	SAR	-	-	Review of hydrodynamic studies in agitated reactors
Roberts and Chang ⁽⁸⁵⁾	WC	-	-	Enhancement of mass transfer due to turbulent waves
Vazquez-Una et al. ⁽⁸⁶⁾	RT	CO ₂ /Water	-	Effect of wave frequency on k_L . Negligible effect of waves on a

B: Blade, DT: Disk turbine, RT: Rushton turbine, PT: Pitched turbine, P: Propeller, Pa: Paddles; WC: Wetted Column

Table 8: Hydrodynamic Studies in Gas Inducing Reactors

Authors	Reactor	Gas/Liquid	Reactor characteristics	Remarks
Zlokarnik ⁽⁸⁷⁾	GIR	Air/Water	d_T : 0.15-1.00/Hollow Shaft 4 types: 0.06	Effect of N on Q_{GI}
Zlokarnik ⁽⁸⁸⁾	GIR	Air/Water	$d_T/d_{Imp.}$: 2.42-5.00/hollow shaft 4 types: 0.06, 0.12	Effect of mixing speed, liquid height and impeller submergence on Q_{GI}
Martin ⁽⁸⁹⁾	GIR	Air/water	d_T : 0.28/Baffles/Hollow Shaft Flat, angles T: 0.254	Q_{GI} is function of the contact angle. Scale-up of GIR
Topiwala and Hamer ⁽⁹⁰⁾	GIR	O ₂ /K ₂ SO ₄ sol., bacterial broth	d_T : 0.158/4-Baffles Hollow T: 0.075	Q_{GI} increases with N and decreases with K ₂ SO ₄ . Effect of liquid properties on d_S , ε_G
White and de Villiers ⁽⁹¹⁾	GIR	Air/Tap water, glycerin-water-teepol	d_T : 0.29/Stator, Hollow shaft 12-vanes rotor: 0.056	Q_{GI} increases with μ_L
Joshi and Sharma ⁽⁹²⁾	GIR	Air/water, DEG, Sodium dithionite	d_T : 0.41-1.00/4-Baffles, Hollow shaft/Pipe T: 0.2-0.5 Flat cylind. T: 0.250-0.395	Q_{GI} increases with orifice area, N , $d_{Imp.}$, and decreases with H and μ_L . No effect of σ_L on Q_{GI}
Sawant and Joshi ⁽⁹³⁾	GIR	Air/water, isopropanol, PEG	Denver d_T : 0.1-0.172, $d_{Imp.}$: 0.070-0.115 Wenco d_T : 0.3 $d_{Imp.}$: 0.050	Q_{GI} increases with N and $d_{Imp.}$, decreases with H and μ_L , and is independent of σ_L and ρ_L . N_{CRI} affected by μ_L
Zundeleovich ⁽⁹⁴⁾	GIR	Air/Water	d_T : 0.4/Stator, Hollow shaft Rotor Stator: 0.08, 0.10, 0.12	Effect of $d_{Imp.}$ and H on Q_{GI} and P_G^*
Sawant et al. ⁽⁹⁵⁾	GIR	Air/Water, PEG/dolomite	d_T : 0.30/Stator, Hollow shaft Wenco: 0.10	Q_{GI} increases with N and decreases with H , and μ_L
Sawant et al. ⁽⁹⁶⁾	GIR	Air/Water, PEG/dolomite	d_T : 0.1-0.172, 0.380 $d_{Imp.}$: 0.070-0.115/Stator	Q_{GI} increases with N and $d_{Imp.}$, decreases with H and μ_L
Joshi et al. ⁽⁷⁰⁾	GIR	-	-	Review on agitated gas-liquid contactors
Raidoo et al. ⁽⁹⁷⁾	GIR	Air/Water	d_T : 0.57/Stator, Hollow shaft 6-B DT: 0.15-0.25 6-B T/6-B PT: 0.25	Q_{GI} increases with ΔP , $d_{Imp.}$ and N . At high N , Q_{GI} flattens off
Chang ⁽²⁴⁹⁾	GIR	H ₂ , N ₂ , CO, CH ₄ /n-C ₆ H ₁₄ , n-C ₁₀ H ₂₂ , n-C ₁₄ H ₃₀ , c-C ₆ H ₁₂	d_T : 0.127/4 Baffles 6-B RT: 0.0635, Hollow shaft	Determination of N_{CR}
He et al. ⁽⁹⁸⁾	GIR	Air/Water+CMC, water+triton-X-114	d_T : 0.075/4 Baffles 6-B DT: 0.032	N_{CR} increases with μ_L , H and σ_L ; a , ε_G increases with N , and decreases with H , σ_L . ε_G increases and decreases with μ_L

Table 8 (Cont'd)

Authors	Reactor	Gas/Liquid	Reactor characteristics	Remarks
Rielly et al. ⁽⁹⁹⁾	GIR	Air/Water	d_T : 0.30, 0.45, 0.60/4 Baffles 2-B Flat Pa: 0.215 2-B Concave T: 0.215	Bubble coalescence increases with Q_{GI} . Model to determine N_{CR} and Q_{GI}
Aldrich and van Deventer ⁽¹⁰⁰⁾	GIR	Air/H ₂ O, resin, brine sol., sucrose/nylon, polystyrene	d_T : 0.19/Baffles, Draft tube 6, 12-B RT: 0.05, 0.057 4-B Pipe T: 0.065	Q_{GI} decreases with μ_L and ρ_L
Aldrich and van Deventer ⁽¹⁰¹⁾	GIR	Air/Water, aqueous ethyl alcohol, sucrose, glycerin	d_T : 0.19/Baffles, Draft tube 6, 12-B RT: 0.05, 0.057	At low μ_L , Q_{GI} increases with μ_L , and decreases with μ_L at high μ_L . Q_{GI} decreases with ρ_L
Saravanan et al. ⁽¹⁰²⁾	GIR	Air/H ₂ O	d_T : 0.57, 1.0, 1.5/Baffles 6-B DT: 0.19-0.55, Draft tube	Scale-up effect on N_{CR} and Q_{GI} .
Aldrich and van Deventer ⁽¹⁰³⁾	GIR	Air/water, sucrose, ethanol, brine solution	d_T : 0.19/Baffles, Draft tube 6, 12-B RT: 0.05, 0.057	Effect of H , $d_{Imp.}$, μ_L and ρ_L on Fr_C and Ae
Al Taweel and Cheng ⁽¹⁰⁴⁾	GIR	Air/water+PGME	d_T : 0.19/Baffles, Draft tube 8-B RT: 0.096	Effect of liquid properties on a and ε_G . Additives retards the coalescence
Hsu and Huang ⁽¹⁰⁵⁾	GIR	Ozone/water	d_T : 0.170/Baffles, Draft tube 6-B PT: 0.060	Bubble coalescence Increases with Q_{GI}
Heim et al. ⁽¹⁰⁶⁾	GIR	Air/water-fermentation mixture	d_T : 0.30/4-Baffles/hollow shaft 4-B Pipe/6-B Pipe T: 0.125 6-B DT: 0.100, 0.150	Q_{GI} is a function of N , $d_{Imp.}$, H , μ_L , and increases with μ_L
Saravanan and Joshi ⁽¹⁰⁷⁾	GIR	Air/H ₂ O	d_T : 0.57, 1.0, 1.5/Baffles 6-B DT: 0.19-0.55, Draft tube	Review on modeling and experimental studies of N_{CR} , ε_G and Q_{GI} in GIR
Hsu and Huang ⁽¹⁰⁸⁾	GIR	Ozone/water	d_T : 0.29/4-Baffles 2 6-B PT: 0.09-0.12	Effect of impeller submergence on N_{CR} and the mixing time
Hsu et al. ⁽¹⁰⁹⁾	GIR	Ozone/water	d_T : 0.170/Baffles, Draft tube 6-B PT: 0.35-0.50 d_T	Effect of N and $d_{Imp.}$ on N_{CR} , ε_G , d_s , Q_{GI} and a
Patwardhan and Joshi ⁽¹¹⁰⁾	GIR	Air/H ₂ O	d_T : 1.5/Baffles, Draft tube 2 6-B DT: 0.50	Review on modeling and experimental studies of N_{CR} , ε_G and Q_{GI} in GIR
Tekie ⁽²³⁾	GIR	N ₂ , O ₂ /Cyclohexane	d_T : 0.1154-Baffles 6-B RT: 0.0508, Hollow shaft	No effect of pressure, temperature, mixing speed and liquid height on d_s
Forrester et al. ⁽¹¹¹⁾	GIR	Air/Water	d_T : 0.45/4 Baffles, hollow Shaft 26-B Concave T: 0.154	Q_{GI} increases with number of gas outlets
Hsu et al. ⁽¹¹²⁾	GIR	Ozone/water	d_T : 0.29/4-Baffles 2 6-B PT: 0.09-0.12	Effect of N and $d_{Imp.}$ on N_{CR} , and P_G^*
Patwardhan and Joshi ⁽⁸⁴⁾	GIR GSR	-	-	Review of hydrodynamic studies in agitated reactors

Table 8 (Cont'd)

Authors	Reactor	Gas/Liquid	Reactor characteristics	Remarks
Patil and Joshi ⁽¹¹³⁾	GIR	Air/H ₂ O	d_T : 1.0/Baffles, Draft tube 12-B PT: -/4-24 vanes Stator T:-	Q_{GI} exhibit a hysteresis behavior. Effect of impeller design on Q_{GI}
Patwardhan and Joshi ⁽¹¹⁴⁾	GIR	-	-	Review of experimental and modeling studies on GIR
Fillion ⁽³⁴⁹⁾	GIR GSR	H ₂ , N ₂ /Soybean oil	d_T : 0.115/4-Baffles hollow shaft 6-B RT: 0.0508/Spider sparger	Effect of P , T , N , H and Q_{GI} on d_S and ε_G

B: Blade, DT: Disk turbine, RT: Rushton turbine, PT: Pitched turbine, P: Propeller, Pa: Paddles

In the GIR, several correlations have been proposed in the literature in order to predict N_{CR} ^(349, 93, 94, 102, 103, 106, 108-110), as shown in Table A-2. Using a hollow shaft, Evans et al. ^(115, 116) extended the earlier model proposed by Martin ⁽⁸⁹⁾ and employed the theory of flow past immersed body along with Bernoulli's equation to obtain the critical mixing speed for gas induction in GIRs as follows:

$$P(\theta) = (P_T + \rho_L g H_L) - \frac{1}{2} \rho_L C_p(\theta) \times \left(2\pi N \frac{d_{imp.}}{2} (1 - K) \right)^2 \quad (2-1)$$

Where $P(\theta)$ and $C_p(\theta)$ are defined as the pressure and the pressure coefficient at any angular position, respectively, and K is a factor accounting for the slip between the impeller and the fluid. Therefore, the critical speed of induction is:

$$N_{CR} = \sqrt{\frac{2gH_L}{C_p(\theta) \times (\pi \times d_{imp.} (1 - K))^2}} \quad (2-2)$$

With the values of $C_p(\theta)$ is calculated from the potential flow theory for inviscid flow around a cylinder in an infinite medium:

$$C_p(\theta) = 4 \sin^2(\theta) \quad (2-3)$$

Saravanan and Joshi ⁽¹⁰⁷⁾ and White and de Villiers ⁽⁹¹⁾ used a similar model in a hollow shaft stator-diffuser type impeller. Increasing liquid viscosity has been reported to increase the critical mixing speed of gas induction ^(349, 93, 103) to a power ranging from 0.1 to 0.13, while negligible effects of liquid density and surface tension were reported. On the other hand, increasing liquid height or decreasing impeller diameter was found ^(349, 93, 103) to increase the critical mixing speed of gas induction.

In the GSR, as shown in Table A-3, van Dierendonck et al. ⁽¹⁵⁰⁾ determined the critical speed of gas dispersion using gas holdup measurements, which correspond to the beginning of the loading regime ^(135, 136). Warmoeskerken and Smith ⁽¹³⁶⁾ calculated the critical speed of flooding at given gas flow rates, and Westerterp et al. ⁽¹²⁰⁾ reported the critical speed of surface aeration in a GSR.

As can be seen in Table A-4, scarce studies ^(71, 129, 141, 143, 117) have reported the rate of surface entrainment, which can be attributed to the complexity, and inconsistency of the measurement method. In the SAR, only Matsumara et al. ⁽⁷¹⁾ reported the rate of gas entrainment, and found that increasing liquid viscosity and surface tension resulted in a decrease of the superficial gas entrainment velocity, U_E , while increasing the mixing speed, impeller diameter or decreasing the tank diameter, enhanced U_E . In the GSR, similar effect of physical properties, operating conditions, and impeller and reactor dimensions on the gas flow rate of entrainment was reported ^(129, 141, 143, 117, 457).

Table 9: Hydrodynamic Studies in Gas Sparging Reactors

Authors	Reactor	Gas/Liquid	Reactor characteristics	Remarks
Calderbank ⁽¹¹⁸⁾	GSR	Air/Water, toluene, alcohols, glycols, CCl ₄ , nitrobenzene, ethyl acetate	d_T : 0.19, 0.51/4-Baffles 6-B DT: $d_T/3$	Effect of liquid properties on ε_G , d_S and a and of gas entrainment on the total a
Calderbank ⁽¹¹⁹⁾	GSR	Air/Water, toluene, alcohols, glycols, CCl ₄ , nitrobenzene, ethyl acetate	d_T : 0.3, 0.375, 0.51/4-Baffles 6-B DT: $d_T/3$	Effect of liquid properties on N_{CRE} under sparged conditions
Westerterp et al. ⁽¹²⁰⁾	GSR	Air/Sulphite solution	d_T : 0.14- 0.90/4-Baffles 6-B DT, 4-B Pa, 2-B Pa, 3-B P: 0.2-0.7 d_T	Effect of impeller design and reactor sizes on a and N_{CRD}
Westerterp ⁽¹²¹⁾	GSR	Air/Sulphite solution	d_T : 0.14- 0.90/4 Baffles 6-B DT, 4-B Pa, 2-B Pa, 3-B P: 0.2-0.7 d_T	Determination of the optimum agitator design and operating conditions
Rushton and Bimbinet ⁽¹²²⁾	GSR	Air/Water + corn syrup	d_T : 0.23, 0.29, 0.46, 0.61, 0.91/4-Baffles/Orifice sparger 6-B RT: 0.0051-0.305	Characterization of flooding. Effect of d_T , $d_{imp.}$, U_G and μ_L on ε_G
Lee and Meyrick ⁽¹²³⁾	GSR	Air/ Solutions of sodium chloride and sulphate	d_T : 0.191/4-Baffles, Orifice 6-B DT: 0.10	Effect of mixing speed and superficial gas velocity on ε_G
Reith and Beek ⁽¹²⁴⁾	GSR	Air/Water, sulphite solution	d_T : 0.30/4-Baffles/ring sparger 6-B T: 0.076	Statistical determination of the bubbles coalescence rate
Fuchs et al. ⁽¹²⁵⁾	GSR	O ₂ /Water	-(1-51,000 liters)	Effect of reactor size on gas entrainment
Mehta and Sharma ⁽⁶⁴⁾	GSR SAR	Air, CO ₂ , O ₂ /H ₂ O+MEA, +DIPA, +DEG, +NaOH, +Na ₂ S ₂ O ₄ , CuCl +HCl, +NaCl, +CuCl ₂	d_T : 0.125-0.700/4-Baffles 6-B DT: 0.04-0.33 4-B, 6-B curved T, 5-B DT	Effect of reactor mode and diameter, impeller type, H , viscosity, surface tension, ionic strength, N and U_G on a
Miller ⁽¹²⁶⁾	GSR	CO ₂ , Air / Aqueous solution	d_T : 0.1524, 0.305, 0.686 4-B Pa: 0.1016, 0.203, 0.457 4-Baffles, Ring sparger	Minimum N to get a significant increase in a due to the mechanical agitation. Effect P^* and U_G on d_S and ε_G
Hassan and Robinson ⁽¹²⁷⁾	GSR	Air/H ₂ O, propionic acid, methylacetate, ethylene glycol, glycerol, sodium sulfate	d_T : 0.152, 0.291/4-Baffles 6-B RT, 6-B Pa: $d_T/3$ 4-B Pa: $d_T/3$, Orifice sparger	Effect of liquid properties on ε_G .
Loiseau et al. ⁽¹²⁸⁾	GSR	Air/Water, glycol, water alcohols, sodium sulfite	d_T : 0.22/4-Baffles 6-B RT: $d_T/3$, Orifice and ring	Effect of foaming and non-foaming systems on P^*_G and ε_G .
Matsumura et al. ⁽¹²⁹⁾	GSR	Water, alcohols	d_T : 0.218/3-Baffles 6-B DT: 0.487 d_T	Effect of gas entrainment on P^* and ε_G

Table 9 (Cont'd)

Authors	Reactor	Gas/Liquid	Reactor characteristics	Remarks
Lopes de Figueiredo and Calderbank ⁽¹³⁰⁾	GSR	O ₂ /Water	d_T : 0.91/4 Baffles 6-B RT: 0.27	Effect of reactor size on gas d_s , a , ε_G , entrainment, and P^* for scale-up
Nienow et al. ⁽¹³¹⁾	GSR	Air/Water	d_T : 0.61/4 Baffles 6-B RT: 0.305	Evaluation of surface gassing under sparging conditions
Sridhar and Potter ⁽¹³²⁾	GSR	Air/Cyclohexane	d_T : 0.13/4-Baffles, Nozzle sparger 6-B RT: 0.045	Effect of pressure on d_s and ε_G
Sridhar and Potter ⁽¹³³⁾	GSR	Air/Cyclohexane	d_T : 0.13/4-Baffles, Nozzle sparger 6-B RT: 0.045	Effect of temperature, pressure, N and U_G on a
Hughmark ⁽¹³⁴⁾	GSR	-	12 publications	Review of correlations on a , d_s and ε_G
Joshi et al. ⁽⁷⁰⁾	GSR	-	-	Review on agitated gas-liquid contactors
Chapman et al. ⁽¹³⁵⁾	GSR	Air/Water	d_T : 0.56/4-Baffles 6-B DT: 0.28	Characterization of the conditions for total gas dispersion
Warmoeskerken et al. ⁽¹³⁶⁾	GSR	Air/Water	d_T : 0.44, 0.64, 1.20/4-Baffles/Ring 6-B RT: 0.176, 0.256, 0.480	Characterization of the onset of Flooding
Hudcova et al. ⁽¹³⁷⁾	GSR	Air/Water	d_T : 0.44, 0.56/Variou sparger	No effect of H_L on flooding-loading
Greaves and Barigou ⁽¹³⁸⁾	GSR	Air/Water, NaCl sol.	d_T : 1.0/4 Baffles/orifice sparger 6-B DT: 0.250, 0.333, 0.500	Effect of cavity type on ε_G
Oyevaar et al. ⁽¹³⁹⁾	GSR	CO ₂ +N ₂ /DEA	d_T : 0.088/4 Baffles/Orifice 6-B DT: 0. d_T	Effect of pressure, mixing speed and superficial gas velocity on ε_G
Lu and Ju ⁽¹⁴⁰⁾	GSR	Air/Water	d_T : 0.288/4 Baffles/Ring sparger 6-B DT: 0.072 4-B DT, 8-B DT: 0.096	Characterization of the cavity configuration and flooding
Veljkovic and Skala ⁽¹⁴¹⁾	GSR	N ₂ /Water	d_T : 0.22/4 Baffles 1 or 2 6-B DT	Effect of gas entrainment on P^* , under sparged conditions
Oyevaar et al. ⁽¹⁴²⁾	GSR	CO ₂ +N ₂ /DEA	d_T : 0.081/4 Baffles 6-B DT: 0.4, 0. d_T , Orifices	Effect of pressure, mixing speed and superficial gas velocity on a
Veljkovic et al. ⁽¹⁴³⁾	GSR	N ₂ /Water	d_T : 0.20, 0.30, 0.45, 0.675 4 Baffles/6-B DT: $d_T/3$	Effect of gas entrainment on P^* , under sparged and unsparged conditions
Barigou and Greaves ⁽¹⁴⁴⁾	GSR	Air/Water, NaCl sol.	d_T : 1.0/4 Baffles/orifice sparger 6-B DT: 0.333	Effect of U_G and N on the bubble size at different locations in the vessel
Takahashi and Nienow ⁽¹⁴⁵⁾	GSR	He, air, CO ₂ /Deionized water, saturated CO ₂ water	d_T : 0.29/4 Baffles/Ring sparger 6-B RT: $d_T/3$	Effect of gas density on P_G^* and on the flooding-loading transition

Table 9 (Cont'd)

Authors	Reactor	Gas/Liquid	Reactor characteristics	Remarks
Parthasarathy and Ahmed ⁽¹⁴⁶⁾	GSR	Air/Water+methyl isobutyl carbinol	d_T : 0.195/4 Baffles 6-B RT: 0.065/Sintered plate	Effect of mixing speed on the equilibrium bubble size
Khare and Niranjana ⁽¹⁴⁷⁾	GSR	Air/CMC, castor oil, rapeseed oil	d_T : 0.3/4 Baffles/Ring sparger 6-B DT: $d_T/3$	Effect of N and U_G on small, large and total bubbles holdup
Wu ⁽⁸¹⁾	SAR, GSR	Air/H ₂ O	d_T : 0.202, 0.305/4 Baffles 6-B DT: 0.6 d_T	Effect of H_L/d_T on $k_L a$ in surface aeration and N_{CRE}
Roman and Tudose ⁽¹⁴⁸⁾	GSR	-	d_T : 0.25/4 Baffles Modified RT: $d_T/3$	Effect of impeller height and type on P^*
Murugesan ⁽¹⁴⁹⁾	GSR	Air/Water, Toluene, glycerol	d_T : 0.15/4-Baffles/Plate sparger 6-B RT: 0.05, 0.07	Correlation of ε_G
Patwardhan and Joshi ⁽⁸⁴⁾	GIR GSR	-	-	Review of hydrodynamic studies in agitated reactors
Fillion ⁽³⁴⁹⁾	GIR GSR	H ₂ , N ₂ /Soybean oil	d_T : 0.115/4-Baffles/hollow shaft 6-B RT: 0.0508, Spider sparger	Effect of P , T , N , H and Q_G on d_s and ε_G

B: Blade, DT: Disk turbine, RT: Rushton turbine, PT: Pitched turbine, P: Propeller, Pa: Paddles

In the GIR, extensive quantitative studies on the rate of gas induction can be found in the literature^(349, 89-91, 94-97, 100-103, 106, 107-109, 151). While the effect of liquid surface tension on the induction rate appears to be negligible, the impact of liquid viscosity is critical. In fact, several investigators reported a decrease of the gas flow rate with increasing liquid viscosity^(349, 92, 94-96), whereas others reported an increase^(91, 103). Furthermore, recent studies found that the rate of gas induction was first increased and then decreased with increasing liquid viscosity^(100, 101, 151). Liquid density, however, has been reported to decrease the gas induction rate^(100, 101, 103), due to the increase of the buoyancy. While the effects of temperature and pressure on the induced gas flow rate have been scarcely reported^(349, 151), the effects of mixing speed, liquid height, impeller and reactor diameter are well established as shown in Table A-4. In fact, Fillion et al.⁽¹⁵¹⁾ found that the effect of increasing temperature on gas induction rate was similar to the effect of decreasing viscosity, whereas an increase of pressure decreases the induction rate by influencing the cavities structure. Decreasing the liquid height, vessel diameter or increasing the impeller diameter increases the pumping capacity of the impeller, hence the induction rate as generally reported^(89, 91, 94-97, 102, 106).

Several techniques have been developed to determine critical mixing speeds in agitated reactors. The most commonly used method is the photographic technique, which had been successfully carried out in the SAR^(68, 75, 76) and GIR^(349, 103, 92). Methods for the determination of the impeller speed at which $k_L a$ or a values increase sharply have also been used in the GSR^(118, 126, 141, 143) and in the GIR⁽²⁴⁹⁾. Another commonly accepted technique developed by Clark and Vermulen⁽⁶⁰⁾, resides in monitoring the mixing speed at which the power input decreases steeply. In the GSR, van Dierendonck et al.⁽¹⁵⁰⁾ determined the gas bubbles dispersion critical speed by plotting the mixing speed versus ε_G and extrapolating it towards $\varepsilon_G = 0$. In the GSR, Matsumura et al.⁽¹²⁹⁾, Veljkovic et al.⁽¹⁴¹⁾ and Veljkovic et al.⁽¹⁴³⁾ determined the ratio of surface aeration rate to sparged rate and the intensification of surface aeration by using a gas tracer. In the GIR, Fillion⁽³⁴⁹⁾ and Fillion et al.⁽¹⁵¹⁾ used a sealed bearing device and recirculation loop to measure the gas flow rate with a Coriolis mass flow meter.

2.4.3 Hydrodynamic Parameters in Bubble Column Reactors (BCR)

In bubble column reactor, as reported in the literature presented in Table 10, different hydrodynamic regimes can occur depending on the gas flow rate, column diameter and system pressure^(173, 176, 178, 186, 188, 192, 193). Specifically, three different hydrodynamic regimes were reported⁽¹⁵²⁾. The first regime is the bubbly flow regime, or homogeneous regime, which is characterized by rising gas bubbles without significant interactions among them. As a result, the gas bubbles residence time is constant and is expressed as a function of the bubble rise velocity. The gas velocity mainly dictates this regime, and the reactor diameter was not found to play a critical role. The maximum gas linear velocity in this regime is low; usually less than 0.05 m/s, and the mean bubble velocity defined by Equation (2-4) is lower than 0.3 m/s⁽¹⁵²⁾:

$$u_b = \frac{U_G}{\varepsilon_G} \quad (2-4)$$

The liquid phase can be considered stationary, since no major re-circulation of the liquid occurs in the reactor. As the velocity increases, the drag force increases due to bubbles rise, which induces mixing in the liquid phase. In small diameter columns, this increase of the gas velocity leads to a slug flow regime, which prevails when gas bubbles are flowing upward. Gas bubbles tend to grow to sizes close to the reactor diameter and rise pushing the liquid in slugs. Thus, this regime is characterized by the presence of large gas bubbles; hence low mass and heat transfer coefficients, which result in severe concentration profiles of the reactants. In large columns, however, as the gas velocity increases, the heterogeneous or churn-turbulent regime appears. In this regime, the rising gas bubbles tend to create circulation patterns in the whole reactor, and accordingly the gas holdup does not linearly increase with the gas velocity as expected in the homogeneous regime. Large gas bubbles rise in the reactor in a plug flow mode whereas small bubbles re-circulate in the liquid phase. Thus, high gas-liquid mass transfer coefficients, and intensity of mixing characterize such a regime.

Several flow regime maps were proposed to delineate the hydrodynamic flow regimes in BCRs as the one by Oshinowo and Charles⁽¹⁵³⁾, which identifies six different flow regimes in an upward flow; and that by Deckwer et al.⁽¹⁵⁴⁾ based on the reactor diameter and gas velocity for air/water system. In BCRs operating at superficial gas velocities ≤ 0.05 m/s, the bubbly or homogenous flow regime prevails, which is characterized by a homogeneous gas bubbles distribution, weak interactions among gas bubbles, and almost constant gas bubbles residence time. In this regime, the gas injection point was reported to have a strong impact on the gas bubbles formation, whereas the reactor diameter was not as important^(186, 193). In small BCRs with internal diameters less than 0.15 m, increasing the superficial gas velocity could lead to the formation of large gas bubbles in the form of slugs, which is designated as a slug flow regime. In this regime, the wall effect^(155, 156) is important and has a strong impact on the hydrodynamic and mass transfer parameters. In large-scale BCRs, however, increasing the superficial gas velocity leads the reactor to operate in the heterogeneous or churn-turbulent flow regime. In this regime, large and fast-rising gas bubbles induce strong circulations and create back-mixing or re-circulation zones in the reactor where small bubbles are entrained^(157, 219, 344). In the churn-turbulent flow regime, visual observations and photographic methods revealed the coexistence of small and large (two-bubble class) bubbles in BCRs and SBCRs^(157, 158, 188) and therefore the knowledge of the hydrodynamic and mass transfer of these bubbles is required^(159, 160, 161) for modeling BCRs. It should be mentioned that although these three flow regimes are often defined in terms of reactor diameter and superficial gas velocity^(154, 219), the transition between any two regimes was reported to be strongly dependent on the sparger design^(162, 203); reactor length to diameter ratio (H/D_C)⁽¹⁶³⁾; system pressure^(183, 184, 188, 223) and temperature^(207, 223). The development of non-intrusive measuring techniques, such as Computer-Automated Radioactive Particle Tracking (CARPT)^(164, 165), Particle Image Velocimetry (PIV)^(164, 166, 167), Laser Doppler Anemometry (LDA)^(162, 168) and Computed Tomography (CT)^(164, 479), allowing the determination of the liquid, gas, and solid averaged velocities/profiles, turbulent kinetic energy, Reynolds stresses and void fraction distribution, could be used in Computational Fluid Dynamic (CFD) to establish more accurate flow regime maps. Unfortunately, these techniques are currently being tested in relatively small diameter reactors, usually operating with air-water system under ambient conditions. Thus, to date flow-regime maps in large-scale BCRs operating under industrial conditions

(high-pressures, high-temperatures, and organic media) are not available despite the fact that they are needed for proper understanding of the hydrodynamic behavior of these reactors. Fair et al. ⁽⁵⁰⁴⁾, Yoshida and Akita ⁽²¹⁸⁾, and Shah et al. ⁽²¹⁹⁾ pointed out the lack of experimental data on the hydrodynamics of BCRs and SBCRs operating under typical commercial process conditions; and more recently, Behkish et al. ⁽¹⁵⁸⁾ gave a comprehensive survey of available literature data on the gas holdup in BCRs and SBCRs and concluded that the gas holdup data obtained in large-scale reactors under industrial conditions are scanty.

Table 10: Hydrodynamic Studies Using Bubble Columns Larger than 0.15 m

Authors	Gas-Liquid	Column, m	Sparger	Conditions U_G , m/s	Remarks
Argo and Cova ⁽¹⁶⁹⁾	N ₂ +H ₂ / Water	$D_C = 0.45$, $H = 8.1$	SO	$U_G < 0.16$	No effect of P
Akita and Yoshida ⁽¹⁷⁰⁾	He, Air, O ₂ , CO ₂ / Water + Sol.	$D_C = 0.15, 0.3, 0.6$ $H = 2$	SO	Atm.	Effect of ρ_G
Godbole et al. ⁽¹⁷¹⁾	Air/Sotrol,Turpentine 5	$D_C = 0.305$, $H = 2.6$	PP	$U_G < 0.32$	Small and large bubbles
Tarmy et al. ⁽¹⁷²⁾	N ₂ /C ₇ H ₁₆	$D_C = 0.61$, $H = 8.5$	BC	$U_G < 0.20$	Effect of P
Molerus and Kurtin ⁽¹⁷³⁾	Air / Water + butanol	$D_C = 0.19$, $H = 2.5$	PP, PoP	-	In the bubbly regime, bubble sizes deduced from gas throughput and ε_G
Guy et al. ⁽¹⁹⁸⁾	Air / Water, glycerol, cellulose,polyacrylamide	$D_C = 0.254$, $H = 0.9$	Several PP	$U_G < 0.10$	Effect of μ_L and sparger plate on ε_G
Daly et al. ⁽¹⁷⁴⁾	N ₂ /FT-300 paraffin, SASOL wax	$D_C = 0.05/0.20$, $H = 3$	PP	$U_G < 0.14$	Effect of axial position, column diameter and temperature
Grund et al. ⁽¹⁷⁵⁾	Air/H ₂ O,Oils,CH ₃ OH	$D_C = 0.15$, $H = 4.3$	PP	$U_G < 0.2$	Effect of liquid properties
Wilkinson et al. ⁽¹⁷⁶⁾	N ₂ /n-Heptane, water, mono-ethylene glycol	$D_C = 0.16, 0.23$ $H_L = 1.5, 1.2$	-	$U_G < 0.55$	Effect of D_C , H , sparger design, ρ_G and liquid properties on ε_G and flow regime
Chabot and de Lasa ⁽¹⁷⁷⁾	N ₂ / paraffinic oil (LP-100)	$D_C = 0.2$, $H = 2.4$	PP	$U_G < 0.15$	Effect of T , z and U_G on ε_G and d_B
Reilly et al. ⁽¹⁷⁸⁾	He, N ₂ , Air, Ar, CO ₂ / Water, varsol, TCE, isopar G / M	$D_C = 0.15$, $H = 2.7$	X-type sparger	$U_G < 0.23$	Effect of M_G on ε_G under bubbly and churn-turbulent flow regimes
De Swart ⁽¹⁷⁹⁾	Air / Oil,H ₂ O,alcohol	$D_C = 0.05, 0.174, 0.19, 0.38$; $H = 4$	SP50,200 μ m	$U_G < 0.55$	-
Stegeman et al. ⁽¹⁸⁰⁾	CO ₂ ,N ₂ /H ₂ O,DEA,ETG	$D_C = 0.156$	PP 0.4mm	$U_G < 0.06$	Effect of P , U_G , μ_L on ε_G and a
Laari et al. ⁽¹⁸¹⁾	Air / Water +phenol	$D_C = 0.19, 0.97$ $H = 0.67-4.64$	T-nozzle	$U_G < 0.03$	Effect of D_C , U_G , additives on ε_G , d_B
Letzel et al. ⁽¹⁸²⁾	N ₂ / Water	$D_C = 0.15$, $H = 1.2$	PP	$U_G < 0.30$	Effect of P on flow regimes and Utrans
Letzel et al. ⁽¹⁸³⁾	N ₂ / Water	$D_C = 0.15$, $H = 1.2$	PP	$U_G < 0.30$	Effect of P on flow regimes and Utrans

Table 10 (Cont'd)

Authors	Gas-Liquid	Column, m	Sparger	Conditions U_G , m/s	Remarks
Letzel et al. ⁽¹⁸⁴⁾	N ₂ / Water	$D_C = 0.15$, $H = 1.2$	PP	$U_G < 0.30$	Effect of ρ_G on ε_G of large bubble
Kang et al. ⁽¹⁸⁵⁾	Air / CMC	$D_C = 0.152$, $H = 2.0$	PP	$U_G < 0.20$	Effect of pressure on ε_G
Sarrafi et al. ⁽¹⁸⁶⁾	Air / Water	0.10x0.15x1.50 $D_C = 0.08, 0.155$	PP	$U_G < 0.08$	Effect of column geometry, sparger on transition velocity and ε_G
Pohorecki et al. ⁽¹⁸⁷⁾	N ₂ / Water	$D_C = 0.3$, $H = 4$	Several O	$U_G < 0.020$	No effect of P , T , z and sparger on d_s , ε_G only dependent on U_G
Krishna et al. ⁽¹⁸⁸⁾	Air / Water +alcohol	$D_C = 0.15$, $H = 4$	SP	$U_G < 0.5$	Effect of P on the flow regime, ε_G , d_b .
Bouaifi et al. ⁽¹⁸⁹⁾	Air / Water	$D_C = 0.15, 0.20$, $H = 2$	PP,SP,PM	$U_G < 0.04$	Effect of power input on ε_G
Jordan and Schumpe ⁽¹⁹⁰⁾ , Jordan et al. ⁽¹⁹¹⁾	He, N ₂ , Air / C ₂ H ₅ OH, C ₄ H ₉ OH, decalin, C ₇ H ₈	$D_C = 0.1, 0.115$ $H = 1.3, 1$	Several PP	$U_G < 0.21$	Effect of D_C , distributors, gas velocity, ρ_G and T on ε_G
Kemoun et al. ⁽¹⁹²⁾	Air / Water	$D_C = 0.162$, $H = 2.5$	PP	$U_G < 0.18$	P delayed the churn –turbulent regime
Magaud et al. ⁽¹⁹³⁾	Air / Water,polarographic sol.	0.1x0.3x4	PP	$U_G < 0.07$ $U_L < 0.125$	Study of the wall and core region in the homogeneous regime
Moustiri et al. ⁽¹⁹⁴⁾	Air / Water	$D_C = 0.15, 0.20$ $H = 4.25, 4.5$	PM	$U_G < 0.055$ $U_L < 0.022$	Effects of D_C on ε_G and liquid mixing
Pohorecki et al ⁽¹⁹⁵⁾	N ₂ / cyclohexane	$D_C = 0.3$, $H = 4$	Several O	$U_G < 0.055$	Effects of P and T on d_s and ε_G
Pohorecki et al ⁽¹⁹⁶⁾	Air/C ₆ H ₁₂ ,C ₇ H ₈ ,CH ₃ OH,n-C ₇ H ₁₆ ,CH ₃ COH, CH ₂ O,iso-C ₃ H ₇ OH	$D_C = 0.09, 0.3$, $H = 2, 4$	SO	$U_G < 0.027$	Effects of U_G on d_s

PP= Perforated Plate, SO= Single Orifice, BC= Bubble Cap, SP= Sintered Plate, PM= Perforated Membrane, PoP: Porous plate, O= Orifice

2.4.4 Gas Bubbles in Agitated Reactors

The gas phase quality in the liquid is often characterized by the bubble size and distribution, which along with the gas holdup control the gas-liquid interfacial area, the bubble rise velocity, and the contact time. In agitated reactors, as described in Section 2.4.1, the gas bubbles are formed at the surface in the SAR, under the impeller in the GIR, and at the bottom of the reactor in the GSR. Therefore, depending on the type of reactor the gas bubble size can be controlled by the energy of the gas stream, impeller type and size, sparger size and spacing as well as liquid properties. In fact, for a single bubble formation, the forces controlling the bubble size are:

1. the forces of buoyancy:

$$F_{buoyancy} = \frac{\pi}{6} d_b^3 \Delta \rho g \quad (2-5)$$

2. the surface tension forces:

$$F_{surface\ tension} = \pi d_{orif} \sigma \cos \theta \times f \quad (2-6)$$

where f is the shape factor which equals 1 for a sphere and, θ , the contact angle equals 0 for a perfectly wet orifice. Under these conditions the spherical bubble diameter is:

$$d_b = \left(\frac{6 d_{orif} \sigma}{\Delta \rho g} \right)^{1/3} \quad (2-7)$$

In agitated reactors, however, this approach is rather simple due to the formation of multiple bubbles, which can collide, break up, coalesce or be consumed by reaction. Therefore, the effect of physical properties, operating conditions and reactor design reported in the literature on d_s will be discussed in the following.

From Table A-5 d_s has been unanimously found to increase with liquid surface tension^(349, 72, 118, 125, 132, 134, 458, 459), and decrease with increasing liquid viscosity as reported by Vermulen et al.⁽⁴⁵⁸⁾ and Matsumura et al.⁽⁷²⁾. On the other hand, liquid and gas⁽¹³²⁾ densities have been reported to decrease the bubble diameter as can be observed in Table A-5. The effect of gas viscosity reported by Vermulen et al.⁽⁴⁵⁸⁾, however, should be taken as a fitting parameter rather than as an actual physical effect. Also, it should be mentioned that the effect of gas holdup on the bubble diameter reported by Calderbank⁽¹¹⁹⁾, Miller⁽¹²⁶⁾, Shridhar and Potter⁽¹³²⁾ and Hughmark⁽¹³⁴⁾ reflects the coalescing behavior of the liquid employed.

The mixing speed and superficial gas velocity, i.e. the mixing power input, have been reported to decrease the bubbles diameter^(72, 349, 119, 126, 132, 134, 458, 459), whereas the effect of temperature and pressure on the gas bubble sizes has been scarcely reported. It seems, however, that increasing temperature, which decreases the liquid viscosity, decreases the bubble diameter. Fillion⁽³⁴⁹⁾ reported negligible effect of pressure up to 4 bar on the Sauter mean bubble diameter, whereas Shridhar and Potter⁽¹³²⁾ found that increasing pressure from 1 to 10 atmospheres resulted in a slight decrease of the bubble diameter in a GSR. While the Sauter mean bubble diameter was found to decrease

with the number of impellers and their diameters⁽⁷²⁾, the effect of sparger design in the GSR has been found to have tremendous impact on the Sauter mean bubble diameter^(118, 119). This can directly be related to Equation (2-6), which underlines the critical role of the orifice diameter during the bubble formation. Fillion⁽³⁴⁹⁾ reported that the reactor type has an important impact on the bubble size, which is the result of different modes of bubble formation in the different reactor types. It should be mentioned that few studies have been carried out under typical industrial conditions for the toluene-N₂ and -O₂ systems, and it is therefore necessary to investigate the effect of process variable on the bubbles size in agitated reactors.

2.4.5 Gas Bubbles in Bubble Column Reactors

In BCRs, the gas phase quality in the reactor is also characterized by the bubbles size and distribution. The bubbles size formed at the bottom of the reactor is controlled by the energy of the gas streams, sparger size and spacing as well as liquid properties as described by Equations (2-5) and (2-6). The bubble formation at an orifice or a nozzle depends on the linear gas velocity; hence low velocities allow the formation of consecutive individual bubbles, while at higher gas velocities jets are created generating a turbulent zone in the liquid located at the vicinity of the nozzle. The bubble size generated at the gas sparger may not remain the same along the column, since it may grow due to coalescence or may decrease in size due to reaction or rupture with turbulence. The equilibrium bubble size depends then on the gas and liquid properties as well as the turbulence in the reactor. A number of pertinent studies to predict bubble sizes are given in Table A-6. Several correlations to predict the bubble rise velocity are given in Table A-7 and most of them follow the Davies-Taylor⁽¹⁹⁷⁾ relationship, Equation (2-8):

$$u_b = \alpha(gd_b)^\beta \quad (2-8)$$

One of the limitations of these correlations, however, is that they were proposed for one single bubble in a steady liquid, which is not the case in a BCR operating in the churn-turbulent flow regime. In this regime, the large bubbles travel upward creating swarms which increase the small bubbles back-mixing. The liquid circulation velocity u_c created by the rise of these bubbles is added to the terminal velocity of the bubbles ($u_{b,\infty}$) as in Equation (2-9):

$$u_b = u_{b,\infty} + u_c \quad (2-9)$$

Although this complicates the problem, the common approach is to separate each velocity component and assess each one independently. In the homogeneous flow regime, however, the bubbles rise can be estimated from Stokes law⁽¹⁹⁸⁾ as given in Table A-7.

d_s has been reported to increase with liquid surface tension^(119, 461-465) and decrease with liquid viscosity as reported by Peebles and Garber⁽⁴⁶⁰⁾, Akita and Yoshida⁽⁴⁶²⁾ and Wilkinson⁽⁴⁶⁵⁾. On the other hand, the bubble diameter appeared to decrease with both increasing liquid and gas density^(199, 465). Wilkinson et al.⁽²⁰⁰⁾ developed a Kelvin-Helmholtz stability analysis in order to explain the effect of gas density on the bubbles.

While the superficial gas velocity has been reported^(195, 196, 199, 200, 462, 465) to decrease the bubble diameter at low superficial gas velocity, Gaddis and Vogelpoohl⁽⁴⁶³⁾, Inga⁽⁵⁶⁾ and Behkish et al.⁽²¹⁴⁾ observed an increase of the bubble size at high superficial gas velocity, which was attributed the increase of the coalescence rate with UG in the

churn-turbulent flow regime. Increasing temperature has been reported ⁽¹⁷⁷⁾ to decrease the gas bubbles size, whereas increasing pressure was commonly found to decrease the bubbles size ^(56, 214, 188, 199, 235, 468, 469, 478).

It seems obvious from Section 2.3.2 that the column diameter and height to diameter ratio have a critical impact on the bubble size. In fact, due to their influence on the hydrodynamic regime they are expected to play a critical role. For instance, at small column diameter, since slug flow regime is governing, the bubbles size is enhanced due to wall effect ⁽²⁰¹⁾. The gas distributor design can also have an important effect on the Sauter mean bubble diameter. In fact, according to Mersmann ⁽⁴⁷³⁾ and Neubauer ⁽²⁰²⁾, the Weber number has to be greater than two in order to insure bubble breakage and axial mixing in the liquid:

$$We = \frac{\rho_G U_{G,0}^2 d_0}{\sigma_L} = \frac{\rho_G U_G^2 D^4}{N_s^2 d_0^3 \sigma_L} \quad (2-10)$$

where d_0 is the orifice diameter and N_s the number of orifices. The types of gas distributor have also been shown to have a significant impact on the bubble diameter as reported by Bouafi et al. ⁽¹⁸⁹⁾ as well as Camarasa et al. ⁽²⁰³⁾.

2.4.6 Bubble Size Measurement Techniques in gas-Liquid Contactors

The bubble size measurement techniques can be classified into two main categories ⁽²³⁾:

- Direct optical techniques
- Indirect techniques

Several direct techniques have been used to measure the gas bubble sizes in both agitated and bubble column reactors. High speed flash photography ^(23, 349, 144, 146, 154, 175, 186, 189, 194, 195, 204, 205, 206, 207, 459, 235, 238, 462, 318) as well as light scattering ^(119, 208) have been used in order to evaluate statistically the Sauter mean bubble diameter and the bubble size distribution in gas-liquid contactors. Indirect techniques such as ultra-sound ⁽²⁰⁹⁾, electrical resistivity probe ^(210, 177, 211, 230), photoelectric capillary ⁽²¹²⁾, acoustic ⁽²¹³⁾, capillary probe ⁽¹⁴⁴⁾ and gas disengagement ^(56, 174, 175, 214, 215) have also been carried out to measure the gas bubble size. Since most of these techniques provide local measurement of the bubble size, it should be mentioned that unless tedious study of the entire reactor at different positions is carried out, extreme care should be taken to use these measurement in overall calculations. It is also important to point out that most of these techniques have been extensively used at atmospheric pressure and room temperature, but due to the lack of adequate instrumentation only few studies have been completed under typical industrial conditions, i.e. high temperatures and pressures ⁽²¹⁶⁾.

2.4.7 Gas Holdup in Agitated Reactors

The gas holdup, ε_G , defined as the gas volume fraction present in the expanded volume of the reactor, has tremendous impact on the hydrodynamics and heat as well as mass transfer, since it can control the gas-liquid interfacial area ⁽⁵⁶⁾. Thus, it is necessary to study the effect of operating conditions, physical properties and reactor design on ε_G in order to assess the parameters influencing the gas-liquid interfacial area. In the following, different

techniques used to determine the gas holdup in gas-liquid contactors will first be reviewed. Then, the effect of physical properties, operating conditions and reactor design on the gas holdup will be discussed.

As shown in Table A-8, ε_G has been reported to decrease with increasing liquid surface tension^(72, 75, 76, 104, 118, 126, 128, 129, 132, 134, 149) and decreasing liquid density^(72, 106, 107, 118, 126, 129, 132, 149) in the three types of agitated reactors. The effect of liquid viscosity on ε_G , on the other hand, appears to be controversial, since Matsumura et al.⁽⁷²⁾ in the SAR, Saravanan and Joshi⁽¹⁰⁷⁾, Heim et al.⁽¹⁰⁶⁾ and Tekie⁽²³⁾ in the GIR, and Loiseau et al.⁽¹²⁸⁾ in the GSR found that ε_G decreases with increasing liquid viscosity, whereas Murugesan found that ε_G values increase with increasing liquid viscosity in the GSR. Furthermore, He et al.⁽⁹⁸⁾ in the GIR and Rushton and Bimbenet⁽¹²²⁾ in the GSR found that ε_G first increases and then decreases with increasing liquid viscosity, revealing a maximum. In addition, Shridhar and Potter⁽¹³²⁾ reported an increase of ε_G with increasing gas density, which was attributed to the increase of gas momentum⁽¹⁷⁸⁾.

The mixing speed^(23, 349, 72, 80, 104, 106, 134, 149), superficial gas velocity^(72, 107, 118, 122, 126, 128, 129, 132, 134, 149) and power input^(75, 76, 96, 98, 107, 118, 122, 126, 128, 130, 132) have been reported to increase ε_G whereas the effect of temperature on ε_G appeared to be reactor dependent. Fillion⁽³⁴⁹⁾ found that ε_G decreases with temperature in the GIR and increases in the GSR. Few and controversial studies on the effect of pressure on ε_G can be found, since for instance, Fillion⁽³⁴⁹⁾ reported negligible effect of pressure on ε_G , while Shridhar and Potter⁽¹³²⁾ found an increase of ε_G with pressure in agitated reactor.

The effect of impeller and reactor types and diameter has been reported to have an important influence on the gas holdup^(72, 75, 76, 106, 107, 120, 121, 134, 149). An increase of the number of impellers and diameter has been observed to increase ε_G , whereas an increase of reactor diameter was found to decrease ε_G . The sparger design in the GSR has also been found^(70, 84, 134) to have a tremendous impact on the gas holdup, due to the critical role played by the orifice during the bubble formation. Although extensive studies on ε_G have been carried out, it should be stressed that Table A-8 clearly shows a lack of experimental data under typical industrial conditions, i.e. high pressures^(349, 132, 145) and temperatures^(349, 132).

2.4.8 Gas Holdup in Bubble Column Reactors

Effect of physical properties on ε_G in bubble column reactors: In Table A-9, ε_G has commonly been found to decrease with increasing liquid surface tension^(178, 187, 190, 191, 470, 471, 473-475, 477, 478) and viscosity^(190, 191, 472, 474, 476-478). The effect of liquid density on ε_G , however, is questionable since ε_G has been reported to increase^(190, 191, 471, 473, 476, 477) and decrease^(178, 470, 472, 475, 478) with increasing liquid density. This controversial behavior appeared to be linked to the coalescing nature of the liquid employed. The gas density, on the other hand, was generally found to increase ε_G ^(178, 190, 191, 474, 475, 478). It should also be mentioned that a number of investigators^(182-184, 190, 191, 238, 217), using the dynamic gas disengagement technique, characterized the fraction of total ε_G that corresponds to small and large gas bubbles. Krishna and Ellenberger⁽²¹⁷⁾ found that the fraction that corresponded to small gas bubbles was strongly dependent

on the system physical properties, whereas the fraction corresponding to large bubbles was independent of the liquid properties.

The superficial gas velocity^(176, 178, 190, 191, 195, 470-478) has been reported to increase ε_G . The effect of temperature has been found to increase ε_G ^(177, 187, 195, 477) due to the decrease of both liquid surface tension and viscosity. Also, increasing pressure appeared to significantly increase ε_G ^(172, 180, 182, 183, 185, 188, 192), which was generally attributed to an increase of gas density.

The effect of column geometry has a major influence on ε_G . In fact, as can be observed the hydrodynamic parameters in Table A-9 are only reported for column diameter greater than 0.15 m. Fair et al.⁽⁵⁰⁴⁾ and Yoshida and Akita⁽²¹⁸⁾ reported a strong effect of column diameter below 0.15 m on ε_G , and this was further inferred by Shah et al.⁽²¹⁹⁾ who showed that ε_G was independent of column diameter if the column diameter was above 0.1-0.15 m. Moustiri et al.⁽¹⁹⁴⁾ and Eickenbusch et al.⁽³²⁰⁾ also reported, that no noticeable effect of column diameter and column height on ε_G could be observed in the churn turbulent flow regime for diameters greater than 0.15 m and height to diameter ratio between 6 and 11. Nonetheless, Moustiri et al.⁽¹⁹⁴⁾ reported a pronounced effect of column diameter on ε_G at low gas velocity. Pino et al.⁽²²⁰⁾ and Guy et al.⁽¹⁹⁸⁾ found that ε_G was unaffected by the column dimensions for height to diameter ratio between 6 and 12 and 3 and 12, respectively. The design of the gas distributor has also been reported to have a tremendous effect on ε_G values⁽²²¹⁾, especially at low gas velocities. In fact, depending on the gas sparger design, orifices number and diameters, the energy consumption changes and can affect considerably the bubble size, flow regime and ε_G ^(189, 195, 202, 203, 473). ε_G has been extensively studied, as shown in Table A-9, using air/water system, under atmospheric conditions and in small diameter columns. There are obviously serious limitations of these studies, when using them for scale-up purposes of organic chemical processes operating under high pressures and temperatures in large reactors. Numerous publications concerning ε_G in BCRs are available, but unfortunately only few were obtained in large diameter columns (≥ 0.15 m) under typical industrial conditions^(177, 187, 195, 207, 222, 223). Therefore, it is essential to investigate ε_G behavior under typical industrial conditions.

2.4.9 Gas Holdup Measurement Techniques in gas-Liquid Contactors

Several methods have been developed in order to measure the gas holdup in gas-liquid contactors. The dispersion height technique is a direct method, where the liquid height is measured under gassed and ungassed conditions⁽²²⁴⁾. This method, however, has been reported to lack accuracy when waves or foam are formed at the liquid surface⁽²¹⁶⁾. An alternative to this technique is the manometric method or gas disengagement technique^(23, 56, 118, 174, 214, 225, 281), which indirectly measures the gas holdup. In fact, by using high accuracy differential pressure cells (DP), the pressure difference between two points in the reactor is measured. The gas holdup is then calculated precisely even under high temperatures and pressures. Other techniques such as ultrasound and real time neutron radiography⁽²⁰⁹⁾, X- and γ -ray⁽²²⁶⁾ and electrical resistivity probe⁽²²⁷⁾ have also been employed but less frequently in gas-liquid contactors to measure the gas holdup.

Table 11: Comparison of Small and Large Bubble Diameters in the BCR

<i>Authors</i>	<i>Distributor</i>	<i>Gas/Liquid</i>	<i>Remarks</i>
Quicker and Deckwer ⁽²²⁸⁾	S-ON / PoP / PP $d_o = 0.9\text{mm}$.	N_2 / Vestowax	$d_b = 0.5\text{-}0.6\text{ mm}$.
Godbole et al. ⁽¹⁷¹⁾	PP / 1.66mm	Air / Sotrol	$u_{b,small} = 0.1\text{m/s}$
Molerus and Kurtin ⁽¹⁷³⁾	PP/Porous plate $d_o = 0.5, 1\text{mm}$	Air / Water + butanol	Bubble sizes deduce from gas throughput and mean void fraction in the homogeneous bubbly regime
Fan et al. ⁽²²⁹⁾	Packed Bed	Air / Alcohol Solutions	$d_b = 0.5\text{-}1.5\text{ mm}$
Fukuma et al. ⁽²³⁰⁾	M-ON / 2.6 mm	Air / Water glycerol	$d_b = 0.01\text{m}$, $u_G = 0.1\text{ m/s}$, 0 wt.% / $d_b = 0.03\text{m}$, ~20 wt.%
Patel et al. ^(231, 232)	PP / 2 mm	N_2 / Waxes	FT300 $d_{b,small} = 0.3\text{-}0.9\text{mm}$ / $d_{b,large} = 9\text{-}58\text{mm}$
Daly et al. ⁽¹⁷⁴⁾	PP / $d_o = 2\text{ mm}$	N_2 / Wax	$d_b = 0.5\text{-}2\text{mm}$
Grund et al. ⁽¹⁷⁵⁾	PP / 2.3 mm SP / 0.2 mm	Air / Water, methanol, toluene, ligroin	$u_{b,small} = 0.2\text{m/s}$, $u_{b,large} = 0.6\text{m/s}$ $d_{b,small} = 2\text{-}3\text{ mm}$.
Solanki et al. ⁽²³³⁾	Filter cloth / 2mm	Air / Solutions	$d_{b,small} = 1\text{mm}$, $d_{b,large} = 11\text{ mm}$.
Hyndman and Guy ⁽²³⁴⁾	PP / 1mm	Air / Water	Bubbly Flow $u_b = 0.2\text{ m/s}$ Churn-turbulent $u_b = 0.35\text{ m/s}$
Jiang et al. ⁽²³⁵⁾	M-ON / 3mm	N_2 / Paratherm Oil	Effect of Pressure can reduce d_b from 5mm to 0.7 mm
Kundakovic and Novakovic ⁽²³⁶⁾	S-ON / 4mm	Air / Water	$d_{b,small} = 0.5\text{ mm}$, $d_{b,large} = 3\text{-}5\text{ mm}$, $d_p = 2.5\text{ mm}$.
Smith et al. ⁽²³⁷⁾	PP / 3 mm	Air / Water glycerol	$d_b = 16.5\text{ mm}$, 1bar, 10wt%/ $d_b = 7\text{ mm}$, 8 bar, 10 wt.%
De Swart ⁽¹⁷⁹⁾	SP / 0.2 mm	Air / Oil	$d_b = 1\text{ mm}$, 0 wt.% / $d_b = 0.1\text{ m}$, 32 wt.%
Inga ⁽⁵⁶⁾	Spider / 5 mm	$H_2, N_2, CO, CH_4 / C_6$	$d_{b,small} = 3\text{mm}$ $u_{b,small} = 0.2\text{m/s}$, $d_b = 4\text{-}10\text{mm}$ 0 wt.%, $d_b = 20\text{-}40\text{mm}$ 50wt.%
Krishna et al. ⁽²³⁸⁾	S-ON	Air / water	Estimation of large bubble swarm velocity
Large et al. ⁽²³⁹⁾	PP / 0.5 mm	Air / Aqueous isopropanol	Homogeneous regime for velocity lower than 0.05 m.s^{-1}
Krishna et al. ⁽¹⁸⁸⁾	SP / 0.5mm	Air / Water + alcohol	Pressure promotes the break up of large bubbles
Kemoun et al. ⁽¹⁹²⁾	PP / 0.4mm	Air / Water	Churn-turbulent regime delayed by pressure

PP=Perforated Plate, S-ON=Single Orifice, SP=Sintered Plate, PM=Perforated Membrane, M-ON=Multiple Orifices, PoP:Porous Plate

2.5 MASS TRANSFER CHARACTERISTICS

Despite the known impact of mass transfer on the liquid-phase toluene oxidation process^(8, 240, 241), few data are available in the literature. Bejan et al.⁽²⁴¹⁾ studied the electrochemically- assisted liquid-phase oxidation of toluene in acetic acid in the presence of cobalt catalyst, and pointed out the major impact of the oxygen flow rate and mass transfer rate on the yield of benzoic acid. Mills et al.⁽⁸⁾, who underlined the importance of mass and heat transfer in oxidation processes, also reported the importance of a critical oxygen ratio in the reactor inlet in order to achieve maximum efficiency under steady state for liquid-phase catalytic oxidation following red-ox mechanism. Panneerlvam et al.⁽²⁴⁰⁾ studied the kinetics of liquid-phase oxidation of toluene to benzoic acid in a packed bed reactor and noticed the importance of the mass transfer and hydrodynamic characteristics of the system in order to model and optimize the process. Based on a correlation from Mohunta et al.⁽²⁴²⁾, their model provided an overall rate for the process; including both kinetic and mass transfer resistance. Alternatively, in the BCR Ozturk et al.⁽²⁴³⁾, Grund et al.⁽¹⁷⁵⁾ as well as Jordan and Schumpe⁽¹⁹⁰⁾ and Jordan et al.⁽¹⁹¹⁾ reported mass transfer parameters for air and nitrogen in toluene. In the following, a review of the different techniques used to measure the gas-liquid interfacial area, volumetric mass transfer coefficient and mass transfer coefficient will be presented. Then, through the analysis of physical models, the effect of physical properties, operating conditions and reactor geometrical parameters on a , $k_L a$ and k_L reported in the literature will be discussed for the agitated reactors and the BCR.

2.5.1 Mass Transfer Measurement Techniques in Gas-Liquid Contactors

Several methods have been developed in order to measure the gas-liquid interfacial area, a in gas-liquid contactors. The gas-liquid interfacial area can be measured using physical or chemical methods. Optical methods, such as photographic⁽¹¹⁸⁾, light reflection^(118, 244) and light scattering⁽²⁴⁵⁾ were used as physical techniques, however, they were restricted to transparent contactors having low gas holdup⁽²⁰⁹⁾. Other physical methods including γ -ray radiography⁽²⁰⁹⁾ and real time neutron radiography⁽²⁰⁹⁾ have also been used to estimate a . The chemical techniques, on the other hand, were used to measure the gas-liquid interfacial area. Midoux and Charpentier⁽²⁴⁶⁾ reviewed various chemical reactions, where it is possible to measure a . The limitation of this method is that the reaction kinetics are needed before measuring a . While these previous procedures mainly help to reveal the bubble contributions to a , other measuring techniques have been used in ripple tank to determine a at the gas-liquid interface. Muenz and Marchello^(61, 62), measured the wave frequency using a stroboscope and determined the amplitude through the analysis of the refractive surface properties via a Photovolt photometer and densitometer. Recently, Vazquez-Una et al.⁽⁸⁶⁾ used a CDD camera viewing the surface at a 45° angle to calculate through digitized images analysis the wavelength λ . The surface peak-to-peak amplitude and frequency were determined from the surface displacement recorded using a vertically oriented laser triple-range distance-measuring device.

Depending on the systems used, likewise a , both the chemical or physical method^(247, 248) have been employed to measure $k_L a$ in gas-liquid contactors. In the physical methods, the physical gas absorption or desorption is monitored by pressure transducers or gas probes⁽²³⁾ as a function of time under defined conditions. The transient pressure decline technique appears to be the most successful method used^(11, 23; 249). For instance, Chang and Morsi^(250, 251, 252) developed a powerful model to describe the transient pressure decline, based on a modified Peng-Robinson EOS and mass balance. The improvement brought by this model is discussed elsewhere⁽²⁴⁹⁾. In the chemical methods, reviewed by Danckwert et al.⁽²⁵³⁾, $k_L a$ data are obtained by combining known kinetics and mass transfer under chemical reaction conditions. The difficulty of temperature control, as well as the lack of kinetics data, however, seem to set the boundaries of the chemical method. The direct determination of k_L is only possible through the chemical method⁽²²⁴⁾, but can, however, be indirectly calculated from the measurement of $k_L a$ and a ^(118, 133, 224, 247, 253).

2.5.2 Gas-liquid Interfacial Area in Gas-Liquid Contactors, a

The gas-liquid interfacial area, a strongly affect the volumetric mass transfer coefficient, $k_L a$. Thus, it is critical to study the effect of operating conditions, physical properties and reactor geometry on a to evaluate the criteria influencing the mass transfer parameters. In the following, the different techniques used to determine a in gas-liquid contactors will be reviewed and the effect of physical properties, operating conditions and reactor design on a reported in the literature will then be discussed.

In the SAR, a has been usually calculated as the reciprocal of the liquid height, by assuming that the liquid surface remains flat^(11, 23, 56, 349, 67). However, as discussed in Section 2.4.1, under specific conditions gas bubbles are entrained from the surface and therefore can have a significant impact on the total interfacial area^(72, 79, 120). Matsumura et al.⁽⁷²⁾ found an increase of a with the number of impellers and a decrease with the impeller height below the surface. While these previous investigators studied the effect of gas entrainment in the SAR, recently Vazquez-Una et al.⁽⁸⁶⁾ discussed the effect of ripples at the surface of rippled tanks. This study is important since it is well accepted that the agitator creates ripples at the liquid surface of agitated reactors even equipped with baffles. Vazquez-Una et al.⁽⁸⁶⁾, however, concluded that the wavy interface had more influence on the enhancement of the mass transfer coefficient than on the increase of a , which could be considered unaffected by the ripples. Under sparged conditions, it was found that a increases with the number of impellers^(129, 138). Calderbank⁽¹¹⁸⁾, Fuchs et al.⁽¹²⁵⁾ and Miller⁽¹²⁶⁾ also reported an unexpected increase of a under elevated agitation, due to gas bubbles entrainment from the surface. Fuchs et al.⁽¹²⁵⁾ and Miller⁽¹²⁶⁾, who studied the impact of gas entrainment on the GSR scale-up, concluded, however, that the effect of gas entrainment diminishes significantly with the reactor size, becoming negligible for tanks greater than 0.2 m³ in volume. Although the effect of reactor geometry on a in the GIR^(23, 349) and BCR⁽¹⁴²⁾ has been scarcely studied, Filion⁽³⁴⁹⁾ and Tekie⁽²³⁾ observed an increase of a with decreasing liquid height in the GIR. From the literature data shown in Table A-10, it can be concluded that a is expected to follow:

$$\text{BCR} > \text{GSR} > \text{GIR} \gg \text{SAR} \quad (2-11)$$

While a has been reported to decrease with both the liquid surface tension^(72, 118, 120, 126, 133, 134, 462) and viscosity^(72, 142, 171, 462, 506), the liquid density^(72, 118, 120, 126, 133, 134, 462) seemed to increase a in all reactor types. a was also found to increase with gas density in the GSR and BCR⁽¹³³⁾.

a has been reported to increase with increasing mixing speed^(72, 104, 120, 134), superficial gas velocity^(72, 104, 118, 126, 130, 133, 134, 171, 506) and power input^(95, 96, 104, 118, 126, 130, 133), while the effect of temperature has been scarcely reported^(23, 349). In fact, Fillion⁽³⁴⁹⁾ reported a decrease of a with temperature in the GIR, and an increase in the GSR. Tekie⁽²³⁾, on the other hand, found that temperature had negligible effect on a . Fillion⁽³⁴⁹⁾ also reported negligible effect of pressure on a in both the GSR and GIR, whereas Shridhar and Potter⁽¹³²⁾ found that increasing pressure resulted in an increase of a in the GSR. Few studies have reported the gas-liquid interfacial area in the BCR, SAR or GIR under typical industrial conditions as clearly shown in Table A-10. Thus, it is essential to investigate the effect of process variable on the gas-liquid interfacial area behavior under typical industrial conditions for the liquid-phase toluene oxidation process.

2.5.3 Volumetric Mass Transfer Coefficient, k_La

Empirical, statistical and phenomenological correlations have been used to predict the volumetric mass transfer coefficient in agitated reactors. In the SAR, it appears that k_La follows essentially the trend of the mass transfer coefficient, k_L ^(11, 23, 67, 249, 349), since the absorption takes place at the free gas-liquid interface. Thus, an increase in mixing speed, power input, impeller diameter or a decrease in the liquid height and vessel diameter, will result in an increase of the volumetric mass transfer coefficient^(11, 23, 67, 249, 349). The diffusivity, on the other hand, has been reported in all correlations to be proportional to k_La to power ranging between 0.5 and 1, which is in good agreement with the penetration theory and film model, respectively. While it appears that there is a good agreement on the effect of liquid viscosity on k_La , the effect of liquid density and surface tension are controversial. In fact, increasing liquid viscosity is generally found in Table A-11 to decrease k_La , whereas increasing liquid density and surface tension were reported to increase or decrease^(11, 23, 67, 266, 457, 482) k_La . Additional controversial findings on the effect of pressure were reported k_La . In contrast, the temperature was generally reported to increase k_La in the SAR^(11, 23, 67, 349).

In the GIR, below the critical mixing for gas induction, the reactor performs exactly as an SAR, since no gas bubbles are induced in the liquid phase. Therefore, under such conditions k_La behaves as in the SAR. When the critical mixing for gas induction is reached, however, gas bubbles start to be induced and dispersed in the liquid phase, increasing considerably a and therefore k_La . Consequently, both a and k_L can influence k_La values. Increasing the mixing speed, power input, impeller diameter or decreasing the liquid height and vessel diameter increases the turbulences inside the reactor and the pumping capacity of the impeller. Thus, both a and k_L increase and subsequently k_La as often found^(23, 349, 92, 96, 106, 111, 249-252, 271, 272, 485-488). On the other hand, the effect of physical properties on k_La appears to be system-dependent since the overall trends of k_La as shown in Table A-12 with liquid viscosity, density and surface tension are different. It appears also that increasing temperature leads to a decrease of

$k_L a$ ^(23, 349) in the GIR, whereas the effect of pressure seems more complex and was generally found to be negligible^(23, 349).

In the GSR, since the gas is being sparged into the liquid, a has a crucial impact on $k_L a$. $k_L a$ was found to increase substantially with the gas superficial velocity, mixing speed, total power input and impeller diameter^(81, 130, 247, 276, 281, 283, 285, 286, 289, 349). The liquid viscosity, on the other hand, was clearly^(349, 280, 288) reported to decrease $k_L a$ in the GSR, while the density showed an increasing effect^(280, 288). Unlike the GIR, it appears that in the GSR, $k_L a$ increases with temperature^(349, 284). The diffusivity was also reported to be proportional to $k_L a$ to a power n ranging between 0.5 and 1. Thus, despite the fact that extensive studies on $k_L a$ have been reported in the literature for agitated reactors, as shown in Tables A-11 through A-13, the majority of these studies were usually carried out in aqueous media under ambient conditions.

The behavior of BCRs has been reported to be controlled by the gas-liquid interfacial area^(56, 254), hence it is expected that $k_L a$ values follow the trend of the gas-liquid interfacial area. While increasing liquid viscosity and decreasing liquid density were found to reduce the volumetric mass transfer coefficient^(170, 171, 175, 504, 489, 491), the effect of surface tension on $k_L a$ appears to be controversial or somewhat system-dependent^(170, 294, 490). The superficial gas velocity⁽²⁵⁴⁻⁴⁹⁵⁾, pressure^(254, 175, 494, 495) and temperature^(190, 191), on the other hand, have been reported to increase $k_L a$. The column diameter and sparger design have also been reported to have a tremendous impact on $k_L a$. In fact, Jordan and Schumpe⁽¹⁹⁰⁾ in different diameter columns using a single orifice, sintered plate and perforated plate, reported changes in $k_L a$ values of O₂ in toluene emphasizing the impact of gas distributors and column diameters on the mass transfer parameters. Although the volumetric mass transfer coefficients have been extensively reported in the BCR, most of the literature studies were carried out with air and aqueous media, and were usually limited by the operating conditions under which they were obtained, i.e. under atmospheric pressure and ambient temperature^(175, 243). In fact, most of the experiments reported in Table A-14 were obtained in small-scale reactors, increasing the risk of wall effects and limiting the applications of mass transfer values to small diameter columns^(190, 191, 462).

Table 12: Literature Survey on Mass Transfer in Surface Aeration Reactors

<i>References</i>	<i>Gas/Liquid</i>	<i>Operating Conditions</i>	<i>Remarks</i>
Eldib and Albright ⁽²⁵⁵⁾	H ₂ /Cottonseed oil	2-11 bar/388-433 K	G-L mass transfer negligible at high N
Albright et al. ⁽²⁵⁶⁾	H ₂ /Cottonseed oil	3-8 bar /408-418 K	G-L mass transfer negligible at high N
Muenz and Marchello ⁽⁶²⁾	O ₂ , He, CO ₂ , C ₃ H ₆ /Water	Atm.	Effect of wavy interface on D_E
Yoshida et al. ⁽²⁵⁷⁾	O ₂ /H ₂ O, KCl	1-20 bar / 310 K	k_L decreases with P , increases with N
van Dierendonck et al. ⁽⁶⁵⁾	-	-	Effect of reactor geometry on k_L
Kataoka et al. ⁽²⁵⁸⁾	O ₂ ,He,CO ₂ ,H ₂ /Water,ethanol, toluene,benzene	-	Effect of liquid properties, N on k_L
Teramoto et al. ⁽²⁵⁹⁾	H ₂ ,He,Ar,CO ₂ ,N ₂ /H ₂ O,ethanol,p-xylene	2-101 bar / 298 K	k_L decreases with P for p-xylene
Farritor and Hughnark ⁽²⁶⁰⁾	Air/Water	294.5 K / 0.7 Hz	Effect of energy dissipation on kLa
Zwicky and Gut ⁽²⁶¹⁾	H ₂ /o-cresol	10-60 bar/363-433 K	k_La increases with N
Takase et al. ⁽²⁶²⁾	Air/Water	298 K / 1.6-41.6 Hz	Effect of H_L on k_La
Hozawa et al. ⁽²⁶³⁾	O ₂ ,N ₂ /Methanol,CCl ₄ ,benzene,nitrobenzene,H ₂ O	298 K / 2-4 Hz	Effect of surface tension on k_L
Albal et al. ⁽⁶⁷⁾	O ₂ ,He,CO,H ₂ ,N ₂ /wax,H ₂ O,glycerin,CMC,soltrol-130,sodium sulfite	6-97 bar/295-523 K	k_La independent of P , decreases with kL and increases with T and N
Ledakowicz et al. ⁽²⁶⁴⁾	CO, H ₂ , CO ₂ , N ₂ /Vestowax	5-60 bar/354-554 K	k_La increases with N
Deimling et al. ⁽²⁶⁵⁾	CO,H ₂ /F-T liquids	10-40 bar/373-523 K	k_La increases with P , T decreased with CN . k_L was independent of P
Versteeg et al. ⁽²⁶⁶⁾	CO ₂ ,N ₂ O/H ₂ O,H ₂ SO ₄ ,alkanolamine	1-10 bar/291-355 K	k_L increases with N and T
Tekie et al. ⁽²⁶⁷⁾	N ₂ , O ₂ /Cyclohexane	7-35 bar/330-430 K 6-20 Hz/0.171-0.268m	k_La increases with N , decreases with H . independent of P and T
Mohammad ⁽¹¹⁾	N ₂ , O ₂ /Benzoic acid	1-5 bar /423-523 K 100-23.3 Hz	k_La increases with N , and with T and P
Fillion and Morsi ⁽²⁶⁸⁾	N ₂ , H ₂ /Soybean Oil	1-5 bar/373-473 K 10-23 Hz/0.171-0.268m	k_La increases with N and T , decreased with H , no effect of P
Vazquez-Una et al. ⁽⁸⁶⁾	CO ₂ /Water		Effect of wave frequency on k_L
Woodrow and Duke ⁽²⁶⁹⁾	O ₂ /Water		Waves increase k_L by half a fold

Table 13: Literature Survey on Mass Transfer in Gas Inducing Reactor

<i>References</i>	<i>Gas /Liquid</i>	<i>Operating Conditions</i>	<i>Remarks</i>
Topiwala et al. ⁽⁹⁰⁾	Air /K ₂ SO ₄ (aq.)	303 K	$k_L a$ increases with N
Joshi and Sharma ⁽⁹²⁾	Air/Sodium dithionite sol.	Atm./d _{imp} .0.2-0.5/d _T 0.41-1	Effect of reactor size and impeller design on a and $k_L a$
Pawlowski and Kricsfalussy ⁽²⁷⁰⁾	H ₂ /DNT	41 bar / 393-433 K	$k_L a$ is a function of P^*/V_L
Kara et al. ⁽²⁷¹⁾	H ₂ /Tetralin, coal liquid	70-135 bar / 606-684 K	$k_L a$ increases with and decreases with
Karandikar et al. ⁽²⁷²⁾	CO, CH ₄ , CO ₂ , H ₂ / F-T liquids containing water	10-50 bar / 373-573 K	$k_L a$ increases with P , N , P^*/V_L , decreases with H/d_T
Eiras ⁽²⁷³⁾	H ₂ , C ₂ H ₄ , C ₃ H ₆ /n-Hexane	1-40 bar / 313-353 K	$k_L a$ increased with N . Effect of P and T was not clear
Lee and Foster ^(58, 274)	O ₂ , CH ₄ /Silicon fluid, perfluoroalkyl,polyether	10-70 bar / 293-573 K	$k_L a$ increased with N , P and T , $(k_L a)_{O_2} > (k_L a)_{CH_4}$
Zlokamik et al. ⁽²⁷⁵⁾	O ₂ ,N ₂ /Water, Na ₂ SO ₄ , NaCl	2 bar / 293 K	$k_L a$ increases with $(P^*/V_L)^{0.8}$
Chang ⁽²⁴⁹⁾	H ₂ , N ₂ , H ₂ O, CO, CH ₄ /n-C ₆ H ₁₄ , n-C ₁₀ H ₂₂ , n-C ₁₄ H ₃₀ , c-C ₆ H ₁₂	1-60 bar 328-528 K	$k_L a$ increases with N , decreases with H . Effect of P and T on $k_L a$ is system dependent
Al Taweel et al. ⁽¹⁰⁴⁾	Air/Water+ propylene glycol methyl ether	298 K / Atm.	Effect of surface tension on a
Hsu et al. ⁽¹⁰⁹⁾	Ozone/Water	298 K	$k_L a$ increases with N , due to the increase of ε_G
Tekie et al. ⁽²⁶⁷⁾	N ₂ , O ₂ /Cyclohexane	7-35 bar /330-430 K 6-20 Hz/0.171-0.268m	$k_L a$ increases with N , decreases with H . Effect of P on $k_L a$ is system dependent. Effect of T is not clear
Mohammad ⁽¹¹¹⁾	N ₂ , O ₂ /Benzoic acid	1-5 bar /423-523 K 100-23.3 Hz	$k_L a$ increases with N , and slightly with T and P
Fillion and Morsi ⁽²⁶⁸⁾	N ₂ , H ₂ /Soybean Oil	1-5 bar / 373-473 K 10-23 Hz / 0.171-0.268m	$k_L a$ increases with N , decreases with H and T . $k_L a$ is independent of P .

Table 14: Literature Survey on Mass Transfer in Gas-Sparged Reactors

References	Gas /Liquid	Operating Conditions	Remarks
Calderbank ⁽¹¹⁸⁾	Air/Water, toluene, alcohols, glycols, CCl ₄ , nitrobenzene, ethylacetate	298 K / $Re > 10^4$ 0.003-0.02 m.s ⁻¹	Determination of a and effect of surface entrainment on the total a
Yoshida et al. ⁽²⁷⁶⁾	O ₂ , air /H ₂ O, Na ₂ SO ₃ , Na ₂ SO ₄	1 bar / 280-313 K	$k_L a$ increases with N but independent of T , k_L increases with N
Wisniak and Albright ⁽²⁷⁷⁾	H ₂ /Cottonseed oil	11-105 bar / 373-403 K	G-L mass transfer resistance negligible at high N
Westerterp et al. ⁽¹²⁰⁾	Air/Sulphite solution	303 K / 100-3600 rpm 0.001-0.035 m.s ⁻¹	Effect of impeller type on a and k_L
Brian et al. ⁽²⁷⁸⁾	Pivalic acid/H ₂ O	-	Effect of power input on k_L
Mehta and Sharma ⁽⁶⁴⁾	Air/Cuprous chloride	-	Effect of reactor design, liquid properties on $k_L a$, k_L and a
Bossier et al. ⁽⁶⁶⁾	N ₂ , O ₂ /Tetradecane, p-xylene, Nujol, alkyl	293 K / Atm.	Determination of $k_L a$, k_L and a
Prasher and Wills ⁽²⁷⁹⁾	CO ₂ /Water	-	Effect of P^* on k_L
Miller ⁽¹²⁶⁾	CO ₂ /Air/Aq. solution	-	Effect of reactor size and impeller design on $k_L a$
Perez and Sandall ⁽²⁸⁰⁾	CO ₂ /Carbopol solution	Atm./297-308 K/3-9 Hz 0.162-0.466 m.s ⁻¹	$k_L a$ of non-Newtonian fluids in sparged vessels
Robinson and Wilke ⁽²⁸¹⁾	N ₂ , CO ₂ /Aq. solutions	303 K / Atm.	Effect of P^* , N on k_L and a
Yagi and Yoshida ⁽²⁸²⁾	O ₂ , N ₂ /Glycerol-water, Millet -jelly-water	303 K/ 300-600 rpm 0.002-0.08 m.s ⁻¹	Effect of liquid properties on $k_L a$
Bern et al. ⁽²⁸³⁾	Fat	1.2-1.5 bar / 453 K	$k_L a$ increases with N , d_{Imp} , U_G , decreases with V_L
Marangozis et al. ⁽²⁸⁴⁾	H ₂ /Cottonseed oil	2-8 bar / 393-433 K	$k_L a$ increases with N and T but decreases with P
Lopes de Figueiredo and Calderbank ⁽¹³⁰⁾	O ₂ /Water	Atm./ 300-500 rpm 0.41-4.8 kW.m ⁻³ 0.006-0.013 m.s ⁻¹	Effect of reactor size on gas entrainment, P^* and $k_L a$ for scale-up
Matsamura et al. ⁽²⁸⁵⁾	O ₂ , CO ₂ , H ₄ , C ₈ H ₈ /Sodium sulfite, H ₂ O	303 K / 500-800 rpm 0.0005-0.003 m.s ⁻¹	Chemical and physical method used to measure $k_L a$. No effect of flow rates under high P^*
Meister et al. ⁽²⁸⁶⁾	Air/Aqueous solutions	400-1200 rpm 0.005-0.03 m.s ⁻¹	Effect of multi-impeller on $k_L a$.
Sridhar and Potter ^(132,133)	N ₂ /Cyclohexane	1-10 bar / 297-423 K	db decreases with N and P , both ε_G and a increases with N and P

Table 14 (Cont'd)

References	Gas /Liquid	Operating Conditions	Remarks
Nishikawa et al. ⁽²⁸⁷⁾	Air/Water	303 K / 0-1000 rpm 0.085-1.13 m.s ⁻¹	Effect of reactor design on k_La
Judat ⁽²⁸⁸⁾	Data from 13 publications	-	Review on gas-liquid mass transfer in stirred vessels
Gibilaro et al. ⁽²⁸⁹⁾	Air/Water	Atm. / 0.4-7 kW.m ⁻³ 0.005-0.025 m.s ⁻¹	Initial response analysis on mass transfer coefficient
Oyevaar et al. ⁽¹³⁹⁾	N ₂ , CO ₂ /DEA	0-20 bar/ 298 K	a and ε_G increases with N , independent of P .
Oyevaar et al. ⁽¹⁴²⁾	N ₂ , CO ₂ /DEA	0-80 bar / 298 K	a independent of P till 17 bar, then increases
Reisener et al. ⁽²⁹⁰⁾	N ₂ /Electrolyte sol.	-	Use of ANN to model k_La .
Stegeman et al. ⁽²⁹¹⁾	N ₂ , CO ₂ /DEA	0-66 bar / 298 K	a decreases with P at low pressures, increases with P at higher pressures
Wu ⁽⁸¹⁾	Air/Water	Atm. / 0.2-10 kW.m ⁻³ 0.003-0.007m.s ⁻¹	Comparison of SAR and GSR in terms of k_La
Yoshida et al. ⁽²⁹²⁾	Air/Water	Atm. / 150-400 rpm 0.004-0.06 m.s ⁻¹	Effect of sparger design, N and U_G on k_La and ε_G
Yang et al. ⁽²⁹³⁾	O ₂ /-	16 publications	Use of ANN to correlate k_La .
Fillion ⁽³⁴⁹⁾	N ₂ , H ₂ /Soybean Oil	373-473 K/ 10-23.3 Hz 1-5 bar / 10.4-51.9cm ³ .s ⁻¹	k_La increases with N , Q_G and T . No effect of P

Table 15: Literature Survey on Mass Transfer in Bubble Column Reactors

References	Gases U_G Max, m/s	Liquids	D_C , m	H, m	Sparger	Remarks
Akita and Yoshida ⁽⁴⁶²⁾	Air, O_2 / 0.07	H_2O , Glycol, Methanol, glycerol, Na_2SO_3 , CCl_4	0.077, 0.15, 0.30	2.5	PP, PG, S-ON	Effect of D_C on k_La and d_s
Hikita et al. ⁽²⁹⁴⁾	Air, H_2 , CO_2 , CH_4 , C_3H_8 / 0.38	H_2O , 30, methanol, n-butanol	0.10, 0.19	1.5, 2.4	2 and 3 S-ON	Effect of U_G on k_La
Kawase et al. ⁽²⁹⁵⁾	Air / 0.07	Water/CMC	0.23, 0.76 Draft tube	1.22, 3.71	OP, 3 PR	Effect of k_La in Newtonian and non-Newtonian systems
Moo Young and Kawase ⁽²⁹⁶⁾	CO_2 / 0.07	Water/Poly-acrylamide, 0.2 -0.6 %	0.23 Conical bottom	1.22	PP	Elasticity increases ε_G but not k_La
Ozturk et al. ⁽²⁴³⁾	Air, N_2 , CO_2 , He, H_2 / 0.1	Xylene, Tetralin, H_2O , C_7H_8 , Ethylacetate, decalin, Ligno A, B	0.095	0.85	S-ON	ε_G and k_La increases with ρ_G
Popovic et al. ⁽²⁹⁷⁾	Air / 0.1	Water/ Na_2SO_3	0.15, 0.1, 0.05 Down-comer	1.88	1mm S-ON	k_La in Newtonian Fluids
Popovic et al. ⁽²⁹⁸⁾	Air / 0.09	Water/CMC, Na_2SO_3	0.15, 0.10, 0.05 Down-comer	1.88	1mm S-ON	Effect of viscosity in re-circulating BCR
Cho et al. ⁽²⁹⁹⁾	N_2 / 0.054	Aq. sol. C_6H_6 , CCl_4 , $CHCl_3$, $(CH_2Cl)_2$	0.11	0.4	SO, 3 PG	k_La measured by desorption
Akita ⁽³⁰⁰⁾	Air	Water and electrolytes sol.	0.155	3	PP	k_La is system dependant
Allen et al. ⁽³⁰¹⁾	Air					k_La in fermentation sol.
Halard et al. ⁽³⁰²⁾	Air / 0.053	Water/CMC	O.D. 0.76, 0.35	3.2	PR/Draft tube	k_La in viscous solutions
Medic et al. ⁽³⁰³⁾	Air / 0.045	Na_2SO_3 /CoCl ₂ solution	Rect. 1x2	6	Aeration pad	k_La decreases with H
Popovic and Robinson ⁽³⁰⁴⁾	Air / 0.26	Water/CMC	0.15, 0.05 & 0.075 Down-comer	1.88		Down-comer is a dead zone for mass transfer
Uchida et al. ⁽³⁰⁵⁾	Air	Water, glycerol butanol sol.	0.046	1.36	PG, S-ON	k_La not f (gas sparger)
Vatai and Tekic ⁽³⁰⁶⁾	CO_2	Water/CMC	0.05, 0.1, 0.15, 0.2	2.5	SO	k_La decreases with D_C in pseudo-plastic systems
Seno et al. ⁽³⁰⁷⁾	Air	Water, glycerol butanol	0.046	1.36	PG, S-ON	k_La f(U_G , U_L , system)
Huynh et al. ⁽³⁰⁸⁾	Air / 0.25	Water	0.095	0.79		k_La proportional to ε_G
Kawase et al. ⁽³⁰⁹⁾	Air / 0.075	Water/ carboxypoly-methylene	0.23	1.22	PP	-
Rodemerck and Seidel ⁽³¹⁰⁾	Air	n-pentadecane	0.04	2	SP	-
Suh et al. ⁽³¹¹⁾	Air / 0.32	Water/Sucrose/Xantan P.A.A.	0.15	2.9		Effect of elastic fluids on k_La .

Table 15 (Cont'd)

References	Gases U_G Max, m/s	Liquids	D_C , m	H, m	Sparger	Remarks
Terasaka and Tusge ⁽³¹²⁾	Air	Water/ glycerol	0.1 / 0.2	1.21, 2.48	Several	Effect of viscosity and sparger design on $k_L a$.
Goto et al. ⁽³¹³⁾	Air	Water	0.1	3.7	Static mixer	Mixer increases $k_L a$
Merchuk and Ben Zvi ⁽³¹⁴⁾	Air / 0.1	Water	0.19	2.4	PR	Analysis is based on the Power per unit volume
Muller and Davidson ⁽³¹⁵⁾	Air / 0.08	Water	0.14	2.5		$k_L a$ of small bubbles is 20-50% of total
Kawasaki et al. ⁽³¹⁶⁾	Air	Water	0.157	2.03	S-ON	$k_L a$ proportional to G
Kawasaki et al. ⁽³¹⁷⁾	Air / 0.05	Water	0.15 Draft tube	2		Number of tubes increases $k_L a$
Wilkinson et al. ⁽³¹⁸⁾	Air / 0.2	Water, Hydrocarbons	0.158/ 0.25		PP	Effect of Pressure
Zhao et al. ⁽³¹⁹⁾	CO ₂ / 0.06	Water, Hydrocarbons	0.14/ 0.09	2.5	PP	Internals increases $k_L a$
Eickenbusch et al. ⁽³²⁰⁾	O ₂ / 0.10	Xanthan, hydroxypropyl guar sol.	0.19, 0.29, 0.60	2.8, 4.5, 5.75	PP, PP, PR	Effect of pseudoplastic liquid on $k_L a$
Laari et al. ⁽¹⁸¹⁾	Air / 0.03	Water, water+phenol	0.19, 0.97	0.67-4.64	T-nozzle	Effect of H , U_G , C on $k_L a$
Terasaka et al. ⁽³²¹⁾	Air/ 0.15	water, xanthan, gellan	0.06, 0.114	-	PP	Effect of U_G on $k_L a$
Vazquez et al. ^(322, 323)	CO ₂ /0.002	NaHCO ₃ , Na ₂ CO ₃ +surfactants	0.113	1.086	PG	k_L , a decrease with addition of surfactant
Jordan et al. ⁽¹⁹¹⁾	He, N ₂ , Air/0.21	C ₂ H ₅ OH, C ₄ H ₉ OH, decalin, C ₇ H ₈	0.1, 0.115	1.3, 1.0	Several PP	Effect of D_{AB} , distributors, U_G , ρ_G and T on $k_L a$

PP=Perforated Plate, PR=Perforated Ring, S-ON=Single Orifice, BC=Bubble Cap, SP= Sintered Plate, PG= Porous Glass, OP= Orifice Plate

2.5.4 Mass Transfer Coefficient, k_L

The two film model: “Whitemans model” was first introduced by Whiteman in 1923⁽⁴⁹⁷⁾, and considers that the gas is being absorbed by molecular diffusion alone across a stagnant liquid film of thickness δ . While the liquid composition is assumed constant due to mixing in the bulk, the resistance is concentrated in the film and results in a concentration gradient (C^*-C_L) between its two edges. This model leads to the following equation of k_L :

$$k_L = \frac{D_{AB}}{\delta} \quad (2-12)$$

Despite the simplistic physical meaning of this model, it integrates important aspects of the real behavior of the gas-liquid absorption, which are the dissolution and molecular diffusion of the gas into the liquid before its transport by convection. This simplistic model predicts results similar to more complex and realistic model^(253, 208, 500). It is also worth mentioning that the effects of the hydrodynamic parameters on k_L are described by the behavior of the film thickness, whereas the effect of physical properties could have an impact on both the diffusivity and the film thickness. For instance, increasing the viscosity or decreasing the temperature decreases the diffusivity, which reduces k_L . The effects of pressure, liquid surface tension and density on k_L are more complex and appeared to be system dependent^(23, 349).

In 1935, Higbie⁽⁴⁹⁸⁾ proposed the penetration theory or “Higbies model” based on the postulate that transfer occurs by a penetration process, which in fact overlooks the assumption of steady-state transfer. In this model, it is assumed that all liquid surface elements are exposed to the gas for the same amount of time before being replaced. During this exposure time, also called contact time, the element absorbs the same amount of gas per unit area as if it was stagnant and infinitely deep. The contact time is related to k_L as:

$$k_L = 2 \times \sqrt{\frac{D_{AB}}{\pi \times t_C}} \quad (2-13)$$

Assuming that the bubbles slip through the stationary liquid, the contact time in gas-liquid contactors is usually calculated^(324, 490) as follows:

$$t_C = \frac{d_B}{U_T} \quad (2-14)$$

Thus, the effects of physical properties, operating conditions and reactor design on k_L are the resulting consequence on their effects on d_B , U_T and D_{AB} .

The Danckwerts model also called “surface renewal theory” proposed in 1951⁽⁴⁹⁹⁾ is similar to Higbies model⁽⁴⁹⁸⁾. In fact, instead of assuming that all surface elements are exposed to the gas for the same amount of time t_C , it assumes that there is a stationary distribution of the surface exposure. Hence, an element of surface being replaced by a fresh liquid element is independent of the exposure time. The only parameter taking into account the hydrodynamics is in this case s , which is the fractional rate of surface renewal.

$$k_L = \sqrt{D_{AB} \times s} \quad (2-15)$$

Several investigators have introduced empirical and semi-empirical models based on the previously discussed theory, such as “film-renewal model” ^(325, 326). Kishinevskii et al. ⁽³²⁷⁾ and King ⁽⁵⁰⁰⁾ have proposed a different approach where the turbulences were extended to the liquid surface and in which the gas absorption was a combination of molecular and eddy-diffusivity. The correlations shown in Tables A-15 and A-16 have been developed based ^(126, 260, 278, 279, 295, 502, 508) or not ^(62, 72, 462, 323, 208, 504, 501, 503, 506, 507) on these models using experimental data. From these studies, it appears that in all reactor types, the mass transfer coefficient increases with the degree of turbulences, i.e. with increasing superficial velocity, mixing speed, impeller diameter and power input. k_L values were also found to increase with liquid density and decrease with liquid viscosity, while the effect of liquid surface tension is not clear ^(462, 323, 490). k_L was always found to be proportional to the diffusivity to a power ranging between 0.5 and 1, which corresponds to the penetration theory and the film model, respectively. It should also be mentioned that k_L values were commonly found to increase with the bubble size in all gas-liquid contactors ⁽²⁰⁸⁾. Nevertheless, no experimental data on the mass transfer coefficient have been reported in the literature under typical industrial conditions for the liquid-phase toluene oxidation process.

3.0 OBJECTIVES

The preceding literature review reveals that the design, modeling, scale-up and optimization of the liquid-phase toluene oxidation process require, among others, precise knowledge of the kinetics, hydrodynamics and mass as well as heat transfer parameters. Section 2.1 showed that several mechanisms, reaction rates and kinetic data are available in the literature for this process and therefore the kinetics of this process will not be investigated in this study. Sections 2.1, 2.4 and 2.5, on the other hand, showed the lack of experimental thermodynamic, hydrodynamic and mass transfer data for the liquid-phase toluene oxidation process. In addition, the extensive literature studies on these parameters in agitated and bubble column reactors were obtained in narrow ranges of operating conditions, where the effect of temperature and pressure were frequently ignored and the gas-liquid used were surrogate to the real systems. Therefore, the objectives of this study are:

1. To measure, study and correlate the thermodynamic, hydrodynamic and mass transfer parameters of O_2 , N_2 and air in liquid toluene and liquid mixture of toluene, benzoic acid and benzaldehyde under typical industrial conditions in agitated and bubble column reactors,
2. To compare the hydrodynamic and mass transfer performances of the different gas-liquid contactors used under the typical industrial conditions; and
3. To model and design gas-liquid contactors for the toluene oxidation process using available literature kinetic data.

Thus, the data to be obtained in this work could be employed to optimize and scale-up the liquid-phase toluene oxidation process.

4.0 EXPERIMENTAL

4.1 GAS-LIQUID SYSTEMS AND OPERATING VARIABLES

The gas-liquid systems and ranges of the operating variables studied are:

Reactors	: SAR, GIR, GSR and BCR
Gases	: N ₂ (SAR, GIR, GSR, BCR), O ₂ (SAR, GIR) and Air (GIR, BCR)
Liquids	: Toluene, 3 Mixtures of Toluene-Benzaldehyde-Benzoic Acid
Pressure	: 1-14 bar (SAR, GIR, GSR), 2-8 bar (BCR)
Temperature	: 300-453 K (SAR, GIR, GSR), 300 K (BCR)
Mixing Speed	: 800-1200 rpm (SAR, GIR, GSR)
Liquid Height	: 0.171-0.316 m (SAR, GIR), 0.171 m (GSR)
Superficial Gas velocity	: 0-0.004 m.s ⁻¹ (GSR), 0.06-0.14 m.s ⁻¹ (BCR)

Pre-purified N₂, O₂ and air with a purity of 99.99%, 99.96% and 99.9%, respectively, from Valley National Gas and toluene, benzaldehyde and benzoic acid with purities of 98+%, 99.99% and 99+% from Velsicol Chemical Corporation and Sigma-Aldrich, respectively, were used in the agitated reactors and the bubble column reactor.

4.2 PROPERTIES OF THE GAS-LIQUID SYSTEMS USED

Some thermodynamic properties ⁽³²⁸⁾ of the gas-liquid systems used are listed in Table 16. It is also important to mention that the three different mixtures of toluene-benzoic acid-benzaldehyde with compositions given in Table 17 were selected based upon typical industrial yields obtained during the continuous liquid-phase toluene oxidation process ^(10, 13, 14, 15, 16, 17, 18, 55).

Table 16: Thermodynamics properties of toluene, benzoic acid, benzaldehyde, nitrogen and oxygen ⁽³²⁸⁾

<i>Component</i>	<i>Mol wt. kg.kmol⁻¹</i>	<i>T_C</i> <i>K</i>	<i>P_C</i> <i>bar</i>	<i>ω</i> -	<i>[P]_i</i> -	<i>[P]_i</i> ^{(a)(329, 330)} -	<i>δ_i</i> ^(298K) <i>(MPa)^{1/2}</i>
Toluene	92.141	593.10	42.10	0.263	245.1	264.1 ^(b)	18.346
Benzaldehyde	106.124	695.00	44.70	0.305	255.6	-	21.610
Benzoic Acid	122.123	751.00	46.50	0.604	263.4	-	22.432
Mixture #1	94.72	607.17	42.38	0.291	246.7	-	18.81
Mixture #2	94.28	605.85	42.46	0.282	246.5	-	18.77
Mixture #3	93.84	604.57	42.53	0.273	246.3	-	18.74
Air	29.00	132.16	36.85	0.036	36.1	58 ^(a)	11.43
Oxygen	31.999	154.60	50.40	0.025	40.0	55.7 ^(b) , 53.5 ^(a)	14.7
Nitrogen	28.013	126.20	33.90	0.039	35.0	60.2 ^(b) , 60 ^(a)	10.8

^(a) Experimental value reported by Lefrancois and Bourgeois ⁽³²⁹⁾^(b) Experimental value reported by Broseta and Ragil ⁽³³⁰⁾**Table 17: Composition of the Different Liquid Mixtures Used**

<i>Liquid</i>	<i>Toluene</i>	<i>Benzoic Acid</i>	<i>Benzaldehyde</i>
Pure Toluene	100 wt.%	0 wt.%	0 wt.%
Mixture # 1	88 wt.%	10 wt.%	2 wt.%
Mixture # 2	88 wt.%	6 wt.%	6 wt.%
Mixture # 3	88 wt.%	2 wt.%	10 wt.%

4.2.1 Vapor Pressure of Toluene

The vapor pressure of toluene and benzaldehyde were calculated using the Wagner's Equation ⁽³²⁸⁾, which are valid between 306K and 593K and 405K and 695K, respectively.

for toluene:

$$\ln \frac{P_s}{P_C} = \left(\frac{I}{1-X} \right) \times (-7.28607 \times X + 1.38091 \times X^{1.5} - 2.83433 \times X^3 - 2.79168 \times X^6) \quad (4-1)$$

for benzaldehyde:

$$\ln \frac{P_s}{P_C} = \left(\frac{I}{1-X} \right) \times (-7.1653 \times X + 0.5271 \times X^{1.5} - 1.5148 \times X^3 - 7.9291 \times X^6) \quad (4-2)$$

where $X = 1 - T_R$ and $T_R = T/T_C$.

For benzoic acid, the following equation ⁽³²⁸⁾ was used to calculate the vapor pressure between 405K and 560K:

$$P_s = \exp \left(10.5432 - \frac{4190.7}{T - 125.2} \right) \quad (4-3)$$

Figure 5 compares the calculated vapor pressure of toluene using Equation (4-1) with the measured values and a very good agreement can be reported.

For the three mixtures experimental vapor pressure data were collected and were fitted using a Wagner type of equation, which were valid between 293 and 460K. As can be seen in Figure 5, the experimental values were well predicted by Equations (4-4) for the mixture #1, 2 and 3.

$$\ln \frac{P_S}{P_C} = \left(\frac{I}{I-X} \right) \times (aX + bX^{1.5} + cX^3 + dX^6) \quad (4-4)$$

Where a , b , c and d are shown in Table 18.

4.2.2 Density of Toluene

The density values of toluene, benzaldehyde and benzoic acid in kg.m^3 were correlated with the Rackett Equation (4-5)⁽³²⁸⁾ in the temperature range of 178 to 591K, 247 to 695K and 395 to 751K, respectively.

for toluene:

$$\rho_L = 290.6 \times 0.265^{-(I-T_R)^{2/7}} \quad (4-5)$$

for benzaldehyde:

$$\rho_L = 327.59 \times 0.2578^{-(I-T_R)^{0.285}} \quad (4-6)$$

and for benzoic acid:

$$\rho_L = 353.1 \times 0.25^{-(I-T_R)^{2/7}} \quad (4-7)$$

For the three mixtures the modified Rackett Equation⁽³²⁸⁾ for liquid mixtures was used to calculate the liquid densities between 293 to 460 K as follows:

$$\rho_{\text{Mixture}} = \frac{\left(\sum_{i=1}^3 x_i M_{Wi} \right)}{R \left(\sum_{i=1}^3 \frac{x_i T_{Ci}}{P_{Ci}} \right) Z_{RA-\text{Mixture}}} \times Z_{RA-\text{Mixture}} \left(1 - \frac{T}{T_{C-\text{Mixture}}} \right)^{2/7} \quad (4-8)$$

With:

$$Z_{RA-\text{Mixture}} = \sum_{i=1}^3 x_i Z_{RAi} \quad (4-9)$$

With x_i the liquid molar fraction and Z_{RAi} defined in the Rackett Equation for pure liquids:

$$\rho_i = A \times Z_{RAi} \left(1 - \frac{T}{T_{Ci}} \right)^{2/7} \quad (4-10)$$

It is also important to mention that the following Chueh-Prausnitz mixing rules were used in the calculation as recommended by Reid et al.⁽³²⁸⁾:

$$T_{C-Mixture} = \sum_{j=1}^3 \sum_{i=1}^3 \varphi_i \varphi_j T_{Cij} \quad (4-11)$$

$$T_{Cij} = (1 - k_{ij}) (T_{Ci} T_{Cj})^{1/2} \quad (4-12)$$

$$\varphi_i = \frac{x_i V_{Ci}}{\sum_{i=1}^3 x_i V_{Ci}} \quad (4-13)$$

$$1 - k_{ij} = \frac{8(V_{Ci} V_{Cj})^{1/2}}{\left(V_{Ci}^{1/3} + V_{Cj}^{1/3} \right)^3} \quad (4-14)$$

For the three mixtures using the statistical software package, MINITAB Version 9.1 for the Mainframe, the densities values were best fitted using the Rackett Equation as:

$$\rho_{Mixture} = A \times B^{-(1-T_R)^{2/7}} \quad (4-15)$$

Where A and B are shown in Table 18.

The toluene and three mixtures density are shown in Figure 6.

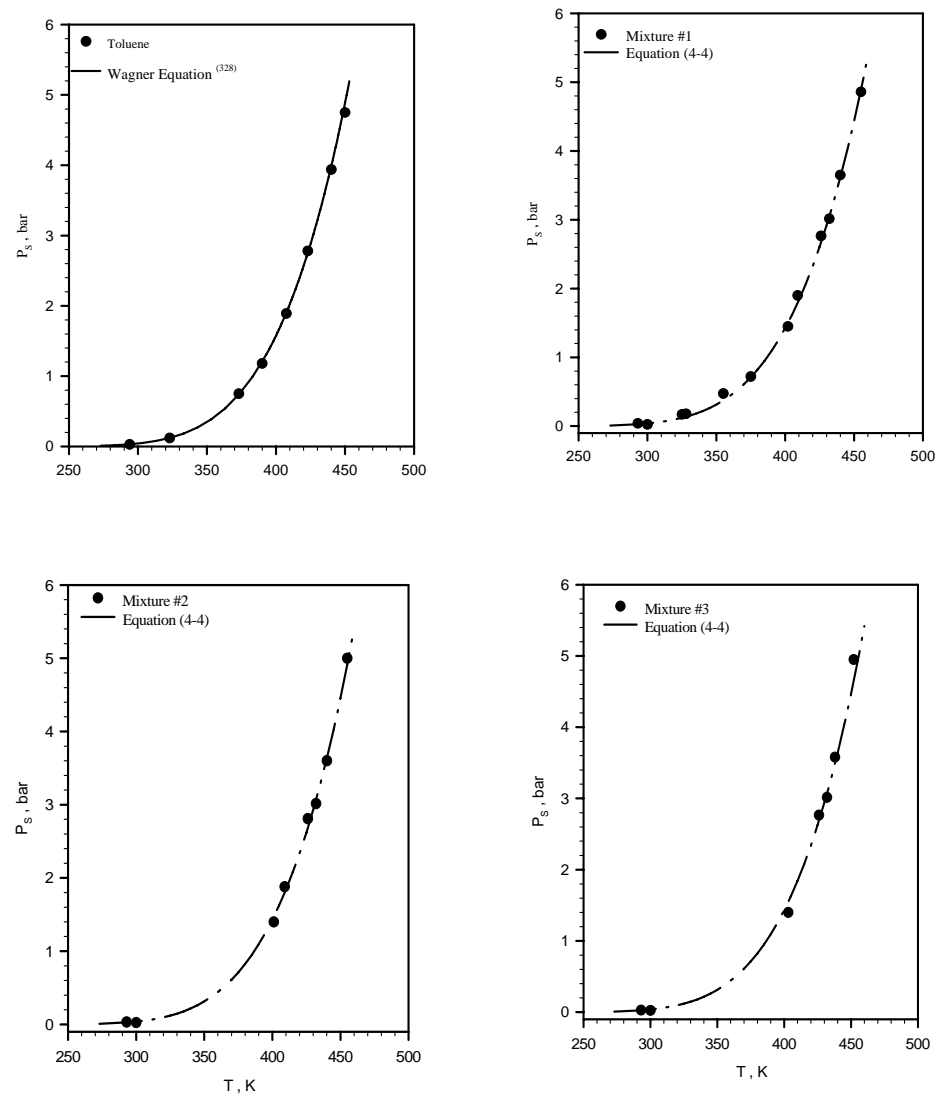


Figure 5: Effect of Temperature on Toluene and Toluene Mixtures Vapor Pressure

Table 18: Physical Properties of the Liquid Systems Used

Reference	Physical Properties	Liquid	Parameters			
P_S , bar			a	b	c	d
Reid et al. (1987)	$\ln \frac{P_S}{P_C} = \left(\frac{I}{1-X} \right) \times \left(aX + bX^{1.5} + cX^3 + dX^6 \right)$ with $X = 1 - \frac{T}{T_C}$, Wagner type of equation	Toluene	-7.29	1.38	-2.83	-2.79
		Mixture #1	-6.34	$-7.75 \cdot 10^{-3}$	-1.48	-4.03
		Mixture #2	-6.52	0.24	-1.70	-3.79
		Mixture #3	-6.67	0.45	-1.87	-3.58
ρ_L , kg/m ³			A		B	
Reid et al. (1987)	$\rho_L = A \times B^{-\left(1-T_R\right)^{2/7}}$ with $T_R = \frac{T}{T_C}$, and Rackett equation for mixtures	Toluene	290.6		0.2650	
		Mixture #1	290.4		0.2529	
		Mixture #2	292.4		0.2555	
		Mixture #3	292.7		0.2564	
μ_L , Pa.s			a	b	$c \times 10^3$	$d \times 10^6$
Perry et al. (1997) and Reid et al. (1987)	$\mu_L = 0.001 \times \exp \left(a + \frac{b}{T} + c \times T + d \times T^2 \right)$ with for the mixtures $\ln \left(\mu_{Mix} \right) = \sum_{i=1}^3 x_i \ln \left(\mu_i \right) + \frac{1}{2} \sum_{i=1}^3 \sum_{j=1}^3 x_i x_j G_{ij}$, Grunberg and Nissan method	Toluene	-5.88	1287	4.56	-4.5
		Mixture #1	-3.23	1285	-6.19	6.8
		Mixture #2	-6.3	1487	4.6	-4.06
		Mixture #3	-6.02	1327	4.78	-4.05
σ_L , N/m			A		n	
Perry et al. (1997) and Reid et al. (1987)	$\sigma = A \times \left(1 - \frac{T}{T_c} \right)^n$ and for the mixtures Winterfeld, David and Scriven Method $\sigma_{Mix} = \sum_{i=1}^n \sum_{j=1}^n \frac{I}{\left(\sum_{k=1}^n x_k v_{L_k} \right)^2} \left(x_i v_{L_i} \right) \left(x_j v_{L_j} \right) \left(\sigma_{L_i} \sigma_{L_j} \right)^{1/2}$	Toluene	0.0668		1.2456	
		Mixture #1	0.0672		1.2389	
		Mixture #2	0.0671		1.2372	
		Mixture #3	0.0671		1.2355	
D_{AB} , m ² /s			ψ	V_A , m ³ .kmol ⁻¹		
				N_2	O_2	Air
Reid et al. (1987)	$D_{AB} = 1.1728 \times 10^{-16} \frac{\left(\psi M_B \right)^{0.5} T}{\mu_B V_A^{0.6}}$ Wilke and Chang's correlation	Toluene	1.0	0.0347	0.0280	0.0329
		Mixture #1	1.0	0.0347	0.0280	0.0329
		Mixture #2	1.0	0.0347	0.0280	0.0329
		Mixture #3	1.0	0.0347	0.0280	0.0329

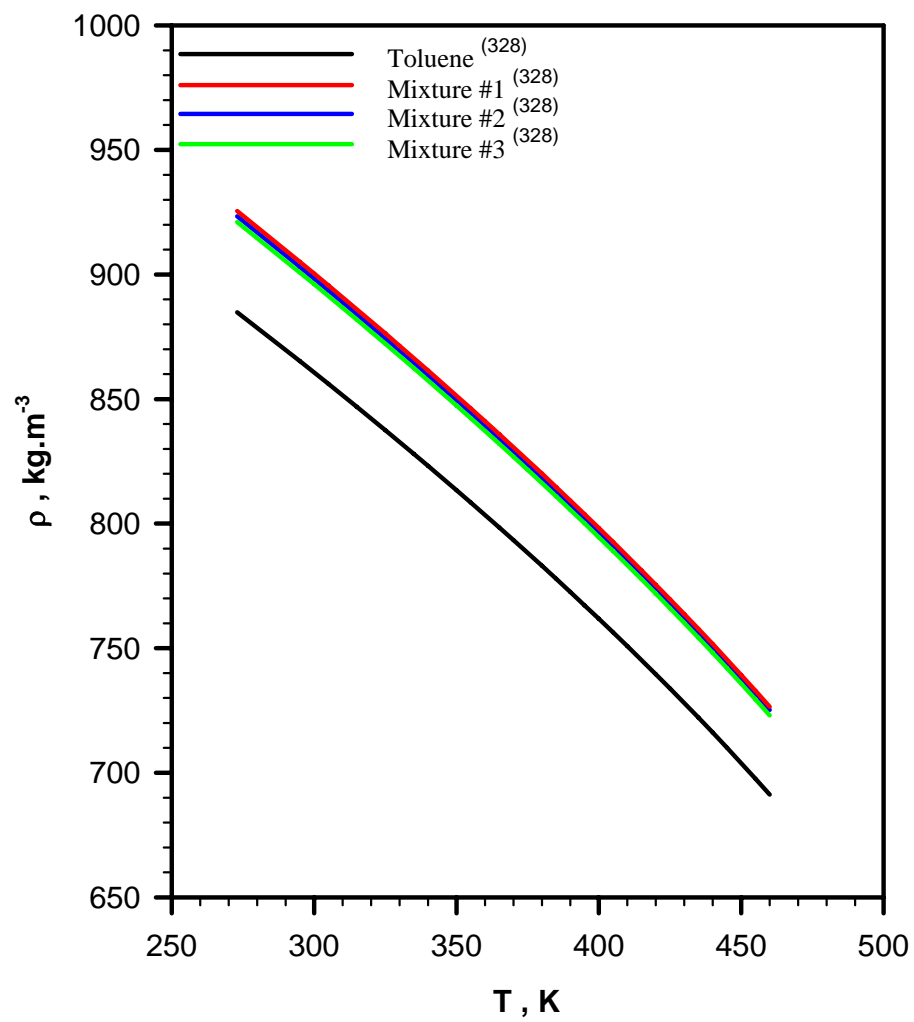


Figure 6: Effect of Temperature on Toluene and the three Mixtures Density

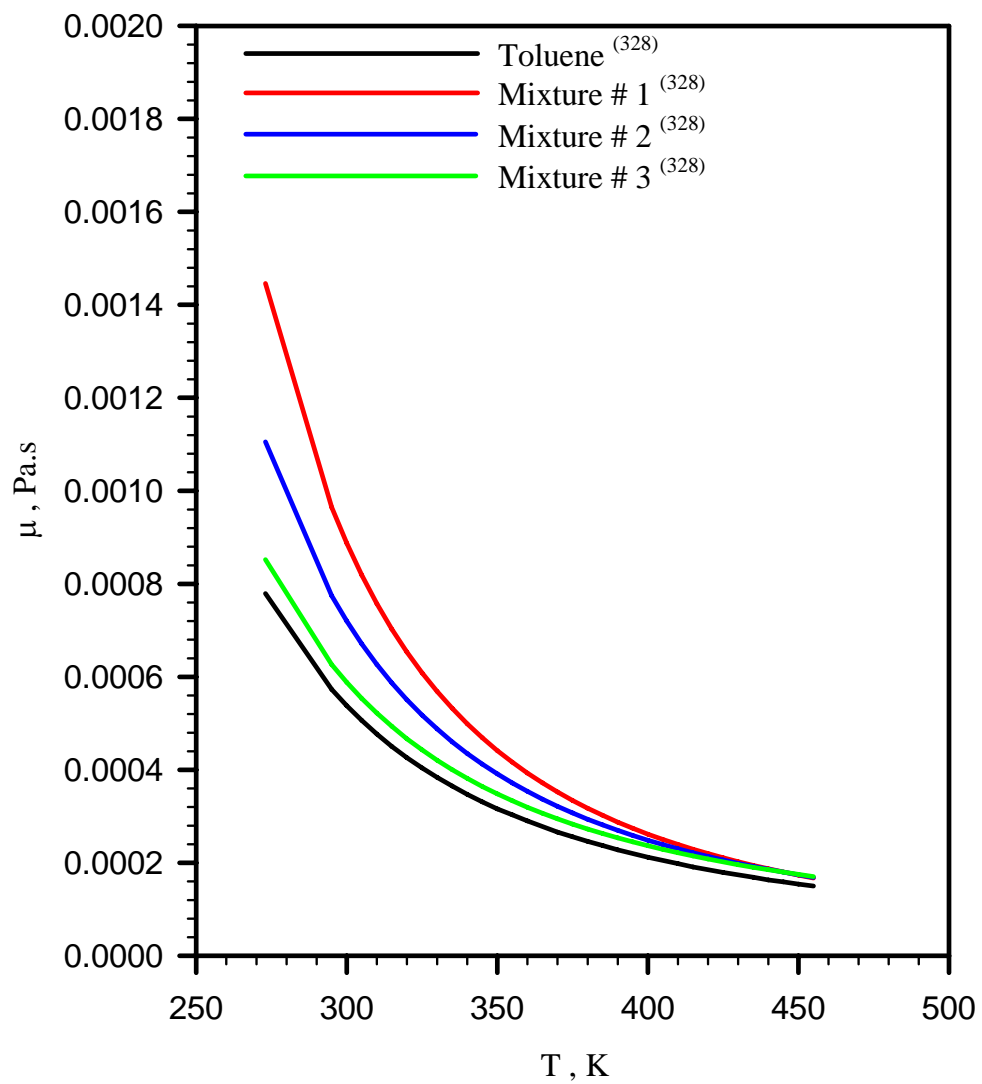


Figure 7: Effect of Temperature on Toluene and the three Mixtures Viscosity

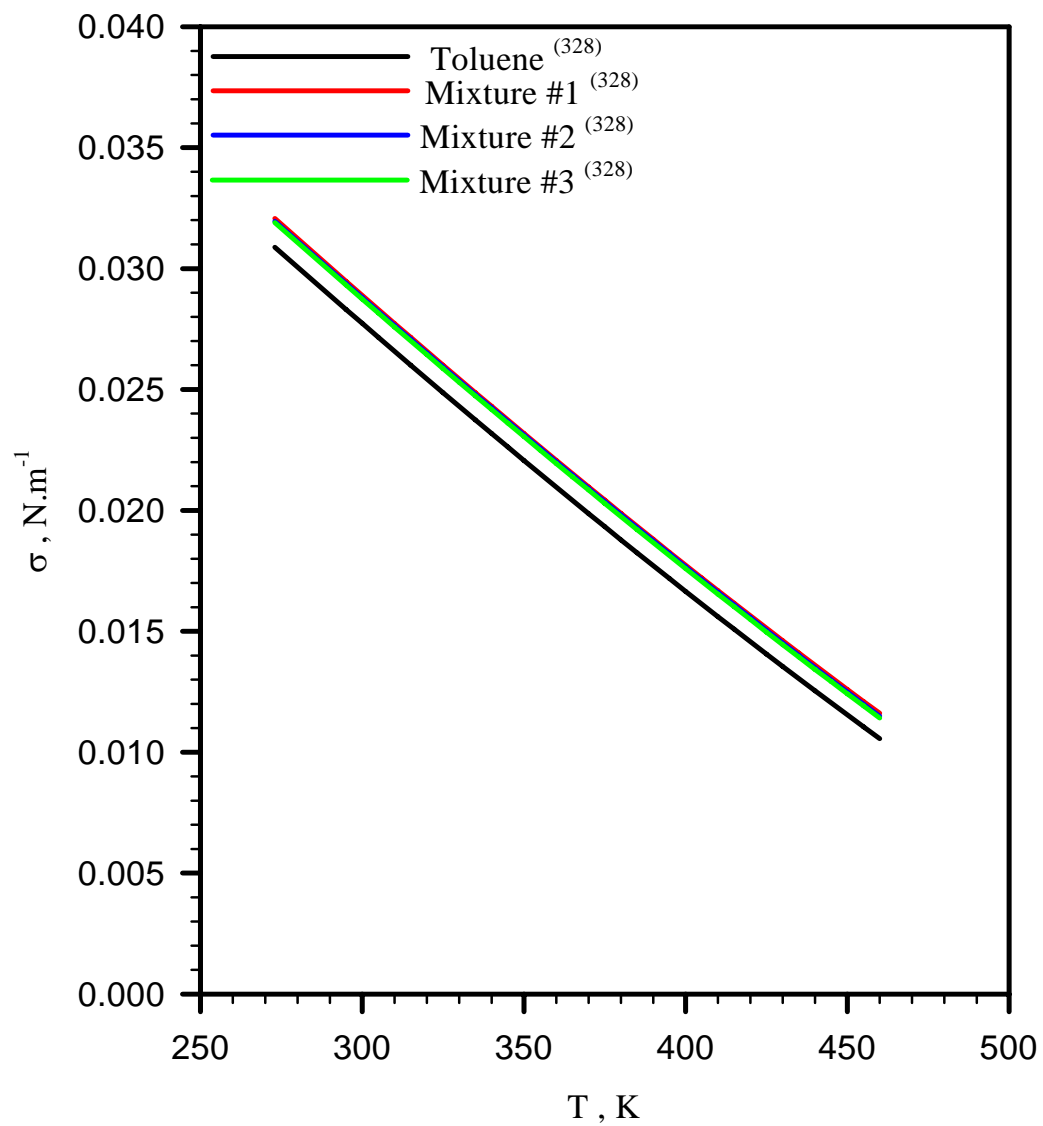


Figure 8: Effect of Temperature on Toluene and the three Mixtures Surface Tension

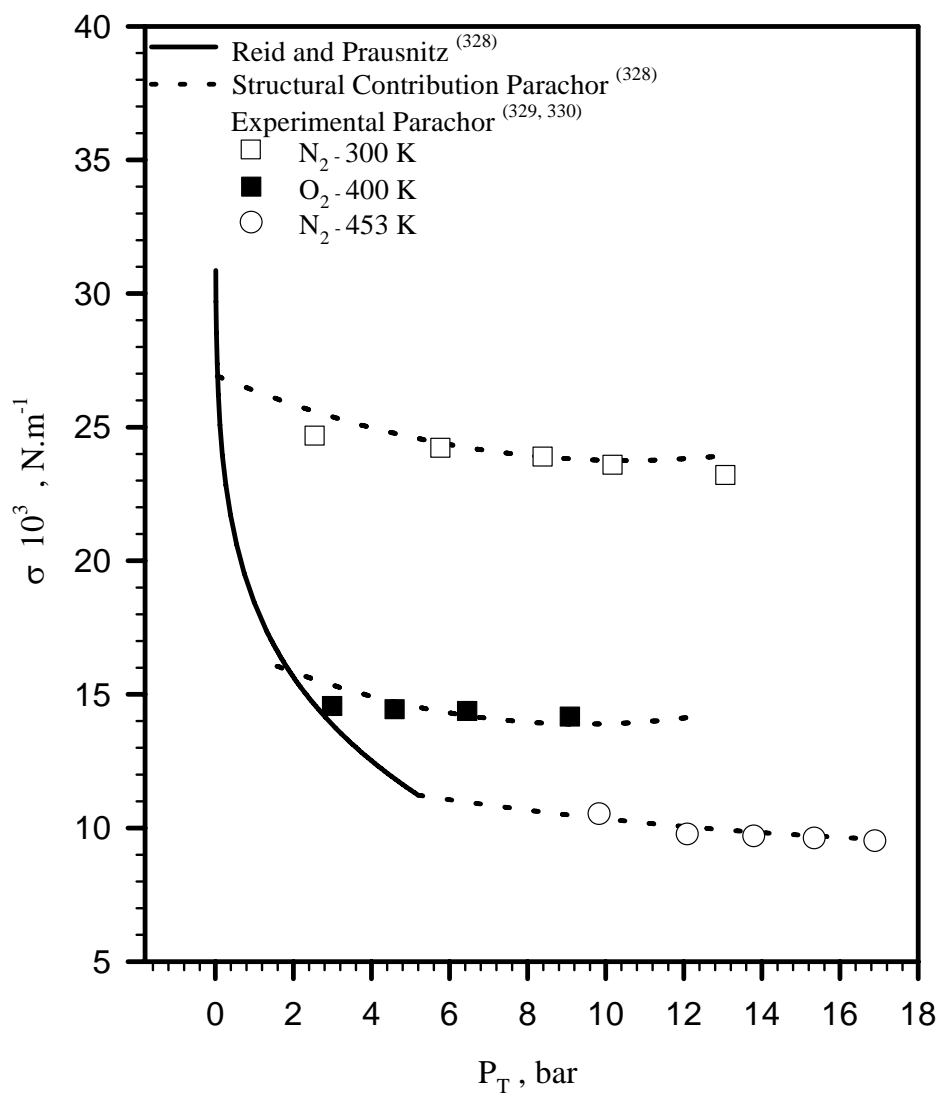


Figure 9: Effect of Pressure and Temperature on Toluene Surface Tension

4.2.3 Viscosity of Toluene

The viscosity of toluene, benzaldehyde and benzoic acid ⁽³²⁸⁾, μ in Pa.s were calculated as:
for toluene:

$$\mu = 0.001 \times \exp \left(-5.878 + \frac{1287}{T} + 4.575 \times 10^{-3} T - 4.499 \times 10^{-6} T^2 \right) \quad (4-16)$$

for benzaldehyde:

$$\mu = \exp \left(-10.563 + \frac{929.1}{T} + 0.14846 \times \ln(T) \right) \quad (4-17)$$

and for benzoic acid:

$$\mu = 0.001 \times \exp \left(-14.78 + \frac{6027}{T} \right) \quad (4-18)$$

For the 3 mixtures, the Grunberg and Nissan method ⁽³²⁸⁾ was used:

$$\ln(\mu_{Mix}) = \sum_{i=1}^3 x_i \ln(\mu_i) + \frac{1}{2} \sum_{i=1}^3 \sum_{j=1}^3 x_i x_j G_{ij} \quad (4-19)$$

With x_i the liquid molar fraction and G_{ij} ⁽³²⁸⁾ an interaction parameter defined at any temperature as

$$G_{ij}(T) = 1 - \left[1 - G_{ij}(298) \right] \frac{573 - T}{275} \quad (4-20)$$

And G_{ij} obtained at 298K from group contribution ⁽³²⁸⁾.

Thus, for the three mixtures using the statistical software package, MINITAB Version 9.1 for the Mainframe, the viscosity values were best fitted using the following Equation as:

$$\mu_L = 0.001 \times \exp \left(a + \frac{b}{T} + c \times T + d \times T^2 \right) \quad (4-21)$$

Where a , b , c and d are shown in Table 18.

A plot of the viscosity of toluene and the tree mixtures as a function of temperature is illustrated in Figure 7.

4.2.4 Surface Tension of Toluene

The surface tension of pure toluene, benzaldehyde and benzoic acid, σ , in N.m⁻¹ were calculated as a function of temperature ⁽³²⁸⁾ in the temperature range of 293.2K to 591K, 247K to 695K and 395K to 751K, respectively. The values obtained are plotted in Figure 8. For the toluene, the following equation was used:

$$\sigma = \sigma_l \left(\frac{T_c - T}{T_c - T_l} \right)^{11/9} \quad (4-22)$$

Where σ_i is the surface tension at T_i , for toluene σ_i is equal to 0.02852 N.m⁻¹ at 293.2K; and for benzaldehyde and benzoic acid, Equation (4-23) was used:

$$\sigma = A \left(1 - \frac{T}{T_c} \right)^n \quad (4-23)$$

With A equals 0.07468 and 0.0734 N.m⁻¹ and n 1.193 and 1.106 for benzaldehyde and benzoic acid, respectively.

For the 3 mixtures, the Winterfeld, David and Scriven Method ⁽³²⁸⁾ was used:

$$\sigma_{Mix} = \sum_{i=1}^n \sum_{j=1}^n \frac{I}{\left(\sum_{k=1}^n x_k v_{L_k} \right)^2} (x_i v_{L_i} x_j v_{L_j} \sigma_{L_i} \sigma_{L_j})^{1/2} \quad (4-24)$$

With v_{iL} is the liquid molar volume and x_i the liquid molar fraction.

Thus, for the three mixtures using the statistical software package, MINITAB Version 9.1 for the Mainframe, the surface tension values were best fitted using the following Equation as:

$$\sigma = A \times \left(1 - \frac{T}{T_c} \right)^n \quad (4-25)$$

Where A and n are shown in Table 18.

A plot of the surface tension of toluene and the tree mixtures as a function of temperature is illustrated in Figure 8.

The surface tension of toluene containing a dissolved gas was determined using the Macleod-Sugden correlation ⁽³²⁸⁾:

$$\sigma = 10^{-3} \left(\sum_{i=1}^n [P]_i \left(\frac{x_i}{v_L} - \frac{y_i}{v_G} \right) \right)^4 \quad (4-26)$$

Where v_L and v_G the molar volumes in the gas and liquid phases in mol.cm⁻³ and $[P]_i$ is the parachor of each component. The parachors shown in Table 16 were either obtained from the structure contributions or experimental values reported in the literature ^(329, 330). Figure 9 shows the effect of dissolved gas on the toluene surface tension for the different Parachor values of O₂ and N₂, and it appears that the mixture surface tension is not affected significantly by the different $[P]_i$ values, as Reid and Prausnitz ⁽³²⁸⁾ stated. In this figure the values of x_i and y_i , shown in Table 19, were obtained under a thermodynamic equilibrium at a given temperature and pressure using a modified Peng-Robinson equation of state as it will be discussed in Section 5.1.1. Under these conditions from the Gibbs phase rules:

$$N_F = C - P + 2 = 2 - 2 + 2 = 2 \quad (4-27)$$

with C the number of component, P the number of phase and N_F the degree of freedom. Hence, since both temperature and pressure are fixed all other properties can be calculated.

Table 19: Phase molar fraction for O₂ and N₂ in toluene

<i>Systems</i>	<i>T, K</i>	<i>P, bar</i>	<i>x_l, -</i>	<i>x₂, -</i>	<i>y_l, -</i>	<i>y₂, -</i>
C ₇ H ₈ -N ₂	300	0.05	1.0000	0.0000	1.000	0.0000
C ₇ H ₈ -N ₂	300	2.54	0.9986	0.0014	0.0156	0.9844
C ₇ H ₈ -N ₂	300	5.76	0.9967	0.0033	0.0077	0.9923
C ₇ H ₈ -N ₂	300	8.38	0.9952	0.0048	0.0056	0.9944
C ₇ H ₈ -N ₂	300	10.17	0.9942	0.0058	0.0050	0.9950
C ₇ H ₈ -N ₂	300	13.06	0.9926	0.0074	0.0042	0.9958
C ₇ H ₈ -O ₂	400	1.58	1.0000	0.0000	1.000	0.0000
C ₇ H ₈ -O ₂	400	2.99	0.9953	0.0047	0.3641	0.6359
C ₇ H ₈ -O ₂	400	4.59	0.9932	0.0068	0.2759	0.7241
C ₇ H ₈ -O ₂	400	6.45	0.9909	0.0091	0.2140	0.7860
C ₇ H ₈ -O ₂	400	9.08	0.9872	0.0128	0.1668	0.8332
C ₇ H ₈ -O ₂	400	12.56	0.9828	0.0172	0.1299	0.8701
C ₇ H ₈ -N ₂	453	5.19	1.0000	0.0000	1.000	0.0000
C ₇ H ₈ -N ₂	453	9.83	0.9931	0.0069	0.4712	0.5288
C ₇ H ₈ -N ₂	453	12.08	0.9905	0.0095	0.4521	0.5479
C ₇ H ₈ -N ₂	453	13.78	0.9885	0.0115	0.4006	0.5994
C ₇ H ₈ -N ₂	453	15.33	0.9865	0.0135	0.3669	0.6331
C ₇ H ₈ -N ₂	453	16.89	0.9849	0.0151	0.3399	0.6601

with 1: Liquid: toluene and 2: Gas: nitrogen or oxygen

4.2.5 Gas Diffusivity in Toluene

The Wilke-Chang ^(328; 331) equation was used to predict the diffusivity, D_{AB} (m².s⁻¹) of N₂ and O₂ in toluene as a function of temperature, as given below:

$$D_{AB} = 1.1728 \times 10^{-16} \frac{(\psi M_B)^{0.5} T}{\mu_B V_A^{0.6}} \quad (4-28)$$

In this Equation, V_A is the molar volume of the diffusing gas (m³.kmol⁻¹) at its normal boiling point, which is 0.034707 for N₂ and 0.028041 for O₂. ψ is the association factor of the solvent which characterizes its polarity and has a value of 1.0 for toluene ⁽³²⁸⁾. The calculated diffusivities of N₂ and O₂ in toluene are presented in Figure 10.

4.2.6 Gas viscosity in Toluene

The gas viscosity at low pressures, μ_G^0 , in μP is calculated using the Lucas equation ⁽³²⁸⁾:

$$\mu_G^0 = \frac{\left[0.807 \times T_R^{0.618} - 0.357 \times \exp(-0.449 \times T_R) + 0.340 \times \exp(-4.058 \times T_R) + 0.018\right]}{0.176 \times \left(\frac{T_C}{M_W^3 P_C^4}\right)^{1/6}} \quad (4-29)$$

The effect of pressure on the gases viscosity was estimated through the Reichenberg method ⁽³²⁸⁾, Equation (4-30):

$$\frac{\mu_G}{\mu_G^0} = 1 + \frac{A \times P_R^{3/2}}{A \times (1.6552 \times T_R - 1.2760) \times P_R + (1 + B \times P_R^C)^{-1}} \quad (4-30)$$

Where:

$$A = \frac{0.0019824}{T_R} e^{5.2683 \times T_R^{-0.5767}} \quad (4-31)$$

$$B = \frac{0.1319}{T_R} e^{3.7035 \times T_R^{-79.8678}} \quad (4-32)$$

$$C = \frac{2.9496}{T_R} e^{2.9190 \times T_R^{-16.6169}} \quad (4-33)$$

As can be seen in Figure 11, the effect of pressure on gas viscosity is negligible, whereas increasing temperature significantly increases the gas viscosity.

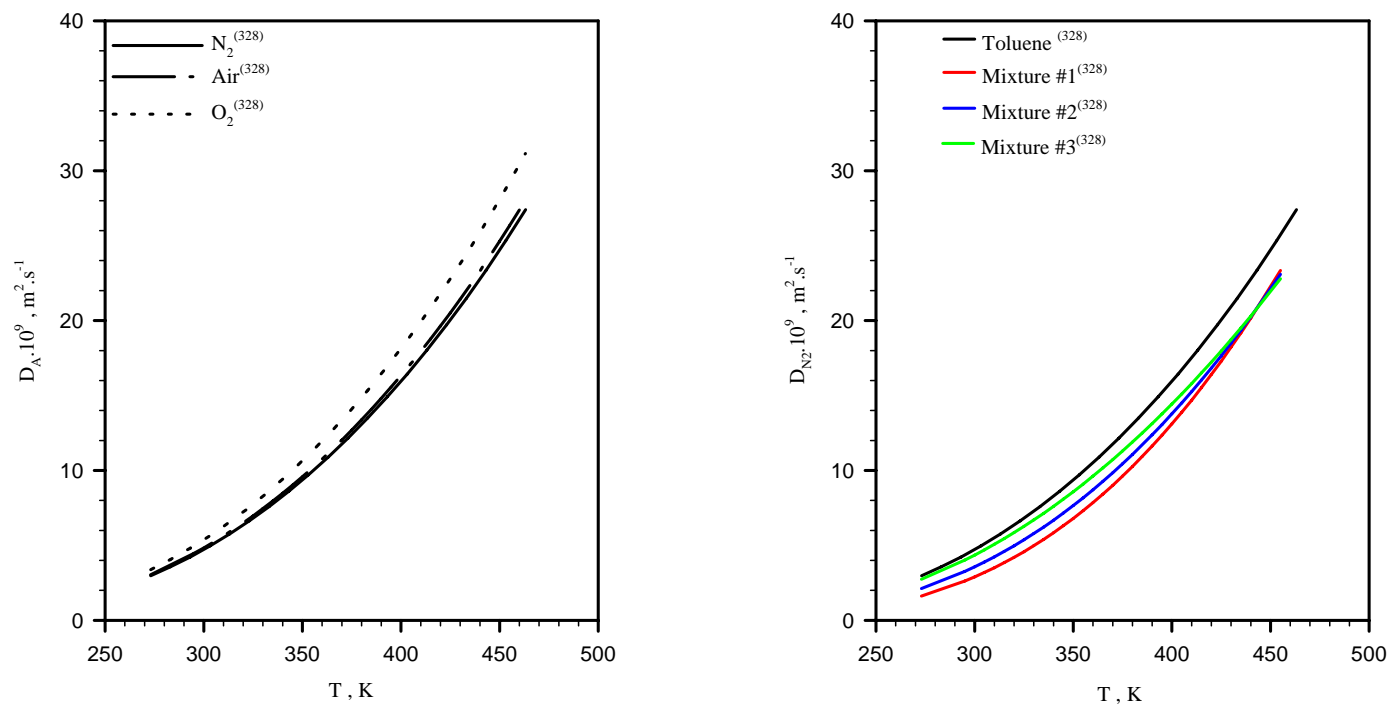


Figure 10: Effect of Temperature on Gas Diffusivity in Toluene and the three Mixtures

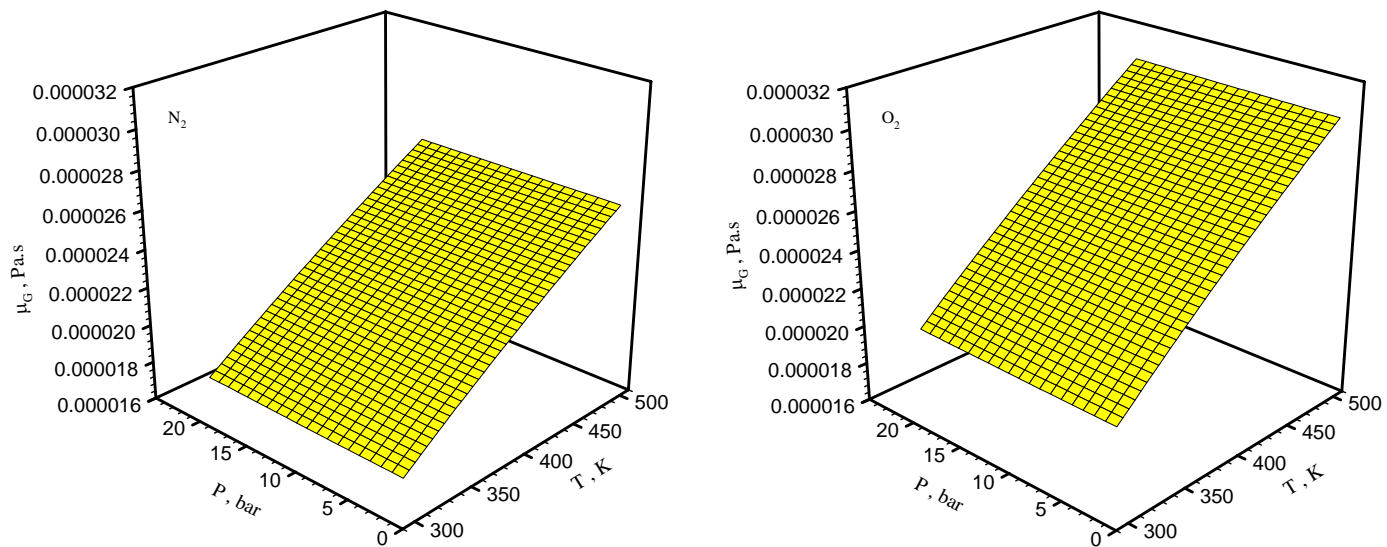


Figure 11: Effect of Temperature and Pressure on Gas Viscosity ⁽³²⁸⁾

4.3 EXPERIMENTAL SET-UP

The experimental set-ups used in this study are described in the following.

4.3.1 Agitated Reactors

The two identical agitated reactors were used in this study are schematically shown in Figures 12 and 13. They consist of the following main units:

1. Reactor
2. Preheater
3. Vacuum system
4. Computer data acquisition system

A 4-liter ZipperClave reactor with an effective volume of $4.03 \cdot 10^{-3} \text{ m}^3$ which can be operated in gas-inducing or surface-aeration mode was used to determine both the mass transfer and thermodynamic parameters. The reactor dimensions are given in Figure 14. For safety reasons, 3 Lexan shields as well as 2 stainless steel doors were installed at the top and bottom of the frames of the reactor, respectively. The reactor is rated at a maximum allowable pressure of 137 bars for a temperature of 505 K. The reactor is equipped with four symmetrically located baffles, a cooling coil, a specially designed heating jacket, a thermo-well and an agitator with a six flat blades impeller and a hollow shaft. Four holes of 0.0015 m diameter each located at the upper and lower end of the shaft allow the reactor to operate in a gas-inducing and surface-aeration mode. Details of the impeller are given in Figure 15. The agitator is driven by a magnetic drive that has enough capacity of dumping any eccentricity. Two K-type chromel alumel thermocouples are used to measure the gas and liquid phase temperature, whereas the pressure inside the reactor is measured using a Setra Model No. 205-2 pressure transducer rated at 0-250 psig. For safety purposes, the reactor is fitted with a relief valve and a rupture disk rated at 71 bar at 295K. Another 4-liter Zipper-Clave, see-through reactor equipped with two Jerguson windows, as shown in Figure 13, was used in order to measure the hydrodynamic parameters under the operating conditions employed. This reactor is identical to the one used for the mass transfer measurements with the exception of the two sight-windows whose details are given in Figure 16. As also illustrated in Figure 13, a leak-free special device was mounted on the shaft and an external re-circulation loop was designed to measure in the GIR the induced gas flow rate through the agitator hollow shaft. Also, some modifications were introduced in order to operate the reactor in a gas-sparging mode, and thus a gas re-circulation loop as shown in Figure 16 was mounted on the unit. The gas was re-circulated externally by means of a gas booster type AGD-4, manufactured by Haskel, Burbank, CA., USA; and the gas sparger used was a cross-shaped distributor, having 12 holes of 1-mm in diameter drilled in the four legs and were oriented downward to

achieve good gas distribution⁽³⁴⁹⁾. It is important to mention that the gas phase is cooled down at the reactor outlet in order to condense any possible liquid vapors, which could damage the compressor.

A CCD camera was used to record the gas bubbles and measure the gas holdup through the Jerguson sight-windows shown in Figure 16. Also, the gas flow rate was measured during the experiment with the re-circulation loop illustrated in Figure 16, using a Coriolis mass flow meter type CMF-010M, manufactured by Micro Motion Inc., Boulder CO. USA.

A high-pressure bomb with an effective volume of $2.237 \cdot 10^{-3} \text{ m}^3$ is used to heat the gas to the desired temperature before it is charged to the reactor. The preheater is maintained at a constant temperature by means of electrical heating tapes and temperature controllers. A K-type shielded thermocouple and a pressure transducer Setra 1000 psig are installed to record both temperature and pressure readings during the experiments.

The vacuum pump used is a Welch duo-seal model 1399, which is an oil sealed mechanical vacuum pump that can reach down to 1000 Pa. The system is used to degas the liquid in the reactor before the start of the experiment. A liquid trap is connected between the reactor outlet and the vacuum pump inlet to collect any possible condensed vapor. The gas from the vacuum pump is then vented to the exhaust.

All pressure transducers and thermocouples used in the setup are interfaced with an on-line personal computer through an interfacing board from Metra Byte Corporation and Keithley, respectively, for the two agitated reactors, used for the mass transfer and hydrodynamic measurements. User-friendly computer programs developed in our laboratory were used to assign the channels for the interface board and to monitor on-line the system pressures and temperatures. At any given condition, the pressures and temperatures of both phases are displayed on the computer screen. During gas absorption, the pressure decline is recorded and displayed as a function of time. Also, the pressures and temperatures in the preheater are recorded before and after the gas is charged into the reactor to build a mass balance in the gas phase.

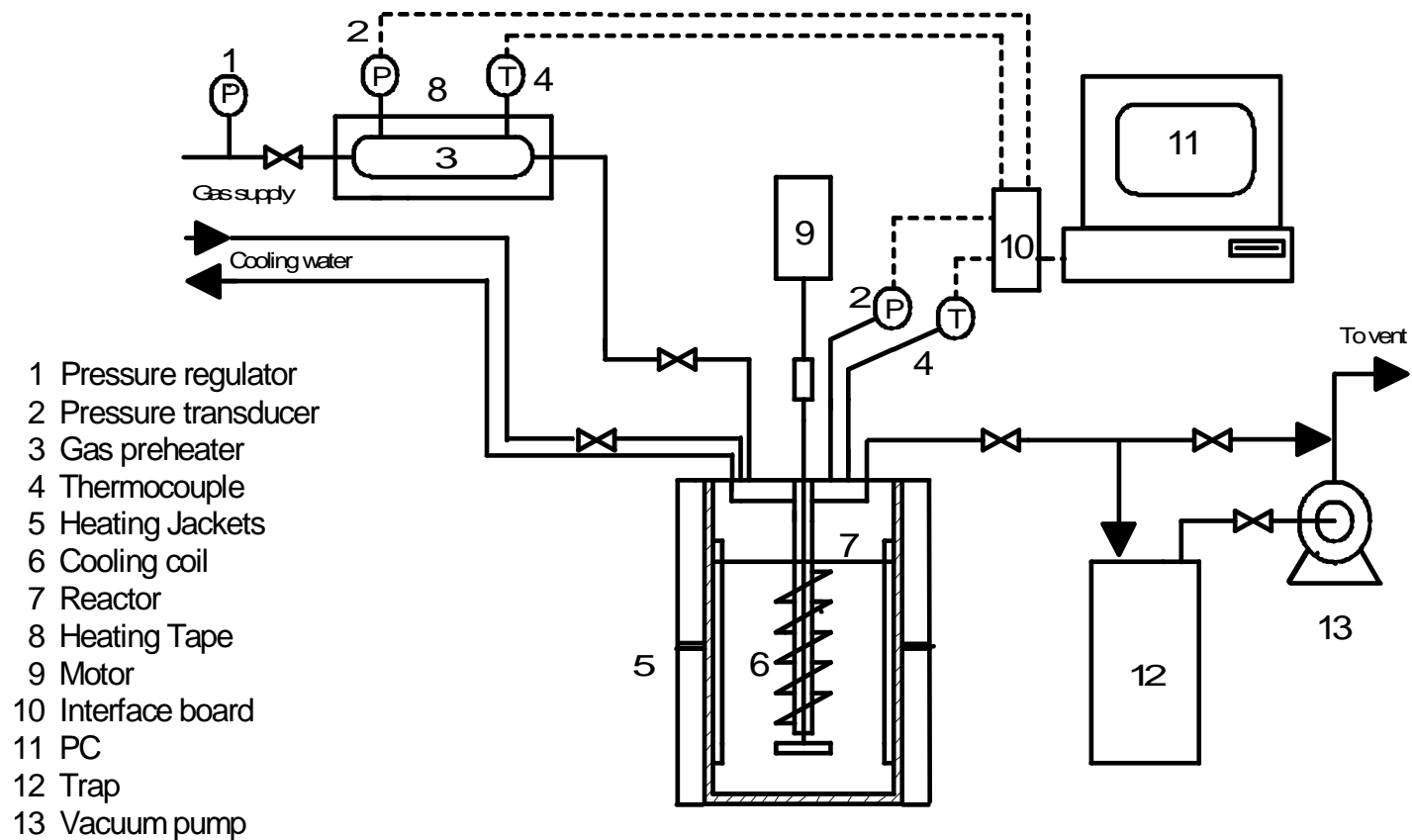


Figure 12: Schematic of the Experimental Setup for Mass Transfer Measurements

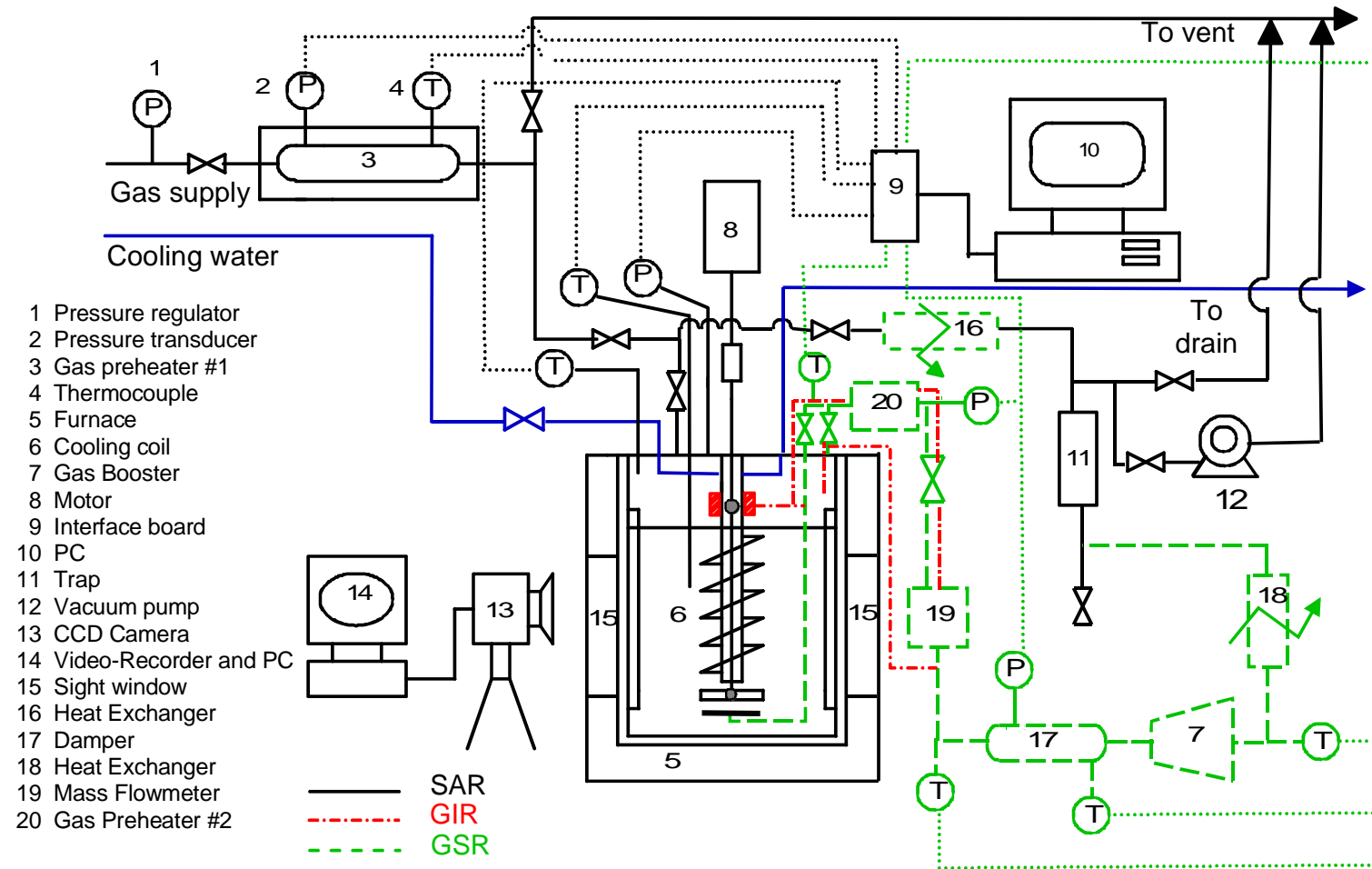


Figure 13: Schematic of the Experimental Setup for Hydrodynamic Measurements

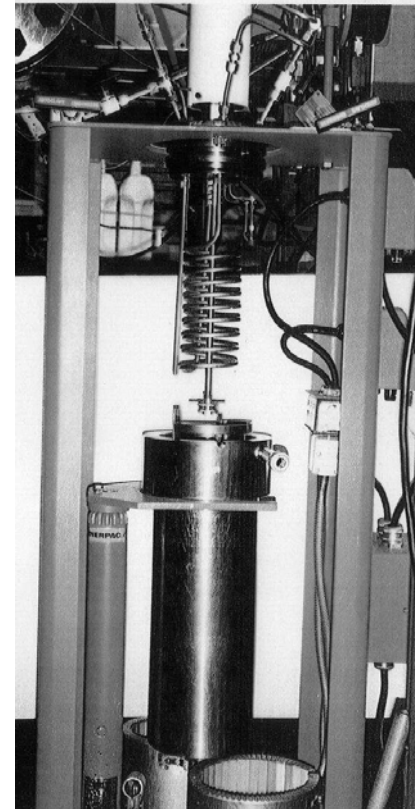
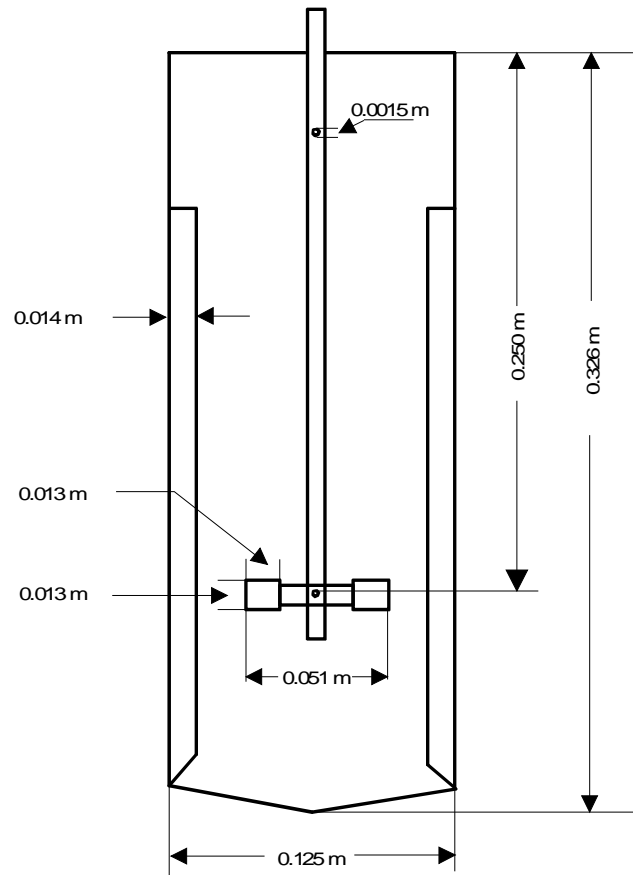
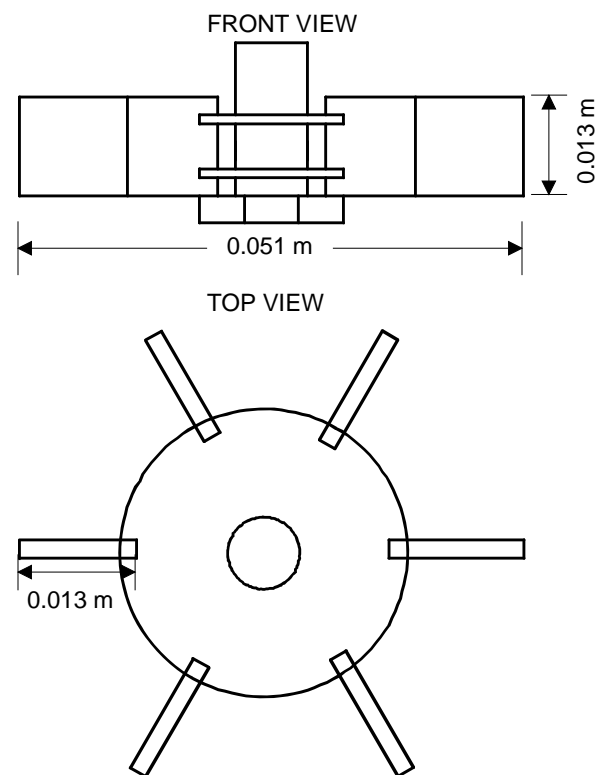
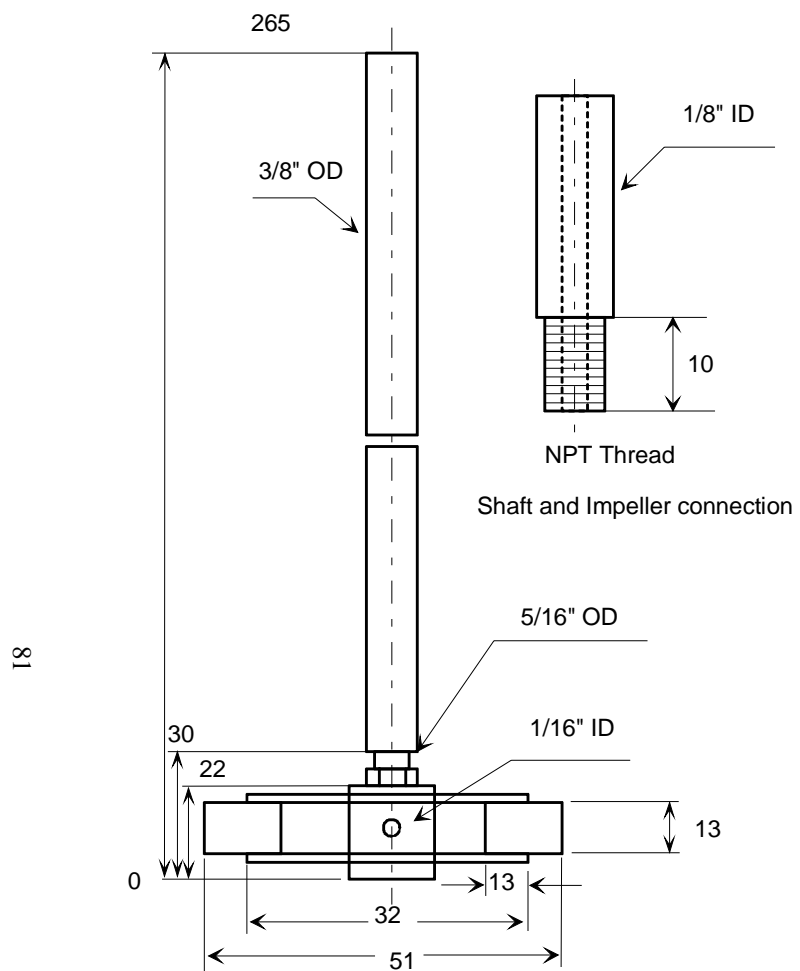


Figure 14: Details of the Agitated Reactors Dimensions



All dimensions are in mm unless otherwise indicated

Figure 15: Impeller and Shaft Design in the Agitated Reactors

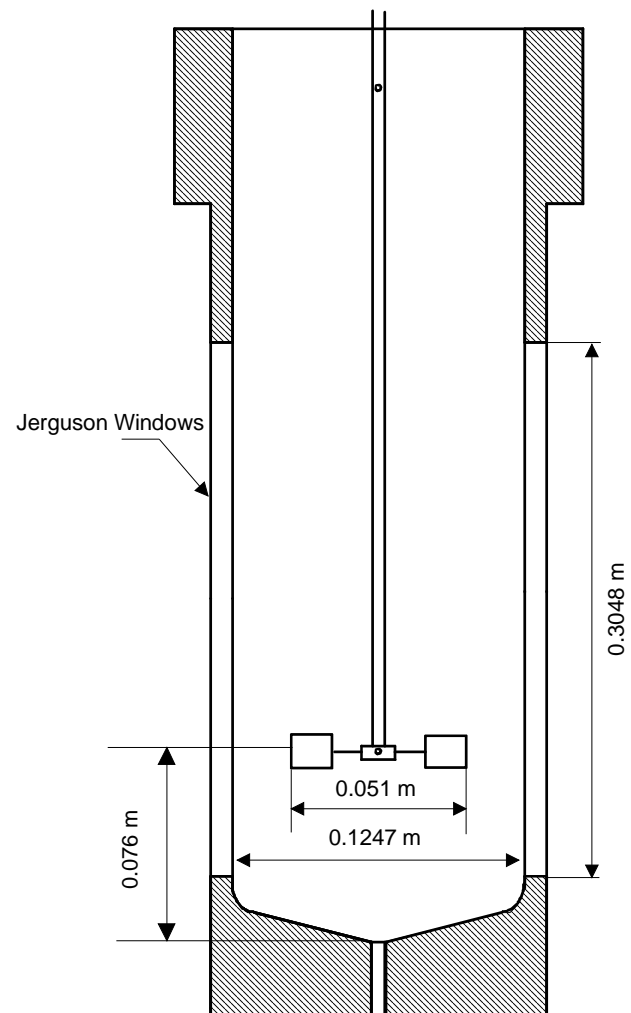


Figure 16: Design of the Jerguson Windows and Position of the Impeller

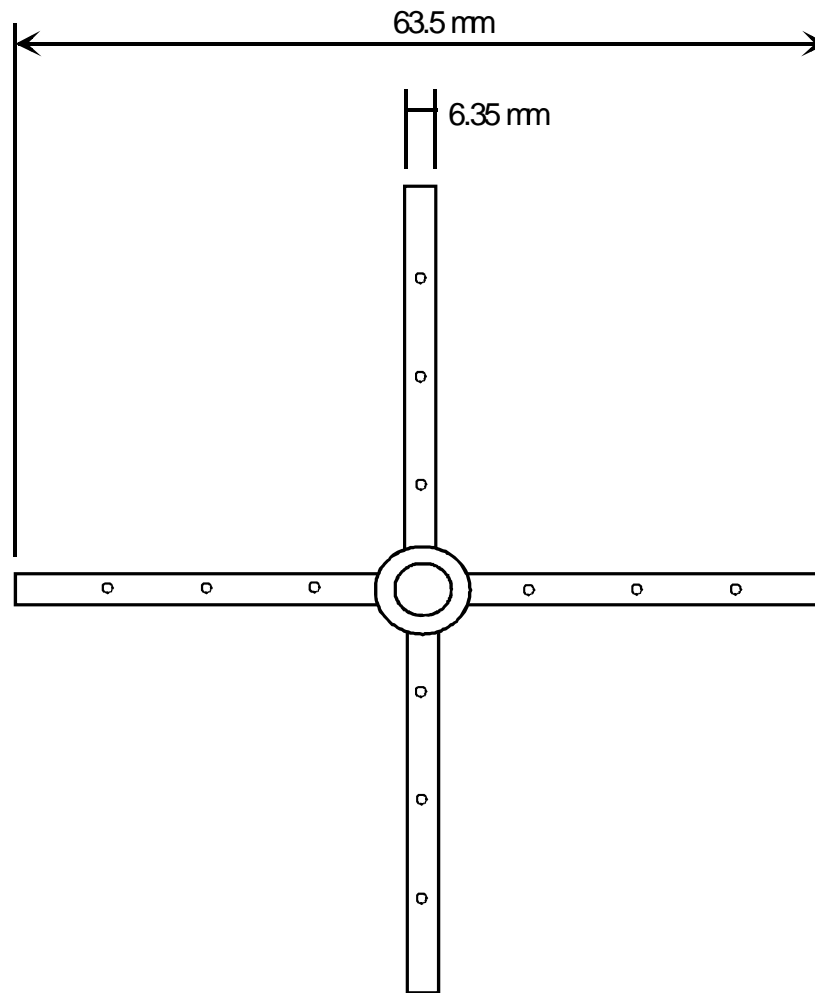


Figure 17: Bottom View of the Gas Distributor in The GSR

4.3.2 Bubble Column Reactor (BCR)

A schematic diagram of the BCR used in this study is shown in Figure 18. The setup is identical to that used by Inga⁽⁵⁶⁾ and Bekhish et al.⁽²¹⁴⁾, and consists of the following main units:

1. Reactor
2. Damper
3. Demister
4. Compressor
5. Supply Vessel
6. Vacuum System
7. DP Cells
8. Data Acquisition System
9. Orifice Meter
10. Sparger

The reactor (column) is constructed from SS 304L, SCH 5 with a maximum pressure rating of 10.3bar (150psig). The reactor inside diameter is 0.316m and its height is 2.811 m. The column consists of two parts provided with flanges. The gas enters from the bottom of the column through a sparger shown in Figure 19⁽⁵⁶⁾. There are two thermocouples and two pressure transducers on the column itself. The hydrostatic pressure is measured through nine lines connected to two ultra-sensitive dP cells manufactured by Foxboro Co. with ratings of 15 and 18.5 inches of water. All thermocouples are type J and pressure transducers are manufactured by Setra model 205-2 rated at 0-100 psig.

The damper has a 0.101m diameter and a length of 0.305m and is constructed from SS 316 SCH 40. It is used to absorb the pressure fluctuations created by the compressor and reduce the noises in the pressure readings.

The demister unit has the same size as the damper. It is placed between the column and the compressor and its purpose is to trap any liquid droplets or mists, which can be carried with the exit gas stream from entering the compressor.

The compressor is model 8 AGD-1 manufactured by Haskel Inc. It is a double-acting, single-stage gas booster operating with house air at 90psig. The maximum output pressure is 300psig.

The supply vessel is a high-pressure unit made of 4" SCH 80 SS 304L with an inside diameter of 0.0984 m and a height of 0.965 m. One Setra model pressure transducer and one J-type thermocouple are connected to this unit in order to calculate the number of moles of gas before and after charging the reactor.

The two vacuum pumps used are model Cit-Alcatel type 2012A, which are oil sealed mechanical vacuum pumps with a 0.75HP motor that can reach pressures down to 1000Pa in the reactor.

The two dP cells used in the reactor are manufactured by Foxboro Co. and have ratings of 15 and 18.5 inches of water, respectively. They are connected to the column through the nine lines as illustrated in Figure 20.

The gas being introduced at the bottom of the column is sparged in the liquid through a six-arm spider type sparger with 5 mm ID holes as shown in Figure 19.

All the pressure transducers, dP cells and thermocouples are connected to a personal computer through a Keithley Data Acquisition Interface, model KDAC 500. This unit allows the storage of data at a very high frequency.

The gas superficial velocity is measured using two different calibrated orifice meters. The orifice used in our study for N₂ has a 16 mm diameter.

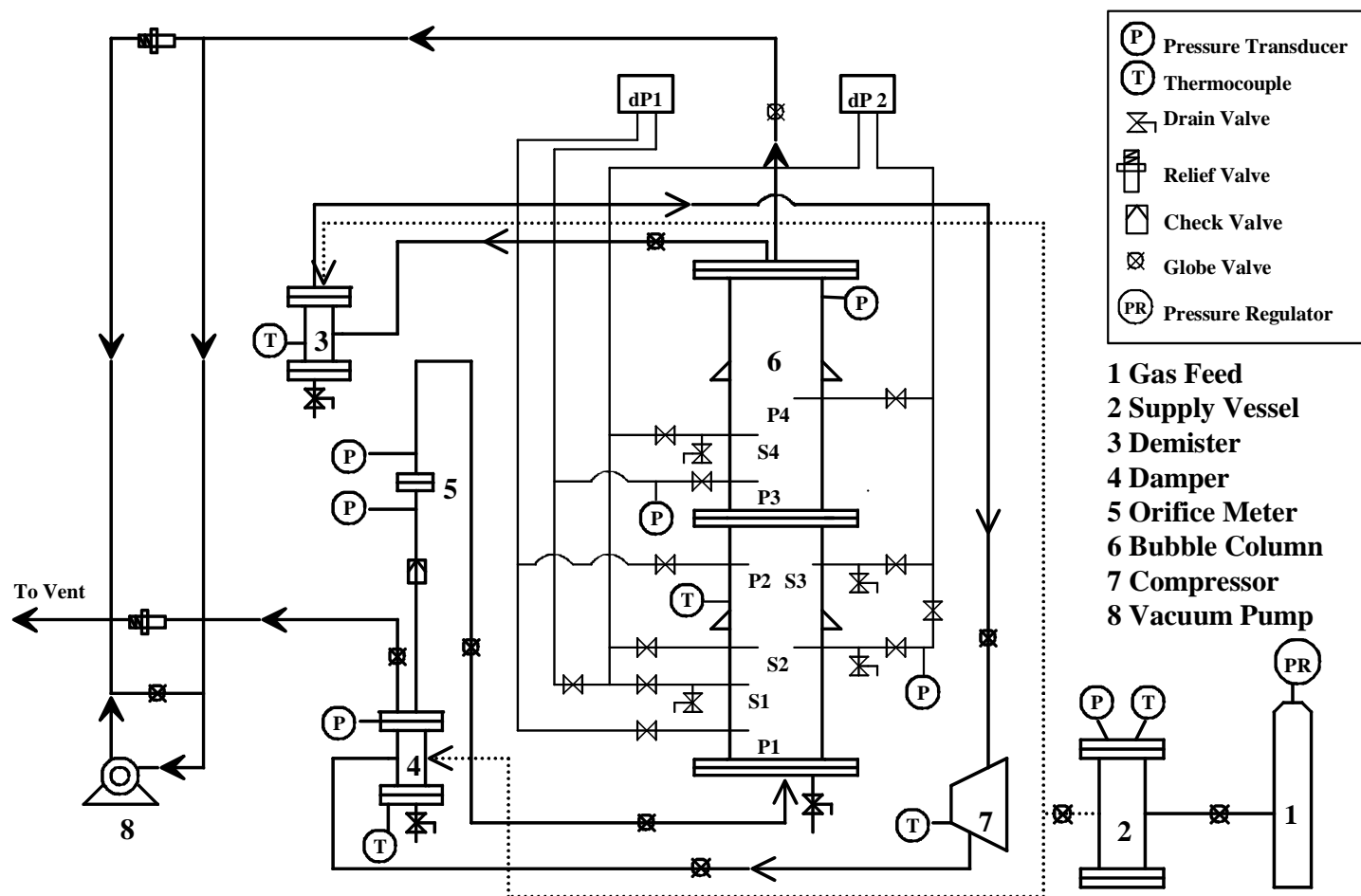


Figure 18: Schematic of the Bubble Column Reactor

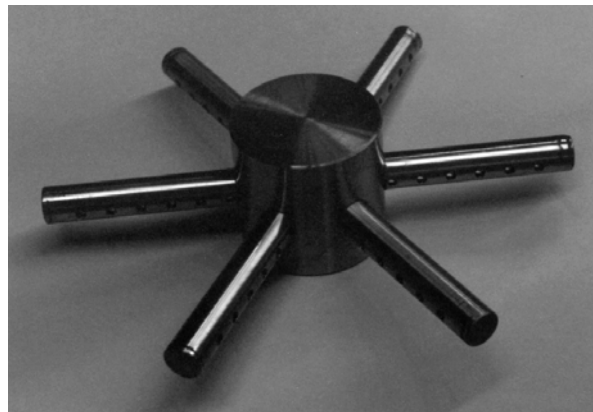
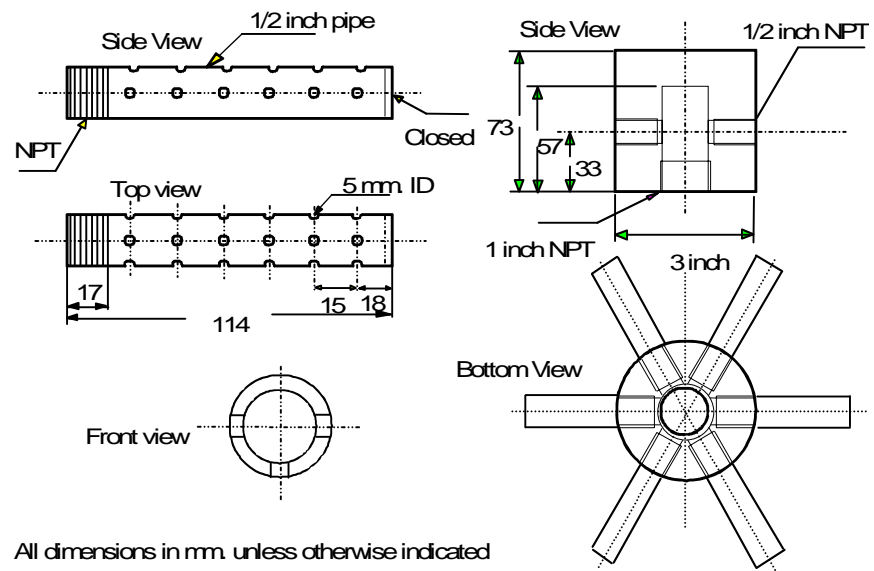


Figure 19: Spider Type Sparger Design ⁽⁵⁶⁾

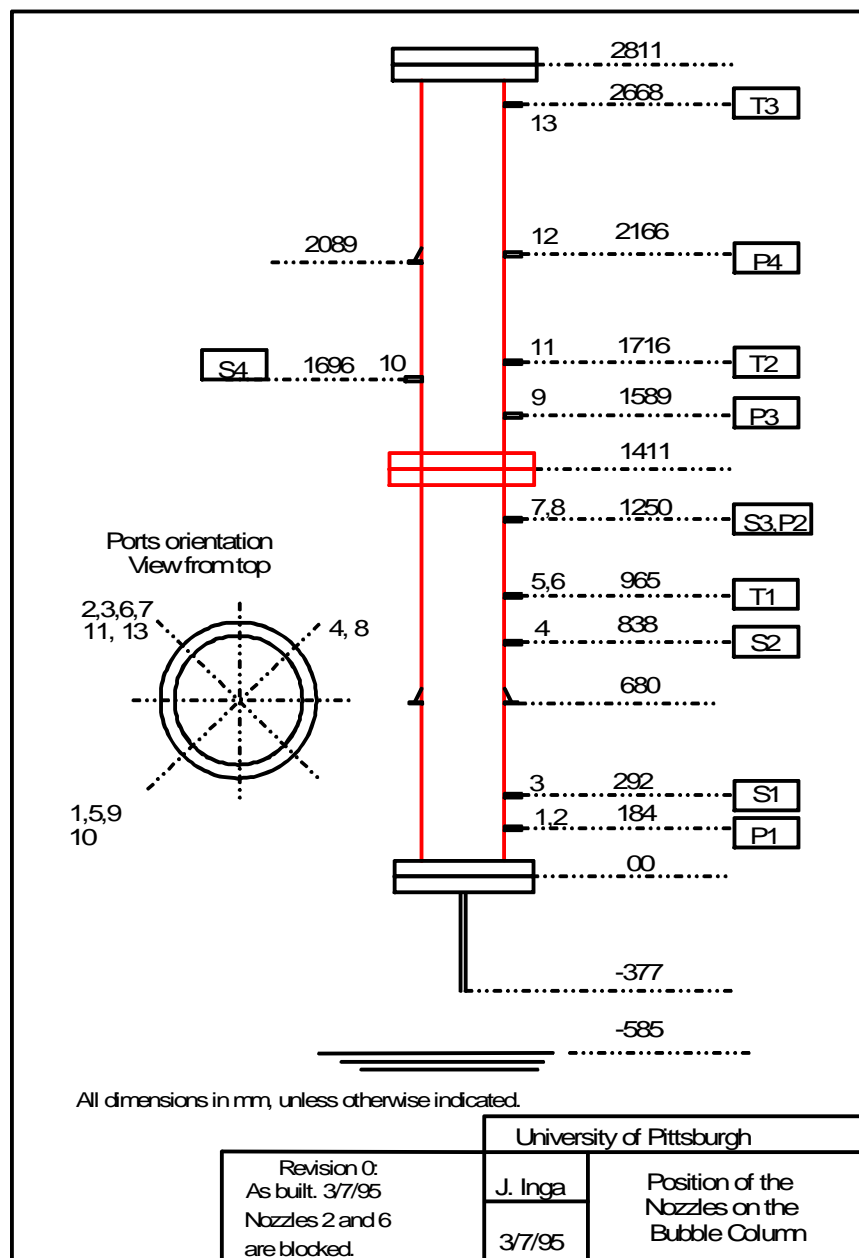


Figure 20: dP Legs Position along the BCR ⁽⁵⁶⁾

4.4 EXPERIMENTAL PROCEDURES

4.4.1 Mass Transfer and Thermodynamic Parameters in the Agitated Reactors

In the agitated reactors, the multi-step physical gas absorption method was used to obtain the equilibrium solubility and the mass transfer coefficient values of N_2 , O_2 and air in the liquid used. This experimental procedure used is similar to that reported by Chang ⁽²⁴⁹⁾; Chang et al. ⁽²⁵⁰⁾; Chang and Morsi ^(251, 252); and Tekie et al. ⁽²⁶⁷⁾. It should also be mentioned that the toluene was changed at regular time intervals in order to avoid any changes in the chemical and physical properties. The experimental procedures followed are given below:

1. A predetermined volume of liquid is charged at room temperature into the reactor.
2. The reactor is closed and the liquid is degassed using the vacuum pump in order to reach the saturation pressure of the liquid.
3. N_2 or O_2 gas is charged into the preheater after purging the remaining air.
4. The contents of the reactor and the preheater were heated to a desired temperature.
5. The initial pressure (P_{LP}) and temperature (T_{LP}) in the preheater were recorded.
6. The gas was charged to the reactor at the same temperature and at an initial predetermined pressure (P_i).

In the SAR and GIR:

8. The reactor content was stirred at a given mixing speed until the thermodynamic equilibrium, characterized by a constant final pressure in the reactor (P_F), was reached. The pressure decline (P_i) was recorded as a function of time.

In the GSR:

8. The gas booster is turned on and the gas flowrate is regulated with a needle valve. The gas is recycled through a bypass. Once the desired gas flowrate is achieved, the reactor is stirred at a predetermined mixing speed. The bypass loop is then closed and the gas is thus sparged into the liquid. The reactor content is stirred until it reaches the thermodynamic equilibrium which is characterized by a constant final pressure (P_F). The pressure decline (P_i) as well as the temperatures as a function of time in each section of the bypass loop are recorded.
9. Steps 5 through 8 were repeated to collect multiple data points at different pressures as shown in Figure 21.

This experimental procedure was followed at each run with different temperature, mixing speed, superficial gas velocity and liquid height. After each run, C^* and $k_L a$ were calculated using a modified Peng-Robinson Equation of State. Detailed calculations of these two values are given in Sections 4. The computer programs developed by Chang ⁽²⁴⁹⁾, to calculate C^* and $k_L a$ were modified for the present gas-liquid systems. The computer programs were designed to:

1. Setup the interfacing channels for data collection.
2. Calibrate the pressure transducers at atmospheric conditions.

3. Record all the operating conditions including temperature, mixing speed, liquid height, etc. of the system in both phases.
4. Monitor the reactor and the preheater temperatures, induced gas flow rate, superficial gas velocity and pressures on a continuous basis.
5. Collect the pressure decline data during the gas absorption on a real time basis.
6. Calculate C^* , x_i , y_i , and K values at equilibrium conditions.
7. Calculate k_La values during the transient period.

4.4.2 Mass Transfer and Thermodynamic Parameters in the BCR

In the BCR the physical gas absorption technique was also employed to measure the gas volumetric mass transfer coefficient in toluene under the operating conditions used. The experimental procedure to obtain k_La is described below:

1. 98 liters of liquid toluene were charged to the reactor.
2. The system was vacuumed to remove any dissolved gases in the liquid. Once the pressure reached the vapor pressure of toluene, the vacuum was stopped.
3. The gas was then charged to the supply vessel and a mass balance was built around it.
4. The gas was then charged to the reactor until the desired pressure was reached.
5. The compressor was started to provide a predetermined superficial gas velocity and the computer started collecting pressure data as a function of time during the gas absorption in the liquid until thermodynamic equilibrium was reached.
6. Once the system reaches equilibrium, data collection was stopped.
7. The C^* was calculated from the reactor initial and final conditions and k_La from the transient part of the pressure-time data, i.e. P-t curve.

In order to obtain C^* and k_La at different pressures, Steps 3-5 were repeated. This experimental procedure was followed at each run with different superficial gas velocity. After each run, C^* and k_La were calculated following the multi-step procedure described previously at constant gas velocity. The computer programs developed by Inga⁽⁵⁶⁾ were modified for the present gas-liquid system. The computer programs were designed to:

1. Setup the interfacing channels for data collection.
2. Calibrate the pressure transducers at atmospheric conditions.
3. Record all the operating conditions of the system in both gas and liquid phases.
4. Monitor the reactor temperature and pressure on a continuous basis.
5. Collect the pressure decline data during the gas absorption on a real time basis.

4.4.3 Hydrodynamic Parameters in the Agitated Reactors

The gas induction and surface entrainment critical mixing speed were estimated by visual observation. For each operating conditions, the mixing speed was increased gradually until the first bubble was induced through the hollow shaft or entrained from the surface into the liquid. In the GIR, the gas induction commences when the reduction in the static pressure near the impeller, caused by its acceleration, is sufficient enough to overcome all the resistances in the path of the gas as described in Section 2.4.2. This mixing speed was designated as the critical mixing for gas induction. In the SAR, the critical mixing speed of gas entrainment was determined when the first gas bubble is entrained from the surface into the liquid. Due to the difficulty of such measurements, the determination of both critical speeds was enhanced by the use of a CDD high-speed video camera in order to achieve more accurate and reproducible values of N_{CR} .

A Coriolis mass flow meter was used to measure the induced gas flow rate by determining the mass flow rate through the agitator hollow shaft under different operating conditions in the GIR. The measurements and recordings of the gas mass flow rate was made possible because of the special design of a leak-free device and external recirculation loop mounted on the shaft and reactor as illustrated in Figure 13. The corresponding Q_{GI} values were then calculated, as it will be described in the next section. Also, using the same Coriolis mass flow meter, the superficial gas velocity was measured in the GSR under the different operating conditions used.

The photographic method, similar to that employed by Fillion and Morsi⁽²⁶⁸⁾, was used to measure the bubble size. The bubbles were recorded through the Jerguson sight window with a CDD camera, manufactured by SONY, during the SAR, GIR and GSR experiments and under the desired operating conditions. The camera was focused on the cooling coil, located above the impeller; and a light source was mounted over the camera in order to provide an optimal lighting. The cooling coil of known outside diameter of 0.00635m, was used to calibrate the bubble size analysis software. The focus of the camera on the cooling coil was essential to avoid and prevent interferences among bubbles, and only discernable bubbles in the focus plan were taken into consideration. The recorded images were then selected and transferred through an image Grabber Software, Snappy 4.0, to a PC. Using Adobe Photoshop 7.0 software, the cooling coil and over 200 bubbles were selected. Their contours were then treated and converted in a black and white image, where the selection appeared in white. A typical image of the gas bubbles is shown in Figure 22. Particle analysis software, Optimas Version 4.1 from Bioscan, was then used to analyze the digitized images.

In the agitated reactors, the dispersion height technique was used to measure the gas holdup under the designed operating conditions. A CCD video camera was located in front of the Jerguson glass window of the reactor, and focused at the gas-liquid interface. As a reference, a ruler was placed along the sight window and the enlarged images on the TV screen were used to precisely measure the dispersion height. Therefore, at any given mixing speed, the gas holdup was determined from the difference between the dispersion height, H_D , and the clear liquid height, H .

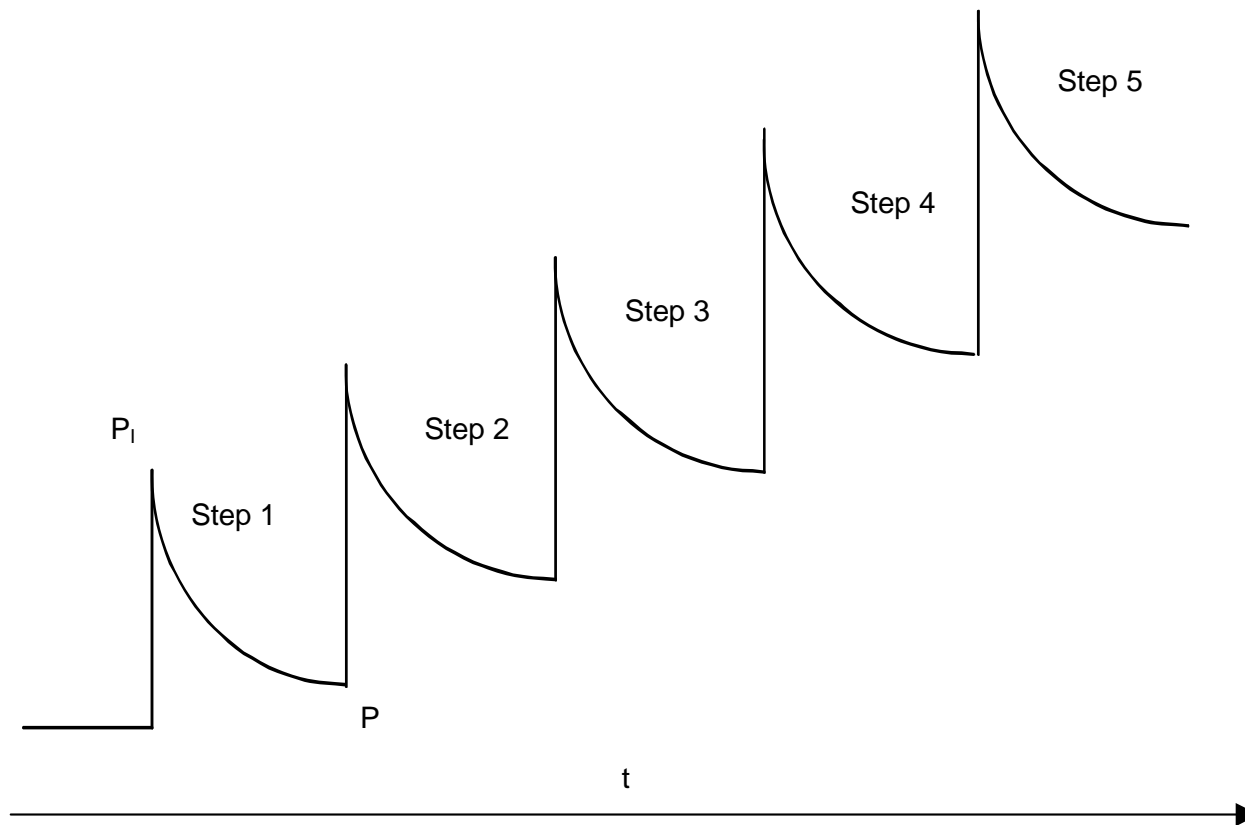


Figure 21: Schematic of the Multi-Step Procedure at Constant Temperature, Mixing Speed and Liquid Height

In the agitated reactors, the bubble contributions to the gas-liquid interfacial area were estimated using the gas holdup and the Sauter mean bubble diameter. The enhancement of the gas-liquid area at the surface due to ripples or waves formation was assessed via the measurement of both wave frequencies and amplitudes. From these measurements, using the small-amplitude wave theory reviewed by Faber⁽³³²⁾, the wave surface was estimated and subsequently the wavy surface contribution to the gas-liquid interfacial area. The frequencies and amplitudes of the surface wave were measured by the analysis of digitized images taken from a high-speed video Phantom camera unit, which enabled the recording of the surface every 3333 μ s, insuring as such a high accuracy of the measured parameters. The unit was provided with a software analysis package especially designed for the measurement of distances, speeds and accelerations, which facilitated the treatment of the recorded images.

4.4.4 Hydrodynamic Parameters in the BCR

In the BCR, the dynamic gas disengagement technique was used to obtain the bubble size and the bubble size distribution. The procedure for the bubble size distribution measurement is as follows:

1. The dP cell legs at a given position were opened.
2. When the compressor was stopped, the dP readings were recorded until all the gas was completely disengaged and the pressure leveled off.

The dP data points recorded were then analyzed and used for both the determination of the bubble size distribution and the Sauter mean bubble diameter, which will be described in Section 5.2.8.

In the BCR, the manometric method was used to obtain the gas holdup values under the operating conditions used. The experimental procedure to obtain ε_G in the BCR is described below:

1. The dP cell legs were purged of liquid.
2. At the predetermined gas velocity, the hydrostatic pressure was measured at different positions along the height of the reactor by opening and closing the corresponding valves.
3. The computer collected the dP cell readings and calculated ε_G at given position.

In order to obtain ε_G at different gas velocities, Steps 1-3 were repeated. The dP readings were then treated to calculate the gas holdup along the column using a computer program developed by Inga⁽⁵⁶⁾ which was modified for the present gas-liquid system. The computer program was designed to:

1. Collect the temperature and pressure along the reactor.
2. Calculate the superficial gas velocity and the gas holdup along the reactor from the differential pressure cells.

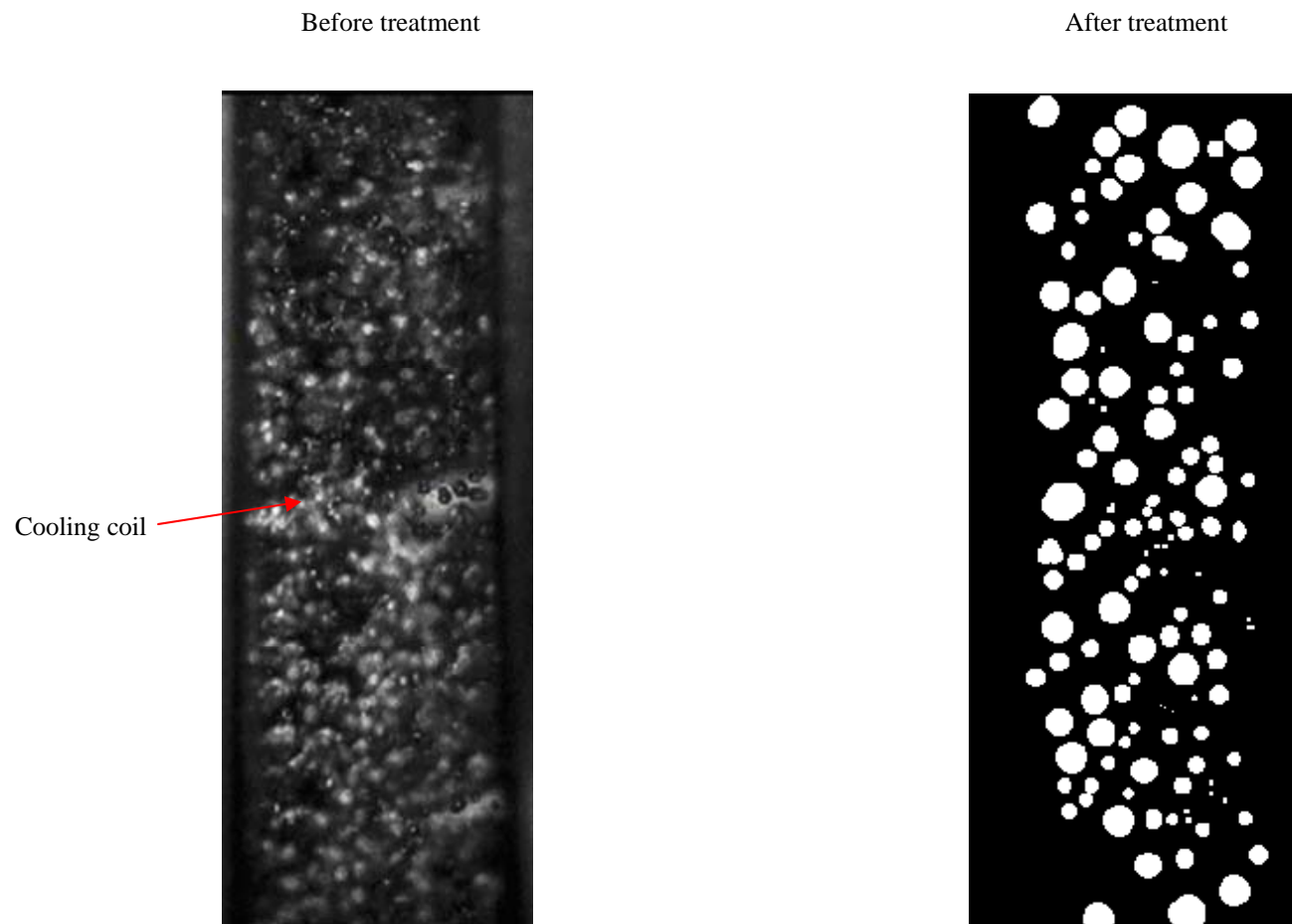


Figure 22: Typical Image of Gas Bubbles before and after Processing in Agitated Reactors

4.5 SAFETY ISSUES

In order to insure safe operation, due to the combustible nature of O₂-toluene mixtures, the explosion limits were investigated under the present experimental conditions. Tables 18 and 19 show the ignition temperatures for the air-toluene system, as well as several experimental flammability limits, reported by Goethals et al. ⁽³³³⁾, Burgoyne et al. ⁽³³⁴⁾, Norrish et al. ⁽³³⁵⁾ and Rozlovskii et al. ⁽³³⁶⁾. Unfortunately, no experimental values were found for the O₂-toluene mixtures. Therefore, calculations were made in order to evaluate the risk of explosion for the O₂-toluene system, using air-toluene experimental data along with a modified equation for the upper limit described by Bodurtha ⁽³³⁷⁾:

$$UFL_{O_2} \% = UFL_{Air} + 70 \times (\text{Log}(C_{O_2}) - 1.321) \quad (4-34)$$

Figure 23 shows the flammability limits for the O₂-toluene system under different conditions as a function of the volumetric percentage of toluene and O₂ pressure. As can be seen, under the operating conditions of this study, only at the highest temperatures, the mixture will be used inside the flammability range. Therefore, a particulate care was taken during those experiments, insuring that the stirred tank is perfectly grounded, in order to avoid any accumulation of static charges at the gas-liquid surface.

Table 20: Ignition temperature for air-toluene mixture ^(334, 335, 336)

<i>P</i> , bar	<i>T</i> , K
2	830
2.5	820
4.7	770
6	730
10	720

4.6 OXIDATION ISSUES

In order to insure both safe operation as discussed above and “non reactive” mass transfer measurements, the liquid phase of each run in the case of O₂ under high temperature was systematically analyzed using a gas chromatograph. As can be seen from the GC and GC-MS analysis provided in Appendix A, the measurements were carried out during the induction period, estimated to be 40 minutes in our study, and accordingly the chemical reaction did not occur during the time of experiments. However, as can be seen in Figure B-1, the run OTS5329 was deliberately carried out for more than 40 minutes, and as expected chemical reaction started to take place, leading to the formation of benzaldehyde shown in Figure B-2.

Table 21: Flammability limits of air and O₂-toluene mixtures in the vapor phase

<i>Operating Conditions</i>				<i>Air</i>		<i>Pure O₂</i>	
<i>P</i> , (bar)	<i>T</i> , (K)	<i>Vol % Toluene</i>	<i>MOC</i> , (Vol %)	<i>LFL</i> , (Vol %)	<i>UFL</i> , (Vol %)	<i>LFL</i> , (Vol %)	<i>UFL</i> , (Vol %)
1	523			0.8	8.1	0.8	55.63
1	503			0.9	8	0.9	55.53
1	473			1	7.8	1	55.33
1	423			1	7.5	1	55.03
1	393			1.1	7.3	1.1	54.83
1	373			1.1	7.2	1.1	54.73
1	333			1.15	7.1	1.15	54.63
1	323			1.2	7	1.2	54.53
8	473	95.4	4.9	0.8	26.6	0.8	74.13
8	463	79.3	5.1	0.8	26.5	0.8	74.03
8	453	65.4	5.3	0.8	26.5	0.8	74.03
8	443	59.6	5.4	0.8	26.4	0.8	73.93
8	433	43.1	5.6	0.9	26.4	0.9	73.93
8	423	34.4	5.8	0.9	26.3	0.9	73.83
8	413	27.1	6	0.9	26.3	0.9	73.83
8	408	24	6.1	0.9	26.2	0.9	73.73
8	403	21.3	6.2	0.9	26.2	0.9	73.73
8	393	16.3	6.3	0.9	26.1	0.9	73.63
8	383	12.4	6.5	1	26.1	1	73.63
8	373	9.1	6.7	1	26	1	73.53
8	363	6.8	6.9	1	26	1	73.53
8	353	4.8	7.1	1	25.9	1	73.43
8	343	2.3	7.2	1.1	25.9	1.1	73.43
8	333	3.4	7.4	1.1	25.8	1.1	73.33
8	323	1.5	7.6	1.1	25.7	1.1	73.23
8	313	1	7.8	1.1	25.7	1.1	73.23

Table 21 (Cont'd)

Operating Conditions				Air		Pure O ₂	
P , (bar)	T , (K)	Vol % Toluene	MOC , (Vol %)	LFL , (Vol %)	UFL , (Vol (Vol %)	LFL , (Vol %)	UFL , (Vol %)
8	303	0.6	8	1.2	25.6	1.2	73.13
8	293	0.4	8.1	1.2	25.6	1.2	73.13
8	283	0.3	8.3	1.2	25.5	1.2	73.03
20	523	85.9	3.4	0.6	35.1	0.6	82.63
20	513	74.1	3.6	0.6	35	0.6	82.53
20	503	63.4	3.8	0.7	35	0.7	82.53
20	493	54	3.9	0.7	34.9	0.7	82.43
20	483	45.6	4.1	0.7	34.8	0.7	82.33
20	473	38.2	4.3	0.7	34.8	0.7	82.33
20	463	31.7	4.5	0.7	34.7	0.7	82.23
20	453	26.2	4.7	0.8	34.7	0.8	82.23
20	443	21.4	4.8	0.8	34.6	0.8	82.13
20	433	17.3	5	0.8	34.6	0.8	82.13
20	423	13.8	5.2	0.8	34.5	0.8	82.03
20	413	10.9	5.4	0.9	34.5	0.9	82.03
20	403	8.5	5.6	0.9	34.4	0.9	81.93
20	393	6.5	5.7	0.9	34.3	0.9	81.83
20	383	5	5.9	0.9	34.3	0.9	81.83
20	373	3.7	6.1	1	34.2	1	81.73
20	363	2.7	6.3	1	34.2	1	81.73
20	353	1.9	6.5	1	34.1	1	81.63
20	343	1.4	6.6	1	34.1	1	81.63
20	333	0.9	6.8	1	34	1	81.53
20	323	0.6	7	1.1	33.9	1.1	81.43
20	313	0.4	7.2	1.1	33.9	1.1	81.43
20	303	0.3	7.4	1.1	33.8	1.1	81.33
20	293	0.2	7.5	1.1	33.8	1.1	81.33
20	283	0.1	7.7	1.2	33.7	1.2	81.23

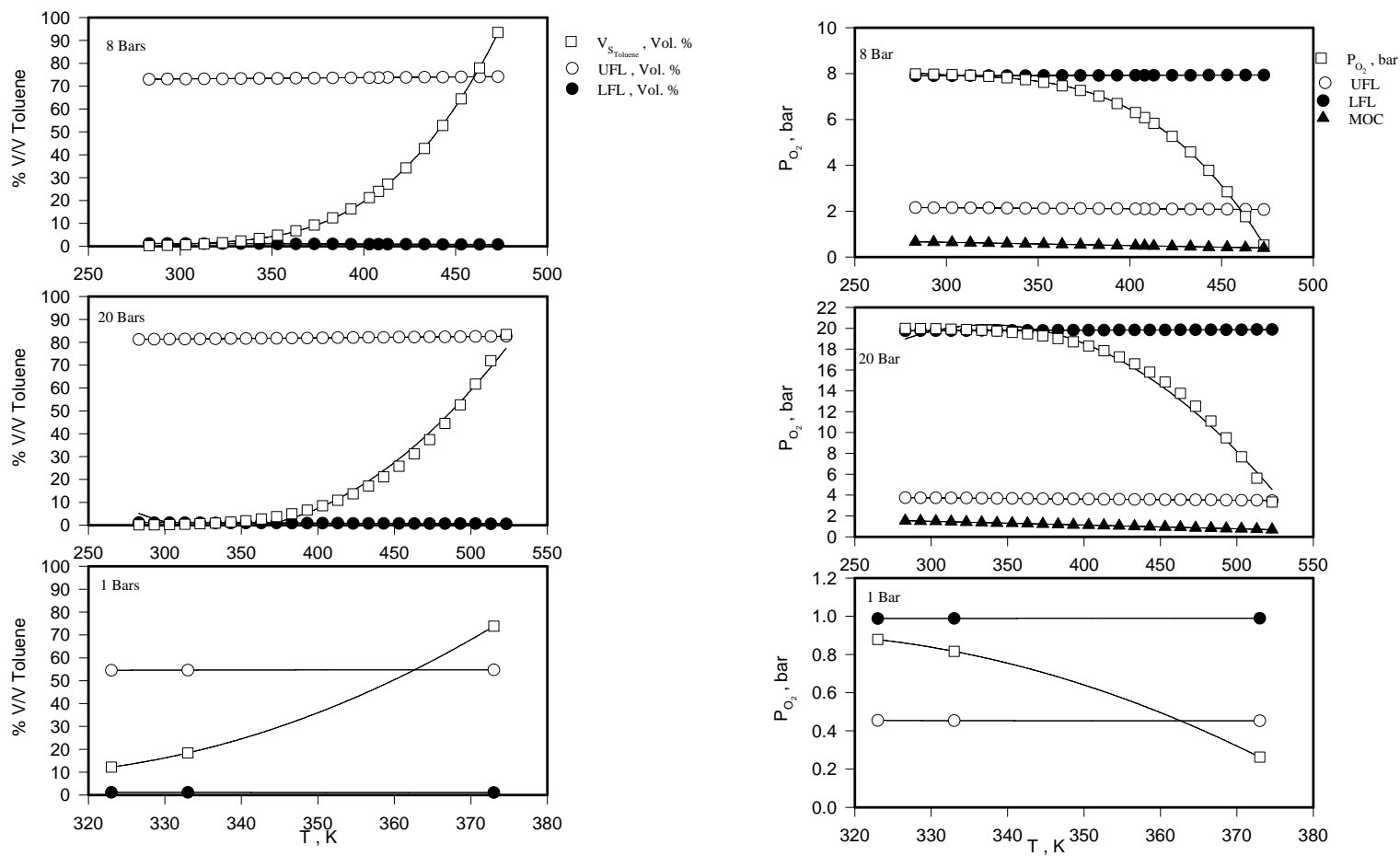


Figure 23: Flammability Limits of O_2 in Toluene as Function of % V/V Toluene and O_2 Partial Pressure

5.0 CALCULATIONS

In the following, the methods for the calculations of thermodynamic, mass transfer and hydrodynamic parameters are reviewed.

5.1 THERMODYNAMIC PARAMETERS

5.1.1 Calculation of C^* in the SAR and GIR

The calculations of C^* were carried out under the following assumptions:

1. Non-ideal behavior of the liquid and gas phases.
2. The liquid phase is well mixed.
3. The amount of gas-absorbed prior to the agitation was also accounted which made the calculation of C^* more rigorous and accurate compared with previous studies^(23, 249).

The Peng-Robinson Equation of State (PR-EOS)^(249, 328, 338) can be written as:

$$P = \frac{RT}{v-b} - \frac{a(T)}{v(v+b)+b(v-b)} \quad (5-1)$$

This equation can be expressed in terms of the compressibility factor, Z as:

$$Z^3 - (1-B)Z^2 + (A-3B^2-2B)Z - (AB-B^2-B^3) = 0 \quad (5-2)$$

where

$$A = \frac{aP}{R^2T^2} \quad (5-3)$$

$$B = \frac{bP}{RT} \quad (5-4)$$

$$z = \frac{Pv}{RT} \quad (5-5)$$

For a single-component, two-phase system the solution of Equation (5-2) results in three roots with the largest positive root corresponding to the vapor phase and the smallest positive root greater than “ b ” corresponding to the liquid phase. At the critical point:

$$a(T_c) = 0.45724 \frac{R^2 T_c^2}{P_c} \quad (5-6)$$

$$b(T_C) = 0.07780 \frac{RT_C}{P_C} \quad (5-7)$$

At any temperature:

$$a(T) = a(T_C) \alpha(T_R \omega) \quad (5-8)$$

$$b(T) = b(T_C) \quad (5-9)$$

$$\alpha^{1/2} = 1 + \kappa(1 - T_R^{1/2}) \quad \text{with} \quad (5-10)$$

$$\kappa = 0.37464 + 1.5422 \omega - 0.26992 \omega^2 \quad (5-11)$$

The fugacity of a pure component is written as:

$$\ln\left(\frac{f}{P}\right) = Z - 1 - \ln(Z - B) - \frac{A}{2\sqrt{2}B} \ln \frac{Z + (1 + \sqrt{2})B}{Z + (1 - \sqrt{2})B} \quad (5-12)$$

For a binary system, the binary interaction parameter δ_{ij} is required in order to use the PR-EOS. The mixing rules are defined as follows:

$$a = \sum_i \sum_j x_i x_j a_{i,j} \quad (5-13)$$

$$b = \sum_i x_i b_i \quad (5-14)$$

$$a_{ij} = (1 - \delta_{ij}) a_i^{1/2} a_j^{1/2} \quad (5-15)$$

The fugacity of each component in the liquid phase is calculated from:

$$\ln \frac{f_k}{x_k P} = \frac{b_k}{b} (Z - 1) - \ln(z - B) - \frac{A}{2\sqrt{2}B} \left(\frac{\sum_i x_i a_{ik}}{a} \right) \ln \frac{Z + (1 + \sqrt{2})B}{Z + (1 - \sqrt{2})B} \quad (5-16)$$

If the values of x_i and x_j are replaced by y_i and y_j , Equations (5-13), (5-14) and (5-16) can be used for the vapor phase.

The PR-EOS was selected to calculate the liquid and gas phase densities of the system used, as well as the solubility of the gases, C^* , the concentration of the gases in the liquid, C_L , and the total liquid volume, V_L , which were subsequently used in the $k_L a$ calculations. In order to check the accuracy of the PR-EOS, the following steps were followed:

1. The saturated liquid density of the liquid was calculated using the Rackett Equation (4-15).
2. The PR-EOS was used to calculate the saturated liquid density of the liquid, where the pressure of the saturated liquid is the vapor pressure estimated from the Wagner's Equation (4-4).
3. These density values were compared, as shown in Figure 24, and a significant difference can be observed.

Since the Rackett equation provides accurate estimates of the saturated liquid density of toluene, two parameters Ψ_1 and Ψ_2 were introduced in the sub-functions of the PR-EOS in order to correct the predicted liquid-phase density of the PR-EOS as previously reported by Enick et al. ⁽³³⁹⁾, Chang ⁽²⁴⁹⁾ and Tekie ⁽²³⁾. The two corrections factors, Ψ_1 and Ψ_2 , were introduced into the two sub-functions in the PR-EOS as Enick et al. ⁽³³⁹⁾:

$$\alpha^{1/2} = 1 + \Psi_1 \kappa (1 - T_R^{1/2}) \quad (5-17)$$

$$b(T_c) = \Psi_2 0.07780 \frac{RT_c}{P_c} \quad (5-18)$$

Ψ_1 and Ψ_2 were then optimized during an iteration process in which the squared error between the saturated liquid densities obtained by the modified PR-EOS and the Rackett Equation (4-15) was minimized. The optimized values of Ψ_1 and Ψ_2 were then correlated as a function of temperature with the following equations:

$$\Psi_1 = A + B 10^{-3} T + C 10^{-6} T^2 + D 10^{-8} T^3 \quad (5-19)$$

$$\Psi_2 = E + F 10^{-3} T + G 10^{-6} T^2 \quad (5-20)$$

with T in K in Equations (5-19) and (5-20) and ranging from 290 to 460K. The Values of the constants A, B, C, D, E and F can be found in for each liquid.

Table 22: Constants in Equations (5-19) and (5-20)

Liquid	A	B	C	D	E	F	G
Pure Toluene	0.72	1.78	-2.07	-	0.83	1.06	-1.40
Mixture # 1	0.49	2.29	-3.45	-	0.82	0.92	-1.15
Mixture # 2	1.66	-7.24	22.81	-2.37	0.81	0.95	-1.19
Mixture # 3	1.71	-7.50	23.60	-2.43	0.81	0.95	-1.21

Figure 24 shows the saturated liquid density of toluene from the Rackett equation, the PR-EOS without correction and the modified PR-EOS, and as can be seen in this figure, a very good agreement was found between the modified PR-EOS and the Rackett equation.

The modified Peng-Robinson Equation of State (PR-EOS) coupled with components mole and volume balances were used for the calculation of the equilibrium solubility of the gases in toluene. For a two-component, two-phase system at equilibrium, the fugacities of each component in each phase are equal:

$$f_i^L = f_i^G \quad (5-21)$$

The fugacities were calculated using Equation (5-16). From the mass balance equation, the total number of moles in the reactor stays the same as:

$$N_T = N_G + N_L \quad (5-22)$$

The component balance could be written as:

$$N_1 = N_G y_1 + N_L x_1 \quad (5-23)$$

$$N_2 = N_G y_2 + N_L x_2 \quad (5-24)$$

The overall volume balance is:

$$V_R = V_L + V_G \quad (5-25)$$

V_L and V_G were calculated using the number of moles and the molar volumes (v_G and v_L) obtained from the modified PR-EOS as:

$$V_G = N_G v_G \quad (5-26)$$

$$V_L = N_L v_L \quad (5-27)$$

In addition to these equations, the number of moles charged to the reactor, N_I , is calculated from the difference between the initial and final conditions in the preheater, using the PR-EOS. The equations used for the calculation of the initial and final molar volumes are:

$$v_G^I = \frac{RT_I Z_G^I}{P_I} \quad (5-28)$$

$$v_G^F = \frac{RT_F Z_G^F}{P_F} \quad (5-29)$$

Subsequently, the number of moles charged becomes:

$$N_I = V_{preh} \left(\frac{1}{v_G^I} - \frac{1}{v_G^F} \right) \quad (5-30)$$

where V_{preh} is the volume of the preheater. The initial number of moles of liquid in the reactor was determined from the amount of liquid charged and its molar volume at ambient conditions as:

$$N_2 = \frac{V_L}{v_L} \quad (5-31)$$

The liquid molar volume can be calculated from:

$$v_L = \frac{Z_L RT}{P_T} \quad (5-32)$$

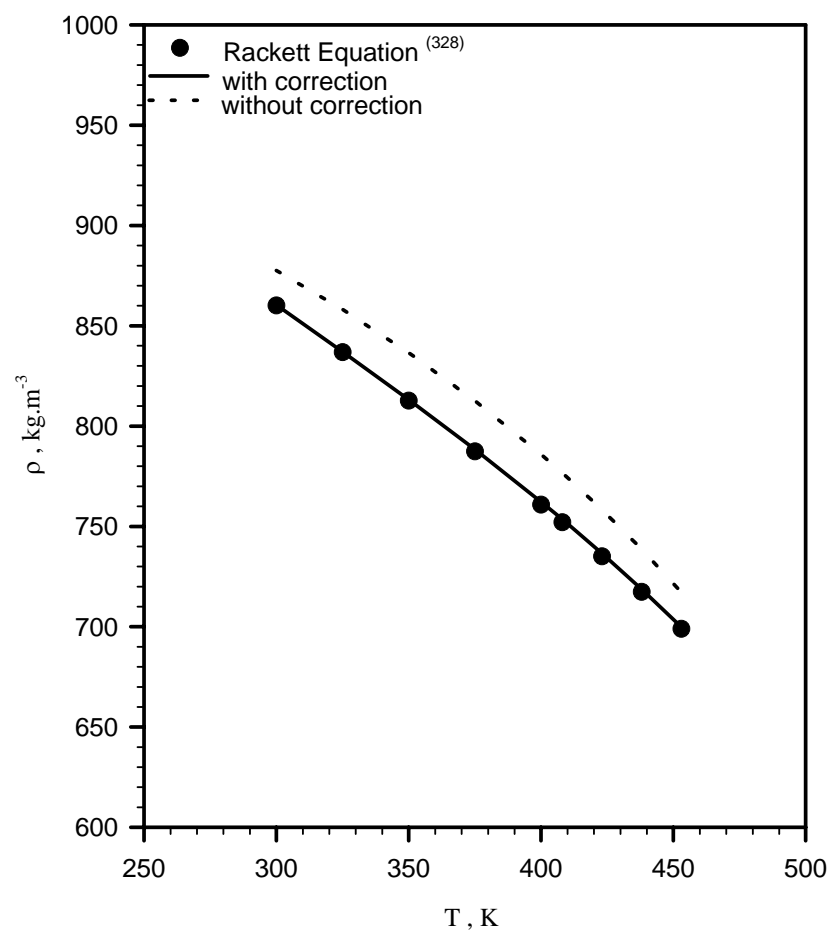


Figure 24: Validation of the Modified PR-EOS by Density Calculation

Based on the above equations, an iterative calculation algorithm of C^* initially developed by Chang ⁽²⁴⁹⁾ was modified for the present systems and used. The main steps of this algorithm are depicted in Figure 26 and are summarized in the following.

1. The vapor pressure P_s of toluene is calculated using Wagner Equation (4-4); and the initial values of $y_2 = P_s/P_T$ and $x_1 = 0$ are assumed.
2. A value of the binary interaction parameter, δ_{ij} is assumed.
3. y_1 is calculated as $y_1 = 1 - y_2$.
4. Z_G is calculated using Equations (5-2) to (5-5), (5-13) and (5-14).
5. The molar volume of the gas phase v_G is calculated from:

$$v_G = \frac{Z_G RT}{P_T} \quad (5-33)$$

6. The vapor phase fugacities of both components are calculated using Equation (5-16).
7. x_2 is calculated from $x_2 = 1 - x_1$.
8. Z_L is calculated using Equations (5-2) to (5-5), (5-13) and (5-14).
9. The molar volume of the liquid phase v_L is calculated from:

$$v_L = \frac{Z_L RT}{P_T} \quad (5-34)$$

10. At equilibrium, $f_1^L = f_1^G$ from which a new value of x_1 , \bar{x}_1 is obtained.
11. If the error calculated from $\Delta x = |\bar{x}_1 - x_1|$ is not less than the specified accuracy (10^{-6}), steps 7 to 11 are repeated with the new value of $x_1 = \bar{x}_1$.
12. f_2^L is obtained from Equation (5-16), since x_1 is fixed.
13. At equilibrium, $f_2^L = f_2^G$ must be true, and a new value of y_2 , \bar{y}_2 is obtained.
14. Again, if the error calculated from $\Delta y = |\bar{y}_2 - y_2|$ is not less than the specified accuracy (10^{-6}), steps 3 to 13 are repeated with the new value $y_2 = \bar{y}_2$.
15. From Equations (5-23) and (5-24), N_L and N_G are calculated.
16. The gas and liquid phase volumes are determined from $V_G = (v_G \times N_G)$ and $V_L = (v_L \times N_L)$, respectively.
17. A volume balance is confirmed if $V_R = V_G + V_L$, otherwise a new value of the interaction parameter δ_{ij} is assumed and steps 2 through 15 are repeated.
18. If the volume balance is confirmed, the equilibrium values of x_1 , y_1 , v_L and v_G are obtained at the corresponding pressure and temperature. Finally C^* is calculated from:

$$C^* = \frac{x_1}{v_L} \quad (5-35)$$

Using these data, an expression of the gas solubility C^* as a function of pressure can be developed at a constant temperature as:

$$C^* = E_o P_{IF} + E_I P_{IF}^2 \quad (5-36)$$

with $E_I=0$ if the gas-liquid system obeys Henry's law.

5.1.2 Calculation of C^* in the GSR

In the GSR, the number of mole of the gaseous component in the gas phase at any instant, t , was obtained from a mass balance built on the reactor and the re-circulation loop units (Figure 25) as:

$$N_{G,t} = N_{G-Reactor,t} + N_{Heat\ Exchangers,t} + N_{Gas-Booster,t} + N_{Damper,t} + N_{Flowmeter,t} + N_{Preheater\#2,t} \quad (5-37)$$

$$N_{G,t} = \frac{(P_R - P_S)(V_R - V_L)}{ZRT_{G-Reactor}} + \frac{(P_R - P_S)V_{Heat\ Exchangers}}{ZRT_{Heat\ Exchangers}} + \frac{P_{Gas-Booster}V_{Gas-Booster}}{ZRT_{Gas-Booster}} + \frac{P_{Damper}V_{Damper}}{ZRT_{Damper}} + \frac{P_{Flowmeter}V_{Flowmeter}}{ZRT_{Flowmeter}} + \frac{P_{Preheater\#2}V_{Preheater\#2}}{ZRT_{Preheater\#2}} \quad (5-38)$$

Since the gas phase is cooled down at the reactor exit and all vapors are condensed in the liquid trap, the gas entering the gas booster can be considered dry. The solubility at the equilibrium final gas partial pressure, $P_{I,f}$, and temperature in the reactor can therefore be calculated at thermodynamic equilibrium from:

$$C^* = \frac{N_T - N_{G,f}}{V_L} \quad (5-39)$$

N_T is the initial number of gas moles charged in the unit, which is calculated through a mass balance on the preheater #1 (Figure 13).

5.1.3 Calculation of C^* in the Bubble Column Reactor

The solubility of air and N_2 in the liquids used is not the main objective of the design experiments in the BCR; however, for the sake of comparison with the stirred reactor data, the equilibrium solubility values in the BCR were calculated. The calculation was carried out using the PR-EOS, which was modified for the different liquid used as described previously. The details of the calculation of C^* and the general assumptions made are given below:

1. In the feed tank, a non-ideal gas was assumed and the PR-EOS was used.
2. In the BCR, the binary mixture behavior was assumed to be ideal.
3. The gas and liquid were assumed well mixed, i.e., the concentration of the gas component in the liquid phase was assumed to be homogeneous.
4. There is no change in the liquid volume due to gas absorption.
5. The compression heat is negligible.
6. There is a negligible absorption prior to the start of the compressor

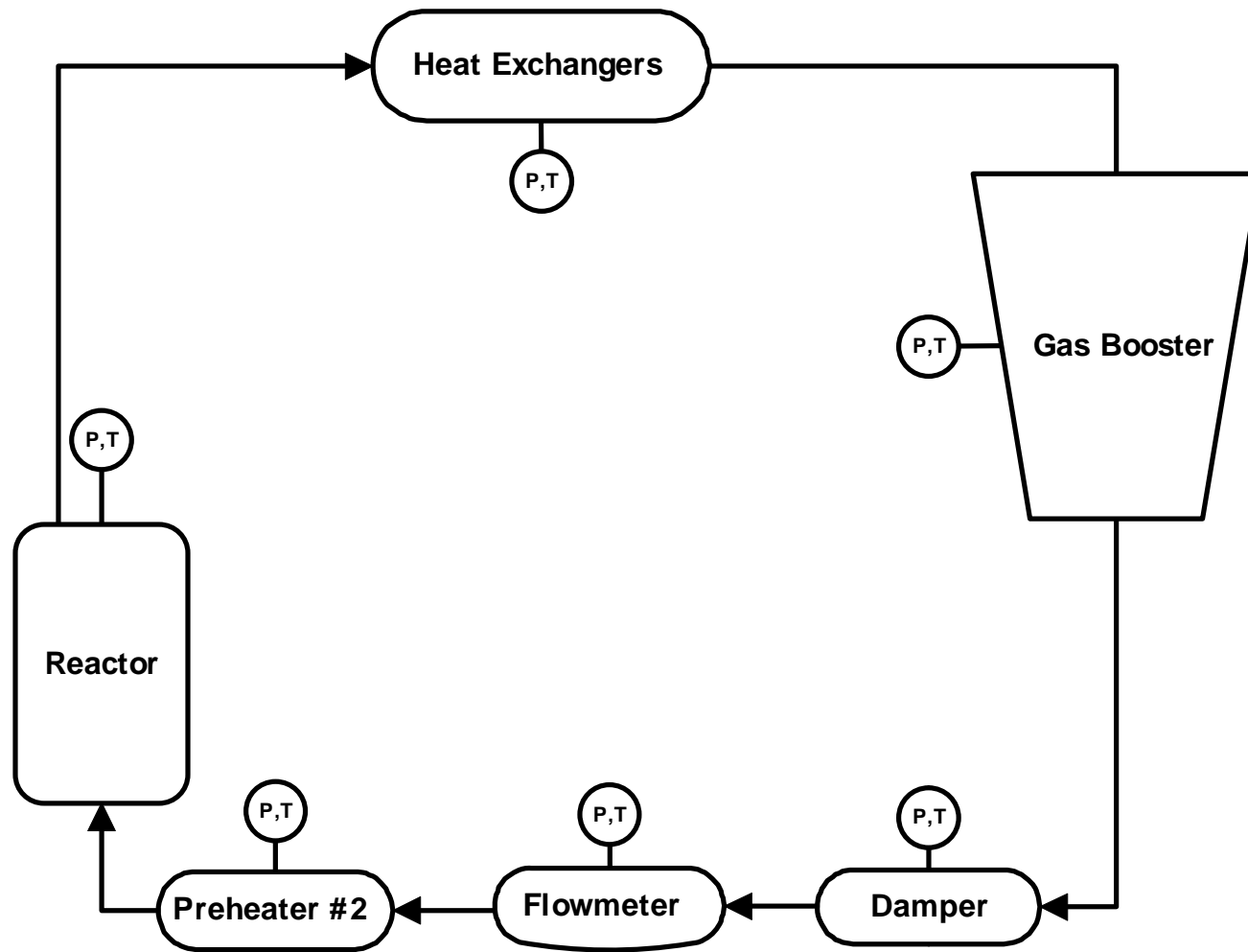


Figure 25: Flow Diagram of the re-circulation Path in the GSR

Since the pressure in the feed tank was high, the first assumption was essential to insure better accuracy in the mass balance. The second assumption was justified from the operating conditions, since both pressure and temperature were low. The homogeneity of the liquid phase was validated by the churn turbulent flow regime under which the BCR was operated. The fourth assumption was based on the analysis of the solubility values obtained in the stirred reactor and the maximum pressure used in the bubble column. The calculated increase of the liquid phase volume in the BCR was found to be negligible and equal to 2.5%. The fifth assumption was experimentally verified, since the absorption process lasted less than 40 seconds and subsequently the time for the compressor to heat and increase the gas temperature was very small, maintaining the gas and liquid temperatures constant. The last assumption was also experimentally verified, since the pressure was found to be independent of time until the compressor startup.

The calculation method of C^* in the BCR was based upon a material balance on the gas charged in the reactor, which was calculated from:

$$N_0 = \frac{P_{Charged}(V_{Reactor} - V_{Liquid})}{z_{Charged}RT} \quad (5-40)$$

The PR-EOS was used to calculate the compressibility factors of the gas, $z_{Charged}$. In the column, the solute gas mole balance can be expressed as:

$$N_0 = N_{i,G} + N_{i,L} \quad (5-41)$$

At equilibrium:

$$P_T = P_v + P_I \quad (5-42)$$

Since P_v is known from Equation (4-4), the partial pressure of the solute gas can be calculated from the total pressure. The material balance of the solute in the gas phase is then:

$$N_{i,G} = \sum \frac{P_{T,j}V_j}{RT_j} - \sum \frac{P_vV_j}{RT_j} \quad (5-43)$$

The measurement of the pressure and temperature at different points across the system allows the calculation of the number of moles in the entire system. It should be mentioned that, when comparing the volume of each part of the setup, we concluded that more than 90% of the total gas moles is in the reactor. Thus, it is reasonable to assume that: $\sum P_i V_i = P \sum V_i = P V_G$, and the concentration of the solute gas in the liquid phase can then be calculated from:

$$C_{i,L} = \frac{N_0 - N_{i,G}}{V_L} = \frac{N_0 - (P_T - P_v)V_G/RT}{V_L} \quad (5-44)$$

At equilibrium, the solubility C^* is calculated as:

$$C^* = \frac{N_0 - (P_{T,F} - P_v)V_G/RT}{V_L} \quad (5-45)$$

where $P_{T,F}$ is the final total equilibrium pressure.

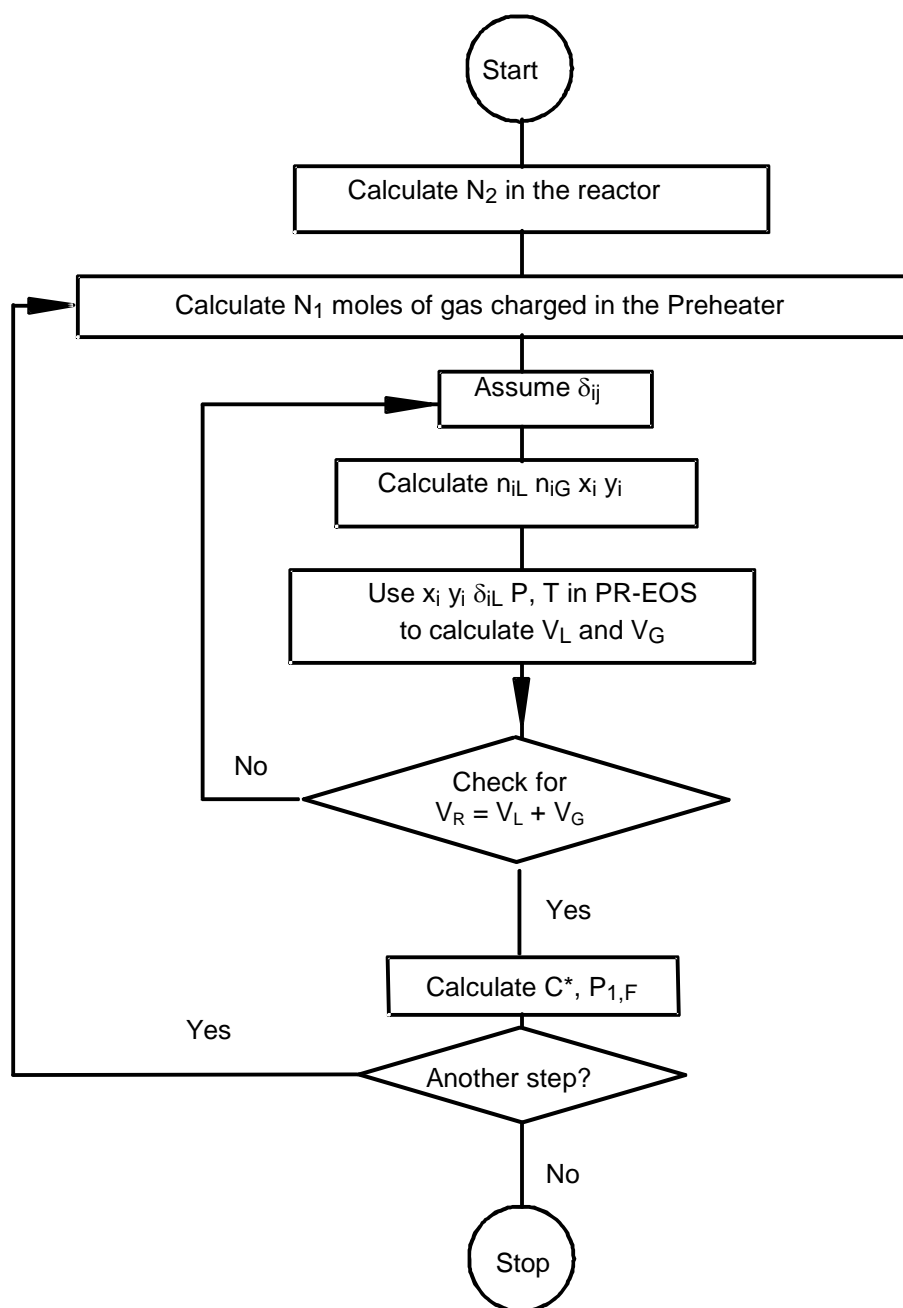


Figure 26: Algorithm for C^* Calculation in the Agitated Reactors⁽²⁴⁹⁾

5.2 HYDRODYNAMIC PARAMETERS

In the following, the critical mixing speed, induced gas flow rate, bubble size and gas holdup calculation procedures are reviewed in details for the gas-liquid contactors used in this study. It should be mentioned, that the critical mixing speed, induced gas flow rate, gas hold up and bubbles size, in the agitated reactors were initially carried out in another reactor, with identical geometry to the one employed for k_{La} measurements, and therefore systematic checks and calculations were performed in order to detect any differences or changes in the k_{La} values. In fact, as shown in Figure 27, a very good agreement, in the order of the experimental error, was found, which validates our experimental data.

5.2.1 Critical Mixing Speed Measurement, N_{CR} , in the Agitated Reactors

The critical mixing speed for gas induction was measured under wide ranges of operating conditions, following the procedure described in Section 4.4.3. Using a high-speed video camera, the mixing speed was simply increased until the appearance of the first gas bubble in the liquid toluene in the SAR and GIR. In the SAR, the gas was entrained into the liquid and therefore special care was taken to monitor the gas-liquid surface, whereas in the GIR since the gas was induced from the hollow shaft, the impeller region was examined carefully.

5.2.2 Calculation of the Gas Flow Rate, Q_{GI} , in the Agitated Reactors

In the GIR, a Coriolis mass flow meter Type CMF-010M manufactured by Micro Motion Inc., Boulder, CO was used to measure the induced gas mass flow rate, $M^*_{Measured}$ through the agitator hollow shaft under different operating conditions. Q_{GI} was calculated as follows assuming ideal mixture in the gas phase:

$$y_{Gas} = \frac{P_{Gas}}{P_T} ; y_{Tol.} = \frac{P_{Tol.}}{P_T} \quad (5-46)$$

$$\rho_{mixture} = y_{Gas} \frac{P_T M_{W-Gas}}{RT} + y_{Tol.} \frac{P_T M_{W-Tol.}}{RT} \text{ then:} \quad (5-47)$$

$$Q_{GI} = y_{Gas} \times \frac{M^*_{Measured}}{\rho_{mixture}} \quad (5-48)$$

5.2.3 Calculation of the Gas Flow Rate, Q_G , in the BCR

In the BCR, using the theory of flow through orifices and nozzles⁽³⁴⁰⁾, the volumetric flow rate was calculated using the following equation:

$$Q_{Gas} = Y \times C \times \Omega \times \sqrt{\frac{2g \times (144) \times \Delta P}{\rho_G}} \quad (5-49)$$

where Ω is the orifice cross section area in ft^2 , Y is the expansion factor and C is the flow coefficient, and P is in Psi and ρ_G in lb.ft^{-3} . Since two pressure transducers measured the ΔP across the orifice, the values of C and Y were computed through iterative calculations of the gas Reynolds number ⁽³⁴⁰⁾ for a pipe to orifice diameter ratio of 0.6, and pressure ratio ⁽³⁴⁰⁾, respectively. The iterative programs developed by Inga ⁽⁵⁶⁾ were used and modified for the present gas-liquid system.

5.2.4 Calculation of the Superficial Gas Velocity, U_G , in both Contactors

The superficial, terminal and orifice gas velocity were respectively calculated as:

$$U_G = 4 \frac{Q_{Gl}}{\pi(d_T)^2} \quad (5-50)$$

$$U_T = \sqrt{\frac{2\sigma_L}{d_B(\rho_L + \rho_G)} + \frac{gd_B}{2}} \quad (5-51)$$

$$U_{orifice} = \frac{1}{n} \times 4 \frac{Q_G}{\pi(d_{orifice})^2} \quad (5-52)$$

where n is the number of orifices. Equation (5-51) was taken from Jamialahmadi et al. ⁽³⁴¹⁾ who developed this general correlation for the prediction of the terminal bubble rise velocity using air-toluene as part of the systems investigated. In the both gas-liquid contactors, the superficial gas velocity was calculated through the measurement of the gas flow rate at the orifice meter using Equation (5-50). The contact time, t_C , was define as follows, assuming that the bubble is a cylinder of length d_s rising vertically through the liquid at the velocity U_G as follows:

$$t_C = \frac{d_s}{U_T} = \frac{d_s V_L \varepsilon_G}{Q_G H_L (1 - \varepsilon_G)} \quad (5-53)$$

5.2.5 Gas Holdup in the Agitated Reactors, ε_G

In the agitated reactors, the dispersion height technique was used to measure the gas holdup under the designed operating conditions, since the manometric method was reportedly unsuccessful by Tekie ⁽²³⁾ due to considerable turbulences created by the impeller, affecting the dP cells signal. Therefore, at any given mixing speed using the experimental method described in Section 4.4.3, ε_G was determined from the difference between the dispersion height, H_D , and clear liquid height, H , as:

$$\varepsilon_G = \frac{H_D - H}{H_D} \quad (5-54)$$

5.2.6 Gas Holdup in the BCR, ε_G

The gas holdup ε_G in the BCR was determined using the hydrostatic head method, also called manometric method. This method is based on the measurement of the gas volume fraction in the reactor under given operating conditions with the following assumptions: (1) the reactor is operating under steady-state condition; (2) the liquid and gas phases are well mixed; and (3) the impacts of the frictional effects on the pressure drop are negligible. In the experiments, enough time was allowed for the gas-liquid system to reach steady state, which was confirmed by plotting the gas holdup in the column as a function of time for each dP positions, as shown in Figure 28. The gas holdup values between position 1 (dP1) and the bed height (between dP3 and dP4) shown in Figure 29 are almost the same, indicating that large gas bubbles have created strong liquid circulation and bubbles back-mixing throughout the entire reactor ⁽⁵⁶⁾ and subsequently the liquid and gas phases can be assumed well mixed. Also, Gharat and Joshi ⁽³⁴²⁾ and Boyer et al. ⁽³⁴³⁾ reported slight impact of the frictional effects on the pressure drop in the Manometric method under both the homogeneous and churn-turbulent regime in BCRs, which confirms the third assumption. Essentially, the ε_G at two different positions in the BCR is measured using the two dP cells. Since the distance between the dP legs (ΔL_{dP}) and the density of the phases are known, ε_G can be calculated for each dP leg positions using the following equation:

$$\varepsilon_G = \left(\frac{\rho_L}{\rho_L - \rho_G} \right) \times \left[1 - \frac{\Delta P_{Cell}}{\rho_L \Delta L_{dP} g} \right] \quad (5-55)$$

An average gas holdup was then calculated in the column. In addition, in the BCR, large bubbles with high gas holdup are expected to rise quickly through the liquid and create back-mixing, whereas the smaller ones, entrained in the re-circulation path ⁽⁵⁶⁾, rise slowly to the surface. The coexistence of small and large gas bubbles in bubble column reactors have been reported using visual observations and photographic methods ^(179, 229, 235, 462, 465, 344). Rupture and coalescence of the bubbles may take place at any point inside the reactor, and could be explained by two competing forces, namely the surface tension and inertia. The surface tension force tends to maintain the gas bubbles in a spherical shape, whereas the inertial force tends to elongate the gas bubbles. Therefore, due to the existence of these two classes of bubbles in BCRs, the gas holdup of small and large bubbles was determined based on an arbitrary bubble diameter of:

$$d_{B-Small} \leq 1.5mm \quad (5-56)$$

The corresponding gas holdups were calculated by analyzing the dP cell signal after the sudden interruption of the compressor, using the Dynamic Gas Disengagement technique, which will be discussed in the following section. It should also be mentioned that the gas and liquid were assumed well mixed and enough time was given to reach steady state, which was confirmed by the actual plot of the axial profile of the gas holdup. In fact, as can be seen in Figure 28, the actual readings from the dP cells were not affected by time and the gas holdup values compared well at each positions on the column. Figure 29 also indicates that the liquid circulation was present along the entire column, since a small increase of the gas holdup values with the column height was observed. This was attributed to

the bubble expansion and high gas momentum of the large bubble, which was able to carry circulating bubbles through the re-circulation zone.

5.2.7 Bubble Size Distribution and Sauter Mean Bubble Diameter in the Agitated Reactors, d_s

The photographic method reviewed in Section 4.4.3 was employed to measure the gas bubbles size in the agitated reactors under wide range of operating conditions as outlined earlier. The mechanical factors affecting the bubble measurement were optimal lighting and proper focus on the cooling coil, which insured an accurate calibration of the bubble size analysis software. It should be mentioned that the bubble sizes and d_s were determined for each run using one shot, however, several shots were taken during each experiment with sufficient elapsed time to check the reproducibility of the results. 200 bubbles were also assumed to be sufficient from a statistical point of view to insure accurate results and reproducibility of the experimental data. Assuming spherical bubbles, the size was determined and found to follow a log-normal distribution as shown in Figure 30. Forrester et al. ⁽¹¹¹⁾ observed similar distribution for the air-water system in the GIR. The log-normal density function distribution is given by:

$$f(d_B) = \frac{1}{\ln(\bar{\sigma}) \times d_B \times \sqrt{2\pi}} \exp \left[-\frac{1}{2} \left(\frac{\ln(d_B) - \ln(\bar{\mu})}{\ln(\bar{\sigma})} \right)^2 \right] \quad (5-57)$$

where $\bar{\mu}$ is the geometric mean bubble diameter and σ the standard deviation. These two parameters can be calculated from the plot of d_B with the cumulative density in a log-normal probability graph. d_s was then calculated from the bubble volume to area ratio as ^(23, 349):

$$d_s = \frac{\sum_{i=1}^k d_{Bi}^3}{\sum_{i=1}^k d_{Bi}^2} \quad (5-58)$$

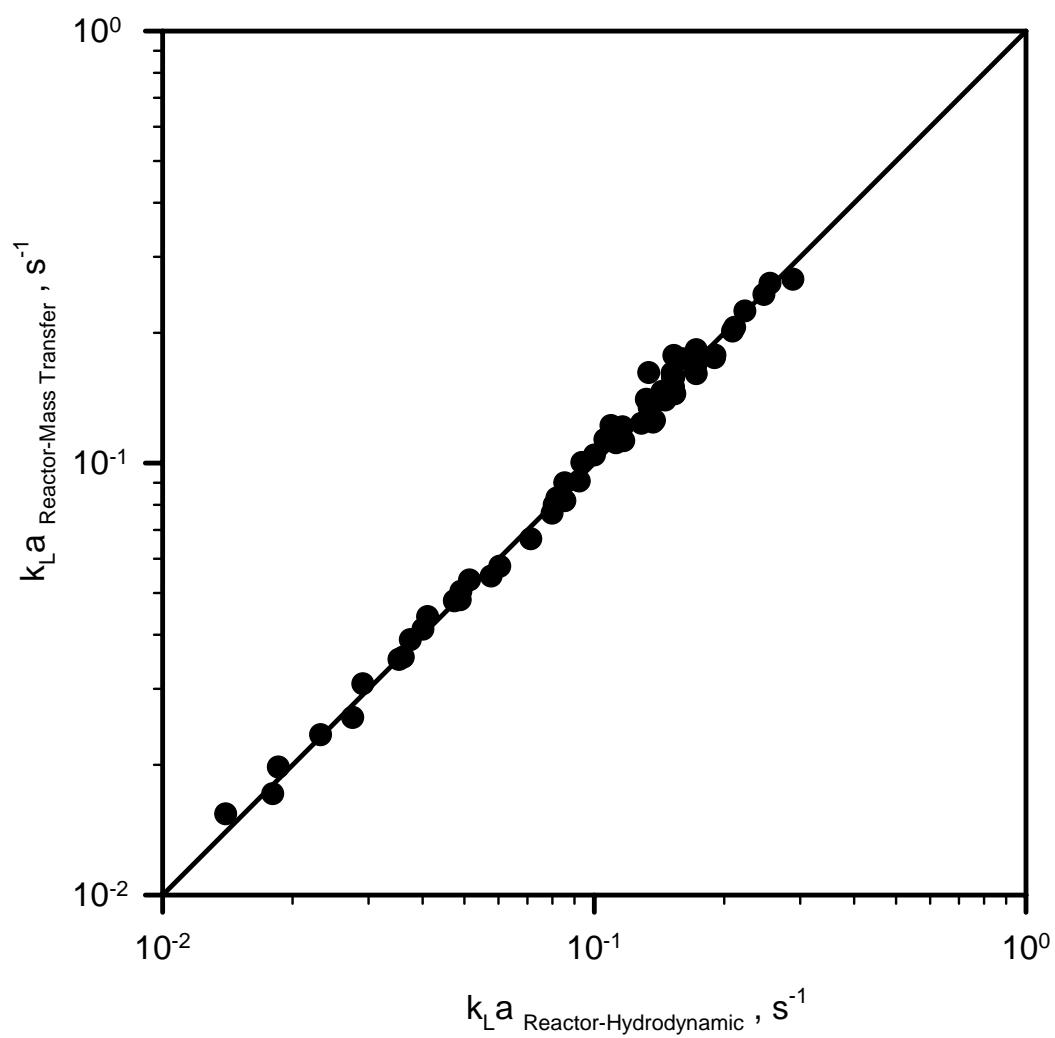


Figure 27: Comparison Between $k_L a$ Values Obtained in the Two Agitated Reactors Used

5.2.8 Bubble Size Distribution and Sauter Mean Bubble Diameter in the BCR, d_s

The Dynamic Gas Disengagement technique ⁽²¹⁵⁾ was used to determine the bubble size distribution in the BCR. This method is based on the determination of the bubbles size in the expanded bed as they leave by monitoring the rate of gas disengagement as a function of the bubble rise velocity of a given gas fraction. This is usually carried out using two approaches:

1. Measuring the actual drop of the bed height ^(215, 231, 345, 346).
2. Measuring the hydrostatic pressure change with time ^(56, 174, 215, 347).

The limitation of the first approach is related to the method of monitoring the change of the bed height, which may be carried out by visual observations or floating devices. The second approach relies on the dP cells and is only limited by their specifications. Using the second approach, from the position of the dP cell taps and the recorded time after the compressor has been stopped, the bubble rise velocity was calculated from the following expression:

$$u_b = \left(\frac{L_T}{t} \right) \quad (5-59)$$

Using this value, the bubble diameter was determined from the following equation ⁽²³⁰⁾:

$$d_b = 0.5917 \times \left(\frac{u_b^2}{g} \right) \quad (5-60)$$

As can be seen in Figure 28, the pressure drop across the two dP taps increases as the gas disengages due to the decrease of ε_G . Therefore, using Equation (5-55), ε_G was calculated leading to the estimation of the rate of disengagement of each “size” of bubbles as a function of u_b . In fact, If at time $t = 0$ the compressor is stopped and a homogenous distribution of bubbles along the column is assumed, then ε_G at time t can be coupled with $u_{b,i}$, L_T/t , assuming that the bubbles affecting the dP reading are exactly the bubbles disengaging at t . This leads to the assumption that the large bubbles would disengage first from t_1 to t_2 , while the small bubbles would take longer time to disengage with velocities $u_{b,Small}$ ranging from L_T/t_2 to L_T/t_3 . Thus, the observed decrease of ε_G at t , represents the volume of bubbles leaving the dP zone at L_T , hence the following equations apply:

$$\Delta \varepsilon_{G,i} = \int_{t_{i-1}}^{t_i} \frac{d\varepsilon_G}{dt} dt \quad (5-61)$$

$$u_{b,i} = \frac{L_T}{t_i} \quad (5-62)$$

$$\varepsilon_G = \sum_{i=1}^n \varepsilon_{G,i} \quad (5-63)$$

In order to obtain $\Delta \varepsilon_{G,i}$, $u_{b,i}$ and ε_G , the following four assumptions were made:

1. The rate of gas disengagement of each bubble type i is constant throughout the experiment, meaning that $u_{b,i}$ does not change, therefore $d\varepsilon_G/dt$ is replaced by $\Delta \varepsilon_G / \Delta t$.

2. Once the gas flow is stopped, there is no coalescence or rupture of gas bubbles, meaning that the bubbles size remains constant as they disengage.
3. There is no interaction between the different bubbles as they rise.
4. The liquid circulation does not affect the bubble rise velocity.

Sriram and Mann ⁽²¹⁵⁾ pointed that if the last assumption is not true, its effect on the final results is not significant. Once $u_{b,i}$ are calculated, d_B can be estimated using one of the correlations listed in Table A-7. It should be noted, however, that the estimated d_B might vary from one correlation to the other as described by Inga ⁽⁵⁶⁾. In this study, the correlation proposed by Fukuma et al. ⁽²³⁰⁾, given in Table A-7, was selected. Their study was conducted in a 0.15m diameter BCR operating under atmospheric pressures and using an air/water/glass beads system with solid concentrations from 0 to 50 % by volume, which validated the use of their correlation in this study. d_s of the small, large and total bubble population were then calculated using the volume to area ratio commonly accepted ^(118, 124, 144) shown in Equation (5-58).

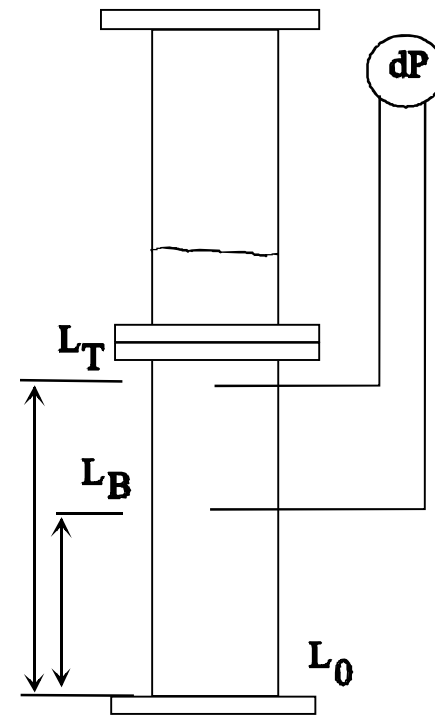
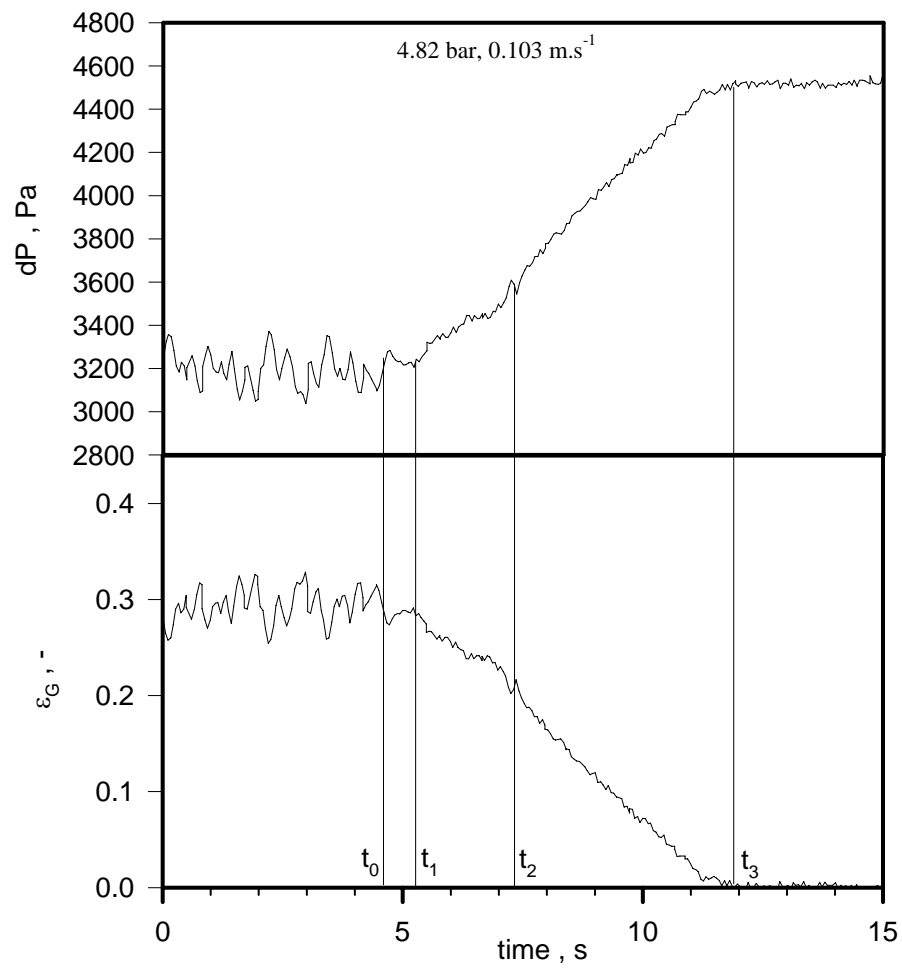


Figure 28: Dynamic Gas Disengagement Technique and dP Cells Position for the Bubble Size Measurement in the BCR

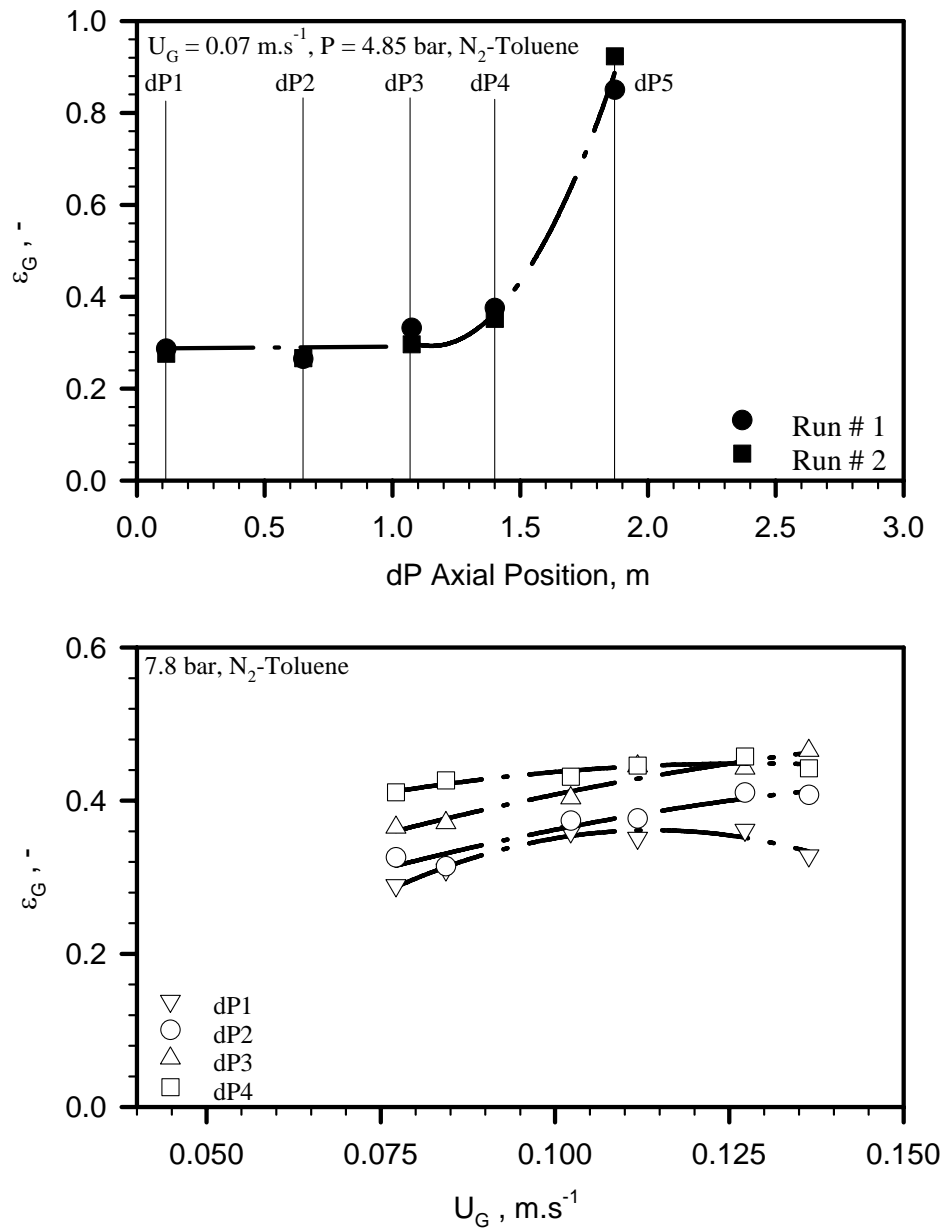


Figure 29: Effect of the dP Cells Position and Gas Velocity on Axial Distribution of the Gas Holdup

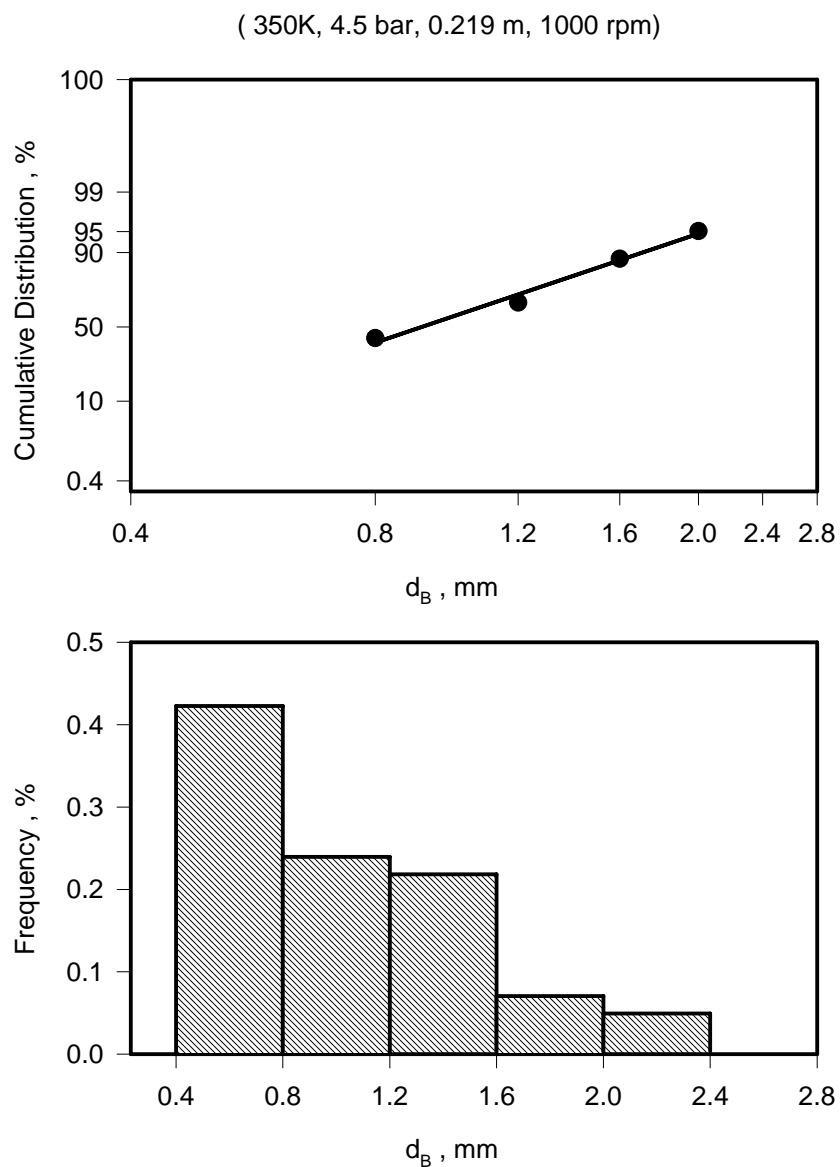


Figure 30: Bubble Size Distribution for N_2 in Toluene in the Agitated Reactors

5.3 MASS TRANSFER PARAMETERS

In this section, the mass transfer parameters calculation methods in both gas-liquid contactors are described.

5.3.1 Calculation of the Gas-Liquid Interfacial Areas, a , in the Agitated Reactors

In the SAR, it is generally assumed from the flat surface model that the enhancement of interface due to the wavy motion is negligible and subsequently gas-liquid interface area, a_{SAR} , is estimated using Equation (5-64) ^(11, 23, 349).

$$a_{SAR} = \frac{A_{Interface}}{V_L} \approx \frac{\pi d_T^2/4}{H\pi r_T^2/4} = \frac{1}{H} \quad (5-64)$$

In this study, in order to estimate and assess the contribution of the wavy surface to the gas-liquid interfacial area, the small-amplitude wave theory reviewed by Faber ⁽³³²⁾ was employed. Under steady-state conditions, the commonly accepted relations ^(61, 62, 86, 332) for the displacement, $\xi(r)$, and the wave frequency, ω_{Wave} are as follow:

$$\xi(r, t) = \xi_{Max} \sin(kr - \omega_{Wave} t) \quad (5-65)$$

$$\omega_{Wave}^2 = \left[\frac{\rho_L - \rho_G}{\rho_L + \rho_G} gk + \frac{\sigma_L k^3}{\rho_L + \rho_G} \right] \tanh(kH) \quad (5-66)$$

In these equations, k is the wave number, r is the radial coordinate, and ξ_{Max} is the wave amplitude. Under given operating conditions, ω_{Wave} and ξ_{Max} were measured in liquid toluene by analyzing the digitized images taken by the high-speed video Phantom camera unit, which enabled recording of the surface every 3333 μ s. By inserting ω_{Wave} values in Equation (5-66), k was computed. It was also assumed that no damping effect occurred, due to the relatively low toluene viscosity, and subsequently a_{Wave} was estimated by the following integral:

$$a_{Wave} = \frac{\int_0^{d_T/2} 2\pi \times r \sqrt{1 + \xi_{Max}^2 k^2 \times \cos^2(kr)} dr}{V_L} \quad (5-67)$$

In the SAR, GIR and GSR, the interfacial area of the entrained, induced and sparged bubbles was calculated from ε_G and d_S values measured under identical operating conditions as:

$$a_{Entrained} = \frac{6\varepsilon_{G-SAR}}{d_{S-SAR}(1 - \varepsilon_{G-SAR})} \quad (5-68)$$

$$a_{Induced} = \frac{6\varepsilon_{G-GIR}}{d_{S-GIR}(1 - \varepsilon_{G-GIR})} \quad (5-69)$$

$$a_{Sparged} = \frac{6\varepsilon_{G-GSR}}{d_{S-GSR}(1 - \varepsilon_{G-GSR})} \quad (5-70)$$

Using a_{Wave} and Equations (5-68), (5-69) and (5-70), a_{SAR} , a_{GIR} and a_{GSR} were calculated as:

$$a_{SAR} = a_{Entrained} + a_{Wave} \quad (5-71)$$

$$a_{GIR} = a_{Induced} + a_{Wave} \quad (5-72)$$

$$a_{GSR} = a_{Sparged} + a_{Wave} \quad (5-73)$$

5.3.2 Calculation of the Gas-Liquid Interfacial Areas, a , in the BCR

The average ε_G and d_s in the column were coupled to obtain the gas-liquid interfacial area, a as:

$$a = \frac{6\varepsilon_G}{d_s(1-\varepsilon_G)} \quad (5-74)$$

Since the contribution of the flat gas-liquid interface to the total a_{BCR} can be assumed negligible in the BCR, the following equation was used:

$$a_{BCR} = a = \frac{6\varepsilon_G}{d_s(1-\varepsilon_G)} \quad (5-75)$$

Similarly, the gas-liquid interfacial areas of small and large gas bubbles were calculated:

$$a_{Small} = \frac{6\varepsilon_{G-Small}}{d_{S-Small}(1-\varepsilon_G)} \quad (5-76)$$

$$a_{Large} = \frac{6\varepsilon_{G-Large}}{d_{S-Large}(1-\varepsilon_G)} \quad (5-77)$$

5.3.3 Calculation of the Volumetric Mass Transfer Coefficient, k_La , in the Agitated Reactors

In the SAR and GIR, the calculation of k_La was carried out under the following assumptions:

1. Non-ideal behavior of the liquid and gas phases.
2. The liquid phase is well mixed
3. The mass transfer resistance of the gas phase is negligible compared to the liquid phase.

The transient physical gas absorption technique, where the decline of the total pressure of the system with time is recorded, in conjunction with total mole and volume balances was used to calculate k_La values of O_2 and N_2 in toluene. The rate of mass transfer from the solute gas to the liquid phase is calculated using the two-film model as:

$$\frac{dn_{iL}}{dt} = k_La(C^* - C_L) \times V_L \quad (5-78)$$

where n_{iL} is the number of moles of component i transferred from the gas phase into the liquid phase, C^* is the concentration of the solute gas at the gas-liquid interface, C_L is the concentration of the gas in liquid bulk, and V_L is the volume of liquid toluene. In order to calculate k_La from Equation (5-78), C^* , C_L , V_L and n_{iL} were determined as a function of the solute gas partial pressure P_i . At the gas-liquid interface, the liquid is assumed to be in instantaneous equilibrium with the partial pressure P_i of the gas phase, hence P_{iF} is replaced by P_i in Equation (5-36) to obtain C^* . C_L , V_L and n_{iL} were calculated using the flash vaporization method described by Chang et al. ⁽²⁴⁹⁻²⁵²⁾. The

calculation algorithm is shown in Figure 31. At any pressure $P(t)$ between the initial pressure P_i and equilibrium pressure P_F , Δn number of moles of solute gas is assumed to vaporize from the liquid phase to the gas phase and the binary interaction parameter δ_{ij} , optimized at the corresponding equilibrium temperature and pressure P_F , is used in the calculation. It should be mentioned that δ_{ij} was assumed to be independent of pressure. The essential steps in the calculation are:

1. When Δn of the solute gas is vaporized back to the gas phase at time t , the composition of the solute gas (component 1) in the gas and liquid phases becomes:

$$x_1(t) = \frac{n_{1L} - \Delta n}{N_L - \Delta n} \quad (5-79)$$

$$y_1(t) = \frac{n_{1G} - \Delta n}{N_G - \Delta n} \quad (5-80)$$

2. Z_G and Z_L are calculated using Equation (5-2).
3. v_G and v_L are calculated using Equations (5-33) and (5-34), respectively.
4. $V_L = (N_L - \Delta n) v_L$ and $V_G = (N_G + \Delta n) v_G$ are calculated.
5. The volume balance $V_R = V_L + V_G$ is checked. If the volume balance is not confirmed, steps 1 to 4 are repeated.
6. The values of C_L and V_L are calculated from the following equations:

$$C_L = \frac{x_1}{v_L} \quad (5-81)$$

$$V_L = v_L (N_L - \Delta n) \quad (5-82)$$

The calculations shown in Figures 26 and 31, were executed at every tested pressure from P_F to P_i , and the values of C_L and V_L obtained at each operating condition were correlated as a function of P_i :

$$C_L = C_1 + C_2 P_i + C_3 P_i^2 \quad (5-83)$$

$$V_L = F_0 + F_1 P_i + F_2 P_i^2 \quad (5-84)$$

Ultimately, n_{1L} is calculated from

$$n_{1L} = C_L \times V_L \quad (5-85)$$

Coupling Equations (5-36), (5-83), (5-84) and (5-85) with (5-78) and integrating:

$$\frac{\xi_1}{F_2(E_1 - C_3)} \int \frac{(P_{1,f}^3 + \xi_2 P_{1,f}^2 + \xi_4)}{(P_{1,f}^2 + \beta_1 P_{1,f} + \beta_2) \times (P_{1,f}^2 + \beta_3 P_{1,f} + \beta_4)} dt = k_L a \int dt \quad \text{where:} \quad (5-86)$$

$$\beta_1 = \frac{E_0 - C_2}{E_1 - C_3} \quad (5-87)$$

$$\beta_2 = -\frac{C_1}{E_1 - C_3} \quad (5-88)$$

$$\beta_3 = \frac{F_1}{F_2} \quad (5-89)$$

$$\beta_4 = \frac{F_o}{F_2} \quad (5-90)$$

$$\xi_1 = 4C_3F_2 \quad (5-91)$$

$$\xi_2 = \frac{3(C_2F_2 + C_3F_1)}{\xi_1} \quad (5-92)$$

$$\xi_3 = \frac{2(C_1F_2 + C_2F_1 + C_3F_o)}{\xi_1} \quad (5-93)$$

$$\xi_4 = \frac{C_1F_1 + C_2F_o}{\xi_1} \quad (5-94)$$

Equation (5-86) could be expressed as:

$$\frac{\xi_1}{F_2(E_1 - C_3)} \int \left\{ \frac{\gamma_1 P_{lf} + \gamma_2}{P_{lf}^2 + \beta_1 P_{lf} + \beta_2} + \frac{\gamma_3 P_{lf} + \gamma_4}{P_{lf}^2 + \beta_3 P_{lf} + \beta_4} \right\} dP_{lf} = k_L a \int dt \text{ where:} \quad (5-95)$$

$$\gamma_1 = \frac{(\beta_2 - \beta_4) \times \left(\xi_3 - \beta_2 - \xi_4 \frac{\beta_1}{\beta_2} \right) + (\beta_3 \beta_2 + \beta_1 \beta_4) \times \left(\xi_2 - \beta_1 - \frac{\xi_4}{\beta_2} \right)}{(\beta_2 \beta_3 - \beta_1 \beta_4) \times (\beta_1 - \beta_3) - (\beta_4 - \beta_2)^2} \quad (5-96)$$

$$\gamma_2 = \frac{\left(\xi_2 - \beta_1 - \frac{\xi_4}{\beta_2} \right) + (\beta_1 - \beta_3) \gamma_1}{1 - \beta_4 / \beta_2} \quad (5-97)$$

$$\gamma_3 = 1 - \gamma_1 \quad (5-98)$$

$$\gamma_4 = \frac{\xi_4 - \gamma_2 \beta_4}{\beta_2} \quad (5-99)$$

Equation (4-60) can be simplified as:

$$\gamma_1 \int \frac{P_{lf}}{A_1} dP_{lf} + \gamma_2 \int \frac{dP_{lf}}{A_1} + \gamma_3 \int \frac{P_{lf}}{A_2} dP_{lf} + \gamma_4 \int \frac{dP_{lf}}{A_2} = k_L a \int dt \quad (5-100)$$

$$\text{where: } A_1 = P_{lf}^2 + \beta_1 P_{lf} + \beta_2 \text{ and } A_2 = P_{lf}^2 + \beta_3 P_{lf} + \beta_4 \quad (5-101)$$

The first and third terms of Equation (5-100) are:

$$\int \frac{P_{lf}}{A_1} dP_{lf} = \left[\frac{1}{2} \ln(A_1) \right] - \frac{\beta_1}{2} \int \frac{dP_{lf}}{A_1} \quad (5-102)$$

$$\int \frac{P_{lf}}{A_2} dP_{lf} = \left[\frac{1}{2} \ln(A_2) \right] - \frac{\beta_3}{2} \int \frac{dP_{lf}}{A_2} \quad (5-103)$$

Assigning values to:

$$I_1 = \int \frac{dP_{lf}}{A_1} \text{ and } I_2 = \int \frac{dP_{lf}}{A_2} \quad (5-104)$$

Substituting Equations (5-102), (5-103), (5-104) and (5-101) into Equation (5-100) gives:

$$\frac{\gamma_1}{2}[\ln(A_1)] + \frac{\gamma_3}{2}[\ln(A_2)] + \frac{\gamma_2\beta_1\gamma_1}{2}I_1 + \frac{\gamma_4\beta_3\gamma_3}{2}I_2 = k_L a \int dt \quad (5-105)$$

The integration of I_1 and I_2 depends on the value of the discriminant $4ac-b^2$ in $I = \int \frac{dx}{ax^2+bx+c}$

$$I = \int \frac{2}{\sqrt{4ac-b^2}} \tan^{-1} \frac{2ax+b}{\sqrt{4ac-b^2}} \text{ for } (4ac-b^2) > 0 \quad (5-106)$$

$$I = -\frac{1}{ax+b/2} \text{ for } (4ac-b^2) = 0 \quad (5-107)$$

$$I = \frac{1}{\sqrt{b^2-4ac}} \times \ln \left[\frac{2ax+b-\sqrt{b^2-4ac}}{2ax+b+\sqrt{b^2-4ac}} \right] \text{ for } (4ac-b^2) < 0 \quad (5-108)$$

Using Equations (5-106) to (5-108), the expressions of I_1 can be re-written:

$$I_1 = \frac{2}{\sqrt{4\beta_2-\beta_1^2}} \tan^{-1} \frac{2P_{If}+\beta_1}{\sqrt{4\beta_2-\beta_1^2}} \text{ for } 4\beta_2 > \beta_1^2 \quad (5-109)$$

$$I_1 = \frac{-1}{P_{If} + \frac{\beta_1}{2}} \text{ for } 4\beta_2 = \beta_1^2 \quad (5-110)$$

$$I_1 = \frac{1}{\sqrt{\beta_1^2-4\beta_2}} \ln \left| \frac{2P_{If}+\beta_1-\sqrt{\beta_1^2-4\beta_2}}{2P_{If}+\beta_1+\sqrt{\beta_1^2-4\beta_2}} \right| \text{ for } 4\beta_2 < \beta_1^2 \quad (5-111)$$

Similarly, I_2 is determined by the value of the discriminant $(4\beta_4-\beta_3^2)$:

$$I_2 = \frac{2}{\sqrt{4\beta_4-\beta_3^2}} \tan^{-1} \frac{2P_{If}+\beta_3}{\sqrt{4\beta_4-\beta_3^2}} \text{ for } 4\beta_4-\beta_3^2 > 0 \quad (5-112)$$

$$I_2 = \frac{-1}{P_{If} + \frac{\beta_3}{2}} \text{ for } 4\beta_4-\beta_3^2 = 0 \quad (5-113)$$

$$I_2 = \frac{1}{\sqrt{\beta_3^2-4\beta_4}} \ln \left| \frac{2P_{If}+\beta_3-\sqrt{\beta_3^2-4\beta_4}}{2P_{If}+\beta_3+\sqrt{\beta_3^2-4\beta_4}} \right| \text{ for } 4\beta_4-\beta_3^2 < 0 \quad (5-114)$$

Thus, Equation (5-105) can be integrated from time $t = 0$ ($P_{It} = P_{II}$) to anytime t ($P_{If} = P_{It}$):

$$\frac{\zeta_I}{F_2(E_I - C_3)} \left[\frac{\gamma_1}{2} \ln|A_1| + \frac{\gamma_3}{2} \ln|A_2| + \frac{\gamma_2\gamma_1\beta_1}{2} I_1 + \frac{\gamma_4\gamma_3\beta_3}{2} I_2 \right] \Bigg|_{P_{II}}^{P_{It}} = k_L a \times t \Big|_{P_{II}}^{P_{It}} \quad (5-115)$$

The above equation can also be written as:

$$F(t) = k_L a \times t \quad (5-116)$$

Finally, the left hand side of the Equation (5-116) was plotted versus time, and if a straight line is obtained, its slope will correspond to $k_L a$, as shown in Appendix C.

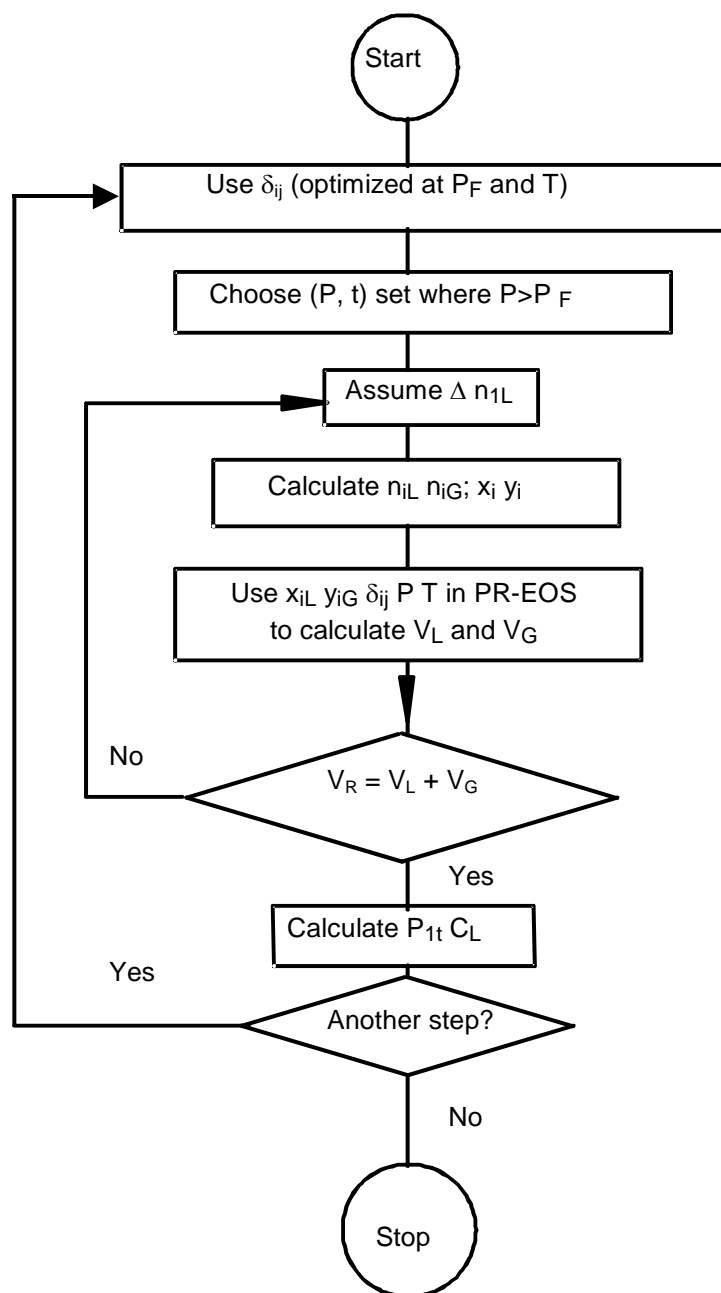


Figure 31: Algorithm for C_L and V_L Calculation in the Agitated Reactors ⁽²⁴⁹⁾

In the GSR, using the two-film model, the rate of mass transfer from the solute gas into the liquid phase can be expressed as:

$$\frac{dN_{L,t}}{dt} = -\frac{dN_{G,t}}{dt} = k_L a (C^* - C_{L,t}) V_L \quad (5-117)$$

The solubility, C^* , is calculated from Equation (5-39), and the gas concentration in the liquid at any time, t , is defined as:

$$C_{L,t} = \frac{N_T - N_{G,t}}{V_L} \quad (5-118)$$

Assuming no volume change due to gas solubility, Equation (5-118) could be simplified as:

$$\frac{dC_{L,t}}{(C^* - C_{L,t})} = k_L a \, dt \quad (5-119)$$

The integration of Equation (5-119) between the limits from $C_{L,0}$ at $t = 0$ to $C_{L,t}$ at any time t , gives:

$$\ln \left(\frac{C^* - C_{L,0}}{C^* - C_{L,t}} \right) = k_L a \, t \quad (5-120)$$

The above equation can also be rewritten as:

$$F(t) = k_L a \, t \quad (5-121)$$

When $F(t)$ values are plotted against time, t , and a straight line is found, $k_L a$ will be its slope.

5.3.4 Calculation of the Volumetric Mass Transfer Coefficient, $k_L a$, in the BCR

The physical gas absorption technique was also used to obtain $k_L a$ in the BCR. The calculation details and assumptions made are described below:

1. The binary mixture behavior was assumed to be ideal. The operating conditions justified such an assumption since both pressure and temperature were low.
2. The gas and liquid were assumed well mixed: the liquid and gas concentration in the liquid phase were assumed to be homogeneous.

The rate of mass transfer from the solute gas to the liquid phase is calculated using the two-film model as in Equation (5-78). Inga ⁽⁵⁶⁾ developed three methods for the $k_L a$ calculation in the slurry bubble column reactor (SBCR): the integral, the differential, and the multiple linear regression method. These three methods gave similar results; however, the selection of one of them should be based upon the mathematical stability of the final function.

In the integral method, the solubility values can be modeled by Henry's Law as:

$$C^* = (P_T - P_v) / H_e \quad (5-122)$$

Using Equations (5-44) and (5-122), Equation (5-78) is rewritten as:

$$-\frac{V_G}{RT} \frac{dP_T}{dt} = V_L k_L a \times \left(\frac{P_T}{He} - \frac{P_v}{He} - \frac{N_0 - \frac{(P_T - P_v)V_G}{RT}}{V_L} \right) \quad (5-123)$$

separating the variables:

$$\frac{V_G}{RT} \frac{dP_T}{\left(\theta (P_T - P_v) - \frac{N_0}{V_L} \right)} = -V_L k_L a \cdot dt \quad \text{with } \theta = \frac{1}{He} + \frac{V_G}{V_L RT} \quad (5-124)$$

by integrating both sides, the following relation is obtained:

$$\frac{V_G}{V_L RT} \times \frac{1}{\theta} \times \ln \left(\theta (P_T - P_v) - \frac{N_0}{V_L} \right) = -k_L a \times t + C \quad (5-125)$$

If the left-hand side of the Equation (5-125) is plotted vs. time t , and gives a straight line the slope of this line equals $k_L a$. This method was used to obtain $k_L a$ in the present study.

In the differential method, Equation (5-123) is solved by approximating dP as ΔP and dt as Δt . Since the readings were taken at $\Delta t < 0.05$ s, this assumption seems reasonable. Hence, it gives:

$$A_L \times \Delta P = -V_L \times k_L a \times \Delta t \quad (5-126)$$

If the ratio between $A_L \Delta P$ and $-V_L \Delta t$ is constant, the resulting value will correspond to $k_L a$.

The multiple linear regression method is based on the linearization of Equation (5-123), which can be rewritten as a linear expression:

$$A_1 \times \Delta P = A_2 \times P_T \times \Delta t + A_3 \times \Delta t + A_4 \quad \text{where:} \quad (5-127)$$

$$A_1 = \frac{-V_G}{RT V_L k_L a} \quad (5-128)$$

$$A_2 = \theta \quad (5-129)$$

$$A_3 = \frac{-N_0}{V_L} - P_v \theta \quad (5-130)$$

$$A_4 = \text{constant} \quad (5-131)$$

Using multiple linear regressions, the coefficients A_1 , A_2 , A_3 and A_4 can be found.

5.3.5 Calculation of the Gas-Liquid Mass Transfer Coefficient, k_L , in the Agitated Reactors

The mass transfer coefficients, k_L in the SAR, GIR and GSR can be deduced from a and $k_L a$ data as:

$$k_{L-SAR} = \frac{(k_L a)_{SAR}}{a_{SAR}} \quad (5-132)$$

$$k_{L-GIR} = \frac{(k_L a)_{GIR}}{a_{GIR}} \quad (5-133)$$

$$k_{L-GSR} = \frac{(k_L a)_{GSR}}{a_{GSR}} \quad (5-134)$$

5.3.6 Calculation of the Gas-Liquid Mass Transfer Coefficient, k_L , in the BCR

The gas-liquid mass transfer coefficient, k_L can be obtained by dividing $k_L a$ by Equation (5-75):

$$k_L = \frac{k_L a}{a} = k_L a \frac{d_s (1 - \varepsilon_G)}{6 \varepsilon_G} \quad (5-135)$$

In the BCR, the contribution of the flat gas-liquid interface to the total gas-liquid interfacial area, a can be assumed negligible and accordingly:

$$k_L \approx k_{L-Bubbles} \quad (5-136)$$

6.0 RESULTS AND DISCUSSION

In this section, the effects of operating variables on the thermodynamic, hydrodynamic and mass transfer parameters are discussed. Details of the statistical design and analysis techniques used in this study are given in Appendix E. The experimental conditions used in the agitated and bubble column reactors are given in Tables 23 and 24, respectively, with the corresponding coded variables of the Central Composite Statistical Design shown in Tables 24 and 25. It is important to mention that in the agitated reactors, the effect of pressure, P , temperature, T , mixing speed, N , and liquid height, H , on the hydrodynamic and mass transfer parameters were statistically investigated in the SAR and GIR, whereas in the GSR the effect of liquid height was replaced by the superficial gas velocity, $U_{G,}$.

Table 23: Operating variables and their ranges for the agitated reactors

No.	$N, \text{ Hz}$	$P, \text{ bar}$	H, m (SAR, GIR)	$U_G, \text{ cm.s}^{-1}$ (GSR)	T, K	
					All gas-liquid systems used	All gas-liquid systems used, except Air-Toluene
1	15.0	4.5	0.195	0.1	325	408
2	15.0	4.5	0.244	0.3	325	408
3	15.0	11.5	0.195	0.1	325	408
4	15.0	11.5	0.244	0.3	325	408
5	18.3	4.5	0.195	0.1	325	408
6	18.3	4.5	0.244	0.3	325	408
7	18.3	11.5	0.195	0.1	325	408
8	18.3	11.5	0.244	0.3	325	408
9	15.0	4.5	0.195	0.1	375	438
10	15.0	4.5	0.244	0.3	375	438
11	15.0	11.5	0.195	0.1	375	438
12	15.0	11.5	0.244	0.3	375	438
13	18.3	4.5	0.195	0.1	375	438
14	18.3	4.5	0.244	0.3	375	438
15	18.3	11.5	0.195	0.1	375	438
16	18.3	11.5	0.244	0.3	375	438
17	16.7	8.0	0.219	0.2	300	393
18	16.7	8.0	0.219	0.2	400	453
19	13.3	8.0	0.219	0.2	350	423
20	20.0	8.0	0.219	0.2	350	423
21	16.7	1.0	0.219	0.2	350	423
22	16.7	15.0	0.219	0.2	350	423
23	16.7	8.0	0.171	0.0	350	423
24	16.7	8.0	0.268	0.4	350	423
25	16.7	8.0	0.219	0.2	350	423
26	16.7	8.0	0.219	0.2	350	423
27	16.7	8.0	0.219	0.2	350	423
28	16.7	8.0	0.219	0.2	350	423
29	16.7	8.0	0.219	0.2	350	423
30	16.7	8.0	0.219	0.2	350	423
31	16.7	8.0	0.219	0.2	350	423

Table 24: Operating, Coded variables and their Ranges for the BCR

No.	P , MPa	U_G , $m.s^{-1}$	x_1 , -	x_2 , -	
1	0.29	0.072	-1	-1	Factorial points
2	0.29	0.128	-1	1	
3	0.71	0.072	1	-1	
4	0.71	0.128	1	1	
5	0.20	0.100	$-\sqrt{2}$	0	Axial points
6	0.80	0.100	$\sqrt{2}$	0	
7	0.50	0.060	0	$-\sqrt{2}$	
8	0.50	0.140	0	$\sqrt{2}$	
9	0.50	0.100	0	0	Central points
10	0.50	0.100	0	0	
11	0.50	0.100	0	0	
12	0.50	0.100	0	0	
13	0.50	0.100	0	0	

Table 25: Experimental conditions and coded variables for the agitated reactors

Toluene and Organic Mixtures						
Operating Variables		Value of the Variable				
Matrix 1: Air-Toluene; N ₂ -Toluene; and N ₂ -Toluene mixtures 1, 2, and 3						
	Coded Variables	-2	-1	0	1	2
Temperature, K	x_1	300	325	350	375	400
Mixing speed, rpm	x_2	800	900	1000	1100	1200
Pressure, bar	x_3	1.0	4.5	8.0	11.5	15.0
Liquid height, m	x_4	0.171	0.195	0.219	0.244	0.268
Superficial gas velocity, cm/s	x_4	0	0.1	0.2	0.3	0.4
Matrix 2: N ₂ -Toluene ; and N ₂ -Toluene mixtures 1, 2, and 3						
	Coded Variables	-2	-1	0	1	2
Temperature, K	x_1	393	408	423	438	453
Mixing speed, rpm	x_2	800	900	1000	1100	1200
Pressure, bar	x_3	4.0	6.0	8.0	10.0	12.0
Liquid height, m	x_4	0.171	0.195	0.219	0.244	0.268
Superficial gas velocity, cm/s	x_4	0	0.1	0.2	0.3	0.4

6.1 THERMODYNAMIC PARAMETERS

6.1.1 Gas Solubility in the Liquids Studied

The effect of pressure, temperature gas and liquid nature on the solubility values, obtained in the temperature range of 300-453 K and pressure range of 1-15 bars and covering the industrial operating conditions of the process, are described in the following. The reproducibility of C^* data for gases in the different liquids used shown in Figure 33 is with an average deviation of less than 10%. A comparison between the solubility data obtained in this study and those given in Table 4 is shown in Figure 34, and a reasonably good agreement with literature data within $\pm 10\%$ deviation can be reported. Also, the solubility data obtained in the agitated reactors and those in the BCR were plotted in Figure 32 for the sake of comparison. As can be seen in this figure, a very good agreement can be found and thus the solubility data obtained in the agitated reactors are the one to be used for modeling purposes due to larger ranges of operating conditions and better accuracy.

Figure 33 shows that in the pressure and temperature ranges investigated, C^* values of the O_2 , N_2 and air in the liquids used vary linearly with pressure at constant temperature and accordingly Henry's law was used to model C^* values as:

$$C^* = \frac{P_{l,f}}{He} \quad (6-1)$$

He is the Henry's constant and $P_{l,f}$ is the equilibrium (final) partial pressure of the gas.

The regressed Henry's law constant (He) values within the entire operating conditions used are listed in Table 26. The experimental values of He are listed in under the entire operating conditions used in this study. Similar effect of pressure on the gas solubility in liquids has been reported in the literature ^(11, 23, 56, 249) for various systems. In fact, increasing pressure increases the concentration gradient of the gas species between the two phases, which leads to an increase of the gas solubility in the liquid. Furthermore, in the "low" pressure ranges usually investigated for the design of gas-liquid processes, Henry's law generally describes rather well the pressure dependency of gas solubility, assuming ideal solutions. The most important characteristic of Henry's law is that it implies linearity between the gas solubility and the gas partial pressure. While Henry's law is commonly used in the design of chemical processes, it should be mentioned that its applicability is usually restricted to low pressure systems. In fact, under elevated pressures, Henry's law fails to describe the system behavior due to the high gas concentration, which results in a non-linearity between the gas solubility and pressure.

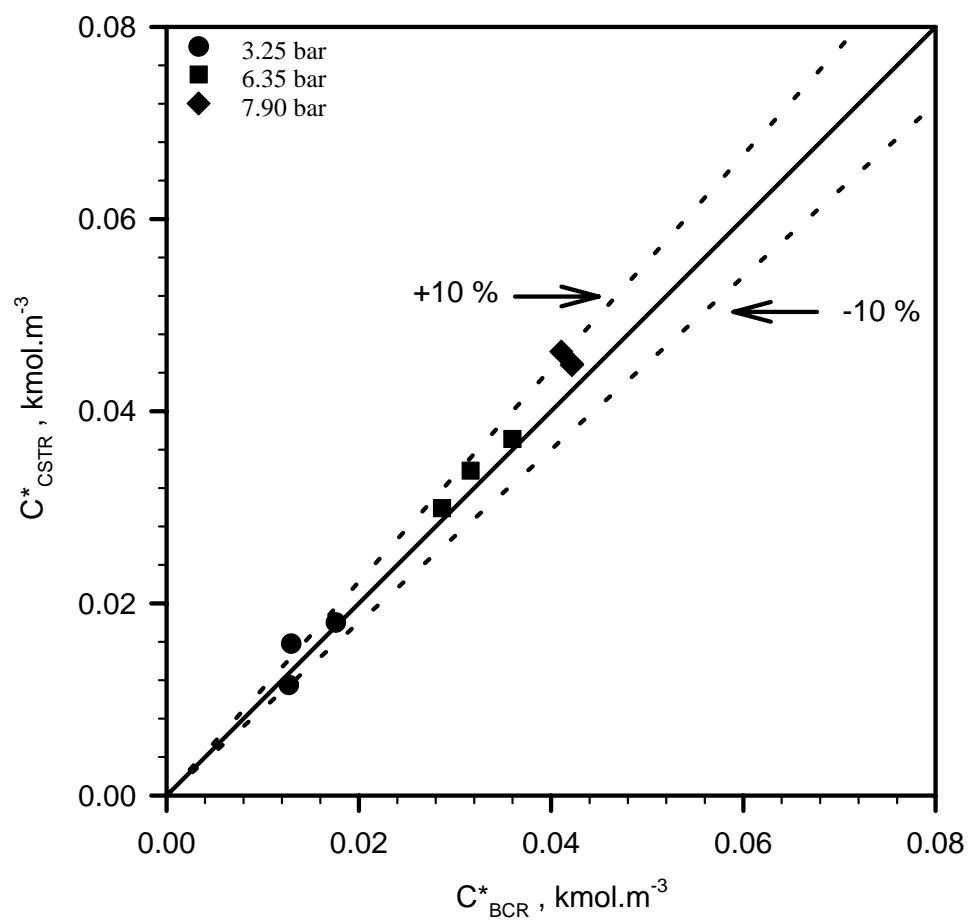


Figure 32: Comparison Between the C^* Values Obtained in the Bubble Column and the Agitated Reactors

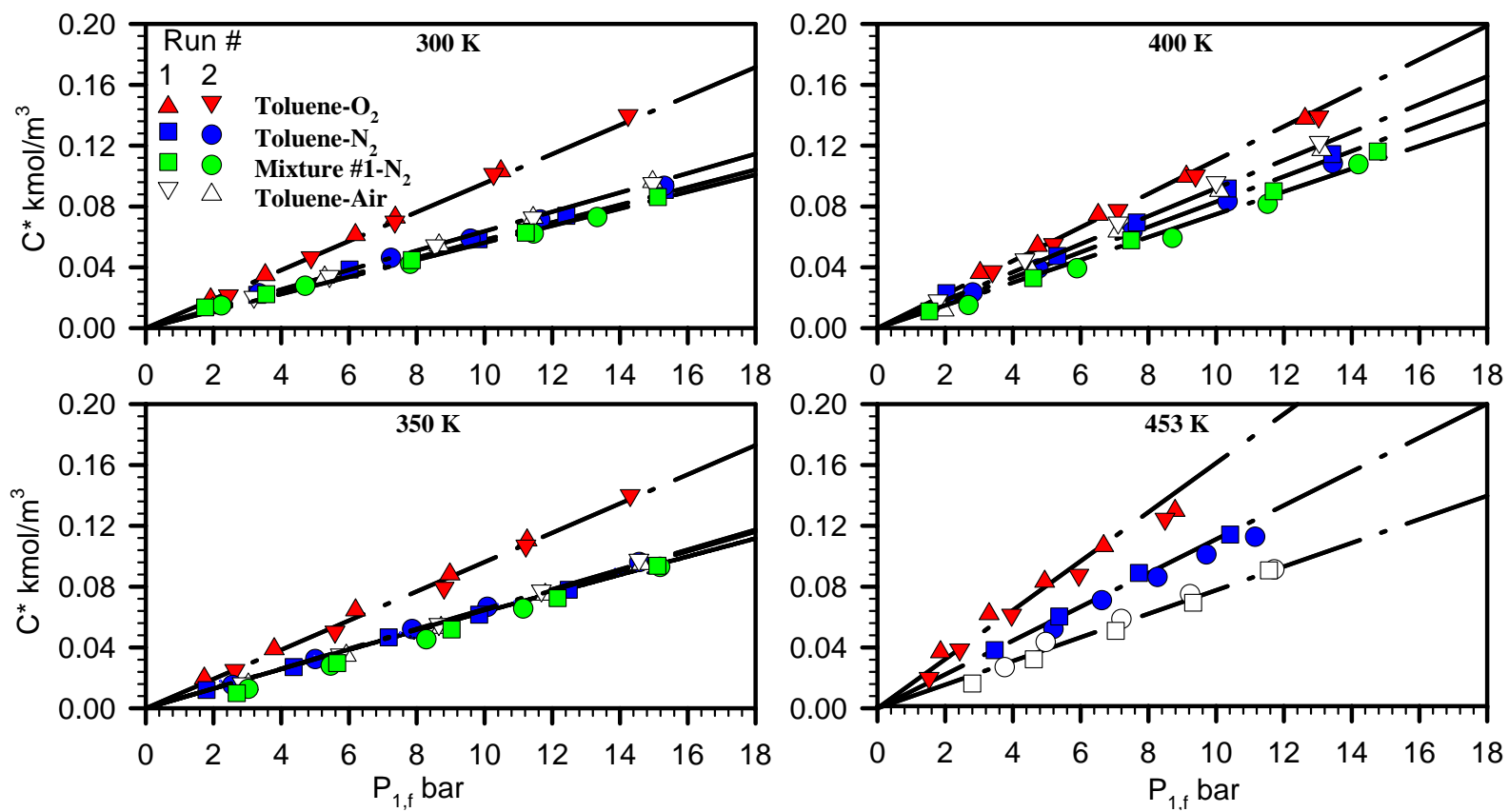


Figure 33: Reproducibility and Effect of Pressure, Temperature, and Gas and Liquid Nature on C^* Values

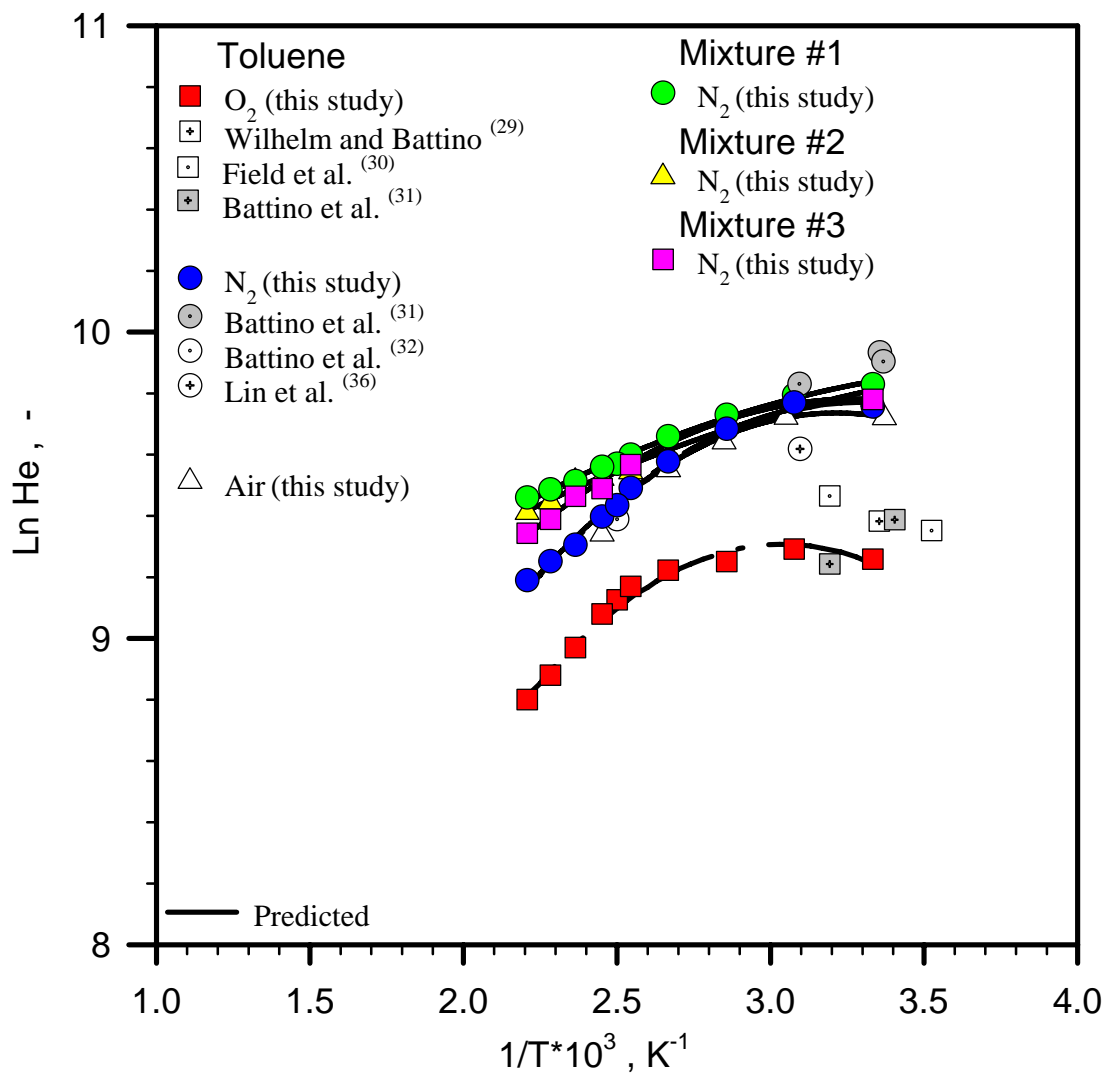


Figure 34: Effect of Temperature on Henry Constants for N_2 and O_2 in Toluene

The effect of temperature on C^* values, on the other hand, has been reported to be system dependent^(486, 348) and is generally studied through the Henry's law constants and apparent activation energy of absorption^(11, 23, 349, 350, 351, 352, 26, 29, 30, 31, 32, 36). In a small temperature range, an Arrhenius-type, Equation (6-2), is usually used to predict the effect of temperature on He , assuming that the apparent activation energies of absorption (ΔE) are constant^(11, 23, 349, 350, 351, 352, 353, 354, 355, 29, 30, 31, 32, 249).

$$He = H_o \times \exp\left(\frac{-\Delta E}{RT}\right) \quad (6-2)$$

In a wide temperature range, however, ΔE might not be constant and accordingly Equation (6-3) can be used^(350-353, 355, 29-32).

$$\frac{\Delta E}{R} = - \left[\frac{\partial(\ln(He))}{\partial(1/T)} \right] \quad (6-3)$$

In fact, for numerous gas-liquid systems^(356, 357), as reported by Hilmmlblau⁽³⁵⁰⁾, Schulze and Prausnitz⁽³⁵¹⁾ and Carroll et al.⁽³⁵²⁾, it appears that there is a turn-around point where the temperature dependency of the gas solubility changes. It is clear from these studies that C^* first decreases until it reaches a minimum, i.e. turn around point, and then increases with temperature. In the present study, as Figure 34 shows, He appears to increase with T , until T_{MAX} , the turn-around point, and then decreases with further increase of temperature. Figure 35 shows a comparison between our data and those reported by Hilmmlblau⁽³⁵⁰⁾, for N_2 -water and O_2 -water, where a similar behavior was found, when the modified Henry's law constants, defined in Equation (6-4), were plotted versus the reciprocal temperature.

$$He_{Mod.} = \frac{P_{l,f}}{x_l} \quad (6-4)$$

Hilmmlblau⁽³⁵⁰⁾, Schulze and Prausnitz⁽³⁵¹⁾, Battino et al.⁽³¹⁾ and Carroll et al.⁽³⁵²⁾ used polynomial functions of temperature or inverse temperature in order to represent the temperature dependency of the gas solubility under these conditions. Following a similar procedure developed by Hilmmlblau⁽³⁵⁰⁾, the behavior of C^* with temperature was described using a dimensionless equation for O_2 , N_2 and air in the toluene and mixtures used as:

$$\ln(He^*) = A + \frac{B}{T^*} + \frac{C}{T^{*2}} \quad \text{with:} \quad (6-5)$$

$$\frac{1}{T^*} = \frac{\left(\frac{1}{T} - \frac{1}{T_C} \right)}{\left(\frac{1}{T_{MAX}} - \frac{1}{T_C} \right)} \quad (6-6)$$

$$He^* = \frac{He}{He_{MAX}} \quad (6-7)$$

T_C represents the toluene critical temperature; T_{MAX} and He_{MAX} (see Table 27) are the temperature and Henry's Law constant corresponding to the turn around point for each gas-liquid system used. The coefficients in Equation (6-5) were estimated with a regression coefficient $> 99.5 \%$ as can be seen in the parity plot of Figure 36.

The effect of gas nature on C^* was studied through the solubility parameters, since Prausnitz and Lichtenthaler⁽³⁵⁸⁾ suggested that the gas molar fraction in liquids, x_l can be expressed by:

$$x_l = F(f) \times \exp\left(-\frac{v_l^L \times (\delta_l - \delta_2)^2 \times \Phi_2^2}{RT}\right) \quad (6-8)$$

Where $F(f)$ is a function of the fugacity, v_l^L is the gas molar volume, δ_l and δ_2 are the solubility parameters of component 1 and 2, respectively, and Φ_2 is the volume fraction of the liquid. As can be seen in Equation (6-8), when the difference between δ_l and δ_2 is small, x_l becomes large and thus a high C^* is expected. The solubility parameters of liquids and gases for organic and inorganic compounds are ascertained at any temperature from the data of heat of vaporization, H_v , and liquid volume, V_L , as shown in the following equation⁽³⁵⁹⁾:

$$\delta = \left(\frac{H_v - RT}{V_L}\right)^{1/2} \quad (6-9)$$

Although the solubility parameters are function of temperature as shown from Equation (6-9) and the values listed in Table 16 were reported at 298 K, Prausnitz and Lichtenthaler⁽³⁵⁸⁾ reported that the difference between the solubility parameters of two components is independent of temperature. In fact, these findings are in agreement with the regular solution theory⁽³²⁸⁾, which assumes that the excess entropy equals 0. Thus, it can be concluded that:

$$RT \times \ln(f_l) = Cst \quad (6-10)$$

Thus, it can be shown using Equation (6-8) that for any temperature:

$$(\delta_l - \delta_2)^2 = Cst \quad (6-11)$$

Since the gas-liquid systems used in this study are considered non-polar, the theory of regular solution is applicable, which leads to the findings of Prausnitz and Lichtenthaler⁽³⁵⁸⁾. Hence, from Equation (6-8) and the solubility parameter data given in Table 16, both C^* of gases in toluene and C^* of N_2 in liquids should follow inequalities (6-12) and (6-13), respectively:

$$(C^*)_{O_2}^{Toluene} > (C^*)_{Air}^{Toluene} > (C^*)_{N_2}^{Toluene} \quad (6-12)$$

$$(C^*)_{N_2}^{Toluene} > (C^*)_{N_2}^{Mixture \#3} > (C^*)_{N_2}^{Mixture \#2} > (C^*)_{N_2}^{Mixture \#1} \quad (6-13)$$

Figure 33 shows that these two inequalities hold for the gases and liquids used in this study, and accordingly the effects of gas and liquid natures on C^* appeared to follow Equation (6-8) suggested by Prausnitz and Lichtenthaler⁽³⁵⁸⁾. At temperatures close to the liquid critical temperature, however, Beutier and Renon⁽³⁶⁰⁾ showed that it is impossible to predict the gas solubility without any experimental data under these conditions. In addition, as commonly accepted in the literature^(350, 351, 352, 353, 354, 355, 358, 26, 27, 30, 31), Beutier and Renon⁽³⁶⁰⁾ reported that the solubilities of all gases in a specific solvent converge at the critical temperature towards the same value.

6.1.2 Activation Energy of Air, N₂ and O₂ in Toluene

The apparent activation energies of absorption for N₂, O₂ and air in toluene and toluene mixtures were obtained by Equation (6-3) ^(350-353, 355, 29-32). Table 26 shows ΔE values of both gases in toluene in the temperature range of 300-453 K. The apparent activation energy values were also correlated using Equations (6-3) and (6-5):

$$\Delta E = \frac{-R}{\left(\frac{1}{T_{MAX}} - \frac{1}{T_C}\right)} \times \left(B + \frac{2C}{T^*}\right) \quad (6-14)$$

The knowledge of the apparent activation energy of absorption (ΔE) is important to verify the occurrence of chemical reaction during the physical absorption in the range of temperature studied. In fact, Doraiswamy and Sharma ⁽³⁶¹⁾ reported that ΔE for mass transfer without chemical reaction should be $< 21000 \text{ kJ.kmol}^{-1}$, which is in agreement with the values listed in Table 26, hence no chemical reaction took place during the absorption experiments conducted in this study.

Table 26: Henry's law constant and apparent activation energy of absorption

<i>Gas/Liquid</i>	Nitrogen/Toluene									
<i>T, K</i>	300	325	350	375	400	393	408	423	438	453
<i>He, bar.m³/kmol</i>	172.80	175.01	160.70	144.38	125.1	132.48	120.57	110.01	104.24	98.02
<i>ΔE, kJ/kmol</i>	391	-1832	-3737	-5389	-6834	-6448	-7259	-8012	-8714	-9370
<i>Gas/Liquid</i>	Oxygen/Toluene									
<i>He, bar.m³/kmol</i>	104.91	108.44	104.10	101.21	91.91	96.05	87.78	78.64	71.87	66.34
<i>ΔE, kJ/kmol</i>	3810	631	-2093	-4454	-6520	-5968	-7128	-8205	-9208	-10146
<i>Gas/Liquid</i>	Air/Toluene									
<i>He, bar.m³/kmol</i>	166.47	166.74	153.83	140.45	113.84	-	-	-	-	-
<i>ΔE, kJ/kmol</i>	1482	-1544	-3449	-5158	-7195	-	-	-	-	-
<i>Gas/Liquid</i>	Nitrogen/Mixture #1									
<i>He, bar.m³/kmol</i>	185.83	179.44	168.15	156.78	147.65	143.28	141.86	135.40	131.78	128.36
<i>ΔE, kJ/kmol</i>	1680	-791	-2910	-4745	-5923	-6352	-6824	-7662	-8443	-9171
<i>Gas/Liquid</i>	Nitrogen/Mixture #2									
<i>He, bar.m³/kmol</i>	182.66	-	-	-	-	139.58	136.53	135.24	126.46	122.25
<i>ΔE, kJ/kmol</i>	1125	-	-	-	-	-6030	-6878	-7666	-8400	-9086
<i>Gas/Liquid</i>	Nitrogen/Mixture #3									
<i>He, bar.m³/kmol</i>	176.77	-	-	-	-	142.85	132.15	128.85	119.50	114.19
<i>ΔE, kJ/kmol</i>	631	-	-	-	-	-6113	-6912	-7655	-8348	-8994

Table 27: Parameters for the General Solubility Correlation Equation (6-5)

	<i>N₂-Toluene</i>	<i>O₂-Toluene</i>	<i>Air-Toluene</i>	<i>N₂-Mixture #1</i>	<i>N₂-Mixture #2</i>	<i>N₂-Mixture #3</i>
<i>A</i>	-1.328	-1.328	-1.328	-0.722	-0.922	-0.968
<i>B</i>	2.635	2.635	2.635	1.047	1.603	1.791
<i>C</i>	-1.310	-1.310	-1.310	-0.349	-0.706	-0.834
<i>He_{MAX}, bar.m³/kmol</i>	175.50	110.40	169.50	185.00	184.00	178.00
<i>T_{MAX}, K</i>	304	330	312	317	313	308

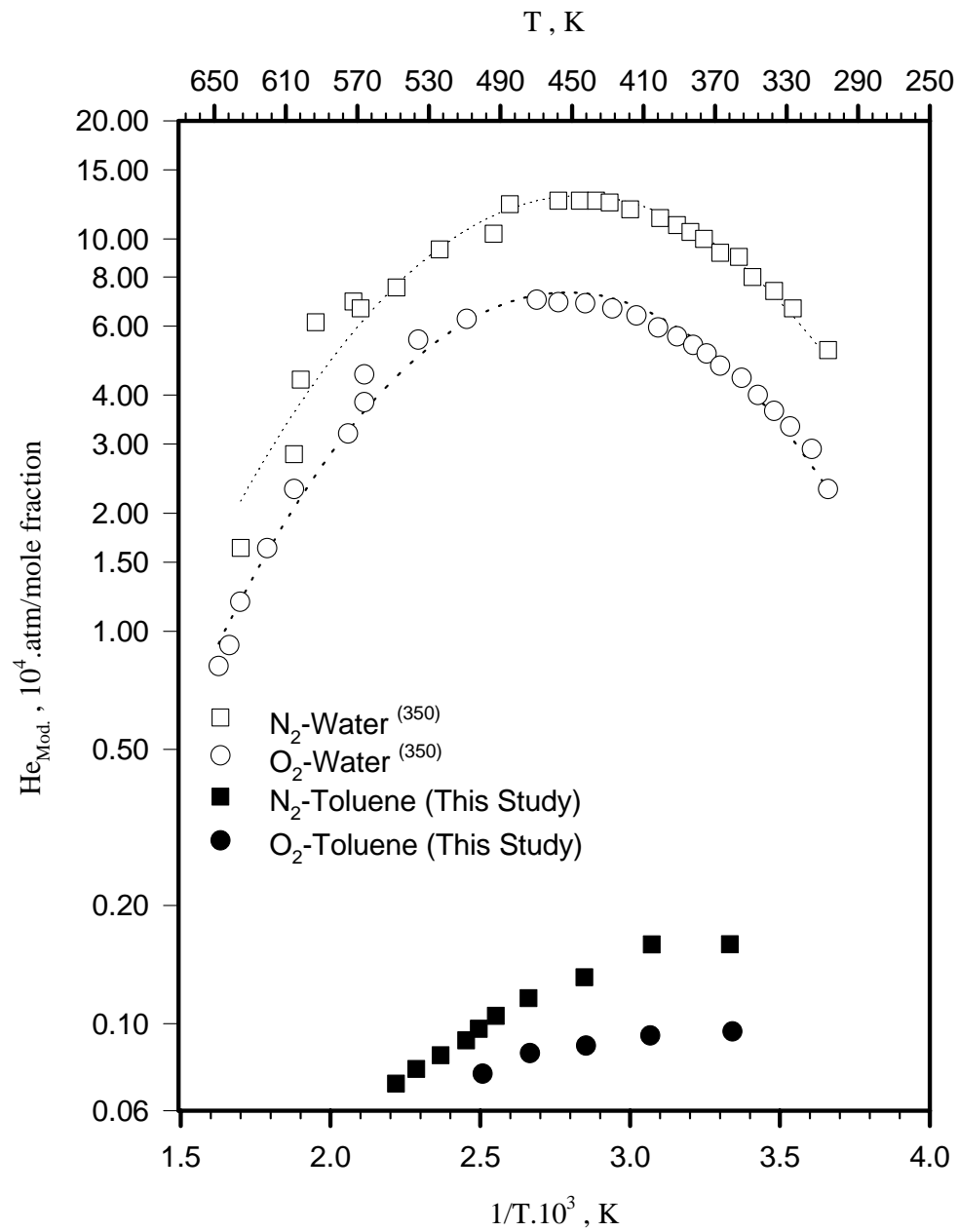


Figure 35: Turn Around Temperature Effect on C^* Values in Water⁽³⁵⁰⁾ and Toluene

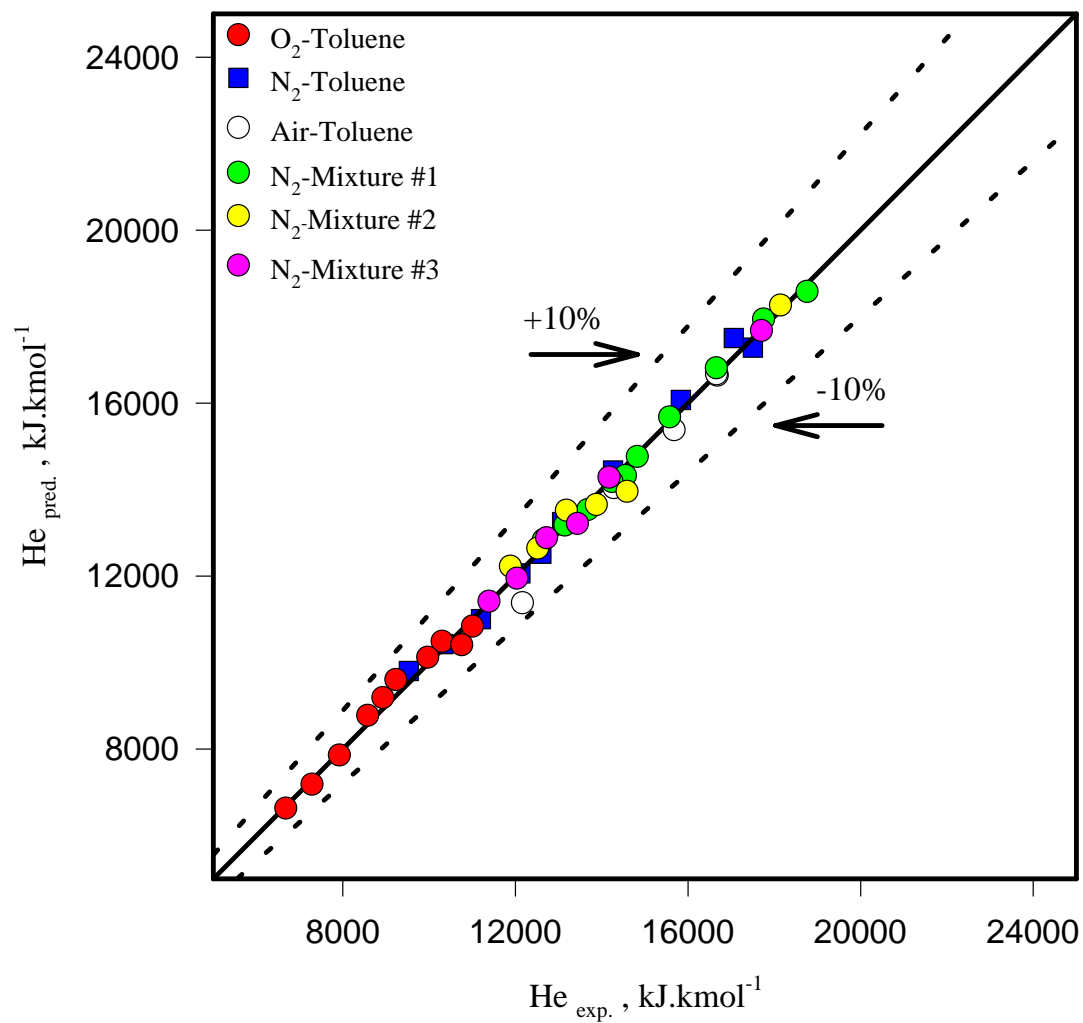


Figure 36: Comparison Between Experimental and Predicted Henry Constants from Equation (6-5)

6.2 HYDRODYNAMIC AND MASS TRANSFER PARAMETERS IN AGITATED REACTORS

In this section, the effects of operating variables on the critical mixing speeds, induced gas flow rate, bubble size, gas holdup, gas-liquid interfacial area, volumetric mass transfer coefficient and mass transfer coefficient are discussed. The reproducibility of $k_L a$, N_{CR} , Q_{GI} , d_S , ε_G , a_{Wave} , a and k_L values presented in Figures 37 through 52 were obtained with an average deviation of < 15, 10, 15, 15, 15, 10, 15 and 15 %, respectively.

6.2.1 Effect of Mixing Speed on the Hydrodynamic and Mass Transfer Parameters

Figure 37 indicates that in the SAR, GIR and GSR, increasing mixing speed from 13.33 to 20.00 Hz appears to increase $k_L a$ values by about 200, 500 and 100%, respectively. This behavior is in agreement with various literature findings^(267, 268, 483), and can be explained by the effect of N on both k_L and a .

In fact, increasing mixing speed increases the gas entrainment rate in the SAR, gas induction rate in the GIR (Figure 39) or gas re-circulation rate in the GSR and thus ε_{G-SAR} , ε_{G-GIR} and ε_{G-GSR} increases by about 100, 400 and 60%, respectively when mixing speed is increased from 13.33 to 20.00 Hz as shown in Figure 38. This behavior is due to the increase of turbulence at the gas-liquid surface in the SAR^(72, 75, 76, 106, 107, 120, 121, 134, 149), the increase of the pumping capacity of the impeller in GIRs^(89, 103, 111, 114), and the increase of gas bubbles re-circulation and dispersion in the GSR, which is in agreement with several literature findings^(72, 107, 120, 121, 122, 128, 139, 149). It is also important to notice that in all reactor types at high mixing speeds, ε_G values level off due to the establishment of a fully developed hydrodynamic regime.

Furthermore, increasing mixing speed from 13.33 to 20.00 Hz appears to slightly decrease d_{S-SAR} and d_{S-GSR} by 15 and 10%, respectively, which can be attributed to the increase of the bubble breakup probability with increasing N , as more and more entrained gas bubbles became dispersed throughout the vessel in the SAR^(72, 349, 119, 126, 132, 134, 458, 459), and as sparged gas bubbles rising from the distributor reach the impeller blades in the GSR^(118, 126, 132, 146).

Thus, as shown in Figure 40, a increases by about 275 and 80% with increasing mixing speed in the SAR and GSR from 13.33 to 20.00 Hz, which is expected from Equations (5-71) and (5-73) and the reported behavior of a_{Wave} . In fact, Figure 39 shows the effect of mixing speed on the wavy gas-liquid interfacial area; and as can be seen increasing mixing speed increases a_{Wave} , which can be quantified in terms of the enhancement of the gas-liquid interfacial area $E(a)$. Increasing mixing speed increases the turbulence at the gas-liquid interface, which increases the frequency as well as the amplitude of the surface waves created, leading to the observed increase of a_{Wave} .

In the GIR, however, d_{S-GIR} values appear to increase by about 30% with increasing mixing speed, which is similar to the findings by Fillion and Morsi⁽²⁶⁸⁾ and Hsu and Huang⁽¹⁰⁹⁾. These data suggest that the reactor has reached its fully developed hydrodynamic or flooding regime, and consequently an increase of the bubble coalescence probability is expected due to the presence of large population of induced gas bubbles. Nonetheless,

a_{GIR} and $a_{Induced}$ appear to increase by about 250% with increasing N , as the gas holdup values seem to control the behavior of the gas-liquid interfacial area in the GIR under such conditions.

It is also important to notice that in both the GIR and GSR, the trends of d_s and a were less pronounced in the organic mixtures than in toluene, as the presence of benzaldehyde and benzoic acid appears to have decreased the toluene coalescence tendency.

In the SAR, GIR and GSR, k_L is found to increase by about 10, 30 and 5%, respectively, with increasing mixing speed as can be seen in Figure 40, which can be related to the reduction of the film thickness with increasing turbulence^(267, 483). It is also important to mention that the increase of k_L with N is stronger in the GIR than in the SAR and GSR, which can be attributed to a greater increase of d_s with N in the GIR, since Calderbank and Moo-Young (1961) reported that k_L is directly proportional to d_s . At high mixing speeds in all three types of reactor, however, k_L tends to become almost independent of N , which is in agreement with the findings by Ganguli and van den Berg⁽³⁶²⁾. Thus, since in the three reactor types used, both a and k_L were found to increase with N , increasing mixing speed was expected to increase $k_L a$ values.

6.2.2 Effect of Liquid Height on the Hydrodynamic and Mass Transfer Parameters

Figure 41 shows that increasing liquid height from 0.171 to 0.268m decreases $k_L a$ values in both the SAR and GIR by up to 90 and 80%, respectively.

In fact, increasing H decreases the turbulence at the gas-liquid surface and as a result N_{CRE} increases^(60, 65, 68, 71, 73-77) in the SAR, as shown in Figure 42. In the GIR, the decrease of turbulence increases the hydrostatic head above the impeller, which increases the pressure drop needed to induce the gas into the liquid, and thus reduces the pumping capacity of the impeller^(349, 93, 103), and subsequently increasing the liquid height increases N_{CRI} ^(89, 92, 111), as shown in Figure 42.

Therefore, both rate of gas entrainment and induced gas flow rate, Q_{GI} , (Figure 42) decrease, respectively, in the SAR and GIR, leading to a sharp decrease of ε_{G-SAR} and ε_{G-GIR} ^(95, 96, 98, 106, 109, 114, 267, 483) as illustrated in Figure 43. At mixing speeds > 16 Hz in the GIR, however, Q_{GI} becomes independent of liquid height, as shown in Figure 42, and could be attributed to the fully developed hydrodynamic regime reached by the reactor under such conditions.

Figure 43 also shows that increasing liquid height from 0.171 to 0.219m increases d_{S-SAR} by 20%, as the decrease of turbulence and population of entrained gas bubbles led to a decrease of the bubble breakup probability. This behavior is different in the GIR, as the reactor under the operating conditions used reached a fully developed hydrodynamic regime, where increasing liquid height decreases Q_{GI} as well as the rate of gas bubbles coalescence. Also, as bubbles coalescence appears to dominate the gas bubble sizes distribution in pure toluene, the presence of benzaldehyde and benzoic acid seems to have hindered coalescence, since the decrease of d_{S-GIR} with H in toluene mixtures is only 5% when compared with 30% in toluene as can be observed in Figure 43.

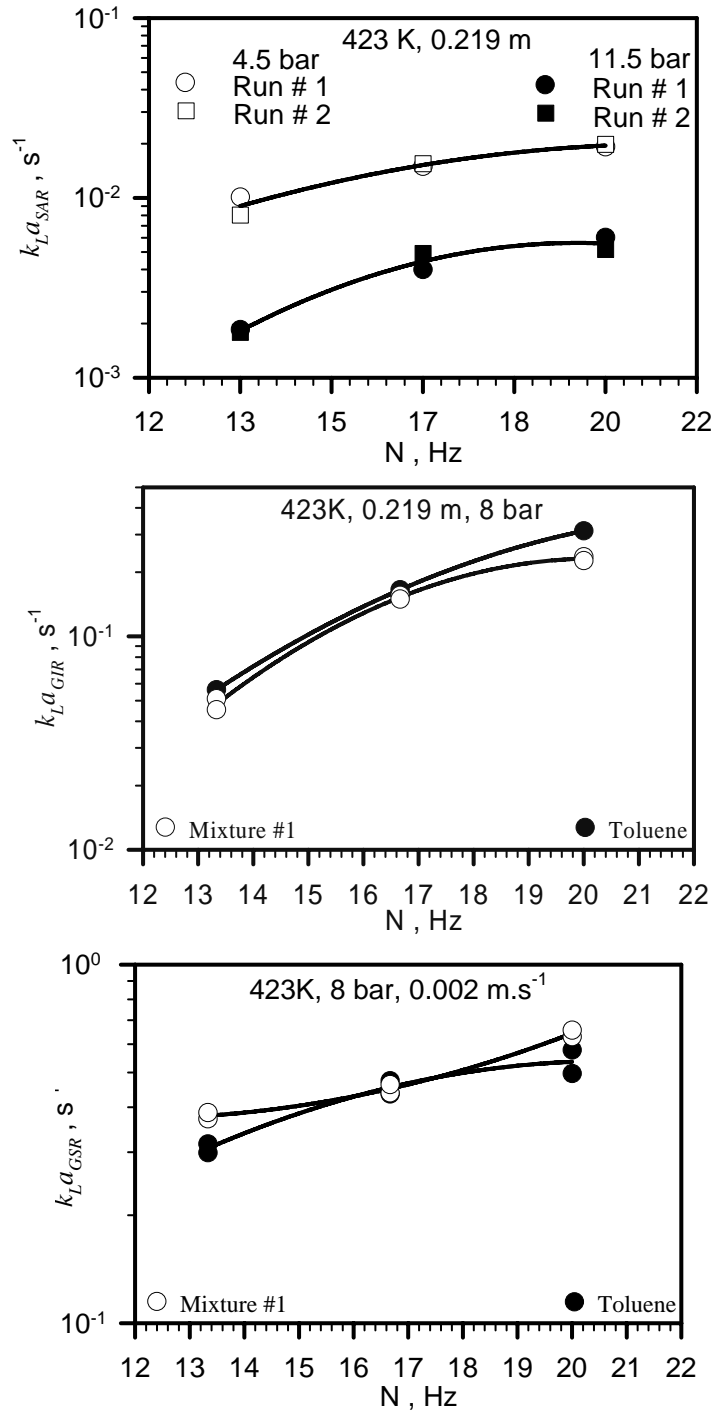


Figure 37: Effect of Mixing Speed, Pressure and Liquid Nature on k_{La} values in the SAR, GIR and GSR

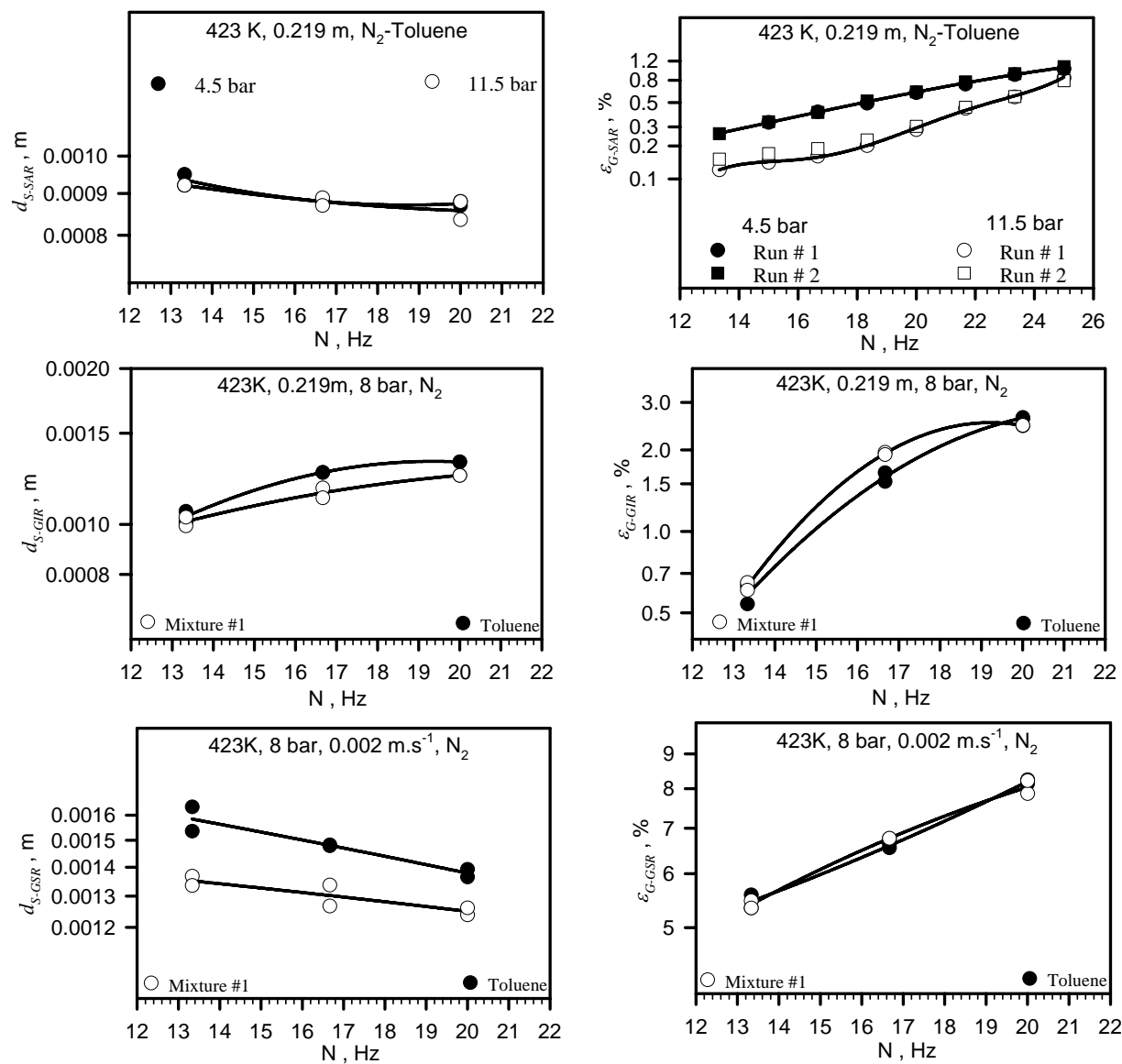


Figure 38: Effect of Mixing Speed, Pressure and Liquid Nature on d_s and ε_G values in the SAR, GIR and GSR

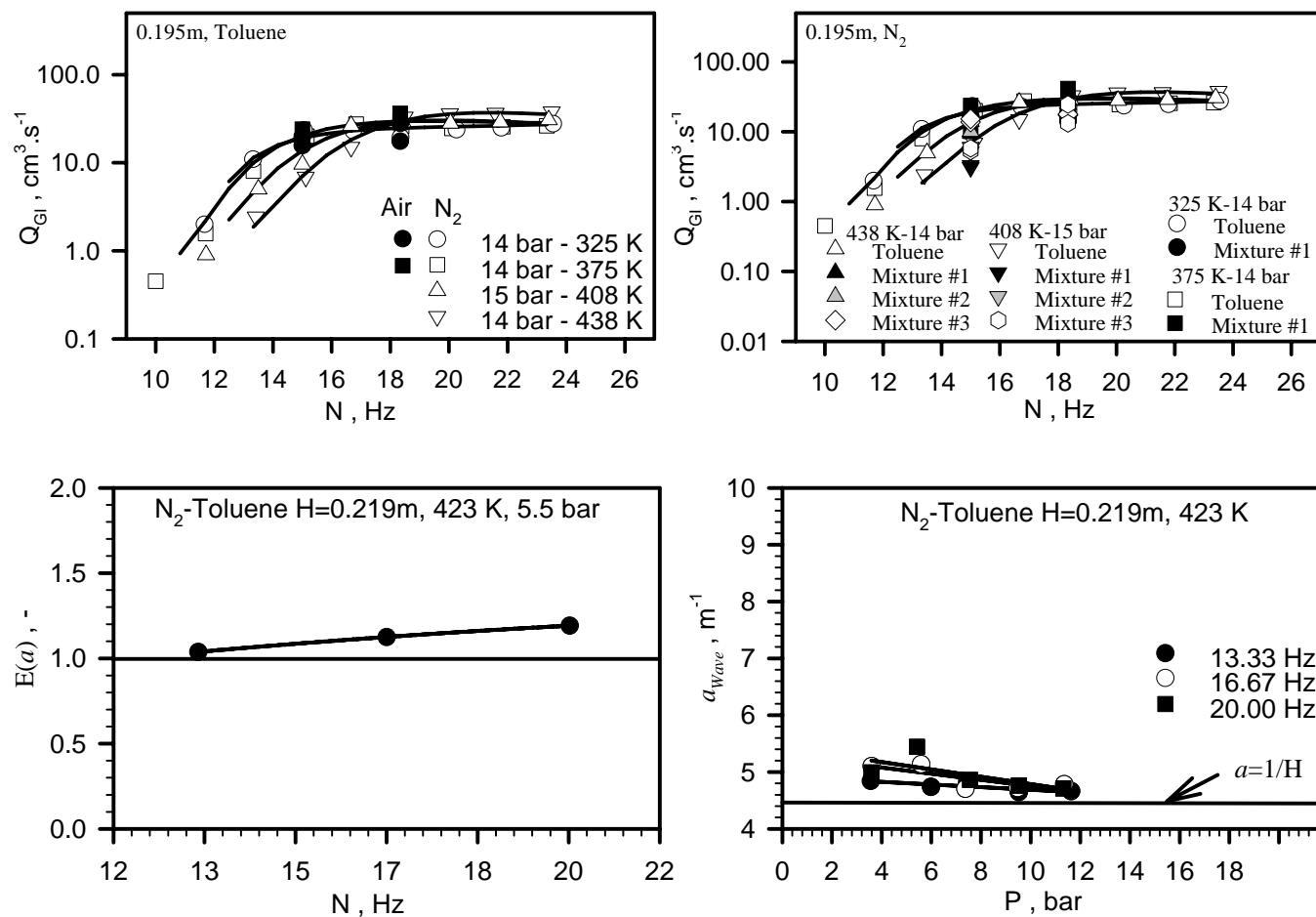


Figure 39: Effect of Mixing Speed, Pressure and Liquid Nature on Q_{GI} and a_{Wave} values in the SAR, GIR and GSR

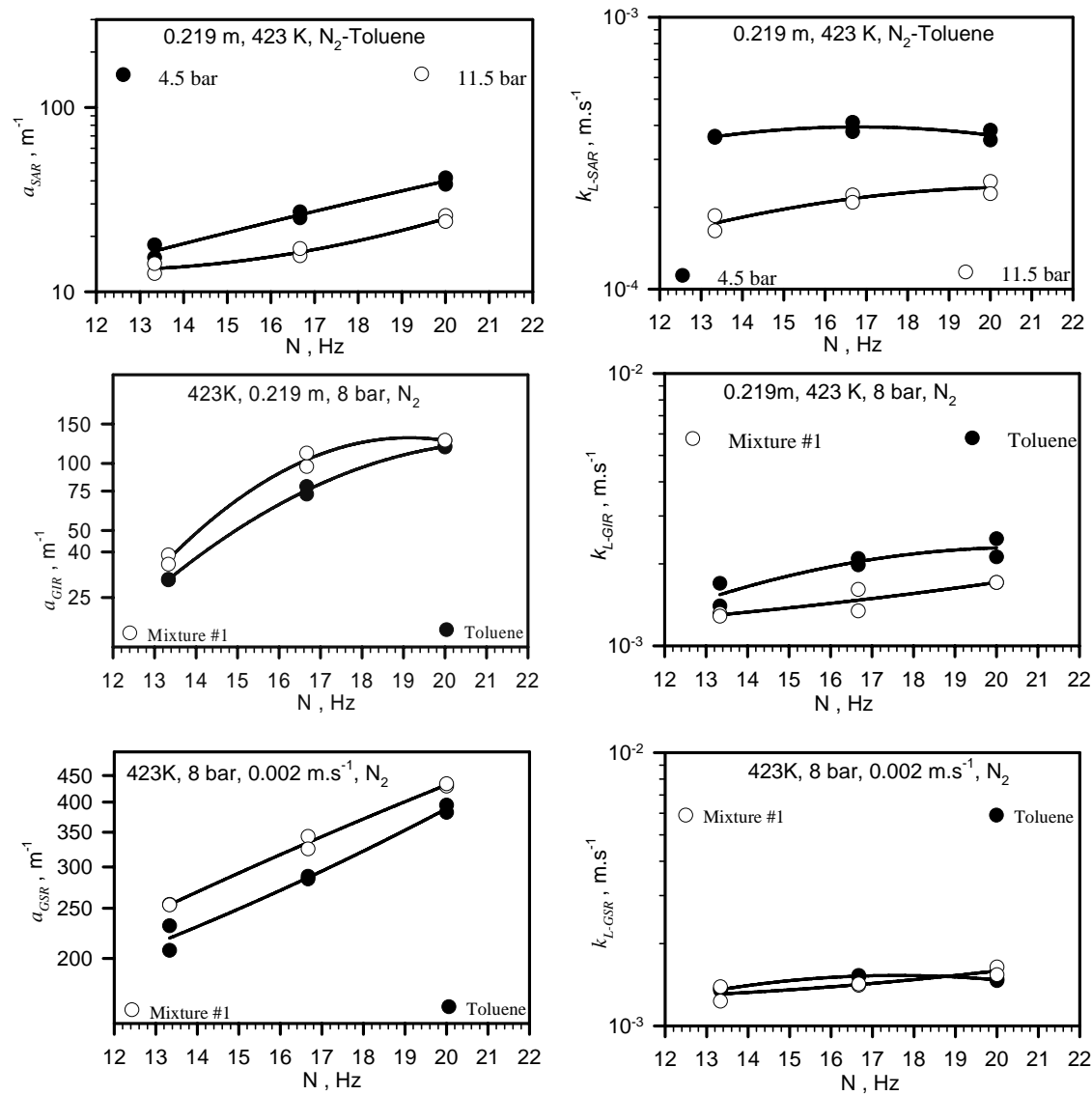


Figure 40: Effect of Mixing Speed, Pressure and Liquid Nature on a and k_L values in the SAR, GIR and GSR

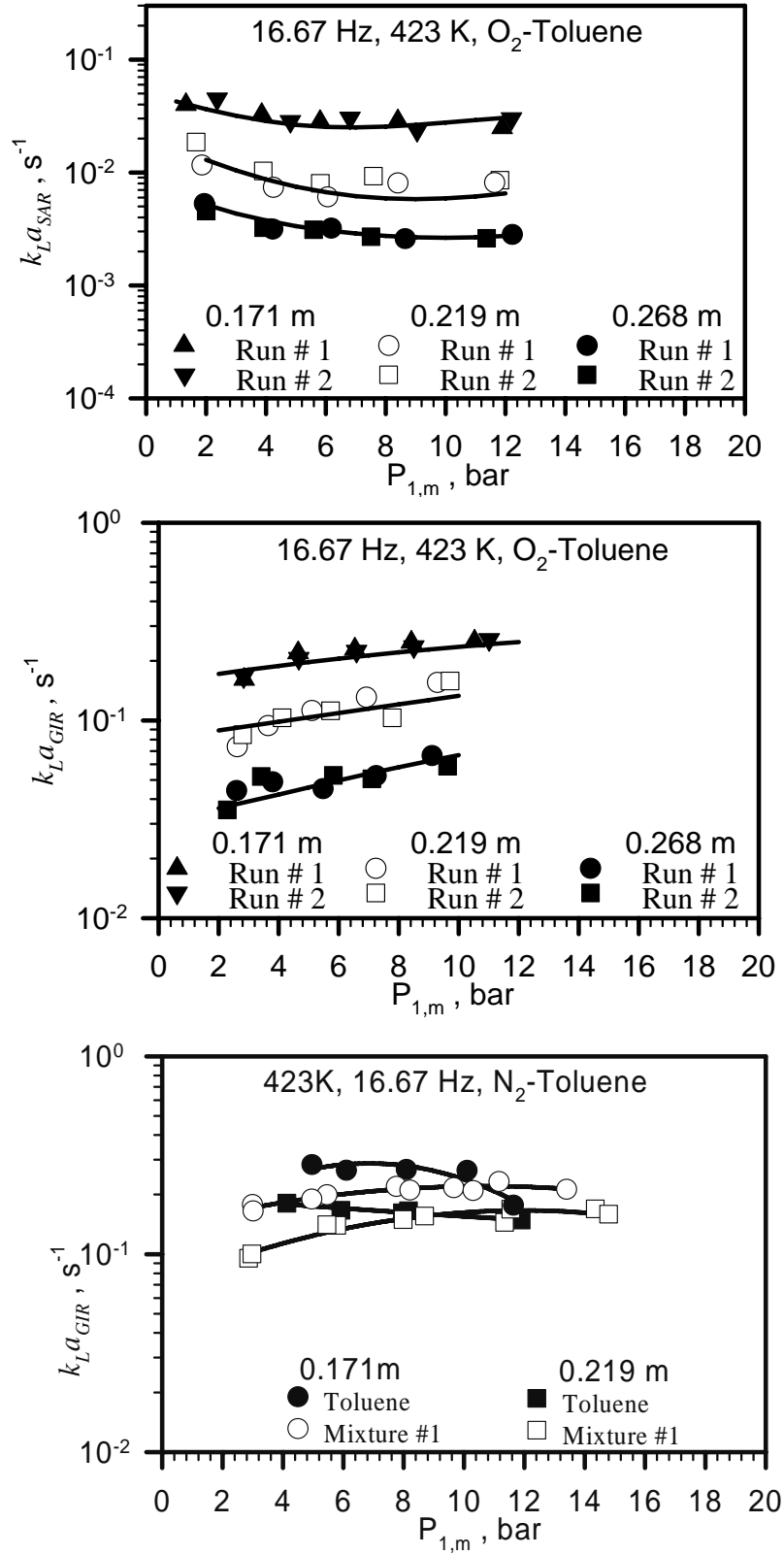


Figure 41: Effect of Liquid Height, Pressure and Liquid Nature on $k_L a$ values in the SAR and GIR

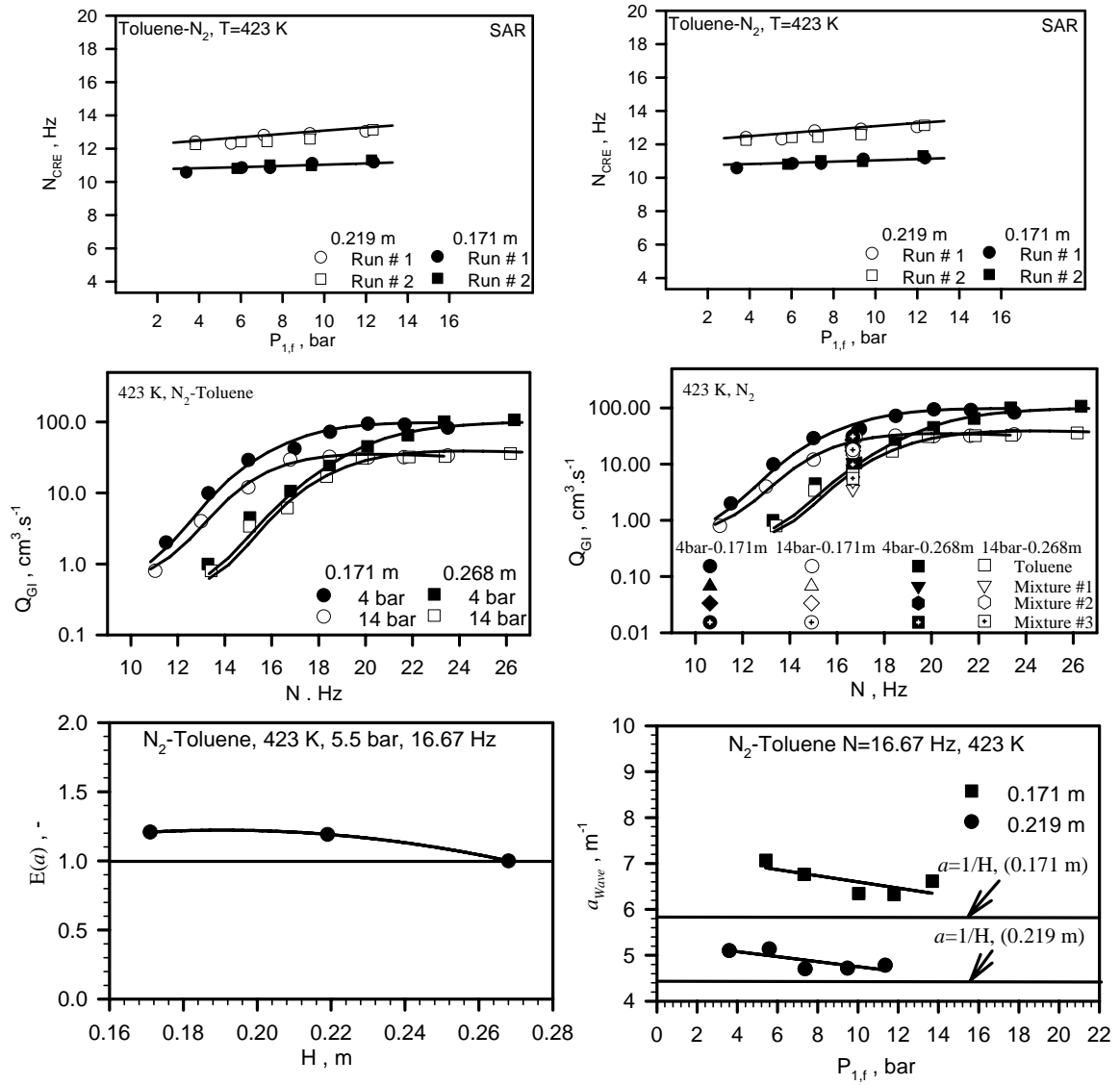


Figure 42: Effect of Liquid Height, Pressure and Liquid Nature on N_{CRE} , N_{CRI} , Q_{GI} and a_{Wave} values in the SAR and GIR

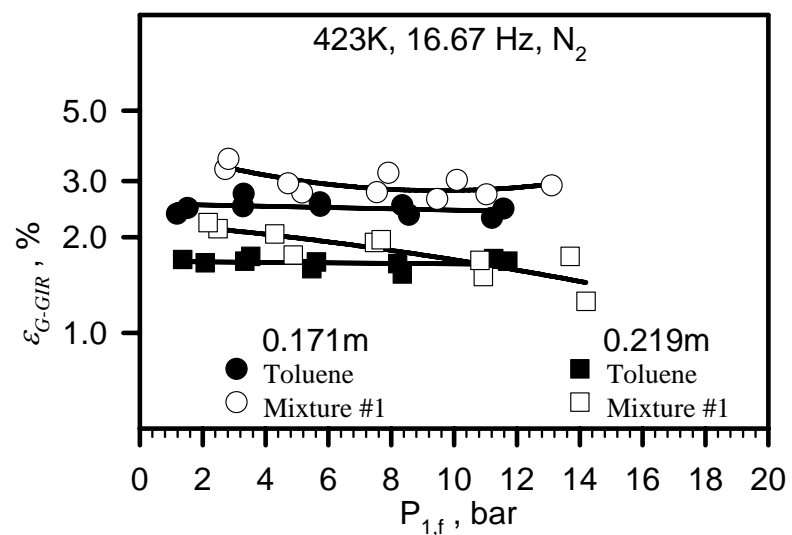
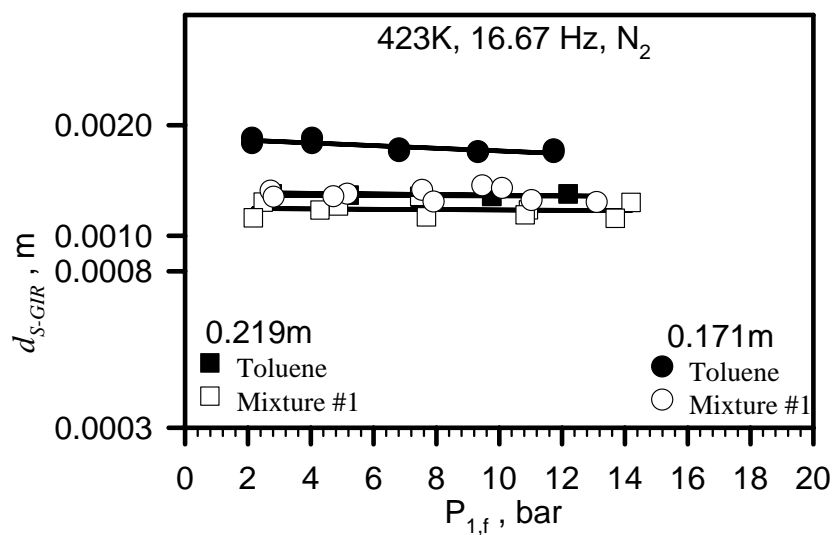
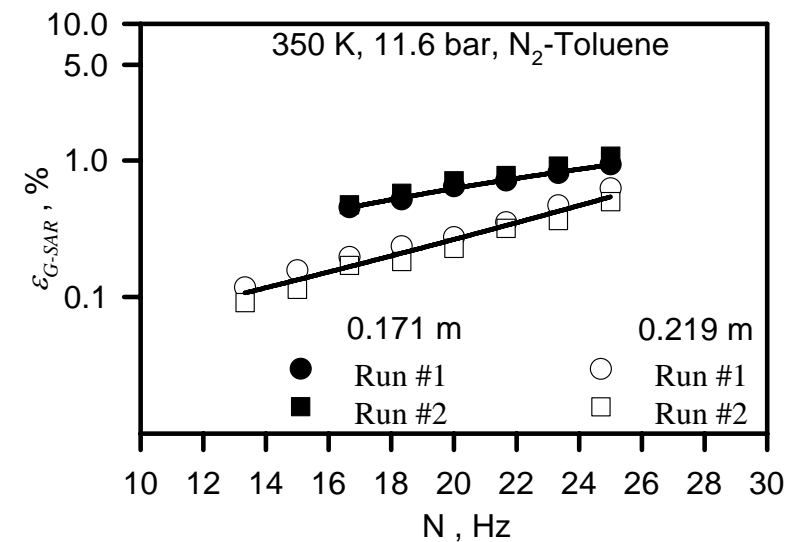
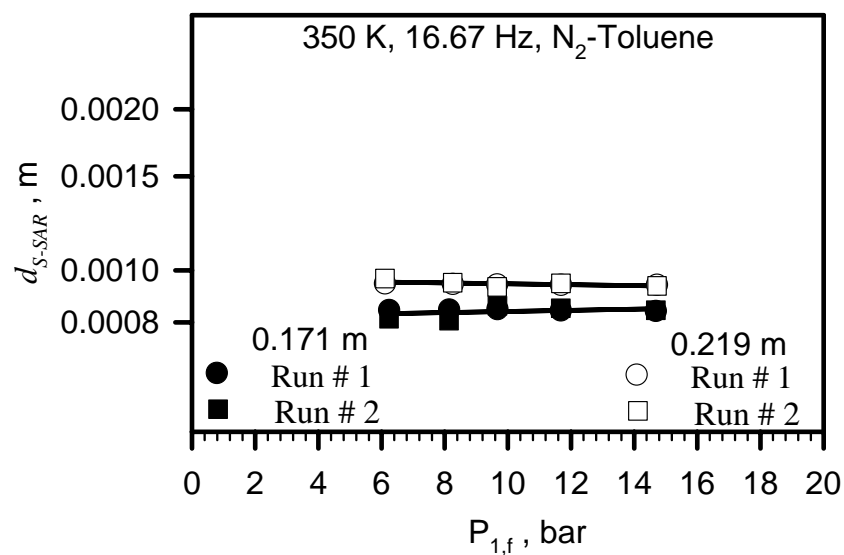


Figure 43: Effect of Liquid Height, Pressure and Liquid Nature on d_S and ϵ_G values in the SAR and GIR

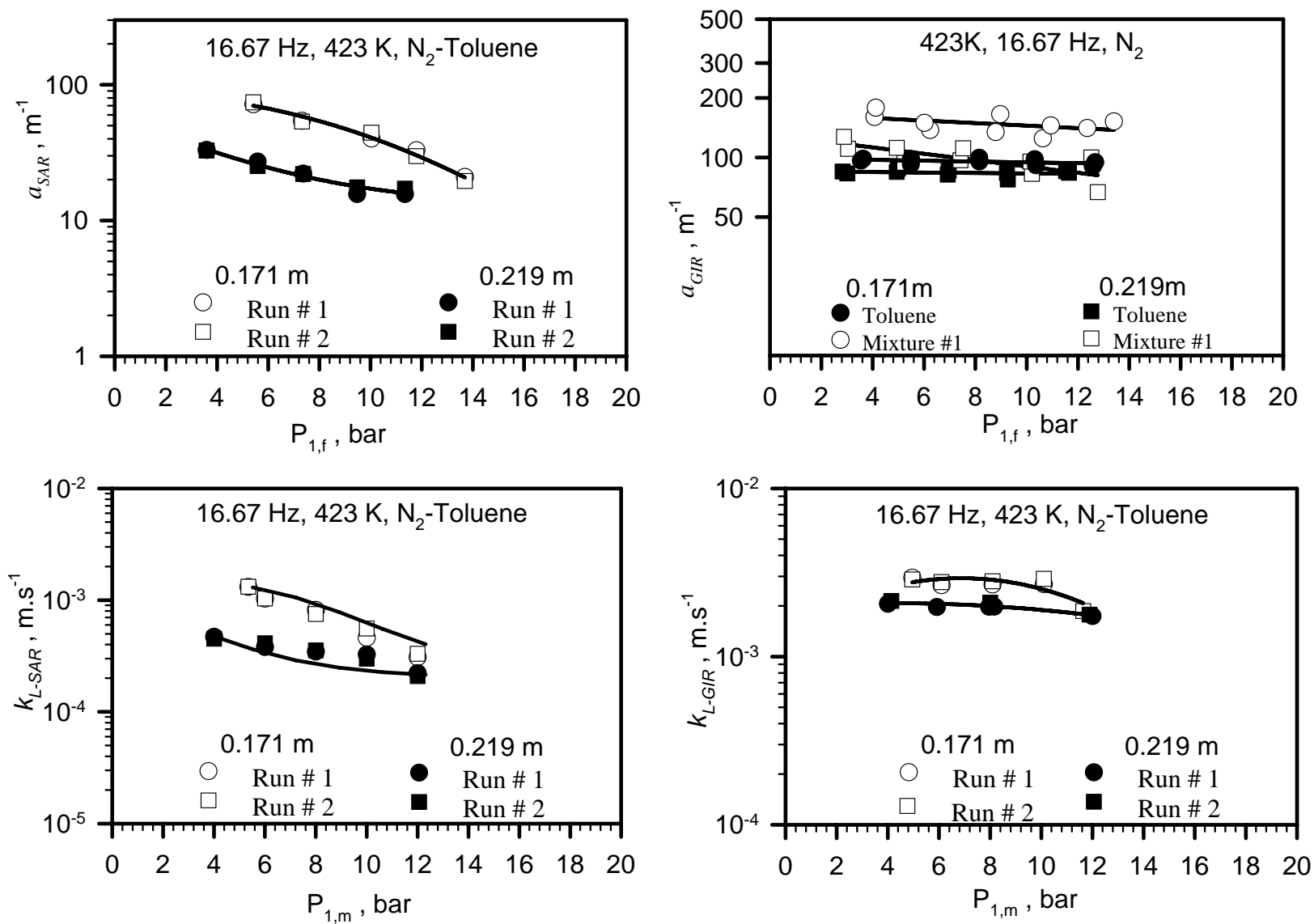


Figure 44: Effect of Liquid Height, Pressure and Liquid Nature on a and k_L values in the SAR and GIR

The a_{Wave} , on the other hand, appears to decrease with liquid height, H , as can be observed in Figure 42. In fact, increasing H decreases the turbulence, which results in a decrease of the a_{Wave} and subsequently $E(a)$ by about 25%. From Equation (5-71) and (5-72), and the behavior of a_{Wave} , a_{SAR} is expected to decrease by about 20% with increasing liquid height from 0.171 to 0.219m, whereas for a_{GIR} , the observed decrease with H is not that obvious, as it appears to be predominantly due to the decrease of Q_{GI} and subsequently ε_{G-GIR} . This signifies that the gas holdup in the GIR controls the gas-liquid interfacial area, as it is shown in Figure 44.

Increasing the liquid height also decreases the power input per unit volume and the degree of turbulence, and thus decreases both k_{L-SAR} and k_{L-GIR} by about 50 and 25%, respectively as depicted in Figure 44. Therefore, since increasing H decreases both a and k_L the observed decrease of $k_L a$ values with increasing liquid height are expected.

6.2.3 Effect of Superficial Gas Velocity on the Hydrodynamic and Mass Transfer Parameters

The effect of superficial gas velocity, U_G , on $k_L a_{GSR}$ is shown in Figure 45, and it appears that $k_L a_{GSR}$ increases by about 30 % with increasing U_G from 0.002 to 0.004m/s, which was expected due to the observed increase of ε_{G-GSR} , a_{GSR} and k_{L-GSR} with U_G .

In fact, on one hand, ε_{G-GSR} increases by 50% with increasing superficial gas velocity, since increasing U_G increases the bubble population, gas dispersion and re-circulation zone in the reactor. On the other hand, increasing U_G increases the bubbles coalescence probability and decreases the mixing power input per unit volume ⁽¹²⁸⁾, which subsequently decreases the bubbles breakup rate, and thus increases d_{S-GSR} values. Therefore, due to these combined effects, an increase by 35% of d_{S-GSR} values with increasing U_G occurs in the GSR, as observed in Figure 45. It is, however, important to mention that this behavior is less pronounced in mixture #1 (only 20%), due to the non-coalescence (frothing) nature of this mixture.

This increase of d_{S-GSR} values with U_G appears, however, to be minor as a_{GSR} increases by about 20% with U_G , indicating that ε_{G-GSR} has a controlling effect on a_{GSR} under these conditions.

Increasing the superficial gas velocity U_G decreases the energy dissipated, and according to the “eddy” cell model ^(279, 363) k_{L-GSR} is expected to decrease which disagrees with our experimental findings. Linek et al. ⁽³⁶³⁾, on the other hand, recently pointed out that the “slip velocity” model predicts a decrease of k_L with increasing the dissipated power, which is in contradiction with the predictions of the “eddy” cell model. In this study, however, increasing U_G appeared to increase d_{S-GSR} and hence k_{L-GSR} should a priori increase as suggested by Calderbank and Moon-Young ⁽²⁰⁸⁾, Miller et al., ⁽¹²⁶⁾ and Linek et al. ⁽³⁶⁴⁾. Thus, increasing U_G increases both a_{GSR} and k_{L-GSR} and consequently $k_L a_{GSR}$.

6.2.4 Effect of Temperature on the Hydrodynamic and Mass Transfer Parameters

The temperature effect on $k_L a_{SAR}$ is usually related to the changes of the physicochemical properties of the gas-liquid system used ^(11, 23, 349, 224, 249). In this study, as shown in Figure 46, $k_L a$ increases by about 400 and 300% with increasing T from 300 to 453 K, respectively for all gases in toluene in the SAR and GSR, and by 20% in mixture #1

in the GSR, whereas in the GIR, $k_L a$ is observed to increase and then slightly decrease in toluene and appears to systematically decrease in the organic mixtures. This effect of T on $k_L a$ in the SAR, GIR and GSR can be explained by the effect of temperature on a and k_L .

In toluene, increasing temperature from 300 to 453 K appears to decrease d_{S-SAR} , d_{S-GIR} and d_{S-GSR} , by 15, 30 and 20 %, respectively as can be observed in Figure 49. This effect can be directly attributed to the decrease of liquid viscosity^(72, 458) and surface tension^(349, 72, 118, 125, 132, 134, 458, 459) with T , as similar findings have been reported in the literature^(71, 118, 126, 132, 134, 146, 458). In the organic mixtures, however, d_{S-GIR} and d_{S-GSR} values seem to behave differently with increasing temperature. In fact, d_{S-GIR} and d_{S-GSR} values in the liquid mixtures first increase and then decrease with increasing temperature. This trend closely matches the behavior of the mixtures frothing characteristics, since at temperatures < 380 K, it was observed that froth was formed at the gas-liquid interface; and as the temperature was increased the froth started to slowly diminish and completely disappeared for $T > 410$ K. Consequently, since smaller bubble sizes are expected in the presence of froth, d_{S-GIR} and d_{S-GSR} values started to increase with temperature until the froth disappeared (between 380 to 410 K), then with further temperature increase, d_s values in the mixtures decreased as in pure toluene.

Increasing temperature decreases both liquid viscosity and surface tension, and led, in the SAR, to the decrease of N_{CRE} due to the increase of the surface turbulence. Similar findings were observed and reported by Tanaka et al.⁽⁷⁴⁾ and Tanaka and Izumi⁽⁷⁷⁾. Thus, the rate of gas entrainment in the SAR and the re-circulation rate⁽¹²²⁾ in the GSR increase, resulting in an increase with T of ε_{G-SAR} and ε_{G-GSR} by 25 and 50%, respectively in toluene, as it was confirmed in Figure 49. In the GIR, Figure 47 shows that N_{CRI} slightly decreases with increasing temperature, which can be related to the decrease of liquid viscosity as previously reported by several investigators^(349, 93, 103). Furthermore, using the experimental data by Fillion⁽³⁴⁹⁾ obtained in a geometrically identical GIR (see Table 28) along with those obtained in this study, the effect of physicochemical properties on the critical mixing speed was investigated as depicted in Figure 48. It appears, from this figure that increasing liquid viscosity or density increases N_{CRI} , which is in agreement with the finding by Patwardhan and Joshi⁽¹¹⁴⁾.

However, as illustrated in Figure 47, the induced gas-flow rate for toluene and mixtures in the GIR appears to increase and then decreases with temperature. This behavior is analogous to the effect of liquid viscosity on the gas induction flow rate found by Aldrich and van Deventer^(100, 101), and could be the result of the formation of different types of cavities around the impeller, revealing a transition of flow regime as reported by van't Riet and Smith⁽³⁶⁵⁾ and Bruijn et al.⁽³⁶⁶⁾. They studied this behavior in terms of cavity formation and observed that at low viscosity (corresponding to high temperatures) small cavities designated “clinging cavities” are formed around the impeller. As the viscosity increases, i.e., temperature decreases, these cavities become bigger, leading to a decrease of the pressure behind the blade and consequently the pumping capacity of the impeller increases. Bruijn et al.⁽³⁶⁶⁾ also showed that with further increase in liquid viscosity (corresponding to very low temperatures), more stable cavities are formed and the impeller suction efficiency diminishes. To further verify this effect of liquid viscosity on Q_{GI} values, Q_{GI} of N_2 in soybean oil and toluene were compared in Figure 48. As can be observed in this figure increasing liquid viscosity first increases and then decreases Q_{GI} , which is confirming the literature findings^(101, 365, 366) as well as the effect of temperature on Q_{GI} observed in toluene. Figure 48 also shows that increasing liquid

density decreases Q_{GI} , which again is in agreement with the results by Aldrich and van Deventer⁽¹⁰¹⁾, who observed a decrease of Q_{GI} with increasing liquid density from 798 to 998 kg/m³. Thus, it can be concluded that a maximum in Q_{GI} values as function of temperature, i.e. liquid viscosity is expected. This explanation in terms of cavity formations provided by van't Riet and Smith⁽³⁶⁵⁾ and Bruijn et al.⁽³⁶⁶⁾ to interpret the flow regime transition could also be perceived as a consequence of the impeller flooding. In fact, Warmoeskerken and Smith⁽¹³⁶⁾ observed similar cavities structure in the “loading-flooding” transition in a gas-sparging reactor (GSRs). Hence, the effect of temperature could be attributed to the impeller flooding, and be explained as a transition of flow regime with changes in liquid viscosity as observed by Aldrich and van Deventer^(100, 101). At mixing speeds >16 Hz, however, the induced gas flow rate appears to be independent of temperature, meaning that the reactor seems to have reached a fully developed hydrodynamic regime. Consequently, due to the effect of temperature or “viscosity” on Q_{GI} , ε_{G-GIR} appears to increase and then decrease with temperature in toluene, which is in agreement with the findings of He et al.⁽⁹⁸⁾ and Aldrich and van Deventer⁽¹⁰¹⁾ in GIRs.

In the organic mixtures, however, the presence of froth and the effect of temperature on its stability affected the gas holdup, and thus different behaviors were observed. In fact, at low T , the froth led to an enhancement of ε_{G-GIR} values, which disappeared at high T as the froth faded. Therefore, ε_{G-GIR} values in the mixtures were affected and controlled by both the froth and Q_{GI} , as a systematic decrease with temperature can be seen in Figure 49. In the GSR, ε_{G-GSR} trend in mixture #1 is only controlled by the presence of froth, as ε_{G-GSR} values in mixture # 1 were found to decrease and increase with T . In fact, as temperature increased the froth decayed, thus ε_{G-GSR} decreased until $T > 410$ K, where the organic mixture started to behave like toluene, resulting in an increase of ε_{G-GSR} with T .

Furthermore, under the conditions used, a_{Wave} and $E(a)$ appear to increase with increasing temperature as illustrated in Figure 47. This effect of temperature can be attributed to the decrease of liquid viscosity and surface tension with increasing T , which leads to the increase of the amplitude of a_{Wave} ⁽⁸⁶⁾ resulting in an increase of $E(a)$ by 40% at 5.5 bar.

Consequently, as d_{S-SAR} , d_{S-GIR} and d_{S-GSR} decrease, and a_{Wave} increases with T in toluene, a_{SAR} , a_{GIR} and a_{GSR} are expected to follow the behavior exhibited by the gas holdup in the SAR, GIR and GSR, which is confirmed by comparing Figures 49 and 50. In the liquid mixtures, the froth controls the gas holdup behavior which dominates the trends of a in both the GIR and GSR. Thus, a_{GIR} decrease in liquid mixtures, and a_{GSR} first decrease and then increase with increasing T , as can be seen in Figure 50.

Increasing temperature was also found to increase k_L values by about 75, 100 and 100 %, respectively in the SAR, GIR and GSR in all systems studied, as can be seen in Figure 50. This effect was expected, as increasing T increases the gas diffusivity, D_{AB} , and subsequently k_L , because it is well accepted that k_L is directly proportional to D_{AB} to a power n (Equation (6-15)) ranging from 0.5 for the penetration theory to 1.0 for the two-film model⁽³⁶⁷⁾.

$$k_L \propto D_{AB}^n \quad (6-15)$$

From the balance effect of T on both a and k_L , it appears that in toluene $k_L a$ increases in the SAR and GSR, and increase and slightly decreases in the GIR. In the organic mixtures, however, $k_L a$ appears to systematically decrease in the GIR and decrease and then increase in the GSR. These trends seem to imply that the SAR is controlled mostly by k_L , and the GIR and GSR by both k_L and a , especially under frothing conditions.

Table 28: Geometrical and Operating Parameters Used by Fillion ⁽³⁴⁹⁾

<i>Systems</i>	
<i>Gas</i>	H_2, N_2
<i>Liquid</i>	<i>Soybean Oil</i>
<i>Physical Properties</i>	
$\rho_L, kg.m^{-3}$	800-866
$\mu_L, Pa.s$	0.0023-0.0067
$\sigma_L, N.m^{-1}$	0.024-.030
<i>Operating Conditions</i>	
T, K	373-473
P, bar	1-5
H, m	0.146-0.268
N, Hz	11.7-28.3
<i>Reactor Geometry</i>	
<i>Inducing Type</i>	<i>Hollow shaft</i>
d_{imp}, m	0.0508
d_{orif}, m	0.0024
d_T, m	0.114
H_{imp}, m	0.0635

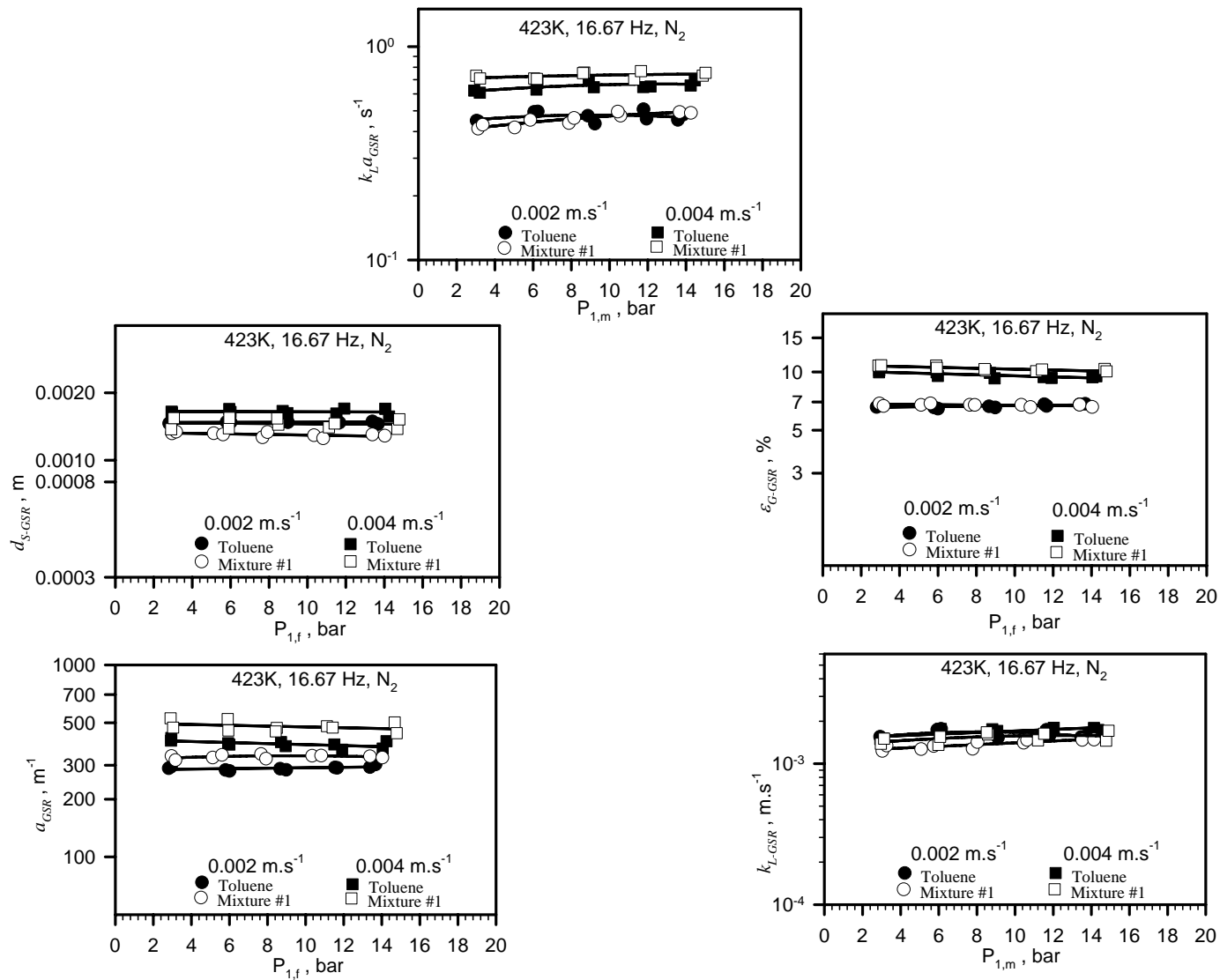


Figure 45: Effect of Superficial Gas Velocity, Pressure and Liquid Nature on $k_L a$, d_S , ε_G , a and k_L in the GSR

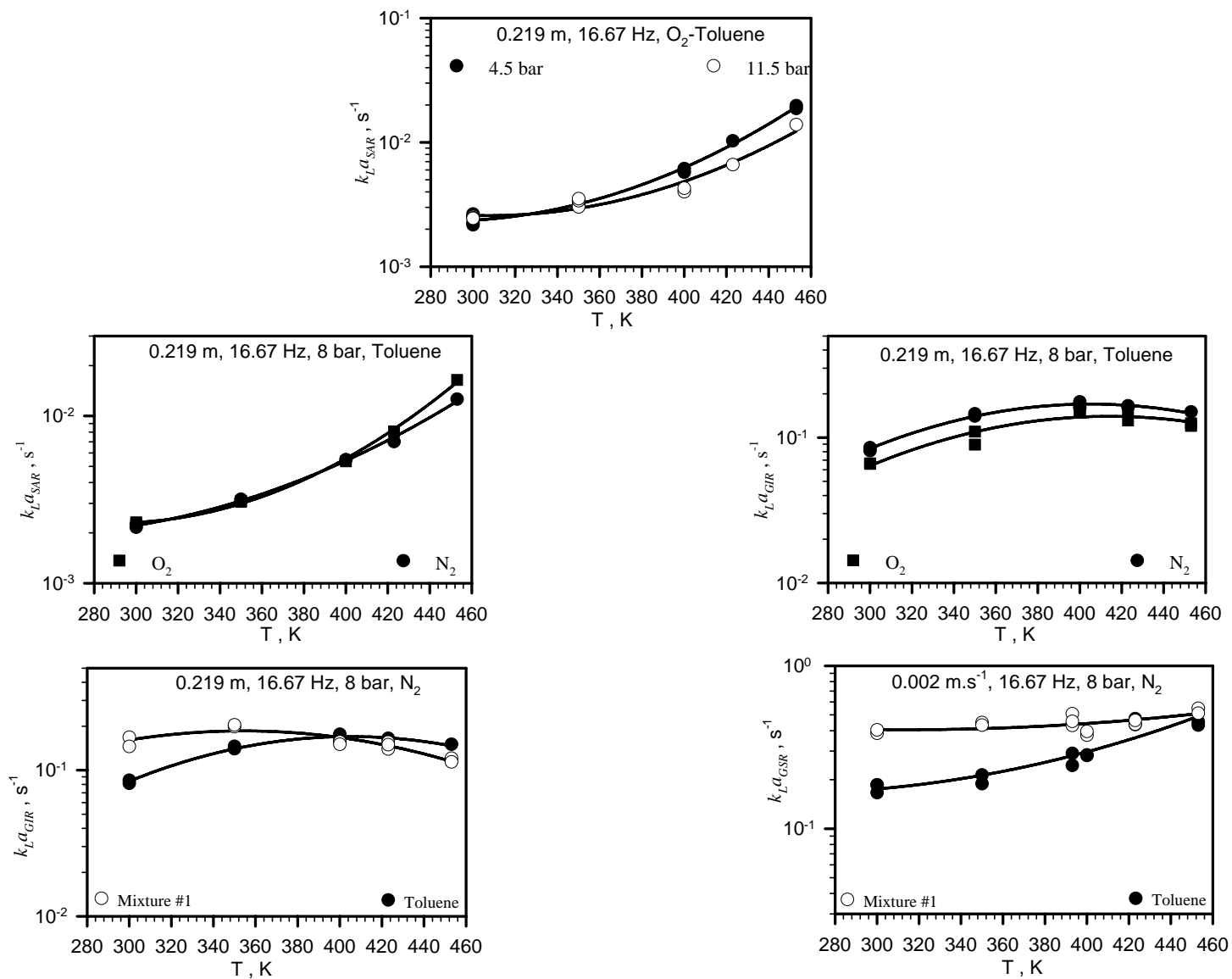


Figure 46: Effect of Temperature, Pressure and Gas Nature on $k_L a$ in the SAR, GIR and GSR

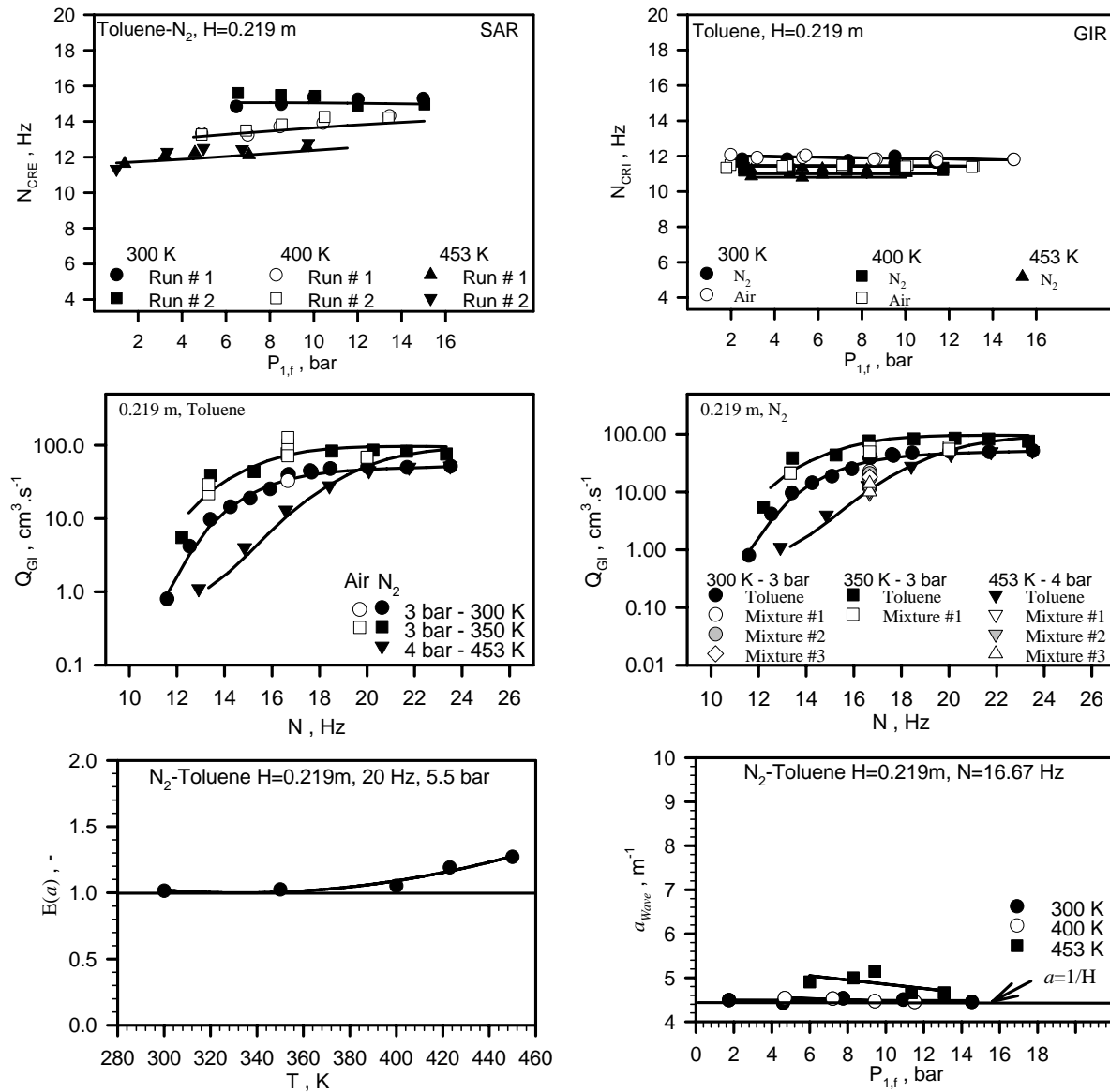


Figure 47: Effect of Temperature, Pressure, Gas and Liquid Nature on N_{CRE} , N_{CRI} , Q_{GI} and a_{Wave} in the SAR, GIR and GSR

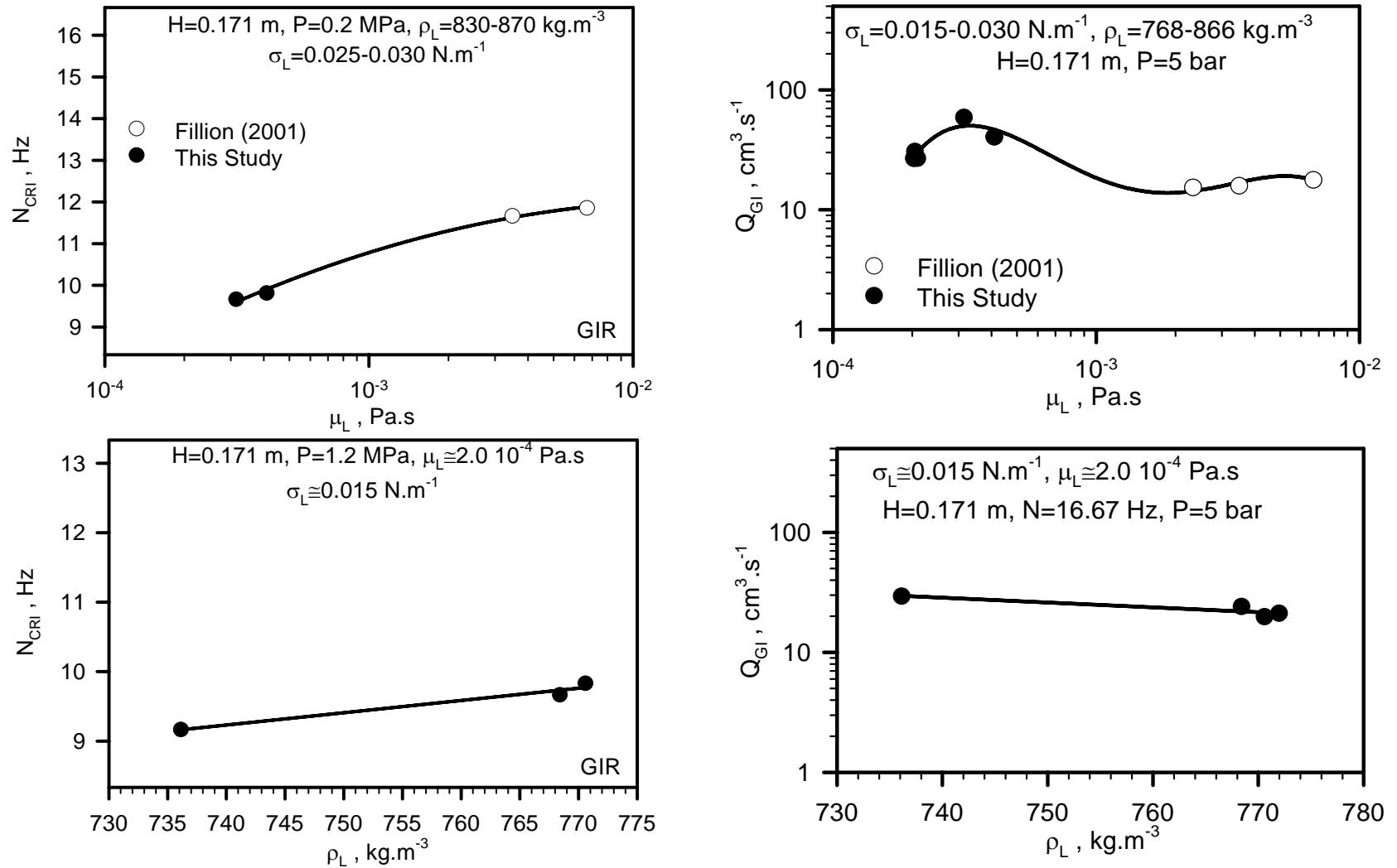


Figure 48: Effect of Viscosity and Density on N_{CRI} and Q_{GI} in the GIR

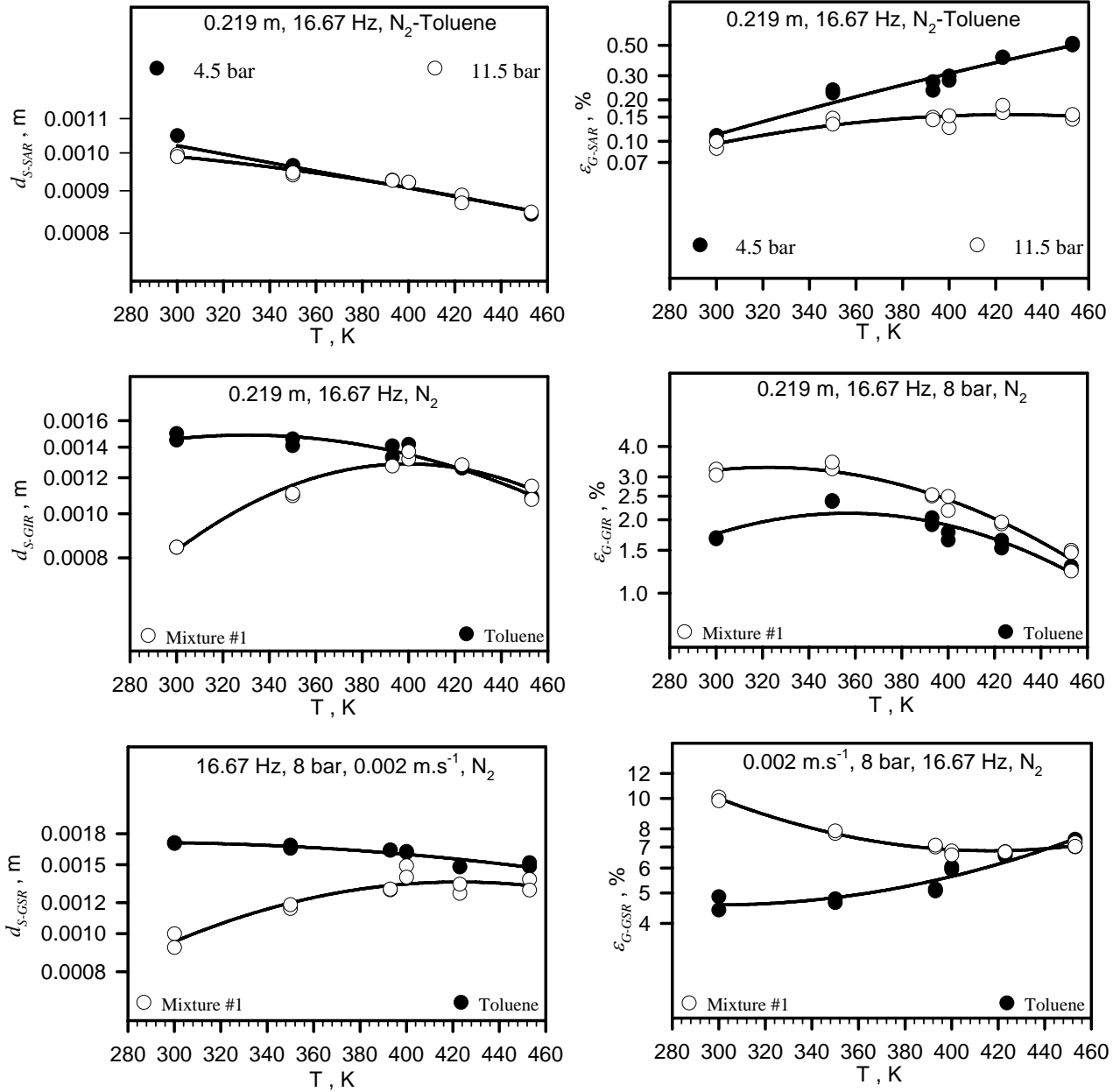


Figure 49: Effect of Temperature and Pressure on d_s and ϵ_g in the SAR, GIR and GSR

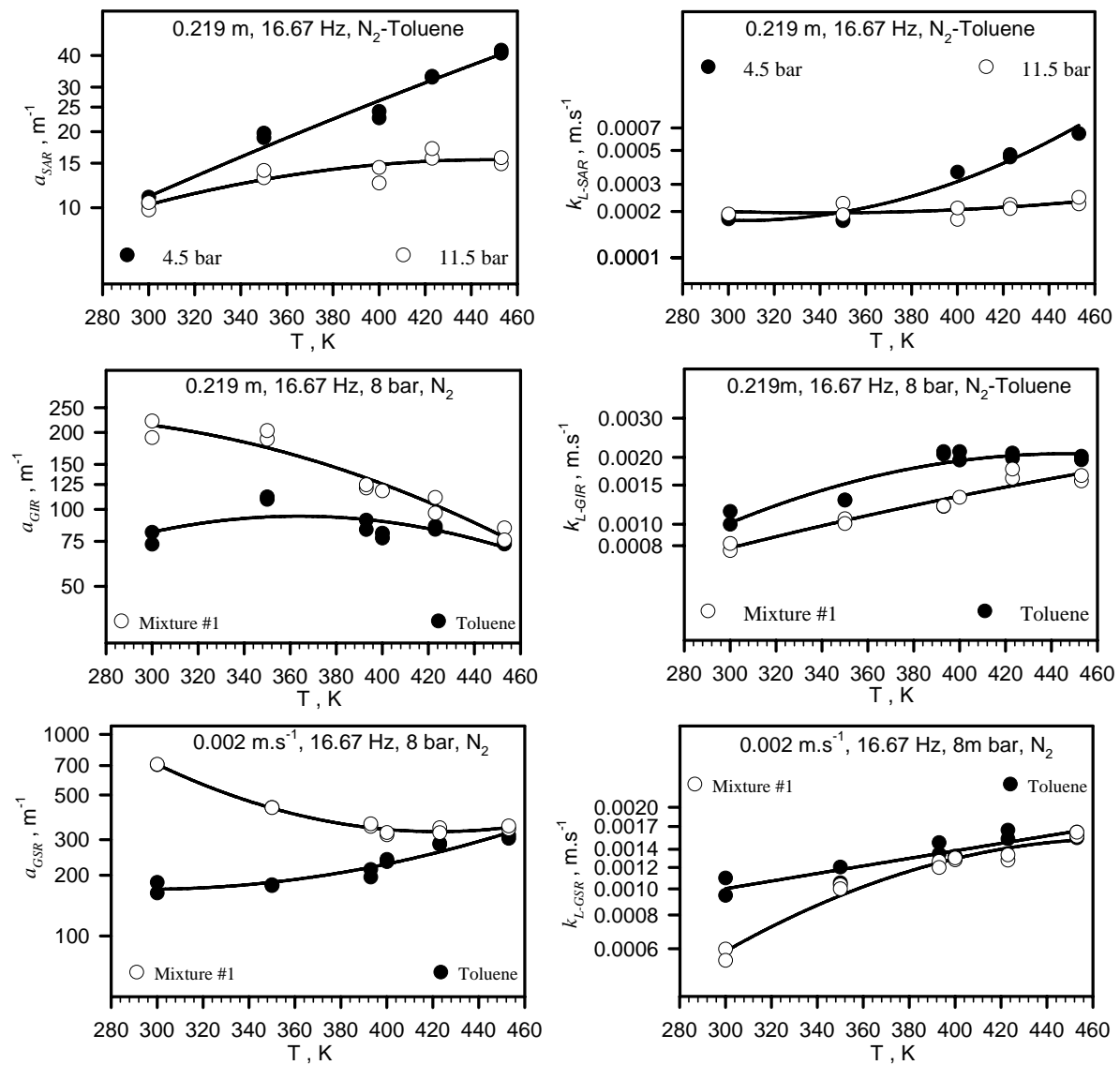


Figure 50: Effect of Temperature and Pressure on a and k_L in the SAR, GIR and GSR

6.2.5 Effect of Pressure on the Hydrodynamic and Mass Transfer Parameters

In Figures 37, 41, 45, 46 and 51, $k_L a_{SAR}$ values appear to be independent of pressure at low T and to decrease with P at high T , while $k_L a_{GIR}$ and $k_L a_{GSR}$ values appear to be almost independent of P . These behaviors can be interpreted in the light of the dependency of k_L and a on P , as the effect of P on $k_L a$ have been reported to be controversial ⁽²³⁾.

Figures 38, 43, 45, 49 and 51 illustrate that d_{S-SAR} , d_{S-GIR} and d_{S-GSR} are not affected by pressure, indicating that the bubbles are small enough to resist the force generated by P ^(23, 349). In Figure 42, it also appears that the pressure does not significantly affect N_{CRE} values within the experimental conditions used, as the liquid not the gas physicochemical properties, seem to control the N_{CRE} behavior in the SAR. Similar findings in the GIR can be observed in Figure 42. This figure indicates that within the range investigated, pressure has no effect on N_{CRI} , which can be explained by the behavior of the pumping mechanism in the GIR. At low mixing speeds, the hollow shaft is full or partially full of liquid, and as the mixing speed increases, the liquid level inside the hollow shaft decreases until the first gas bubbles exits through the orifice, indicating N_{CRI} . Thus, at mixing speeds below N_{CRI} , the pumping capacity of the impeller is mainly dependent on the liquid and not the gas properties as discussed by Patwardhan and Joshi ⁽¹¹⁴⁾.

In the SAR, it can also be noticed in Figures 38, 43, 45, 49 and 51, that ε_{G-SAR} values decrease by about 40% with increasing pressure at high temperatures (> 350 K), while ε_{G-GIR} and ε_{G-GSR} values are almost independent of P . Increasing pressure can alter the gas-liquid physical properties, such as liquid viscosity and surface tension, or create a smoother liquid surface (force/area). Since in all reactor types, very little change was observed by increasing pressure on the Sauter mean bubble diameter or critical mixing speeds, it can be concluded that the change of physicochemical properties with pressure is negligible.

In the SAR, however, it seems that increasing P reduced the degree of turbulence inside the reactor as in Figures 39, 42 and 47 the values of a_{Wave} and $E(a)$ decrease with increasing P , especially at high temperature. This behavior could be attributed to the increase of the forces applied on the gas-liquid surface with increasing pressure, which might have flattened the wavy surface. In fact, increasing pressure tends to decrease the waves' amplitude and squeeze the gas-liquid surface leading to a decrease of a_{Wave} ⁽¹⁵¹⁾. Thus, a decrease in a_{Wave} can be expected, especially at low liquid viscosity and surface tension, i.e. high temperature. In these figures, it also appears that depending on the operating conditions used, a_{Wave} could increase reaching an $E(a)$ of about 40%, which means that its determination is critical in calculating and assessing the true mass transfer coefficient, k_L . Also, the knowledge of a_{Wave} values could have a strong impact on the scale-up of SARs, if taken into account, as suggested by Miller ⁽¹²⁶⁾. Consequently, the overall bubble population decreases with pressure, leading to the observed decrease of gas holdup especially at high temperature. In fact, at high T , lower values of liquid viscosity and surface tension are expected, and as pressure increases, the gas-liquid surface tends to smooth out leading to less and less entrainment of gas bubbles, i.e. ε_{G-SAR} .

It is also important to mention that even though small effect of P on ε_{G-GIR} can be seen, a meticulous study of the gas holdup values shows a slight decrease, which can be explained by the effect of pressure on Q_{GI} . In fact, the

induced gas flow rate is observed to decrease with pressure as illustrated in Figure 42, and can be related to the change of density. Increasing pressure increases the local density of the gas-liquid system, and therefore the hydrostatic head above the impeller as well as the pressure drop across the orifices increase, leading to a decrease of Q_{GI} . This behavior is in accordance with the findings for H₂-, N₂-soybean oil systems reported by Fillion⁽³⁴⁹⁾, who found that Q_{GI} values decreased with increasing gas density. Consequently, since very little effect of pressure on the Sauter mean bubble diameter was observed, it is expected that the gas-liquid interfacial area follow the behavior exhibited by the gas holdup in all reactor types, as can be seen in Figures 40, 44, 45, 50 and 52.

Also, k_{L-SAR} has been reported to be independent^(265, 267), decrease^(257, 259) or increase⁽⁶⁷⁾ with P , depending on the gas-liquid physicochemical properties and the operating conditions used. In this study, k_{L-SAR} appears to decrease by 40% with pressure, particularly at temperatures > 350 K, whereas k_{L-GIR} and k_{L-GSR} appear to be independent of pressure in Figures 40, 44, 45, 50 and 52. Increasing pressure increases C^* , which reduces both liquid viscosity and surface tension. Decreasing liquid viscosity increases k_L , since D_{AB} is inversely proportional to the liquid viscosity; however, decreasing liquid surface tension decreases k_L by decreasing the rate of surface renewal. Thus, increasing pressure has two opposite effects on k_L , nonetheless since no effect of pressure were found on d_s , k_{L-GIR} and k_{L-GSR} , it is likely that increasing pressure did not sufficiently change the physical properties to affect both hydrodynamic and mass transfer parameters. However, it seems that increasing P reduces the degree of turbulence in the SAR by stabilizing the gas-liquid surface, which decreases the overall bubble population and led to the observed decrease of k_{L-SAR} , which is in accordance with the relationship between k_L and d_s reported by Calderbank and Moon-Young⁽²⁰⁸⁾. This phenomenon did not occur in both the GIR and GSR, and consequently, the effect of pressure on k_L is negligible, as the gas-liquid physicochemical properties were unchanged. Therefore, both k_{L-SAR} and a_{SAR} decrease with increasing pressure, which resulted in the observed decrease of $k_L a_{SAR}$ values, whereas $k_L a_{GIR}$ and $k_L a_{GSR}$ values remained unchanged by increasing P as both gas holdups and Sauter mean bubble diameters in these two reactor types were unchanged by the pressure.

6.2.6 Effect of Gas Nature on the Hydrodynamic and Mass Transfer Parameters

As depicted in Figures 46 and 51, the effect of gas nature on $k_L a$ values is in agreement with the available literature^(11, 23, 56, 349, 249), as in the SAR, $k_L a_{SAR}$ values of O₂ are similar or greater than those obtained for N₂, following the diffusivity trend, i.e. k_L , and as in the GIR, $k_L a_{GIR}$ values of N₂ are slightly greater than those of air, which are greater than those of O₂. In the GIR, the trend does not follow that of the diffusivity, but follows that of a_{GIR} ⁽²³⁾, indicating the strong effect of a values on $k_L a$ in the GIR. In order to explain these different behaviors, the effect of gas nature on d_s , ε_G and thus on both a and k_L is clarified in the following for the GIR.

As can be observed in Figure 51, no change between d_{S-GIR} values of N₂ and air was found, which is expected since their molecular weights; hence gas densities, are almost the same. An increase of about 10% between ε_{G-GIR} values of N₂ and of air is, however, shown in Figure 51, and can be attributed to the effect of gas nature on Q_{GI} . In fact, in Figure 39 Q_{GI} values are slightly higher for N₂ than for air in toluene. This behavior could be attributed to the

closeness of their molecular weights and subsequently their densities. Consequently, the effect of gas nature on a_{GIR} can be correlated with the ε_{G-GIR} behavior as no change in bubble diameter was observed.

The difference, however, in the gas-liquid interfacial area between the two gases is so small that it can be considered within the experimental error range, which is more likely since N_2 and air have close molecular weights. The effect of gas nature on k_{L-GIR} , which can be seen in Figure 52, shows that k_{L-GIR} values of air are 5% greater than those of N_2 , which is in agreement with literature findings (Tekie et al., 1997; Fillion and Morsi, 2000) since air has slightly higher diffusivity values than N_2 under the same operating conditions. Thus, from a and k_L values in the GIR, it appears that $k_L a_{GIR}$ values of N_2 are slightly greater than those of air, greater than those of O_2 . While the difference between N_2 and air values is small and probably within the experimental error, it seems that the small difference is due to the effect of gas nature on the gas holdup, thus a_{GIR} has an important impact in the control of $k_L a_{GIR}$ values.

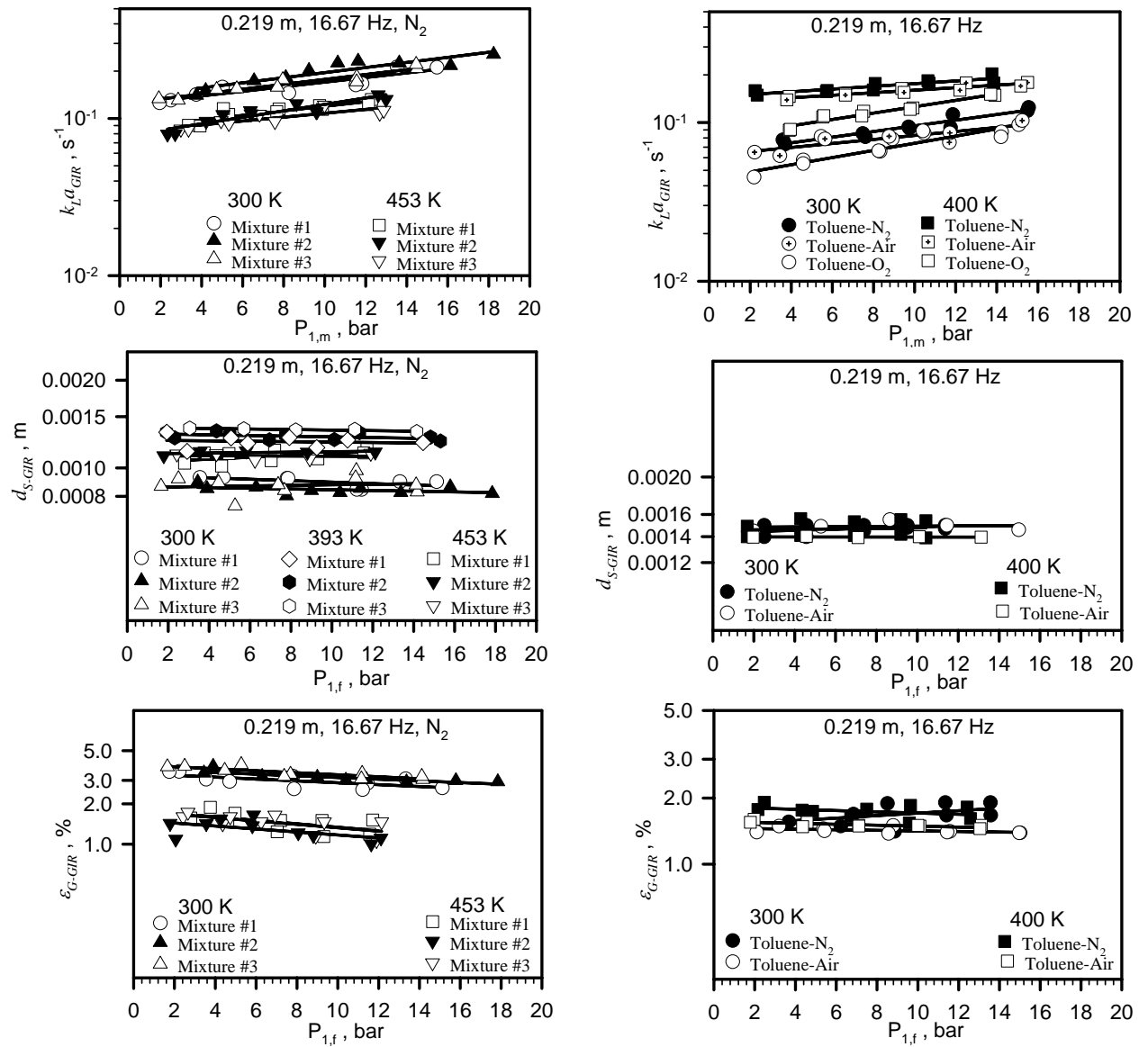


Figure 51: Effect of Liquid, Gas Nature and Pressure on k_La , d_S and ϵ_G in the GIR

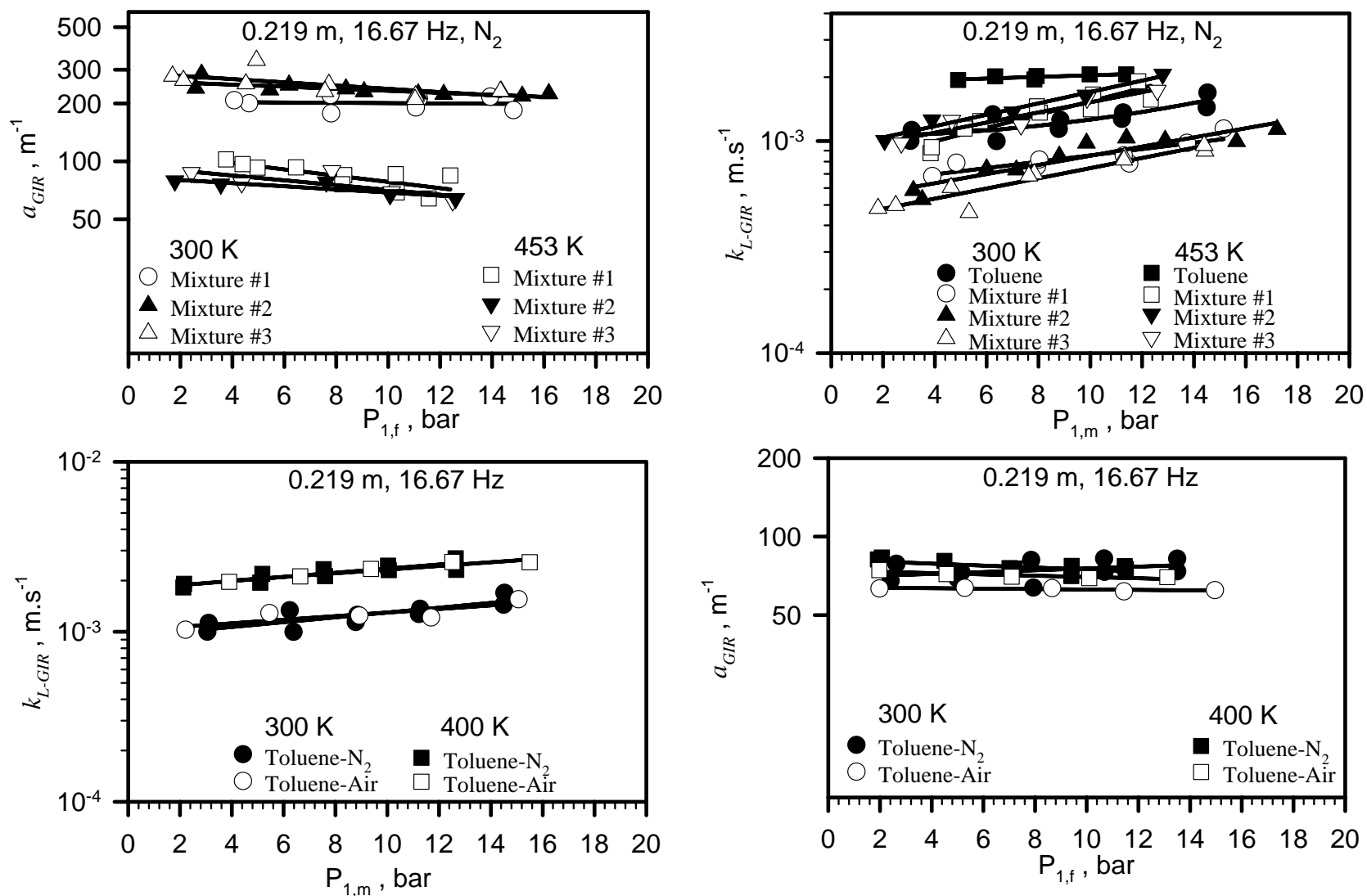


Figure 52: Effect of Liquid, Gas Nature and Pressure on a and k_L in the GIR

6.2.7 Effect of Froth, Liquid Nature on the Hydrodynamic and Mass Transfer Parameters

The effect of liquid nature on $k_L a$ values in the GIR and GSR is shown in Figures 45 and 51; and as can be deduced the addition of benzaldehyde and benzoic acid to toluene, aimed at mimicking the continuous LPTO process, strongly increases both $k_L a_{GIR}$ (60-70%) and $k_L a_{GSR}$ (100-120%) values at low T . At higher T , however, negligible effect and even a reduction of 15 % in $k_L a_{GIR}$ can be reported in the GIR, whereas in the GSR an enhancement (up to 30%) in $k_L a_{GSR}$ can be seen in Figures 45 and 51. The effect of benzaldehyde and benzoic acid concentration on $k_L a$ can be elucidated by the behaviors of both a and k_L .

The addition of benzaldehyde and benzoic acid to toluene decreased d_{S-GIR} values by up to 50 % at low T whereas at high T , a decrease of 0-10% occurs as shown in Figure 51. Figure 45 shows that d_{S-GSR} values decrease with the addition of benzaldehyde and benzoic acid to toluene by almost 50 % at low T and by 5-10% at high T . This behavior can be directly related to the presence of stable froth at low temperature because the addition of benzaldehyde and benzoic acid to toluene appears to strongly decrease the coalescence tendency of gas bubbles. As temperature increases the froth stability steadily decreases till it vanishes at high T (> 410 K). The reduction of the bubble size is also dependent on the degree of turbulences, i.e., U_G , N , and H , which affect the coalescence probability. Thus, depending on the degree of turbulence, larger or smaller differences between d_S values in pure toluene and those in its mixtures can be expected in both the GIR and GSR, as depicted in Figures 38, 43, 45, 49 and 51. The effect of additives concentrations within the range used, however, did not appear to influence d_{S-GIR} values as similar trends and values were observed in mixture # 1, 2 and 3 in the GIR.

The effect of liquid nature at low T (< 380 K) on ε_G values is illustrated in Figures 45 and 51, where an increase of up to 75 % and 110 % can be seen in the GIR and GSR, respectively. As temperature increases, the froth stability decreases resulting only in an enhancement of ε_G values, of 15% in the GIR and 30% in the GSR. At low T , the presence of froth had a tremendous impact on the gas holdup as smaller gas bubbles with larger re-circulation pattern were formed. At high temperature the froth tend to disappear resulting in a weaker effect on the gas holdup in both reactor types.

Furthermore, in Figure 48, it can be seen that N_{CRI} is higher in the mixtures than in toluene, which is explained by the higher liquid viscosity and density of the liquid mixtures ⁽¹¹⁴⁾.

Also, in Figures 42 and 48, the effect of liquid nature on Q_{GI} is presented, and as can be seen, the values are always higher in toluene than those in toluene mixtures. This is in good agreements with the findings by Aldrich and van Deventer ⁽¹⁰¹⁾, and can be attributed to the higher liquid density and viscosity of the mixtures (see Section 4.2) when compared with those of pure toluene under identical operating conditions.

Therefore, ε_{G-GIR} values in the mixtures were affected and controlled by both the froth and Q_{GI} , as the enhancement of ε_G values diminishes substantially with temperature. Thus, as the Sauter mean bubble diameter decreases with the presence of benzaldehyde and benzoic acid; and as the gas holdup increases in both the GIR and GSR, larger values of gas-liquid interfacial area, a were expected as shown in Figures 45 and 52.

In the same figures it can also be observed that larger values of k_{L-GIR} and k_{L-GSR} are obtained in toluene than in the liquid mixtures which can be attributed to the increase of liquid viscosity and decrease of diffusivity with the addition of benzaldehyde and benzoic acid to toluene, and to the presence of small gas bubbles size in the organic mixtures⁽²⁰⁸⁾. Thus, from the behavior of both a and k_L , it appears that a strong increase of $k_L a$ values was possible at low T and high mixing characteristics, i.e. high N and U_G or low H , in both the GIR and GSR due to the presence of froth created by the addition of benzaldehyde and benzoic acid to toluene. On the other hand, as temperature increases or the degree of mixing decreases, the froth stability decreases leading to almost negligible impact on $k_L a$ values. It is also important to mention that in the presence of froth, the gas-liquid interfacial area is controlling the behavior of the GIR and GSR, as the enhancement is strong enough to overcome the behavior displayed by k_L . Quantitatively, the effect of the addition of benzoic acid and benzaldehyde to toluene on d_s , ε_G and $k_L a$ is summarized in Tables 29 and 30. It is also important to mention that the LPTO process is usually carried out between 350 and 440K^(10, 13, 55), which corresponds exactly to the range where the froth was observed to disappear.

Table 29: Quantitative Effect of Benzaldehyde and Benzoic Acid Addition to Toluene on d_S , ε_G , and $k_L a$ in the GIR

T, K	N, Hz	P, bar	H, m	<i>Liquid</i>	d_{S-Tol}, m	$\varepsilon_{G-Tol}, \%$	$k_L a_{Tol}, s^{-1}$
300	16.7	10	0.219	Toluene	0.0016	2.15	0.113
400	16.7	10	0.219	Toluene	0.0012	1.69	0.162
300	13.3	10	0.219	Toluene	0.0014	1.25	0.019
300	20.0	10	0.219	Toluene	0.0019	3.38	0.233
300	16.7	1	0.219	Toluene	0.0016	2.18	0.089
300	16.7	10	0.219	Toluene	0.0016	2.15	0.113
350	16.7	10	0.171	Toluene	0.0018	3.14	0.276
350	16.7	10	0.268	Toluene	0.0015	1.25	0.051
T, K	N, Hz	P, bar	H, m	<i>Liquid</i>	$E(d_{S-Mixture}), \%$	$E(\varepsilon_{G-Mixture}), \%$	$E(k_L a_{Mixture}), \%$
300	16.7	10	0.219	Mixture #1	-43	60	54
				Mixture #2	-47	63	60
				Mixture #3	-46	58	67
400	16.7	10	0.219	Mixture #1	-1	14	-18
				Mixture #2	5	12	-25
				Mixture #3	3	1	-22
300	13.3	10	0.219	Mixture #1	-37	75	240
				Mixture #2	-28	74	259
				Mixture #3	-42	79	275
300	20.0	10	0.219	Mixture #1	-48	51	135
				Mixture #2	-63	40	121
				Mixture #3	-50	58	116
300	16.7	1	0.219	Mixture #1	-43	77	29
				Mixture #2	-47	89	42
				Mixture #3	-46	65	35
300	16.7	10	0.219	Mixture #1	-43	60	54
				Mixture #2	-47	63	60
				Mixture #3	-46	58	67
350	16.7	10	0.171	Mixture #1	-46	21	26
				Mixture #2	-41	14	26
				Mixture #3	-45	17	29
350	16.7	10	0.268	Mixture #1	-26	25	23
				Mixture #2	-21	28	26
				Mixture #3	-16	22	31

Table 30: Quantitative Effect of Benzaldehyde and Benzoic Acid Addition to Toluene on d_S , ε_G , and $k_L a$ in the GSR

T, K	N, Hz	P, bar	$U_G, m.s^{-1}$	<i>Liquid</i>	d_{S-Tol}, m	$\varepsilon_{G-Tol}, \%$	$k_L a_{Tol}, s^{-1}$
300	16.7	10	0.002	Toluene	0.0016	2.15	0.113
400	16.7	10	0.002	Toluene	0.0012	1.69	0.162
300	13.3	10	0.002	Toluene	0.0014	1.25	0.019
300	20.0	10	0.002	Toluene	0.0019	3.38	0.233
300	16.7	1	0.002	Toluene	0.0016	2.18	0.089
300	16.7	10	0.002	Toluene	0.0016	2.15	0.113
350	16.7	10	0.001	Toluene	0.0018	3.14	0.276
350	16.7	10	0.004	Toluene	0.0015	1.25	0.051
T, K	N, Hz	P, bar	$U_G, m.s^{-1}$	<i>Liquid</i>	$E(d_{S-Mixture}), \%$	$E(\varepsilon_{G-Mixture}), \%$	$E(k_L a_{Mixture}), \%$
300	16.7	10	0.002	Mixture #1	-33	107	112
400	16.7	10	0.002	Mixture #1	-15	30	29
300	13.3	10	0.002	Mixture #1	-36	106	116
300	20.0	10	0.002	Mixture #1	-30	89	107
300	16.7	1	0.002	Mixture #1	-32	76	85
300	16.7	10	0.002	Mixture #1	-33	107	112
350	16.7	10	0.001	Mixture #1	-19	95	98
350	16.7	10	0.004	Mixture #1	-33	31	72

6.2.8 Effect of Reactor Mode on the Hydrodynamic and Mass Transfer Parameters

Even though an identical 6-blades Rushton type impeller provided the mixing in the SAR, GIR and GSR, the performance of these agitated reactors were found to be different due to their distinct gas dispersion characteristics. Entraining, inducing or sparging the gas into the liquid-phase led to different hydrodynamic and mass transfer characteristics of the gas-liquid contactors studied. Using the mixing power input per unit liquid volume, a comparison among the three operating modes was made. In the SAR, the impeller power input (W/m^3) was calculated using the commonly accepted Equation (30) ^(23, 349):

$$\frac{P_{SAR}^*}{V_L} = N_p d_{imp}^5 \rho_L N^3 \quad (6-16)$$

In the GIR, the gassed power input per unit liquid volume was calculated using Equation (31) reported by Heim et al. ⁽¹⁰⁶⁾, which was developed in a GIR equipped with a six-pipe impeller and a hollow shaft:

$$\frac{P_{GIR}^*}{V_L} = \frac{P_{SAR}^*}{V_L} \left(1 - \exp \left(-0.591 - \frac{0.638}{\sqrt{Fr}} - 3.79 \times 10^{-8} Re \right) \right) \quad (6-17)$$

In the GSR, Equation (32) from Loiseau et al. ⁽¹²⁸⁾ was used:

$$\frac{P_{GSR}^*}{V_L} = \frac{C}{V_L} \left(\frac{P_{SAR}^* N d_{imp}^3}{Q_G^{0.56}} \right)^n = \frac{C}{V_L} M^n \quad (6-18)$$

With $C = 0.83$ and $n = 0.45$ for non-foaming system, and for foaming system $C = 0.65$, $n = 0.45$ if $M < 2.10^3$, and 1.88, 0.83, respectively if $M \geq 2.10^3$.

As can be seen in Figure 53, at the same power input per unit liquid volume, $k_L a$ values obtained in the GSR are greater than those in the GIR and SAR. The difference between $k_L a$ values in the GSR and GIR can be attributed to higher ε_G , and thus higher a values in the GSR, because of the relatively similar k_L and d_s data between the two reactor types, as depicted in Figure 53. In the SAR, however, not only ε_G and a , but also k_L and d_s were found to be smaller than those obtained in the GSR and GIR. Thus, the difference among the three reactor types indicates that the mass transfer behavior of the SAR is controlled by k_L , whereas those of the GIR and GSR are controlled by both a and k_L . It should, however, be mentioned that the effect of gas-liquid interfacial area on $k_L a$ becomes more important with increasing the power input per unit liquid volume and with the presence of froth as additional gas-liquid interfacial areas are created.

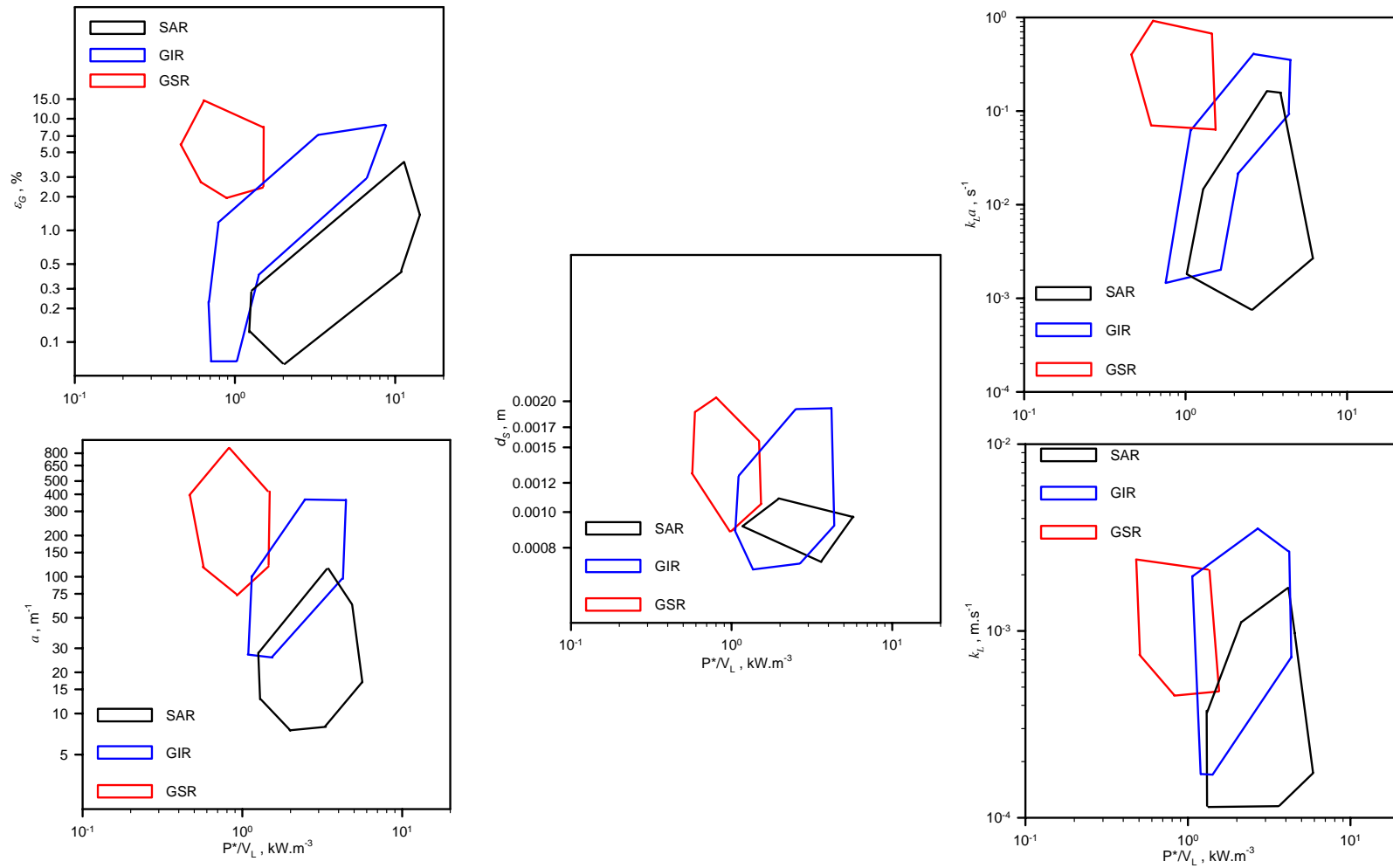


Figure 53: Comparison of the Hydrodynamic and Mass Transfer Parameters in the SAR, GIR and GSR

6.3 HYDRODYNAMIC AND MASS TRANSFER PARAMETERS IN THE BCR

6.3.1 Effect of Pressure on the Hydrodynamic and Mass Transfer Parameters

The effect of pressure on $k_L a$ values can be directly related to its effect on a and k_L . Inga and Morsi⁽³⁶⁸⁾ and Behkish et al.⁽²⁵⁴⁾ reported that $k_L a$ values in BCRs, operating in a fully developed churn-turbulent regime, were controlled by the gas-liquid interfacial area, a ^(369, 254). Figure 62 shows that $k_L a$ values increase with pressure, which is similar to the behavior exhibited by a . These data indicate that the gas-liquid interfacial area is controlling the behavior of the BCR because k_L values could increase, decrease or be independent of pressure as mentioned by numerous investigators^(208, 371, 498, 499).

Figure 54 shows that the Sauter mean bubble diameter, d_s decreases with increasing pressure for all gas-liquid systems studied, and Figure 55 indicates that at any given superficial gas velocity, increasing pressure gradually shifts the bubble size distribution toward smaller gas bubbles. These findings are in agreement with those by Inga⁽⁵⁶⁾, Letzel et al.⁽¹⁸⁴⁾, Lin et al.⁽²⁰⁷⁾ and Behkish et al.⁽²¹⁴⁾, who suggested that increasing pressure increases gas density and shrinks gas bubbles, which exhibit a more rigid shape.

At constant superficial gas velocity, U_G , Figure 57 shows that ε_G values in toluene and its mixtures are doubled when the pressure is increased by 0.6 MPa, indicating that ε_G is a strong function of gas density^(172, 176, 178). Similar findings were reported for various systems by a number of investigators^(56, 184, 172, 176, 180, 185, 188, 192, 195, 196, 214). Figures 57 and 58 illustrate that the increase of the total gas holdup with pressure can be related to the increase of ε_G of the small gas bubbles because their behavior with pressure are similar, i.e. ε_G of large gas bubble remains almost unchanged. Thus, increasing pressure leads to the formation of a large number of small rigid gas bubbles, contributing to the increase of the total ε_G . These results are in agreement with data previously reported by Inga⁽⁵⁶⁾, Krishna et al.⁽¹⁸⁸⁾ and Behkish et al.⁽²¹⁴⁾.

As previously described, d_s values decreased whereas ε_G values increased with pressure and subsequently the gas-liquid interfacial area, a is expected to increase with pressure by simply inspecting Equation (5-75). Figure 60 actually shows that the gas-liquid interfacial areas for air and N_2 increase with pressure at constant gas superficial velocity, U_G , which is in agreement with previous literature findings^(56, 142, 214, 254, 370).

At constant superficial gas velocity, increasing pressure slightly decreased d_s and k_L as depicted in Figures 54 and 63, respectively. These results are in agreement with previous findings by Calderbank and Moo-Young⁽²⁰⁸⁾, who reported for various systems and reactor types that k_L was dependent on the bubble size and by Marrucci⁽³⁷¹⁾, who reported that k_L was proportional to d_s to a power 1/2.

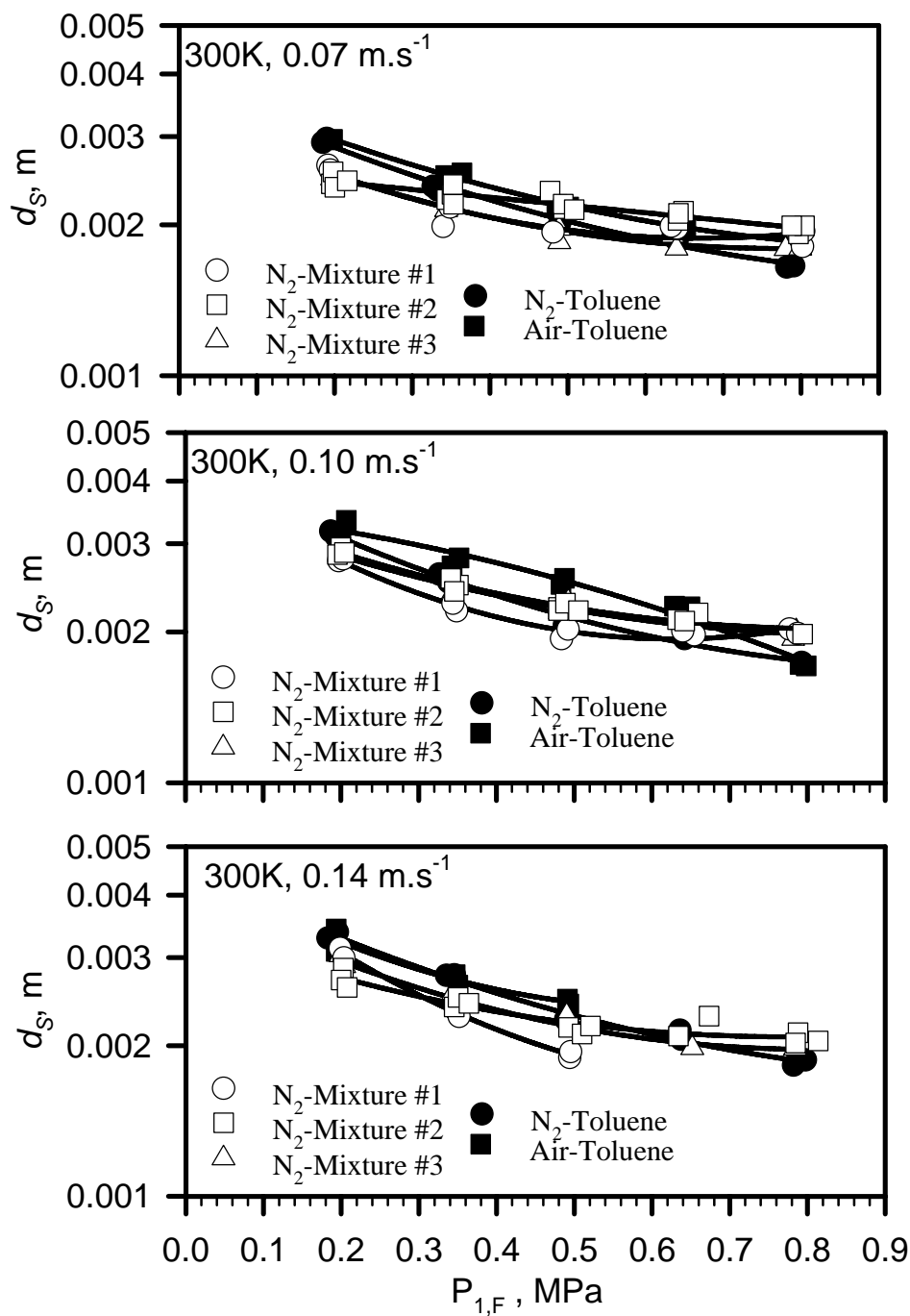


Figure 54: Effect of Pressure and Superficial Gas velocity on d_S of N_2 and Air in the Liquids Studied

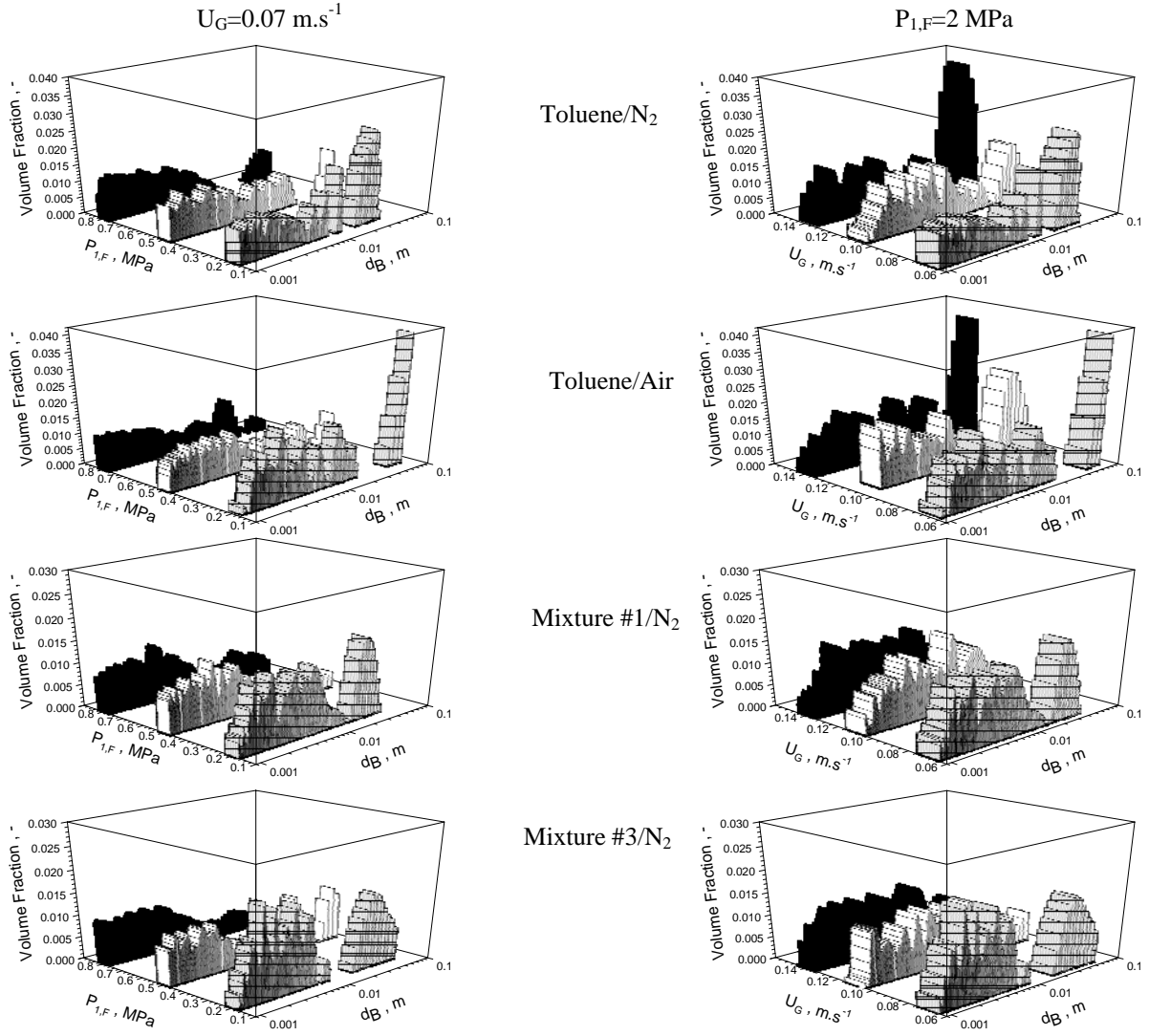


Figure 55: Effect of Pressure and Superficial Gas Velocity on the Bubble Size Distribution

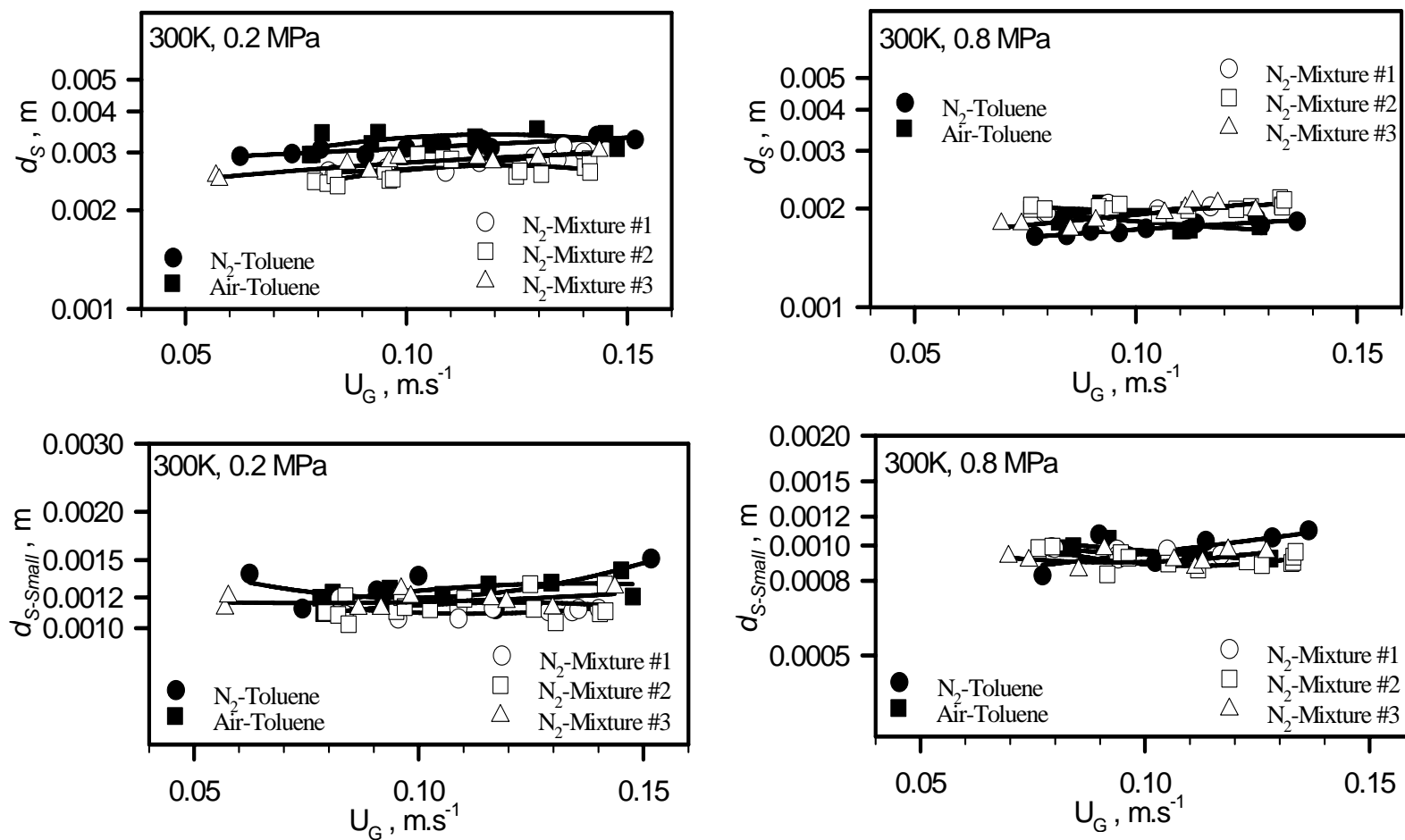


Figure 56: Effect of Pressure and Superficial Gas Velocity on d_s and $d_{s-small}$ of N_2 and Air in the Liquids Studied

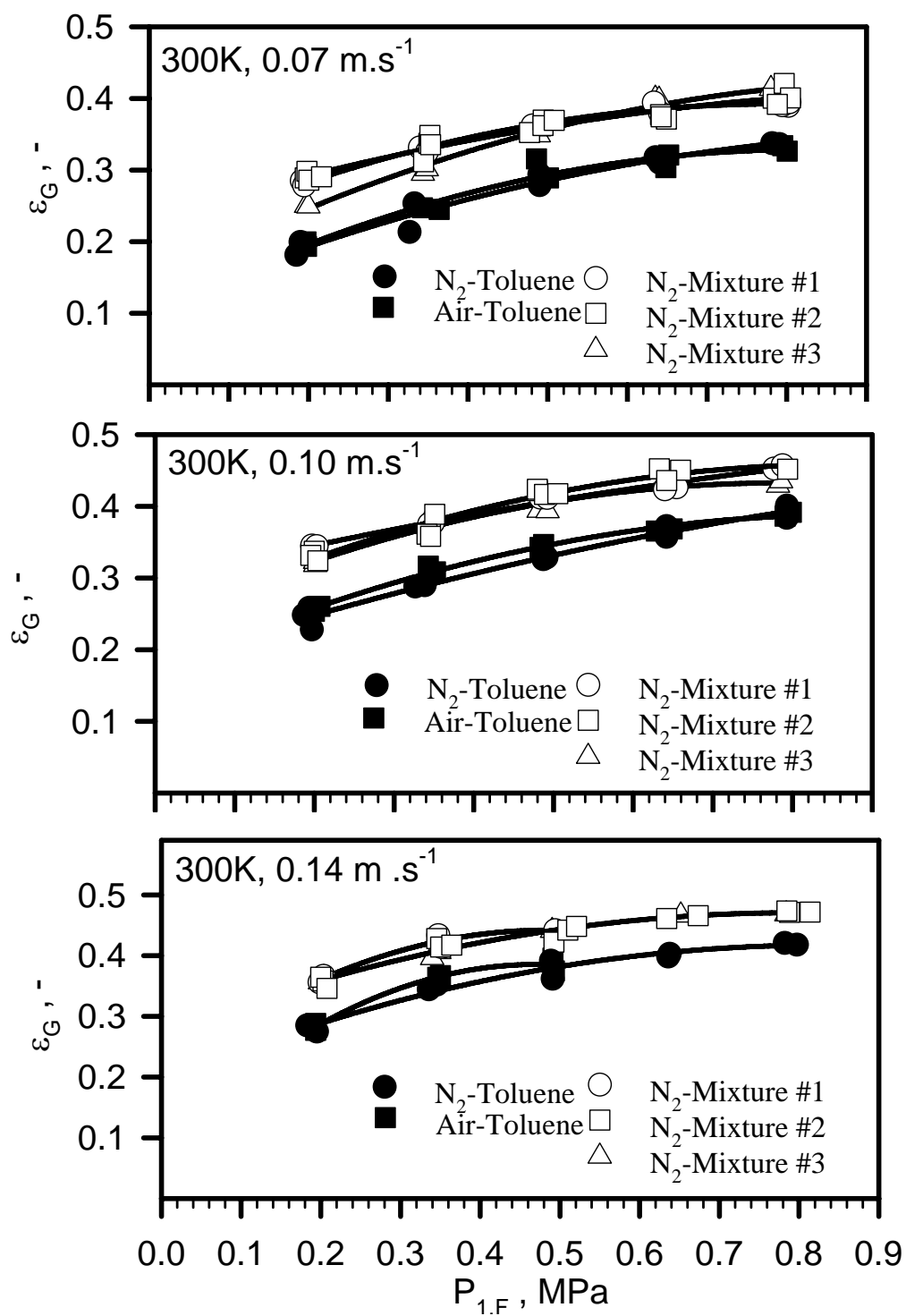


Figure 57: Effect of Pressure and Superficial Gas velocity on ε_G of N₂ and Air in the Liquids Studied

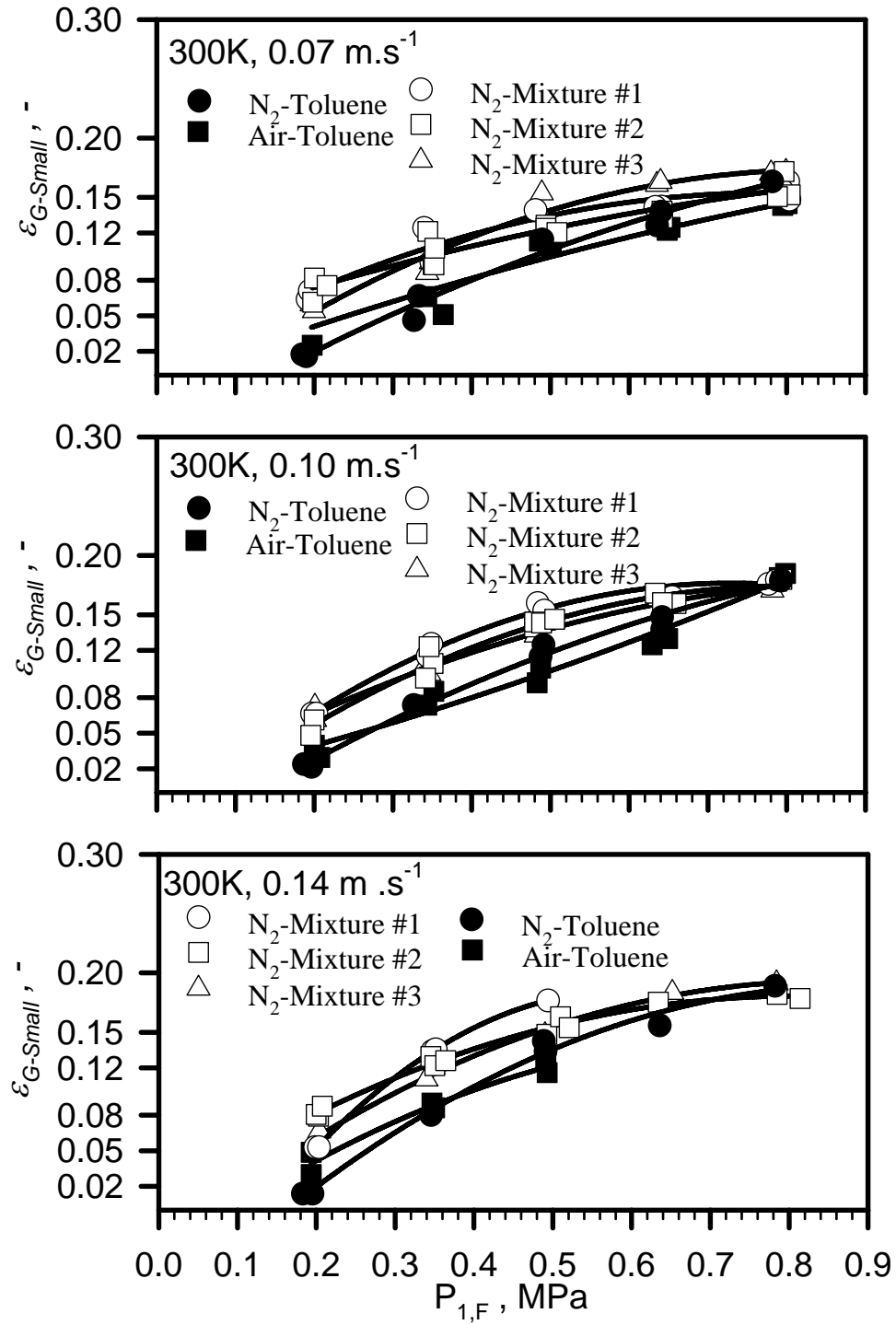


Figure 58: Effect of Pressure and Superficial Gas velocity on $\epsilon_{G-Small}$ of N_2 and Air in the Liquids Studied

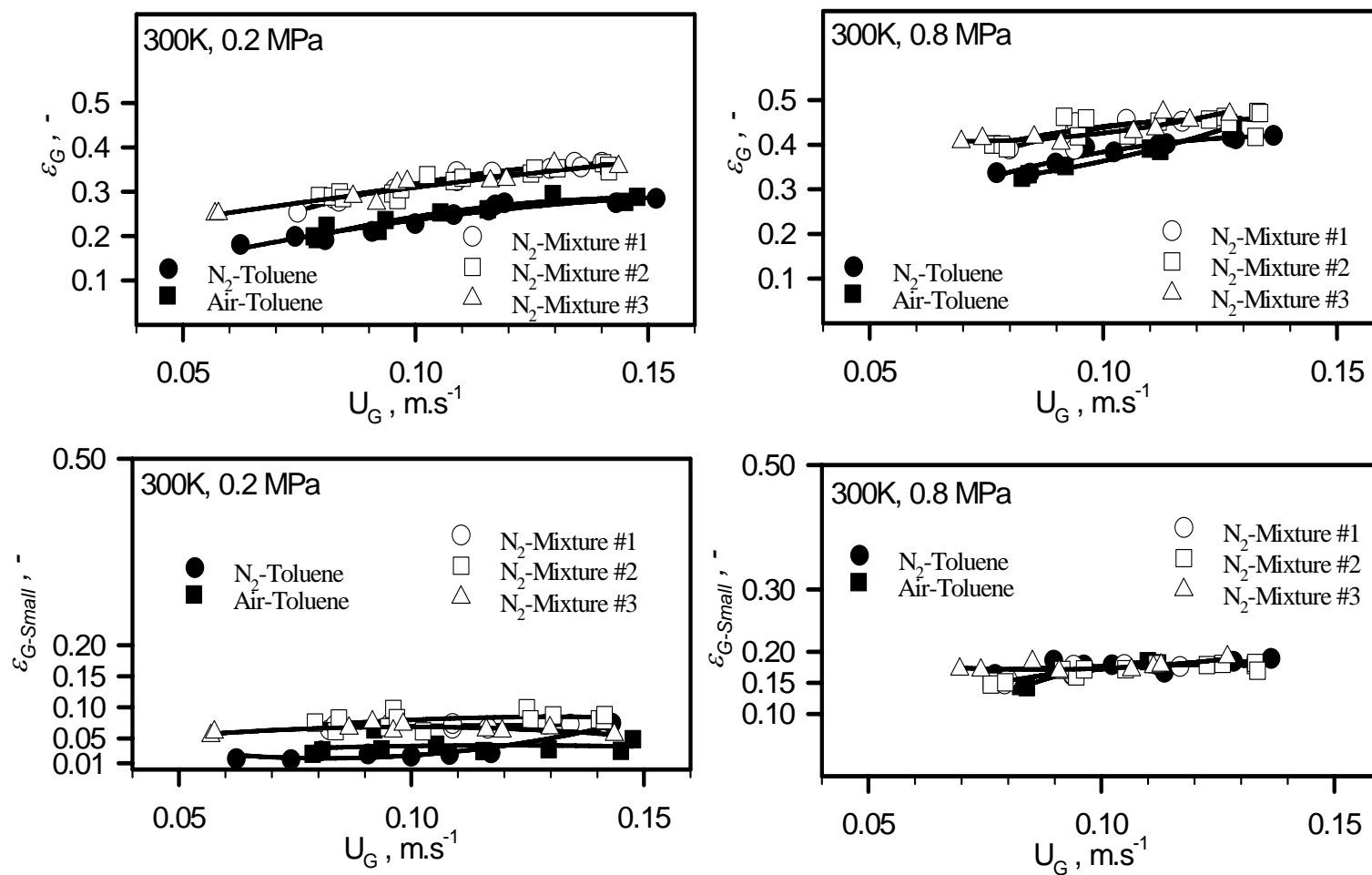


Figure 59: Effect of Pressure and Superficial Gas Velocity on ϵ_G and $\epsilon_{G-Small}$ of N_2 and Air in the Liquids Studied

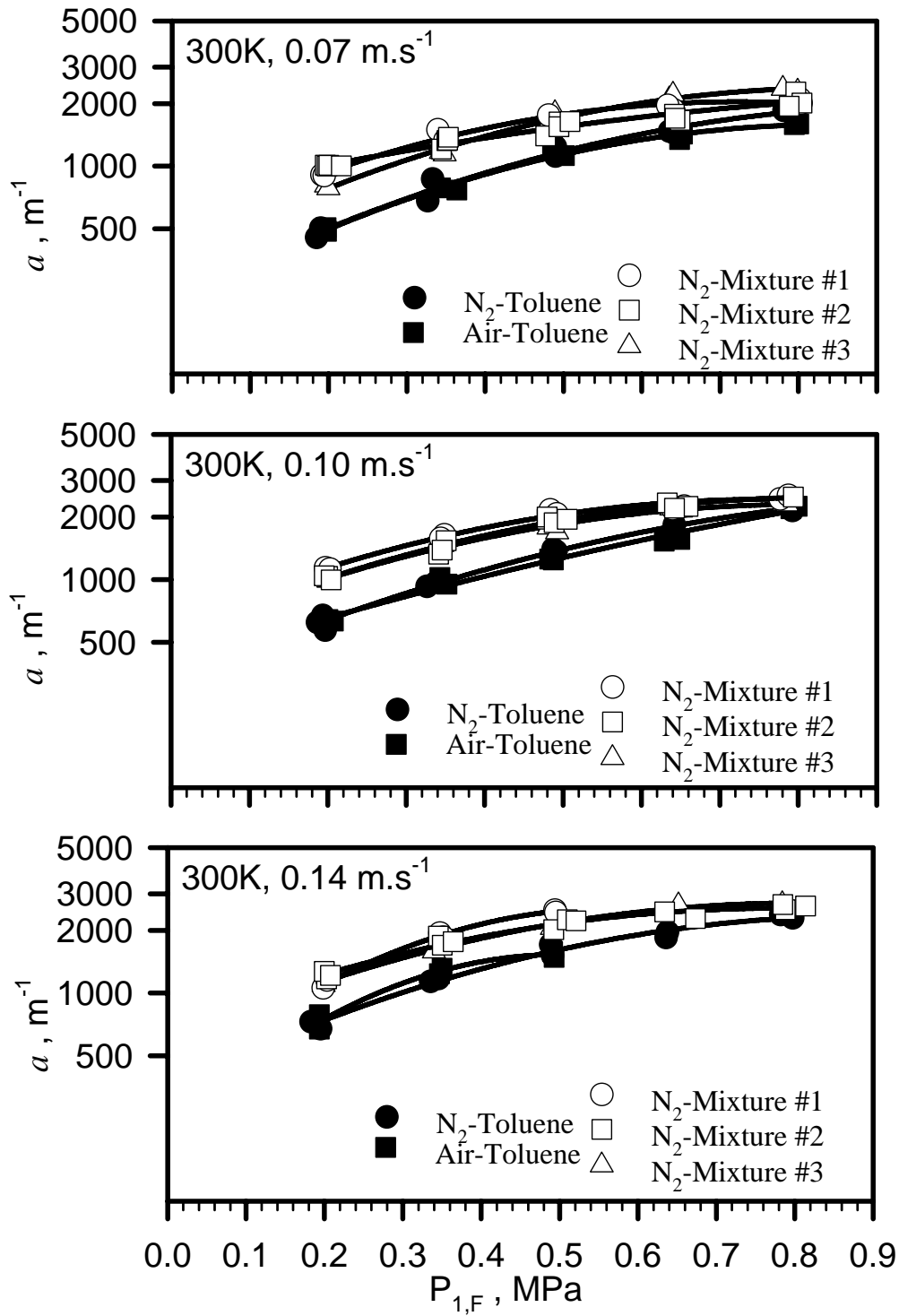


Figure 60: Effect of Pressure and Superficial Gas velocity on a of N_2 and Air in the Liquids Studied

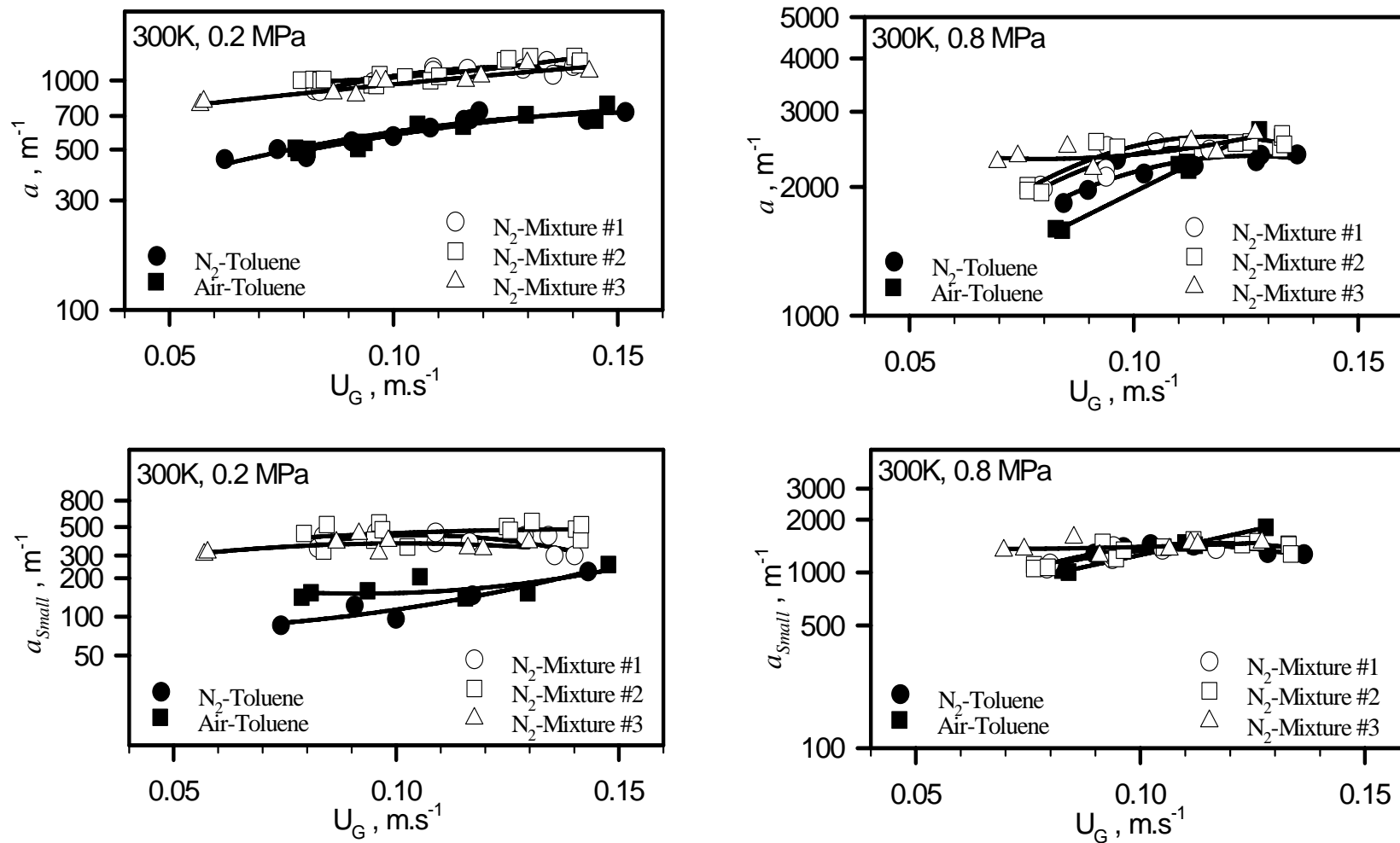


Figure 61: Effect of Pressure and Superficial Gas Velocity on a and a_{small} of N₂ and Air in the Liquids Studied

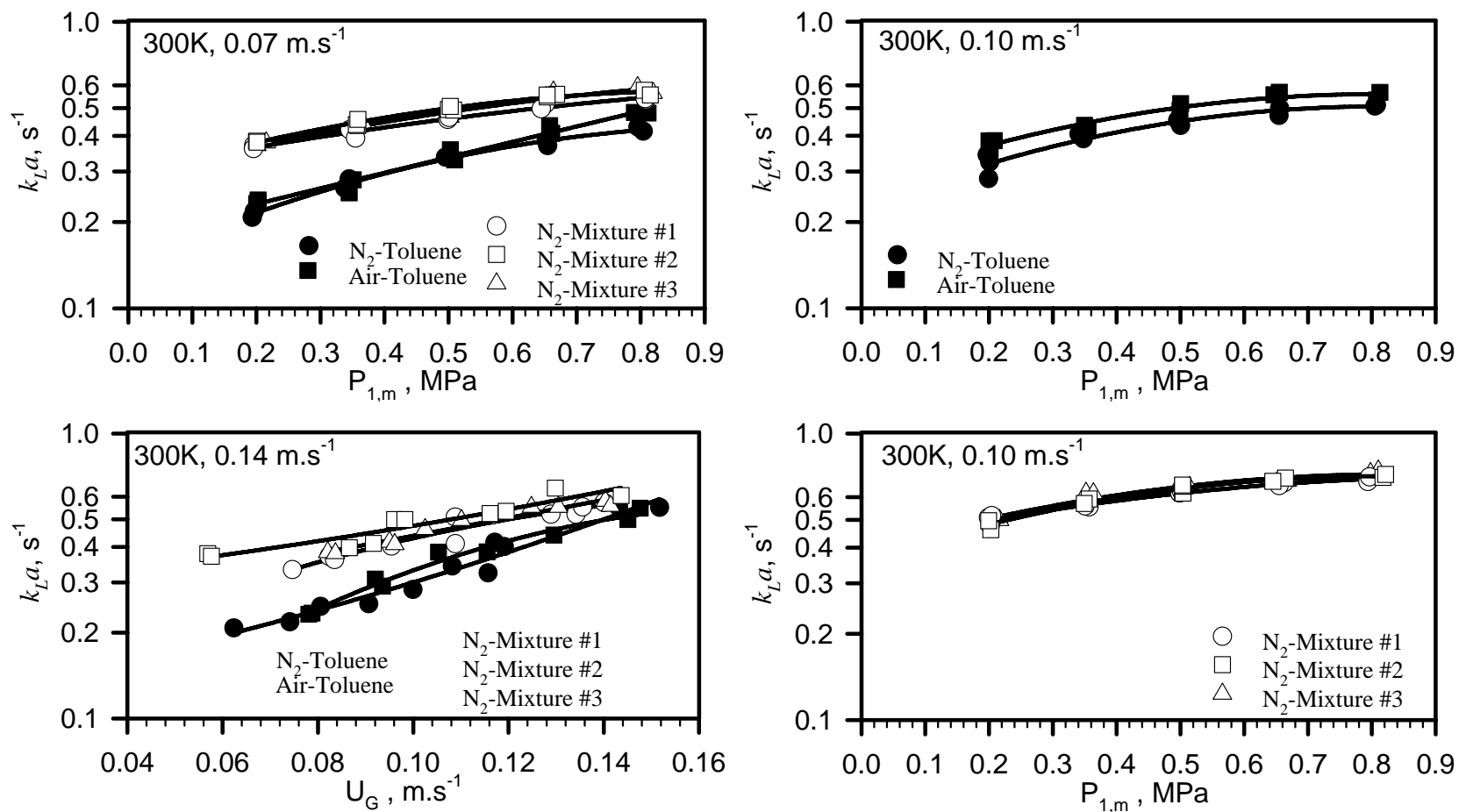


Figure 62: Effect of Pressure and Superficial Gas velocity on k_{La} of N_2 and Air in the Liquids Studied

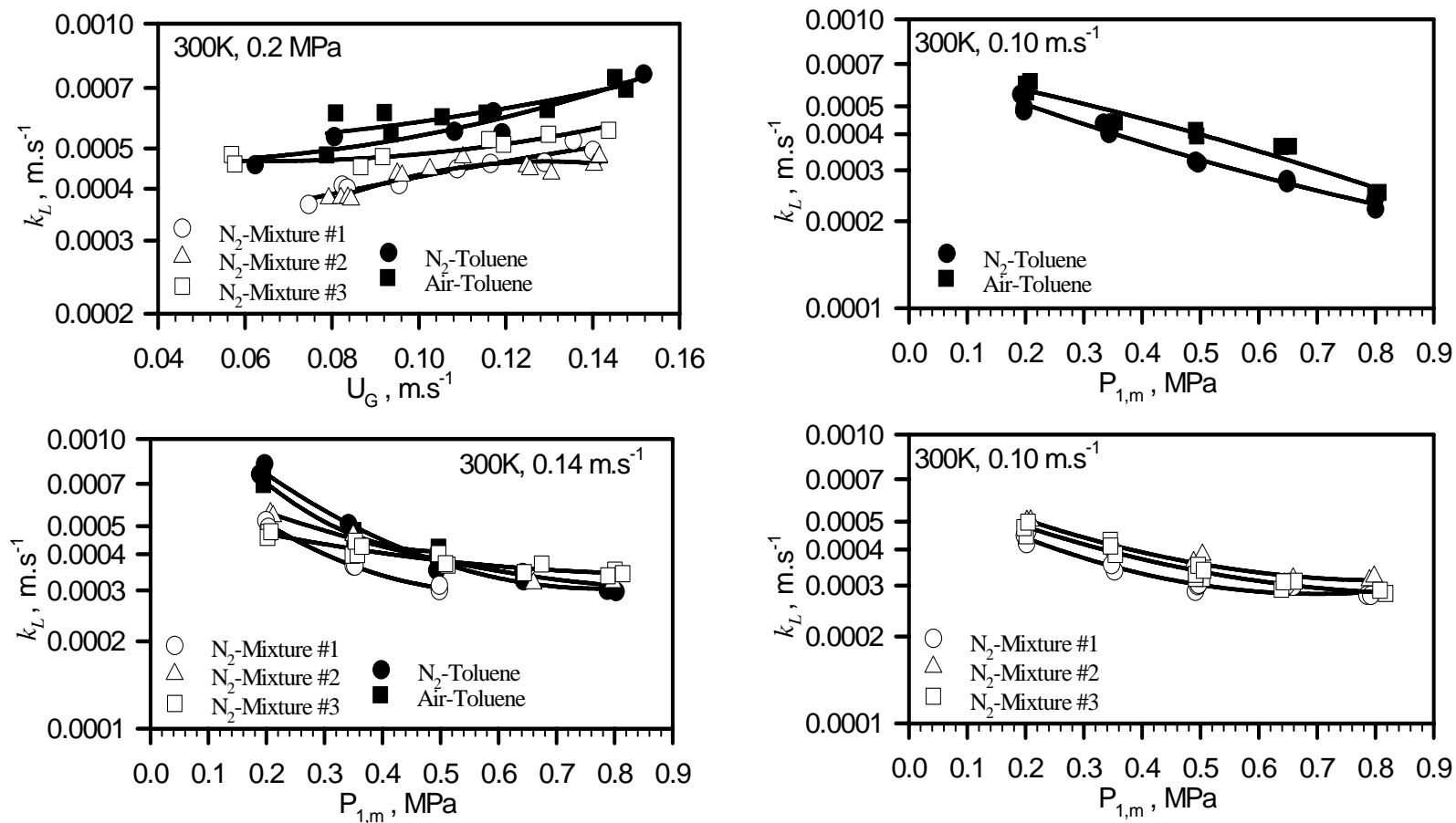


Figure 63: Effect of Pressure and Superficial Gas velocity on k_L of N₂ and Air in the Liquids Studied

6.3.2 Effect of Superficial Gas Velocity on the Hydrodynamic and Mass Transfer Parameters

Figure 62 shows that $k_L a$ values increase with the superficial gas velocity, U_G , which is in agreement with the findings by Ozturk et al. ⁽²⁴³⁾, Grund et al. ⁽¹⁷⁵⁾, Inga ⁽⁵⁶⁾, Jordan and Schumpe ⁽¹⁹⁰⁾, Jordan et al. ⁽¹⁹¹⁾ and Behkish et al. ⁽²⁵⁴⁾. This behavior can be explained by the effect of increasing gas velocity on the gas-liquid interfacial area, a , and the liquid-side mass transfer coefficient, k_L . Since the gas-liquid interfacial area, a was found to increase with U_G , and k_L values are also expected to increase with U_G due to the increase of turbulences and the decrease of the film thickness ^(309, 322, 504, 506).

Figure 55 depicts the effect of the superficial gas velocity, U_G on the bubble size distribution at constant pressure; and as can be observed, the volume fraction of large bubbles increases with increasing U_G , while the volume fraction of small bubbles remains almost constant. This trend is also confirmed by Figure 56, where d_s values of the small bubbles appear to remain constant with increasing superficial gas velocity, while the overall d_s values increases. This increase, attributed to the increase of the large bubbles population, can be related to a higher probability of bubble collisions, which leads to more bubble coalescence as previously reported by Inga ⁽⁵⁶⁾, Letzel et al. ⁽¹⁸⁴⁾, Lin et al. ⁽²⁰⁷⁾ and Behkish et al. ⁽²¹⁴⁾.

At constant pressure, Figure 59 shows that ε_G values increase with U_G and this increase is strongly due to the increase of ε_G of the large gas bubbles, since that corresponding to small bubbles appears to be almost independent of U_G . These data are in accordance with those shown in Figure 55, since the volume fraction of the large gas bubbles appears to significantly increase with U_G at constant P , whereas that of small bubbles remains almost constant. Similar results for different systems were reported in the literature ^(56, 175, 188, 190, 214).

At constant pressure, increasing the superficial gas velocity, U_G , increased both ε_G and d_s values, which means that the resulting effect on the gas-liquid interfacial area, a would not be obvious. Figure 61, however, shows that at constant pressure, the gas-liquid interfacial areas increase with U_G , which is in agreement with available literature ^(56, 142, 214, 254, 372). These results clearly indicate that ε_G controls the behavior of a , even though the Sauter mean bubble diameter, d_s appeared to slightly increase with increasing U_G under the operating conditions used. Figure 61 also shows that the increase of the gas-liquid interfacial area can be related to the presence of small gas bubbles which is in agreement with earlier findings ^(56, 188, 214, 254).

At constant pressure, Figure 63 illustrates that k_L values increase with superficial gas velocity, U_G , which could be related to the increase of d_s and $\varepsilon_{G-Large}$. Increasing the superficial gas velocity increases d_s and is supposed to increase k_L according to their direct proportionality as reported by Calderbank and Moo-Young ⁽²⁰⁸⁾ and Marrucci ⁽³⁷¹⁾. Also, increasing the superficial gas velocity increases the holdup of large gas bubbles, which enhances the liquid back-mixing and turbulence and consequently k_L .

6.3.3 Effect of Gas Nature on the Hydrodynamic and Mass Transfer Parameters

The effect of gas nature on $k_L a$ was negligible as its effect on the gas holdup, Sauter mean bubble diameter and gas-liquid interfacial area.

Figure 54 also shows the effect of gas nature (nitrogen vs. air) on d_s , and as can be seen the values seem to be independent of the gas nature, which was expected due to the relatively close molecular weights of N_2 and air.

Figure 57 indicates that the effect of gas nature on ε_G values in toluene and mixtures is negligible. Reilly et al. (1994), Inga (1997) and Jordan and Schumpe (2001) reported that the gas holdup in BCRs is a strong function of the gas momentum. Thus, the observed behavior was expected, since under the same pressure (density) and gas velocity, the difference between air and nitrogen momentums is negligible due to the closeness of their molecular weights.

Figure 60 indicates a negligible effect of gas nature (nitrogen vs. air) on the gas liquid interfacial area, which was expected since the gas holdup and the Sauter mean bubble diameter were not affected by the gas nature due to the negligible difference between the molecular weights of the two gases.

Figure 63 also shows that k_L values obtained for air were slightly higher when compared with those for nitrogen under similar operating conditions. This can be attributed to the fact that air has slightly higher diffusivity than N_2 under these conditions.

6.3.4 Effect of Liquid Nature on the Hydrodynamic and Mass Transfer Parameters

The presence of benzaldehyde and benzoic acid in toluene, however, appears to strongly affect $k_L a$ values as shown in Figure 62. Quantitatively, $k_L a$ data for nitrogen in toluene mixtures were found to increase by 50-70 % at low pressure (0.2 MPa) for $U_G = 0.06$ m/s and by 40-60 % at high pressure (0.5 MPa) for $U_G = 0.10$ m/s when compared with those obtained in pure toluene. This behavior can be attributed to the fact that the presence of benzaldehyde and benzoic acid in toluene led to the formation of froth, particularly under low pressure, which increased the gas-liquid interfacial area and subsequently $k_L a$.

The effect of benzaldehyde and benzoic acid presence, on the other hand, appeared to slightly decrease d_s values for nitrogen by approximately 10 % when compared with the data obtained in toluene at low pressure (0.2 MPa); and no effect was estimated at higher pressure (0.5 MPa) as can be seen in Figure 54. This behavior can be attributed to the observed frothing when using toluene mixtures under, particularly, low pressures. Actually, the presence of froth with toluene containing benzaldehyde and benzoic acid was observed in our laboratory using a 4-liter see-through agitated reactor. The decrease of liquid nature impact at high pressures indicates that pressure has a greater effect on the size of gas bubbles in toluene as a coalescing system (characterized by the formation of large gas bubbles) when compared with that in toluene mixtures as a non-coalescing system (characterized by the presence of froth) where the bubbles are already small.

The effect of benzaldehyde and benzoic acid presence in toluene, on the other hand, appears to strongly affect the total gas holdup. Quantitatively, the gas holdup data for nitrogen in toluene mixtures were found to increase by

30-35 % at low pressure (0.2 MPa) and by 25-30 % at high pressure (0.5 MPa) when compared with those obtained in pure toluene. This behavior can be attributed to the fact that toluene is a coalescing system and the presence of benzaldehyde and benzoic acid in toluene resulted in a non-coalescing system. It should be mentioned that in Figures 58 and 59, as the pressure increases, the gas holdup of small gas bubbles becomes almost the same for toluene and its mixtures. This means that increasing pressure decreases the froth stability of the toluene mixtures and under these conditions the holdup of small gas bubbles becomes similar for toluene and its mixtures.

The effect of benzaldehyde and benzoic acid presence in toluene, on the other hand, appears to strongly affect the gas-liquid interfacial area as can be seen in Figure 60. This significant increase of the gas-liquid interfacial area can be attributed to the presence of froth when using toluene-benzaldehyde-benzoic acid mixtures. It also should be mentioned that in Figure 60 as the pressure increases, its effect on the gas-liquid interfacial area diminishes, which can be attributed to the decrease of the froth stability exhibited with toluene mixtures under high pressures.

Figure 63 also demonstrates that k_L values for N_2 are higher in toluene than in the three toluene mixtures particularly at low pressures. This can be related to the increase of liquid viscosity (see Section 4.2), which resulted in a decrease of the diffusivity and consequently k_L upon the addition of benzaldehyde and benzoic acid to toluene. Also, the decrease of froth stability with increasing pressure can explain the negligible effect of addition of benzaldehyde and benzoic acid to toluene on d_s and consequently k_L since k_L and d_s are directly related^(208, 371).

Thus, the effect of benzaldehyde and benzoic acid addition to toluene on d_s , ε_G , and $k_L a$ for nitrogen can be summarized in Table 31.

Table 31: Quantitative Effect of Benzaldehyde and Benzoic Acid Addition to Toluene on d_s , ε_G , and $k_L a$ in the BCR

U_G , m/s	P , MPa	Liquid	d_{S-Tol} , m	ε_{G-Tol} , %	$k_L a_{Tol}$, s ⁻¹
0.06	0.2	Toluene	0.00292	0.19	0.22
	0.5	Toluene	0.00203	0.26	0.28
0.10	0.2	Toluene	0.00306	0.24	0.32
	0.5	Toluene	0.00214	0.32	0.41
U_G , m/s	P , MPa	Liquid	$E(d_{S-Mixture})$, %	$(\varepsilon_{G-Mixture})$, %	$(k_L a_{Mixture})$, %
0.06	0.2	Mixture #1	-9	33	67
		Mixture #2	-10	34	70
		Mixture #3	-11	36	74
	0.5	Mixture #1	≈ 0	31	57
		Mixture #2	≈ 0	32	60
		Mixture #3	≈ 0	33	62
0.10	0.2	Mixture #1	-8	28	49
		Mixture #2	-9	29	51
		Mixture #3	-10	30	53
	0.5	Mixture #1	≈ 0	23	42
		Mixture #2	≈ 0	24	44
		Mixture #3	≈ 0	25	46

6.4 CORRELATIONS AND CALCULATION ALGORITHM IN THE AGITATED REACTORS

While understanding the effect of process variables on the hydrodynamic and mass transfer parameters of a gas-liquid contactor is essential for scale-up purposes⁽³⁷³⁾, it is as critical to be able to calculate these parameters for a given geometry. In the following, a comparison between the data obtained in this study and those reported in the literature is first presented. Then, as obvious differences are found due to limitations in literature correlations, novel hydrodynamic and mass transfer correlations are developed. Three types of correlations were derived: Empirical, Statistical and Back-Propagation Neural Network correlations, and were used to predict a large data bank (7374 data points) of experimental data obtained in this study and in the literature. Finally, calculation algorithms based on the empirical and BPNN correlations developed in this study were introduced in order to determine all the hydrodynamic and mass transfer parameters for the liquid-phase toluene oxidation process in agitated and bubble column reactors.

6.4.1 Empirical Correlations of the Hydrodynamic and Mass transfer Parameters in the Agitated Reactors

A total of 7374 experimental points, shown in Table 32, obtained in our laboratories as well as from the literature on hydrodynamic and mass transfer parameters were used to develop empirical correlations for predicting the critical mixing speed for entrainment, N_{CRE} , in the SAR and induction, N_{CRI} , in the GIR, the induced gas flow rate, Q_{GI} , and the wavy surface, a_{Wave} , the gas holdup, ε_G , the Sauter mean bubble diameter, d_S and the volumetric mass transfer coefficient, $k_L a$ in SARs, GIRs, and GSRs. Table 33 lists the ranges of operating variables, physical properties and reactor geometry used in these correlations. As can be seen in these tables, these ranges were wide enough to cover various industrial processes. It should also be pointed out that large reactor sizes (up to 3.6-m) were included in the data bank, which validates the scale-up capability of such correlations.

In the SAR, N_{CRE} values can be predicted using Equation (6-19):

$$\frac{N_{CRE}^2 d_{Imp.}}{g} = 0.441 \times \left(\frac{\mu_L}{\mu_{Water}} \right)^{0.100} \left(\frac{\sigma_L}{\sigma_{Water}} \right)^{-0.430} \left(\frac{\rho_L}{\rho_{Water}} \right)^{2.960} \left(\frac{H_L}{d_T} \right)^{-0.100} e^{0.378 \frac{H_L}{d_{Imp.}}} \quad (6-19)$$

In the GIR, Equation (6-20) can be used to predict N_{CRI} with a regression coefficient of 96%, as can be seen in Figure 64.

$$\frac{N_{CRI}^2 d_{Imp.}}{g} = 0.512 \times \left(\frac{\mu_L}{\mu_{Water}} \right)^{0.146} \left(\frac{\sigma_L}{\sigma_{Water}} \right)^{-0.180} \left(\frac{\rho_L}{\rho_{Water}} \right)^{-0.265} \left(\frac{H_L}{d_T} \right) \quad (6-20)$$

In the GIR, Q_{GI} values can be predicted using Equation (6-21), with a regression coefficient of 70% as depicted in Figure 64.

$$Ae = \frac{Q_{GI}}{Nd_{Imp.}^3} = 50.03 \times \frac{n_{Imp.}^{1.695} d_T^{2.584} \mu_L^{0.627} \rho_L^{1.991} \rho_G^{2.847}}{\sigma_L^{4.440} M_{W_{Gas}}^{3.203}} \exp \left(-3.957 \times \frac{Eu^{0.142} We^{0.174}}{Re^{0.048} (Fr - Fr_C)^{0.042}} \right) \quad (6-21)$$

A regression coefficient of 92% was obtained as seen in Figure 65 to predict a_{wave} using Equation (6-22):

$$a_{Wave} = \frac{1}{H} + \frac{1}{H_L} \times \frac{Re^{1.75} We^{3.00}}{Eu^{3.00}} \left(\frac{\rho_L}{\rho_G} \right)^{-2.67} e^{-12.95 \times H - 0.59 \times N} \quad (6-22)$$

For predicting the gas holdup in the SARs:

$$\varepsilon_{G-SAR} = 16.3 \times \left(\frac{P_{SAR}^*}{V_L} \right)^{\alpha_{SAR}} (Fr - Fr_C)^{\beta_{SAR}} \quad (6-23)$$

$$\alpha_{SAR} = -0.573 \times d_T^{-0.142} N^{-0.400} \mu_L^{-0.137} \rho_G^{0.101} \quad (6-24)$$

$$\beta_{SAR} = 1.36 \times 10^{-5} \times d_{Imp.}^{0.001} H_L^{-0.001} N^{0.130} \rho_L^{1.920} \mu_L^{0.932} \sigma_L^{-1.360} \quad (6-25)$$

For predicting the gas holdup in the GIRs:

$$\varepsilon_{GIR} = 0.102 \times \left(\frac{P_{GIR}^*}{V_L} \right)^{\alpha_{GIR}} U_G^{\beta_{GIR}} \times \exp(-0.349 X_W) \quad (6-26)$$

$$\alpha_{GIR} = 3.770 \times 10^{-5} \times d_T^{-2.540} N^{0.005} \mu_L^{-0.012} \sigma_L^{-0.603} \rho_G^{-0.122} \quad (6-27)$$

$$\beta_{GIR} = 0.087 \times d_{Imp.}^{-0.819} H_L^{0.617} N^{-0.854} \rho_L^{-0.036} \mu_L^{-0.043} \sigma_L^{-0.560} \quad (6-28)$$

For predicting the gas holdup in the GSRs:

$$\varepsilon_{G-GSR} = 9.620 \times 10^{-3} \times \left(\frac{P_{GSR}^*}{V_L} \right)^{\alpha_{GSR}} U_G^{\beta_{GSR}} \times \exp(-0.216 X_W) \quad (6-29)$$

$$\alpha_{GSR} = 0.190 \times d_T^{-0.179} N^{0.043} \mu_L^{-0.228} \sigma_L^{0.261} \rho_G^{-0.011} \quad (6-30)$$

$$\beta_{GSR} = 1.86 \times 10^{12} \times d_{Imp.}^{-0.087} H_L^{-0.279} N^{0.063} \rho_L^{-4.270} \mu_L^{-0.464} \sigma_L^{1.380} \quad (6-31)$$

It should be mentioned that the quantity (P^*/V_L) is the total energy dissipated which corresponds to the sum of the power input (impeller and gas sparged) per unit liquid volume⁽³⁷⁴⁾. Several correlations to predict the impeller and gas power input per unit liquid volume for SARs⁽²³⁾, GIRs^(92, 106, 102, 375, 376) and GSRs^(126, 128, 132, 134, 377, 378) can be found:

The power input per unit volume in SARs was calculated as follows:

$$\frac{P_{SAR}^*}{V_L} = \frac{N_P \times d_{Imp.}^5 \times \rho_L \times N^3}{V_L} \quad (6-32)$$

N_p , the power number, is function of the impeller type and geometry as well as the Reynolds number⁽²³⁾

The gassed power input per unit liquid volume in GIRs equipped with a hollow shaft was calculated from Heim et al.⁽¹⁰⁶⁾:

$$\frac{P_{GIR}^*}{V_L} = \frac{P_{SAR}^*}{V_L} \times \left(1 - \exp \left(A + \frac{a_1}{\sqrt{Fr}} + a_2 Re \right) \right) \quad (6-33)$$

A , a_1 and a_2 are constants which are function of the impeller design.

For GIRs equipped with a draft tube, the expression developed by Saravanan et al.⁽³⁷⁶⁾ was used:

$$\frac{P_{GIR}^*}{V_L} = \frac{\rho_L W N^3 \left(\frac{d_{Imp.}}{2} \right)^4}{V_L} \left(C_{DO}^* - C_{DY}^* \left(1 - \frac{I}{\Phi F_s} \right)^3 \right) + \frac{\tau_{rg} 2\pi N}{V_L} \quad (6-34)$$

W is the impeller width, C_{DO}^* and C_{DY}^* are the impeller drag coefficients in the gas-liquid dispersion conveying and central zone, respectively, Φ is the vortexing constant, F_s is the Froude number based on submergence, and τ_{rg} is the torque representing the effect of recycled fluid on the power input.

In GSRs, the power input per unit volume was calculated from Loiseau et al. ⁽¹²⁸⁾:

$$\frac{P_{GSR}^*}{V_L} = \frac{A}{V_L} \times \left(\frac{P_{SAR}^* N d_{imp}^3}{Q_G^{0.56}} \right)^B + U_G \rho_L g \quad (6-35)$$

A and B are constants.

Also, the power of the sparged gas from the compressor was calculated according to Sridhar and Potter ⁽¹³²⁾ as:

$$U_G \rho_L g \quad (6-36)$$

It is also important to point out that in GIRs and GSRs, X_w was introduced in Equations (6-26) and (6-52) in order to account for the liquid composition and its foamability ⁽²¹⁴⁾. X_w represents the concentration of the primary liquid in the mixture, and its value lies between 0.50 and 1. Consequently, for a single-component and for a complex organic liquid mixture composed of more than three hydrocarbons, such as oils and waxes, X_w equals 1.

For predicting the Sauter mean bubble diameter in SARs:

$$d_{S-SAR} = 1.31 \cdot 10^{-3} \times (Fr - Fr_c)^{\gamma_{SAR}} \epsilon_{G-SAR}^{\lambda_{SAR}} \quad (6-37)$$

$$\gamma_{SAR} = -5.81 \cdot 10^{-6} \times d_{Imp.}^{-1.310} d_T^{1.550} N^{1.300} \mu_L^{-0.588} \quad (6-38)$$

$$\lambda_{SAR} = 0.207 \times \rho_L^{-0.408} \sigma_L^{-0.171} \rho_G^{-0.141} H_L^{-0.657} \quad (6-39)$$

For predicting the Sauter mean bubble diameter in GIRs:

$$d_{S-GIR} = 2.61 \cdot 10^{-3} \times U_G^{\gamma_{GIR}} \epsilon_{G-GIR}^{\lambda_{GIR}} \quad (6-40)$$

$$\gamma_{GIR} = 3.980 \cdot 10^{-2} \times d_{Imp.}^{1.500} d_T^{-2.020} N^{0.419} \mu_L^{0.102} \quad (6-41)$$

$$\lambda_{GIR} = 3.310 \cdot 10^{-2} \times \rho_L^{0.373} \sigma_L^{-0.044} \rho_G^{-0.093} H_L^{0.070} \exp(-1.180 X_w) \quad (6-42)$$

For predicting the Sauter mean bubble diameter in GSRs:

$$d_{S-GSR} = 9.380 \cdot 10^{-3} \times U_G^{\gamma_{GSR}} \epsilon_{G-GSR}^{\lambda_{GSR}} \quad (6-43)$$

$$\gamma_{GSR} = 1.380 \cdot 10^{-2} \times d_{Imp.}^{-0.878} d_T^{0.351} N^{0.563} H_L^{0.185} \quad (6-44)$$

$$\lambda_{GSR} = 1.300 \cdot 10^{-20} \times \rho_L^{7.490} \sigma_L^{-0.240} \rho_G^{-0.196} \exp(-8.470 X_w) \quad (6-45)$$

Also, for predicting the volumetric mass transfer coefficient in SARs:

$$k_L a_{SAR} = 69.961 \times \frac{D_{AB}^{0.500}}{\rho_G^{0.060}} \left(\frac{P_{SAR}^*}{V_L} \right)^{\delta_{SAR}} \left(2.678 \cdot 10^{-2} + \frac{(2.085 \cdot 10^{-3} + d_s)^{0.155} \epsilon_G^{0.234}}{(Fr - Fr_c)^{-\eta_{SAR}}} \right) \quad (6-46)$$

$$\delta_{SAR} = 0.925 \times d_{Imp.}^{1.156} N^{0.348} H_L^{-0.830} \quad (6-47)$$

$$\eta_{SAR} = 0.010 \times d_T^{-2.820} N^{3.570} \mu_L^{-0.679} \sigma_L^{3.998} \quad (6-48)$$

For predicting the volumetric mass transfer coefficient in GIRs:

$$k_L a_{GIR} = 1.383 \cdot 10^5 \times \frac{D_{AB}^{0.500} \epsilon_G^{0.155} d_S^{0.414}}{\rho_G^{0.060}} \left(\frac{P_{GIR}^*}{V_L} \right)^{\delta_{GIR}} U_G^{\eta_{GIR}} \exp(-2.011 X_W) \quad (6-49)$$

$$\delta_{GIR} = 7.010 \cdot 10^{-6} \times d_{imp.}^{-0.395} d_T^{4.183} N^{2.237} \mu_L^{0.126} H_L^{-0.658} \quad (6-50)$$

$$\eta_{GIR} = 0.420 \times d_{imp.}^{-2.385} d_T^{-2.485} N^{-3.238} \sigma_L^{-0.261} H_L^{3.249} \quad (6-51)$$

For predicting the volumetric mass transfer coefficient in GSRs:

$$k_L a_{GSR} = 2.564 \cdot 10^3 \times \frac{D_{AB}^{0.500} \epsilon_G^{0.575}}{\rho_G^{0.060} d_S^{0.402}} \left(\frac{P_{GSR}^*}{V_L} \right)^{\delta_{GSR}} U_G^{\eta_{GSR}} \exp(-2.402 X_W) \quad (6-52)$$

$$\delta_{GSR} = 4.664 \cdot 10^{-4} \times d_T^{0.124} N^{0.593} \mu_L^{-0.769} \quad (6-53)$$

$$\eta_{GSR} = 9.475 \cdot 10^{-5} \times d_{imp.}^{0.363} N^{0.967} \rho_L^{-0.470} \mu_L^{-0.884} H_L^{-1.440} \quad (6-54)$$

Table 32: Data Base on ARs used in this Study

<i>References</i>	<i>Parameters</i>	<i>Gas/Liquid</i>	<i>Reactor</i>	<i>Operating Conditions</i>	<i>Legend</i>
Rushton and Bimbinet ⁽¹²²⁾	ε_G	Air/ Water + corn syrup	GSR	Atm. U _G : 3-30 10 ⁻³ m/s d _T : 0.23-0.91m	◻
Fuchs et al. ⁽¹²⁵⁾	N_{CRE}, k_{LA}	Air, N ₂ , O ₂ /Water	SAR GSR	Atm. U _G : 0-53 10 ⁻³ m/s d _T : 0.13-3.33m	◆
Martin ⁽⁸⁹⁾	N_{CRI}, Q_{GI}	Air /Water	GIR (HS)	Atm. N: 4.3-6.0Hz d _T : 0.280m	▲
Miller ⁽¹²⁶⁾	$\varepsilon_G, d_S, k_{LA}$	CO ₂ , Air/Aqueous sol.	GSR	Atm. N: 0.4-7Hz U _G : 8-150 10 ⁻³ m/s d _T : 0.15-0.67m	⊙
Robinson and Wilke ⁽²⁸¹⁾	$\varepsilon_G, d_S, k_{LA}$	N ₂ , O ₂ , CO ₂ /Water, alkaline sol.	GSR	Atm. 303 K N: 6.7-36.7Hz U _G : 1-4.6 10 ⁻³ m/s d _T : 0.1524m	●
Bern et al. ⁽²⁸³⁾	k_{LA}	H ₂ /Fat	GSR	P: 0.12-0.14MPa T: 453 K N: 3-12.5Hz U _G : 35-300 10 ⁻³ m/s d _T : 0.25,0.65,2.4m	◆
Loiseau ⁽³⁷⁸⁾	$\varepsilon_G, d_S, k_{LA}$	Air, O ₂ /Water, glycol, ethanol, sugar, acetic acid, CuCl, sodium sulfite	GSR	Atm. N: 6.7-50.0 Hz U _G : 0.75-85.0 10 ⁻³ m/s d _T : 0.225m	◈
Joshi and Sharma ⁽⁹²⁾	$N_{CRI}, Q_{GI},$ $\varepsilon_G, d_S(a),$ k_{LA}	CO ₂ , Air / Water, sodium dithionite, Na ₂ CO ₃ + NaHCO ₃	GIR (HS)	Atm. N: 3-11.7 Hz d _T : 0.41,0.57,1.0m	▽
Lopes de Figueiredo and Calderbank ⁽¹³⁰⁾	$\varepsilon_G, d_S, k_{LA}$	O ₂ /Water	GSR	Atm. N: 5-8 Hz U _G : 6-13 10 ⁻³ m/s d _T : 0.91m	◻

Table 32 (Cont'd)					
References	Parameters	Gas/Liquid	Reactor	Operating Conditions	Legend
Botton et al. ⁽³⁷⁹⁾	N_{CRE} , ε_G , k_{La}	Air /Water, glycol, Sodium sulphite	SAR GSR	Atm. N: 0-50Hz U_G : < 0.1m/s d_T : 0.085,0.12,0.25,0.60	▲
Sridhar and Potter ⁽¹³²⁾	ε_G , d_S	Air/Cyclohexane	GSR	P: 0.1-1.0 MPa N: 8-30Hz U_G : <0.032 m/s d_T : 0.13m	⊗
Matsumura et al. ⁽¹²⁹⁾	N_{CRE} , d_S	Air, O ₂ /Water + sodium alginate	SAR	Atm. N: 7-16.5Hz d_T : 0.190,0.242,0.316m	▼
Greaves and Barigou ⁽¹³⁸⁾	ε_G	Air/Water	GSR	Atm. N: 0.6-8.33Hz U_G : 6.3-10.7 10 ⁻³ m/s d_T : 1.0m	▲
Chang ⁽²⁴⁹⁾	k_{La}	H ₂ , N ₂ , CO, CH ₄ /Water, n-hexane, n-decane, n-tetradecane, cyclohexane	GIR (HS)	P: 0.5-5.96MPa T: 328-378K N: 13.3-20.0Hz d_T : 0.127m	▲
He et al. ⁽⁹⁸⁾	N_{CRI} , ε_G	Air/Water + CMC, water+triton-X-114	GIR (HS)	Atm. N: 3.3-33.3Hz d_T : 0.075m	●
Smith et al. ⁽³⁸⁰⁾	ε_G	Air/Water	GSR	Atm. N: 0.45-4.0Hz U_G : 8.8-28.7 10 ⁻³ m/s d_T : 1.2,1.6,1.8,1.8,2.7m	▼
Koneripalli ⁽³⁸¹⁾	k_{La}	N ₂ , CO, H ₂ , CH ₄ , CO ₂ /Methanol, ethanol	GIR (HS)	P: 0.33-5.48MPa T: 328-428K N: 13.3-23.3Hz d_T : 0.127m	▲
Mizan ⁽³⁸²⁾	k_{La}	H ₂ , C ₂ H ₄ , C ₃ H ₆ /n-hexane, propylene	SAR	P: 0.16-3.16MPa T: 297-353 K N: 13.3-20.0Hz d_T : 0.125m	■
Rielly et al. ⁽⁹⁹⁾	N_{CRI} , Q_{GI}	Air /Water	GIR (HS)	Atm. N: 3.4-9.0Hz d_T : 0.3-0.6 m	▼

Table 32 (Cont'd)					
References	Parameters	Gas/Liquid	Reactor	Operating Conditions	Legend
Rewatkar et al. (383)	ε_G	Air/Water	GSR	Atm. N: 0.85-8.0Hz U_G : 6.3-30.0 10^{-3} m/s d_T : 1.0, 1.5m	◆
Aldrich and van Deventer (100)	N_{CRI} , Q_{GI}	Air / Water, ethyl alcohol, sucrose sol.	GIR (DT)	Atm. N: 9.2-20.0Hz d_T : 0.19 m	●
Nienow et al. (384)	ε_G	Air/Water, dirty water	GSR	Atm. N: 0.67-2.5Hz U_G : 10-75 10^{-3} m/s d_T : 1.98m	▲
Saravanan et al. (102)	N_{CRI} , Q_{GI}	Air /Water	GIR (DT)	Atm. N: 0.13-13.5Hz d_T : 0.57, 1, 1.5m	⊙
Aldrich and van Deventer (103)	Q_{GI}	Air /Water, brine, alcohol, sucrose sol.	GIR (DT)	Atm. T: 291-350K N: 13.3-16.3Hz d_T : 0.19m	◆
Al Taweel and Cheng (104)	ε_G	Air/water + PGME	GIR (DT)	Atm. N: 12.5-25Hz d_T : 0.19m	■
Li (385)	k_{La}	H ₂ , C ₃ H ₈ , C ₂ H ₄ , C ₃ H ₆ /propane, n-hexane	SAR	P: 0.14-5.8MPa T: 297-353 K N: 13.3-20.0Hz d_T : 0.125m	■
Saravanan and Joshi (386)	N_{CRI} , Q_{GI}	Air /Water	GIR (DT)	Atm. N: 0.3-15.45Hz d_T : 0.57, 1, 1.5m	▣
Saravanan and Joshi (107)	ε_G	Air/H ₂ O	GIR (DT)	Atm. N: 0.3-15.5Hz d_T : 0.57, 1, 1.5m	●
Yoshida et al. (292)	ε_G , k_{La}	Air/Water	GSR	Atm. N: 2.5-6.7Hz U_G : 4-60 10^{-3} m/s d_T : 0.25m	▼

Table 32 (Cont'd)					
References	Parameters	Gas/Liquid	Reactor	Operating Conditions	Legend
Tekie ⁽²³⁾	$d_s, k_L a$	N ₂ , O ₂ /Cyclohexane	SAR GIR (HS)	P: 0.7-3.5MPa T: 330-430K N: 6.7-20Hz d _T : 0.11	●
Forrester et al. ⁽¹¹¹⁾	$Q_{GI}, d_s, k_L a$	Air /Water	GIR (HS)	Atm. N: 5.0-10.0Hz d _T : 0.45m	◆
Murugesan ⁽¹⁴⁹⁾	ε_G	Air/Water, Toluene, glycerol	GSR	Atm. N: 3.3-23.3Hz U _G : 1-66 10 ⁻³ m/s d _T : 0.15m	△
Solomakha and Tarasova ⁽³⁸⁷⁾	$\varepsilon_G, k_L a$	-	GSR	Atm. U _G : 2-87 10 ⁻³ m/s d _T : 0.2-3.6m	●
Mohammad ⁽¹¹⁾	$k_L a$	O ₂ , N ₂ /Benzoic acid	SAR GIR (HS)	P: 0.09-0.5MPa T: 473K N: 16.7Hz d _T : 0.076	▲
Patil and Joshi ⁽¹¹³⁾	N_{CRI}, Q_{GI}	Air /Water	GIR (DT)	Atm. N: 3.5-10.0Hz d _T : 1.0m	△
Vrabel et al. ⁽³⁸⁸⁾	ε_G	Air /Water, NaCl	GSR	Atm. N: 1.5-2.5Hz U _G : 10-40 10 ⁻³ m/s d _T : 1.876,2.09m	⊙
Bouaifi et al. ⁽³⁷⁷⁾	$\varepsilon_G, d_s, k_L a$	Air /Water	GSR	Atm. N: 1.66-11.67Hz U _G : 0.54-2.63 10 ⁻³ m/s d _T : 0.43m	◆
Fillion ⁽³⁴⁹⁾	$N_{CRI}, Q_{GI}, \varepsilon_G, d_s, k_L a$	N ₂ , H ₂ /Soybean oil	SAR GIR (HS) GSR	P: 0.1-0.5 MPa T: 373-473 K N: 10-23.3 Hz H: 0.171-0.268m Q _G : 10.4-51.9 10 ⁻⁶ m ³ /s d _T : 0.115m	○
Poncin et al. ⁽³⁷⁵⁾	$N_{CRI}, Q_{GI}, \varepsilon_G, k_L a$	Air /Water	SAR GIR (HS)	Atm. d _T : 0.6m	■








Table 32 (Cont'd)					
References	Parameters	Gas/Liquid	Reactor	Operating Conditions	Legend
Yawalkar et al. (389)	ε_G	Air /Water	GSR	Atm. N: 1.0-11.0Hz U _G : 3.9-15.7 10 ⁻³ m/s d _T : 0.57m	
Alves et al. (390) [72]	ε_G, d_S, k_La	Air O ₂ /Water, sodium sulphate, PEG	GSR	Atm. N: 4.2-10.0Hz U _G : 2.5-5.0 10 ⁻³ m/s d _T : 0.292m	
Lemoine et al. (391) [73]	N_{CRE}, N_{CRI}, Q_{GI}	Air, N ₂ /Toluene, benzaldehyde, benzoic acid	SAR GIR (HS)	P: 0.1-1.5 MPa T: 300-453K N: 10.3-12.3 Hz d _T : 0.125 m	
Linek et al. (363)	ε_G, k_La	Air, O ₂ /Water, water+NaSO ₄	GSR	Atm. N: 4.17-14.17 Hz U _G : 2.12-8.48 10 ⁻³ m/s d _T : 0.29 m	
Heintz (392)	$N_{CRI}, Q_{GI}, \varepsilon_G, d_S, k_La$	N ₂ , CO ₂ /Fluorinated liquids	GIR(HS)	P: 0.2-3.0 MPa T: 300-500K N: 10-12.3 Hz d _T : 0.115 m	
Lemoine and Morsi (393)	ε_G, d_S, k_La	Air, N ₂ /Toluene, benzaldehyde, benzoic acid	SAR GIR (HS) GSR	P: 0.1-1.5 MPa T: 300-453K N: 10.3-12.3 Hz U _G : 0-4 10 ⁻³ m/s d _T : 0.125 m	
Soriano (394)	k_La	CO, N ₂ , H ₂ , He/PAO-8, Sasol wax	GIR (HS)	P: 0.7-3.5 MPa T: 423-523K N: 13.3-20.0 Hz d _T : 0.076 m	

Table 33: Upper and Lower limits of the variables used in Equations (6-19) through (6-54)

<i>Variables</i>	<i>Minimum value</i>	<i>Maximum value</i>
$U_G, m/s$	0	0.3
N, Hz	0	54.0
H, m	0.064	6.542
H_L, m	$1.15 \cdot 10^{-2}$	4.97
d_T, m	0.075	3.600
d_{imp}, m	0.032	1.370
$\rho_L, kg/m^3$	310	2042
$\mu_L, Pa \cdot s$	$5.00 \cdot 10^{-5}$	0.09
$\sigma_L, N/m$	$1.20 \cdot 10^{-3}$	0.077
$\rho_G, kg/m^3$	0.05	194.90
$X_w, wt.$	0.5589	1.0000
$D_{AB}, 10^9 \cdot m^2/s$	0.08	153.94
n_{imp}, s	1	8
$M_{W-Gas}, kg/kmol$	2	44

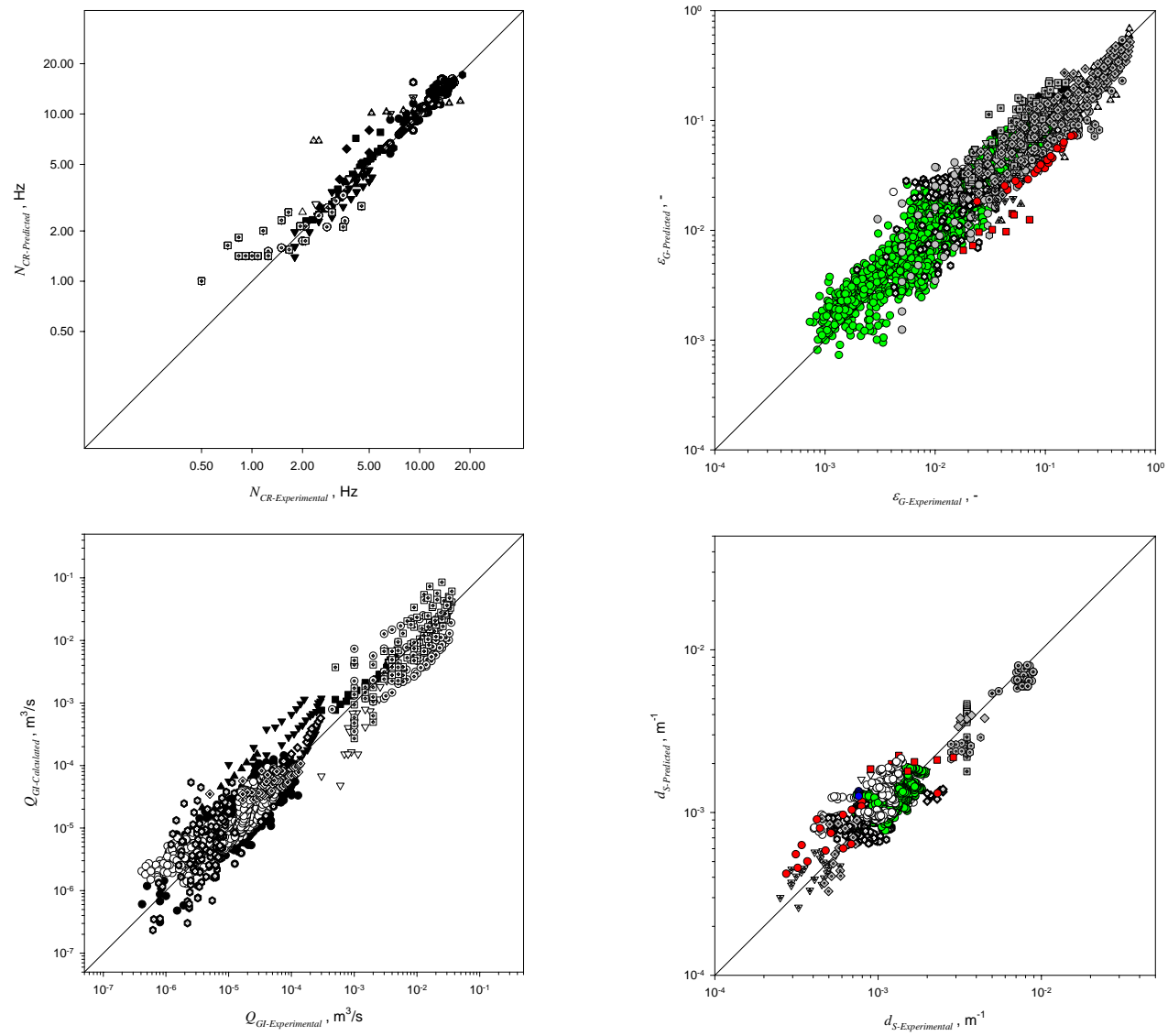


Figure 64: Comparison between Experimental and Predicted N_{CR} , Q_{GL} , ϵ_G and d_S Values using Empirical Correlations

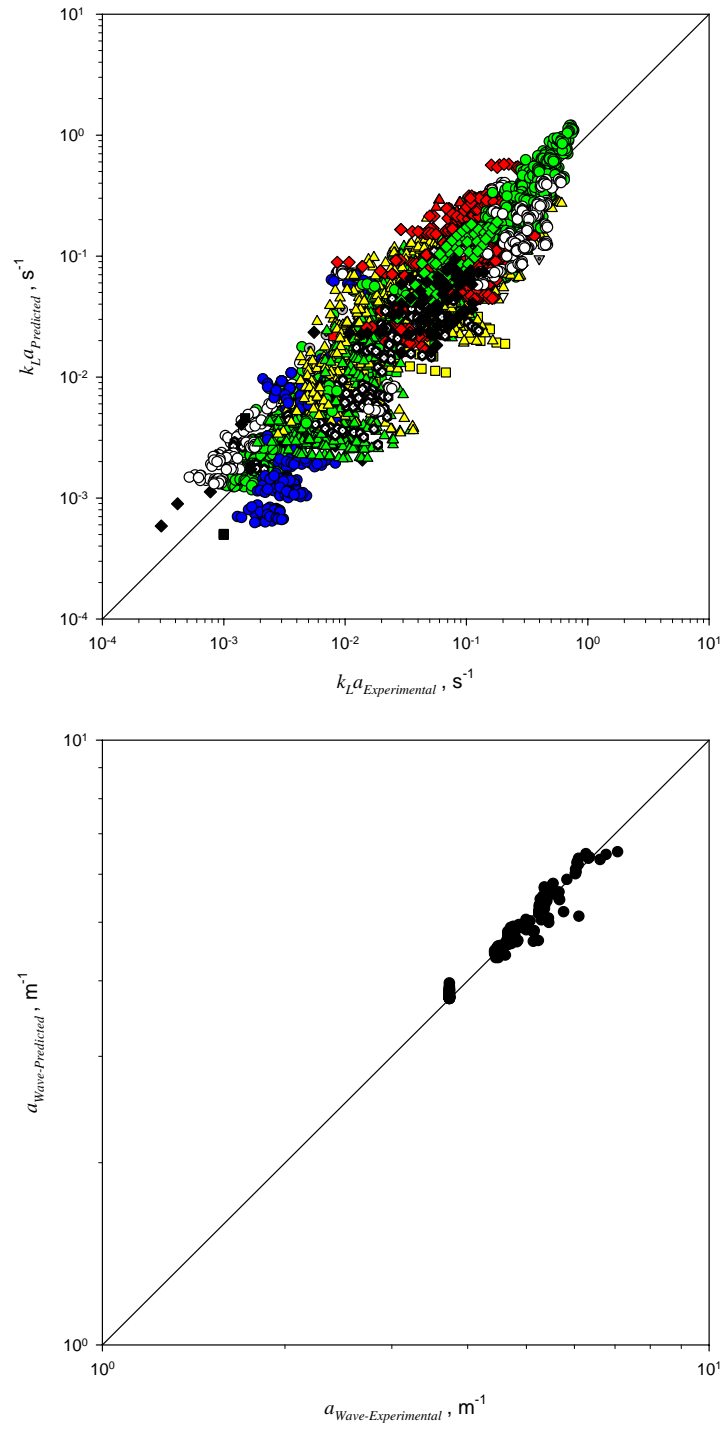


Figure 65: Comparison between Experimental and Predicted $k_L a$ and a_{Wave} Values using Empirical Correlations

6.4.2 Statistical Correlations of the Hydrodynamic and Mass transfer Parameters in the Agitated Reactors

Statistical correlations were also developed for each system investigated in this study using the statistical software package, Minitab Version 9.1 for Mainframe, since statistical correlations, though limited to the systems used, were reported to enjoy high confidence levels and much greater regression coefficients when compared with those of dimensionless correlations^(11, 23, 349, 385). The following general statistical correlation was found for N_{CRE} , N_{CRI} , Q_{GI} , a_{wave} , d_S , ε_G , a , $k_L a$ and k_L .

$$\ln(Y) = \beta_0 + \sum_{i=1}^4 \beta_i x_i + \sum_{i=1}^4 \sum_{j=1}^4 \beta_{ij} x_i x_j + \sum_{i=1}^4 \alpha_i \exp(\gamma_i x_i) + \sum_{i=1}^4 \sum_{\substack{j=1 \\ j \neq i}}^4 \kappa_{ij} \times \exp(\lambda_{ij} x_i x_j) + \zeta \times \exp\left(\sum_{i=1}^4 \zeta_i x_i\right) \quad (6-55)$$

The coefficients in Equation (6-55) are given in Tables 34 through 39, and the parity plot between the experimental and predicted N_{CRE} , N_{CRI} , Q_{GI} , a_{wave} , d_S , ε_G , a , $k_L a$ and k_L values are illustrated in Figures 66 and 67. As can be noticed in this figure, the predictions using the statistical correlations are with average regression coefficients of 97, 98, 90, 96, 97, 96, 98, 97 and 96%, respectively which are much greater than those obtained for the empirical correlations developed above. It should be mentioned that the coded variables, x_1 , x_2 , x_3 and x_4 , in Equation (6-55) were calculated based on the gas-liquid system and the reactor types used as follows:

For air-toluene in the GIR:

$$x_1 = 2 \left[\frac{2T - (400 + 300)}{(400 - 300)} \right] \quad (6-56)$$

For all other systems used, except air-toluene in the SAR, GIR, and GSR:

$$x_1 = 2 \left[\frac{2T - (453 + 300)}{(453 - 300)} \right] \quad (6-57)$$

For all gas-liquid systems used in the SAR, GIR, and GSR:

$$x_2 = 2 \left[\frac{2N - (1200 + 800)}{(1200 - 800)} \right] \quad (6-58)$$

$$x_3 = 2 \left[\frac{2P - (15 + 1)}{(15 - 1)} \right] \quad (6-59)$$

For all gas-liquid systems used in the SAR and GIR:

$$x_4 = 2 \left[\frac{2H - (0.268 + 0.171)}{(0.268 - 0.171)} \right] \quad (6-60)$$

For all gas-liquid systems used in the GSR:

$$x_4 = 2 \left[\frac{2U_G - 0.004}{0.004} \right] \quad (6-61)$$

Table 34: Coefficients of the Statistical Correlations for N_{CR} , a_{Wave} and Q_{GI}

N_{CRE}			$Toluene-N_2$		a_{Wave}		$Toluene-N_2$	
		$Confidence\ Level$	95%			$Confidence\ Level$	95%	
		β_0	6.31			β_0	$4.34\ 10^{-1}$	
		β_1	$-8.48\ 10^{-2}$			β_1	$6.98\ 10^{-3}$	
		β_3	$-3.40\ 10^{-2}$			β_2	$-1.09\ 10^{-1}$	
		β_4	$7.92\ 10^{-2}$			β_3	$-4.65\ 10^{-3}$	
		ξ	$3.82\ 10^{-1}$			β_4	$-2.43\ 10^{-1}$	
		ζ_1	$1.13\ 10^{-1}$			β_{22}	$-1.03\ 10^{-2}$	
		ζ_3	$1.15\ 10^{-1}$			β_{44}	$-2.25\ 10^{-3}$	
		ζ_4	$2.83\ 10^{-3}$			α_1	$2.31\ 10^{-4}$	
					γ_1	3.06		
					α_2	$5.06\ 10^{-1}$		
					γ_2	$2.17\ 10^{-1}$		
					α_3	$8.38\ 10^{-2}$		
					γ_3	$-1.17\ 10^{-3}$		
					α_4	$5.00\ 10^{-1}$		
					γ_4	$2.22\ 10^{-1}$		
N_{CRI}		$Toluene-N_2$	$Toluene-air$	$Mixture\ \#1-N_2$	$Mixture\ \#2-N_2$	$Mixture\ \#3-N_2$		
	$Confidence\ Level$	95%	95%	95%	95%	95%		
	β_0	$9.64\ 10^{-1}$	6.50	5.09	5.89	5.87		
	β_1	$-4.83\ 10^{-1}$	$-4.30\ 10^{-2}$	$-2.28\ 10^{-1}$	$-1.10\ 10^{-1}$	$-1.40\ 10^{-1}$		
	β_3	$-2.90\ 10^{-3}$	$-1.79\ 10^{-3}$	$1.22\ 10^{-4}$	$3.50\ 10^{-4}$	$-1.14\ 10^{-4}$		
	β_4	$7.54\ 10^{-2}$	$7.65\ 10^{-2}$	$7.36\ 10^{-2}$	$7.47\ 10^{-2}$	$7.70\ 10^{-2}$		
	ξ	5.52	$1.95\ 10^{-4}$	1.42	$6.42\ 10^{-1}$	$6.42\ 10^{-1}$		
	ζ_1	$8.47\ 10^{-2}$	2.81	$1.45\ 10^{-1}$	$1.41\ 10^{-1}$	$1.88\ 10^{-1}$		
Q_{GI}	$Confidence\ Level$	85%	90%	90%	90%	90%		
	β_0	$-1.20\ 10^3$	$-1.19\ 10^1$	$-1.60\ 10^1$	$-1.16\ 10^1$	$-1.06\ 10^1$		
	β_1	-2.20	$-9.36\ 10^{-1}$	-2.12	$-1.72\ 10^{-1}$	$-2.83\ 10^{-1}$		
	β_2	$-4.09\ 10^1$	$9.03\ 10^{-2}$	$-2.97\ 10^{-1}$	$6.23\ 10^{-1}$	$2.18\ 10^{-1}$		
	β_3	$2.10\ 10^{-2}$	$-4.14\ 10^{-1}$	$-3.31\ 10^{-1}$	$-6.36\ 10^{-1}$	$-3.30\ 10^{-1}$		
	β_4	-3.13	$3.11\ 10^{-1}$	$4.47\ 10^{-2}$	$-2.74\ 10^{-1}$	$-3.69\ 10^{-1}$		
	β_{11}	$-2.04\ 10^{-1}$	$-4.11\ 10^{-1}$	$-6.29\ 10^{-1}$	$-2.00\ 10^{-1}$	$-3.54\ 10^{-1}$		
	β_{22}	$-8.53\ 10^{-1}$	$-9.16\ 10^{-2}$	$-1.45\ 10^{-1}$	$-1.15\ 10^{-1}$	$-2.37\ 10^{-1}$		
	ξ	$1.19\ 10^3$	1.71	5.81	$8.84\ 10^{-1}$	$1.15\ 10^{-1}$		
	ζ_1	$1.72\ 10^{-3}$	$5.16\ 10^{-1}$	$3.15\ 10^{-1}$	$7.92\ 10^{-2}$	$9.86\ 10^{-1}$		
	ζ_2	$3.47\ 10^{-2}$	$6.85\ 10^{-2}$	$1.05\ 10^{-1}$	$-4.73\ 10^{-3}$	$7.45\ 10^{-1}$		
	ζ_3	$-2.55\ 10^{-4}$	$3.21\ 10^{-2}$	$1.51\ 10^{-2}$	$3.81\ 10^{-1}$	$1.32\ 10^{-1}$		
	ζ_4	$2.35\ 10^{-3}$	$-1.74\ 10^{-1}$	$-3.23\ 10^{-2}$	$1.31\ 10^{-2}$	$1.88\ 10^{-1}$		

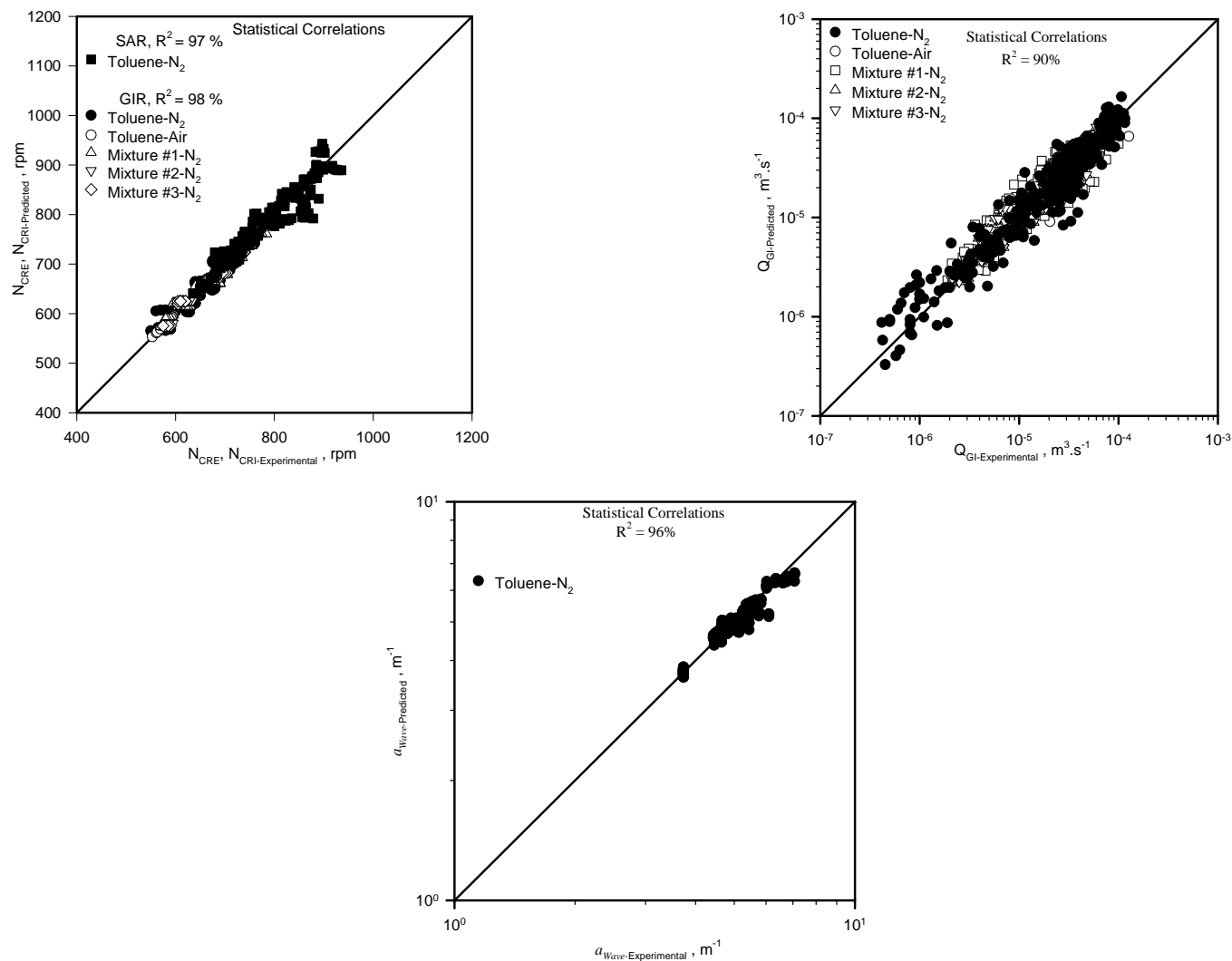


Figure 66: Comparison between Experimental and Predicted N_{CRE} , N_{CRb} , Q_{GI} and a_{Wave} Values Using the Statistical Correlations

Table 35: Coefficients of the Statistical Correlations for d_s

[illegible]

Table 36: Coefficients of the Statistical Correlations for ε_G

[illegible]

Table 37: Coefficients of the Statistical Correlations for $k_J a$

[illegible]

Table 38: Coefficients of the Statistical Correlations for a

[illegible]

Table 39: Coefficients of the Statistical Correlations for k_L

[illegible]

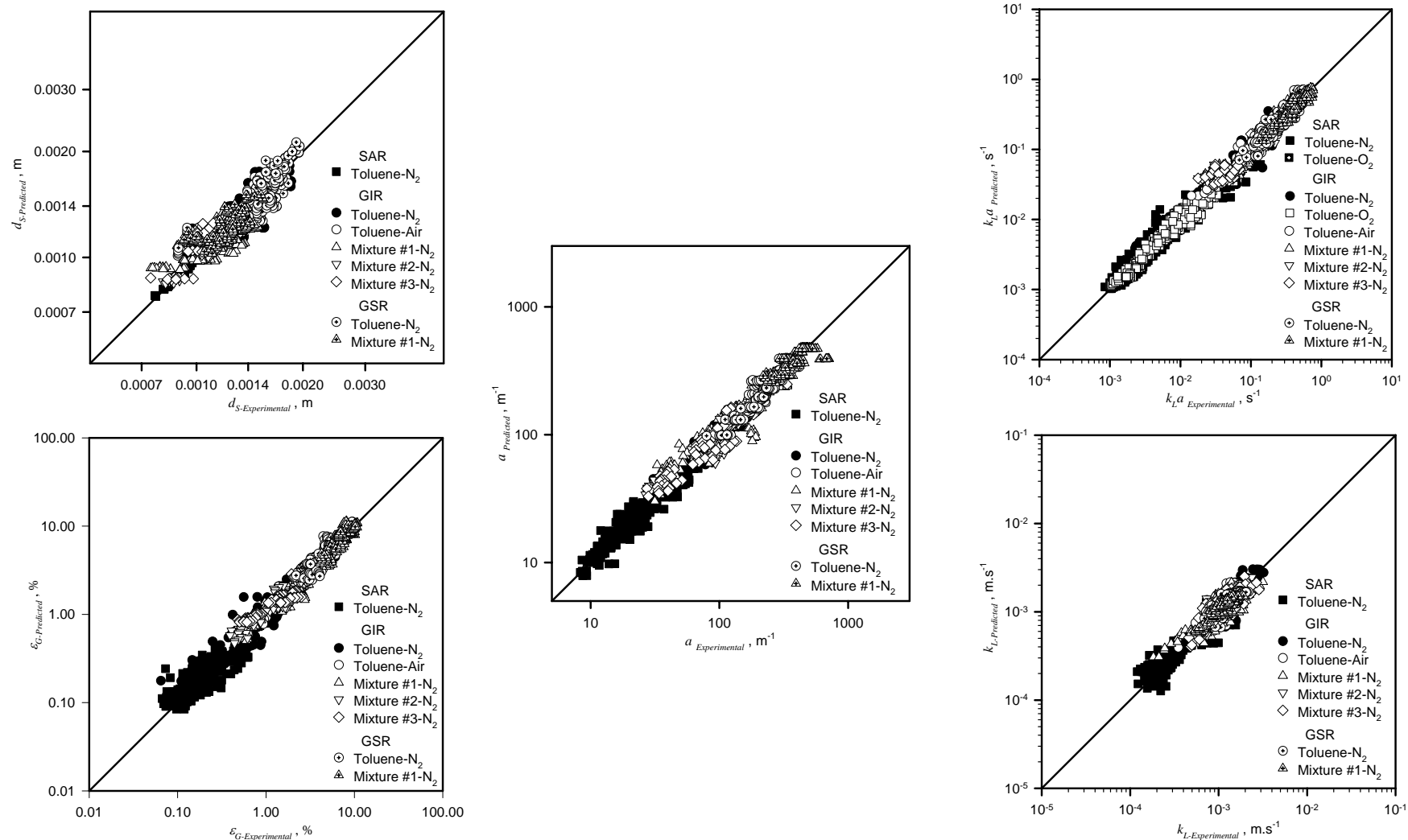


Figure 67: Comparison between Experimental and Predicted d_S , ε_G , a , $k_L a$ and k_L Values Using the Statistical Correlations

6.4.3 BPNN Correlations of the Hydrodynamic and Mass transfer Parameters in the Agitated Reactors

In the SAR, GIR and BCR, the PITTNET software package was then used to build the BPNN correlations. The same database (7374 experimental points) shown in Table 32 was also used to develop BPNN correlations for predicting the critical mixing speed, induced gas flow rate, wavy gas-liquid surface, gas holdup, Sauter mean bubble diameter and volumetric mass transfer coefficients for the corresponding reactor types. The BPNNs developed were validated using 25% of the total number of data points and the cross validation technique described in Appendix E. Tables 40 and 43 through 48 presents the input variables, architecture and weights of the constructed BPNNs for predicting N_{CR} , Q_{GI} , a_{Wave} , ε_G , d_S and k_{La} . Also, Table 41 shows the regression coefficient (R^2), standard deviation (σ) and average absolute relative error (AARE) for the empirical and BPNN correlations. These statistical errors prove that the developed BPNNs can predict the values of N_{CR} , Q_{GI} , a_{Wave} , ε_G , d_S and k_{La} with much higher accuracies than those of the empirical correlations as can be observed in Figures 68 and 69. It should also be mentioned that the reactor and gas dispersion mode were assigned in the BPNN correlations as shown in Table 42.

Table 40: Architecture and Input Variables of the N_{CR} , Q_{GI} , ε_G , d_S , a_{Wave} and k_{La} BPNN Correlations

Parameters	$\ln N_{CR}$			$\ln Q_{GI}$			$\ln \varepsilon_G$			$\ln d_S$			$\ln k_{La}$			$\ln a_{Wave} \cdot H$		
	Max	Min		Max	Min		Max	Min		Max	Min		Max	Min		Max	Min	
	7.762	3.401		-3.324	-15.613		-0.528	-9.871		-4.720	-8.557		-0.265	-8.093		0.452	0	
Variables	Position in BPNN	Max	Min	Position in BPNN	Max	Min	Position in BPNN	Max	Min	Position in BPNN	Max	Min	Position in BPNN	Max	Min	Position in BPNN	Max	Min
Reactor	1	1	0	-	-	-	1	1	0	1	1	0	-	-	-	-	-	-
Type, -																		
H , m	2	6.227	0.064	1	1.67	0.14	3	6.542	0.082	-	-	-	-	-	-	-	-	-
H_L , m	3	4.66	$\frac{1.15}{10^{-2}}$	2	1.000	0.083	12	4.97	$\frac{3.75}{10^{-2}}$	-	-	-	-	-	-	-	-	-
U_G , m/s	-	-	-	-	-	-	4	0.3	0.0	3	0.3	0	2	0.3	0.0	-	-	-
N , rpm	-	-	-	3	1729	36	2	3235	0.09	2	2400	0.09	1	2100	0	3	1400	75
ρ_L , kg/m ³	4	2042	310	4	2042	700	5	2042	429	4	2042	310	3	2042	310	6	1844	310
μ_L , Pa s	5	0.09	$\frac{5.00}{10^{-5}}$	5	0.09	$\frac{1.50}{10^{-4}}$	6	0.09	$\frac{5.00}{10^{-5}}$	5	0.09	$\frac{5.00}{10^{-5}}$	4	0.09	$\frac{5.00}{10^{-5}}$	7	$6.7 \cdot 10^{-3}$	$\frac{5.0}{10^{-5}}$
σ_L , N/m	6	0.077	$\frac{1.20}{10^{-3}}$	6	0.077	0.008	7	0.077	$\frac{1.20}{10^{-3}}$	6	0.074	$\frac{1.20}{10^{-3}}$	5	0.072	$\frac{1.20}{10^{-3}}$	8	0.072	$\frac{1.20}{10^{-3}}$
ρ_G , kg/m ³	7	194.90	0.05	7	53.86	0.05	8	53.86	0.06	7	55.27	0.05	6	55.27	0.05	9	55.17	0.05
M_{W-gas} , kg/kmol				8	44	2	11	44	2	8	44	2	-	-	-	-	-	-
d_T , m	8	3.330	0.075	9	1.500	0.113	9	3.600	0.075	-	-	-	7	3.330	0.076	-	-	-
d_{imp} , m	9	1.370	0.032	10	0.5	0.05	10	1.350	0.032	-	-	-	-	-	-	-	-	-
N_{CR} , rpm	-	-	-	12	1106	30	-	-	-	-	-	-	-	-	-	-	-	-
X_w , wt. %	-	-	-	-	-	-	13	100.00	55.89	9	100	88	-	-	-	-	-	-
D_{AB} , m ² /s	-	-	-	-	-	-	-	-	-	-	-	-	8	$1.5 \cdot 10^{-7}$	$\frac{8.4}{11} \cdot 10^{-7}$	-	-	-
Gas dispersion type, -	10	1	0	11	1	0	-	-	-	-	-	-	-	-	-	-	-	-
ε_G , -	-	-	-	-	-	-	-	-	-	10	0.59	$\frac{5.30}{10^{-5}}$	9	0.54	0	-	-	-
d_S , m	-	-	-	-	-	-	-	-	-	-	-	-	10	$8.9 \cdot 10^{-3}$	0	-	-	-
T , K	-	-	-	-	-	-	-	-	-	-	-	-	-	-	-	1	473	297
P , MPa	-	-	-	-	-	-	-	-	-	-	-	-	-	-	-	2	5.96	0.09
d_T/H , -	-	-	-	-	-	-	-	-	-	-	-	-	-	-	-	4	1.00	0.39
d_{imp}/H_L , -	-	-	-	-	-	-	-	-	-	-	-	-	-	-	-	5	0.67	0.21

Table 41: Statistical Analysis of the Empirical and BPNN Correlations

<i>Parameters</i>	<i>Regression Coefficient</i> R^2 , %		<i>Standard Deviation</i> σ , %		<i>Average absolute relative error</i> AARE, %	
	Empirical	BPNN	Empirical	BPNN	Empirical	BPNN
N_{CR}	96	97	14	4	7	3
Q_{GI}	70	97	50	20	35	15
a_{Wave}	92	97	5	2	3	2
ε_G	87	92	48	27	24	16
d_S	92	97	23	12	13	8
k_La	80	91	52	28	32	18

Table 42: Input Variables for Gas distribution and Reactor Type used in the BPNN Correlations

<i>Gas distribution type</i>	<i>Reactor Mode</i>	<i>Values for the BPNN</i>
<i>Surface aeration</i>	<i>SAR</i>	0
<i>Hollow shaft</i>	<i>GIR</i>	0.5
<i>Draft tube</i>	<i>GSR</i>	1

Table 43: Architecture, Weights of the N_{CR} BPNN Correlation

1^{st} hidden Layer Weights $u_{i,j}$	1	2	3	4	5	6	7	8	9	10
1	8.35	26.78	-30.16	2.63	1.72	-5.37	0.54	3.64	-1.90	-13.24
2	-28.29	-33.32	60.17	-4.83	4.48	7.00	-0.73	50.43	-69.38	32.63
3	-12.15	34.83	-80.39	6.31	-7.04	-4.18	0.82	-55.17	60.85	0.24
4	4.52	34.25	-73.91	-4.10	0.98	-3.50	-0.54	81.09	28.72	-3.49
5	-6.21	-42.45	51.52	1.45	0.92	8.78	-2.19	-11.24	1.59	13.96
6	-1.70	-27.57	-5.17	3.74	-1.58	-6.71	2.62	11.16	-20.47	2.79
7	-14.74	-29.14	-44.81	3.12	-6.13	-2.07	1.28	20.15	-23.49	1.78
8	-6.97	-6.54	-33.78	1.41	-0.68	-3.43	1.86	7.65	-10.75	0.91
Bias of 1^{st} hidden Layer $u_{0,i}$	1	2	3	4	5	6	7	8		
	4.85	-3.93	3.75	6.92	-11.05	5.52	5.01	9.85		
Output Layer Weights w_i	1	2	3	4	5	6	7	8		
	14.02	8.42	17.05	-33.35	4.38	4.07	-16.60	-4.15		
Bias of Output Neuron w_0					19.89					

Table 44: Architecture, Weights of the Q_{GI} BPNN Correlation

I^{st} hidden Layer Weights u_{ij}	1	2	3	4	5	6	7	8	9	10	11	12
1	-14.15	8.50	-7.38	-4.82	-7.26	-11.92	-2.60	4.68	2.29	-0.89	22.17	14.43
2	-6.31	0.83	4.64	-9.98	-3.71	1.32	2.13	3.44	7.23	4.39	-9.67	20.24
3	-9.90	9.56	-7.69	-3.34	-17.75	-0.80	0.05	2.85	4.80	-6.12	5.86	-0.30
4	5.19	-5.30	-16.27	0.81	-16.10	0.65	1.44	0.88	0.96	2.20	-0.89	13.58
5	18.75	-14.83	2.10	8.76	0.52	-0.92	2.20	0.07	-8.23	0.37	-3.11	0.56
6	-14.27	3.30	-9.12	-3.73	-16.10	-5.30	-0.29	5.63	2.65	8.07	10.14	7.89
7	-47.58	1.04	-5.45	-26.94	-21.08	18.79	0.37	9.25	-47.74	6.08	-11.01	11.30
8	-0.66	9.05	-8.41	-1.13	0.97	-12.44	-0.11	-3.41	-12.49	-6.43	-3.67	0.59
Bias of I^{st} hidden Layer $u_{0,i}$	1	2	3	4	5	6	7	8				
	-13.35	2.35	-0.48	-4.77	-1.94	-4.33	-13.89	5.79				
Output Layer Weights w_i	1	2	3	4	5	6	7	8				
	-4.95	8.09	-5.90	-7.91	-2.67	8.75	-28.30	-7.14				
Bias of Output Neuron w_0						-6.36						

Table 45: Architecture, Weights of the ε_G BPNN Correlation

I^{st} hidden Layer Weights u_{ij}	1	2	3	4	5	6	7	8	9	10	11	12	13
1	-18.65	13.91	-9.73	-2.87	2.46	-34.93	-10.02	-4.88	32.85	6.69	0.57	-17.83	3.04
2	-17.66	14.99	3.83	5.82	6.51	-0.99	1.57	6.64	0.81	6.17	1.14	5.55	-1.68
3	-1.52	1.94	0.90	-22.86	-5.65	0.19	3.81	3.09	6.38	-0.99	-3.10	-2.95	2.81
4	-0.09	7.78	-12.13	-4.16	2.46	4.34	13.73	-2.41	10.69	-0.19	-0.92	-4.79	-0.79
5	4.33	-1.52	-7.36	3.77	-1.03	-0.29	-3.72	1.61	-4.96	3.77	1.95	-4.53	0.61
6	1.71	-10.63	-1.31	-29.96	4.46	-1.36	-7.26	-9.25	-0.03	-5.51	9.98	-16.02	1.86
7	2.36	5.02	-0.81	6.96	7.03	-0.66	4.62	-2.82	16.71	7.23	-0.42	-12.60	-2.28
8	-14.89	10.62	-10.55	3.45	0.73	-5.76	-8.67	-5.38	-15.38	1.08	0.67	-9.04	1.13
9	-15.53	10.15	0.49	-6.09	11.92	1.88	6.77	-1.01	1.47	5.21	-2.00	7.93	-2.56
10	2.97	-2.43	17.06	19.45	5.69	-2.78	1.32	4.15	-2.59	31.89	0.31	22.51	-1.76
Bias of I^{st} hidden Layer $u_{0,i}$	1	2	3	4	5	6	7	8	9	10			
	-2.38	4.84	-5.78	-0.39	-5.13	-0.59	-5.00	0.72	0.10	-1.09			
Output Layer Weights w_i	1	2	3	4	5	6	7	8	9	10			
	13.01	2.72	-8.58	6.90	8.73	-0.88	3.78	-12.50	-2.65	-3.76			
Bias of Output Neuron w_0							-5.54						

Table 46: Architecture, Weights of the d_s BPNN Correlation[illegible]

Table 47: Architecture, Weights of the k_{Ia} BPNN Correlation

1^{st} hidden Layer Weights u_{ij}	1	2	3	4	5	6	7	8	9	10
1	2.88	4.87	-0.58	-9.02	5.98	-0.17	-3.67	-0.67	-7.76	-22.32
2	-2.09	9.11	3.01	8.08	-9.03	-0.09	-29.15	-18.32	3.53	-5.85
3	9.81	-19.61	0.31	-17.34	-5.20	6.11	-0.32	-9.38	13.21	-20.79
4	-1.20	-9.28	-15.05	8.45	1.68	-1.56	1.47	-4.67	1.07	1.38
5	-9.35	2.52	6.38	-24.46	-1.51	-0.18	-7.52	3.38	-5.27	7.29
6	-2.07	-12.16	38.68	-10.52	-15.93	-1.72	-0.70	-6.62	-6.22	0.68
7	-0.10	7.14	-24.48	-22.50	7.56	-1.97	-3.66	-8.07	12.88	-3.50
8	-9.56	6.55	-11.73	0.70	9.45	-6.24	0.58	8.97	81.82	-0.49
9	0.95	5.94	-5.27	25.29	0.95	0.48	-3.14	-9.46	4.65	36.31
10	1.78	-7.27	11.60	25.96	-19.65	-0.46	-21.74	1.35	11.97	3.81
$Bias\ of\ 1^{st}\ hidden\ Layer\ u_{0,i}$	1	2	3	4	5	6	7	8	9	10
	0.82	4.52	-2.16	5.09	0.72	-3.21	1.80	5.67	-1.96	-3.57
2^{nd} hidden Layer Weights v_{ij}	1	2	3	4	5	6	7	8	9	10
1	1.27	-9.88	-0.42	1.58	-1.63	16.16	4.88	-3.03	8.32	5.63
2	-7.05	-2.78	0.72	20.23	-19.60	1.37	9.44	-1.67	6.20	-26.30
3	16.65	-12.39	-2.78	4.43	11.46	-8.95	-9.19	0.46	21.81	22.59
4	7.31	-1.24	-5.42	2.73	-2.78	9.01	-3.16	-7.21	2.29	14.68
5	7.55	-4.91	-0.20	5.70	1.45	-5.28	-2.31	-0.10	12.16	4.73
6	1.75	-1.59	0.94	-1.45	1.51	4.43	-17.00	1.17	-0.05	-8.04
7	4.46	3.24	-1.33	7.23	4.54	-7.43	0.51	-1.09	1.77	-0.62
8	-8.50	-0.83	-22.08	6.93	-3.57	7.13	-11.62	-21.44	-5.45	-22.50
$Bias\ of\ 2^{nd}\ hidden\ Layer\ v_{0,i}$	1	2	3	4	5	6	7	8		
	-10.66	-12.17	-21.03	-7.88	-14.04	-1.62	-9.50	18.08		
$Output\ Layer\ Weights\ w_i$	1	2	3	4	5	6	7	8		
	2.61	-1.25	-1.29	-3.12	2.51	-2.90	-3.51	-10.20		
$Bias\ of\ Output\ Neuron\ w_0$					1.99					

Table 48: Architecture, Weights of the a_{Wave} BPNN Correlation

I^{st} hidden Layer Weights $u_{i,j}$	1	2	3	4	5	6	7	8	9
1	1.73	14.79	-3.45	-5.05	7.50	2.72	8.19	12.41	-6.86
2	-7.48	7.36	-0.88	33.75	-23.57	-14.92	7.99	-7.91	-6.53
3	8.31	3.18	-1.56	-15.79	-10.94	20.27	2.21	26.92	-6.14
4	4.56	-11.59	1.52	-7.97	-2.97	13.38	0.84	8.53	14.59
$Bias\ of\ I^{st}\ hidden\ Layer\ u_{0,i}$	1	2			3			4	
	-1.48	10.15			-10.95			1.47	
$Output\ Layer\ Weights\ w_i$	1	2			3			4	
	-7.50	-11.14			-21.93			9.98	
$Bias\ of\ Output\ Neuron\ w_0$	4.22								

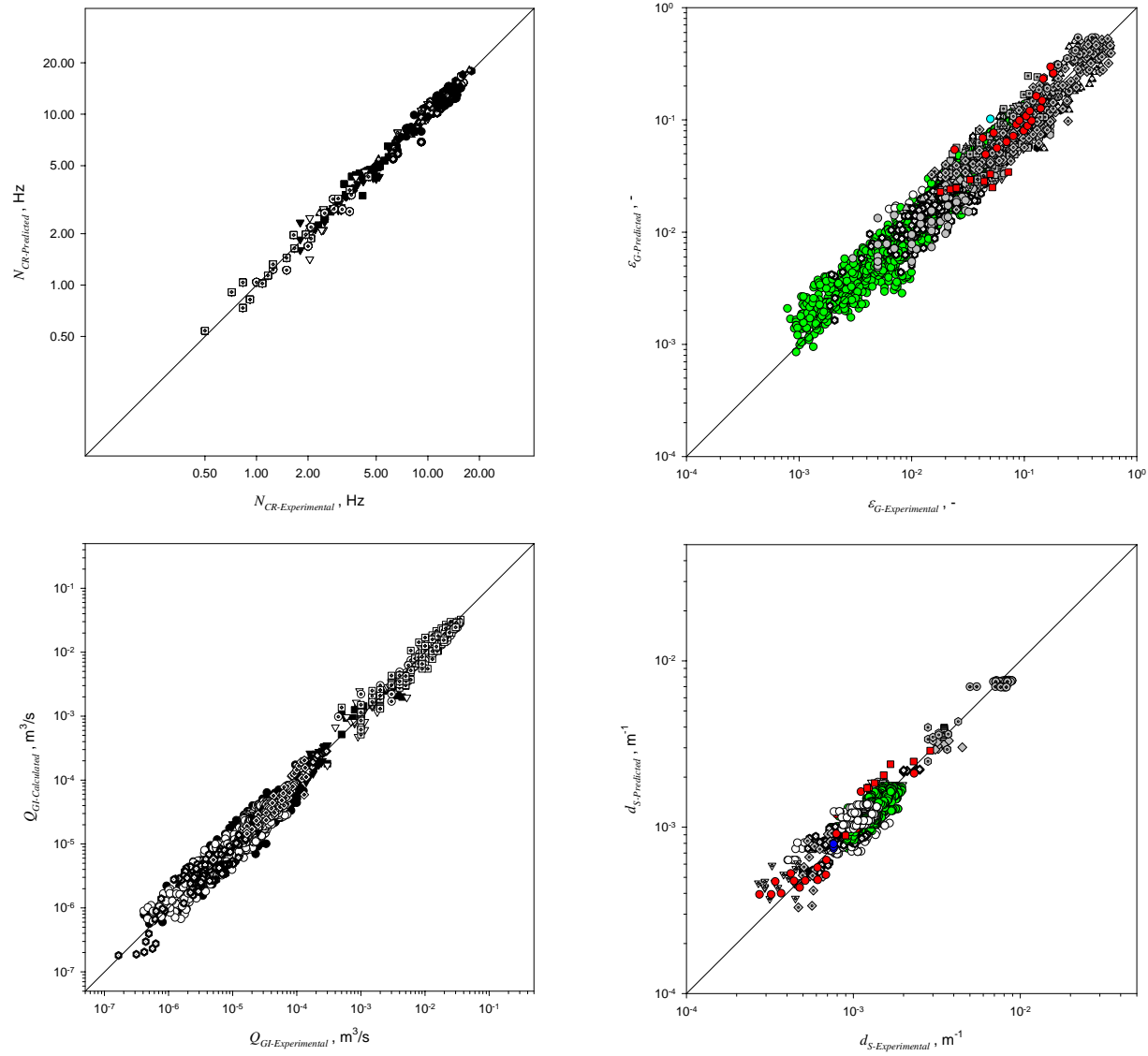


Figure 68: Comparison between Experimental and Predicted N_{CR} , Q_{GI} , ϵ_G and d_S Values using BPNN Correlations

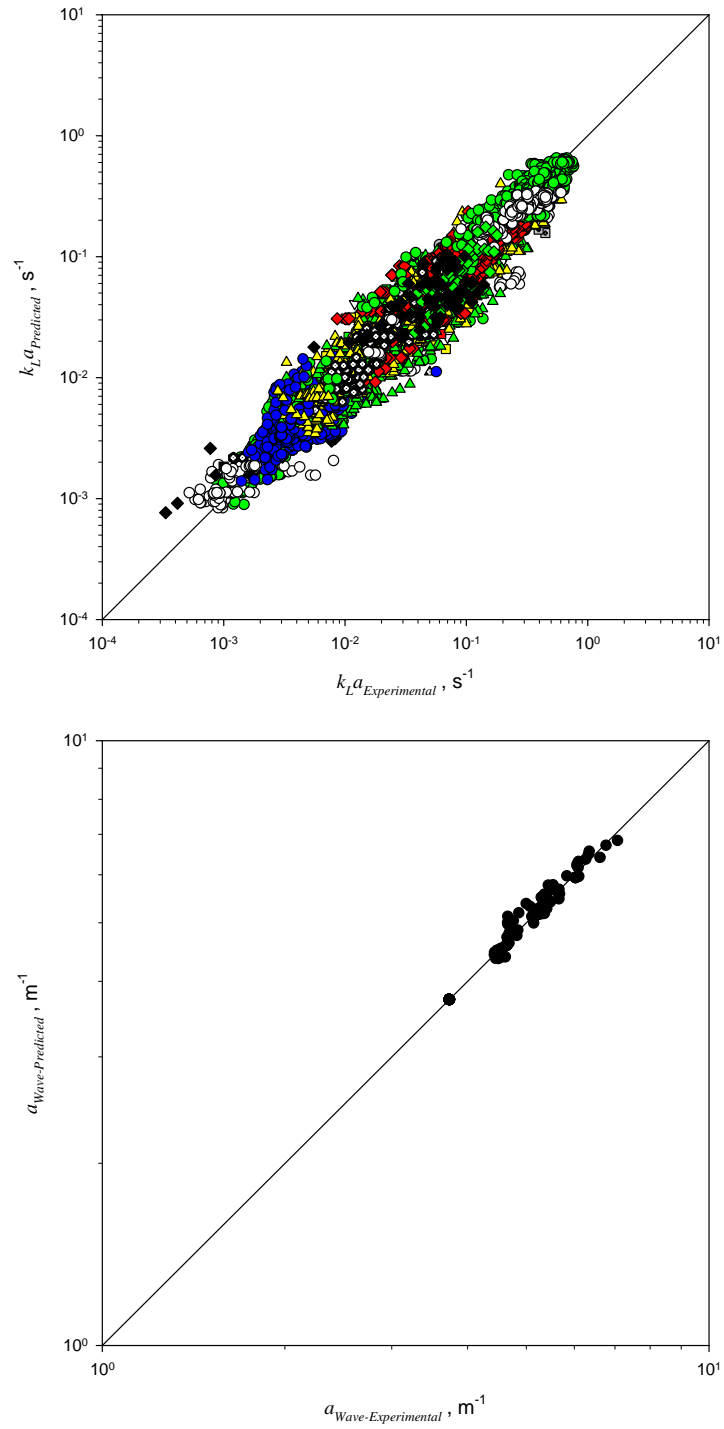


Figure 69: Comparison between Experimental and Predicted $k_L a$ and a_{Wave} Values using BPNN Correlations

6.4.4 Calculation Algorithm of the Hydrodynamic and Mass transfer Parameters in the Agitated Reactors

In this study, the empirical correlations and BPNNs were used in parallel to develop the calculation algorithm, which could be employed to predict the hydrodynamic and mass transfer parameters in agitated reactors as depicted in Figure 70. The calculation algorithm consists of the following steps:

1. Calculate N_{CRE} for SARs, Equation (6-19) or N_{CRI} for GIRs, Equation (6-20), or the BPNN in Table 43.
2. If $N_{CRI} < N$, calculate Q_{GI} for GIRs, Equation (6-21) or Table 44, otherwise $Q_{GI} = 0$ and the reactor is an SAR.
3. Obtain P^*/V_L in SARs, GIRs, and GSRs using the empirical literature correlation. If using BPNNs correlations, go to step 4.
4. Calculate ε_G , Equations (6-23) for SARs, (6-26) for GIRs and (6-29) for GSRs, or Table 45.
5. Calculate d_s using Equations (6-37) for SARs, (6-40) for GIRs and (6-43) GSRs, or Table 46.
6. Calculate $k_L a$, Equations (6-46), (6-49) and (6-52) or the BPNN in Table 47.
7. Calculate a_{Wave} from Equation (6-22) or the BPNN in Table 48.
8. Calculate a , Equation (6-62):

$$a = \frac{6\varepsilon_G}{(1-\varepsilon_G)d_s} + a_{Wave} \quad (6-62)$$

9. Calculate k_L , Equation (6-63):

$$k_L = \frac{k_L a}{a} \quad (6-63)$$

It should be mentioned that a_{Wave} was used in Equation (6-62) in order to take into account the effect of the wavy surface area, which can have a significant impact, particularly in small-scale agitated reactors ⁽¹²⁶⁾.

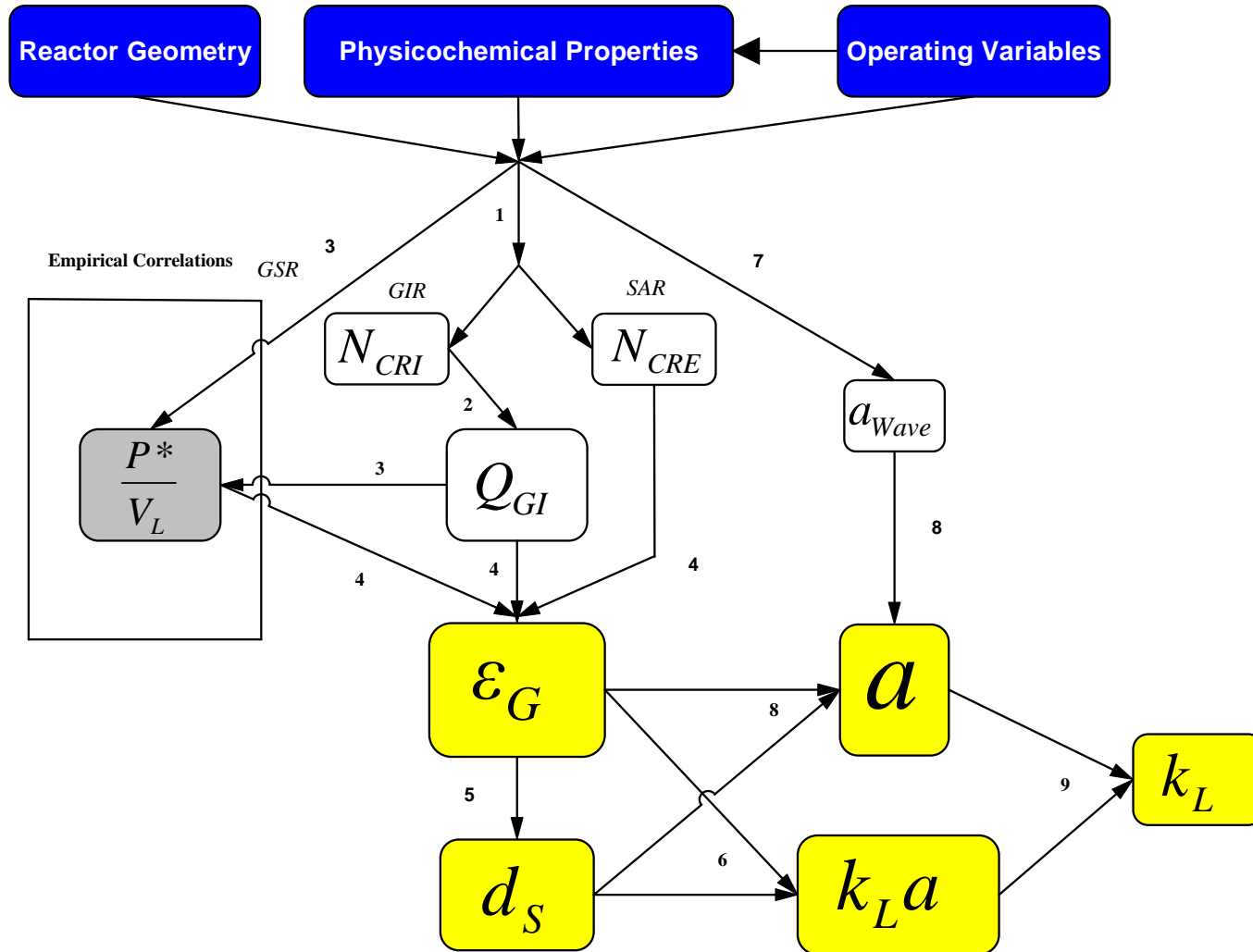


Figure 70: Calculation Algorithm for the Hydrodynamic and Mass Transfer Parameters Using the Empirical and BPNN Correlations

6.5 CORRELATIONS AND CALCULATION ALGORITHM IN THE BCR

As in the agitated reactors, empirical, statistical and BPNN correlations were developed to predict both hydrodynamic and mass transfer parameters in BCRs. The different types of correlations are first presented, and then because of the large data bank used (3881 data points), the developed the empirical and BPNN correlations were used to build a simple algorithm, enabling the calculation of the hydrodynamic and mass transfer parameters.

6.5.1 Empirical Correlations of the Hydrodynamic and Mass Transfer Parameters in the BCR

The correlation proposed by Behkish⁽³⁹⁵⁾ was modified in order to take into account the foamability of the liquids, hence the following correlations for predicting the total gas holdup (ε_G) and the holdup of large gas bubbles ($\varepsilon_{G-Large}$) were developed using the 3881 data points shown in Table 49:

$$\varepsilon_G = 4.94 \times 10^{-3} \left(\frac{\rho_L^{0.42} \rho_G^{0.18}}{\mu_L^{0.17} \sigma_L^{0.27}} \right) U_G^{0.55} \left(\frac{P_T}{P_T - P_S} \right)^{0.20} \left(\frac{D_C}{D_C + I} \right)^{-0.12} \Gamma^{0.05} \exp(-2.23C_V - 0.16(\rho_p d_p) - 0.24X_w) \quad (6-64)$$

$$\varepsilon_{G-Large} = \varepsilon_G^{0.84} \left(1 - 3.04 \times 10^{-6} \frac{\rho_L^{0.97}}{\mu_L^{0.16}} e^{4.50X_w - 4.49C_V} \right) = \varepsilon^{0.84}(F) \quad (6-65)$$

From the knowledge of the total gas holdup (ε_G), Equation (6-64) and the holdup of large gas bubbles, Equation (6-65), the holdup of small gas bubbles ($\varepsilon_{G-Small}$) can be deduced as:

$$\varepsilon_{G-Small} = \varepsilon_G - \varepsilon_{G-Large} \quad (6-66)$$

It should be noted that coupling Equations (6-64) and (6-65) leads to the following possibilities:

1. If ε_G is $\leq (F)^{25/4}$, small gas bubbles do not exist; and Equation (6-66) cannot be used to split ε_G into $\varepsilon_{G-Large}$ and $\varepsilon_{G-Small}$.

2. If ε_G is $> (F)^{25/4}$, small and large gas bubbles coexist; and Equations (6-65) and (6-66) can be used.

In the Equation (6-67), Γ represents the gas sparger type and is defined as:

$$\Gamma = (K_d \times N_o d_o^\alpha) \quad (6-67)$$

K_d is the distributor coefficient, N_o is the number of orifices in the sparger, and d_o is the diameter of the orifice. The values of K_d and the exponent α for several distributors can be found in Table 50. For perforated plates, the exponent α depends on ζ , and can be expressed as:

$$\zeta = N_o \left(\frac{d_o}{D_C} \right)^2 \quad (6-68)$$

X_W in Equation (6-64) designates the concentration of the primary liquid in a liquid mixture, and its value varies between 0.5 and 1. For a single-component or an organic liquid mixture, consisting of several hydrocarbons, such as oils and waxes, X_W equals 1. It should also be mentioned that in the case of BCRs, C_V , ρ_P , and d_P are zeros.

To predict the Sauter mean bubble diameter of all gas bubbles in the reactor, the following correlation was obtained:

$$d_s = 37.19 \times \frac{\mu_L^{0.08} \sigma_L^{1.22} \rho_G^{0.02} T^{1.66}}{\rho_L^{1.52} M_{W-Gas}^{0.12}} U_G^{0.14} \left(\frac{D_C}{D_C + 1} \right)^{0.30} (1 - \varepsilon_G)^{1.56} \Gamma^{-0.02} e^{-2.29X_W + 2.81C_V + 2.77\rho_P d_P} \quad (6-69)$$

In the case where small and large gas bubbles coexist ($\varepsilon_G > (F)^{25/4}$), the Sauter mean bubble diameter of large gas bubbles was correlated as:

$$d_{S-Large} = d_s^{0.96} \left(1 - 10^{-5} \rho_L^{0.22} \mu_L^{0.03} \sigma_L^{8.60} U_G^{0.04} \varepsilon_G^{2.37} \varepsilon_{G-Large}^{2.74} \right) \quad (6-70)$$

Also, for predicting the volumetric mass transfer coefficient, the following correlation was developed.

$$k_L a = 6.14 \times 10^4 \frac{\rho_L^{0.26} \mu_L^{0.12}}{\sigma_L^{0.52} \rho_G^{0.06}} \frac{\varepsilon_G^{1.21}}{U_G^{0.12} d_s^{0.05}} \frac{D_{AB}^{0.50}}{T^{0.68}} \Gamma^{0.11} \left(\frac{D_C}{D_C + 1} \right)^{0.40} \quad (6-71)$$

Table 51 presents the ranges of the conditions of applicability of Equations (6-64) through (6-71); and Table 53 shows the regression coefficients and standard deviations of the correlations developed for each parameter.

It should be noted that the above correlations are valid when the volume of internals, commonly used in BCRs and SBCRS for cooling or heating purposes, is $\leq 20\%$ of the reactor volume. This is because several literature findings (155, 396, 397, 398, 399, 400, 401, 402, 403) showed limited or no effect of internals on the hydrodynamic and mass transfer parameters as long as their volume fraction remains under 20%. Also, these correlations should be valid for reactor height/diameter ratio (H/D_C) from 4 to 20, hence a considerable number of data points available in the literature (194, 198, 219, 220, 320) and used to develop these correlations cover such an H/D_C range.

Table 49: Database used in this study on BCRs and SBCRs

Authors	Parameters	Gas	Liquid	Solid	Operating variable	D_G, m	Sparger	Legend
Towell et al. ⁽⁴⁰⁴⁾	k_{La}	CO ₂	Water	-	P : atm./ T : 300 K// U_G : 0.07 m/s	0.407	S-ON	▣
Bhaga et al. ⁽⁴⁰⁵⁾	ε_G	N ₂	n-octane+toluene, cumene+ams, toluene+ethanol, +ams, +cumene, +ethylbenzene, acetone+benezene	-	P : atm./ T : 298, 333 K/ U_G : 0.021-0.035 m/s	0.0382	PfP	⊙
Botton et al. ⁽⁴⁰⁶⁾	ε_G	Air	Water, water+glycol, +tensioactive+trisodium phosphate	-	P : atm./ T : amb./ U_G : 4.7 10 ⁻³ -14.0 m/s	0.02, 0.075, 0.200, 0.480	PfP, R, S	▼
Jackson and Shen ⁽⁴⁰⁷⁾	k_{La}	Air	Water+sodium sulfite	-	P : atm./ T : 283-303 K/ U_G : 0.001-0.004 m/s	0.076, 1.800, 7.600	S-ON, M-ON	⊙
Kataoka et al. ⁽⁴⁰⁸⁾	$\varepsilon_G, d_s, k_{La}$	CO ₂	Water	-	P : atm./ T : 0.05 m/s	5.5	M-ON	⊙
Deckwer et al. ⁽¹⁵⁴⁾	ε_G	N ₂	Wax	Al ₂ O ₃	P : 0.4 M Pa/ T : 523 K/ U_G : 0.004-0.034 m/s/ C_V : 0-1.21 vol.%	0.1	SP	⊙
Kastanek et al. ⁽⁴⁰⁹⁾	k_{La}	Air	Water	-	P : atm./ T : amb./ U_G : 0.005-0.025 m/s	0.15, 0.30, 1.00	PfP	△
Hikita et al. ⁽²⁹⁴⁾	k_{La}	Air, O ₂ , H ₂ , CO ₂ , CH ₄ , C ₃ H ₈	Water, +sucrose, +n-butanol, +methanol, +Na ₂ SO ₄ , +K ₂ SO ₄ , +K ₃ PO ₄ , +KNO ₃ , +CaCl ₂ , +AlCl ₃ , +KCl, +NaCl	-	P : atm./ T : 298 K/ U_G : 0.042-0.38 m/s	0.10, 0.19	S-ON	⊙
Vermeer and Krishna ⁽¹⁵⁷⁾	$\varepsilon_G, \varepsilon_{G-Small}, \varepsilon_{G-Large}, k_{La}$	Air	Turpentine 5	-	P : 0.1 MPa/ T : 290 K/ U_G : 0.1-0.3 m/s	0.19	Cross	⊙
Godbole ⁽⁴¹⁰⁾	ε_G, k_{La}	Air	Water, +CMC, +0.8 M sodium sulfite, +ethanol, +propanol, +butanol, +methanol, +glycerine, Sotrol-130	Polystyrene, coal, oil shell, sand	P : atm./ T : 298 K/ U_G : 0.017-0.57 m/s/ C_V : 0-26.3 vol.%	0.305	PfP	◆
Moujaes ⁽⁴¹¹⁾	ε_G, k_{La}	N ₂ , air	Tetraline, water, ethylene glycol	-	P : atm./ T : 275-293 K/ U_G : 0.015-0.117 m/s	0.127, 0.3048, 1.8288	S-ON, M-ON	△
Tarmy et al. ⁽¹⁷²⁾	ε_G	N ₂	n-Heptane	-	P : 0.12-0.62 MPa/ T : amb./ U_G : 0.12 m/s	0.61	S-ON	△
Shah et al. ⁽⁴¹²⁾	ε_G	Air	Water+Ethanol	-	P : atm./ T : amb./ U_G : 0.106-0.208 m/s	0.1	SP	△
Grover et al. ⁽⁴¹³⁾	ε_G	Air	Water	-	P : atm./ T : 303-353 K/ U_G : 0.012-0.041 m/s	0.1	SP	▽

Authors	Parameters	Gas	Liquid	Solid	Operating variable	D _c , m	Sparger	Legend
Idogawa et al. (⁴¹⁴)	ε_G, d_S	Air	Water	-	P : 0.1-15.0 MPa/ T : 293 K/ U_G : 0.005-0.050 m/s	0.05	S-ON, PfP, PoP	◇
Wezorke (⁴¹⁵)	ε_G	Air	Mono-ethylene glycol	-	P : atm/ T : amb./ U_G : 0.11-0.41 m/s	0.44	S-ON	▽
Bukur and Daly (⁴¹⁶)	ε_G	O ₂	Wax	-	P : atm/ T : 473, 538 K/ U_G : 0.01-0.15 m/s	0.229	PfP	⬢
Idogawa et al. (⁴¹⁷)	ε_G, d_S	Air, He, H ₂	Water, methanol, acetone, ethanol, isoamyl-alcohol+water, ethanol+water	-	P : 0.1-15.0 MPa/ T : 293 K/ U_G : 0.005-0.050 m/s	0.05	PfP	⬢
O'Dowd et al. (⁴¹⁸)	ε_G	N ₂	Water	Glass beads	P : atm/ T : amb./ U_G : 0.031-0.194 m/s/ C_V : 4.17-10.74 vol.%	0.108	PfP	⬢
Ozturk et al. (²⁴³)	$\varepsilon_G, k_L a$	Air, H ₂ , N ₂ , He, CO ₂	Xylene, p-xylene, aniline, toluene+ethanol, ligroin, ethylbenzene, ethylacetate, CCl ₄ , 1,4-dioxane, acetone, nitrobenzene, 1,2-dichloroethane	-	P : atm/ T : 293 K/ U_G : 0.03-0.08 m/s	0.095	S-ON	⬢
Zou et al. (⁴¹⁹)	ε_G	Air	Water, ethanol	-	P : atm/ T : 313-369.5 K/ U_G : 0.04-0.17 m/s/ U_L : 0.007 m/s	0.1	S-ON	△
Halard et al. (⁴²⁰)	$\varepsilon_G, k_L a$	Air	Water-CMC sol.	-	P : atm/ T : amb./ U_G : 0.02-0.05 m/s	0.76	R	⬢
Pino et al. (⁴²¹)	ε_G	Air	Kerosene	-	P : atm/ T : 298 K/ U_G : 0.1-0.175	0.29	PfP	⊙
Daly et al. (¹⁷⁴)	ε_G, d_S	Air	Sasol wax	-	P : atm/ T : 538 K/ U_G : 0.02-0.12	0.05	PfP	⬢
Grund et al. (¹⁷⁵)	$\varepsilon_G, \varepsilon_{G-Small}, k_L a, \varepsilon_{G-Large}, d_{S-Small}, d_{S-Large}$	Air	Water, methanol, toluene, ligroin	-	P : atm/ T : 293/ U_G : 0.103-0.195 m/s	0.15	PfP	⬢
Saxena et al. (⁴²²)	ε_G	Air	Water	-	P : atm/ T : 343, 353 K/ U_G : 0.01-0.3 m/s	0.305	BC	⬢
Wilkinson et al. (¹⁷⁶)	ε_G	SF ₆ , He, Ar, N ₂ , CO ₂	Water, mono-ethylene glycol, n-heptane	-	P : 0.1-2 MPa/ T : 293, 313K/ U_G : 0.03-0.28 m/s	0.158, 0.23	R	△
Chabot and Lasa (¹⁷⁷)	ε_G	N ₂	Paraffin oil	-	P : atm/ T : 373, 448 K/ U_G : 0.022-0.146 m/s	0.2	PfP	▽

Authors	Parameters	Gas	Liquid	Solid	Operating variable	D _C , m	Sparger	Legend
Ellenberger and Krishna ⁽⁴²³⁾	$\varepsilon_G, \varepsilon_{G-Small}, \varepsilon_{G-Large}$	Air, Ar, He, SF ₆	Water, tetradecane, paraffin oil	-	P : atm./ T : 298K/ U_G : 0.06-0.7 m/s	0.10, 0.19, 0.38	SP	▲
Wilkinson et al. ⁽²⁰⁰⁾	$\varepsilon_G, d_S, k_{La}$	SF ₆ , He, Ar, N ₂ , CO ₂	0.8M sodium sulfite+water, water, mono-ethylene glycol, n-heptane	-	P : 0.1-2 MPa/ T : 293K/ U_G : 0.03-0.28 m/s	0.15, 0.158, 0.23	R	▲
Dewes et al. ⁽³⁷⁰⁾	ε_G, k_{La}	Air	Water+0.8M sodium sulfate	-	P : 0.1-0.8 MPa/ T : amb./ U_G : 0.03-0.08 m/s	0.115	PfP	▲
Eickenbusch et al. ⁽³²⁰⁾	ε_G, k_{La}	Air	Water + hydroxypropyl guar	-	P : atm./ T : amb./ U_G : 0.009-0.09 m/s P : 0.1-12.2 MPa/ T : amb./ U_G : 0.027-0.075 m/s	0.19, 0.29, 0.60	PfP, R	■
Jiang et al. ⁽²³⁵⁾	ε_G, d_S	N ₂	Paratherm NF	-	P : atm./ T : amb./ U_G : 0.02-0.08 m/s/ C_V : 3 vol.%	0.0508	R	◆
Choi et al. ⁽⁴²⁴⁾	ε_G, k_{La}	Air	Water	Glass beads	P : atm./ T : amb./ U_G : 0.02-0.08 m/s/ C_V : 3 vol.%	Rect: 0.456x0.153	PfP	▲
Hyndman et al. ⁽⁴²⁵⁾	$\varepsilon_G, \varepsilon_{G-Small}, \varepsilon_{G-Large}$	Air, Ar	Water	-	P : atm./ T : amb./ U_G : 0.04-0.15 m/s P : 0.126-0.767 MPa/ T : amb.	0.20	PfP	▼
Inga ⁽⁵⁶⁾	$\varepsilon_G, \varepsilon_{G-Small}, k_{La}, \varepsilon_{G-Large}, d_{S-Small}, d_{S-Large}$	H ₂ , CO, CH ₄ , N ₂	Hexanes	Iron oxides	U_G : 0.06-0.35 m/s/ C_V : 0-21.76 vol.% P : atm./ T : amb./ U_G : 0.085-0.218 m/s/ C_V : 0-36 vol.%	0.316	S	▲
Krishna et al. ⁽⁴²⁶⁾	ε_G	Air	Paraffin oil	Silica	P : atm./ T : amb./ U_G : 0.018-0.038 m/s P : 0.1-0.9 MPa/ T : amb./ U_G : 0.12-0.2 m/s	0.38	SP	⊙
Laari et al. ⁽¹⁸¹⁾	ε_G, k_{La}	Air	Water	-	P : atm./ T : amb./ U_G : 0.013-0.15 m/s P : atm./ T : amb./ U_G : 0.05-0.26 m/s C_V : 10-35 vol.%	0.98	S-ON	◆
Letzel et al. ⁽¹⁸²⁾	ε_G	N ₂	Water	-	P : atm./ T : amb./ U_G : 0.013-0.15 m/s	0.15	PfP	●
Camarasa et al. ⁽²⁰³⁾	ε_G, d_S	Air	Water	-	P : atm./ T : amb./ U_G : 0.013-0.15 m/s	0.1	PoP	▽
Gandhi et al. ⁽⁴²⁷⁾	ε_G	Air	Water	Glass beads	P : atm./ T : amb./ U_G : 0.05-0.26 m/s C_V : 10-35 vol.%	0.15	S	◆

Authors	Parameters	Gas	Liquid	Solid	Operating variable	D _C , m	Sparger	Legend
Inga and Morsi (368)	ε_G	H ₂ , CO, CH ₄ , N ₂	Hexanes	Iron oxides	P : 0.126-0.767 MPa/ T : amb./ U_G : 0.06-0.35 m/s/ C_V : 0-21.76 vol.% P : 0.1-0.6 MPa/ T : amb./	0.316	S	▲
Kang et al. (185)	ε_G, k_{La}	Air	Water+CMC	-	U_G : 0.02-0.20 m/s P : 0.1-1.3 MPa/ T : amb./	0.152	M-ON	▽
Letzel et al. (183)	ε_G, k_{La}	N ₂	Water	-	U_G : 0.12-0.5 m/s P : 0.1-2.86 MPa/ T : 301 K/ U_G : 0.04-0.333 m/s/ C_V : 0-19.1 vol.%	0.15	PfP	●
Luo et al. (428)	ε_G	N ₂	Paratherm NF	Alumina	P : atm./ T : amb./ U_G : 0.01-0.5 m/s P : atm./ T : 298 K/ U_G : 0.008-0.033 m/s	0.102	PfP	◊
Krishna et al. (429)	ε_G	Air	Water + ethanol	Silica	P : atm./ T : amb./ U_G : 0.01-0.5 m/s P : atm./ T : 298 K/ U_G : 0.008-0.033 m/s	0.15	PfP	■
Shimizu et al. (430)	ε_G, k_{La}	Air	Water	-	P : atm./ T : amb./ U_G : 0.023-0.090 m/s	0.155-0.200	PfP, R	⊗
Chen et al. (431)	ε_G	Air	Water	-	P : atm./ T : amb./ U_G : 0.023-0.090 m/s	0.2, 0.4, 0.8	PfP	●
Jamialahmadi et al. (432)	d_S	Air	Water, +methanol, +ethanol, +propanol, +isopropanol, +glycerol, +potassium chloride	-	P : atm./ T : 295 K/ U_G : 0.003-0.0086 m/s	0.1, Rect: 0.05x0.1	S-ON	⊠
Jordan and Schumpe (190)	ε_G, k_{La}	N ₂ , He, Air	Ethanol, decalin, 1-butanol, toluene	-	P : 0.1- 4.0 MPa/ T : 293, 343 K/ U_G : 0.02-0.22 m/s P : atm./ T : amb./ U_G : 0.04-0.11 m/s/ C_V : 0-1.429 10 ⁻³ vol.% P : 1.1 MPa/ T : 373-433 K/ U_G : 0.0035 m/s	0.1	PfP	▲
Kluytmans et al. (433)	ε_G	N ₂	Water	Carbon	P : atm./ T : amb./ U_G : 0.04-0.11 m/s/ C_V : 0-1.429 10 ⁻³ vol.% P : 1.1 MPa/ T : 373-433 K/ U_G : 0.0035 m/s	0.3	PfP	▽
Pohorecki et al. (195)	ε_G, d_S	N ₂	Cyclohexane	-	P : atm./ T : amb./ U_G : 0.06-0.29 m/s P : 0.1- 4.0 MPa/ T : 293, 343 K/ U_G : 0.02-0.22 m/s	0.304	M-ON	⊗
Veera et al. (434)	ε_G	Air	Water, water + n-butanol	-	P : atm./ T : amb./ U_G : 0.06-0.29 m/s P : 0.1- 4.0 MPa/ T : 293, 343 K/ U_G : 0.02-0.22 m/s	0.385	PfP, S-ON	⊠
Jordan et al. (191)	ε_G, k_{La}	N ₂ , He	Ethanol, decalin, 1-butanol, toluene	-	P : 0.1- 4.0 MPa/ T : 293, 343 K/ U_G : 0.02-0.22 m/s	0.1	PfP	▲

Authors	Parameters	Gas	Liquid	Solid	Operating variable	D _C , m	Sparger	Legend
Schäfer et al. (435)	d_S	N ₂	Water, ethanol, cyclohexane, cyclohexanone, cyclohexanol	-	P : 0.1-4.5 MPa/ T : 293-448 K/ U_G : 0.65-2.5 10 ⁻³ m/s	0.058	R, PoP	⊙
Syeda et al. (436)	ε_G	Air	Methanol+propanol, ethylene glycol+water, propanol+water	-	P : atm./ T : amb./ U_G : 0.32 m/s	0.09	PfP	⊠
Jordan et al. (437)	$\varepsilon_G, \varepsilon_{G-Small}, \varepsilon_{G-Large}$	N ₂ , He	Ethanol, decalin, 1-butanol, toluene	-	P : 0.1- 4.0 MPa/ T : 293K/ U_G : 0.01-0.22 m/s	0.1	PfP, PoP	△
Li et al. (438)	$\varepsilon_G, \varepsilon_{G-Small}, \varepsilon_{G-Large}$	Air	Water	Glass beads	P : atm./ T : amb./ U_G : 0.05-0.3 m/s	0.28	S	◇
Behkish et al. (254)	$\varepsilon_G, \varepsilon_{G-Small}, \varepsilon_{G-Large}, d_{S-Small}, d_{S-Large}$	N ₂ , He	Isopar-M	Al ₂ O ₃	P : 0.7-3.0 MPa/ T : 300-453 K/ U_G : 0.07-0.39 m/s/ C_V : 0-20 vol.%	0.29	S	■
Behkish (395)	$\varepsilon_G, \varepsilon_{G-Small}, \varepsilon_{G-Large}, d_{S-Small}, d_{S-Large}, k_{La}$	H ₂ , N ₂ , CO, He, CH ₄	Isopar-M	Glass beads, Al ₂ O ₃	P : 0.17-3.00 MPa/ T : 298 K/ U_G : 0.06-0.39 m/s/ C_V : 0-36 vol.%	0.29, 0.316	S	○
Lau et al. (439)	ε_G, k_{La}	Air	Paratherm NF	-	P : 0.1-4.24 MPa/ T : 298, 365 K/ U_G : 0.019-0.039 m/s/ U_L : 0.8-3.2 10 ⁻³ m/s	0.1016	PfP	⊕
Sehabiague et al. (440)	$\varepsilon_G, k_{La}, \varepsilon_{G-Small}, \varepsilon_{G-Large}, d_{S-Small}, d_{S-Large}$	H ₂ , N ₂	Sasol wax, Isopar M	Al ₂ O ₃ , Iron oxides	P : 0.17-3.00 MPa/ T : 298-453 K/ U_G : 0.06-0.39 m/s/ C_V : 0-20 vol.%	0.29	S	□
Vandu and Krishna (441)	ε_G, k_{La}	N ₂	Water, tetradecane, paraffin oil, ethanol, tellus oil	Silica	P : atm./ T : amb./ U_G : 0.01-0.42 m/s/ C_V : 0-25 vol.%	0.10, 0.15, 0.38, 0.63	S, PfP	●
This Study (442)	$\varepsilon_G, \varepsilon_{G-Small}, \varepsilon_{G-Large}, d_{S-Small}, d_{S-Large}, k_{La}$	N ₂ , air	Toluene, toluene+benzoic acid+benzaldehyde	-	P : 0.18-0.82 MPa/ T : amb./ U_G : 0.056-0.15 m/s	0.316	S	●

Table 50: Value of α used in Equation (6-67)

<i>Distributor</i>	ζ , %	α , -	K_d , $m^{-\alpha}$
PfP	< 0.055	0.017	1.364
PfP	≥ 0.055 and ≤ 0.3	0.303	1.364
PfP	> 0.3	0.293	1.364
M-ON		0.303	1.364
S-ON		0.134	1.205
R, S		0.015	1.000
BC		0.500	1.553
PoP, SP		0.650	1.533

Table 51: Upper and Lower limits of the variables in Equations (6-64) through (6-71)

<i>Variables</i>	<i>Minimum value</i>	<i>Maximum value</i>
P_T , MPa	0.1	19.8
P_S , MPa	0.0	0.7
U_G , m/s	$3.5 \cdot 10^{-3}$	0.574
C_v , vol%	0	36
X_w , wt. %	50	100
T , K	275	538
M_B , kg/kmol	18	730
M_A , kg/kmol	2	44
D_{AB} , m^2/s	$2.78 \cdot 10^{-8}$	$1.25 \cdot 10^{-11}$
dp , m	$4.2 \cdot 10^{-5}$	0.0003
ρ_P , kg/m^3	700	4000
ρ_G , kg/m^3	0.06	223.77
ρ_L , kg/m^3	633	1583
μ_L , $10^{-3} Pa \cdot s$	0.16	398.80
σ_L , $10^{-3} N/m$	8.4	75
D_C , m	0.0382	7.6200
Γ , -	0.06	143800
ζ , %	0.0097	75

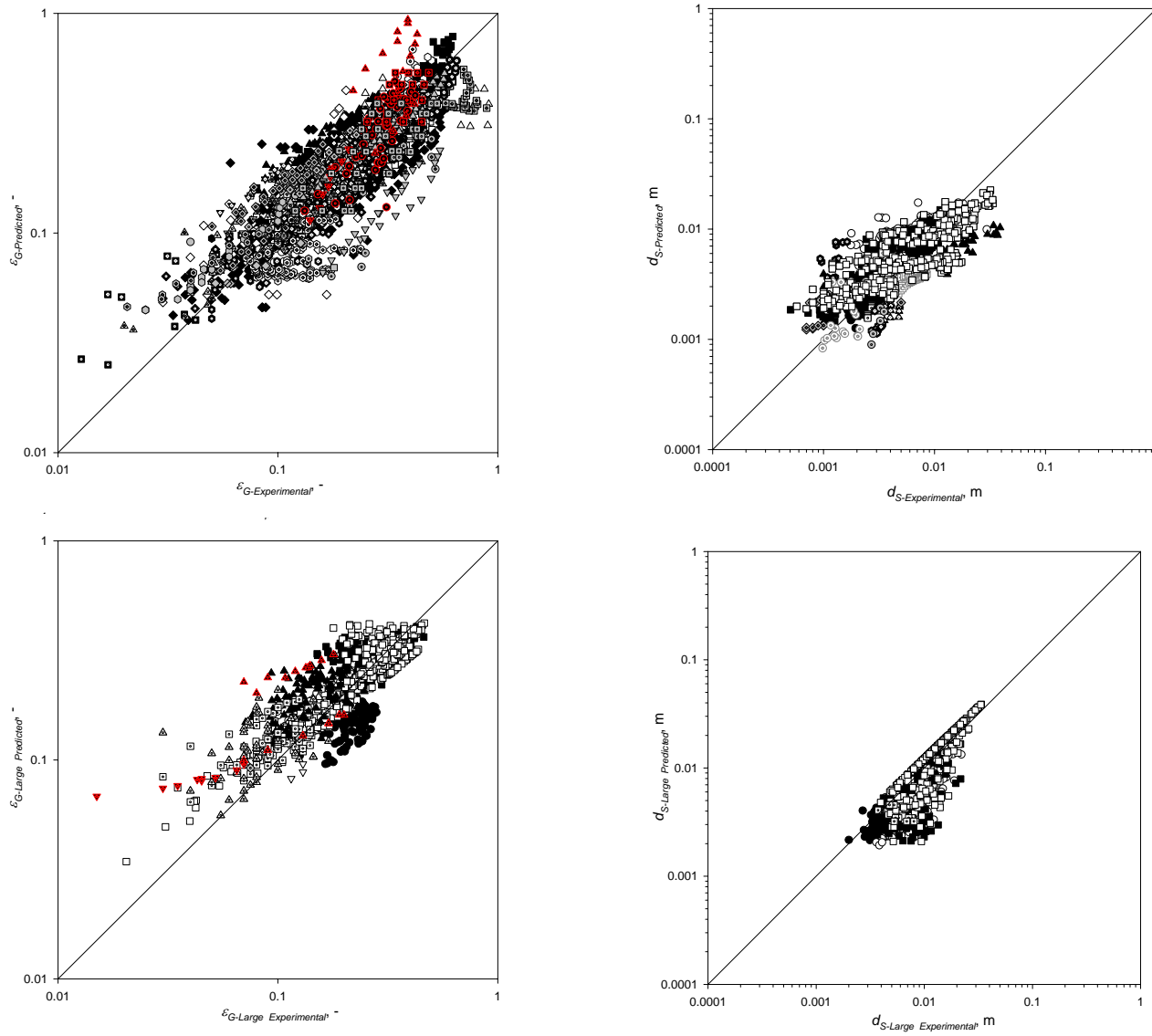


Figure 71: Comparison between ε_G , $\varepsilon_{G-Large}$, d_S and $d_{S-Large}$ Experimental and Predicted values using Empirical Correlations

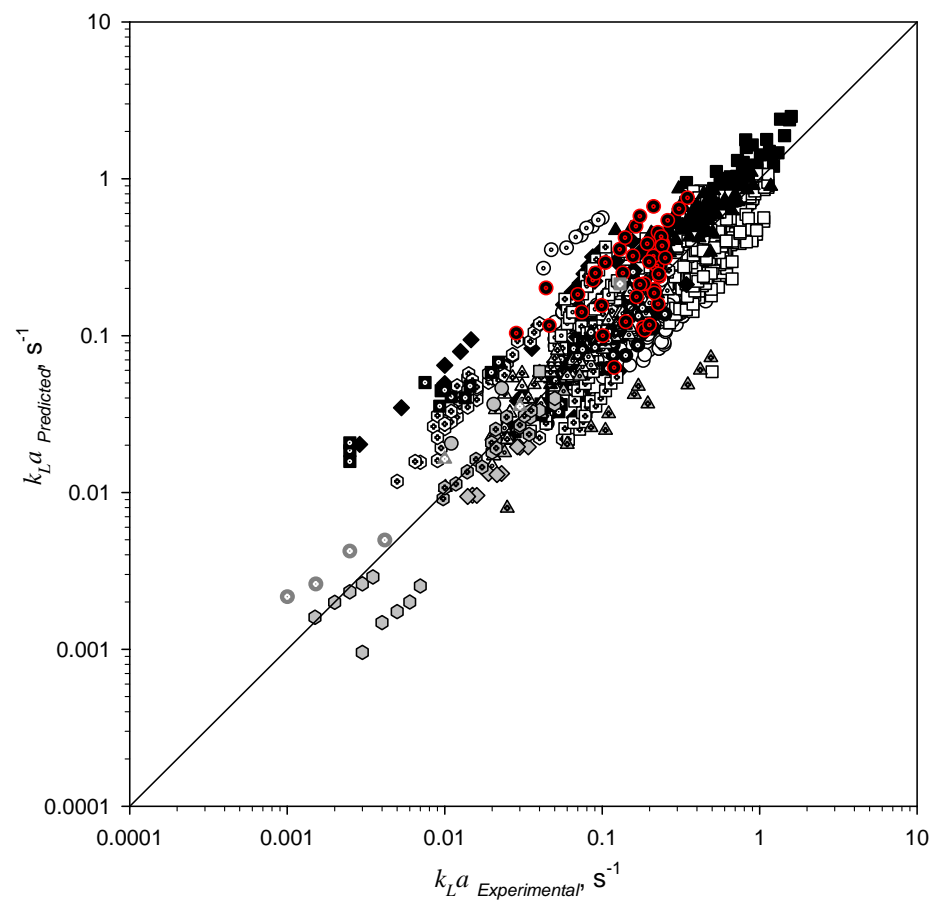


Figure 72: Comparison between $k_L a$ Experimental and Predicted values using Empirical Correlations

6.5.2 Statistical Correlations of the Hydrodynamic and Mass Transfer Parameters in the BCR

In order to improve the predictions of the hydrodynamic and mass transfer parameters and incorporate the effect of benzoic acid and benzaldehyde presence during the liquid-phase toluene oxidation process, statistical correlations were developed. It should also be mentioned that despite the fact statistical correlations are valid exclusively for the systems used to obtain them; they are easier to develop and enjoy extremely high confidence levels when compared with conventional “empirical” correlations. In this study, statistical correlations were developed for the systems studied using the statistical software package, Minitab Version 9.1 for Mainframe. The correlations are in the form of Equation (6-72).

$$\ln(Y) = \beta_0 + \sum_{i=1}^5 \beta_i x_i + \sum_{i=1}^5 \sum_{j=1}^5 \beta_{ij} x_i x_j + \zeta \exp\left(\sum_{i=1}^5 \zeta_i x_i\right) + \sum_{i=1}^5 \alpha_i \exp(\gamma_i x_i) \quad (6-72)$$

where the coded variables are for Pressure:

$$x_1 = \frac{\sqrt{2}}{0.3} (P - 0.5) \quad (6-73)$$

for gas velocity

$$x_2 = \frac{\sqrt{2}}{0.04} (U_G - 0.1) \quad (6-74)$$

for wt. % of Benzoic Acid added

$$x_3 = \frac{\sqrt{2}}{5} (\text{wt. \%}_{BZC} - 5) \quad (6-75)$$

for wt. % of Benzaldehyde added

$$x_4 = \frac{\sqrt{2}}{5} (\text{wt. \%}_{BZL} - 5) \quad (6-76)$$

for Molecular weight of the gas

$$x_5 = 2\sqrt{2} (M_{W-Gas} - 28.5) \quad (6-77)$$

and the corresponding coefficients are given Table 52. Figures 73 and 74 present a comparison between experimental and predicted d_s , ε_G , a , $k_L a$ and k_L values, and as can be observed the predictions using the statistical correlations are more accurate (95% confidence levels) than those using empirical correlations.

Table 52: Coefficients of the Statistical Correlations for the Hydrodynamic and Mass Transfer Parameters

<i>Coefficients</i>	d_S	$d_{S-Small}$	ε_G	$\varepsilon_{G-Large}$	a	a_{-Small}	$k_L a$	k_L
β_0	-9.92	-6.89	$-8.42 \cdot 10^{-1}$	-1.52	7.08	4.02	$-9.08 \cdot 10^{-1}$	-9.80
β_1	$-6.80 \cdot 10^{-1}$	$-8.11 \cdot 10^{-2}$	$1.57 \cdot 10^{-1}$	$5.75 \cdot 10^{-3}$	$4.01 \cdot 10^{-1}$	$-4.88 \cdot 10^{-1}$	$1.65 \cdot 10^{-1}$	$-6.15 \cdot 10^{-1}$
β_2		$1.88 \cdot 10^{-2}$	$1.49 \cdot 10^{-1}$	$1.05 \cdot 10^{-1}$	$1.63 \cdot 10^{-1}$	$5.79 \cdot 10^{-3}$	$2.63 \cdot 10^{-1}$	$9.66 \cdot 10^{-2}$
β_3	$-1.76 \cdot 10^{-1}$	$-1.55 \cdot 10^{-2}$	$9.76 \cdot 10^{-2}$	-	-	-	-	$-2.20 \cdot 10^{-1}$
β_4	$-1.63 \cdot 10^{-1}$	$-1.64 \cdot 10^{-2}$	$1.04 \cdot 10^{-1}$	-	-	-	-	$-3.98 \cdot 10^{-2}$
β_{11}	-	$2.42 \cdot 10^{-2}$	$-4.35 \cdot 10^{-2}$	-	-	$-6.88 \cdot 10^{-1}$	-	-
β_{22}	-	-	-	$-3.30 \cdot 10^{-2}$	-	$-3.69 \cdot 10^{-2}$	-	-
β_{12}	-	-	-	-	-	$-2.62 \cdot 10^{-2}$	-	-
ξ	3.82	$-9.84 \cdot 10^{-2}$	$-4.01 \cdot 10^{-2}$	$4.22 \cdot 10^{-1}$	$9.23 \cdot 10^{-2}$	$5.51 \cdot 10^{-1}$	$5.23 \cdot 10^{-1}$	1.80
ζ_1	$1.44 \cdot 10^{-1}$	$4.43 \cdot 10^{-3}$	$2.53 \cdot 10^{-1}$	$6.68 \cdot 10^{-2}$	$-2.35 \cdot 10^{-1}$	$-6.02 \cdot 10^{-1}$	$-9.17 \cdot 10^{-2}$	$2.50 \cdot 10^{-1}$
ζ_2	$1.19 \cdot 10^{-2}$	$6.94 \cdot 10^{-1}$	$4.37 \cdot 10^{-1}$	$7.44 \cdot 10^{-2}$	$-9.94 \cdot 10^{-2}$	$-1.34 \cdot 10^{-1}$	$-1.80 \cdot 10^{-1}$	$-2.59 \cdot 10^{-5}$
ζ_3	$5.15 \cdot 10^{-2}$	2.51	2.44	1.65	2.41	1.29	1.08	$1.10 \cdot 10^{-1}$
ζ_4	$4.53 \cdot 10^{-2}$	1.99	2.44	1.68	2.38	1.23	1.11	$4.94 \cdot 10^{-2}$
ζ_5	$7.42 \cdot 10^{-3}$	1.83	$1.74 \cdot 10^{-1}$	1.28	$1.60 \cdot 10^{-2}$	$6.21 \cdot 10^{-1}$	$6.80 \cdot 10^{-1}$	$2.26 \cdot 10^{-2}$
α_1	-	-	-	-	-	1.55	-	-
γ_1	-	-	-	-	-	$7.05 \cdot 10^{-1}$	-	-
α_2	-	-	-	-	-	1.28	-	-
γ_2	-	-	-	-	-	$1.53 \cdot 10^{-1}$	-	-

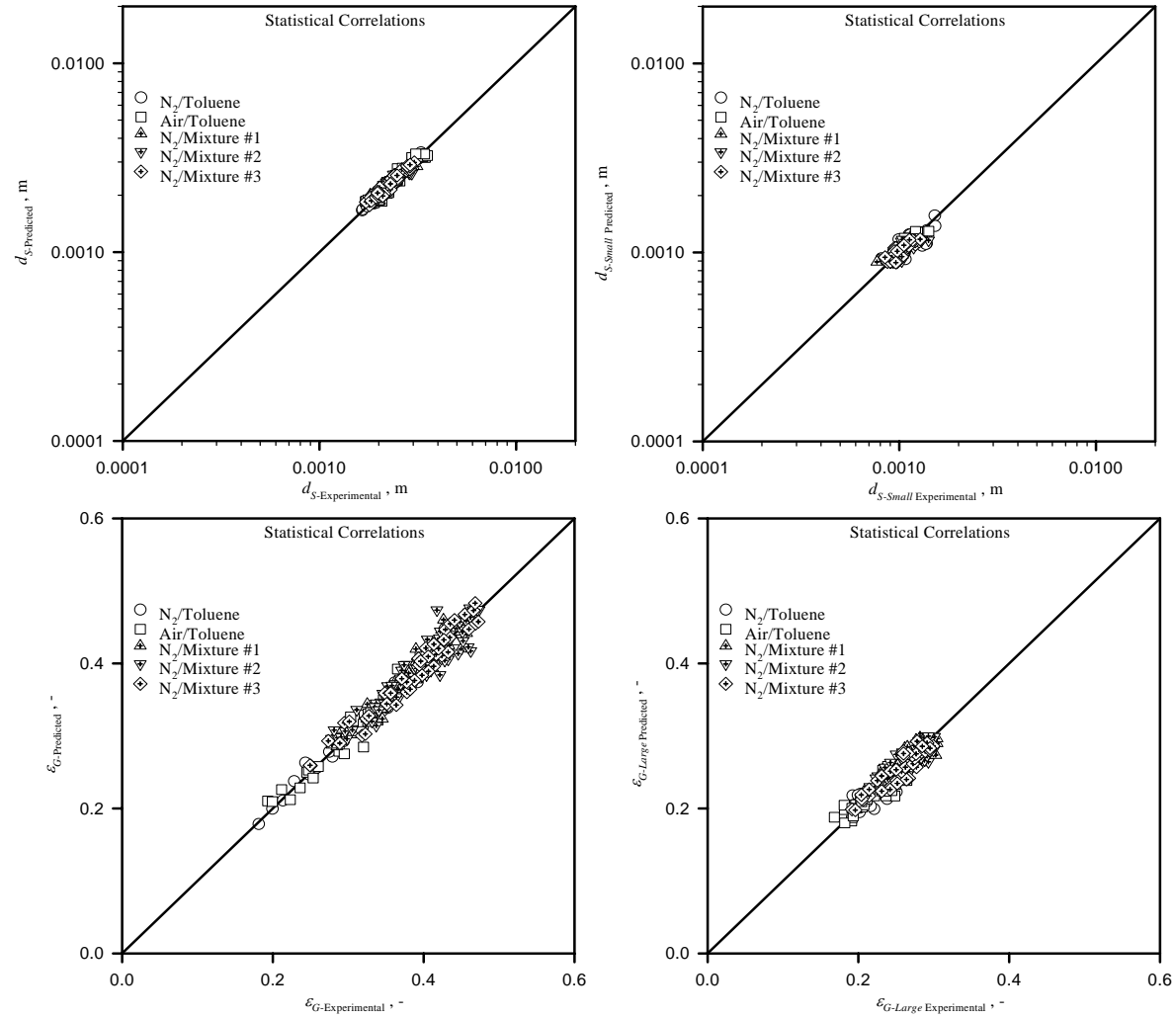


Figure 73: Comparison between Experimental and Predicted d_S , $d_{S-Small}$, ϵ_G and $\epsilon_{G-Large}$ Values Using the Statistical Correlations

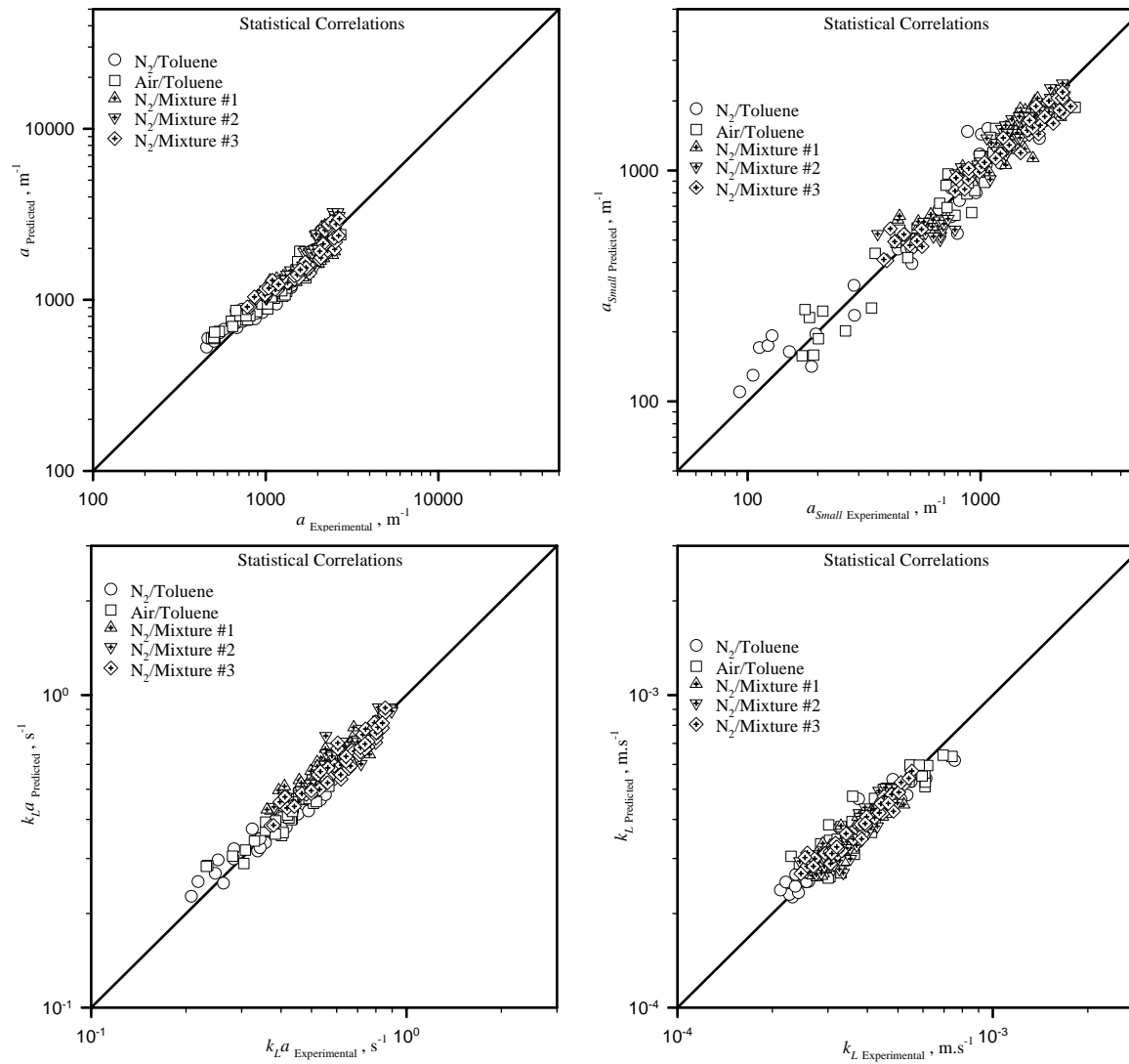


Figure 74: Comparison between Experimental and Predicted a , a_{Small} , $k_L a$ and k_L Values Using the Statistical Correlations

6.5.3 BPNN Correlations of the Hydrodynamic and Mass Transfer Parameters in the BCR

The PITTNET software package was next used to build the BPNNs. The same database (3881 experimental points) as mentioned above was used to develop BPNN correlations for ε_G , $\varepsilon_{G-Large}$, d_S , $d_{S-Large}$ and $k_L a$. The BPNNs developed for these parameters were validated using 25% of the total database and the cross validation technique. Table 53 shows the regression coefficient (R^2) and standard deviation (σ) and Tables 54 through 59 present the input variables, architecture and weights of the constructed BPNNs for predicting ε_G , $\varepsilon_{G-Large}$, d_S , $d_{S-Large}$ and $k_L a$. This statistical analysis proves that the developed BPNNs can predict the values of ε_G , $\varepsilon_{G-Large}$, d_S , $d_{S-Large}$ and $k_L a$ with much higher accuracy than that of the corresponding empirical correlations as can be also observed in Table 53 and Figures 75 and 76.

6.5.4 Calculation Algorithm of the Hydrodynamic and Mass Transfer Parameters in the BCR

The empirical and BPNNs correlations developed in this study were used, in parallel, in the algorithm to predict the hydrodynamic and mass transfer parameters in BCRs and SBCRs as depicted in Figure 77. The algorithm consists of the following steps:

1. Calculate ε_G , Equation (6-64) or Table 55
2. Calculate d_S , Equation (6-70) or Table 57
3. Obtain a using Equation (6-78):

$$a = \frac{6\varepsilon_G}{(1-\varepsilon_G)d_S} \quad (6-78)$$

4. Calculate $k_L a$, Equation (6-71) or Table 59
5. Obtain k_L using Equation (6-79):

$$k_L = \frac{k_L a}{a} = \frac{k_L a (1-\varepsilon_G) d_S}{6\varepsilon_G} \quad (6-79)$$

6. Calculate $\varepsilon_{G-Large}$, Equation (6-65) or Table 56
7. If $\varepsilon_{G-Large}$ is greater than or equal to ε_G , there is only one class of bubbles and calculations are complete. If $\varepsilon_{G-Large}$ is less than ε_G , small and large gas bubbles coexist and proceed with the calculation.
8. Calculate $\varepsilon_{G-Small}$, Equation (6-66)
9. Calculate $d_{S-Large}$, Equation (6-70) or Table 58
10. Calculate $d_{S-Small}$, Equation (6-80):

$$\frac{\varepsilon_{G-Small}}{d_{S-Small}} = \frac{\varepsilon_G}{d_S} - \frac{\varepsilon_{G-Large}}{d_{S-Large}} \quad (6-80)$$

11. Calculate a_{Large} , Equation (6-81):

$$a_{Large} = \frac{6\varepsilon_{G-Large}}{(1-\varepsilon_G)d_{S-Large}} \quad (6-81)$$

12. Calculate a_{Small} , Equation (6-82):

$$a_{Small} = a - a_{Large} \quad (6-82)$$

13. Calculate $k_L a_{Large}$ using Equation (6-71) or Table 59 by employing $\varepsilon_{G-Large}$ and $d_{S-Large}$ instead of ε_G and d_S

14. Calculate $k_L a_{Small}$ using Equation (6-71) or Table 59 by inserting $\varepsilon_{G-Small}$ and $d_{S-Small}$ instead of ε_G and d_S

15. Calculate $k_{L-Large}$ using Equation (6-79) by employing $k_L a_{Large}$ and a_{Large}

16. Calculate $k_{L-Small}$ using Equation (6-79) by employing $k_L a_{Small}$ and a_{Small} .

It should be mentioned that the use of Equation (6-71) to calculate $k_L a$ for small and large gas bubbles using their corresponding gas holdup and Sauter mean bubble diameter is an accurate approach; because it underscores the fact that the mass transfer behavior of BCRs and SBCRs is controlled by the gas-liquid interfacial area [35,65,84], which is a function of d_S and ε_G as shown in Equation (6-71). de Swart and Krishna [94] estimated $k_L a$ for large and small gas bubbles by measuring the corresponding gas-liquid interfacial areas and calculating k_L for large and small bubbles using the correlations for mobile and rigid gas bubbles developed by Calderbank and Moo-Young [82]. This indirect method by de Swart and Krishna [94] for estimating $k_L a$ of small and large gas bubbles, however, may result in inaccurate $k_L a$ values due to the compounded errors in both k_L and a . Also, Grund et al. [49] reported that the Sauter mean bubble diameter is independent of the gas velocity; and proposed Equation (6-83) for calculating $k_L a_{Small}$ in the churn-turbulent flow regime:

$$\left(\frac{k_L a}{\varepsilon_G} \right)_{Small} = \left(\frac{k_L a}{\varepsilon_G} \right)_{Homogeneous} \quad (6-83)$$

If d_S is constant, i.e. independent of the flow regime, Equation (6-83) gives that $(k_L)_{Small}$ in the churn-turbulent flow regime = $(k_L)_{Homogeneous}$ which is invalid given that the Churn-turbulent flow regime is characterized by strong turbulence and back-mixing which enhance both k_L and a .

Table 53: Statistical Analysis of the Empirical and BPNN Correlations

<i>Parameters</i>	<i>R², %</i>		<i>Standard Deviation, %</i>	
	Empirical	BPNN	Empirical	BPNN
ε_G	75	90	21	19
$\varepsilon_{G-Large}$	71	93	27	14
d_S	70	90	30	18
$d_{S-Large}$	79	95	18	12
k_{La}	85	93	18	10

Table 54: Architecture, Weights of the d_S , $d_{S-Large}$ and k_{La} BPNN Correlations

Parameters	$Ln \varepsilon_G$						$ln d_S$			$d_{S-Large}$			$ln k_{La}$		
	Max	Min		Max	Min		Max	Min		Max	Min		Max	Min	
	-0.094	-4.775		0.463	0		-3.244	-7.593		0.059	0.002		0.465	-6.725	
Variables	Position in BPNN	Max	Min	Position in BPNN	Max	Min	Position in BPNN	Max	Min	Position in BPNN	Max	Min	Position in BPNN	Max	Min
$U_G, m/s$	1	0.75	0.003	1	0.75	0.04	1	0.3640	0.0003	1	0.3640	0.0569	1	0.4000	0.0015
$\rho_L, kg/m^3$	2	1583	633	2	1000	680	2	1113	633	2	1000	688	2	1583	680
$\mu_L, Pa/s$	3	0.3988	0.00019	3	0.0092	0.00032	3	0.04430	0.00016	3	0.00920	0.00047	3	0.10139	0.00031
$\sigma_L, N/m$	4	0.075	0.0084	4	0.0728	0.0162	4	0.0750	0.0084	4	0.0728	0.0162	4	0.0750	0.0162
$M_{W-1}, kg/kmol$	5	730	18	5	567.38	18	5	730	18	5	567	18	-	-	-
$D_{AB}, m^2/s$	-			6	29.79	0.166	-	-	-	-	-	-	5	$2.78 \cdot 10^{-8}$	$1.25 \cdot 10^{-11}$
$\rho_G, kg/m^3$	6	178.44	0.07	7	29	2	6	223.77	0.09	6	29.10	0.14	6	46.00	0.08
$M_{W-2}, kg/kmol$	7	44	2	-	-	-	7	44	2	7	29	2	-	-	-
D_C, m	8	5.5	0.0382	-	-	-	8	5.5	0.05	-	-	-	7	7.6200	0.0508
$\zeta, \%$	9	75	0.0096	8	75	0.07	9	75.00	0.015	-	-	-	-	-	-
d_p, m	10	0.0003	0	9	$4.2 \cdot 10^{-5}$	0	10	$4.2 \cdot 10^{-5}$	0	8	$4.2 \cdot 10^{-5}$	0	8	0.0003	0
$\rho_P, kg/m^3$	11	4000	0	10	4000	0	11	4000	0	9	3218	0	9	4000	0
$\varepsilon_G, -$	-	-	-	11	0.66	0.03	12	0.62	0.03	10	0.62	0.08	10	0.62	0.01
d_S, m	-	-	-	-	-	-	-	-	-	11	0.0336	0.0005	11	0.0336	0.0006
$\varepsilon_{G-Small}, -$	-	-	-	-	-	-	-	-	-	12	0.46	0	-	-	-
$\varepsilon_{G-Large}, -$	-	-	-	-	-	-	-	-	-	13	0.46	0.02	-	-	-
$X_{W_s}, -$	12	100	50	12	100	88	13	100.0	54.2	14	100	88	12	100.0	56.2
$C_{V_s}, -$	13	36	0	13	36	0	14	36	0	15	36	0	13	36	0
Sparger type	14	1	0	14	1	0	15	1	0	-	-	-	-	-	-

Table 56: Architecture, Weights of the $\varepsilon_{G-Large}$ BPNN Correlation

<i>1st hidden Layer</i> <i>Weights $u_{i,j}$</i>	1	2	3	4	5	6	7	8	9	10	11	12	13	14
1	3.37	-1.14	2.76	5.58	-7.47	1.00	3.27	2.94	2.69	-6.77	0.72	-0.69	-9.70	1.24
2	4.64	1.71	-4.60	3.55	-8.14	0.74	0.89	0.57	0.63	3.06	-2.22	1.03	-3.09	0.30
3	3.92	-7.68	-0.99	1.50	-0.20	-0.45	-0.10	0.87	-3.26	-2.94	2.87	-1.10	-5.07	1.68
4	1.70	0.00	9.03	-1.94	-7.52	-0.14	-0.64	-1.21	-2.75	0.57	-4.37	0.24	10.34	-11.82
5	1.55	-0.03	0.47	-0.44	0.13	0.16	0.08	-0.12	2.42	-2.92	-4.67	0.04	1.37	0.49
6	-3.18	1.45	3.93	-5.07	2.77	6.64	-1.02	-0.73	0.85	-1.59	2.90	0.28	7.18	-1.70
7	5.16	-0.99	1.96	1.01	-0.72	-0.04	0.20	1.44	4.30	-2.62	4.70	-1.06	3.10	-8.22
8	1.45	1.13	-0.89	-3.88	0.19	0.60	0.31	2.28	-0.51	-2.00	3.60	0.58	-1.28	9.86
<i>Bias of 1st hidden Layer</i> <i>$u_{0,i}$</i>	1	2	3	4	5	6	7	8						
	0.13	-3.36	-1.20	14.23	-1.10	0.83	1.59	-7.96						
<i>Output Layer Weights</i> <i>w_i</i>	1	2	3	4	5	6	7	8						
	-1.47	-1.65	-1.61	2.45	-2.95	-1.89	1.82	3.11						
<i>Bias of Output Neuron</i> <i>w_0</i>	-1.53													

Table 57: Architecture, Weights of the d_s BPNN Correlation

1^{st} hidden Layer Weights		1	2	3	4	5	6	7	8	9	10	11	12	13	14	15
u_{ij}																
1		4.00	7.60	2.39	-2.67	2.20	-1.57	-4.37	4.21	3.58	-1.25	-0.07	1.80	0.58	1.41	-8.84
2		-2.55	0.75	2.33	2.66	2.82	0.08	2.20	1.08	-0.29	-3.46	0.31	0.03	-2.11	3.38	12.98
3		0.54	-5.00	8.17	-8.14	2.18	2.67	3.01	-3.63	-7.04	-3.78	7.72	3.15	-2.32	-8.97	-1.78
4		2.28	-0.06	2.10	0.01	-3.90	-0.62	-3.12	6.90	-0.63	4.43	0.84	-5.36	-3.51	12.83	-1.45
5		1.51	3.67	-4.44	-4.04	-1.03	-2.20	-0.58	5.32	-1.56	-2.98	-1.91	2.76	0.63	2.95	0.52
6		-2.20	5.10	1.99	-1.24	-2.99	2.04	4.24	-3.13	-2.05	1.66	-3.29	3.46	-1.57	7.54	3.47
7		2.41	-2.08	11.69	6.56	-0.01	-2.67	1.92	6.76	0.69	2.89	-0.30	2.46	-0.16	1.30	-5.32
8		4.35	-0.98	0.74	-7.50	-10.18	-6.81	1.44	4.75	1.31	-0.21	-0.05	-2.56	2.50	0.20	-0.86
9		1.22	-3.55	-5.48	-1.87	1.92	1.30	0.16	2.15	3.63	6.26	-3.08	2.22	-1.94	-2.92	-0.34
$Bias\ of\ 1^{st}\ hidden\ Layer$		1	2	3	4	5	6	7	8	9						
$u_{0,i}$		2.17	-7.32	-1.14	-4.73	-2.50	-3.77	-3.55	-1.44	-0.54						
2^{nd} hidden Layer Weights		1	2	3	4	5	6	7	8	9						
v_{ij}																
1		-3.04	-0.33	2.49	-2.71	6.73	0.05	-2.63	-2.24	3.98						
2		1.44	0.31	1.85	-4.67	-4.09	-0.84	-3.53	0.11	-2.24						
3		-6.24	1.59	-0.29	2.78	-0.48	-2.54	2.21	-9.92	-2.48						
4		-3.85	6.43	-3.06	3.45	-4.58	-0.47	-2.58	-0.52	4.52						
5		2.69	0.05	0.50	-2.27	0.00	-0.77	1.23	1.40	-4.55						
6		-2.80	4.23	-7.59	2.72	-3.41	-9.87	7.09	0.43	-4.61						
7		-1.13	-6.93	-5.12	-1.59	-0.34	-4.73	2.06	-6.59	6.57						
$Bias\ of\ 2^{nd}\ hidden\ Layer$		1	2	3	4	5	6	7								
$v_{0,i}$		-3.29	0.02	3.06	-2.50	-4.55	1.20	-1.48								
$Output\ Layer\ Weights\ w_i$		1	2	3	4	5	6	7								
		-2.59	-3.11	-2.63	1.93	-4.53	2.91	-0.69								
$Bias\ of\ Output\ Neuron\ w_0$		0.74														

Table 58: Architecture, Weights of the $d_{S-Large}$ BPNN Correlation

<i>1st hidden Layer</i> <i>Weights u_{ij}</i>	1	2	3	4	5	6	7	8	9	10	11	12	13	14	15
1	-0.63	1.27	-1.52	-1.55	-1.01	0.23	0.36	0.93	-1.01	-0.09	8.60	-0.16	0.09	0.08	-5.31
2	1.13	0.59	0.24	-1.04	0.95	0.62	-1.40	0.44	-1.26	-1.67	5.04	-22.03	0.01	-0.81	2.82
3	2.85	-1.30	1.46	0.36	0.58	-3.08	1.03	2.14	2.11	-1.35	13.30	0.84	8.36	-2.72	-0.31
4	0.18	-3.43	0.38	6.10	0.86	-0.19	-0.04	1.59	-1.73	-0.38	5.29	0.65	0.79	0.24	1.50
5	0.75	-0.15	1.41	-3.98	-3.89	0.97	-0.73	0.94	-3.15	1.50	-5.09	-0.50	-6.98	0.94	-4.14
6	-0.86	-0.95	5.20	-3.59	1.05	-1.52	4.11	-0.74	2.21	7.07	-14.70	1.13	3.77	2.04	7.36
7	1.33	-0.36	-3.55	9.12	-0.76	0.69	-2.14	-1.92	3.01	-1.97	2.12	-8.48	-1.08	-1.65	2.57
<i>Bias of 1st hidden Layer</i> <i>$u_{0,i}$</i>	1	2	3	4	5	6	7								
	0.31	-1.61	-1.25	-3.96	4.07	-1.46	-0.93								
<i>2nd hidden Layer</i> <i>Weights v_{ij}</i>	1	2	3	4	5	6	7								
1	-0.76	-16.00	0.28	6.75	-2.71	1.59	7.40								
2	-3.82	1.80	-0.72	0.98	-4.95	3.92	-0.01								
3	-2.17	0.74	-13.25	-11.13	7.11	9.33	-2.61								
4	0.75	-0.75	1.26	3.28	0.25	-0.15	0.61								
5	-3.50	-6.76	2.53	-4.50	3.90	-8.76	1.72								
<i>Bias of 2nd hidden Layer</i> <i>$v_{0,i}$</i>	1	2	3	4	5										
	1.09	3.45	6.63	-4.35	7.29										
<i>Output Layer Weights</i> <i>w_i</i>	1	2	3	4	5										
	0.23	0.46	-2.82	3.80	3.19										
<i>Bias of Output Neuron</i> <i>w_0</i>	-2.53														

Table 59: Architecture, Weights of the k_{Ia} BPNN Correlation

1^{st} hidden Layer Weights													
u_{ij}	1	2	3	4	5	6	7	8	9	10	11	12	13
1	-0.66	0.83	3.23	-4.44	-10.51	-0.92	-0.34	-10.77	-0.49	5.48	4.85	-4.64	1.09
2	-0.74	1.83	-17.81	-9.59	-11.60	-1.54	-3.90	4.37	-0.02	-0.79	-0.12	0.87	1.10
3	-1.05	-0.48	2.10	3.26	-24.01	-1.76	3.84	2.51	2.10	5.13	2.14	1.30	0.43
4	3.53	-0.53	-4.34	-4.83	-3.39	2.96	5.43	-7.05	4.21	-6.12	-1.93	-0.81	4.00
5	-0.15	12.81	13.82	-1.07	3.94	-1.46	-7.81	0.71	3.47	-1.00	-9.26	-9.20	-0.79
6	-0.38	-1.90	-0.23	0.37	-0.27	0.21	-2.18	-4.49	1.01	-4.18	-0.85	6.15	0.17
7	-4.66	-4.47	9.93	-2.94	-5.15	-3.02	15.54	3.42	-0.01	-1.91	-8.21	1.58	16.53
8	-0.81	5.35	-3.04	0.34	1.71	-1.26	-2.72	-0.58	3.10	1.72	-4.09	4.33	-1.04
$Bias\ of\ 1^{st}\ hidden\ Layer$	1	2	3	4	5	6	7	8					
$u_{0,i}$	2.35	2.83	-5.31	4.33	9.52	-4.91	4.06	-4.07					
2^{nd} hidden Layer Weights													
v_{ij}	1	2	3	4	5	6	7	8					
1	0.34	-3.68	-2.94	-6.36	2.01	-5.40	3.26	6.42					
2	-8.13	-4.29	-1.08	3.02	-3.20	12.34	-3.59	-5.25					
3	0.01	-8.98	3.26	-2.80	-3.52	0.70	-1.60	3.62					
4	11.53	-13.66	-8.49	13.99	4.83	0.32	7.37	3.31					
5	4.22	-4.54	-12.72	-8.00	-7.81	3.00	0.27	3.26					
6	-1.28	-0.70	5.85	-8.48	8.08	5.41	3.88	-7.07					
$Bias\ of\ 2^{nd}\ hidden\ Layer$	1	2	3	4	5	6							
$v_{0,i}$	-3.86	1.12	-1.00	-16.20	4.71	-1.31							
$Output\ Layer\ Weights\ w_i$	1	2	3	4	5	6							
	1.73	-1.36	2.68	1.25	1.63	-2.60							
$Bias\ of\ Output\ Neuron$													
w_0	0.36												

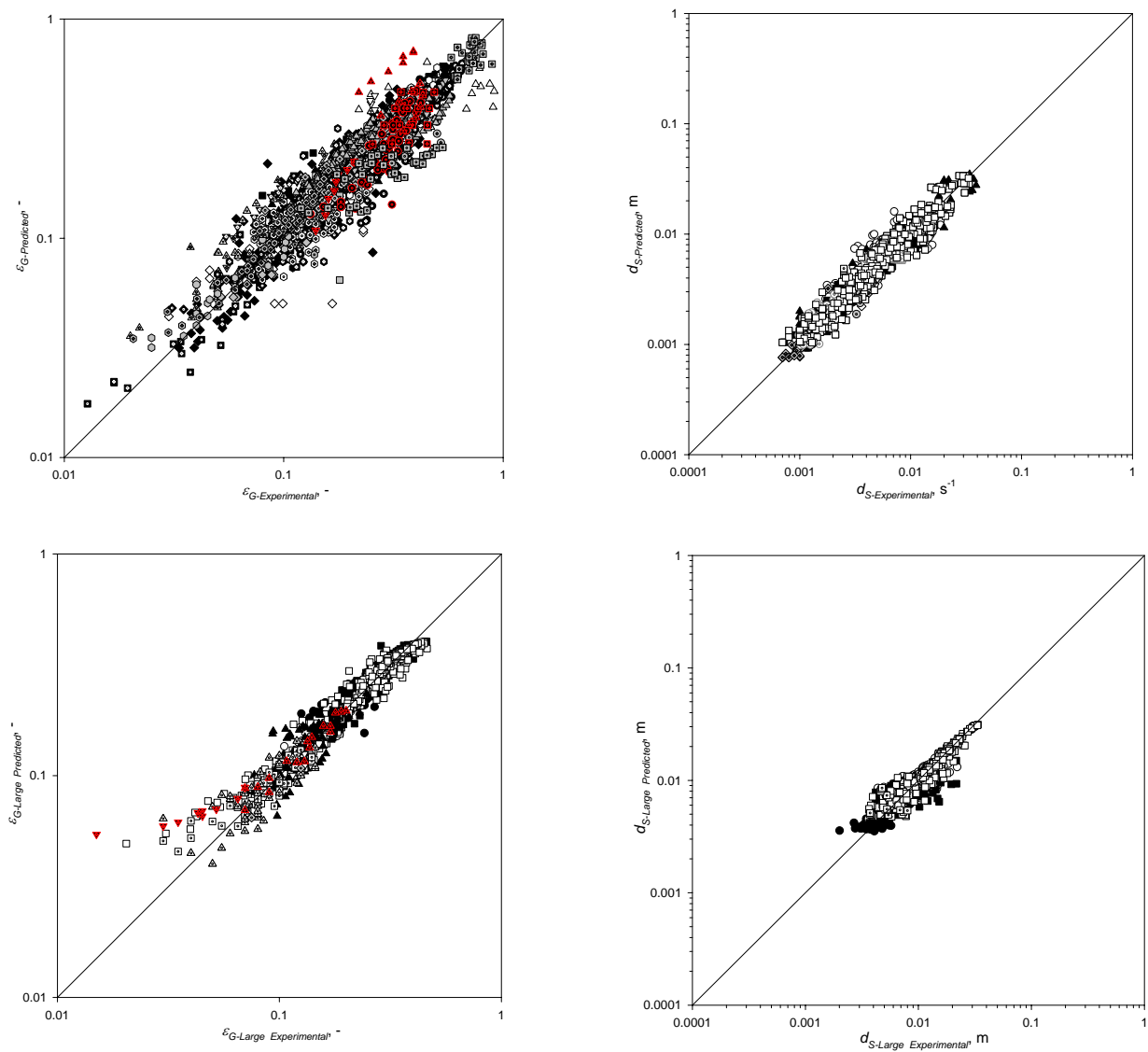


Figure 75: Comparison between ε_G , $\varepsilon_{G-Large}$, d_S and $d_{S-Large}$ Experimental and Predicted values using BPNN Correlations

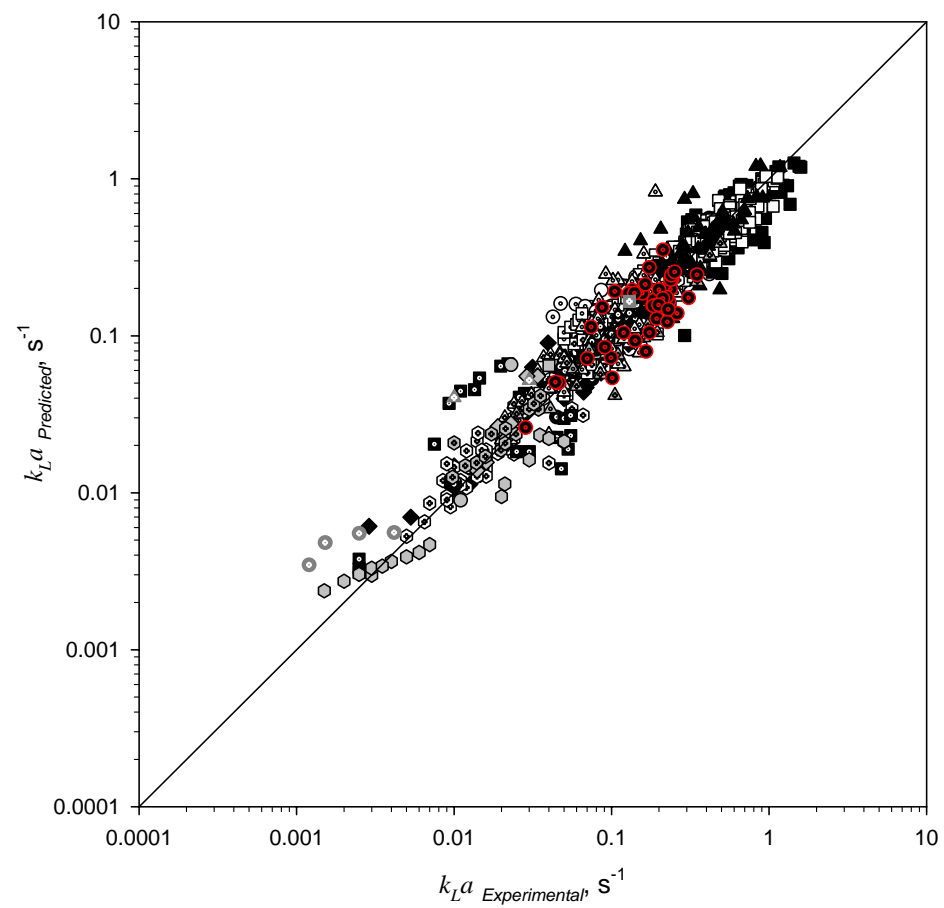


Figure 76: Comparison between $k_L a$ Experimental and Predicted values using BPNN Correlations

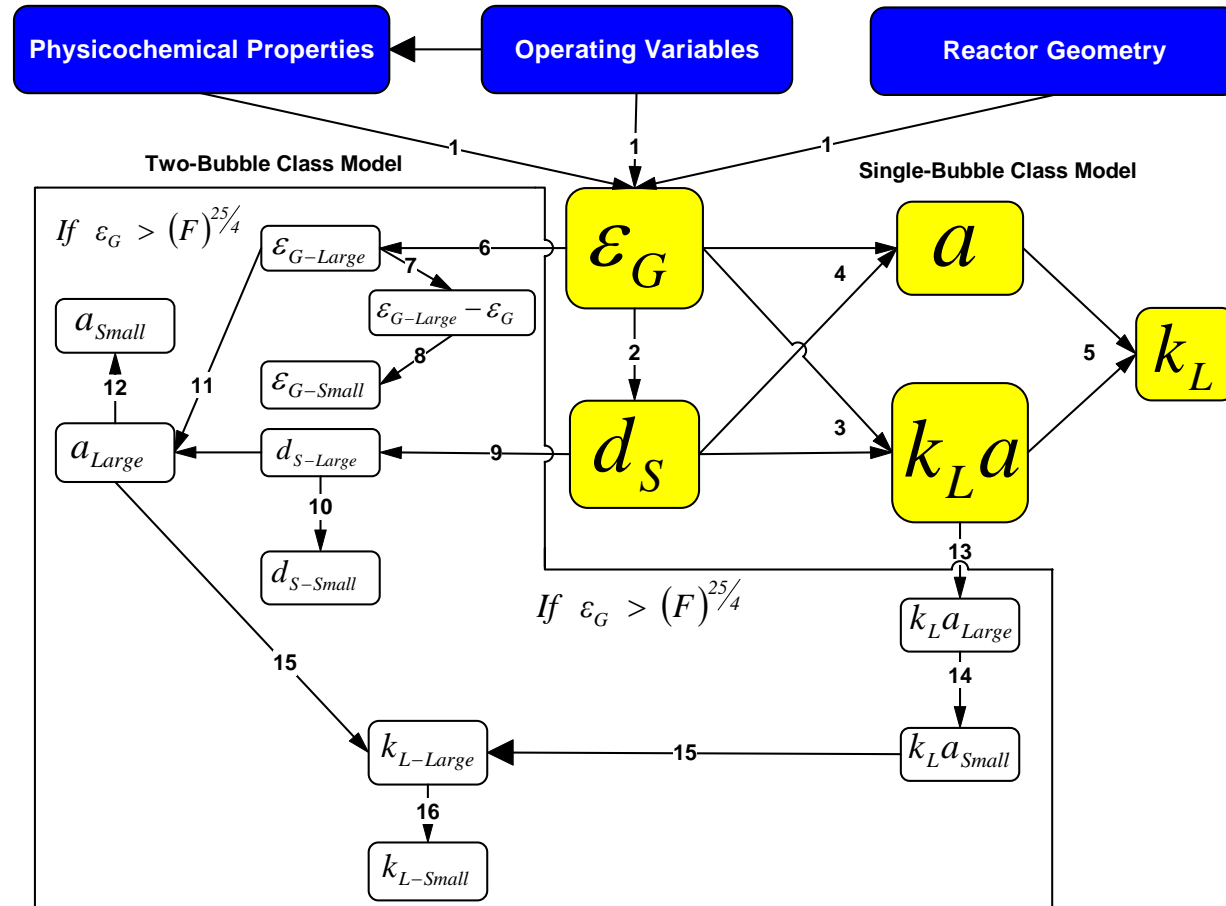


Figure 77: Algorithm for Calculating the Hydrodynamic and Mass Transfer Parameters in BCRs and SBCRs

6.6 SIMULATION

The design and scale-up of Ars and BCRs requires, among others, precise knowledge of the kinetics, thermodynamics, hydrodynamics and heat as well as mass transfer parameters. The two desirable products of the LPTO process are benzoic acid and benzaldehyde, however, since these products are highly reactive intermediates in the free radical chain reaction, numerous undesirable by-products are also formed^(7, 8, 10, 21). Thus, controlling the oxygen/toluene ratio in the feed to the reactor will affect the kinetics, hydrodynamics, and heat as well as mass transfer, which in turn will impact the performance of the oxidation process^(8,9). Also, since the hydrodynamic, heat/mass transfer parameters in ARs and BCRs are different, the selection of the reactor type to carry out the oxidation process will impact the selectivity and yield of the desired products. In this section, the LPTO process is simulated in commercial-size BCRs and ARs using our correlations of the thermodynamics, hydrodynamics, and mass transfer parameters, along with literature data on the heat transfer and toluene oxidation reaction kinetics. Also, a comparison between the performances of these two reactor types is made.

6.6.1 Modeling of LPTO Process in a BCR

Several investigators visually observed small and large gas bubbles in BCRs, where large ones move upward through the liquid in a plug-flow manner^(157, 219, 344), whereas the small ones, which are entrained in the recirculations created by the rising large gas bubbles, are completely back-mixed. The dispersions of these small and large gas bubbles was described using the axial dispersion model^(157, 160, 179, 219, 344), since this model in conjunction with the two-class (small + large) gas bubbles model was reported to be suitable for the assessment of the performance of BCRs^(160, 179, 344, 443, 444). Actually, de Swart and Krishna⁽¹⁶⁰⁾ questioned the use of a single parameter to account for the flow and mixing characteristics of the gas and liquid phases. Also, Mills et al.⁽⁴⁴³⁾, Deckwer and Schumpe⁽³⁷³⁾ and Dudukovic et al.⁽⁴⁴⁵⁾ questioned the correctness of using a single lumped axial dispersion coefficient to describe the circulation and mixing characteristics, i.e., the axial and radial flow of the liquid-phase and the behaviors of small and large gas bubbles. Shah et al.⁽³⁹⁸⁾, Joseph⁽³⁹⁹⁾ and Chen et al.⁽⁴⁰¹⁾ reported limited or no effect of internals on the hydrodynamics of BCR if their volume fraction were less than 20%, and Forret et al.⁽⁴⁰³⁾ showed in a large-scale BCR that the internals significantly affect the bubbles recirculation and local dispersion when their volume was greater than 22% of the dispersed volume.

In this study, the LPTO process in a BCR was modeled according to Figure 78, and as can be seen the reactor is equipped with a bundle of cooling tubes, a multiple-orifices gas distributor, external insulations, and gas as well as liquid inlet and outlet. The gas is sparged from the bottom of the reactor into the liquid-phase through a multiple-orifice gas distributor. The BCR is operated continuously in a co-current upflow with respect to the gas and liquid phases. The heat of reaction is removed from the BCR using cooling tubes, which along with the external insulation

allow controlling the reactor temperature. The basic geometrical ratios of the BCR used are given in Table 60. The volume fraction of the internals in the BCR is selected to be less than 5% and accordingly the cooling tubes are assumed to have no effect on the axial dispersion coefficient as well as on the hydrodynamic, heat and mass transfer parameters. The BCR is assumed to operate in the churn-turbulent flow regime under steady-state conditions. Due to the considerable back-mixing anticipated in such a flow regime, the gas bubbles were classified in large and small ^(160, 179, 344, 442, 444) which behave differently in the reactor. In addition, the following assumptions, which are similar to those proposed by Mills et al. ⁽⁴⁴³⁾ and de Swart and Krishna ⁽¹⁶⁰⁾, are made: (1) the mass transfer resistance is in liquid-side, (2) the gas-phase is in thermal equilibrium with the liquid-phase, (3) the liquid superficial velocity is constant, (4) no gas is dissolved in the liquid feed, (5) the change in gas flow rate is accounted for through mass balance, (6) the oxidation reaction is slow ⁽¹⁰⁾ and takes place in the liquid bulk, and (7) the BCR operates under steady state conditions. The dispersions of these small and large gas bubbles were described using the axial dispersion model.

Table 60: Geometrical Ratios of Bubble Column Reactors

<i>Ratios</i>	<i>Ranges</i>
H/D_C , -	4-10 ⁽⁵⁶⁾
D_C , m	>0.30 ⁽⁵⁶⁾
ζ , % (M-ON)	0.01-0.10 ⁽²¹⁴⁾
Internal volume ratio , %	1-16 ^(155, 396-403)

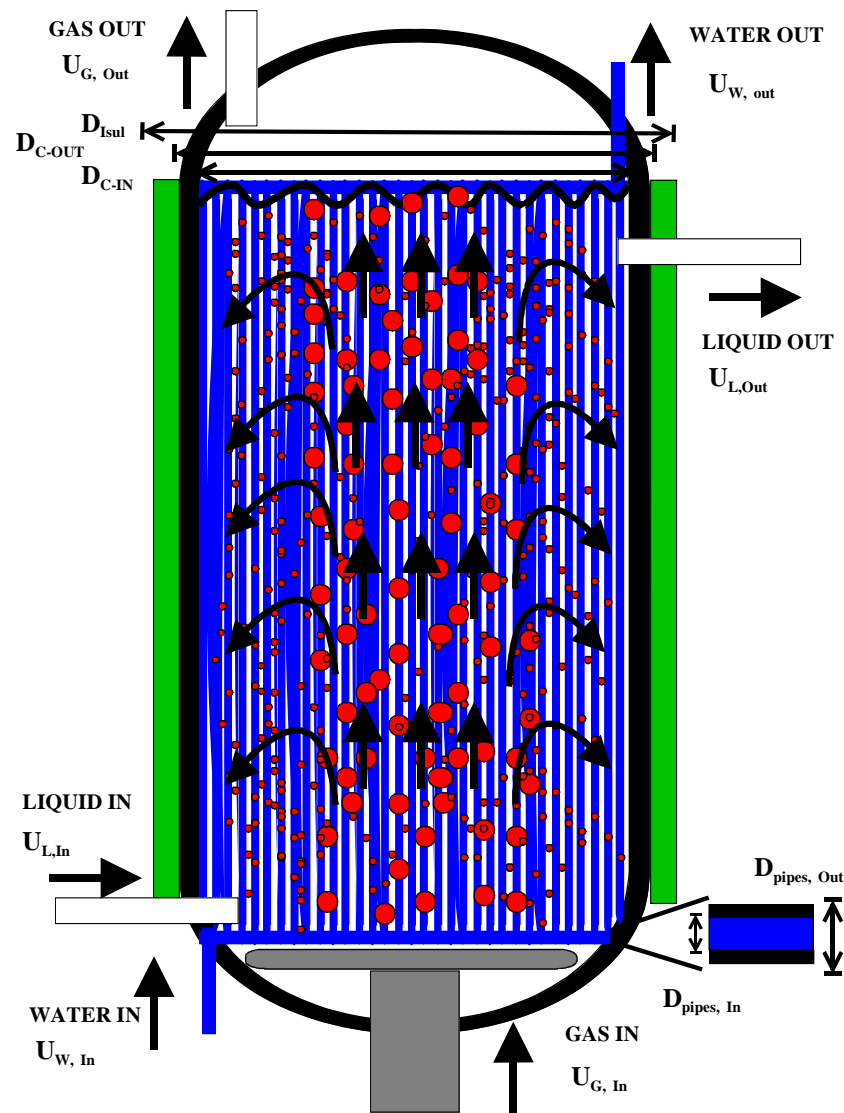


Figure 78: Geometry of the BCRs used

The mass and energy balances are derived over a differential element of the reactor and the resulting equations are given below.

Oxygen or nitrogen mass balance in large gas bubbles:

$$\frac{\partial}{\partial z} \left(\varepsilon_{G-Large} D_G \frac{\partial C_{i,G,Large}}{\partial z} \right) - \frac{\partial (U_{G,Large} C_{i,G,Large})}{\partial z} - (k_L a)_{i,Large} (1 - \varepsilon_G) \left(\frac{C_{i,G,Large}}{He_i / RT} - C_{i,L} \right) = 0 \quad (6-84)$$

Oxygen or nitrogen mass balance in small bubbles:

$$\frac{\partial}{\partial z} \left(\varepsilon_{G-Small} D_L \frac{\partial C_{i,G,Small}}{\partial z} \right) - \frac{\partial (U_{G,Small} C_{i,G,Small})}{\partial z} - (k_L a)_{i,Small} (1 - \varepsilon_G) \left(\frac{C_{i,G,Small}}{He_i / RT} - C_{i,L} \right) = 0 \quad (6-85)$$

Oxygen, nitrogen, toluene, benzaldehyde and benzoic acid mass balance in the liquid phase:

$$\begin{aligned} \frac{\partial}{\partial z} \left((1 - \varepsilon_G) D_L \frac{\partial C_{i,L}}{\partial z} \right) - \frac{\partial (U_L C_{i,L})}{\partial z} + (k_L a)_{i,Large} (1 - \varepsilon_G) \left(\frac{C_{i,G,Large}}{He_i / RT} - C_{i,L} \right) + \\ (k_L a)_{i,Small} (1 - \varepsilon_G) \left(\frac{C_{i,G,Small}}{He_i / RT} - C_{i,L} \right) + (1 - \varepsilon_G) r_i = 0 \end{aligned} \quad (6-86)$$

The energy balance, which includes dispersion, convection, heat of reaction, and heat removal through the cooling tubes and reactor wall, is as follows:

$$\begin{aligned} \frac{\partial}{\partial z} \left((1 - \varepsilon_G) \rho_L C_{p,L} D_L \frac{\partial T_L}{\partial z} \right) - \frac{\partial (U_L \rho_L C_{p,L} T_L)}{\partial z} + (1 - \varepsilon_G) (-\Delta H_{R,i}) r_i - \\ U_{pipes} a_{pipes} (T_L - T_W) - U_{wall} a_{wall} (T_L - T_{outside}) = 0 \end{aligned} \quad (6-87)$$

The overall heat transfer coefficients through the pipes and the reactor wall were estimated as:

$$\frac{1}{U_{pipes} a_{pipes}} = \frac{1}{h_L a_{pipes}} + \frac{V_R \ln \left(\frac{D_{pipes,out}}{D_{pipes,in}} \right)}{2\pi H \lambda_{pipes} n_{pipes}} \quad (6-88)$$

$$\frac{1}{U_{wall} a_{wall}} = \frac{1}{h_L a_{wall}} + \frac{V_R \ln \left(\frac{D_{C,out}}{D_{C,in}} \right)}{2\pi H \lambda_R} + \frac{V_R \ln \left(\frac{D_{isol.}}{D_{C,out}} \right)}{2\pi H \lambda_{isol.}} \quad (6-89)$$

The variation of gas flow rate due to chemical reaction was calculated using the total gas-phase mass balance as:

$$\frac{\partial}{\partial z} (C_G U_G) + (1 - \varepsilon_G) \sum_i \left[(k_L a)_{i,Large} \left(\frac{C_{i,G,Large}}{He / RT} - C_{i,L} \right) + (k_L a)_{i,Small} \left(\frac{C_{i,G,Small}}{He / RT} - C_{i,L} \right) \right] = 0 \quad (6-90)$$

The pressure profile was obtained from ⁽⁴⁴⁶⁾:

$$\frac{\partial (P_T)}{\partial z} + (1 - \varepsilon_G) g \rho_L + (\varepsilon_G) g \rho_G = 0 \quad (6-91)$$

The mass balance of the water in the cooling pipes was expressed by:

$$\frac{\partial (U_W \rho_W)}{\partial z} = 0 \quad (6-92)$$

The pressure drop in each pipe was calculated using Equation (6-93) where f is the Fanning friction factor ⁽⁴⁴⁷⁾:

$$\frac{\partial(P_w)}{\partial z} + g\rho_w + \frac{\partial(\rho_w U_w^2 / 2)}{\partial z} + 4f\left(\frac{\rho_w U_w^2}{2d_{pipe}}\right) = 0 \quad (6-93)$$

In this study, however, it is assumed that the friction loss in the pipe (ΔP_F) defined in Equation (6-94) is negligible.

$$\Delta P_F = 4fH\left(\frac{\rho_w U_w^2}{2d_{pipe}}\right) \quad (6-94)$$

The energy balance on the cooling pipes was defined in Equations (6-95) through (6-97); and as can be seen it depends on the saturation temperature of water (T_S) as steam can be formed in the pipe. The value of T_S was obtained by computing the water phase equilibria using the procedure described by Fernandez-Prini and Dooley⁽⁴⁴⁸⁾.

If $T_W < T_S$:

$$\varepsilon_{pipes} \frac{\partial}{\partial z} \left(\rho_{L,W} C_{p,L,W} D_{L,W} \frac{\partial T_W}{\partial z} \right) - \varepsilon_{pipes} \frac{\partial(U_W \rho_{L,W} C_{p,L,W} T_W)}{\partial z} + U_{pipes} a_{pipes} (T_L - T_W) = 0 \quad (6-95)$$

If $T_W = T_S$, the steam mole fraction can be obtained as:

$$y = \frac{\int_{z_l}^{z_2} U_{pipes} a_{pipes} (T_L - T_W) dz}{\varepsilon_{pipes} U_W \Delta H_{vap.}} \quad (6-96)$$

If $T_W > T_S$:

$$\varepsilon_{pipes} \frac{\partial}{\partial z} \left(\rho_{G,W} C_{p,G,W} D_{G,W} \frac{\partial T_W}{\partial z} \right) - \varepsilon_{pipes} \frac{\partial(U_W \rho_{G,W} C_{p,G,W} T_W)}{\partial z} + U_{pipes} a_{pipes} (T_L - T_W) = 0 \quad (6-97)$$

The boundary conditions at the inlet of the BCR were Danckwerts' type, which account for the balance of dispersive and convective fluxes:

At $z = 0$

$$\varepsilon_{G-Large} D_G \frac{\partial C_{i,G,Large}}{\partial z} = U_{G,Large} C_{i,G,Large} - U_{Go,Large} C_{i,Go,Large} \quad (6-98)$$

$$\varepsilon_{G-Small} D_L \frac{\partial C_{i,G,Small}}{\partial z} = U_{G,Small} C_{i,G,Small} - U_{Go,Small} C_{i,Go,Small} \quad (6-99)$$

$$(1 - \varepsilon_G) D_L \frac{\partial C_{i,L}}{\partial z} = U_L C_{i,L} - U_{Lo} C_{i,Lo} \quad (6-100)$$

$$(1 - \varepsilon_G) \rho_L C_{p,L} D_L \frac{\partial T_L}{\partial z} = U_L \rho_L C_{p,L} T_L - U_{Lo} \rho_{Lo} C_{p,Lo} T_{Lo} \quad (6-101)$$

At the exit of the BCR, the following boundary conditions were assumed:

At $z = H$

$$\frac{\partial C_{i,G,Large}}{\partial z} = 0 \quad (6-102)$$

$$\frac{\partial C_{i,G,Small}}{\partial z} = 0 \quad (6-103)$$

$$\frac{\partial C_{i,L}}{\partial z} = 0 \quad (6-104)$$

$$\frac{\partial T_L}{\partial z} = 0 \quad (6-105)$$

6.6.2 Modeling of LPTO Process in a Cascade of GSRs

In this study, the cascade arrangement of GSRs was chosen in the simulation of the LPTO process as depicted in Figure 79, which shows that each GSR is insulated and equipped with three impellers, a gas distributor, cooling tubes, baffles, and gas as well as liquid inlet and outlet. The gas is sparged at the bottom of the reactor into the liquid through a multiple-orifices gas distributor. The gas/liquid mixing is insured using multiple impellers. The gas and liquid phases are fed continuously to the GSRs, which are operated in a co-current scheme. The same gas is introduced in each GSR, whereas the liquid exiting the n^{th} reactor represents the feed for the $(n+1)^{\text{th}}$ reactor. The heat of reaction is removed from the GSRs using cooling tubes (coils), which along with the reactor insulation jacket allow controlling the reactor temperature. The “standard” geometrical ratios accepted in the literature ⁽⁵⁷⁾ for such reactors are given in Table 6.

In the proposed cascade of GSRs, the liquid phase was considered to be well mixed, whereas the gas phase was assumed to move through the liquid in a plug flow. This assumption can be justified considering the low mixing speed (poor mixing) often encountered in large-scale agitated reactors owing to their inherent mechanical limitations. In addition, the following assumptions were made: (1) the resistance to gas-liquid mass transfer is in the liquid-side, (2) the gas phase is in thermal equilibrium with the liquid phase, (3) the gas and liquid superficial gas velocities are constants, (4) no gas is dissolved in the liquid feed, (5) the oxidation reaction is slow ⁽¹⁰⁾ and takes place in the liquid bulk, and (6) the GSRs operate under steady state conditions. The mass and energy balance are written over a differential element of the reactor and the resulting equations are given in the following:

Oxygen or nitrogen mass balance in the gas-phase is:

$$\frac{d(U_{G,R_i} C_{i,G,R_i})}{dz} - (k_L a)_{i,R_i} (I - \varepsilon_{G,R_i}) \left(\frac{C_{i,G,R_i}}{He_{R_i} / RT} - C_{i,L,R_i} \right) = 0 \quad (6-106)$$

Oxygen, nitrogen, toluene, benzaldehyde and benzoic acid mass balance in the liquid-phase:

$$-\frac{(U_{L,R_{i-out}} C_{i,L,R_{i-out}} - U_{L,R_{i-in}} C_{i,L,R_{i-in}})}{H} + (k_L a)_{i,R_i} (I - \varepsilon_{G,R_i}) \left(\frac{C_{i,G,R_i}}{He_{R_i} / RT} - C_{i,L,R_i} \right) + r_i = 0 \quad (6-107)$$

The energy balance, which includes convection, heat of reaction, and heat removal through the cooling tubes and reactor wall, is as follows:

$$\begin{aligned} & -\frac{(U_L \rho_L C_{pL} T_L)_{R_{i-out}} - (U_L \rho_L C_{pL} T_L)_{R_{i-in}}}{H} + (I - \varepsilon_{G,R_i}) (-\Delta H_{R,i,R_i}) r_i - \\ & U_{pipes,R_i} a_{pipes,R_i} (T_{L,R_i} - T_{W,R_i}) - U_{wall,R_i} a_{wall,R_i} (T_{L,R_i} - T_{outside,R_i}) = 0 \end{aligned} \quad (6-108)$$

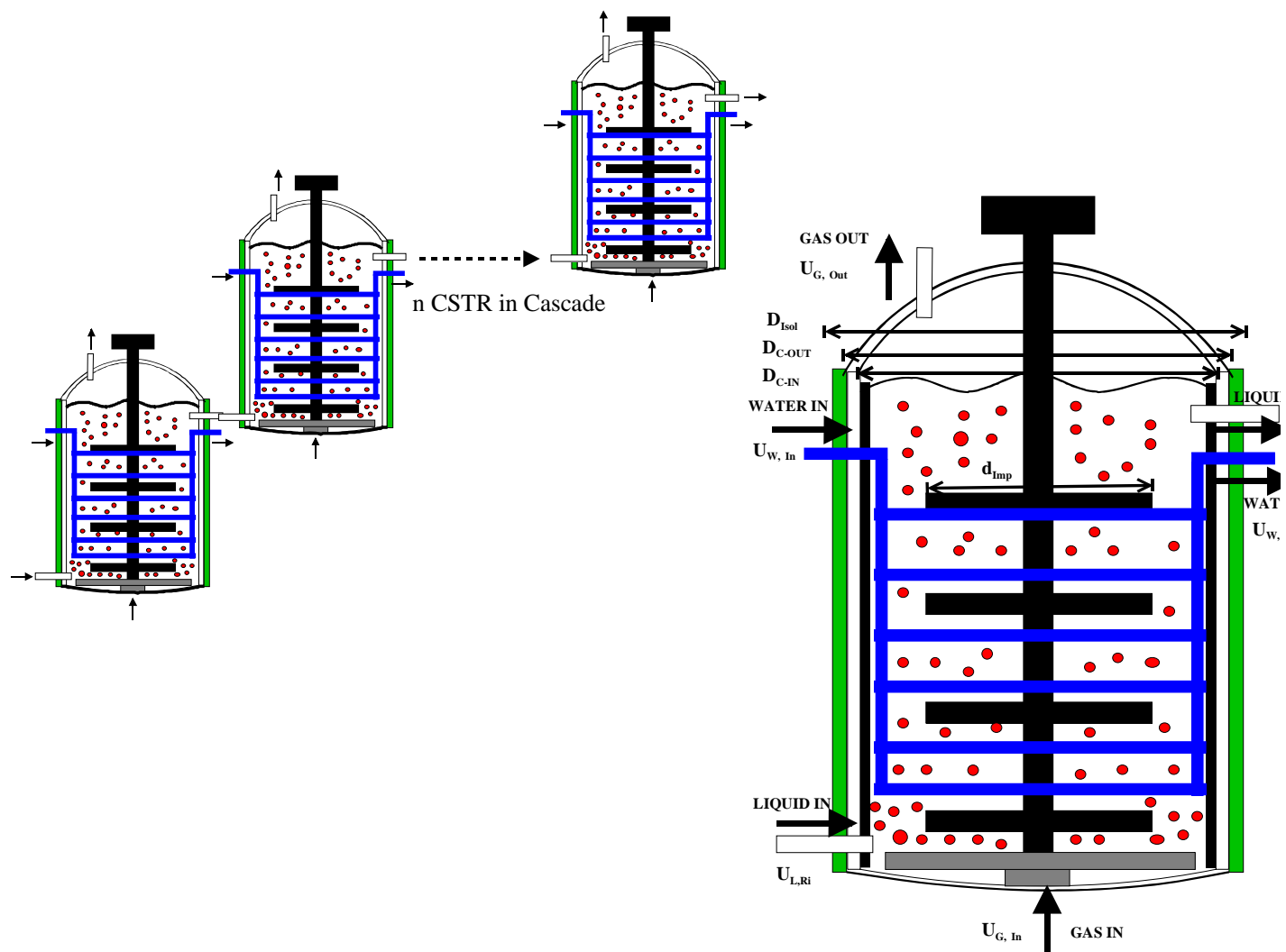


Figure 79: Arrangement of n -GSRs in Series

The boundary conditions for these equations are:

At $z = 0$

$$U_{G,R_i} C_{i,G,R_i} - U_{G,R_i} C_{i,G} = 0 \quad (6-109)$$

$$U_{L,R_i} C_{i,L,R_i} - U_{L,R_{i+1}} C_{i,L,R_{i+1}} = 0 \quad (6-110)$$

$$(U_L \rho_L C_{p,L} T_L)_{R_i} - (U_L \rho_L C_{p,L} T_L)_{R_{i+1}} = 0 \quad (6-111)$$

The BCR and GSRs models with their respective boundary conditions were solved using the modified Newton method included in the Athena Visual Workbench, Version 8.3, developed by Stewarts and Associates Engineering Software, Inc. and the results are discussed below.

6.6.3 Kinetic Model and parameters

The LPTO is usually described as a free radical autocatalytic chain reaction, involving three different steps: (1) chain initiation for generating free radicals, (2) rapid chain propagation via hydro-peroxide formations⁽²¹⁾, and (3) chain termination as a result of reactions among free radicals, according to Emmanuel et al.⁽³⁸⁾ and Sheldon et al.⁽²¹⁾. Several authors proposed different mechanisms for the LPTO as summarized in Table 5, which shows that the oxidation reaction typically occurs in an acetic acid medium with cobalt acetate as a catalyst and bromide as a promoter. The presence of acetic acid increases the catalyst solubility, which is critical in its recovery for reusability^(10, 39, 55), and the bromide promoter reduces the induction period of the reaction^(10, 55) and increases the benzaldehyde yield^(10, 21, 55) by protecting it from further oxidation. It should be mentioned that the separation stage required in the LPTO process represents a disadvantage^(10, 55) and underlines the need for process optimization.

Despite the fact that numerous studies have been conducted on the kinetics of toluene oxidation, few data are available and no intrinsic kinetic models can be found in the literature. In this study, a simple intrinsic kinetic model based on the experimental data by Borgaonkar et al.⁽¹⁰⁾ and Kantam et al.⁽⁵⁵⁾ was developed. Borgaonkar et al.⁽¹⁰⁾ carried the toluene oxidation in acetic medium with cobalt acetate as catalyst and sodium bromide as a promoter. Their study covered wide ranges of temperature, pressure, toluene, cobalt acetate, and sodium bromide concentrations as can be seen in Table 5. During their experiments, however, they only identified toluene, benzaldehyde and benzoic acid; and therefore the overall scheme of the LPTO reaction can be described by Equation (6-112) and/or Equation (6-113). Kantam et al.⁽⁵⁵⁾ also carried out toluene oxidation in acetic medium with cobalt acetate as catalyst and sodium bromide as a promoter, aiming at improving the benzaldehyde and benzyl alcohol selectivities and the recovery process of a new Co/Mn/Br-composite catalyst. During their measurements, however, they identified benzyl alcohol and benzyl acetate in addition to toluene, benzaldehyde and benzoic acid; and as a result different and more complex scheme than Equations (6-112) and (6-113) was proposed as can be seen in Table 5. It should be mentioned that the experiments by Borgaonkar et al.⁽¹⁰⁾ and Kantam et al.⁽⁵⁵⁾ were carried out in a small-scale apparatus, in which the mass transfer resistance was neglected and the oxygen concentration was maintained at the saturation.



The intrinsic kinetic model developed in this study does intend to delineate the precise effects of all the kinetic variables studied by Borgaonkar et al. ⁽¹⁰⁾ and Kantam et al. ⁽⁵⁵⁾, such as temperature, pressure, toluene, cobalt acetate, and sodium bromide concentrations, but its main purpose is to predict with a good degree of accuracy the concentration profiles obtained by these authors. The rate equations for the disappearance of toluene and formation of benzoic acid and benzaldehyde, obtained based on the findings by Mills and Chaudhari ⁽⁴⁴⁹⁾, were as follows:

$$r_{TOL} = k_1 \times \frac{k_2 C_{TOL}^{m_1} C_{O_2}^{m_2} (I + k_3 C_{NaBr}^{m_3}) + k_4 C_{O_2}^{m_4} C_{BZL}^{m_5} C_{Co}^{m_6}}{(I + k_5 C_{O_2}^{m_7} + k_6 C_{BZL}^{m_8})^{m_9}} \quad (6-114)$$

$$r_{BZC} = \frac{k_7 C_{BZL}^{m_{10}} C_{O_2}^{m_{11}} C_{Co}^{m_{12}} (I + k_8 C_{NaBr}^{m_{13}})}{(I + k_9 C_{BZL}^{m_{14}})^{m_{15}}} \quad (6-115)$$

$$r_{BZL} = r_{TOL} - r_{BZC} \quad (6-116)$$

The reaction rate constant (k_i) was assumed to follow an Arrhenius-type equation for the temperature dependency, and was expressed as:

$$k_i = k_{i,Ref.} \times \exp\left(\frac{\Delta E_i}{RT_{Ref.}} \left(\frac{T_{Ref.} - T}{T}\right)\right) \quad (6-117)$$

Where $T_{Ref.}$ is an arbitrary temperature set at 368.15K.

The rate of oxygen consumption for producing benzaldehyde can be related to the toluene consumption given in Equation (6-118) as:

$$r_{O_2} = \frac{r_{TOL}}{2} \quad (6-118)$$

Also, the rate of oxygen consumption for producing benzoic acid can be related to toluene consumption given in Equation (6-119) as:

$$r_{O_2} = r_{TOL} \quad (6-119)$$

In general, the oxygen reaction rate can be expressed as:

$$r_{O_2} = k_{Kinetics} C_L^{m_1} C_{TOL}^{m_2} C_{Catalyst}^{m_3} = K' \Phi_K C_L \quad (6-120)$$

Using the modified Newton method included in the Athena Visual Workbench, Version 8.3, developed by Stewarts and Associates Engineering Software, Inc., the least square error using 73 experimental data points was minimized, and the corresponding m_i , $k_{i,Ref.}$ and ΔE_i can be found in Table 61. The kinetic model was validated using 25% of the data points; and a comparison between the experimental and predicted values is depicted in Figure 80. The figure shows that the toluene, benzaldehyde and benzoic acid concentration are predicted with a regression coefficient (R^2) of 99%, a standard deviation (σ) of 25% and an average absolute relative error (AARE) of 14%. Figure 80 also

shows the reactant and product concentration profiles as a function of time, and a fairly good agreement between the predicted and experimental values can be observed.

The enthalpies of the toluene oxidation reactions for benzaldehyde and benzoic acid production according to Equation (6-121) and (6-122), respectively were also obtained using Aspen +11.1 flash drum calculations; and the following equations were obtained

$$\Delta H_{R,TOL} = -0.102 \times T^2 + 0.493 \times T - 1.846 \times 10^5 \quad (6-121)$$

$$\Delta H_{R,BZC} = -0.016 \times T^2 + 0.474 \times T - 2.788 \times 10^5 \quad (6-122)$$

Table 61: Kinetics Parameters

m_1	m_2	m_3	m_4	m_5	m_6	m_7	m_8	m_9	m_{10}	m_{11}	m_{12}	m_{13}	m_{14}	m_{15}			
1.67	5.00	7.57	5.10	2.95	5.92	1.88	5.00	2.87	5.00	1.04	7.24	1.37	5.00	1.71			
$k_{1,Ref}$		$k_{2,Ref}$		$k_{3,Ref}$		$k_{4,Ref}$		$k_{5,Ref}$		$k_{6,Ref}$		$k_{7,Ref}$		$k_{8,Ref}$		$k_{9,Ref}$	
1.33 10 ⁻²		12.90		3.23		0.24		84.1		79.00		6.22 10 ⁻²		-1.00 10 ⁻²		2.06 10 ⁻²	
ΔE_1		ΔE_2		ΔE_3		ΔE_4		ΔE_5		ΔE_6		ΔE_7		ΔE_8		ΔE_9	
-4.21 10 ³		-1.92 10 ³		-1.34 10 ³		-1.75 10 ³		-5.30 10 ²		-2.69 10 ⁻¹		-9.90		-1.12 10 ³		-8.39 10 ²	

6.6.4 Hydrodynamic and Mass transfer Parameters

These calculation algorithms developed in Sections 6.4.4 and 6.5.4 were used to obtain the hydrodynamic and mass transfer parameters needed in the model equations for the LPTO process in ARS and BCR, respectively.

6.6.5 Liquid and Gas-Phase Mixing Parameters

The axial liquid dispersion coefficient was taken from Krishna et al. ⁽⁴⁵⁰⁾:

$$D_L = 0.31 \times V_L(0) D_C \quad (6-123)$$

$$V_L(0) = 0.2 \times (g D_C)^{0.5} \left(\frac{U_G \rho_L}{g \mu_L} \right)^{1/8} \quad (6-124)$$

The small gas bubbles were assumed to have the same dispersion coefficient as that of the liquid as suggested by de Swart ⁽¹⁷⁹⁾ and confirmed using CFD simulation ⁽⁴⁵¹⁾.

The axial dispersion coefficient of the large bubbles was taken from Deckwer and Schumpe ⁽³⁷³⁾:

$$D_{G,Large} = 56.4 \times \left(\frac{U_G}{\varepsilon_G} \right)^{3.56} D_C^{4/3} \quad (6-125)$$

The axial dispersion coefficient of the water in the cooling pipes D_W was obtained from Shah et al. ⁽²¹⁹⁾:

$$D_w = 0.35 \times (gU_G)^{1/3} D_C^{4/3} \quad (6-126)$$

Wilkinson ⁽⁴⁶⁵⁾ measured the rise velocity of small gas bubbles and proposed Equation (6-127):

$$U_{R,Small} = 2.25 \frac{\sigma_L}{\mu_L} \left(\frac{\sigma_L^3 \rho_L}{g \mu_L^4} \right)^{-0.273} \left(\frac{\rho_L}{\rho_G} \right)^{0.03} \quad (6-127)$$

de Swart and Krishna ⁽¹⁶⁰⁾ assumed that in the churn-turbulent flow regime, the superficial gas velocity of the small gas bubbles can be calculated from Equation (6-128):

$$U_{G,Small} = \varepsilon_{G-Small} U_{R,Small} \quad (6-128)$$

The superficial gas velocity of the large gas bubbles can be obtained as follows ⁽¹⁶⁰⁾:

$$U_{G,Large} = U_G - U_{G,Small} \quad (6-129)$$

6.6.6 Heat Transfer Parameters

In this study, the correlation proposed by Karcz ⁽⁴⁵²⁾ in ARs, which takes into account the effect of multiple impellers and presence of gas on the heat transfer coefficients, as shown in Equation (6-130), was used.

$$\frac{h_L d_T}{\lambda_L} = 0.769 \times \left(\frac{Nd_{imp}^2 \rho_L}{\mu_L} \right)^{0.67} \left(\frac{\mu_L Cp_L}{\lambda_L} \right)^{0.33} \left(\frac{\mu_L}{\mu_w} \right)^{0.14} \quad (6-130)$$

In the BCR, the equations proposed by Schluter et al. ⁽⁴⁵³⁾, which takes into account the effect of internal geometry on the heat transfer coefficients, as shown in Equation (6-131) was employed.

$$\frac{h_L d_s}{\lambda_L} = 0.664 \times \sqrt{\frac{v_{C,loc} d_s \rho_L}{\mu_L}} \sqrt{\frac{\mu_L Cp_L}{\lambda_L} \left(\frac{\mu_L}{\mu_w} \right)^{0.23}} \left(1 + \frac{\delta}{D_C} \right) \quad (6-131)$$

$$\delta = 2.32 \times \sqrt{\frac{d_s \mu_L}{v_{C,loc} \rho_L}} \quad (6-132)$$

$$v_{C,loc} = \sqrt[3]{\xi \frac{(\varepsilon_G \rho_G + (1 - \varepsilon_G) \rho_L)}{(1 - \varepsilon_G) \rho_L} g U_G H_C} \quad (6-133)$$

$$H_C = \begin{cases} D_C & \text{For BCR without bundles} \\ 2t_C & \text{For } \left(\frac{\sigma_L \rho_L}{g \mu_L^4} \right) < 10^6 \\ D_C - D_{pipes} & \text{For } \left(\frac{\sigma_L \rho_L}{g \mu_L^4} \right) < 10^6 \end{cases} \quad (6-134)$$

$$\xi(r) = \frac{\left(1 - \frac{2r}{D_C} \right)^n}{\psi} \quad (6-135)$$

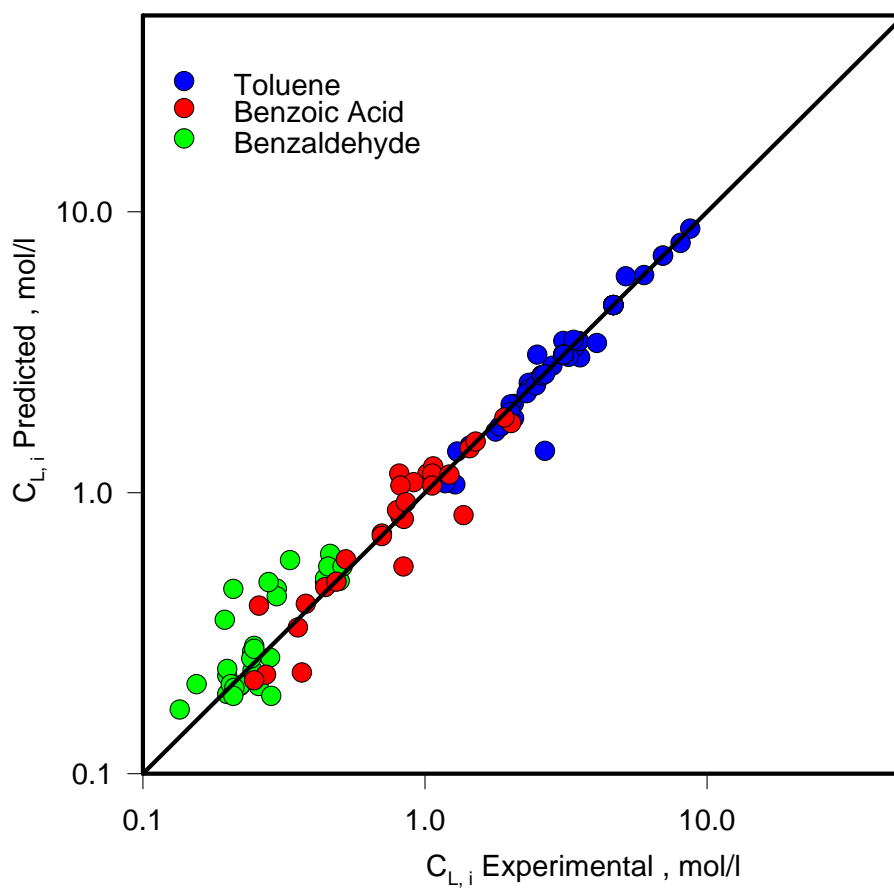
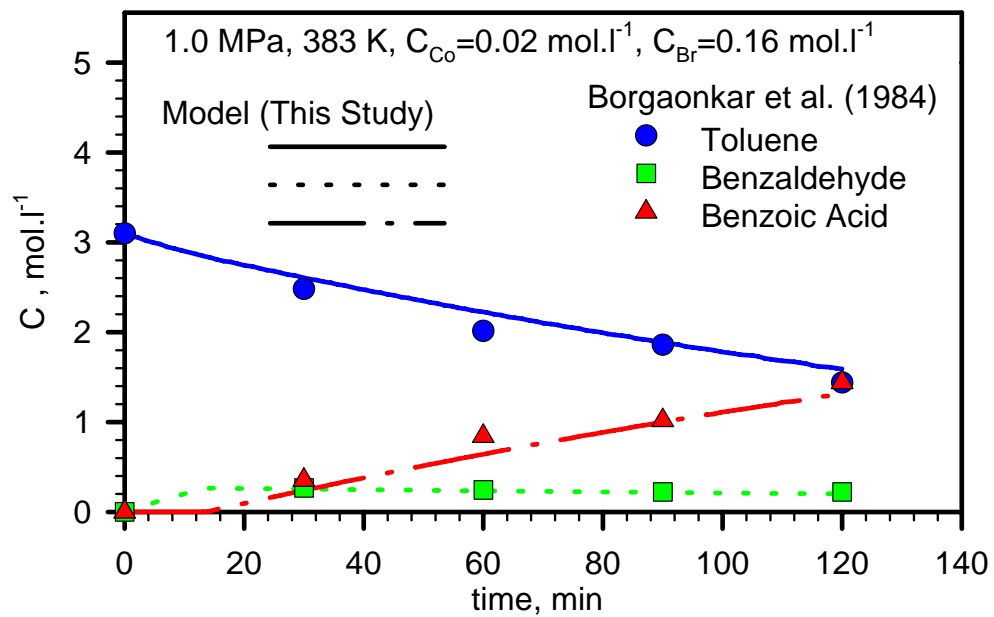


Figure 80: Prediction of Literature Experimental Data using the Kinetic Model Developed

$$n = 0.75 \times \left(\frac{I}{I + 4\varepsilon_s} \right) \quad (6-136)$$

$$\psi = 170 \times \left(\frac{\mu_L^4 g}{\sigma_L^3 \rho_L} \right)^{1/8} \left[1 + 7.85 \cdot 10^{-4} \times \frac{D_{pipes}}{D_C} \sqrt{\left(\frac{D_C^3 g \rho_L^2}{\mu_L^2} \right)^2 \left(\frac{\mu_L^4 g}{\sigma_L^3 \rho_L} \right)} \exp \left(- \frac{10^{-8}}{\left(\frac{\mu_L^4 g}{\sigma_L^3 \rho_L} \right)} \right) \right] \quad (6-137)$$

The thermal conductivity of the pipes and reactor wall in W/m.K was chosen to be ⁽⁴⁵⁴⁾:

$$\lambda_{pipes} = 22.0 \quad (6-138)$$

The thermal conductivity of the insulation material in W/m.K was selected from Pittsburgh Corning foam glass insulation ⁽⁴⁵⁵⁾ as:

$$\lambda_{isol.} = 4.6 \cdot 10^{-11} \times (T')^4 - 2.4 \cdot 10^{-8} \times (T')^3 + 4.3 \cdot 10^{-6} \times (T')^2 - 1.2 \cdot 10^{-4} \times (T') + 0.036 \quad (6-139)$$

The value of T' in Equation (6-139) is in degrees Celsius.

6.6.7 Gas-Liquid thermodynamic and Physicochemical Properties

The Henry's Law constant of O₂ and N₂ obtained in Section 6.1 and modified in order to take into account the effect of liquid concentration. The following dimensionless modified Arrhenius-type equation was obtained:

$$\ln(He^*) = A + \frac{B}{T^*} + \frac{C}{T^{*2}} \quad (6-140)$$

Where:

$$\frac{I}{T^*} = \frac{\left(\frac{I}{T} - \frac{I}{T_C} \right)}{\left(\frac{I}{T_{MAX}} - \frac{I}{T_C} \right)} \quad (6-141)$$

$$He^* = \frac{He}{He_{MAX}} \quad (6-142)$$

$$A = 4.7787 \cdot 10^{-3} T_{C-Mix}^2 - 5.6941 T_{C-Mix} + 1694.85 \quad (6-143)$$

$$B = -0.015784 T_{C-Mix}^2 + 18.83533 T_{C-Mix} + 5616.33 \quad (6-144)$$

$$C = 0.010731 T_{C-Mix}^2 - 12.8135 T_{C-Mix} + 3823.64 \quad (6-145)$$

$$T_{MAX-Gi} = \exp \left(0.666 \ln \left(\frac{\left(\sum_{i=1}^n x_i T_{C,Li} \right)^2}{T_{C-Mix}} \right) + 0.30554 \ln(T_{C,Gi}) \right) \quad (6-146)$$

$$He_{MAX-Gi} = 100 \exp \left(2.4265 \ln \left(\frac{\left(\sum_{i=1}^n x_i T_{C,Li} \right)^2}{T_{C-Mix}} \right) + 2.1371 \ln(T_{C,Gi}) \right) \quad (6-147)$$

The physicochemical properties of the liquid oxidation medium were calculated as described in Section 4.2. Also, the heat capacity and heat conductivity of the liquid-phase were determined as follows ⁽³²⁸⁾:

$$Cp_{Mix} = \sum_{i=1}^3 x_i Cp_i \quad (6-148)$$

$$\lambda_{Mix} = \left(\sum_{i=1}^3 w_i \lambda_i^{-2} \right)^{-0.5} \quad (6-149)$$

6.6.8 Simulation Results on the BCR

The design parameters of the BCR used for simulating the LPTO process are given in Table 62. The ranges of temperature, pressure, catalyst concentration used are within the typical operating conditions of the industrial LPTO given in Table 60. The superficial gas velocity and reactor height to diameter ratio (H/D_C) are in agreement with the ranges used for commercial BCRs ^(56, 179, 443, 446). The liquid (toluene) superficial velocity is chosen to be 0.0005 m/s in order to achieve the desired toluene conversion and benzaldehyde selectivity shown in Table 1. The superficial gas velocity is varied from 0.05 to 0.20 m/s to maintain a churn-turbulent flow regime in BCR ⁽⁴⁴⁶⁾. Vertical internals (cooling tubes) having a volume fraction representing 2% of reactor volume are selected for removing the heat of reaction from the BCR, and since this percentage is less than 20%, these internals are expected to have no effect on the liquid back-mixing and the liquid-phase dispersion coefficient ^(155, 396, 397, 398, 399, 400, 401, 402, 403). Also, the gas is distributed at the bottom of the BCR through a multiple-orifices (M-ON) sparger with an open area (orifices total area/reactor cross-sectional area), ζ of 10%.

Figure 81 shows the oxygen, toluene, benzaldehyde and benzoic acid concentrations as well as liquid-phase and water temperature profiles predicted using the developed model inside a 5-m ID and 15-m high BCR, operating with a superficial gas velocity of 0.1m/s. The gas entering the column consists of a mixture (50/50 by mole) of oxygen and nitrogen; and the oxidation is carried out at a temperature of about 437K, with an inlet reactor pressure of 1.0 MPa, and a Co catalyst concentration of 0.22 wt% and a NaBr promoter concentration of 1.76 wt%. The gas is sparged into the liquid-phase using a gas distributor having 2777 orifices with a 0.03m ID. The heat of reaction generated under such conditions is removed using 127 cooling pipes of 0.0635 m OD, which corresponds to a surface area per unit reactor volume of 1.29 m⁻¹. As can be seen in Figure 81, under steady-state, the oxygen concentration in the liquid-phase near the reactor inlet initially increases due to gas-liquid mass transfer; and then gradually decreases with reactor height due to the chemical reaction with toluene in the liquid-phase, which resulted in the increase of the liquid-phase temperature with reactor height. Figure 81 also shows that the toluene and liquid-

phase oxygen concentrations decrease slightly, whereas the benzaldehyde and benzoic acid concentrations slightly increase with reactor height, indicating the back-mixed character of the liquid-phase in the BCR used. It should be mentioned that the temperature profile in the BCR suggests that the internals volume representing 2% of the reactor volume used was sufficient to remove the heat created in the LPTO process.

The BCR model was also used to predict the effect of reactor geometry on the LPTO process toluene conversion as well as benzaldehyde selectivity and production. The production was based on 330 days of operation with 80% yield in the separation process of benzaldehyde from the rest of the products. Figure 82 depicts the effect of reactor height and height to diameter ratio on the performance of the process carried out in a BCR operating at 420 K, 1.0 MPa, and inlet superficial gas velocity of 0.10 m/s. The internals volume fraction and the distributor open area were kept constant at 2%, and 10%, respectively. As can be seen in this figure, increasing reactor height up to 10 m leads to the increase of the oxygen residence time, which increases the toluene conversion as well as benzaldehyde production, whereas it decreases the benzaldehyde selectivity. This behavior can be related to the increase of the oxygen concentration in the reactor, which resulted in increasing the benzoic acid concentration on the account of benzaldehyde in the liquid-phase. At reactor heights greater than 10 m, however, the decrease of the benzaldehyde selectivity is so important that it affects the benzaldehyde production.

Figure 82 shows that at constant reactor height (H), increasing the reactor height to diameter ratio (H/D_C) slightly increases the toluene conversion, increases the benzaldehyde production and slightly decreases the benzaldehyde selectivity. This is because increasing H/D_C ratio at constant H means that the reactor diameter (D_C) should decrease, which not only decreases the degree of backmixing, but also increases the rate of gas-liquid mass transfer which are expected to increase the toluene conversion and subsequently the benzaldehyde production (yield). Increasing the BCR size intuitively will increase the benzaldehyde production; however, the capital and operating costs, which should be taken into account for the reactor design, will also increase. The model predictions suggest that in order to obtain good toluene conversion, high benzaldehyde selectivity and high benzaldehyde production, a BCR having a height of 10 m with an H/D_C ratio of 5, i.e., $D_C = 2$ m could be a good compromise between the desired reactor performance and economics (capital and operating cost) of the LPTO process.

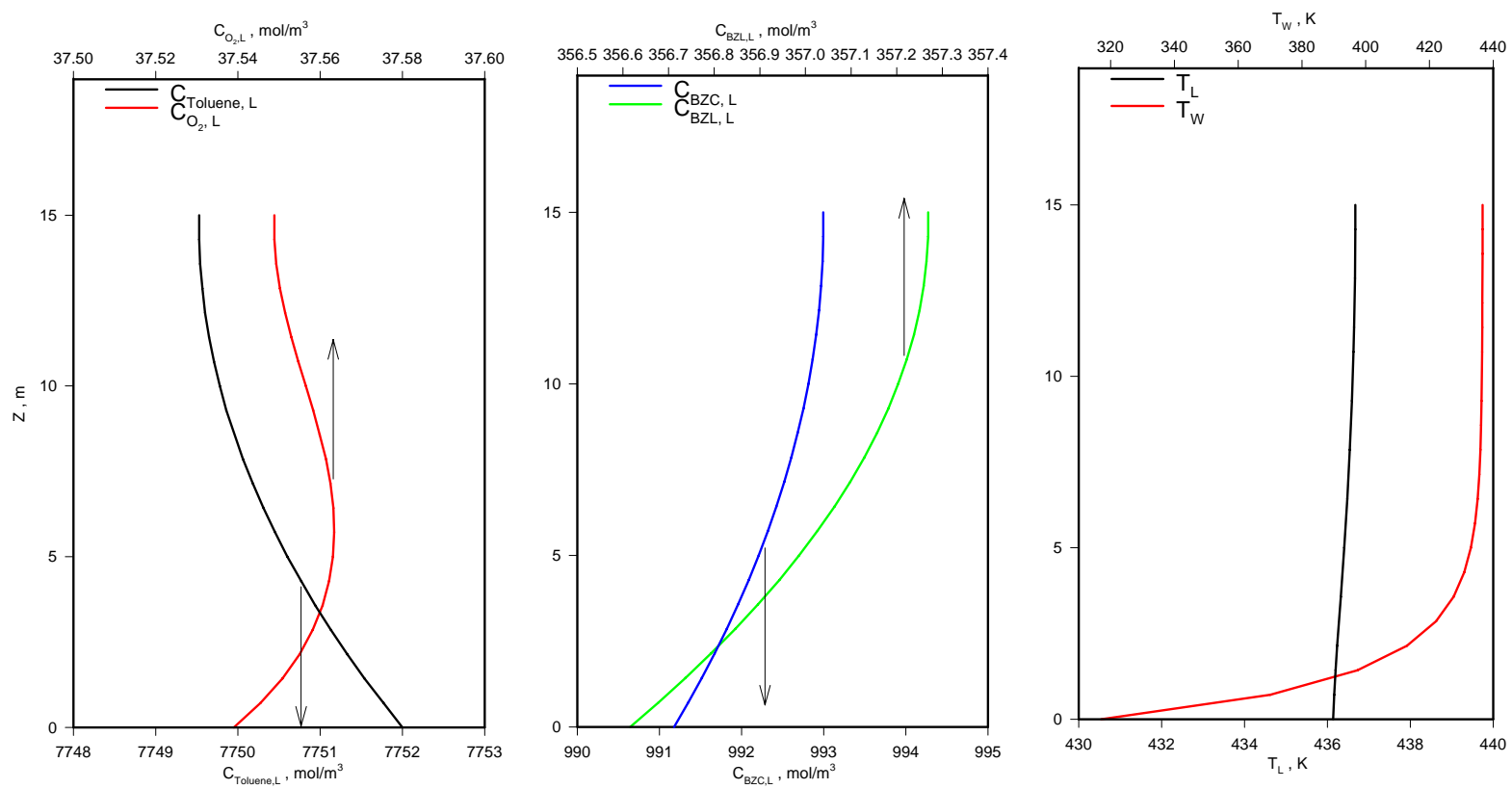
Using this BCR (10-m height and 2-m inside diameter), the effect of superficial gas velocity (U_G) on the process performance was predicted as show in Figure 83. In this figure, increasing U_G values from 0.05 to 0.20 m/s, which correspond to the churn-turbulent flow regime, decrease the toluene conversion and benzaldehyde production, but increase the benzaldehyde selectivity. Figure 83 also shows the effect of U_G on the relevance of gas-liquid mass transfer (β'), represented by the ratio of the gas-liquid mass transfer resistance ($1/k_L a$) and the total resistances (resistance due gas-liquid mass transfer resistance + resistance due to chemical reaction ($1/K'\Phi_K$), Equation (6-150). As can be seen in this figure at low U_G (0.05m/s), the gas-liquid mass transfer is small, whereas the oxygen residence time is long enough to insure high chemical reaction rate. This means that the LPTO process could be controlled by the gas-liquid mass transfer. As the U_G increases, however, the gas-liquid mass transfer increases and the residence time of the gas decreases, and the LPTO process could be controlled by the reaction kinetics. It appears that under kinetically-controlled conditions, the toluene conversion and benzaldehyde production decrease,

whereas the benzaldehyde selectivity constantly increases. Thus, a BCR having 10-m height and 2-m inside diameter operating with an inlet superficial gas velocity of 0.1 m/s could be used to obtain toluene conversion (~12%), benzaldehyde selectivity (40%) and benzaldehyde production (~1500 ton/year), in the LPTO process.

$$\beta' = \frac{\frac{1}{k_L a}}{\frac{1}{k_L a} + \frac{1}{K' \Phi_K}} \quad (6-150)$$

Table 62: Operating Variables for the BCRs

<i>Ratios</i>	<i>Ranges</i>
H/D _C , -	3-10
D _C , m	0.5-5.0
U _G , m/s	0.05-0.20
U _L , m/s	0.0005
P , MPa	1-2
T , K	373-453
C _{CO} , wt%	0.22
C _{NaBr} , wt%	1.76
Orifice type	M-ON
ζ , %	10
Internal volume ratio , %	2
O ₂ mol fraction, %	20-80



$H/D_C = 5m$, $H = 15m$, $T = 437K$, $P = 1.0MPa$, $U_G = 0.10m/s$

Figure 81: Typical Concentration and Temperature profiles in BCRs

$T = 420\text{K}$, $P = 1.0\text{MPa}$, $U_G = 0.10\text{m/s}$

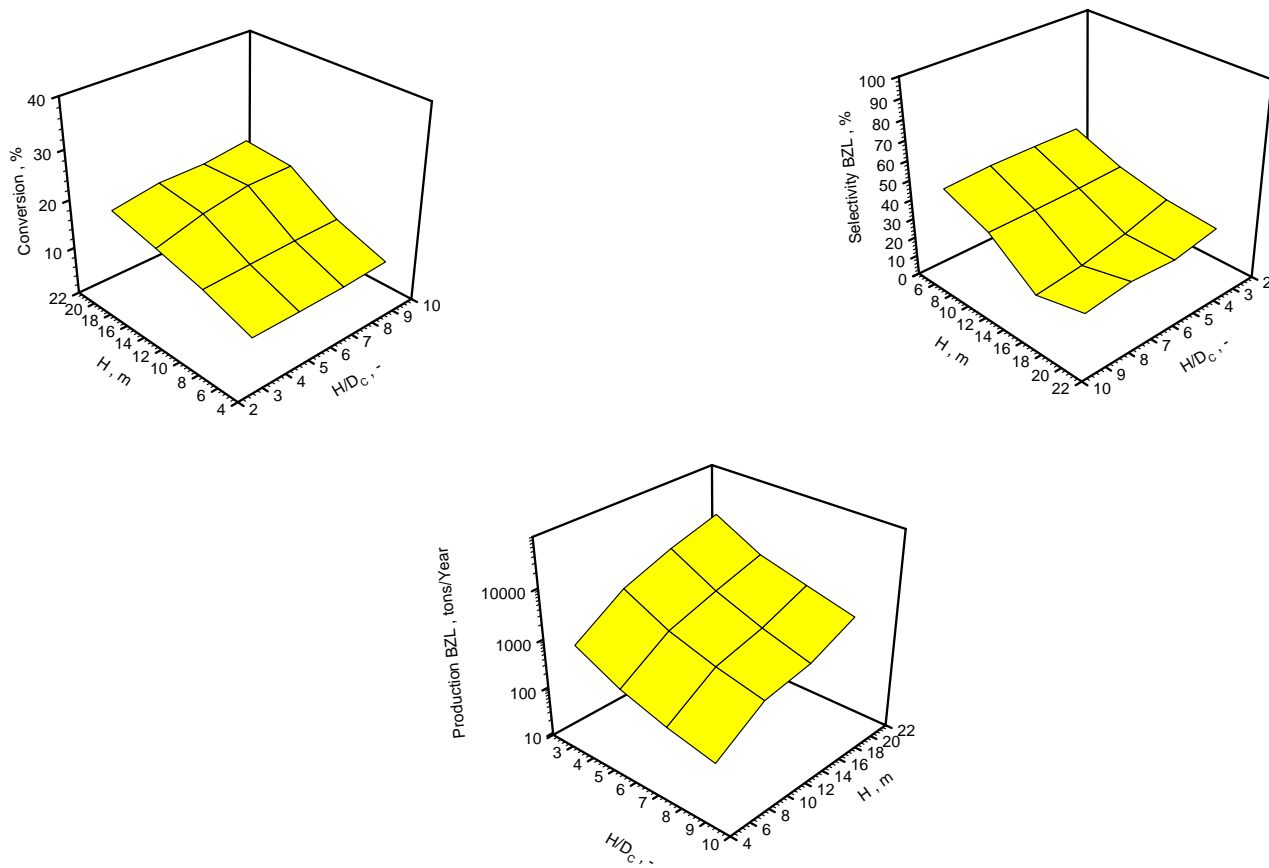


Figure 82: Effect of Column Height and Height to Diameter ratio on the Performances of BCRs

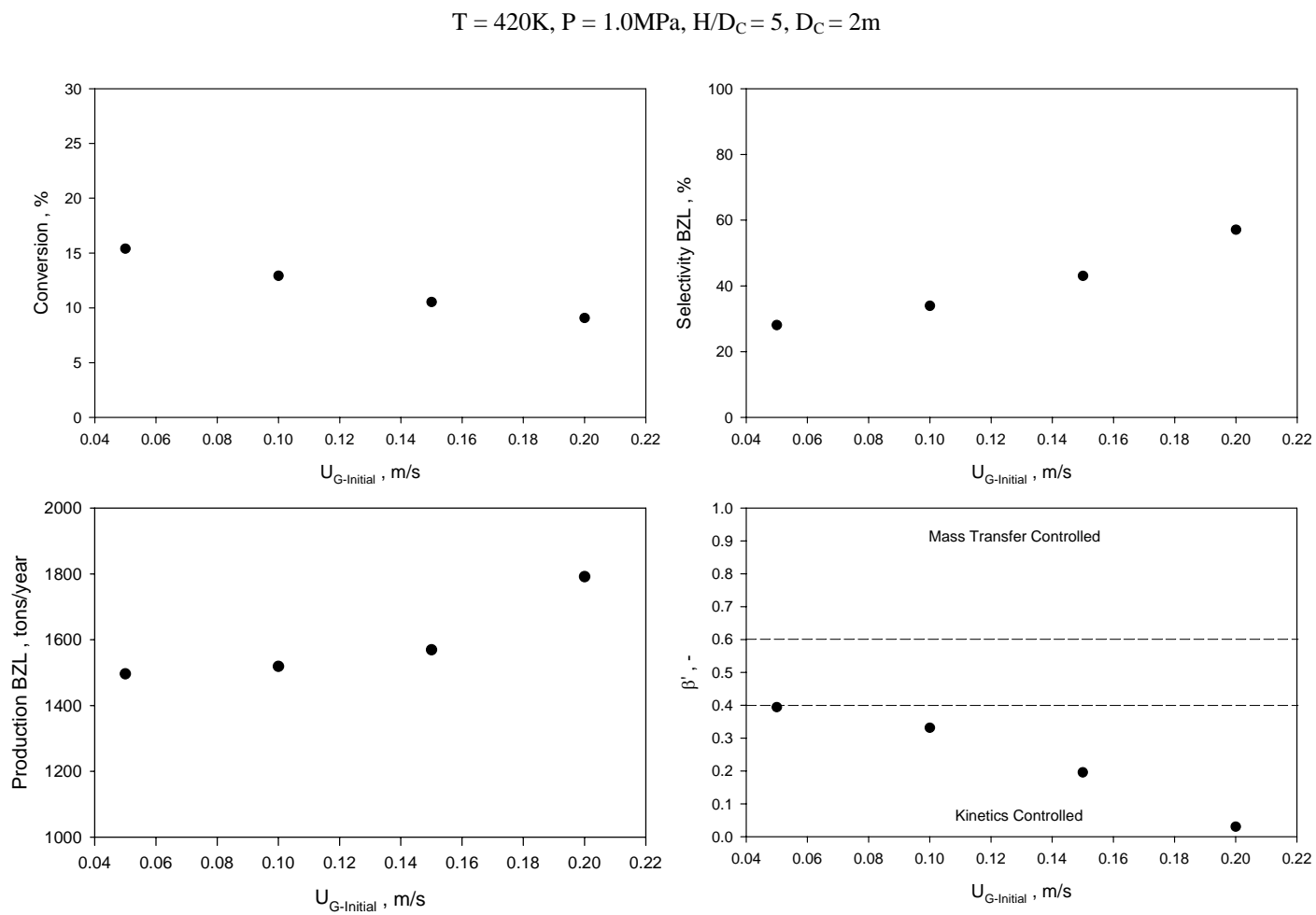


Figure 83: Effect of Superficial Gas Velocity on the Performances of the BCR

6.6.9 The Cascade of GSRs and Comparison with the BCR

A comparison between BCRs and ARs was also conducted, where the reactor volume, liquid residence time and temperature as well as pressure were kept constant in the two contactors. The BCR used in the simulation has a volume of 31.416 m³, and constructing one mechanically agitated reactor having identical volume to the BCR would be almost impossible. Therefore, a number of ARs arranged in series was determined based on the liquid-phase dispersion coefficient, Equation (6-123), using the following relationship^(56, 456):

$$\frac{I}{n} = \frac{2}{Pe_L} - \frac{2}{Pe_L^2} (I - e^{-Pe_L}) \quad (6-151)$$

The number of continuously stirred tank reactors (CSTRs) calculated based on the liquid-phase dispersion coefficient was one. This means that the liquid-phase is completely mixed, however, it is expected that the reactor internals would affect to some extent the degree of mixing even though negligible impact of internal on the mixing characteristics in ARs was reported^(155, 396, 397, 398, 399, 400, 401, 402, 403). The number of CSTRs arranged in series was then calculated based on the gas dispersion coefficient, Equation (6-125); using Equation (6-152); and the number came to be about three^(56, 456). Thus, in this study, it was then decided to simulate the BCR using 3 CSTRs arranged in series, and Table 63 shows the operating conditions used.

$$\frac{I}{n} = \frac{2}{Pe_G} - \frac{2}{Pe_G^2} (I - e^{-Pe_G}) \quad (6-152)$$

Figure 84 shows the effect of superficial gas velocity (U_G) on the performance of the 3-CSTRs in series; and can be seen at U_G values less than 0.01m/s, the toluene conversion and production of benzaldehyde are slightly lower, whereas the selectivity of benzaldehyde is higher than those obtained in the BCR, operating at the same U_G . At U_G value of 0.01 m/s the values of toluene conversion, as well as selectivity and production of benzaldehyde become comparable in the BCR and the 3-CSTRs. At U_G values greater than 0.01m/s, however, the toluene conversion, as well a selectivity and production of benzaldehyde are greater in the BCR when compared with those in the 3-CSTRs. Figure 84 also shows that the toluene conversion in the 3-CSTRs, exhibits a maximum at a superficial gas velocity about 0.01 m/s. This behavior can be attributed to the competing effect of the superficial gas velocity on the gas-liquid mass transfer and the rate of chemical reaction, hence increasing U_G increases the rate of mass transfer while decreases the gas residence time and subsequently the rate of the chemical reaction. It should be mentioned that the increase of the superficial gas velocity in the 3-CSTRs above 0.01 m/s would not only increase the power input requirement and operating cost of the reactors, but also could lead to flooding of the impellers and poor gas-liquid mass transfer, which could control the LPTO process.

In order to overcome the need for such a high superficial gas velocity in the 3-CSTR arrangement, 5 CSTRs arranged in series, where a mixture of 50/50 by mole of oxygen and nitrogen is sparged at the bottom of each reactor, were used. This arrangement may be similar to that used for the cyclohexane oxidation process⁽²³⁾, which similarly to the LPTO process requires low conversion in order to insure optimum selectivities of cyclohexanol and

cyclohexanone. Figure 85 illustrates that the proposed 5-CSTRs configuration gives comparable toluene conversion, as well selectivity and production of benzaldehyde to those obtained in the BCR under similar power input. Figure 85 shows that increasing mixing speed (N) at constant liquid height/reactor diameter (H/d_T) or decreasing H/d_T at constant N increases the toluene conversion, increases the benzaldehyde production, but decreases the benzaldehyde selectivity. This behavior can be related to the increase of the gas-liquid mass transfer coefficient ($k_L a$) with increasing N and/or decreasing H/d_T , resulting in increasing the toluene conversion, which leads to the decrease of the benzaldehyde selectivity. Figure 85 shows also the relevance of the mass transfer (β') in the LPTO process in the 5-CSTRs, and as can be seen β' appears to decrease with increasing N and/or decreasing H/d_T , which indicates that the mass transfer coefficient ($k_L a$) increases under these conditions as reported by Lemoine and Morsi [21].

Figure 86 compares the performance of the BCR and GSRs as a function of the relevance of the mass transfer (β'); and as can be observed under similar power input per unit liquid volume, the BCR operates in a kinetically-controlled regime ($\beta' < 0.42$), whereas the GSRs operate in a regime controlled by both mass transfer and kinetics ($0.4 < \beta' < 0.55$). Thus, BCRs appear to be safer, economical, and more robust to carry out the industrial LPTO process than a cascade of GSRs.

Table 63: Operating Variables for the GSRs

<i>Ratios</i>	<i>Ranges</i>
H/d_T , -	1-2
d_T , m	1.5-2.5
d_{Imp}/d_T , -	1/3
U_G , m/s	0.0005-0.02
U_L , m/s	0.0005
P , MPa	1-2
T , K	373-453
C_{CO} , wt%	0.22
C_{NaBr} , wt%	1.76
O_2 mol fraction, %	20-80

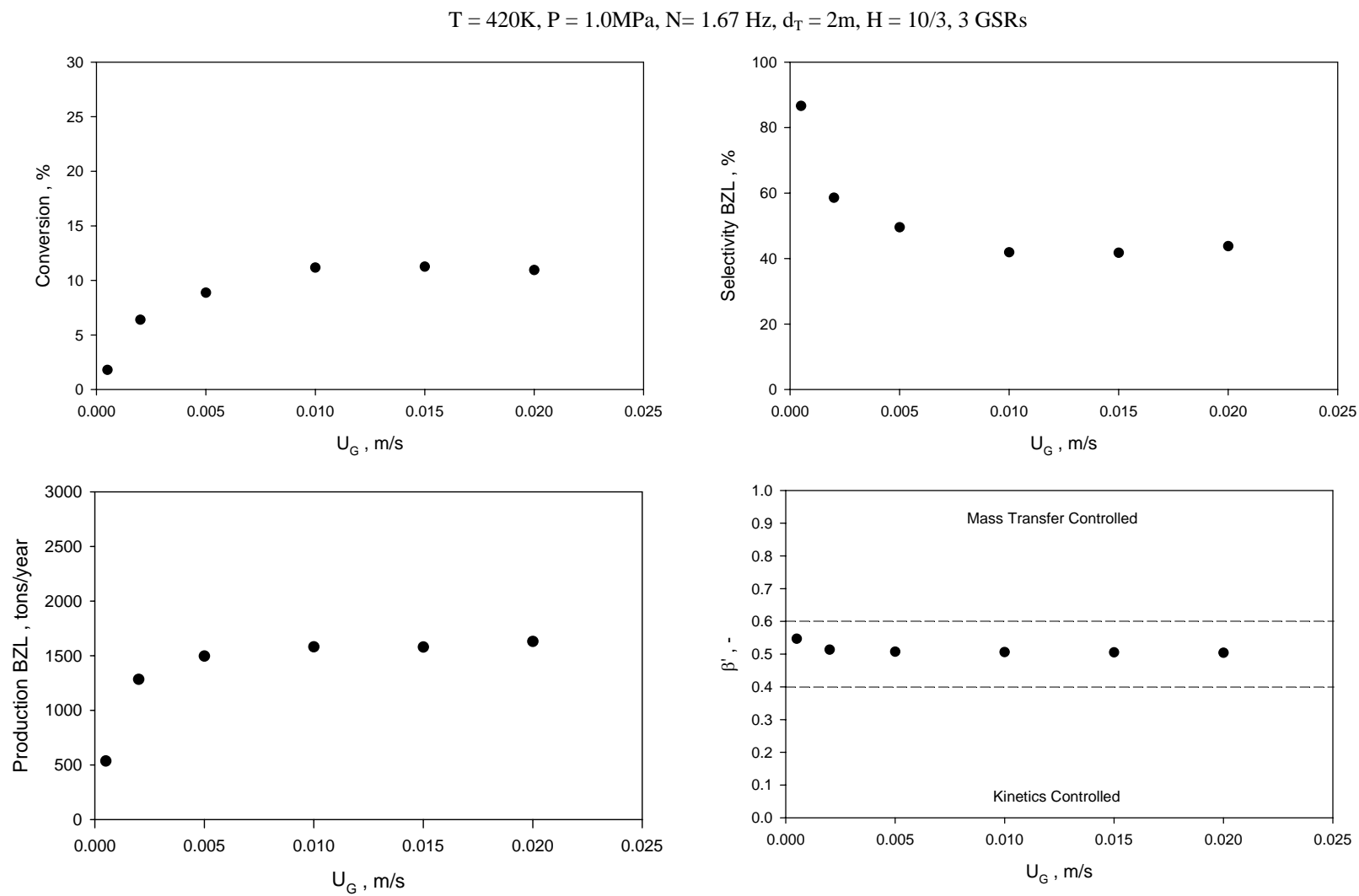


Figure 84: Effect of U_G on the on the Performances of the 3-GSRs

$T = 420\text{K}$, $P = 1.0\text{MPa}$, $U_G = 0.002\text{ m/s}$, $V_R = 31.416\text{ m}^3$, 5 GSRs

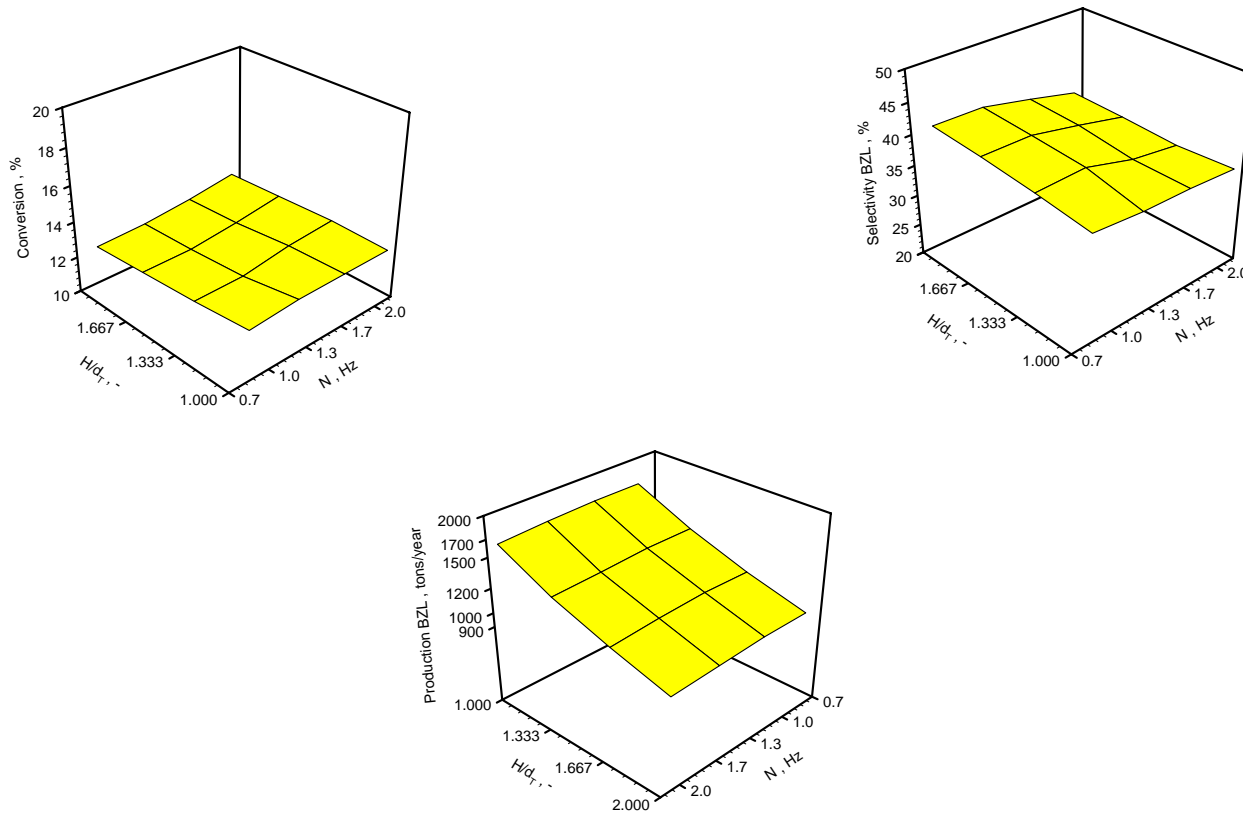


Figure 85: Effect of Height to Diameter Ratio and Mixing Speed on the Performances of the 5-GSRs

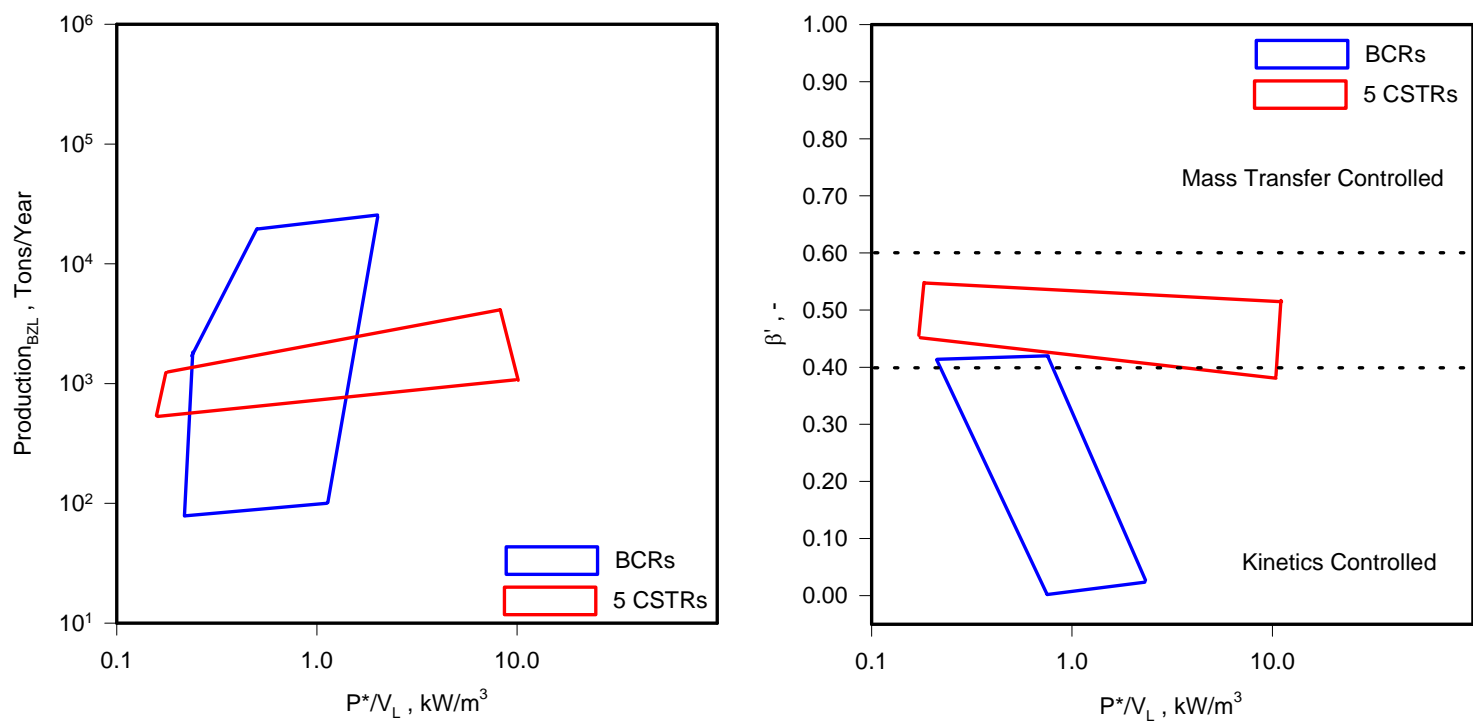


Figure 86: Comparison between the Performances of BCRs and GSRs

CONCLUDING REMARKS

The Central Composite Statistical Design technique was used to obtain the solubility, mass transfer and hydrodynamic parameters of O₂, N₂ and air in four organic liquids (toluene, mixtures of toluene-benzoic acid-benzaldehyde), aimed at mimicking typical yields of the continuous liquid-phase toluene oxidation process, under wide ranges of operating variables in the SAR, GIR, GSR and BCR. From these experimental results, the following conclusions could be reached:

- The solubility values of the gases were found to increase linearly with P and therefore to obey Henry's law at constant temperature. C^* was also observed to first decrease and then increase with T , exhibiting minima in all systems studied. Increasing the gas molecular weight increased C^* values in toluene, while C^* values were found to decrease with the addition of benzaldehyde and benzoic acid. A dimensionless form of Arrhenius type of equation in which the activation energy was dependent of T was developed to predict Henry's law constants with a regression coefficient greater than 99%.

- Increasing N , T or decreasing H was found to increase a_{Wave} , ε_G , a , k_L as well as k_La , and decrease d_S and N_{CRE} values in the SAR, while increasing P appeared to decrease a_{Wave} , ε_G , a , k_L as well as k_La .

- In the GIR, increasing N or decreasing H was found to increase Q_{Gh} , d_S , ε_G , a , k_L as well as k_La , and to decrease N_{CRI} . Also, increasing T appeared to increase and then decrease Q_{Gh} , ε_G and a , and increase k_L as well as k_La , while decreasing d_S and N_{CRI} values. Q_{GI} and ε_G appeared to slightly decrease with P in the GIR, whereas negligible effect was found on N_{CRI} , d_S , a , k_L as well as k_La . The gas holdup appeared to decrease with the gas molecular weight, and so did k_La values in the GIR.

- In the GSR, increasing N , T and U_G appeared to increase ε_G , a , k_L as well as k_La values. d_S values, in contrast, were found to decrease with N and T , while increasing with U_G .

- The addition of benzaldehyde and benzoic acid in the GIR and GSR was found to significantly affect the hydrodynamic parameters (decrease d_S and increase ε_G), especially at low temperature due to frothing, which led to a large increase of the volumetric mass transfer coefficient. Both mass transfer and hydrodynamic characteristics were found to be higher in the GSR than in the GIR, and respectively far greater than in the SAR, which further indicated that the SAR was mainly controlled by k_L , whereas the GSR and GIR appeared to be not only controlled by k_L , but also by a .

- In the BCR, the superficial gas velocity was found to increase the hydrodynamic and mass transfer parameters under the operating conditions studied. Increasing the system pressure, on the other hand, appeared to increase ε_G , a and k_La values, and decrease d_S and k_L values. Negligible effect of the gas nature on both the hydrodynamic and mass transfer parameters was observed and was attributed to the relatively close molecular

weight between N_2 and air. The addition of benzaldehyde and benzoic acid to pure liquid toluene was found to have a strong impact on the hydrodynamic and mass transfer characteristics, since under these conditions froth was formed, enhancing both the gas holdup and volumetric mass transfer coefficients.

- Empirical, statistical and BPNN correlations in both ARs and BCRs using the data obtained in this study along with a large data bank of literature values were used to precisely predict both hydrodynamic and mass transfer parameters. The Empirical and BPNN correlations were then used to construct simple algorithms for predicting these parameters under industrial conditions.

- Using these algorithms, two comprehensive models were developed for a BCR and a series of GSRs to simulate the commercial LPTO process, where the effects of mass and heat transfer, hydrodynamics and kinetics were considered. The model predictions showed that a BCR having 10-m height and 2-m inside diameter operating with an inlet superficial gas velocity of 0.1 m/s could be used to obtain toluene conversion ($\sim 12\%$), benzaldehyde selectivity (40%) and benzaldehyde production (~ 1500 ton/year), in the LPTO process. Similar performances were predicted for a series arrangement of 5 GSRs (2-m inside diameter and 2-m liquid height), operating also with an inlet superficial gas velocity of 0.002 m/s. This BCR was found to operate in the kinetically-controlled regime whereas the 5-GSRs appeared to operate in a regime controlled by both gas-liquid mass transfer and reaction kinetics. For its attractive economics and mechanical constraints of GSRs, the BCR seems to be the reactor of choice for the commercial-scale LPTO process.

APPENDIX A:

LITERATURE SURVEY ON THE HYDRODYNAMIC AND MASS TRANSFER CORRELATIONS

Literature surveys on hydrodynamic and mass transfer correlations are presented in Tables A-1 through A-16.

Table A-1: Literature Correlations of Critical Mixing Speeds in the SAR

<i>Authors</i>	<i>gas/liquid</i>	<i>Reactors</i>	<i>Correlations</i>
Clark and Verneulen ⁽⁶⁰⁾	Water, CCl ₄	SAR	$Fr_E^* \frac{d_{imp}^2 W}{d_T^2 H} \left(\frac{S}{H} \right)^{2/3} = 0.005$
Boerma and Lankester ⁽⁶³⁾	CO ₂ /Sodium carbonate	SAR	$\frac{d_{imp} N_{CRE}}{U_{b\infty}} = A + B \frac{d_T}{d_{imp}}$ with A and B constants
van Dierendonck et al. ⁽⁶⁵⁾	-	SAR	$N_{cir_E} = 1.55 \times \left(\frac{d_T}{d_{imp}} \right) \times \left(\frac{H_L}{d_T} \right)^{1/2}$ and $N_{cir_{IE}} = 2.0 \times \left(\frac{d_T}{d_{imp}} \right) \times \left(\frac{H_L}{d_T} \right)^{1/2}$
Greaves and Kobbacy ⁽⁶⁸⁾	Water, electrolytic solution	SAR	$N_{CRE} = A \frac{(d_T^2 H^2)^{1/3}}{d_{imp}^2} \left(1 - \frac{H - H_L}{H} \right)^{1/3} \left(\frac{P}{P_{Atm.}} \right)^{-0.13}$ A=0.476 for water $N_{CIE} = B \frac{(d_T^2 H^2)^{1/3}}{d_{imp}^2} \left(1 - \frac{H - H_L}{H} \right)^{1/3} \left(\frac{P}{P_{Atm.}} \right)^{-0.13}$ B=0.820 for water
Sverak and Hruby ⁽⁶⁹⁾	Water, glycerin, CCl ₄ , tenside, ethylioside	SAR	$N_{CRE} = k \times g^{0.386} d_{imp}^{-0.614} U_E^{0.228} \left(\frac{\rho_{Ref}}{\rho_L} \right)^{0.317} \left(\frac{V_{Ref}}{V_L} \right)^{0.094}$ (a)
Joshi et al. ⁽⁷⁰⁾	-	-	$\frac{N_{CRE} d_{imp}^{1.980}}{d_T^{1.100}} = 1.65 \times N_P^{-0.125} \left(\frac{g \sigma_L}{\rho_L} \right)^{0.190} \left(\frac{\mu_L}{\mu_G} \right)^{0.031} \left(\frac{W}{d_{imp}} \right)^{0.625}$
Matsumura et al. ⁽⁷¹⁾	O ₂ /Water +sodium alginate	SAR	$\frac{N_{CRE} d_{imp}^3}{d_T^2} = 0.196$ N ₁ is the upper impeller mixing speed
Tanaka et al. ⁽⁷⁴⁾	Aqu. polyvinyl alcohol	SAR	$N = A \times \left(\frac{\mu_L}{\sigma_L} \right)^{0.94} \left(\frac{d_{imp}}{d_T} \right)^{-2.30} \left(\frac{H}{d_T} \right)^{0.44} \left(\frac{H_L}{H} \right)^{0.30}$ (b)
Heywood et al. ⁽⁷³⁾	Aqu. polyvinyl alcohol	SAR	$N_{CRE} = A \times d_T^B d_{imp}^C (H - H_L)^D H^E$ with A, B, C, D and E constants
Ram Mohan ⁽⁷⁵⁾ and Kolte ⁽⁷⁶⁾	Water, sodium chloride, CMC, isopropanol	SAR	$N_{CRE} = A \frac{(d_T^2 H^2)^{1/3}}{d_{imp}^2} \left(1 - \frac{H - H_L}{H} \right)^{1/3}$ (c)
Tanaka and Izumi ⁽⁷⁷⁾	Water	SAR	$Fr_E^* = A \times \left(\frac{\sigma_L}{\sigma_{Water}} \right)^{3.6} \left(\frac{d_{imp}}{d_T} \right)^{-3.6} \left(\frac{H}{d_T} \right)^c \left(\frac{H_L}{H} \right)^d$ (d)

Table A-1 (Cont'd)

<i>Authors</i>	<i>gas/liquid</i>	<i>Reactors</i>	<i>Correlations</i>
Wichterle and Sverak (83)	H ₂ O, glycerin, CCl ₄ , tenside, ethylioside	SAR	$Nc_{ir_E} = (9.336 \pm 0.767) \times Bs^{0.064 \pm 0.022} Rp^{-0.064 \pm 0.012}$ $Nc_{ir_{IE}} = (8.211 \pm 0.765) \times Bs^{0.141 \pm 0.023} Rp^{-0.036 \pm 0.012} \text{ (e)}$

^(a) $V_{Ref} = 1 \text{ m}^3$, $\rho_{Ref} = 1000 \text{ kg.m}^{-3}$, $K = \text{kg}^{0.386}$, $K = 4.8 \text{ (m.s}^{-2})^{0.386}$ for turbine agitator and $K = 9.4 \text{ (m.s}^{-2})^{0.386}$ for agitator with 2 blades, ^(b) $A = 126 \text{ (N}_E)$, $A = 150 \text{ (N}_{IE})$, ^(c) A, B, C, D, E and F constants, ^(d) $A = 0.023$ $c = 0.88$ and $d = 0.60$, ^(e) $7 < B_s < 125.6$ and $6 < B_p < 2500$

Table A-2: Literature Correlations of Critical Mixing Speeds in the GIR

<i>Authors</i>	<i>gas/liquid</i>	<i>Reactors</i>	<i>Correlations</i>
Zlokarnik ⁽⁸⁸⁾	Air/Water	GIR	$Fr_C = 0.156$ for a 4-pipe impeller
Sawant and Joshi ⁽⁹³⁾	Air/water, isopropanol, PEG	GIR	$\frac{N_{CR}^2 d_{imp.}^2}{gH_L} \left(\frac{\mu_W}{\mu_L} \right)^{0.11} = 0.21$
Zundeleovich ⁽⁹⁴⁾	Air/Water	GIR	$N_{CR} = \sqrt{\frac{2gH_L}{K\pi^2 d_{imp.}^2}}$ ^(a)
Saravanan et al. ⁽¹⁰²⁾	Air/Water	GIR	$N_{CR} = \frac{1}{\pi d_{imp.}} \sqrt{2gf_{SP}(H_L - a_C)} \times \left(\Phi_C - \Phi_C \left(\frac{2I_C}{d_{imp.}} \right)^2 \right)^{-1/2}$ ^(b)
Aldrich and van Deventer ⁽¹⁰³⁾	Air/Water, sucrose, ethanol, brine sol.	GIR	$Fr_C = 0.075 \times \left(\frac{\mu_L}{\mu_W} \right)^{0.103} \left(\frac{H_L}{d_{imp.}} \right)^{0.938}$ ^(c) , $Fr_C = 0.130 \times \left(\frac{\mu_L}{\mu_W} \right)^{0.103} \left(\frac{H_L}{d_{imp.}} \right)^{0.570}$ ^(d)
Heim et al. ⁽¹⁰⁶⁾	Air/Water -fermen. mixt.	GIR	$Fr_C = 0.155$ ^(e) , $Fr_C = 0.162$ ^(f) , $Fr_C = 0.230$ ^(g)
Patwardhan and Joshi ⁽¹¹⁰⁾	Air/Water	GIR	$N_{CR} = \frac{1}{\pi d_{imp.}} \sqrt{\frac{2gH_L}{\Phi}}$ ^(h)
Hsu et al. ⁽¹⁰⁹⁾	Ozone/Water	GIR	$Fr_C^* = 3.92 \times \left(\frac{H_L}{d_T} \right)^{1.33} \left(\frac{d_{imp.}}{d_T} \right)^{-2.04} \left(\frac{W}{d_T} \right)^{0.87}$
Fillion ⁽³⁴⁹⁾	H ₂ , N ₂ /Soybean oil	GIR	$Fr_C = 0.289 \times \left(\frac{\mu_L}{\mu_W} \right)^{0.13}$

^(a) K coefficient of head losses in aerator (-), ^(b) $\Phi_C = 1.065$ (-), vortexting constant of PTD at critical condition, $I_C^2 = 0.00342 \text{m}^2$ scale ineffective radius at impeller eye for gas induction, $a_C = 0.0394 \text{m}$ submergence correction at impeller periphery, f_{SP} conformity factor, ^(c) 6-Bladed impeller, ^(d) 12-Bladed impeller, ^(e) 4-pipe impeller, ^(f) 6-pipe impeller, ^(g) disk impeller, ^(h) Φ constant for the slip between the impeller, the liquid and any pressure losses

Table A-3: Literature Correlations of Critical Mixing Speeds in the GSR

<i>Authors</i>	<i>gas/liquid</i>	<i>Reactors</i>	<i>Correlations</i>
Westerterp et al. (120)	Air/Sulphite solution	GSR	$\frac{d_{Imp.} N_{CRE}}{\left(g\sigma_L/\rho_L\right)^{0.25}} = A + B \frac{d_T}{d_{Imp.}}$ with A = 1.22, and B = 1.25 for turbine.
Miller ⁽¹²⁶⁾	CO ₂ , Air/Aqueous solution	GSR	$N_{CR} = \frac{0.01458}{\mu_L d_{Imp.} \sqrt{\frac{d_T \rho_L}{\sigma_L}}}$
Veljkovic et al. (143)	N ₂ /Water	GSR	$N_{CRE} d_{Imp.} = 0.732$ unsparged conditions $N_{CRE} d_{Imp.} - 0.732 = 2812.1 \times U_s d_{Imp.}$ sparged conditions $Re_E (We_E)^{-0.792} (Na_E)^{-0.158} = 104.1$ for $10^{-4} < U_s < 4.10^{-3} \text{ m.s}^{-1(a)}$ $(Re_{SAR})^{0.7} (Na_{SAR})^{0.3} = 18.250$ for $10^{-4} < U_s < 4.10^{-3} \text{ m.s}^{-1(a)}$

^(a) sparged conditions

Table A-4: Literature Correlations of the Induced and Entrainment Gas Flow Rate

Authors	gas/liquid	Reactors	Correlations
Martin ⁽⁸⁹⁾	Air/Water	GIR	$Q_{GIR} = C \times A \times K \times \left[2g(-H_s) \times \left(\frac{\rho_L}{\rho_G} \right) \right]^{1/2} - 0.00085 \times K^{(a)}$
Topilawa ⁽¹¹⁷⁾	Water, potassium sulfate	GSR	$Q_{SAR} \propto \left(\frac{N^5}{Q_{GSR}^{0.4}} \right) \times \left(\frac{S}{H} \right)^{0.6}$
Matsumura et al. ⁽⁴⁵⁷⁾	Water, alcohols	GSR	$\frac{\eta}{(1-\eta)^2} = 1.913 \times 10^{-10} Na^{2.20} Re^{0.10} We^{1.38} (Fr^*)^{0.07} \left(\frac{d_{imp.}}{d_T} \right)^{6.40}$
White and de Villiers ⁽⁹¹⁾	Air/Tap water, glycerin-water-teepol	GIR	$\frac{Q_{GIR}}{Nd_{imp.}^3} \left(\frac{d_{imp.}}{h_R} \right)^{1/2} = 0.0231 \times \left(\frac{N^2 d_{imp.}^3}{gh_R} - \frac{N_{CR}^2 d_{imp.}^3}{gh_R} \right)^{1.84} \quad (b)$ $\frac{Q_{GIR}}{Nd_{imp.}^3} \left(\frac{d_{imp.}}{h_R} \right)^{1/2} = 0.0977 \times \left(\frac{N^2 d_{imp.}^3}{gh_R} - \frac{N_{CR}^2 d_{imp.}^3}{gh_R} \right)^{2.33} \quad (c) \quad h_R = H_L - \frac{\Delta P}{\rho_L g}$
Sawant et al. ⁽⁹⁵⁾	Air/Water,PEG	GIR	$Q_{GIR} = 51.2 \times (Fr - Fr_C)^{0.83} \left(\frac{d_{imp.}}{H_L} \right)^{1/2}$
Sawant et al. ⁽⁹⁶⁾	Air/Water,PEG	GIR	$Q_{GIR} = 0.0021 \times (N^2 - N_{CR}^2)^{0.75} d_{imp.}^3$
Zundelovich ⁽⁹⁴⁾	Air/Water	GIR	$\frac{Q_{GIR}}{P^*} = \frac{Fr}{Np\rho_L g H_L} \left(\frac{1}{Ae} \frac{\left(\frac{Q_G}{d_{imp.}^2} \right)^2 Fr}{g H_L} + \sqrt{\frac{\left(\frac{Q_G}{d_{imp.}^2} \right)^2 Fr}{g H_L}} \right)$
Matsumura et al. ⁽⁷¹⁾	O ₂ /Water +sodium alginate	SAR	$U_E = 7.15 \times 10^{-6} N_1^{1.90} d_{imp.}^{3.95} d_T^{2.50} \left(\frac{\sigma_L}{10^{-3}} \right)^{-2.40} \left(\frac{\mu_L}{10^{-3}} \right)^{-0.15} N_1$ N ₁ : upper impeller speed
Warmoeskerken et al. ⁽¹³⁶⁾	Air/Water	GSR	$Ae = 1.2 \times Fr^* \quad (d), \quad Ae = 0.028 \times d_{imp.}^{0.2} \sqrt{\frac{d_T}{d_{imp.}}} \quad (e)$
Veljkovic et al. ⁽¹⁴³⁾	N ₂ /Water	GSR	$\alpha_E = 2.76 \times 10^{-15} U_S^{-1.5} \left(\frac{P^*}{V_L} \right)^{2.5} \quad (f), \quad \alpha_{SAR} = 3.59 \times 10^{-4} U_S^{-0.67} \quad (g) \quad \alpha_{SAR} = 5.71 \times 10^{-8} U_S^{-1} \frac{P^*}{V_L} \quad (h)$

Table A-4 (Cont'd)

Authors	gas/liquid	Reactors	Correlations
Raidoo et al. ⁽⁹⁷⁾	Air/Water	GIR	$Q_{GIR}^2 = 2.68 \times 10^{-4} (\Delta P \times d_{imp.}^3)^{1.184}$ <p>with $\Delta P + \rho_L g H_L = 0.12 \times 10^3 \left(\frac{\rho_L \pi^2 d_{imp.}^3 N^2}{2} \right)^{0.385}$ for $H/d_T = 1$</p> <p>and $\Delta P + \rho_L g H_L = 0.06 \times 10^3 \left(\frac{\rho_L \pi^2 d_{imp.}^3 N^2}{2} \right)^{0.439}$ for $H/d_T = 0.75$</p> <p>and $\Delta P + \rho_L g H_L = 0.016 \times 10^3 \left(\frac{\rho_L \pi^2 d_{imp.}^3 N^2}{2} \right)^{0.545}$ for $H/d_T = 0.6$</p>
Saravanan et al. ⁽¹⁰²⁾	Air/Water	GIR	$Q_G = \lambda^* N \left(\frac{d_{imp.}}{2} \right)^2 \left[1 - \left(\frac{2I_G}{d_{imp.}} \right)^2 - \frac{2g(H_L f_{SP} - a_G)}{\Phi_G v_{tip}^2} \right] \text{ (i)}$
Aldrich and van Deventer ⁽¹⁰³⁾	Air/Water, sucrose, ethanol, brine solution	GIR	$Ae = 45.39 \times (Fr - Fr_C)^{0.616} \left(\frac{\rho_L}{\rho_W} \right)^{0.735} \left(\frac{\mu_L}{\mu_W} \right)^{0.129} \left(\frac{d_T}{d_{imp.}} \right)^{0.268}$ $\times \exp \left(0.178 \times (Fr - Fr_C) + 0.501 \times \left(\frac{\rho_L}{\rho_W} \right) + 0.268 \times \left(\frac{\mu_L}{\mu_W} \right) + 1.302 \times \left(\frac{d_T}{d_{imp.}} \right) \right)$
Heim et al. ⁽¹⁰⁶⁾	Air/Water - fermentation mixture	GIR	$\frac{Ae}{Ae_\infty} = 1 - e^{(-23.55 \times Fr^{-0.228} Re^{1.788})} \text{ (j)} \quad \frac{Ae}{Ae_\infty} = 1 - e^{(-592.50 \times Fr^{-0.503} Re^{1.638})} \text{ (k)}$ $\frac{Ae}{Ae_\infty} = 1 - e^{(-1792.90 \times Fr^{-0.623} Re^{2.901})} \text{ (l)}$
Saravanan and Joshi ⁽¹⁰⁷⁾	Air/Water	GIR	$Q_G = 129.95 \times N \times \left(\frac{d_{imp.}}{2} \right)^2 \times \left[1 - \frac{2gH_L}{0.85 \times v_{tip}^2} \right]$ $+ 92.42 \times N \times \left(\frac{d_{imp.}}{2} \right)^3 \times \left[1 - 0.30 \left(\frac{2gH_L}{0.85 \times v_{tip}^2} \right)^{3/2} \right]$

Table A-4 (Cont'd)

<i>Authors</i>	<i>gas/liquid</i>	<i>Reactors</i>	<i>Correlations</i>
Hsu et al. ⁽¹¹²⁾	Ozone/Water	GIR	$N_p = 7.89 \times Fr_C^{*-0.53} \left(\frac{H_L}{d_T} \right)^{0.52} \left(\frac{d_{imp.}}{d_T} \right)^{-1.43} \left(\frac{W}{d_T} \right)^{0.79}$
Fillion ⁽³⁴⁹⁾	H ₂ , N ₂ /Soybean oil	GIR	$Q_G = 2.25 \times M_W^{-0.30} (Fr - Fr_C)^{1.89} Re^{-1.17} \left(\frac{d_{imp.}}{H_L} \right)^{-1.62}$ for Fr<0.6 $Q_G = 4.70 \times 10^{-5} M_W^{-0.30} (Fr - Fr_C)^{0.34}$ for Fr>0.6

^(a) C the conventional orifice coefficient (-), A the orifice area (ft²), H_s liquid head (ft), and K the experimental constant (-), ^(b) water, ^(c) water-teepol, ^(d) Flooding transition, ^(e) Transition between large and clinging cavities, ^(f) 10⁻⁴<U_s<4.10⁻³ m.s⁻¹ gassed conditions, ^(g) P*/V_L ≤ P*_{SAR}/V_L, ^(h) P*/V_L > P*_{SAR}/V_L. ⁽ⁱ⁾ i.e. Table A-2, Φ_G=1.101 I_G=0.05828 m, λ* = 0.16937 m, ^(j) 4-pipe impeller Ae_∞ = 0.0205, ^(k) 6-pipe impeller Ae_∞=0.0215, ^(l) disk impeller Ae_∞ = 0.0300

Table A-5: Literature Correlations of the Sauter Mean Bubble Diameter in Agitated Reactors

<i>Authors</i>	<i>gas/liquid</i>	<i>Reactors</i>	<i>Correlations</i>
Vermulen et al. (458)	-	GSR	$d_s = 0.00429 \times \frac{\sigma_L \mu_L^{0.25} \Phi}{N^{1.5} d_{imp} \rho_L^{0.50} \mu_G^{0.75}} \quad \Phi = \exp[1.072 + 0.626 \times \ln(\varepsilon_G) + 0.0733 \times (\ln(\varepsilon_G))^2]$
Calderbank ⁽¹¹⁸⁾	Air/Water, C ₇ H ₈ , alcohols, glycols, CCl ₄ , nitro-benzene, ethyl acetate	GSR	$d_s = 4.15 \times \frac{\sigma_L^{0.6}}{\left(\frac{P^*}{V_L}\right)^{0.4} \rho_C^{0.2}} \times \varepsilon_G^{1/2} + 0.0009$
Miller ⁽¹²⁶⁾	CO ₂ , Air/Aqueous solution	GSR	$d_s = 4.15 \times \frac{\sigma_L^{0.6}}{\left(\frac{P_G^*}{V_L}\right)^{0.4} \rho_L^{0.2}} \times \varepsilon_G^{1/2} + 0.0009$
Sridhar and Potter (132)	Air/Cyclohexane	GSR	$d_s = 4.15 \times \frac{\sigma_L^{0.6}}{\left(\frac{P_G^*}{V_L}\right)^{0.4} \rho_C^{0.2}} \times \left(\frac{\rho_{AIR}}{\rho_G}\right)^{0.16} \left(\frac{P_G^*}{E_T}\right) \times \varepsilon_G^{1/2} + 0.0009$
Hughmark ⁽¹³⁴⁾	-	GSR	$\frac{d_s g \rho_L}{\sigma_L} = 5.5 \times \varepsilon_G^{1/2} \left(\frac{N^2 d_{imp}^3}{d_{imp} g V_L^{2/3} (P_G^* / P^*)^{2/3}} \right)^{-1/2}$
Matsumura et al. (72)	O ₂ /Water +sodium alginate	SAR	$d_s = 7.67 \times 10^{-2} \times \left(\frac{\mu_L^2}{g \rho_L^2} \right)^{1/3} \left(\frac{N_2 d_{imp} \mu_L}{\sigma_L} \right)^{-0.10} \left(\frac{N_2^3 d_{imp}^3 \rho_L}{\mu_L g} \right)^{0.50} \left(\frac{U_E}{N_2 d_{imp}} \right)^{0.22} \quad (a)$
Parthasarathy et al. ⁽⁴⁵⁹⁾	Air/Water + methyl isobutyl carbinol	GSR	$d_s = 2.0 \times \frac{\sigma_L^{3/5}}{\left(\frac{P_G^*}{V_L}\right)^{2/5} \rho_L^{1/5}}$
Fillion ⁽³⁴⁹⁾	H ₂ , N ₂ /Soybean oil	GIR GSR	$d_s = 3.00 \times \frac{\sigma_L^{0.60} Q_G^{0.38}}{\left(\frac{P_G^*}{V_L}\right)^{0.04} \rho_L^{0.20}} \text{ for GIR}$ $d_s = 0.436 \times M_w^{-0.01} \frac{\sigma_L^{0.60} Q_G^{0.20}}{\left(\frac{P_G^*}{V_L}\right)^{0.06} \rho_L^{0.20}} \text{ for GSR}$

(a) N₂ is the lower impeller mixing speed

Table A-6: Literature Correlations of the Sauter Mean Bubble Diameter in the BCR

<i>Authors</i>	<i>Correlations</i>
Peebles and Garber ⁽⁴⁶⁰⁾	$d_b = 4.76 \times \left(\frac{\mu_L}{\rho_L} \right)^{0.41} \frac{u_{b,\infty}^{0.78}}{g^{0.59}}$
Hinze ⁽⁴⁶¹⁾	$d_{max} = J \frac{\sigma^{0.6}}{\rho^{0.2} (P/V)^{0.4}} \text{ with } J = \left(\frac{1}{2} We_{B-CR} \right)^{3/5} \text{ for homogeneous and isotropic}$ turbulent field and WeB-CR critical bubbles Weber number
Calderbank ⁽¹¹⁸⁾	$d_{sm} = 4.15 \frac{\sigma^{0.6}}{\rho^{0.2} \left(\frac{P^*}{V_L} \right)^{0.4}} \epsilon_G^{0.5} + 0.0009$
Akita and Yoshida ⁽⁴⁶²⁾	$d_b = 26 \times Bo^{-0.5} Ga^{-0.12} Fr^{-0.12}$
Gaddis and Vogelpohl ⁽⁴⁶³⁾	$d_b = \left[\left(\frac{6d_0\sigma}{\rho_L g} \right)^{3/4} + \left(\frac{8lvQ_G}{\pi g} \right) + \left(\frac{135 \times Q_G^2}{4\pi^2 g} \right)^{4/5} \right]^{1/4}$
Pandit and Davidson ⁽⁴⁶⁴⁾	$d_{nm} = 0.75 \times (\Delta P)^{-0.27} d_{bi}^{0.2} D_0^{0.53} \sigma^{0.27}$
Wilkinson ⁽⁴⁶⁵⁾	$d_b = 3 \times g^{-0.44} \sigma_L^{0.34} \mu_L^{0.22} \rho_L^{-0.67} \rho_G^{-0.11} U_G^{-0.02}$
Grevskott et al. ⁽⁴⁶⁶⁾	$d_b = a_l k^{a_2} \frac{k^{1.5}}{\epsilon}$
Pohorecki et al. ⁽¹⁹⁵⁾	$d_s = 1.658 \times 10^{-3} \times U_G^{-0.12}$

Table A-7: Literature Correlations for the Bubble Rise Velocity in the BCR

<i>Authors</i>	<i>Correlations</i>
Abou el Hassan ⁽⁴⁶⁷⁾	$N_{v=} = \frac{u_b d_b^{2/3} \rho_L^{1/3}}{\mu_L^{1/3} \sigma d_L^{2/3}} \quad N_{F=} = \frac{g d_b^{8/3} \rho_L^{2/3} (\rho_L - \rho_G)}{\mu_L^{4/3} \sigma_L^{1/3}} \quad N_v = 0.75 (\ln(N_F))^2$
Guy et al. ⁽¹⁹⁸⁾ (Stokes Law)	$u_{b,\infty} = \frac{\rho_L g d_b^2}{18 \mu_L}$
Fukuma et al. ⁽²³⁰⁾	$u_b = 1.3 (g d_b)^{0.5}$
Fan and Tsuchiya ⁽⁴⁶⁸⁾	$u_b^{-1} = \frac{k \mu_L}{\rho_L g d_b^2} + \left[g \frac{d_b}{2} + \frac{2 c \sigma_L}{\rho_L d_b} \right]^{-0.5}$
Wilkinson et al. ⁽¹⁷⁶⁾	$u_{S.B.} = 2.25 \times \frac{\sigma_L}{\mu_L} \left[\frac{\sigma_L^3 \rho_L}{g \mu_L^4} \right]^{-0.273} \left[\frac{\rho_L}{\rho_G} \right]^{0.03} \quad u_{trans.} = 0.5 \times u_{S.B.} \times \exp(-193 \rho_G^{-0.61} \mu_L^{0.50} \sigma_L^{0.11})$ $u_{L.B.} = \frac{\sigma_L}{\mu_L} \times \left[\frac{u_{S.B.} \mu_L}{\sigma_L} + 2.4 \times \left(\frac{(u_{G.} - u_{trans.}) \mu_L}{\sigma_L} \right)^{0.757} \left(\frac{\sigma_L^3 \rho_L}{g \mu_L^4} \right)^{-0.077} \left(\frac{\rho_L}{\rho_G} \right)^{0.077} \right]$
De Swart and Krishna ⁽⁴⁶⁹⁾	$u_b = \varphi_0 d_c^n (g d_b)^{0.5}$
Krishna et al. ⁽²³⁸⁾	$u_{b,LARGE} = 0.71 (g d_b)^{0.5} (SF)(AF) \quad \text{with SF: Scale factor, AF: Acceleration factor}$

Table A-8: Literature Correlations of the Gas Holdup in Agitated Reactors

<i>Authors</i>	<i>gas/liquid</i>	<i>Reactors</i>	<i>Correlations</i>
Calderbank ⁽¹¹⁸⁾	Air/Water, C ₇ H ₈ , alcohols, glycols, CCl ₄ , nitro-benzene, ethyl acetate	GSR	$\varepsilon_G = \left(\frac{U_s \varepsilon_G}{U_T} \right)^{1/2} + 0.000216 \times \frac{\left(\frac{P^*}{V_L} \right)^{0.4} \rho_C^{0.2}}{\sigma_L^{0.6}} \times \left(\frac{U_s}{U_T} \right)^{1/2}$
Westerterp et al. ⁽¹²⁰⁾	Air/Sulphite solution	GSR	$\frac{aH}{1 - \varepsilon_G} = C \times (N - N_{CRE}) d_{imp.} \sqrt{\frac{d_T \rho_L}{\sigma_L}} \quad \text{with C constants}$
Rushton and Bimbinet ⁽¹²²⁾	Air/Water +corn syrup	GSR	$\varepsilon_G = a \times \left(\frac{P_G^*}{V_L} \right)^b U_s^c \quad \text{a and b constants function of } d_{imp.}/d_T, c = 0.6$
Miller ⁽¹²⁶⁾	CO ₂ , Air/Aqueous solution	GSR	$\varepsilon_G = \left(\frac{U_s \varepsilon_G}{U_T + U_s} \right)^{1/2} + 0.000216 \times \frac{\left(\frac{P_G^*}{V_L} \right)^{0.4} \rho_C^{0.2}}{\sigma_L^{0.6}} \times \left(\frac{U_s}{U_T + U_s} \right)^{1/2}$
Loiseau et al. ⁽¹²⁸⁾	Air/Water, glucol, water+alcohols, sodium sulfite	GSR	$\varepsilon_G = 0.011 \times U_s^{0.360} \sigma_L^{-0.360} \mu_L^{-0.056} \left(\frac{P^*}{V_L} + \frac{\rho_G Q_G R T}{M_G V_L \ln(P_{Sparg er} / P_T)} \right)^{0.270}$
Matsumura et al. ⁽¹²⁹⁾	Water, alcohols	GSR	$\varepsilon_G = 6.86 \times 10^{-3} Re^{0.180} We^{0.250} (Na^*)^{-0.200} (Fr^*)^{0.335} \quad (a)$
Lopes de Figueiredo and Calderbank ⁽¹³⁰⁾	O ₂ /Water	GSR	$\varepsilon_G = 0.34 \times \left(\frac{P_G^*}{V_L} \right)^{1/4} U_s^{3/4}$
Sawant et al. ⁽⁹⁶⁾	Air/Water, PEG/dolomite	GIR	$\varepsilon_G = 0.0325 \times \left(\frac{P_G^*}{V_L} \right)^{0.5}$
Sridhar and Potter ⁽¹³²⁾	Air/Cyclohexane	GSR	$\varepsilon_G = \left(\frac{\varepsilon_G U_s}{U_T} \right)^{1/2} + 0.000216 \times \frac{\left(\frac{P_G^*}{V_L} \right)^{0.4} \rho_C^{0.2}}{\sigma_L^{0.6}} \times \left(\frac{U_s}{U_T} \right)^{1/2} \left(\frac{\rho_G}{\rho_{AIR}} \right)^{0.16} \left(\frac{E_T}{P_G^*} \right)$
Hughmark ⁽¹³⁴⁾	-	GSR	$\varepsilon_G = 0.74 \times \left(\frac{Q_G}{NV_L} \right)^{1/2} \left(\frac{N^2 d_{imp.}^4}{d_{imp.} g V_L^{2/3}} \right)^{1/2} \left(\frac{N^2 d_{imp.}^4 d_s}{\sigma_L V_L^{2/3}} \right)^{1/4}$

Table A-8 (Cont'd)

<i>Authors</i>	<i>gas/liquid</i>	<i>Reactors</i>	<i>Correlations</i>
Matsumura et al. (72)	O ₂ /Water+sodium alginate	SAR	$\varepsilon_G = 2.16 \times \left(\frac{N_2 d_{lp} \mu_L}{\sigma_L} \right)^{0.30} \left(\frac{N_2^3 d_{lp}^3 \rho_L}{\mu_L g} \right)^{0.30} \left(\frac{U_E}{N_2 d_{lp}} \right)^{1.05}$ (b)
Ram Mohan ⁽⁷⁵⁾ and Kolte ⁽⁷⁶⁾	Water, sodium chloride, CMC, isopropanol	SAR	$\varepsilon_G = B \left(\frac{P_G^*}{V_L} \right)^C H^D (H - H_L)^E d_{lp}^F$ with A, B, C, D, E and F constants
He et al. ⁽⁹⁸⁾	Air/Water+CMC, water+triton-X-114	GIR	$\varepsilon_G = 3.19 \times 10^{-4} \left(\frac{P_G^*}{V_L} \right)^{1.90}$ (c) $\varepsilon_G = 5.85 \times 10^{-3} \left(\frac{P_G^*}{V_L} \right)^{0.95}$ (d)
Al Taweel and Cheng ⁽¹⁰⁴⁾	Air/Water +PGME	GIR	$\varepsilon_G = 10^{-7.82} N^{2.68} Q_G^{0.15}$ for air / water $\varepsilon_G = 10^{14.5} N^{1.77} Q_G^{0.25} \sigma_L^{-10.4}$ for air / water + additives
Heim et al. ⁽¹⁰⁶⁾	Air/Water - fermentation mixture	GIR	$\varepsilon_G = 28.96 \times Fr^{*0.968} Re^{-0.354} Ae^{0.644} \left(\frac{d_{lp}}{H_L} \right)^{0.176}$ (e) $\varepsilon_G = 199.70 \times Fr^{*1.063} Re^{-0.458} Ae^{0.789} \left(\frac{d_{lp}}{H_L} \right)^{0.316}$ (f) $\varepsilon_G = 25.85 \times Fr^{*0.947} Re^{-0.336} Ae^{0.634} \left(\frac{d_{lp}}{H_L} \right)^{0.255}$ (g)
Wichterle ⁽⁸⁰⁾	H ₂ O, glycerin, CCl ₄ , tenside, ethylsioide	SAR	$\varepsilon_G = 0$ for $N_{cir} < 1.4 N_{cirE}$, $\varepsilon_G = 0.12 \times (N_{cir} - 1.4 \times N_{cirE})$ for $N_{cir} > 1.4 N_{cirE}$
Saravanan and Joshi ⁽¹⁰⁷⁾	Air/Water	GIR	$\varepsilon_G = 6.45 \times 10^{-2} \left(\frac{P_G^*}{V_L} \right)^{0.31} U_G^{0.51}$ $\varepsilon_G = 2.67 \times 10^{-3} \left(\frac{d_{lp}}{d_T} \right)^{1.63} \left(\frac{N^2 Q_G \rho_L}{\mu_L g} \right)^{0.48}$
Tekie ⁽²³⁾	N ₂ ,O ₂ /Cyclohexane	GIR	$\varepsilon_G = 3.85 \times 10^{-2} \times \left(\frac{N - N_0}{N_0} \right)^{1.19} \left(\frac{\mu_G}{\mu_L} \right)^{-0.74} \left(\frac{\rho_G}{\rho_L} \right)^{0.82} \left(\frac{\sigma_L}{\sigma_{L0}} \right)^{1.97}$ with $\sigma_{L0} = 0.025 \text{ N.m}^{-1}$, and $N_0 = 11.6 \text{ Hz}$

Table A-8 (Cont'd)

<i>Authors</i>	<i>gas/liquid</i>	<i>Reactors</i>	<i>Correlations</i>
Murugesan ⁽¹⁴⁹⁾	Air/Water, Toluene, glycerol	GSR	$\varepsilon_G = 31.2 \times \left(U_G \left(\frac{\rho_L^2}{\sigma_L \Delta \rho_L g} \right)^{0.25} \right)^{0.5} Fr^{*0.45} Mo^{0.08} \left(\frac{d_W}{d_T} \right)^{0.85} \left(\frac{d_{imp.}}{d_T} \right)^{0.65}$
Fillion ⁽³⁴⁹⁾	H ₂ , N ₂ /Soybean oil	GIR	$\varepsilon_G = 1.151 \times M_W^{0.07} (Fr - Fr_c)^{0.41} Ae^{0.52}$

^(a) gassed conditions, in Na* U_G calculated from the rate of gas entrainment and the rate of gas sparged ^(b) N₂ is the lower impeller mixing speed, ^(c) P_G*/V_L<20 kW.m⁻³, ^(d) P_G*/V_L>20 kW.m⁻³, ^(e) for a 4-pipe impeller, ^(f) for a 6-pipe impeller, ^(g) for a disk impeller

Table A-9: Literature Correlations of Gas Holdup in Bubble Column Reactors

<i>Authors</i>	<i>System: gas/liquid</i>	<i>Conditions</i>	<i>Correlations</i>
Hughmark ⁽⁴⁷⁰⁾	Air/Water, kerosene, oil	P _{atm} U _G :0.004-0.45m.s ⁻¹	$\varepsilon_G = \left(2 + \left(\frac{0.35}{U_G} \right) \left(\frac{\rho_L \sigma}{72} \right)^{1/3} \right)^{-1}$
Kumar et al. ⁽⁴⁷¹⁾	Air/Water, glycerol, kerosene	P _{atm} , U _G :0.0014-0.14m.s ⁻¹	$\varepsilon_G = 0.728U - 0.485U^2 + 0.0975U^3$ with $U = U_G \left[\rho_L^2 / \sigma (\rho_L - \rho_G) g \right]^{1/4}$
Bach and Pilhofer ⁽⁴⁷²⁾	Air/Alcohol, hydrocarbons	U _G : 0-0.2 m/s	$\frac{\varepsilon_G}{1 - \varepsilon_G} = 0.115 \left(\frac{U_G^3}{v_L g (\rho_L - \rho_G) / \rho_L} \right)^{0.23}$
Mersmann ⁽⁴⁷³⁾	-	-	$\frac{\varepsilon_G}{(1 - \varepsilon_G)^4} = 0.14 \times U_{sg} \left(\frac{\rho_L^3}{\sigma (\rho_L - \rho_G) / g} \right)^{1/4}$
Hikita et al. ⁽⁴⁷⁴⁾	Air,H ₂ ,CO ₂ ,CH ₄ ,C ₃ H ₈ /Water,sucrose,aniline, CH ₃ OH,C ₄ H ₉ OH	P _{atm} , U _G :0.042-0.38m.s ⁻¹	$\varepsilon_G = 0.672 \left(\frac{U_G \mu_L}{\sigma} \right)^{0.578} \left(\frac{\mu_L^4 g}{\rho_L \sigma^3} \right)^{-0.131} \left(\frac{\rho_G}{\rho_L} \right)^{0.062} \left(\frac{\mu_G}{\mu_L} \right)^{0.107}$
Reilly et al. ⁽⁴⁷⁵⁾	Air/Water, Solvent, TCE/glass	U _G : 0.02-0.2m.s-1 C _V : up to 10 vol.%	$\varepsilon_G = 296 \bar{U}_G^{0.44} \rho_L^{-0.98} \sigma^{-0.16} \rho_G^{0.19} + 0.009$
Sauer and Hempel ⁽⁴⁷⁶⁾	Air/Water/10 diff. Solids	P _{atm} , C _V :0-20 vol.% U _G : 0.01-0.08m.s ⁻¹	$\frac{\varepsilon_G}{1 - \varepsilon_G} = 0.0277 \left(\frac{U_G}{(U_G g v_{sl})^{0.25}} \right)^{0.844} \left(\frac{v_{sl}}{v_{eff,rad}} \right)^{-0.136} \left(\frac{C_s}{C_{S0}} \right)^{0.0392}$ (a)
Wilkinson et al. ⁽¹⁷⁶⁾	N ₂ /n-Heptane, water, mono-ethylene glycol	P: 0.1-2.0 MPa. U _G <0.55m.s ⁻¹	$\varepsilon_G = \frac{u_{trans.}}{u_{S.B.}}$ (b,c) $\varepsilon_G = \frac{u_{trans.}}{u_{S.B.}} + \frac{(U_G - u_{trans.})}{u_{L.B.}}$ (b,d)
Renjun et al. ⁽⁴⁷⁷⁾	Air/Water, alcohol, NaCl	P: Atm./T: 25-97°C U _G <0.23m.s ⁻¹ U _L =0.007m.s ⁻¹	$\varepsilon_G = 0.17283 \times \left(\frac{U_G \mu_L}{\sigma} \right)^{0.5897} \left(\frac{\mu_L^4 g}{\rho_L \sigma^3} \right)^{-0.1544} \left(\frac{P + P_s}{P} \right)^{1.6105}$
Reilly et al. ⁽¹⁷⁸⁾	He, N ₂ , Air, Ar, CO ₂ /Water, varsol DX 3139, TCE, isopar G and M	P: Atm.-1.1MPa U _G <0.23 m.s ⁻¹	$\varepsilon_G = A \times M$ in the Bubbly Flow Regime $\varepsilon_G = B \times M^{1/3}$ in the Churn-Turbulent Flow Regime $M = \frac{\rho_G U_G}{(1 - \varepsilon_G) \rho_L}$ with A,B=f(syst.,flow regime)
Jordan and Schumpe ⁽¹⁹⁰⁾ Jordan et al. ⁽¹⁹¹⁾	He,N ₂ ,Air/C ₂ H ₅ OH, C ₄ H ₉ OH, decalin, toluene	ρ _G :0.19-46.7 kg.m ⁻³ U _G < 0.21 m.s ⁻¹	$\frac{\varepsilon_G}{1 - \varepsilon_G} = b_I Bo^{0.16} Ga^{0.04} Fr^{0.70} \times \left(1 + 27.0 \times Fr^{0.52} \left(\frac{\rho_G}{\rho_L} \right)^{0.58} \right)$ (e)

Table A-9 (Cont'd)

<i>Authors</i>	<i>System: gas/liquid</i>	<i>Conditions</i>	<i>Correlations</i>
Fan et al. ⁽⁴⁷⁸⁾	N ₂ /Paratherm NF/alumina	P: 0.1-5.62 MPa U _G < 0.45 m.s ⁻¹ C _V : 8.1-19.1 vol.% T: 28 and 78 °C	$\frac{\varepsilon_G}{1-\varepsilon_G} = \frac{2.9(U_G^4 \rho_G / \sigma g)^\alpha (\rho_G / \rho_{SL})^\beta}{\left[\cosh(Mo_{SL}^{0.054}) \right]^{4.1}} \text{ with } \alpha = 0.21 Mo_{SL}^{0.0079}$ $Mo_{SL} = g(\rho_{SL} - \rho_G)(\zeta \mu_L)^4 / \rho_{SL}^2 \sigma^3 \text{ and, } \beta = 0.096 Mo_{SL}^{-0.011}$ $Ln \zeta = 4.6 C_V \left\{ 5.7 C_V^{0.58} \sinh[-0.71 \exp(-5.8 C_V) \ln Mo^{0.22}] + 1 \right\}$
Pohorecki et al. ⁽¹⁹⁵⁾	N ₂ /Cyclohexane	P: 0.2-1.2 MPa U _G < 0.055 m.s ⁻¹ U _L 0.0014 m.s ⁻¹ T: 30-160 °C	$\varepsilon_G = 0.383 \times \sigma^{-0.52} U_G^{0.65}$
Wu et al. ⁽⁴⁷⁹⁾	Air/Water	P: 0.1-1.0 MPa U _G up to 0.60 m.s ⁻¹ D _C : 0.19-0.44 m	$\varepsilon_{G, Radial} = \varepsilon_{G, Average} \times \left(\frac{n+2}{n+2-2c} \right) \left[1 - c(r/R)^n \right]$ $n = 2188 \times Re_G^{-0.598} Fr_G^{0.146} Mo_L^{-0.004} \text{ and } c = 0.0432 \times Re_G^{0.2492}$

^(a) C_{S0} solid concentration at the bottom of column, kg/m³ $v_{sl} = \mu_L \left[I + 2.5 C_V + 10.05 C_V^2 + 0.00273 e^{16.6 C_V} \right] / \rho_{SL}$ $v_{eff, rad} = 0.011 D_C \sqrt{g D_C} \left(\frac{U_G^3}{g v_L} \right)^{1/8}$ ^(b) u_{S.B.},

u_{L.B.}, utrans. from Table A-7, ^(c) homogeneous bubble flow regime ^(d) transition and heterogeneous regime, ^(e) b₁ f (D, distributor type) (0.153),

Table A-10: Literature Correlations of the Gas-Liquid Interfacial Area

Authors	gas/liquid	Reactors	Correlations
Calderbank ⁽¹¹⁸⁾	Air/Water, toluene, alcohols, glycols, CCl ₄ , nitrobenzene, ethyl acetate	GSR	$a_0 = 1.44 \times \frac{\left(\frac{P^*}{V_L}\right)^{0.4} \rho_C^{0.2}}{\sigma_L^{0.6}} \times \left(\frac{U_S}{U_T}\right)^{1/2} \text{ for } Re^{0.7} \left(\frac{Nd_{imp.}}{U_S}\right)^{0.3} < 20000 \text{ }^{(a)}$ $\log\left(\frac{2.3 \times a}{a_0}\right) = 1.95 \times 10^{-5} Re^{0.7} \left(\frac{Nd_{imp.}}{U_S}\right)^{0.3} \text{ for } Re^{0.7} \left(\frac{Nd_{imp.}}{U_S}\right)^{0.3} > 20000 \text{ }^{(b)}$
Westerterp et al. ⁽¹²⁰⁾	Air/Sulphite solution	GSR	$\frac{aH}{1 - \epsilon_G} = C \times (N - N_{CRE}) d_{imp.} \sqrt{\frac{d_T \rho_L}{\sigma_L}} \text{ with } C = (0.79 \pm 0.16) \mu_L \text{ (}\mu_L \text{ in cP).}$
Muenz and Marchello ⁽⁶²⁾	O ₂ , He, CO ₂ , C ₃ H ₆ /Water	RT	$c^2 = \left[\left(\frac{\lambda g}{2\pi} \right) + \left(\frac{2\pi\sigma_L}{\lambda\rho_L} \right) \right] \tanh\left(\frac{2\pi H}{\lambda}\right) \text{ and } \omega = 2\pi \frac{c}{\lambda} \quad h_2 = h \times \sin\left(\frac{2\pi x}{\lambda} - \omega t\right)$ $v_x = \left[\frac{2\pi hc}{\lambda} \sinh\left(\frac{2\pi H}{\lambda}\right) \right] \cosh\left(\frac{2\pi}{\lambda}(y + H)\right) \sin\left(\frac{2\pi x}{\lambda} - \omega t\right)$ $v_y = - \left[\frac{2\pi hc}{\lambda} \sinh\left(\frac{2\pi H}{\lambda}\right) \right] \cosh\left(\frac{2\pi}{\lambda}(y + H)\right) \cos\left(\frac{2\pi x}{\lambda} - \omega t\right) \text{ }^{(c)}$
Miller ⁽¹²⁶⁾	CO ₂ , Air/Aqueous solution	GSR	$a = 1.44 \times \frac{\left(\frac{P_G^*}{V_L}\right)^{0.4} \rho_C^{0.2}}{\sigma_L^{0.6}} \times \left(\frac{U_S}{U_T + U_S}\right)^{1/2}$
Akita and Yoshida ⁽⁴⁶²⁾	Air, O ₂ /Water, aqueous glycol, glycerol, methanol	BCR	$a = \left(\frac{1}{3D_C}\right) \times \left(\frac{gD_C^2 \rho_L}{\sigma_L}\right)^{0.50} \times \left(\frac{gD_C^3 \rho_L^2}{\mu_L^2}\right)^{0.10} \times \epsilon_G^{1.13}$
Lopes de Figueiredo and Calderbank ⁽¹³⁰⁾	O ₂ /Water	GSR	$a = 593 \times \left(\frac{P_G^*}{V_L}\right)^{1/4} U_S^{3/4}$
Sridhar and Potter ⁽¹³³⁾	Air/Cyclohexane	GSR	$a = 1.44 \times \frac{\left(\frac{P_G^*}{V_L}\right)^{0.4} \rho_C^{0.2}}{\sigma_L^{0.6}} \times \left(\frac{U_S}{U_T}\right)^{1/2} \left(\frac{\rho_G}{\rho_{AIR}}\right)^{0.16} \left(\frac{E_T}{P_G^*}\right)$

Table A-10 (Cont'd)

Authors	gas/liquid	Reactors	Correlations
Nagata ⁽⁴⁸⁰⁾	-	SAR	$\frac{H_V}{d_{lm p.}} = \left(\frac{H}{d_{lm p.}} - \frac{h_1}{d_{lm p.}} \right) + \frac{\pi^2}{2} Fr^* \left(\frac{2r}{d_{lm p.}} \right)^2 \text{ for } \frac{2r}{d_{lm p.}} \leq \frac{2r_C}{d_{lm p.}}$ $\frac{H_V}{d_{lm p.}} = \left(\frac{H}{d_{lm p.}} - \frac{h_2}{d_{lm p.}} \right) + \frac{\pi^2}{2} Fr^* \left(\frac{2r_C}{d_{lm p.}} \right)^4 \left[\left(\frac{d_{lm p.}}{d_T} \right)^2 - \left(\frac{d_{lm p.}}{2r} \right)^2 \right] \text{ for } \frac{2r}{d_{lm p.}} > \frac{2r_C}{d_{lm p.}}$ $\frac{2r_C}{d_{lm p.}} = 1.23 \times \left(0.57 + 0.35 \frac{d_{lm p.}}{d_T} \right) \left(\frac{W}{d_T} \right)^{0.036} n_B^{0.116} \frac{Re}{1000 + 1.43 Re} \text{ for Paddle }^{(d)}$
Hughmark ⁽¹³⁴⁾	-	GSR	$a = 1.38 \times \left(\frac{\rho_L g}{\sigma_L} \right)^{1/2} \left(\frac{Q_G}{NV_L} \right)^{1/3} \left(\frac{N^2 d_{lm p.}^4}{d_{lm p.} g V_L^{2/3}} \right)^{0.592} \left(\frac{N^2 d_{lm p.}^4 d_S}{\sigma_L V_L^{2/3}} \right)^{0.187}$
Sawant et al. ⁽⁹⁵⁾	Air/Water, PEG/dolomite	GIR	$a = 79 \times \left(\frac{P_G^*}{V_L} \right)^{0.86}$
Sawant et al. ⁽⁹⁶⁾	Air/Water, PEG/dolomite	GIR	$a = 75 \times \left(\frac{P_G^*}{V_L} \right)^{0.5}$
Matsumura et al. ⁽⁷²⁾	O ₂ /Water+sodium alginate	SAR	$a_e = 1.69 \times 10^2 \times \left(\frac{\mu_L^2}{g \rho_L^2} \right)^{-1/3} \left(\frac{N_2 d_{lm p.} \mu_L}{\sigma_L} \right)^{0.40} \left(\frac{N_2^3 d_{lm p.}^3 \rho_L}{\mu_L g} \right)^{-0.20} \left(\frac{U_E}{N_2 d_{lm p.}} \right)^{0.84} \text{ }^{(e)}$
Schumpe and Deckwer ⁽⁵⁰⁶⁾	Air/Carboxylmethyl, cellulose+Na ₂ SO ₄	BCR	$a = 0.0465 \times U_G^{0.51} \mu_{eff}^{-0.51} \text{ with } \mu_{eff} = K \times \gamma^{n-1} \text{ and } \gamma = 50 \times U_G \text{ }^{(f)}$
Godbole et al. ⁽¹⁷¹⁾	Air/Water, CMC /Sodium sulfate sol.	BCR	$a = 19.2 \times U_G^{0.47} \mu_{eff}^{-0.76}$
He et al. ⁽⁹⁸⁾	Air/Water+CMC, water+triton-X-114	GIR	$a = 400 \times \left(\frac{P_G^*}{V_L} \right)^{0.24} \varepsilon_G^{0.59}$
Smit and During ⁽⁴⁸¹⁾	-	SAR	$\frac{h_1}{d_{lm p.}} = 2.20 \times Fr^* \text{ with } u_\theta = 0.825 \times \omega r \text{ for } r \leq r_C$ $\frac{h_2}{d_{lm p.}} = 1.13 \times Fr^* \text{ with } u_\theta = 0.825 \times \omega r_C \left(\frac{r_C}{r} \right)^{0.6} \text{ for } r > r_C \text{ }^{(g)}$

Table A-10 (Cont'd)

<i>Authors</i>	<i>gas/liquid</i>	<i>Reactors</i>	<i>Correlations</i>
Al Taweel and Cheng ⁽¹⁰⁴⁾	Air/Water +PGME	GIR	$a = 0.14 \times N^{0.77} Q_G^{0.28}$ for air / water $a = 10^{23.9} N^{2.55} Q_G^{0.06} \sigma_L^{-15.4}$ for air / water + additives
Vazquez-Una et al. ⁽⁸⁶⁾	CO ₂ /Water	RT	$\omega = \sqrt{gk \left(1 + \frac{\sigma_L k^2}{g\rho_L} \right) \tanh(kH)}$ with $c^2 = \left(\frac{g}{k} + \frac{\sigma_L k}{\rho_L} \right) \tanh(kH)$ and $\zeta(r,t) = \frac{\omega}{g \left(1 + \frac{\sigma_L k^2}{g\rho_L} \right)} P \sin(kr - \omega t)$ where P is a constant

^(a) a_0 the interfacial area due to the sparger, ^(b) a is the interfacial area accounting for gas entrainment, ^(c) h_1 is the height of the wave above the mean surface level, y is the vertical distance above the mean level, ^(d) with r_C radius of the vortex, h_1 and h_2 the depth and height of the vortex respectively below and above the mean elevation and H_V mean vortex elevation, ^(e) N_2 is the lower impeller mixing speed, ^(f) a in cm^{-1} , U_G in cm.s^{-1} and μ_L in Pa.s , ^(g) with u_θ the tangential velocity and r_C , h_1 , h_2 defined in Nagata⁽⁴⁸⁰⁾

Table A-11: Literature Correlations of $k_L a$ in the SAR

References	Gas	Liquid	Operating Conditions	Correlation
Matsumura et al. ⁽⁴⁵⁷⁾		Water, Various alcohols	Atm.	$\frac{k_L a}{\sqrt{D_O}} = 309 \times \left(\frac{P^*}{V_L} \right)^{0.6} \varepsilon_G^{0.6}$
Albal et al. ⁽⁶⁷⁾	O ₂	Water	13.8-96.5 bar, 298K 13.3-20 Hz	$k_L a = 2.579 \times 10^{-2} D_A^{0.5} \left(\frac{P^*}{V_L} \right)^{0.6} \varepsilon_G^{0.6}$
Albal et al. ⁽⁶⁷⁾	O ₂	Water, CMC	Atm.	$Sh = 1.41 \times 10^{-2} Sc^{0.5} Re^{0.67} We^{1.29}$
Versteeg et al. ⁽²⁶⁶⁾	CO ₂ , N ₂ O	Water, aqueous alkanol-amine	1-10bar, 291-356 K Re: 0.2-1.2 10 ⁴ Sc: 0.1-1.3 10 ⁴	$Sh = 0.064 \times Sc^{0.5} Re^{0.72}$
Mizan et al. ⁽⁴⁸²⁾	H ₂ , C ₂ H ₄	C ₃ H ₆	Fr: 0.9-2.0, Re: 2-4.5 10 ⁵ We: 741-31060	$Sh = 55.2 \times Fr^{2.07} Re^{1.20} We^{-1.34}$
Wu ⁽⁸¹⁾	Air	Water + Na ₂ SO ₃ + CoSO ₄	1.2 < P [*] /V _L < 8.5 kW/m ³	$k_L a = 6.34 \times 10^{-2} \left(\frac{P^*}{V_L} \right)^{0.65}$
Tekie et al. ⁽²⁶⁷⁾	N ₂ , O ₂	Cyclohexane	We: 2100-13300, Fr: 1-3	$Sh = 4.51 \times 10^3 We^{-0.21} Fr^{0.92}$
Tekie et al. ⁽⁴⁸³⁾	N ₂ , O ₂	Cyclohexane	x ₁ : 6.67 < N < 20.0 Hz x ₂ : 7 < P < 35 bar x ₃ : 330 < T < 430 K x ₄ : 0.171 < H < 0.268m	$\ln(k_L a_{N_2}) = -2.90 + 0.36x_1 + 0.07x_2 + 0.28x_3 - 0.18x_4 - 0.39x_1^2 - 0.06x_2^2 + 0.04x_3^2 + 0.063x_4^2 - 2.90e^{(-0.2(x_1 - 0.204)^2)} + 0.04e^{(0.1(x_1 + 3)(4 - x_4))}$ $\ln(k_L a_{O_2}) = -2.93 + 0.11x_1 + 0.10x_2 + 0.23x_3 - 0.12x_4 - 0.38x_1^2 - 0.05x_2^2 - 0.03x_3^2 + 0.07x_4^2 - 2.90e^{(-0.173(x_1)^2)} + 0.11e^{(0.1(x_1 + 3)(4 - x_4))}$
Fillion and Morsi ⁽²⁶⁸⁾	N ₂ , H ₂	Soybean Oil	x ₁ : 373 < T < 473 K x ₂ : 10 < N < 23.3 Hz x ₃ : 0.171 < H < 0.268m x ₄ : 1 < P < 5 bar	$\ln(k_L a_{N_2}) = -6.50 + 0.177x_1 + 0.474x_2 - 0.407x_3 + 0.053x_3^2 - 0.0798x_2x_3$ $\ln(k_L a_{H_2}) = -5.99 + 0.229x_1 + 0.417x_2 - 0.473x_3 - 0.0445x_1^2 + 0.0524x_3^2 - 0.126x_2x_3$

Table A-12: Literature Correlations of $k_L a$ in the GIR

References	GIR	Gas	Liquid	Operating Conditions	Correlation
Joshi and Sharma ⁽⁹²⁾	HS + Hollow impeller	CO ₂	Na ₂ CO ₃ + NaHCO ₃	3-11.7 Hz/d _T :0.41-1.0 d _{imp} /d _T :0.35-0.75 U _G :0.0003-0.032m.s ⁻¹ P*/V _L :1-15kW/m ³	For U _G <0.005: $k_L a = 6.8 \times 10^{-3} \left(\frac{P^*}{V_L} \right)^{0.55} U_G^{0.5}$ For U _G >0.005: $k_L a = 3.26 \times 10^{-3} \left(\frac{P^*}{V_L} \right)^{0.55} U_G^{0.25}$
Kara ⁽⁴⁸⁴⁾	HS + RT	H ₂	Tetralin SRCII	70-135 bar, 606-684K 0.8-6.6 Hz, P*/V _L <119	$k_L a = (3.42 \pm 1.13) \times 10^{-4} \left(\frac{P^*}{V_L} \right)^{0.80 \pm 0.009} \left(\frac{H_L}{D_T} \right)^{-1.9 \pm 0.66}$
Sawant et al. ⁽⁹⁶⁾	Denver Agitator	Air	Water+ Sodium Sulfate	5<N<36 rev/s 0.5<H'/d _{imp} <1.5	$k_L a = 0.0195 \times \left(\frac{P^*}{V_L} \right)^{0.5}$
Karandikar et al. ⁽²⁷²⁾	HS + RT	CO, H ₂ CO ₂ , CH ₄	F-T Wax + water	7-45 bar, 423-498 K 11.6-16.6 Hz	$k_L a = 0.1607 \times \left(\frac{N}{1000} \right)^{3.42} \exp(0.108 \times P) - 0.046$ ^(a) $k_L a = 0.0171 \times \left(\frac{N}{1000} \right)^{6.05} \exp(0.38 \times P) + 0.00525$ ^(b)
Chang and Morsi ⁽²⁵⁰⁾	HS + RT	N ₂ CH ₄	n-hexane Eau	Eu:0.6-110 ⁴ ,We:0.7-710 ⁴ Sc: 1.4-128,Re: 1-3 10 ⁵	$Sh = 2.39 \times 10^{-28} Re^{4.86} Sc^{2.55} Eu^{0.350} We^{0.34}$
Chang and Morsi ⁽²⁵¹⁾	HS + RT	N ₂ ,H ₂ CH ₄	n-decane	We: 1.6-6.5 10 ⁴ Re: 0.6-2 10 ⁵ ,Fr: 1-3	$Sh = 2.95 \times 10^{14} Re^{-1.41} Fr^{4.74} We^{-1.32}$
Chang ⁽²⁴⁹⁾	HS + RT	CO ₂ , CH ₄	n-C ₆ , n-C ₁₀ , n-C ₁₄	Eu: 0.5-1 10 ⁴ ,Sc: 8-500 Re: 0.3-3 10 ⁵ , Fr 1-3	$Sh = 5.114 \times 10^{-12} Re^{2.18} Sc^{1.63} Eu^{0.28} Fr^{1.73}$
Chang ⁽²⁴⁹⁾	HS + RT	H ₂	n-C ₆ , n-C ₁₀ , n-C ₁₄	Eu: 0.6-1 10 ⁴ , We: 1-7 10 ⁴ Sc: 10-150, Re:0.7-3 10 ⁵	$Sh = 2.74 \times 10^{-18} Re^{3.00} Sc^{2.21} Eu^{-0.42} We^{1.29}$
Hichri et al. ⁽⁴⁸⁵⁾	HS + Turbine impeller	H ₂	2-propanol, o-cresol	Sh:0.1-5 10 ⁵ ,V _G /V _L :1-2 Re: 0.7-13×10 ⁴ Sc: 5-9 103,We: 2-6 103	$Sh = 0.123 \times Re^{0.44} Sc^{0.5} We^{1.27} \left(\frac{V_G}{V_L} \right)^{1.1}$
Tekie et al. ⁽²⁶⁷⁾	HS+ RT	N ₂ ,O ₂	Cyclohexane	We: 0.2-1 10 ⁴ ,Fr: 1-3	$Sh = 4.51 \times 10^3 We^{-0.21} Fr^{0.92} (1 + 1.867 \times 10^3 \varepsilon_G)$
Chang and Morsi ⁽⁴⁸⁶⁾	HS + RT	CO	n-hexane,n-decane n-tetradecane	Eu:0.7-110 ⁴ , We:0.2-110 ⁴ Sc: 8-500,Re: 0.4-3 10 ⁵	$Sh = 3.41 \times 10^{-20} Re^{3.06} Sc^{2.43} Eu^{0.16} We^{0.93}$

Table A-12 (Cont'd)

References	GIR	Gas	Liquid	Operating Conditions	Correlation
Dietrich et al. (487)	RT + HS	H ₂	H ₂ O, Ethanol, hydrogenation mixt.	d _{imp} =0.032m, V _R =500ml 0.25<V _L <0.38 dm ³	For H/DT=1: $Sh = 3 \times 10^{-4} Re^{1.45} Sc^{0.5} We^{0.5}$ For H/DT=1.4: $Sh = 1.5 \times 10^{-4} Re^{1.45} Sc^{0.5} We^{0.5}$
Koneripalli et al. (488)	RT + HS	H ₂ , CO CO ₂	Methanol, Ethanol	Eu:0.3-10103, We:0.2-2104 Sc: 7-200, Re: 0.6-4 10 ⁵	$Sh = 4.88 \times 10^6 Re^{-3.81} Sc^{0.23} We^{4.48} Eu^{0.09}$
Heim et al. (106)	Hollow Pipe	Air	Water-fermentation mixture	0.28<Fr* <1.49 33,000<Re<260,000	$\frac{Sh^*}{9.5 \times 10^{-5}} = 1 - e^{-19.64 Re^{-0.216} Fr^{+1.336}}$ (c) $\frac{Sh^*}{1.06 \times 10^{-4}} = 1 - e^{-21.63 Re^{-0.234} Fr^{+1.207}}$ (d) $\frac{Sh^*}{1.04 \times 10^{-4}} = 1 - e^{-1331.20 Re^{-0.557} Fr^{+2.498}}$ (e)
Tekie et al. (483)	HS + RT	N ₂ O ₂	Cyclohexane	x ₁ : 6.67 <N<20.0 Hz x ₂ : 7<P<35 bar x ₃ : 330<T<430 K x ₄ : 0.171<H<0.268m	$ln(k_L a_{N_2}) = 0.01 - 1.92x_1 + 0.10x_2 + 0.27x_3 - 0.05x_4 + 0.72x_1^2 - 0.10x_2^2 + 0.02x_3^2 + 0.01x_4^2 - 3.40e^{(0.04(x_1 - 4.25)^2)} + 0.27e^{(0.1(x_1 + 3)(4 - x_4))}$ $ln(k_L a_{O_2}) = -3.71 + 1.23x_1 + 0.11x_2 + 0.22x_3 - 0.09x_4 + 0.09x_1^2 - 0.04x_2^2 + 0.01x_3^2 + 0.06x_4^2 - 3.75e^{(-0.17(x_1 - 1.60)^2)} + 0.21e^{(0.1(x_1 + 3)(4 - x_4))}$
Fillion et Morsi (268)	HS + RT	N ₂ H ₂	Soybean oil	x ₁ : 373<T<473 K x ₂ : 10<N<23.3 Hz x ₃ : 0.171<H<0.268m x ₄ : 1<P<5 bar	$ln(k_L a_{N_2}) = -4.86 - 0.18x_1 + 0.71x_2 - 0.60x_3 + 0.08x_1^2 + 0.12x_2^2 - 0.23x_1x_2 - 0.08x_2x_3 - 0.34x_1x_2x_3 - 0.07x_1^3 + 0.0027(x_2 + 2.5)e^{2x_3} + 1.28 \tanh(0.3x_2(5.5 - x_3^2)) + 0.1(2 - 4x_3)$ $ln(k_L a_{H_2}) = -3.87 + 0.52x_2 - 0.79x_3 + 0.22x_1^2 - 0.35e^{x_1} + 0.33e^{x_3} - 0.0038(x_2 + 3)e^{2.5x_3} - 0.93x_1e^{- x_2 } + 2.10 \tanh(0.3x_2(8 - x_3^2)) + 0.1(2 - 6x_3)$

RT: Rushton turbine HS: Hollow Shaft, ^(a) CO and H₂, ^(b) CO₂ and CH₄, ^(c) Four-pipe impeller, ^(d) Six-pipe impeller, ^(e) Disk impeller

Table A-13: Literature Correlations of $k_L a$ in the GSR

References	Sparger Type	Gas	Liquid	Operating Conditions	Correlation
Yoshida et al. (276)	Nozzle	O ₂	Water	280-313K1-10Hz	$k_L a = c \times (N^3 d_T^2)^n U_S^m$ (a)
Robinson and Wilke (281)	Nozzle	N ₂ , CO ₂	Aqueous solutions	303 K	$k_L a = 3.89 \times 10^{-3} \times \left(\frac{P_G^*}{V_L} \right)^{0.74} U_S^{0.36}$
Perez and Sandall (280)	Nozzle	CO ₂	Carbopol solution	297-308K, 3-8Hz 0.162-0.466m.s ⁻¹	$\frac{d_{imp}^2 k_L a}{D_{AB}} = 21.2 \times \left(\frac{N \rho_L d_{imp}^2}{\mu_{eff}} \right)^{1.11} \left(\frac{\mu_{eff}}{\rho_L D_{AB}} \right)^{0.5} \left(\frac{d_{imp} U_S}{\sigma_L} \right)^{0.447} \left(\frac{\mu_G}{\mu_{eff}} \right)^{0.694}$ (b)
Bern et al. (283)	-	H ₂	Fat	12-14 bar, 453 K 180-750 rpm	$k_L a = c \times \left(\frac{N^{3.15} d_T^{5.35}}{V_L^{1.41}} \right)^n U_S^m$ (c)
Lopes de Figueiredo and Calderbank (130)	Nozzle	O ₂	Water	5-8 Hz 0.41-4.8 kW.m ⁻³ 0.006-0.013m.s ⁻¹	$\frac{k_L a V_L}{d_T} = 10^{-3} \times (P^*)^{0.58} U_S^{0.75}$
Matsamura et al. (285)		O ₂ , CO ₂ , CH ₄	Sodium sulfite, water	303 K, 8-13 Hz 0.5-3 10 ⁻⁴ m.s ⁻¹	$\frac{k_L a}{\sqrt{D_{AB}}} = 3.09 \times 10^2 \times \left(\frac{P_G^*}{V_L} \right)^{0.6} \varepsilon_G^{0.6}$
Meister et al. (286)	-	Air	Aqu. Sol.	400-1200 rpm 0.005-0.03 m.s ⁻¹	$k_L a = 69.6 \times \left(\frac{E_T}{V_L} \right)^{0.707} U_S^{0.305}$, $k_L a = 104.9 \times \left(\frac{E_T}{V_L} \right)^{0.801} U_S^{0.248}$ (d)
Van't Riet (247)	-	Air	Ions and Ions-free water	0.002 < V _L < 4.4 0.5-10 kW.m ⁻³	For ions-free water: $k_L a = 2.6 \times 10^{-2} \times \left(\frac{P^*}{V_L} \right)^{0.4} U_S^{0.5}$ For water with ions: $k_L a = 2.0 \times 10^{-3} \times \left(\frac{P^*}{V_L} \right)^{0.7} U_S^{0.2}$
Nishikawa et al. (287)	Perforated Tubes	Air	Water	303 K 0-1000 rpm 0.085-1.13 m.s ⁻¹	Turbine: $k_L a = 3.92 \times 10^{-6} \times \left(\frac{P_G^*}{\rho_L} \right)^{1/3} \left(\frac{P^*}{V_L \rho_L} \right)^{0.8}$ (e) Paddle: $k_L a = 5.69 \times 10^{-6} \times \left(\frac{P_G^*}{\rho_L} \right)^{1/3} \left(\frac{P^*}{V_L \rho_L} \right)^{0.75}$ (e)

Table A-13 (Cont'd)

References	Sparger Type	Gas	Liquid	Operating Conditions	Correlation
Judat ⁽²⁸⁸⁾	Data from 13 publications			-	$k_L a = 9.8 \times 10^{-5} \left(B^{-0.6} + 0.81 \times 10^{-\frac{0.65}{B}} \right)^{-1} \left(\frac{P^*}{V_L \rho_L (\mu_L g^4)^{1/3}} \right)^{0.4} \left(\frac{\mu_L}{\rho_L g^2} \right)^{-1/3}$ ^(f)
Gibilaro et al. ⁽²⁸⁹⁾	-	Air	Water	0.4-7 kW.m ⁻³ 0.005-0.025 m.s ⁻¹	$k_L a = 0.49 \times \left(\frac{P^*}{V_L} \right)^{0.76} U_S^{0.45}$
Wu ⁽⁸¹⁾	Ring	Air	Water	0.2-10 kW.m ⁻³ 0.003-0.007 m.s ⁻¹	$k_L a = 1.06 \times \left(\frac{P^*}{V_L} \right)^{0.67} U_S^{0.56}$
Yoshida et al. ⁽²⁹²⁾	Ring, Nozzle, Spider	Air	Water	150-400 rpm 0.004-0.06 m.s ⁻¹	$k_L a = 2.5 \times N^{1.5 \times (1.7 \times 10^{-7})^{1/5}} U_S^{1.06 ni} U_S^{1.29} ni^{0.10}$ ^(g)
Fillion ⁽³⁴⁹⁾	Spider	N ₂ H ₂	Soybean oil	373-473K, 1-5bar 10-23.3 Hz 10.4-51.9 cm ³ .s ⁻¹	$k_L a = 1226 \times T \mu_L^{-0.10} D_{AB}^{0.62} \left(\frac{P_G^*}{V_L} \right)^{0.31} Q_G^{0.58}$

^(a)turbine with 12 vanes: c=1.10, m=n=2/3, $k_L a$ (hr⁻¹), U_S (ft.hr⁻¹), d_T (ft) ^(b) $\mu_e = \frac{\tau'_{1a}}{\gamma_a}$, ^(c)c=0.326, n=0.37±0.02, m=0.32±0.10 d_T (cm), U_S (cm.s⁻¹), V_L (cm³), ^(d) $k_L a$ (hr⁻¹)

^(f) for 2 and 1 impellers, U_S (mm.s⁻¹), E_T/V_L (W.l⁻¹), ^(e) $P_G^*=U_{Sg}$, ^(f) $B = \frac{Q}{d_T^2} \times \left(\frac{\rho_L}{\mu_L g} \right)^{1/3}$, ^(g) ni number of impeller

Table A-14: Literature Correlations of $k_L a$ in the BCR

References	System	Conditions	Correlation
Fair ⁽⁴⁸⁹⁾	Air/Water	Quiscent regime	$k_L a = 3.3 I \left(\frac{D_L \varepsilon_G}{d_{32}^2} \right) \left(\frac{\mu_L}{\rho_L D_{AB}} \right)^{1/3} \left(\frac{d_{32} \rho_L U_G}{\mu_L \varepsilon_G} \right)^{1/2}$
Akita and Yoshida ⁽¹⁷⁰⁾	Air, O ₂ /Water, Glycol, Methanol	U _G : 0.003-0.4 ms ⁻¹ U _L : 0-0.044 ms ⁻¹ D _C : 0.152-0.6 m H _C : 1.26-3.5 m	$\left(\frac{k_L a D_C^2}{D_{AB}} \right) = 0.6 \left(\frac{\mu_L}{\rho_L D_{AB}} \right)^{0.5} \left(\frac{g D_C^2 \rho_L}{\sigma} \right)^{0.62} \left(\frac{g D_C^3 \rho_L^2}{\mu_L^2} \right)^{0.31} \varepsilon_G^{1.1}$
Gestrich et al. ⁽⁴⁹⁰⁾	135 measurments of 7 different groups	-	$k_L a = 0.0424 U_G^{0.21} \left(\frac{H_s}{D_C} \right)^{-0.561} \left(\frac{\rho_L \sigma^3}{g \mu_L^4} \right)^{0.116} \varepsilon_G^{(a)}$
Hikita et al. ⁽²⁹⁴⁾	Air, H ₂ , CO ₂ , CH ₄ , C ₃ H ₈ /Water, sucrose, alcohol	P _{atm} , U _G : 0.042-0.38ms ⁻¹	$\frac{k_L a U_G}{g} = 14.9 \left(\frac{U_G \mu_L}{\sigma} \right)^{1.76} \left(\frac{\mu_L^4 g}{\rho_L \sigma^3} \right)^{-0.248} \left(\frac{\mu_G}{\mu_L} \right)^{0.243} \left(\frac{\mu_L}{\rho_L D_{AB}} \right)^{-0.604}$
Godbole et al. ⁽¹⁷¹⁾	Air/Water, CMC, Na ₂ SO ₄	Patm, U _G < 0.24ms ⁻¹	$k_L a = 8.35 \times 10^{-4} U_G^{0.44} \mu_{eff}^{-1.01}$
Koide et al. ⁽⁴⁹¹⁾	N ₂ /Water, glycerol, glycol, BaCl ₂ , Na ₂ SO ₄ /Glass, bronze	P _{atm} U _G : 0.03-0.15 ms ⁻¹ C _S : 0-200 kg/m ³	$\frac{k_L a \sigma}{\rho_L D_L g} = \frac{2.1 I \left(\frac{\mu_L}{\rho_L D_{AB}} \right)^{0.5} \left(\frac{g \mu_L^4}{\rho_L \sigma^3} \right)^{-0.159} \varepsilon_G^{1.18}}{1 + 1.47 \times 10^4 \left(\frac{C_s}{\rho_s} \right)^{0.612} \left(\frac{U_{\infty}}{\sqrt{D_C g}} \right)^{0.486} \left(\frac{D_C g \rho_L}{\sigma} \right)^{-0.477} \left(\frac{D_C U_G \rho_L}{\mu_L} \right)^{-0.345}}$
Kawase et al. ⁽²⁹⁵⁾	Air/Water, carbopol, CMC	Semitheoretical	$\frac{k_L a D_C^2}{D_{AB}} = 12 C_4 \frac{1}{\sqrt{\pi}} \sqrt{10.7 n^{1/3} Sc^{1/2} Re^{\frac{2+n}{2+2n}} Fr^{\frac{11n-4}{39(1+n)}} Bo^{3/5}}$ $C_4 = 0.0645 n^{3/2}$ n=1 for Newtonian
Ozturk et al. ⁽²⁴³⁾	Air, N ₂ , He, CO ₂ , H ₂ /Pure organic liq.+ mixtures	P _{atm} , U _G : 0.008-0.1 ms ⁻¹	$\frac{k_L a d_B^2}{D_{AB}} = 0.62 Sc^{0.5} Bo^{0.33} Ga^{0.29} Fr^{0.68} \left(\frac{\rho_G}{\rho_L} \right)^{0.04} \quad (b)$
Schumpe at al. ⁽⁴⁹²⁾	N ₂ , O ₂ /Water, Na ₂ SO ₄ /Carbon, Kieselguhr, Al ₂ O ₃	P _{atm} , U _G : < 0.07ms ⁻¹ C _S : < 300kg/m ³	$k_L a = K U_G^{0.82} \mu_{eff}^{-0.39} \quad (c)$

Table A-14 (Cont'd)

References	System	Conditions	Correlation
Salvacion et al. (493)	Air, N ₂ /Water, alcohols/ Calcium alginate gel, polystyrene	U _G up to: 0.15 ms ⁻¹ C _V : 20 vol. %	$\frac{k_L a \sigma}{\rho_L D_{AB} g} = 12.9 Sc^{0.5} Mo^{-0.159} Bo^{-0.184} \epsilon_G^{1.3}$ $\times \left[0.47 + 0.53 \exp \left(-41.4 \frac{\Pi_\infty k_l}{\mu_L U_p} Re_B^{-1/2} \right) \right] \times (1 + 0.62 C_V)^{-1}$ $\Pi_\infty = -C_B (d\sigma/dC_B) \text{ and } k_l = -(d\sigma/dC_B) (3U_p r_B / 2D_B)^{1/2} / r_B RT^{(d)}$
Dewes and Schumpe ⁽⁴⁹⁴⁾	He, N ₂ , air, sulfur hexafluoride/0.8 M Na ₂ SO ₄ +Xantham/ Kieselghur, alumina	P: 1 to 10 bar U _G : 0.01-0.08 ms ⁻¹ C _V : up to 18 vol. %	$k_L a = U_G^{0.9} \mu_{eff}^{-0.55} \rho_G^{0.46}$
Kojima et al. ⁽⁴⁹⁵⁾	N ₂ , O ₂ /Water, Enzyme solutions (C _E)	P: 0.1-1.1 Mpa U _G : 0.005-0.15ms ⁻¹ C _E : 3-163 mg/dm ³	$k_L a = C \epsilon_G^D (\rho_L Q^2 d_0^{-3} \sigma^{-1})^E (P/P_{atm})^F$ C, D, E and F depend on (C _E)
Kang et al. ⁽¹⁸⁵⁾	Air/CMC	P: 0.1-0.6 Mpa U _G : 0.02-0.2 ms ⁻¹ μ_L : 1-38 mPa s	$k_L a = K \times 10^{-3.08} \left(\frac{D_C U_G \rho_G}{\mu_L} \right)^{0.254}$ K correlation dimension
Chen and Leu (496)	Air/Water/Nickel	U _G up to 0.04 m/s H up to 25000 A/m	$k_L a = 0.40 U_G^{0.625} U_L^{0.26} \exp(1.477 \times 10^{-5} H) \text{ }^{(e)}$
Jordan and Schumpe ⁽¹⁹⁰⁾ Jordan et al. ⁽¹⁹¹⁾	He, N ₂ , Air/C ₂ H ₅ OH, C ₄ H ₉ OH, decalin, toluene	ρ_G : 0.19-46.7 kg.m ⁻³ U _G < 0.21ms ⁻¹	$Sh' = a_1 Sc^{0.50} Bo^{0.34} Ga^{0.27} Fr^{0.72} \times \left(1 + 13.2 \times Fr^{0.37} \left(\frac{\rho_G}{\rho_L} \right)^{0.49} \right)^{(b, f)}$ with a ₁ function of column diameter and distributor type (0.669)

^(a) H_S: Slumped column height, m, ^(b) All dimensionless numbers in terms of d_B (rather than D_C), ^(c) K=0.063 (H₂O/salt solution) K=0.042 (H₂O, 0.8M Na₂SO₄), ^(d) C_B=concentration of alcohol, mol/m³; D_B: Diffusivity of alcohol in the liquid, m²/s, ^(e) H: Applied magnetic field, A/m, ^(f) Sh' being the volumetric mass transfer coefficient referred to liquid volume

Table A-15: Literature Correlations of the Mass Transfer Coefficient in Agitated Reactors

<i>Authors</i>	<i>System: gas/liquid</i>	<i>Conditions</i>	<i>Correlations</i>
Whitman ⁽⁴⁹⁷⁾	Film Theory		$k_L = \frac{D_{AB}}{\delta}$
Higbie ⁽⁴⁹⁸⁾	Penetration Theory		$k_L = \sqrt{\frac{4D_{AB}}{\pi t_C}}$
Danckwerts ⁽⁴⁹⁹⁾	Surface Renewal Theory		$k_L = \sqrt{D_{AB}s}$
King ⁽⁵⁰⁰⁾	Eddy Diffusivity Theory		$k_L = \frac{n}{\pi} a^{1/n} D_{AB}^{1-1/n} \sin\left(\frac{\pi}{n}\right)$ with $E = ay^n$ ^(a)
Muenz and Marchello ⁽⁶²⁾	O ₂ , He, CO ₂ , C ₃ H ₆ /Water	RT	$\frac{D_W}{D_{AB}} = 2.74 \times Sc^{-1/6} \left(\frac{f h^2 \rho_L}{\mu_L} \right)^{1/3}$ ^(b)
Prasher and Wills ⁽²⁷⁹⁾	CO ₂ /Water	Stirred tank	$k_L = 0.592 \times D_{AB}^{0.5} \left(\varepsilon \frac{\mu_L}{\rho_L} \right)^{0.25}$ ^(c)
Brian et al. ⁽²⁷⁸⁾	Pivalic acid/Water	Stirred tank	$\frac{k_L d_s}{D_{AB}} = f \left(\frac{d_s^4 \rho_L^3 \varepsilon}{\mu_L^3}, \frac{\mu_L}{\rho_L D_{AB}}, \frac{g d_s^3 (\rho_s - \rho_L) \rho_L}{\mu_L^2}, \frac{\rho_s}{\rho_L} \right)$ ^(c)
Farritor and Hughmark ⁽²⁶⁰⁾	Air/Water	Stirred tank	$k_L = 0.0256 \times d_{imp}^2 N \times \left(N_p \frac{\mu_L}{\rho_L} \right)^{1/3} Sc^{-1/2}$
Miller ⁽¹²⁶⁾	CO ₂ , Air/Aq. Sol.	GSR	$k_L = 683 \times d_s^{1.376} \sqrt{\frac{4D_{AB}}{\pi t_C}}$
Matsumura et al. ⁽⁷²⁾	O ₂ /Water+sodium alginate	SAR	$k_{L-SAR} = 18.2 \times \left(\frac{\rho_L}{g \mu_L} \right)^{-1/3} \left(\frac{\rho_L D_{AB}}{\mu_L} \right)^{2/3} \left(\frac{N_2^3 d_{imp}^3 \rho_L}{\mu_L g} \right)^{-0.23} \left(\frac{U_E}{N_2 d_{imp}} \right)^{0.84}$ ^(d)
Kawase et al. ⁽³⁰⁹⁾	Newtonian, non-newtonian fluids	Theoretical	$k_L = \frac{2}{\sqrt{\pi}} \sqrt{D_{AB}} \left\{ \frac{U_G g}{K/\rho_L} \right\}^{1/2(1+n)}$ ^(e)
Kuthan and Broz ⁽⁵⁰¹⁾	He, N ₂ , C ₃ H ₈ /Ethylene glycol	Wetted column	$k_L = 0.2 \times \left(\frac{\mu_L g}{\rho_L} \right)^{1/3} \left(\frac{\mu_L}{\rho_L D_{AB}} \right)^{0.306} D_{AB}^{2/3}$

Table A-15 (Cont'd)

<i>Authors</i>	<i>System: gas/liquid</i>	<i>Conditions</i>	<i>Correlations</i>
Yoshimura et al. (502)	O ₂ /Water	Wetted column	$k_L = \xi \times \sqrt{\frac{3.46 \times D_{AB} f_w}{\pi}}$ ^(f)
Roberts and Chang ⁽⁵⁰³⁾	Wave Theory (Falling Film)		$\frac{k_L}{k_{L0}} \approx \left[1 + \frac{9}{16} \left(13.4 \times \frac{Q^{11/9} \rho_L^{2/3} g^{2/9}}{v^{2/9} 3^{7/9}} \right)^2 \alpha^2 \left[1 + \frac{\left(\frac{Q}{v} \right)^2}{200} \right] \right]^{1/2} \text{ for } Q/v < 30$ $\frac{k_L}{k_{L0}} \approx 15.3 \times \left(\frac{Q}{v} \right)^{-1/2} \text{ for } Q/v > 40$ $\frac{k_L}{k_{L0}} \approx 0.002 \times \left(\frac{Q}{v} \right)^{2/3} \sqrt{x} \text{ for } Q/v > 300$ ^(g)

^(a) E is the Eddy diffusivity, y is the distance normal to the interface ^(b) f the wave frequency, h the wave amplitude ^(c) ε the total agitation power per unit mass of fluid ^(d) N₂ is the lower impeller mixing speed ^(e) K the consistency index in a power-law model, Pa.sⁿ and n=1 for Newtonian fluid ^(f) f_w the frequency of roll wave and ξ the parameter of waves sweeping high concentration layer ^(g) Q the inlet flow rate, v the normal velocity and x the dimensional column length

Table A-16: Literature Correlations for the Mass Transfer Coefficient in the BCR

<i>Authors</i>	<i>gas/liquid</i>	<i>Conditions</i>	<i>Correlation</i>
Calderbank and Moo-Young ⁽²⁰⁸⁾	O ₂ , CO ₂ /Glycol, water, brine, polyacrylamide sol.	Sieve and sintered plate	$k_L = 0.31 \times \left(\frac{(\rho_L - \rho_G) \mu_L g}{\rho_L^2} \right)^{1/3} \left(\frac{\mu_L}{\rho_L D_{AB}} \right)^{-2/3} \text{ for } d_s < 1.0 \text{ mm}$ $k_L = 0.0031 \times \left(\frac{(\rho_L - \rho_G) \mu_L g}{\rho_L^2} \right)^{1/3} \left(\frac{\mu_L}{\rho_L D_{AB}} \right)^{-2/3} \text{ for } d_s < 2.5 \text{ mm}$ $k_L = 0.0042 \times \left(\frac{(\rho_L - \rho_G) \mu_L g}{\rho_L^2} \right)^{1/3} \left(\frac{\mu_L}{\rho_L D_{AB}} \right)^{-1/2} \text{ for } d_s > 2.5 \text{ mm}$
Fair ^(504, 489)	Air/Water	Quiescent regime	$\frac{k_L d_s}{D_{AB}} = 2 \times \left(1 + 0.276 \times \left(\frac{d_s \rho_L U_G}{\mu_L} \right)^{1/2} \left(\frac{\mu_L}{\rho_L D_{AB}} \right)^{1/3} \right)$
Lamont and Scott ⁽⁵⁰⁵⁾	CO ₂ /Water	Column	$k_L = 0.4 \times \left(P^* \frac{\mu_L}{\rho_L} \right)^{1/4} Sc^{-1/2}$
Akita and Yoshida ⁽⁴⁶²⁾	Air, O ₂ /Water, glycol, methanol, Na ₂ SO ₃	Atmosph. U _G < 0.07 m.s ⁻¹	$k_L = 0.5 g^{5/8} D_{AB}^{1/2} \rho_L^{3/8} \sigma_L^{-3/8} d_s^{1/2}$
Gestrich et al. ⁽⁴⁹⁰⁾	135 data of 7 different groups	-	$k_L = 0.00163 \times U_G^{0.21} \left(\frac{H_s}{D_C} \right)^{-0.261} \left(\frac{\rho_L \sigma^3}{g \mu_L^4} \right)^{0.119}$
Schumpe et al. ⁽⁵⁰⁶⁾	Air/Carboxy methyl, cellulose and Na ₂ SO ₄	D _C =0.14m 0.004<U _G <0.45 ms ⁻¹ U _L =0.0155 ms ⁻¹	$k_L = 0.0045 \times U_G^{0.05} \mu_{eff}^{-0.32} \text{ with } k_L \text{ and } U_G \text{ in cm.s}^{-1}$
Kawase et al. ⁽³⁰⁹⁾	Newtonian, non-newtonian fluids	Theoretical	$k_L = \frac{2}{\sqrt{\pi}} \sqrt{D_{AB}} \left\{ \frac{U_G g}{K/\rho_L} \right\}^{1/2(I+n)} \quad n=1 \text{ for Newtonian fluid } ^{(a)}$
Cockx et al. ⁽⁵⁰⁷⁾	O ₂ , O ₃ /Water sodium sulfite	D _C =0.2/0.053m, H=4/8m 0.025<U _G <0.15 ms ⁻¹ 1.25<U _L <1.8 ms ⁻¹	$\frac{k_L}{U_I^*} Sc^{0.5} = 0.10 \pm 0.02 \quad U_I^* \text{ is friction velocity at the interface}$

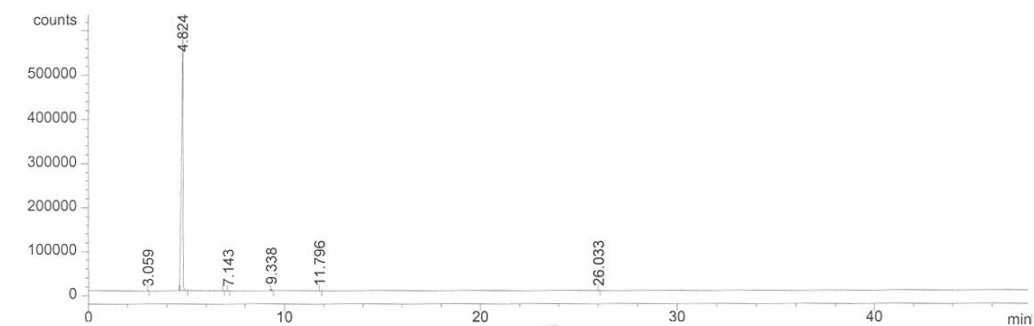
Table A-16 (Cont'd)

<i>Authors</i>	<i>System: gas/liquid/solid</i>	<i>Conditions</i>	<i>Correlation</i>
Tsuchiya et al. (508)	CO ₂ , O ₂ /Water	Column	$k_L = \frac{2}{\sqrt{\pi}} \left[\left(1 - \frac{2.89}{\sqrt{Re}} \right) \frac{D_{AB} U_T f_R}{d_s} \right]^{1/2}$ <p>with $\log(f_R) = 0.5 \times \sqrt{\tanh\left(3.9 \log\left(d_s/0.87\right)\right)} - 1$</p>
Vazquez et al. ⁽³²²⁾	CO ₂ /NaHCO ₃ , Na ₂ CO ₃ +surfactants	D _C =0.113m,H=1.086m U _G <0.002ms ⁻¹	$k_L = K_4 \times U_G^{0.50} \sigma^{1.35}$ with K ₄ function of the bubble plate size

^(a) K the consistency index in a power-law model, Pa.sⁿ

APPENDIX B:

CHEMICAL ANALYSIS



```

=====
                        Area Percent Report
=====
Signal 1: FID1 A,

```

Peak #	RetTime [min]	Type	Width [min]	Area counts*s	Height [counts]	Area %
1	3.059	PP	0.0225	478.08951	301.21088	0.01443
2	4.824	PB	0.0710	3.29594e6	5.96014e5	99.51362
3	6.904	BP	0.0289	378.06326	161.24284	0.01141
4	7.143	PP	0.0394	555.49719	173.42621	0.01677
5	9.338	PB	0.0407	1.14519e4	4355.99707	0.34576
6	11.796	PB	0.0421	2688.05273	802.95117	0.08116
7	26.033	BP	0.0406	557.69275	180.33505	0.01684
Totals :				3.31205e6	6.01989e5	

Figure B-1: Gas Chromatography of Run OTS5321

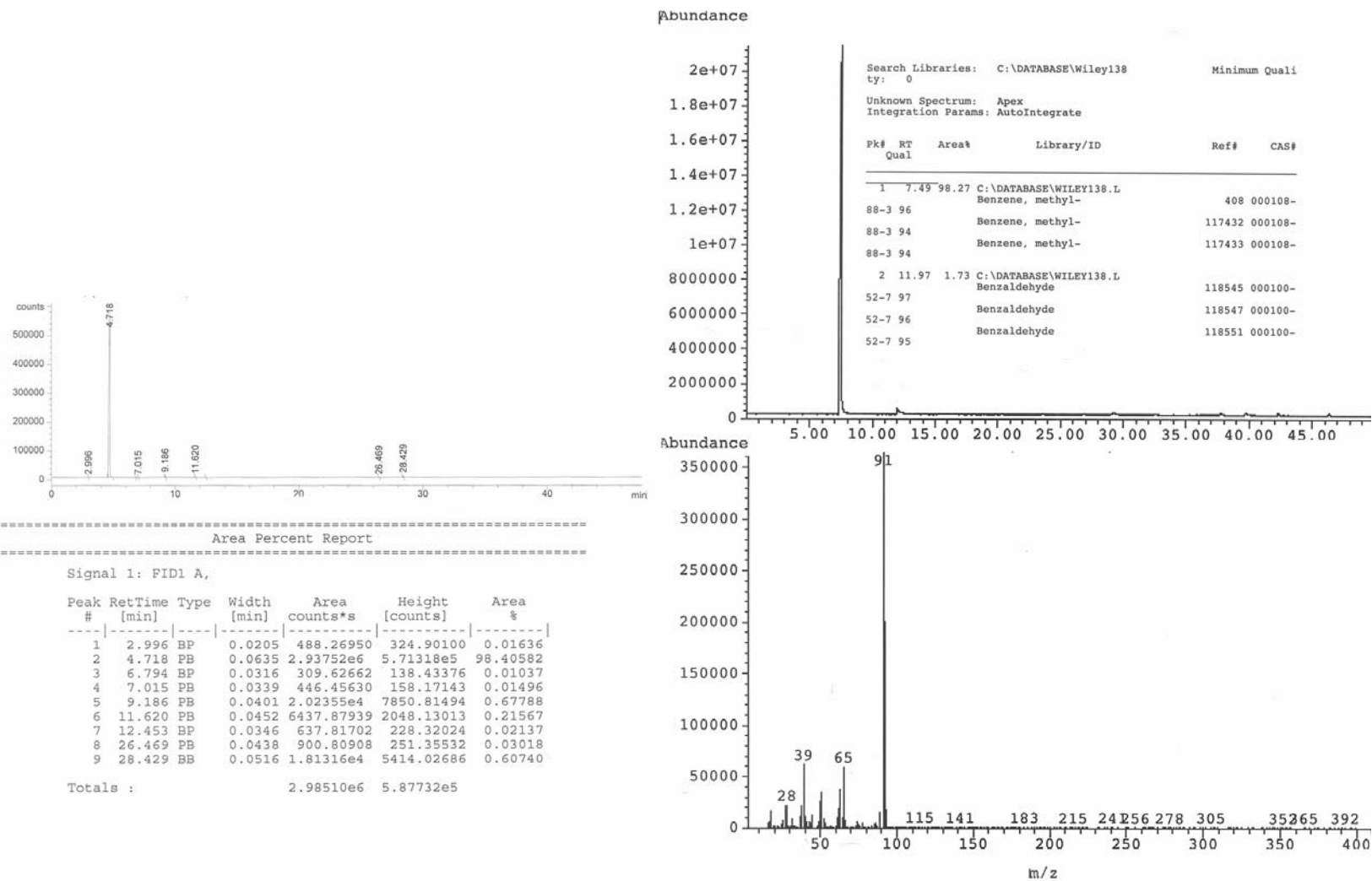


Figure B-2: Gas Chromatography and Mass Spectroscopy of Run OTS5329

APPENDIX C:

ERROR ANALYSIS

Let $Y = f(x_1, \dots, x_n)$ where x_1, \dots, x_n are n independent variables:

$$dY = \sum_{i=1}^n \left(\frac{\partial Y}{\partial x_i} \right)_{x_{j \neq i}} dx_i \quad (C-1)$$

Then, the error is estimated as:

$$\frac{\Delta Y}{Y} \approx \sum_{i=1}^n \left| \frac{\partial Y}{\partial x_i} \right|_{x_{j \neq i}} \frac{\Delta x_i}{Y} \quad (C-2)$$

Hence, expressions of the errors for the different measured parameters are derived in each contactor in the following.

Solubility, C^* :

In the agitated reactors, the solubility C^* is defined as follows:

$$C^* = \left[N_{I,T} - \frac{y_{I,F} P_F (V_R - V_L)}{ZRT} \right] \frac{I}{V_L} \quad (C-3)$$

with

$$N_{I,T} = \left(\frac{I}{v_{I,preh}} - \frac{I}{v_{F,preh}} \right) V_{preh} \quad (C-4)$$

and:

$$v = \frac{ZRT}{P} \quad (C-5)$$

Z , the root of the cubic equation (modified PR-EOS), V_{preh} and V_R , the preheater and reactor volume are assumed to be exact ($\Delta Z=0$, $\Delta V_{preh}=0$, $\Delta V_R=0$). The error on the gas molar fraction was held equal to the specified tolerance in Section 5.1.1. Therefore, the independent variables are:

$$C^* = f(T_{I,preh}, P_{I,preh}, T_{F,preh}, P_{F,preh}, y_{I,F}, P_F, T, V_L) \quad (C-6)$$

Thus, the error on the experimental solubility is approximated as follows:

$$\begin{aligned} \Delta C^* = & \left| \frac{\partial C^*}{\partial T_{l,preh}} \right| \Delta T_{l,preh} + \left| \frac{\partial C^*}{\partial T_{F,preh}} \right| \Delta T_{F,preh} + \left| \frac{\partial C^*}{\partial P_{l,preh}} \right| \Delta P_{l,preh} + \left| \frac{\partial C^*}{\partial P_{F,preh}} \right| \Delta P_{F,preh} \\ & + \left| \frac{\partial C^*}{\partial y_{l,F}} \right| \Delta y_{l,F} + \left| \frac{\partial C^*}{\partial P_F} \right| \Delta P_F + \left| \frac{\partial C^*}{\partial T} \right| \Delta T + \left| \frac{\partial C^*}{\partial V_L} \right| \Delta V_L \end{aligned} \quad (C-7)$$

with the partial derivatives:

$$\frac{\partial C^*}{\partial T_{l,preh}} = \frac{-P_{l,preh} V_{preh}}{Z_l R T_{l,preh}^2 V_L} \quad (C-8)$$

$$\frac{\partial C^*}{\partial P_{l,preh}} = \frac{V_{preh}}{Z_l R T_{l,preh} V_L} \quad (C-9)$$

$$\frac{\partial C^*}{\partial T_{F,preh}} = \frac{P_{l,preh} V_{preh}}{Z_F R T_{F,preh}^2 V_L} \quad (C-10)$$

$$\frac{\partial C^*}{\partial P_{l,preh}} = \frac{V_{preh}}{Z_F R T_{F,preh} V_L} \quad (C-11)$$

$$\frac{\partial C^*}{\partial y_{l,F}} = \frac{-P_F (V_R - V_L)}{Z R T V_L} \quad (C-12)$$

$$\frac{\partial C^*}{\partial P_F} = \frac{-y_{l,F} (V_R - V_L)}{Z R T V_L} \quad (C-13)$$

$$\frac{\partial C^*}{\partial T} = \frac{y_{l,F} P_F (V_R - V_L)}{Z R T^2 V_L} \quad (C-14)$$

$$\frac{\partial C^*}{\partial V_L} = \frac{-C^*}{V_L} \quad (C-15)$$

In the BCR, C^* was calculated using Equation (5-45), which leads to:

$$C^* = f(T_l, P_{l,l}, T_F, P_{l,F}, V_L) \quad (C-16)$$

Thus, the error on the experimental solubility is approximated as follows:

$$\Delta C^* = \left| \frac{\partial C^*}{\partial T_l} \right| \Delta T_l + \left| \frac{\partial C^*}{\partial T_F} \right| \Delta T_F + \left| \frac{\partial C^*}{\partial P_{l,l}} \right| \Delta P_{l,l} + \left| \frac{\partial C^*}{\partial P_{l,F}} \right| \Delta P_{l,F} + \left| \frac{\partial C^*}{\partial V_L} \right| \Delta V_L \quad (C-17)$$

With the partial derivatives:

$$\frac{\partial C^*}{\partial T_l} = \frac{-P_{l,l} (V_R - V_L)}{Z_l R T_l^2 V_L} \quad (C-18)$$

$$\frac{\partial C^*}{\partial P_{l,l}} = \frac{(V_R - V_L)}{Z_l R T_l V_L} \quad (C-19)$$

$$\frac{\partial C^*}{\partial T_F} = \frac{P_{l,F} (V_R - V_L)}{Z_F R T_F^2 V_L} \quad (C-20)$$

$$\frac{\partial C^*}{\partial P_{I,F}} = \frac{-(V_R - V_L)}{Z_F R T_F V_L} \quad (C-21)$$

$$\frac{\partial C^*}{\partial V_L} = -\left(\frac{P_{I,I}}{Z_I R T_I} - \frac{P_{I,F}}{Z_F R T_F}\right) \frac{V_R}{V_L^2} \quad (C-22)$$

Critical Mixing Speed, N_{CR} :

Since the critical mixing speed was read visually, the error on the experimental data was estimated as follows:

$$\Delta N_{CR} = 10 \text{ rpm} \quad (C-23)$$

Induced Gas Flow Rate, Q_{GI} :

In the GIR, the Coriolis mass flow meter Type CMF-010M manufactured by Micro Motion Inc., Boulder, CO was used to measure the induced gas mass flow rate, M^*_{Measured} with the following accuracy:

$$\frac{\Delta M^*}{M^*} = 0.05 \% \quad (C-24)$$

Hence, the error on the induced volumetric gas flow rate was calculated using Equation (5-48), assuming that P_{Tol} is exact in Equation (5-46):

$$Q_{GI} = f(M^*, P_{Gas}, T) \quad (C-25)$$

$$\Delta Q_{GI} = \left| \frac{\partial Q_{GI}}{\partial M^*} \right| \Delta M^* + \left| \frac{\partial Q_{GI}}{\partial P_I} \right| \Delta P_I + \left| \frac{\partial Q_{GI}}{\partial T} \right| \Delta T \quad (C-26)$$

with

$$\frac{\partial Q_{GI}}{\partial M^*} = \frac{y_{Gas}}{\rho_{mixture}} \quad (C-27)$$

$$\frac{\partial Q_{GI}}{\partial P_I} = Q_{GI} \left(\frac{1}{P_I} \frac{P_{Tol} M_{w,Tol}}{M_{w,I} P_I + P_{Tol} M_{w,Tol}} - \frac{1}{P_T} \right) \quad (C-28)$$

$$\frac{\partial Q_{GI}}{\partial T} = \frac{Q_{GI}}{T} \quad (C-29)$$

In the BCR, using the theory on flow through orifices and nozzles⁽⁵⁰⁹⁾, the volumetric flow rate was calculated using the following equation:

$$Q_{Gas} = Y \times C \times \Omega \times \sqrt{\frac{2g \times (144) \times \Delta P}{\rho_G}} \quad (C-30)$$

where Ω is the orifice cross section area, Y the expansion factor and C the flow coefficient. Since Y and C were iteratively computed from the Reynolds number, they were assumed exact. Hence, the error on Q_{Gas} is as follows:

$$Q_{Gas} = f(\Delta P, T, P_I) \quad (C-31)$$

$$\Delta Q_{Gas} = \left| \frac{\partial Q_{Gas}}{\partial \Delta P} \right| \Delta(\Delta P) + \left| \frac{\partial Q_{Gas}}{\partial P_I} \right| \Delta P_I + \left| \frac{\partial Q_{Gas}}{\partial T} \right| \Delta T \quad (C-32)$$

with

$$\frac{\partial Q_{Gas}}{\partial \Delta P} = \frac{1}{2} \frac{Y \times C \times \Omega \times \sqrt{\frac{2g \times 144}{\rho_G}}}{\sqrt{\Delta P}} \quad (C-33)$$

$$\frac{\partial Q_{Gas}}{\partial P_i} = -\frac{1}{2} Y \times C \times \Omega \times \sqrt{\frac{2g \times 144 \times \Delta P}{\rho_G}} \frac{1}{P_i} \quad (C-34)$$

$$\frac{\partial Q_{Gas}}{\partial T} = \frac{1}{2} Y \times C \times \Omega \times \sqrt{\frac{2g \times 144 \times \Delta P}{\rho_G}} \frac{1}{T} \quad (C-35)$$

Sauter Mean Bubble Diameter, d_s :

In the agitated reactors, the Sauter mean bubble diameter is calculated as follows:

$$d_s = \frac{\sum_{i=1}^n d_{Bi}^3}{\sum_{i=1}^n d_{Bi}^2} \quad (C-36)$$

With d_{Bi} estimated from:

$$d_{Bi} = \sqrt{\frac{4A_i}{\pi}} \quad (C-37)$$

A_i is the surface projection of the recorded bubble i determined photographically. From a statistical standpoint, we assumed for $n \geq 200$ that the Sauter mean bubble diameter was independent of the number of bubbles; and the error on d_s is estimated as follows:

$$d_s = f(A_i) \quad (C-38)$$

$$\Delta d_s = \sum_{i=1}^n \left| \frac{\partial d_s}{\partial A_i} \right| \Delta A_i \quad (C-39)$$

with

$$\frac{\partial d_s}{\partial A_i} = \sqrt{\frac{4}{\pi}} \frac{\frac{3}{2} A_i^{1/2} \sum_{j=1}^n A_j - \sum_{j=1}^n A_j^{3/2}}{\left(\sum_{j=1}^n A_j \right)^2} \quad (C-40)$$

In the BCR, on the other hand, the dynamic gas disengagement method was used to calculate d_{Bi} and d_s . Consequently, the bubble diameter was determined from the following equation as explained in Section 5.2.8:

$$d_{Bi} = 0.5917 \times \frac{\left(\frac{L_T}{t_i} \right)^2}{g} \quad (C-41)$$

and its associated error was estimated as follows:

$$d_{Bi} = f(t_i) \quad (C-42)$$

$$\Delta d_{Bi} = \left| \frac{\partial d_{Bi}}{\partial t_i} \right| \Delta t_i \quad (C-43)$$

With

$$\frac{\partial d_{Bi}}{\partial t_i} = -2 \frac{d_{Bi}}{t_i} \quad (C-44)$$

Since Equation (5-58) can be rewritten as:

$$d_S = \frac{\sum_{i=1}^k n_i d_{Bi}^3}{\sum_{i=1}^k n_i d_{Bi}^2} \quad (C-45)$$

With:

$$n_i = \frac{V_G}{\frac{\pi}{6} d_{Bi}^3} = \frac{\varepsilon_{Gi}}{1 - \varepsilon_{Gi}} \frac{V_L}{\frac{\pi}{6} d_{Bi}^3} = \frac{\rho_L}{\rho_L - \rho_G} \frac{\left(1 - \frac{\Delta P_i}{\rho_L g h} \right)}{1 - \frac{\rho_L}{\rho_L - \rho_G} \left(1 - \frac{\Delta P_i}{\rho_L g h} \right)} \frac{V_L}{\frac{\pi}{6} d_{Bi}^3} \quad (C-46)$$

Thus, it follows:

$$d_S = f(d_{Bi}, \Delta P_i, T_{Gi}, T_{Li}, P_i, V_L) \quad (C-47)$$

$$\Delta d_S = \sum_{i=1}^n \left[\left| \frac{\partial d_S}{\partial d_{Bi}} \right| \Delta d_{Bi} + \left| \frac{\partial d_S}{\partial T_{Gi}} \right| \Delta T_{Gi} + \left| \frac{\partial d_S}{\partial T_{Li}} \right| \Delta T_{Li} + \left| \frac{\partial d_S}{\partial P_i} \right| \Delta P_i + \left| \frac{\partial d_S}{\partial (\Delta P_i)} \right| \Delta (\Delta P_i) + \left| \frac{\partial d_S}{\partial V_L} \right| \Delta V_L \right] \quad (C-48)$$

With:

$$\frac{\partial d_S}{\partial d_{Bi}} = \frac{- \sum_{i=1}^k n_i d_{Bi}^3 \times \frac{\rho_L g h - \Delta P_i}{\Delta P_i - \rho_G g h} \frac{V_L}{\frac{\pi}{6} d_{Bi}^2}}{\left(\sum_{i=1}^k n_i d_{Bi}^2 \right)^2} \quad (C-49)$$

$$\frac{\partial d_S}{\partial T_{Gi}} = \frac{-(\rho_L g h - \Delta P_i) \frac{P_i M_{Wi}}{Z R T_{Gi}^2} g h}{(\Delta P_i - \rho_G g h)^2} \frac{V_L}{\frac{\pi}{6}} \left(1 - \frac{\sum_{i=1}^k n_i d_{Bi}^3}{d_{Bi} \sum_{i=1}^k n_i d_{Bi}^2} \right) \frac{1}{\sum_{i=1}^k n_i d_{Bi}^2} \quad (C-50)$$

$$\frac{\partial d_S}{\partial T_{Li}} = \frac{- \frac{2 \ln(0.265)}{7} \frac{1}{T_c} \left(1 - \frac{T_{Li}}{T_c} \right)^{-5/7} \rho_L g h}{(\Delta P_i - \rho_G g h)} \frac{V_L}{\frac{\pi}{6}} \times \left(1 - \frac{\sum_{i=1}^k n_i d_{Bi}^3}{d_{Bi} \sum_{i=1}^k n_i d_{Bi}^2} \right) \frac{1}{\sum_{i=1}^k n_i d_{Bi}^2} \quad (C-51)$$

$$\frac{\partial d_s}{\partial P_i} = \frac{(\rho_L gh - \Delta P_i) \frac{M_{wi}}{ZRT_{Gi}} gh}{(\Delta P_i - \rho_G gh)^2} \frac{V_L}{\frac{\pi}{6}} \times \left(1 - \frac{\sum_{i=1}^k n_i d_{Bi}^3}{d_{Bi} \sum_{i=1}^k n_i d_{Bi}^2} \right) \frac{1}{\sum_{i=1}^k n_i d_{Bi}^2} \quad (C-52)$$

$$\frac{\partial d_s}{\partial (\Delta P_i)} = \frac{(\rho_G - \rho_L) gh}{(\Delta P_i - \rho_G gh)^2} \frac{V_L}{\frac{\pi}{6}} \times \left(1 - \frac{\sum_{i=1}^k n_i d_{Bi}^3}{d_{Bi} \sum_{i=1}^k n_i d_{Bi}^2} \right) \frac{1}{\sum_{i=1}^k n_i d_{Bi}^2} \quad (C-53)$$

$$\frac{\partial d_s}{\partial V_L} = \frac{\rho_L gh - \Delta P_i}{\Delta P_i - \rho_{Gi} gh} \frac{1}{\frac{\pi}{6}} \times \left(1 - \frac{\sum_{i=1}^k n_i d_{Bi}^3}{d_{Bi} \sum_{i=1}^k n_i d_{Bi}^2} \right) \frac{1}{\sum_{i=1}^k n_i d_{Bi}^2} \quad (C-54)$$

Gas Holdup, ε_G :

In the agitated reactors, the gas holdup was determined using the dispersion height technique. Hence, ε_G was calculated from Equation (5-54) and consequently the error was estimated as follow:

$$\varepsilon_G = f(H_D, H) \quad (C-55)$$

$$\Delta \varepsilon_G = \left| \frac{\partial \varepsilon_G}{\partial H_D} \right| \Delta H_D + \left| \frac{\partial \varepsilon_G}{\partial H} \right| \Delta H \quad (C-56)$$

With:

$$\frac{\partial \varepsilon_G}{\partial H_D} = \frac{H}{H_D^2} \quad (C-57)$$

$$\frac{\partial \varepsilon_G}{\partial H} = \frac{-1}{H_D} \quad (C-58)$$

In the BCR, on the other hand, the manometric method was used to calculate the gas holdup as shown in Equation (5-55). Thus, the error on ε_G was estimated as follows:

$$\varepsilon_G = f(T_L, T_G, P_G, \Delta P) \quad (C-59)$$

$$\Delta \varepsilon_G = \left| \frac{\partial \varepsilon_G}{\partial T_L} \right| \Delta T_L + \left| \frac{\partial \varepsilon_G}{\partial T_G} \right| \Delta T_G + \left| \frac{\partial \varepsilon_G}{\partial P_G} \right| \Delta P_G + \left| \frac{\partial \varepsilon_G}{\partial (\Delta P)} \right| \Delta (\Delta P) \quad (C-60)$$

With:

$$\frac{\partial \varepsilon_G}{\partial T_L} = \frac{\frac{2 \ln(0.265)}{T_C} \left(1 - \frac{T_{Li}}{T_C} \right)^{-5/7} \rho_L gh}{(\rho_L gh - \rho_G gh)^2} (\Delta P - \rho_{Gi} gh) \quad (C-61)$$

$$\frac{\partial \varepsilon_G}{\partial T_G} = -\frac{\rho_L \frac{PM_{wi}}{ZRT_G^2} gh}{(\rho_L - \rho_G)^2} \left[1 - \frac{\Delta P}{\rho_L gh} \right] \quad (C-62)$$

$$\frac{\partial \varepsilon_G}{\partial P} = \frac{\rho_L \frac{M_{Wi}}{ZRT_G}}{(\rho_L - \rho_G)^2} \left[1 - \frac{\Delta P}{\rho_L g h} \right] \quad (C-63)$$

$$\frac{\partial \varepsilon_G}{\partial (\Delta P)} = \frac{-1}{(\rho_L - \rho_G) g h} \quad (C-64)$$

Gas-Liquid Interfacial Area, a :

The gas-liquid surface area per unit of liquid volume was estimated by Equation (5-67) and accordingly its error was calculated as follows:

$$a_{Wave} = f(k, V_L, \zeta_{MAX}) \quad (C-65)$$

$$\Delta a_{Wave} = \left| \frac{\partial a_{Wave}}{\partial k} \right| \Delta k + \left| \frac{\partial a_{Wave}}{\partial \zeta_{MAX}} \right| \Delta \zeta_{MAX} + \left| \frac{\partial a_{Wave}}{\partial V_L} \right| \Delta V_L \quad (C-66)$$

and the partial derivatives:

$$\frac{\partial a_{Wave}}{\partial k} = \frac{\int_0^{d_T/2} 2\pi \times r \times k \times \zeta_{MAX}^2 \times \cos(kr) \frac{\cos(kr) - r \times k \times \sin(kr)}{\sqrt{1 + (\zeta_{MAX} \times k \times \cos(kr))^2}} dr}{V_L} \quad (C-67)$$

$$\frac{\partial a_{Wave}}{\partial \zeta_{MAX}} = \frac{\int_0^{d_T/2} 2\pi \times \zeta_{MAX} \times k^2 \times r \frac{(\cos(kr))^2}{\sqrt{1 + (k \times \zeta_{MAX} \times \cos(kr))^2}} dr}{V_L} \quad (C-68)$$

$$\frac{\partial a_{Wave}}{\partial V_L} = \frac{-a_{Wave}}{V_L} \quad (C-69)$$

The gas-liquid interfacial area created by bubbles in the agitated reactors and BCR was always calculated as explained in Sections 5.3.1 and 5.3.2 and its associated error was calculated assuming d_s and ε_G independent as follows:

$$a_B = f(\varepsilon_G, d_s) \quad (C-70)$$

$$\Delta a_B = \left| \frac{\partial a_B}{\partial \varepsilon_G} \right| \Delta \varepsilon_G + \left| \frac{\partial a_B}{\partial d_s} \right| \Delta d_s \quad (C-71)$$

With the partial derivatives:

$$\frac{\partial a_B}{\partial \varepsilon_G} = \frac{6}{d_s (1 - \varepsilon_G)^2} \quad (C-72)$$

$$\frac{\partial a_B}{\partial d_s} = \frac{-a_B}{d_s} \quad (C-73)$$

Volumetric Mass Transfer Coefficient, $k_L a$:

In the agitated reactors, following the procedure described in Section 5.3.3 for the $k_L a$ calculation, an error analysis on Equation (5-115) was derived in the following:

$$k_L a = f(t, P_{l,F}, P_{l,I}) \quad (C-74)$$

Assuming C^* , C_L and V_L only function of pressure at constant T. Hence:

$$\Delta k_L a = \left| \frac{\partial k_L a}{\partial t} \right| \Delta t + \left| \frac{\partial k_L a}{\partial P_{l,F}} \right| \Delta P_{l,F} + \left| \frac{\partial k_L a}{\partial P_{l,I}} \right| \Delta P_{l,I} \quad (C-75)$$

The partial derivatives are:

$$\frac{\partial k_L a}{\partial t} = - \frac{F(P_{l,F}) - F(P_{l,I})}{t^2} \quad (C-76)$$

$$\frac{\partial k_L a}{\partial P_{l,F}} = \frac{1}{t} \frac{\xi_I}{F_2(E_I - C_3)} \left[\frac{\gamma_1 |2P_{l,F} + \beta_I|}{2 \Delta_I} + \frac{\gamma_3 |2P_{l,F} + \beta_3|}{2 \Delta_2} + \frac{\gamma_2 \gamma_1 \beta_I}{2} \Delta I_1 + \frac{\gamma_4 \gamma_3 \beta_3}{2} \Delta I_2 \right] \quad (C-77)$$

$$\frac{\partial k_L a}{\partial P_{l,I}} = \frac{1}{t} \frac{\xi_I}{F_2(E_I - C_3)} \left[\frac{\gamma_1 |2P_{l,I} + \beta_I|}{2 \Delta_I} + \frac{\gamma_3 |2P_{l,I} + \beta_3|}{2 \Delta_2} + \frac{\gamma_2 \gamma_1 \beta_I}{2} \Delta I_1 + \frac{\gamma_4 \gamma_3 \beta_3}{2} \Delta I_2 \right] \quad (C-78)$$

With ΔI_1 and ΔI_2 depending on the value of $4\beta_2 - \beta_1^2$ and $4\beta_4 - \beta_3^2$ respectively.

$$\Delta I_1 = \frac{4}{4\beta_2 - \beta_1^2} \frac{1}{I + \left(\frac{2P + \beta_I}{\sqrt{4\beta_2 - \beta_1^2}} \right)^2} \text{ for } \Delta I_1 \text{ if } 4\beta_2 - \beta_1^2 > 0 \quad (C-79)$$

$$I_1 = \frac{-1}{P_{lf} + \frac{\beta_I}{2}} \text{ if } 4\beta_2 - \beta_1^2 \quad (C-80)$$

$$\Delta I_1 = \frac{2}{\sqrt{\beta_1^2 - 4\beta_2}} \left(\frac{1}{|2P + \beta_I - \sqrt{\beta_1^2 - 4\beta_2}|} - \frac{1}{|2P + \beta_I + \sqrt{\beta_1^2 - 4\beta_2}|} \right) \text{ if } 4\beta_2 - \beta_1^2 < 0 \quad (C-81)$$

$$\Delta I_2 = \frac{4}{4\beta_4 - \beta_3^2} \frac{1}{I + \left(\frac{2P + \beta_3}{\sqrt{4\beta_4 - \beta_3^2}} \right)^2} \text{ for } \Delta I_2 \text{ if } 4\beta_4 - \beta_3^2 > 0 \quad (C-82)$$

$$I_2 = \frac{-1}{P_{lf} + \frac{\beta_3}{2}} \text{ if } 4\beta_4 - \beta_3^2 = 0 \quad (C-83)$$

$$\Delta I_2 = \frac{2}{\sqrt{\beta_3^2 - 4\beta_4}} \left(\frac{1}{|2P + \beta_3 - \sqrt{\beta_3^2 - 4\beta_4}|} - \frac{1}{|2P + \beta_3 + \sqrt{\beta_3^2 - 4\beta_4}|} \right) \text{ if } 4\beta_4 - \beta_3^2 < 0 \quad (C-84)$$

In the BCR, $k_L a$ was calculated from Equation (5-125) and accordingly, assuming that the toluene vapor pressure and reactor volume are exact, He is one variable and the temperature is an average of T_L and T_G , the error was estimated as follows:

$$k_L a = f(t, P_{i,F}, T, V_L, He, P_{i,I}, P_{i,t}) \text{ with} \quad (\text{C-85})$$

$$\begin{aligned} \Delta k_L a = & \left| \frac{\partial k_L a}{\partial t} \right| \Delta t + \left| \frac{\partial k_L a}{\partial P_{i,F}} \right| \Delta P_{i,F} + \left| \frac{\partial k_L a}{\partial P_{i,I}} \right| \Delta P_{i,I} + \left| \frac{\partial k_L a}{\partial V_L} \right| \Delta V_L + \left| \frac{\partial k_L a}{\partial T} \right| \Delta T \\ & + \left| \frac{\partial k_L a}{\partial P_{i,t}} \right| \Delta P_{i,t} + \left| \frac{\partial k_L a}{\partial He} \right| \Delta He \end{aligned} \quad (\text{C-86})$$

The partial derivatives are:

$$\frac{\partial k_L a}{\partial t} = \frac{-I}{t^2} \left(\frac{V_G}{V_L ZRT} \left(\frac{I}{\theta} \right) \ln \left(\theta \times P_{i,t} - \frac{N_0}{V_L} \right) - C \right) \quad (\text{C-87})$$

$$\frac{\partial k_L a}{\partial P_{i,F}} = \frac{I}{t} \left(\frac{V_G}{V_L ZRT} \right)^2 \left(\frac{I}{\theta} \right) \frac{I}{\left(\theta \times P_{i,t} - \frac{N_0}{V_L} \right)} \quad (\text{C-88})$$

$$\frac{\partial k_L a}{\partial P_{i,I}} = \frac{I}{t} \left(\frac{V_G}{V_L ZRT} \right)^2 \left(\frac{I}{\theta} \right) \frac{-I}{\left(\theta \times P_{i,t} - \frac{N_0}{V_L} \right)} \quad (\text{C-89})$$

$$\frac{\partial k_L a}{\partial T} = \frac{I}{t} \frac{V_G}{V_L ZRT} \left(\frac{I}{\theta} \right) \left[\left(\frac{V_G}{\theta V_L ZRT^2} - \frac{I}{T} \right) \ln \left(\theta \times P_{i,t} - \frac{N_0}{V_L} \right) + \frac{\frac{V_G}{V_L ZRT^2} \left(-P_{i,t} + P_{i,I} - P_{i,F} \right)}{\left(\theta \times P_{i,t} - \frac{N_0}{V_L} \right)} \right] \quad (\text{C-90})$$

$$\frac{\partial k_L a}{\partial P_{i,t}} = \frac{I}{t} \frac{V_G}{V_L ZRT} \left(\frac{I}{\theta} \right) \frac{\theta}{\left(\theta \times P_{i,t} - \frac{N_0}{V_L} \right)} \quad (\text{C-91})$$

$$\frac{\partial k_L a}{\partial He} = \frac{I}{t} \frac{V_G}{V_L ZRT} \frac{I}{\theta He^2} \left[\left(\frac{I}{\theta} \right) \ln \left(\theta \times P_{i,t} - \frac{N_0}{V_L} \right) - \frac{P_{i,t}}{\left(\theta \times P_{i,t} - \frac{N_0}{V_L} \right)} \right] \quad (\text{C-92})$$

$$\frac{\partial k_L a}{\partial V_L} = \frac{I}{t} \frac{V_R}{V_L^2 ZRT} \left(\frac{I}{\theta} \right) \left[\left(\frac{V_G}{\theta V_L ZRT} - I \right) \ln \left(\theta \times P_{i,t} - \frac{N_0}{V_L} \right) + \frac{\frac{V_G}{V_R} \left(\frac{N_0}{V_L} - \frac{V_R}{V_L ZRT} \right)}{\left(\theta \times P_{i,t} - \frac{N_0}{V_L} \right)} \right] \quad (\text{C-93})$$

Mass Transfer Coefficient, k_L :

k_L was calculated from Section 5.3, and its associated error was calculated accordingly:

$$k_L = f(k_L a, a) \quad (\text{C-94})$$

$$\Delta k_L = \left| \frac{\partial k_L}{\partial k_L a} \right| \Delta k_L a + \left| \frac{\partial k_L}{\partial a} \right| \Delta a \quad (\text{C-95})$$

With the partial derivatives:

$$\frac{\partial k_L}{\partial k_L a} = \frac{1}{a} \quad (\text{C-96})$$

$$\frac{\partial k_L}{\partial a} = \frac{-k_L}{a} \quad (\text{C-97})$$

Example

In the GIR, under the following conditions: T=400 K, N=1000 rpm, $V_L=0.00247 \text{ m}^3$

$\Delta V_L=10^{-6} \text{ m}^3$, $\Delta P=0.004 \text{ bar}$, $\Delta T=0.1 \text{ K}$, $\Delta t=0$, $\Delta A=0.15 \text{ mm}^2$, $\Delta H_D=\Delta H_P=3 \text{ mm}$

$P_{L,F}$, bar	C^* , kmol.m^{-3}	$\Delta C^*/C^*$, %	$k_L a$, s^{-1}	$\Delta k_L a/k_L a$, %	N_{CR} , rpm	$\Delta N_{CR}/N_{CR}$, %	Q_G , $\text{m}^3.\text{s}^{-1}$	$\Delta Q_G/Q_G$, %	d_s , m	$\Delta d_s/d_s$, %	ε_G , %	$\Delta \varepsilon_G/\varepsilon_G$, %	a , m^{-1}	$\Delta a/a$, %	k_L , m.s^{-1}	$\Delta k_L k_L$, %
2.30	0.0173	9.1	0.1489	20.4	680	1.5	42.9	0.3	0.00140	7.7	1.91	7.6	83.13	15.5	0.00179	35.8
3.89	0.0292	8.5	0.1568	19.3	670	1.5	-	-	0.00141	7.7	1.74	7.4	72.70	15.4	0.00216	34.8
6.48	0.0448	7.3	0.1765	15.2	679	1.5	-	-	0.00141	7.6	1.78	7.4	75.48	15.3	0.00234	30.5
9.42	0.0648	6.5	0.1834	12.8	673	1.5	-	-	0.00142	7.6	1.85	7.5	77.24	15.5	0.00237	28.3
13.16	0.0922	6.1	0.2029	12.5	682	1.5	26.3	0.5	0.00139	7.5	1.82	7.5	75.04	15.6	0.00270	28.1

In the BCR, under the following conditions: T=300 K, $U_G=1000 \text{ m.s}^{-1}$, $V_L=0.098 \text{ m}^3$

$\Delta V_L=0.0001 \text{ m}^3$, $\Delta P=0.004 \text{ bar}$, $\Delta T=0.1 \text{ K}$, $\Delta(\Delta P)=0.1 \text{ Pa}$, $\Delta t=0$

$P_{L,F}$, bar	C^* , kmol.m^{-3}	$\Delta C^*/C^*$, %	$k_L a$, s^{-1}	$\Delta k_L a/k_L a$, %	d_s , m	$\Delta d_s/d_s$, %	ε_G , %	$\Delta \varepsilon_G/\varepsilon_G$, %	a , m^{-1}	$\Delta a/a$, %	k_L , m.s^{-1}	$\Delta k_L k_L$, %
1.81	0.0089	6.2	0.208	3.9	0.00292	2.5	18	1.9	454.5	4.8	0.00046	8.7
3.23	0.0176	5.9	0.263	3.8	0.00239	2.4	21	1.8	681.5	4.6	0.00039	8.4
4.86	0.0207	5.7	0.337	3.7	0.00208	2.2	28	1.7	1117.8	4.6	0.00030	8.3
6.31	0.0360	5.5	0.384	3.6	0.00190	2.1	32	1.7	1474.2	4.6	0.00026	8.2
7.77	0.0378	5.5	0.429	3.6	0.00165	2.1	34	1.6	1854.1	4.5	0.00023	8.1

APPENDIX D:

EXPERIMENTAL PROCEDURE

An experimental $P(t)$ curve of the nitrogen absorption into toluene at 423 K, 1000 rpm and 0.268 m as liquid height, in the GIR mode is depicted in Figure D-1. From these experimental data, the equilibrium solubility was calculated according to the calculation procedure discussed in section 5.1.1. The following results were found:

$T = 423 \text{ K}$	$P_s = 2.788 \text{ bar}$
$N = \text{rpm}$	$\delta_{i,j} = 0.125$
$P_{i,F} = 11.59 \text{ bar}$	$C^* = 0.0988 \text{ kmol/m}^3$
$V_R = 4.030 \cdot 10^{-3} \text{ m}^3$	$V_{L,\text{amp}} = 2.237 \cdot 10^{-3} \text{ m}^3$
$x_1 = 0.012592$	$x_2 = 0.987408$
$y_1 = 0.784956$	$y_2 = 0.215044$
$f_1^L = f_1^G = 11.80$	$f_2^L = f_2^G = 2.68$
$N_G = 0.409547 \cdot 10^{-3} \text{ kmol}$	$N_L = 0.239887 \cdot 10^{-1} \text{ kmol}$
$V_G = 0.956208 \text{ m}^3$	$V_L = 0.305727 \text{ m}^3$

Then, $F(t)$ in Equation (5-116) was calculated from the LHS of Equation (5-115). A plot of $F(t)$ versus t produced a straight line with slope $k_L a$, as can be seen in Figure D-2. $k_L a$ was found to be equal to 0.00587 s^{-1} , and was then used to back-calculate the $P(t)$ - t curve of the absorption. As depicted in Figure D-3, a very good agreement was found.

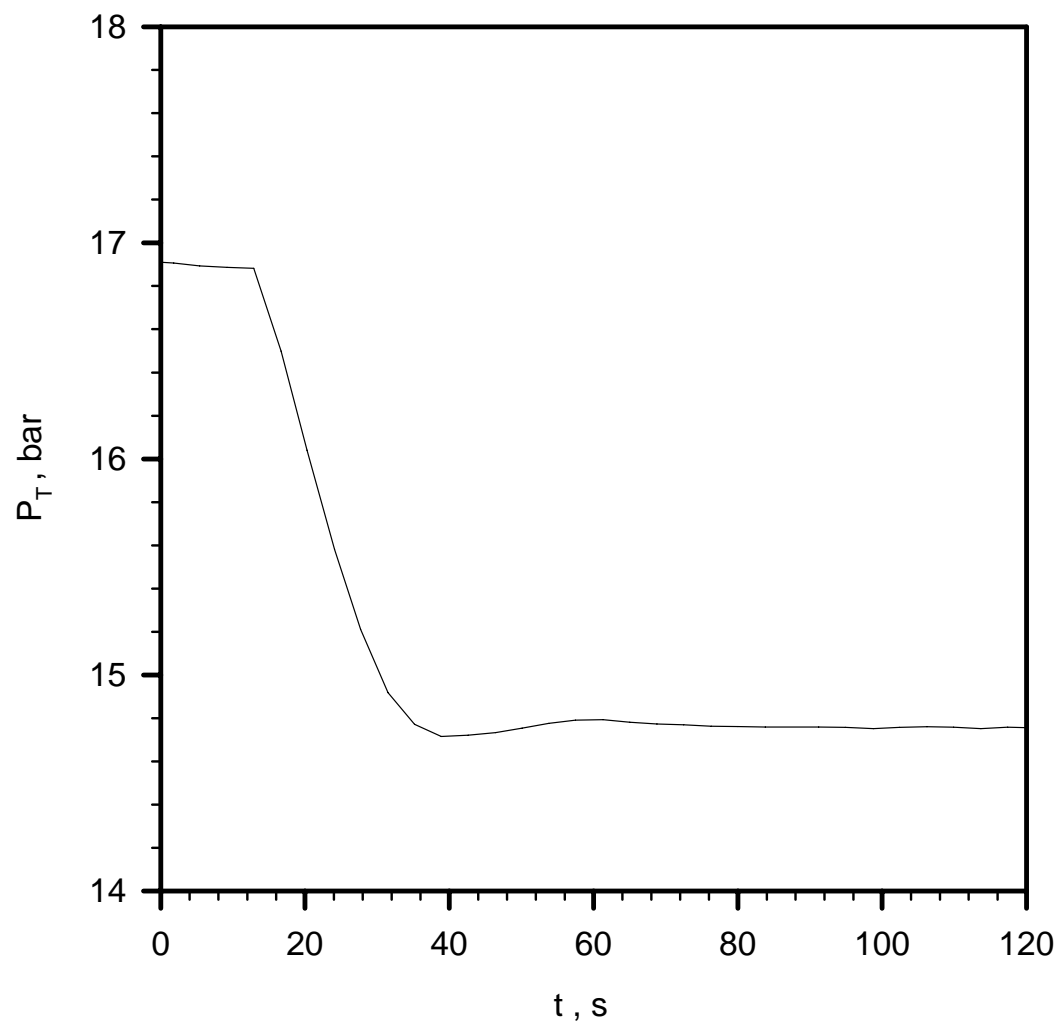


Figure D-1: Typical Experimental $P(t)$ - t Curve For the Transient Gas-Absorption

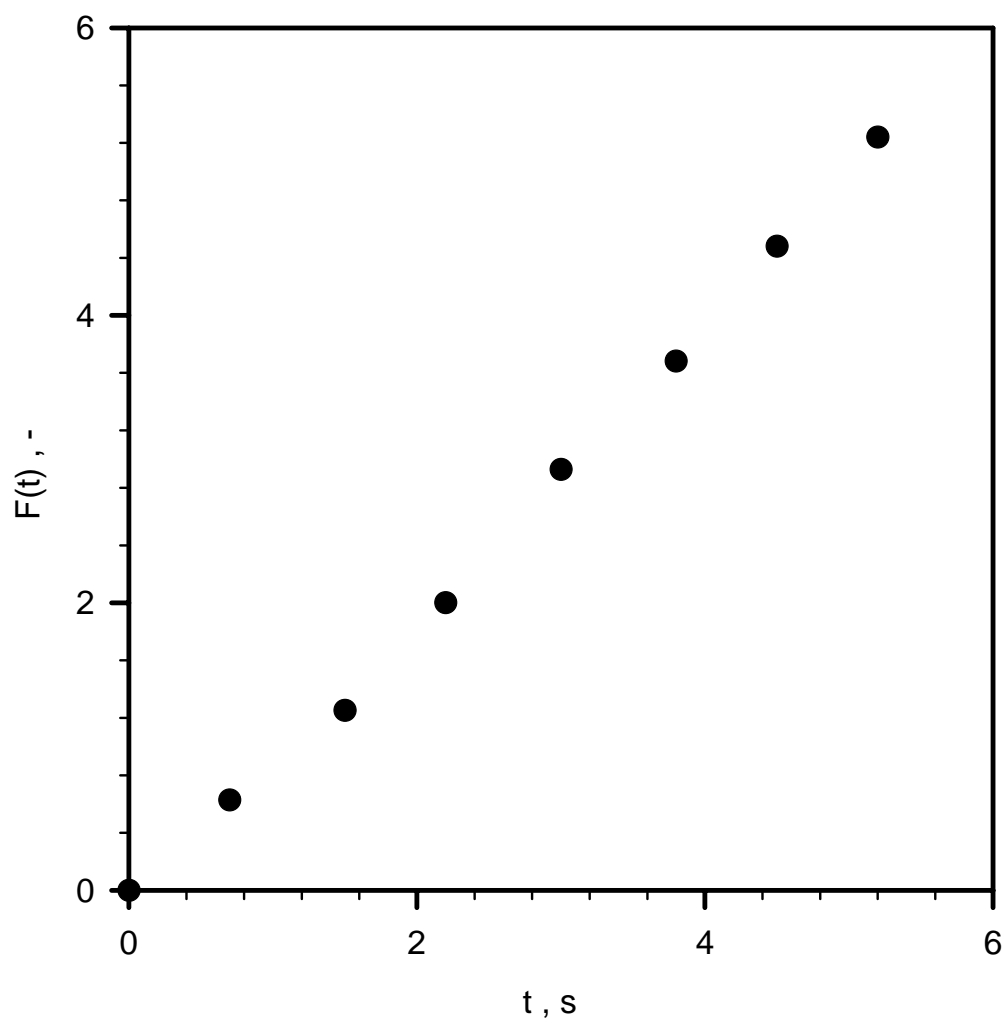


Figure D-2: Plot of $F(t)$ vs. t

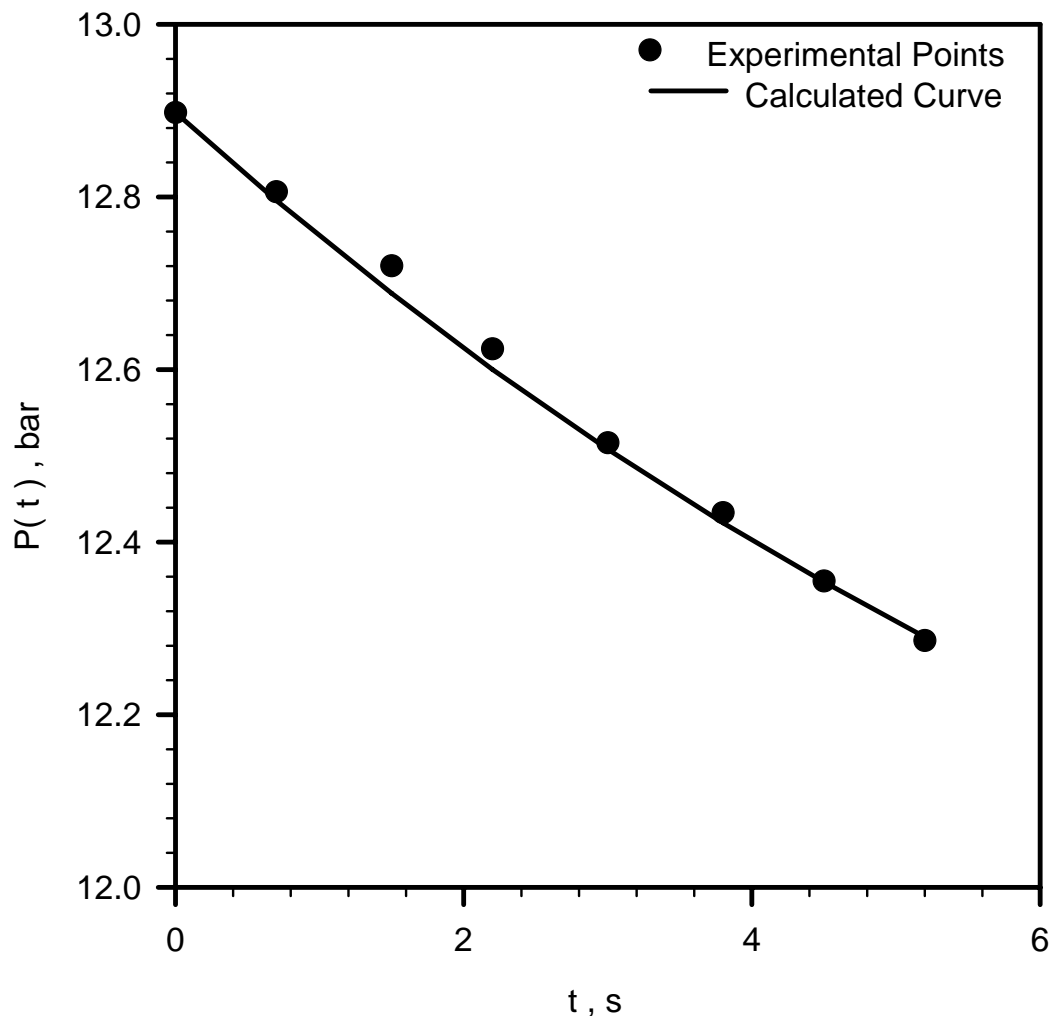


Figure D-3: Comparison Between Experimental and Back-Calculated $P(t)$ vs. t Curve

APPENDIX E:

EXPERIMENTAL DESIGN AND ANALYSIS TECHNIQUES

In this section, different experimental design procedures along with several analysis methodologies are reviewed and described.

Dimensional Analysis

In an attempt to optimize, design and scale-up a process, one should in theory look at the effect of each influencing element independently, which is often complex and impossible. In such situations, however, the theory of similarity is often used to facilitate planning and evaluation of the experimental data. In the following, a comprehensible listing of the variables, which appear to influence the hydrodynamic and mass transfer parameters, is provided. Then, using a dimensional analysis, relationships between the studied parameters and influencing variables will be reduced.

The experimental data collected in this study were obtained in diverse systems, covering wide ranges of operating conditions, reactor types (SAR, GIR, GSR and BCR) and geometries as well as liquid and gas nature. Furthermore, these experimental data were designed to model an industrial process, namely the liquid-phase toluene oxidation process. Since the hydrodynamic and mass transfer parameters are affected by multiple factors, three independent major groups of parameters were first distinguished, allowing a better classification of the studied variables:

Geometrical variables: reactor or column diameter (d_T) or (D_C), impeller diameter ($d_{Imp.}$) and (H_L) liquid height above the impeller, i.e. liquid submergence.

Operating variables: reactor mode (surface aeration reactor: SAR, gas inducing reactor: GIR, gas sparging: GSR), reactor type (BCR and agitated reactors), mixing speed (N), superficial gas velocity (U_G), induced gas flow rate (Q_{G-Gas}), liquid height (H), temperature (T) and gas partial pressure (P_i).

Physicochemical variables: liquid viscosity (μ_L), liquid and gas density (ρ_L et ρ_G), liquid surface tension (σ_L) and the gas diffusion coefficient in the liquid (D_{AB}).

A dimensional analysis ⁽⁵¹⁰⁾ was performed for each studied parameters, where several dimensionless groups were identified depending on the gas-liquid contactors used: Ae , Eu , Fr , Ga , Mo , Re , Sc , We , ρ_G/ρ_L , $HL/D_{Imp.}$. In the agitated reactors, variables affecting the hydrodynamic and mass transfer parameters resulted in the following relationships ⁽⁵¹¹⁾:

$$Fr_{CR} \sim Ga^a \times Mo^b \quad (E-1)$$

$$Ae \sim Mo^a \times Re^b \times Eu^c \times (Fr - Fr_C)^\delta \quad (E-2)$$

$$\frac{d_s}{H_L} \sim Re^\beta \times Eu^\gamma \times Fr^\delta \times We^\epsilon \quad (E-3)$$

$$\varepsilon_G \sim Ae^a \times Re^\beta \times Eu^\chi \times (Fr - Fr_c)^\delta \times We^\epsilon \quad (E-4)$$

$$ad_{Imp.} \sim Ae^a \times Re^\beta \times Eu^\chi \times Fr^\delta \times We^\epsilon \quad (E-5)$$

$$Sh \sim Sc^a \times Re^\beta \times Eu^\chi \times Fr^\delta \times We^\epsilon \times Ae^\eta \quad (E-6)$$

In the BCR, similar expressions were obtained without the critical Froude number and where the impeller diameter was replaced by the column diameter.

It can be argued, however, that some of the dimensionless numbers used either have insignificant impact on the prediction by geometrical similarity or poorly reflect important design criteria. In fact, this is commonly accepted since, as it can be seen in the several dimensionless equations available in the literature, there is a lack of general applications for the developed correlations. It seems that the emerging trend consists of phenomenological correlations, which generate more practical and exploitable results. Therefore, such correlations will be employed when the predictions of dimensionless correlations seem inaccurate.

Statistical Approach

A statistical design and analysis is a powerful tool to study a multi-variable system through a statistically designed number of experiments. The advantages of this tool are reliable observation of variables, minimum number of experiments, and highly accurate statistical correlations⁽⁵¹²⁾.

In this study, the central composite statistical design and analysis technique, similar to that employed by Li et al.⁽⁵¹³⁾, Kim et al.⁽⁵¹⁴⁾, Tekie et al.^(23, 267, 483) and Inga⁽⁵⁶⁾ were used to construct an experimental mapping of the process parameters. Box and Wilson⁽⁵¹⁵⁾ first introduced this design in the 50's as an alternative to 3^k factorials in order to estimate quadratic response surface equations. In this technique, for k independent variables at five levels, the total number of experiments is 2^k factorial points augmented by $2 \times k$ axial points, and with a number of replicates at the central point following Equation (E-7) in order to provide a design with uniform precision⁽⁵¹⁵⁾:

$$N_{Central} = \gamma \times (\sqrt{N_F} + 2)^2 - N_F - 2 \times k \quad (E-7)$$

with $N_{Central}$ the number of replicates at the central point, N_F the number of factorial points, and γ being defined by the following equation:

$$\gamma = \frac{(k+3) + \sqrt{9k^2 + 14k - 7}}{4 \times (k+2)} \quad (E-8)$$

The factorial and axial points are equidistant from the central point to offer rotability properties of the design. In fact, this property becomes important in the examination of the response surface since the orientation of the design does not influence anymore the precision of estimated surfaces. The central composite matrix design was made rotatable by setting the axial point values as follows:

$$\alpha = \sqrt[4]{2^k} \quad (E-9)$$

In this study, four variables, temperature, pressure, mixing speed and liquid height were studied in the agitated reactors and hence $k=4$, $N_{Central}=7$, $N_F=16$ and $\alpha = 2$. The operating conditions used in the SAR, GIR and GSR are

given in Table 23, where two matrices were studied. The coded variables x_i ($i=1,2,3,4$) as defined by Equation (E-10) were used in the distribution and analysis of the experiments.

$$x_i = \frac{E_i - E_{i,c}}{\Delta_i} \quad (\text{E-10})$$

Where E_i and $E_{i,c}$ are the value of the i^{th} variable at any point, and the central point, respectively; and Δ_i is the step size of the i^{th} variable. The distribution of experiments for $k = 4$ can be mathematically represented by Equation (E-11):

$$\sum_{i=1}^4 X_i^2 = \left(\sqrt{N_F}\right)^2 = 2^2 \quad (\text{E-11})$$

The coordinates of the experiments with the coded variables are: (0,0,0,0) for the central point, $(\pm 1, \pm 1, \pm 1, \pm 1)$ for the factorial points, and $(\pm 2, 0, 0, 0)$, $(0, \pm 2, 0, 0)$, $(0, 0, \pm 2, 0)$ and $(0, 0, 0, \pm 2)$ for the axial points. Table E-1 lists the spatial setting of all the experiments and Table 25 shows the range of each variable and its coded value.

Table E-1: Distribution and spatial settings of the experiments according to the central composite statistical design

		H1					H2					H3					H4					H5				
		P1	P2	P3	P4	P5	P1	P2	P3	P4	P5	P1	P2	P3	P4	P5	P1	P2	P3	P4	P5	P1	P2	P3	P4	P5
N1	T1																									
	T2																									
	T3																									
	T4																									
	T5																									
N2	T1																									
	T2																									
	T3																									
	T4																									
	T5																									
N3	T1																									
	T2																									
	T3																									
	T4																									
	T5																									
N4	T1																									
	T2																									
	T3																									
	T4																									
	T5																									
N5	T1																									
	T2																									
	T3																									
	T4																									
	T5																									

The operating conditions used in the bubble column reactor are given in Table 24. A similar central composite statistical design approach to the one used in the agitated reactors with 2 variables was followed in order to determine the number of experiments and assess the significance of the experimental findings. The effect of pressure, P and gas velocity, U_G on the measured experimental data were statistically investigated using this design of two variables at 5 levels, hence $N_C=5$, $N_F=4$ and $\alpha = \sqrt{2}$ from Equations (E-7) through (E-9), leading to numerous combinations of the experimental conditions. Similarly to the agitated reactors design, the coded variables x_i ($i=1,2$) as defined by Equation (E-10) were used in the distribution and analysis of the experiments. The distribution of experiments for $k=2$ can be mathematically represented by Equation (E-12):

$$\sum_{i=1}^4 x_i^2 = \sqrt{2}^2 \quad (E-12)$$

The coordinates of the experiments with the coded variables are: (0,0) for the central point, $(\pm 1, \pm 1)$ for the factorial points, and $(\pm 2, 0)$ and $(0, \pm 2)$ for the axial points. Table 24 also lists the spatial setting of all the experiments and shows the range of each variable along with its coded value.

Conventionally, experimental data obtained using 2^k central composite design are correlated using the quadratic response surface model given in Equation (E-13):

$$\ln(Y_{Pred.}) = \beta_0 + \sum_{i=1}^n (\beta_i x_i) + \sum_{i=1}^n \sum_{j=1}^n (\beta_{ij} x_i x_j) \quad (E-13)$$

Where x_i is the coded variable, β_0 , β_i and β_{ij} are constants and n is the number of variables. In this study, however, the effects of the variables on the experimental output were often found to be non-linear and hence exponential terms were introduced into Equation (E-13) to account for this non-linearity. Therefore, the following general correlation was obtained for $Y_{Pred.}$:

$$\ln(Y_{Pred.}) = \beta_0 + \sum_{i=1}^n \beta_i x_i + \sum_{i=1}^n \sum_{j=1}^n \beta_{ij} x_i x_j + \sum_{i=1}^n \alpha_i \exp(\gamma_i x_i) + \sum_{i=1}^n \sum_{\substack{j=1 \\ j \neq i}}^n \kappa_{ij} \times \exp(\lambda_{ij} x_i x_j) + \xi \times \exp\left(\sum_{i=1}^n \zeta_i x_i\right) \quad (E-14)$$

Where γ_i , α_i , ζ_i , ξ , λ_{ij} and κ_{ij} are constants. The constants in the exponential terms were optimized based on the behavior of $Y_{Pred.}$ with respect to the variables studied. The linear constants were obtained by least-square technique with high confidence level using the statistical software package, Minitab Version 9.1 for Mainframe. However, it should be emphasized that since the central composite statistical design assumes linear quadratic polynomial response surface equation, the non-linearity effects of the process variables on the studied parameters invalidate the model design. Therefore, additional experiments, placed at the boundaries and critical points of the surface curvatures, were inserted in the design matrix in order to compensate for the non-linearity behaviors between the variables and parameters. It should also be mentioned that in the agitated reactors the coded variables were modified in order to obtain one unique statistical correlation for the two central composite statistical designs used. Thus, the new coded variables were determined as follows:

$$\Delta_i = \frac{Max(E_i) - Min(E_i)}{4} \text{ and } x_i = \frac{E_i - (Min(E_i) + 2\Delta_i)}{\Delta_i} \quad (E-15)$$

With $\text{Max}(E_i)$ and $\text{Min}(E_i)$ being the maximum and minimum values of each studied variables for the two central composite statistical design matrices used in this study.

Artificial Neural Network

Artificial neural networks were first introduced in the 1970's and received an increasing attention in the late 1980's and 1990's in various applications, such as signal processing, process control, pattern recognition, medicine, speech recognition, business, and chemical engineering. Despite being traditionally used to model complex non-linear systems⁽⁵¹⁶⁾, artificial neural networks (ANN) appear to be a good alternative to conventional correlations. In fact, since their main advantage is to successfully describe non-linear input-output relationship⁽⁵¹⁷⁾, their manipulation should be much easier than traditional correlations such as empirical, phenomenological or statistical correlations, which frequently assume input-output relations by definition. In the following, after a short introduction on ANN, a precise review of the architecture, calculation and validation process of the back-propagation neural network used in this study is presented.

An artificial neural network is an information-processing system that has certain similarities with the biological neural networks from the brain. As depicted in Figure E-1, the mathematical model of the neural network is based on the assumptions that:

1. Information processing occurs at many simple elements called neurons.
2. The information travels between neurons over connection links.
3. Each connection link has an associated weight that amplifies or not the signal.
4. Each neuron applies an activation function, usually non-linear, to its input to determine the output signal.

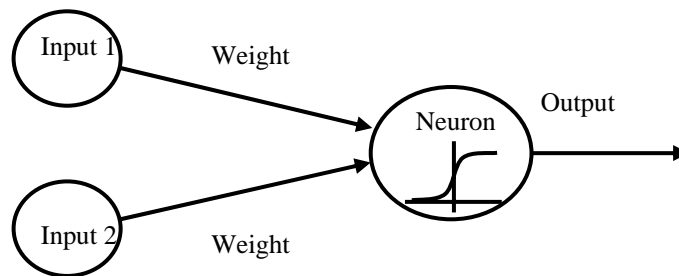


Figure E-1: Schematic of a Simple Artificial Neural Network

Their principal characteristics are as follow:

1. Architecture: pattern of connections between the neurons.
2. Learning Algorithm: iterative procedure to determine the weights between connections.
3. Activation function at the neurons.

Due to their iterative learning abilities, neural networks are able to optimize, correlate and predict with high accuracy in a short period of time a considerable amount of experimental data. Unlike empirical correlations, neural networks are black boxes where no equations are a priori needed. The critical concept in building robust ANNs, However is to create architectures as simple as possible with a fast capacity of learning output data. The robustness of the ANN will therefore be the result of the complex interactions between topology and learning processes. Nonetheless, it is imperative to mention that the choice of the input variables is a key to insure complete description of the systems. It is also clear that the quality and the number of the training observations, i.e. experimental data, have a tremendous impact on both the reliability and performance of the ANN.

One commonly employed neural network for data prediction is the Back-propagation Neural Net as described by Fausett, ⁽⁵¹⁷⁾. The BPNNs used in this study were designed as follows:

- One input layer
- One output node
- p hidden layers
- All neurons are interconnected and all connections are weighted
- Each neuron possess a bias
- The transfer function is a sigmoid of the following from:

$$F(x) = \frac{1}{1 + \exp(-x)} \quad (\text{E-16})$$

This basic architecture of the BPNNs is given in Figure E-2. The number of neurons and hidden layers were determined based on the error analysis during the training phase of the networks ⁽⁵¹⁶⁾. In addition, the PITTNET software package developed at the University of Pittsburgh was used to build and validate the two created BPNNs.

The commonly accepted ^(518, 519, 520) learning algorithm of Back-Propagation was used in this study. During the BPNN training process the gradient descent method is employed in order to adjust the connection weights, as described by Funahashi et al. ⁽⁵¹⁹⁾ and Hornik et al. ⁽⁵²⁰⁾. The training was supervised by means of known output data set, where the squared error is minimized towards the greatest evolution possible. More precisely, the training data sets are feedforward leading to the availability of the calculated output and associated errors. The associated errors are then back-propagated and the adjustment of the weights is completed according to the errors. This process is repeated until satisfactory results are obtained, i.e. the error is lower than the chosen tolerance (10^{-7}). As previously mentioned, the mean squared error between the experimental and calculated output values was the error used, whereas the mean absolute errors (MAE), the root mean squared errors (RMSE) and the R-squared values were also calculated and employed during the validation and construction procedures.

The matrix formulation of the calculation method used in the BPNNs algorithm, depicted in Figure E-3 is summarized in the following.

The net input to (Z_1) is denoted (z_1) and is calculated as follow:

$$(z_1) = (u_0) + [u](x_i) \quad (\text{E-17})$$

The matrix $[u]$ consists of n rows and l columns, corresponding to the number of nodes in the hidden layer and number of input variables:

$$[u] = \begin{bmatrix} u_{1,1} & u_{1,2} & \cdot & \cdot & u_{n,1} \\ u_{2,1} & \cdot & & & \\ \cdot & & \cdot & & \\ \cdot & & & \cdot & \\ u_{n,1} & & & & u_{n,l} \end{bmatrix} \quad (E-18)$$

The activation function is applied to (z_1) to calculate the node output signal denoted (Z_1) :

$$(Z_1) = F((z_1)) \quad (E-19)$$

The net input to (Z_2) is denoted (z_2) and is calculated from the output signal, (Z_1) :

$$(z_2) = (v_0) + [v](Z_1) \quad (E-20)$$

The matrix $[v]$ consists of m rows and n column, corresponding to the number of nodes in the hidden layer 2 and 1:

$$[v] = \begin{bmatrix} v_{1,1} & v_{1,2} & \cdot & \cdot & v_{l,n} \\ v_{2,1} & \cdot & & & \\ \cdot & & \cdot & & \\ \cdot & & & \cdot & \\ v_{m,1} & & & & v_{m,n} \end{bmatrix} \quad (E-21)$$

As in 2., the activation function is applied to (z_2) to calculate the node output signal of the hidden layer 2, denoted (Z_2) :

$$(Z_2) = F((z_2)) \quad (E-22)$$

The net input to (Y_{pred}) is denoted (y_{pred}) and is calculated from the output signal, (Z_2) and the weights, $[w]$ as follow:

$$y_{pred} = w_0 + [w](Z_2) \quad (E-23)$$

Finally, the activation function is applied again to y_{pred} to calculate the output value, Y_{pred} :

$$Y_{pred} = F(y_{pred}) \quad (E-24)$$

During the learning algorithm of back-propagation the MSE is minimized for each epoch, i.e. iteration. In fact, a simultaneous analysis of the MSE and MAE as function of the number of hidden layer and neurons is performed in order to determine the BPNN topology. In order to validate the BPNNs, two approaches were followed. Since ANNs operate as “Black Boxes”, it is almost impossible to determine why a specific network will provide acceptable predictions. Therefore, cross validation methods were first used ^(521, 522) and several networks with identical architecture and parameters were consequently built and trained using all the experimental data set. On the other hand, simultaneously the BPNNs were tested and confirmed through the predictions of untaught output values. This procedure was carried out to ensure that an over- or under-training of the data set did not occur. This was critical to guarantee excellent prediction and interpolation of the training data set from the BPNNs.

INPUTS LAYER 1 LAYER 2 OUTPUT

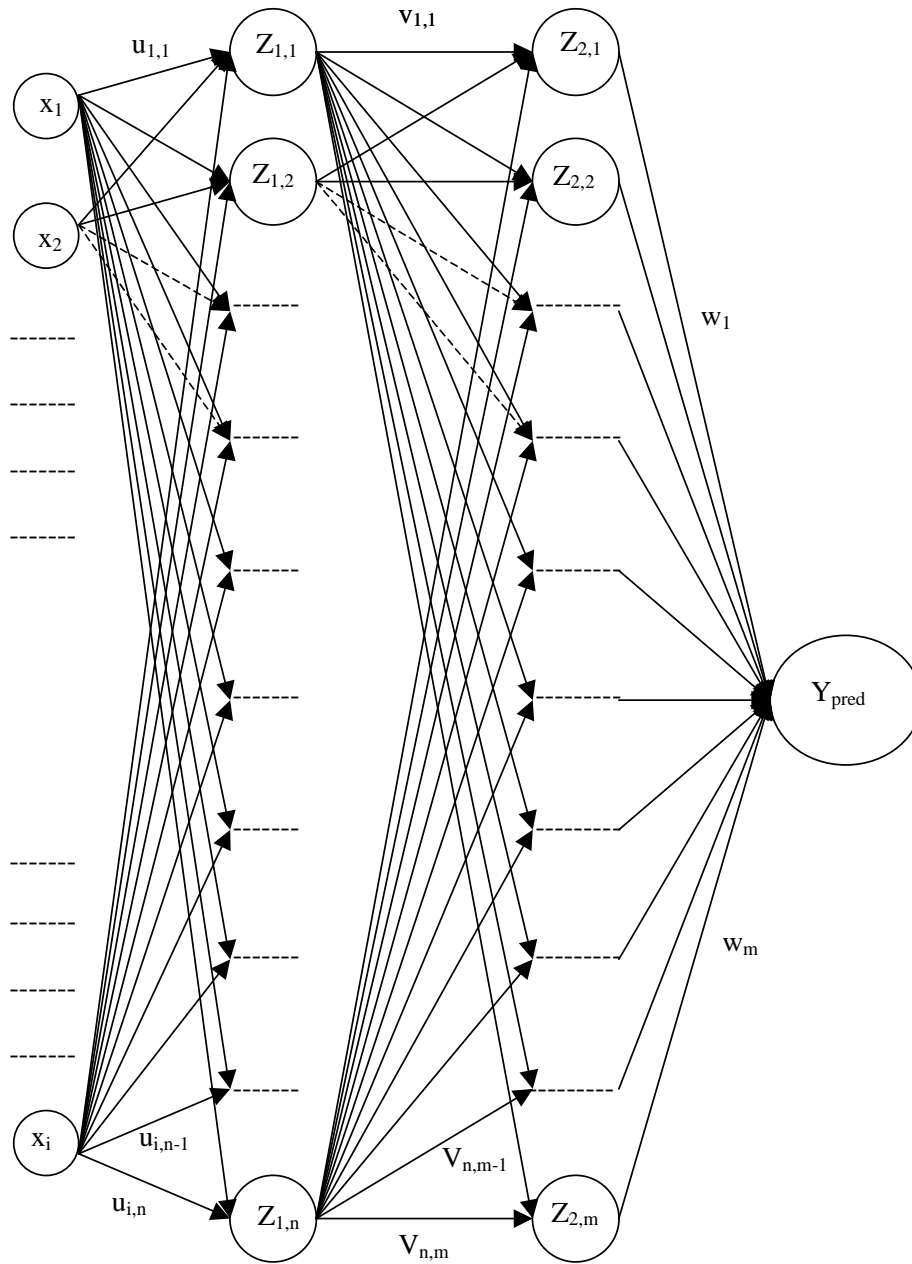


Figure E-2: Basic Architecture of the Neural Networks Employed

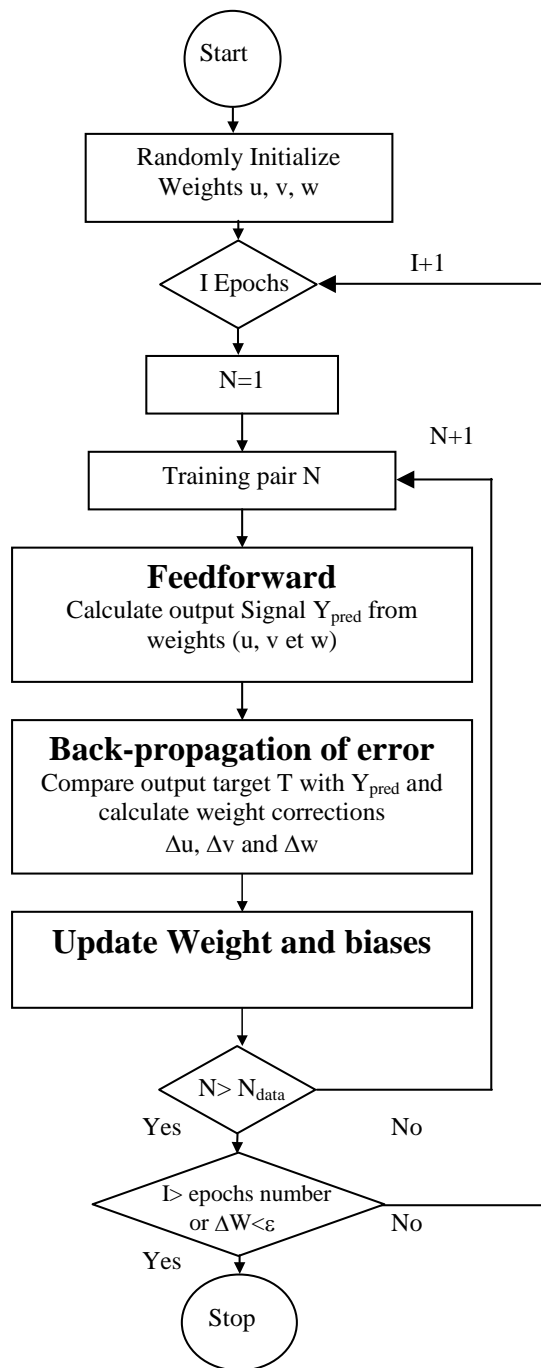


Figure E-3: Training Algorithm of Back-Propagation Neural Networks

REFERENCES

1. Hancock, Toluene, the Xylenes and their Industrial Derivatives (Amsterdam: Elsevier Scientific Publishing Company, 1982).
2. <http://www.gobi.co.uk/>.
3. <http://www.dsm.com/>.
4. McKetta, J. J., Encyclopedia of Chemical Processing and Design, Vol. 4, 24.
5. Kaeding, W.W., "How Dow makes Phenol from toluene," Hydrocarbon Processing, Vol. 1, (1964), pp. 173-176.
6. Kaeding, W.W., Lindblom R.O., Temple, R.G., and Mahon, H. I., "Oxidation of toluene and other alkylated aromatic Hydrocarbons to benzoic acid and phenols," I & EC Process Des. and Dev., Vol. 1, (1968), pp. 97-101.
7. Sheldon, R.A., and Dakka, J., "Heterogeneous catalytic oxidations in the manufacture of fine chemicals," Catalysis Today, Vol. 19, (1994), pp. 215-246.
8. Mills, P.L., and Chaudhari, R.V., "Reaction engineering of emerging oxidation processes," Catalysis Today, Vol. 48, (1999), pp. 17-29.
9. Morimoto, T., and Ogata, Y., "Kinetics of the Autoxidation of Toluene Catalyzed by Cobaltic Acetate," J. Chem. Soc. (B), (1967), pp. 62-67.
10. Borgaonkar, H.V., Raverkar, S.R., and Chandalia, S.B., "Liquid phase oxidation of toluene to Benzaldehyde by air," Ind. Eng. Chem. Prod. Res. Dev., Vol. 23, (1984), pp. 455-458.

11. Mohammad A., "Gas-Liquid Mass Transfer parameters in Benzoic Acid Oxidation Process" (unpublished Ph.D. dissertation, School of Engineering, University of Pittsburgh, 1999).
12. <http://www.the-innovation-group.com/>.
13. Satrio, J.A.B. and Doraiswamy, L.K., "Production of Benzaldehyde: a case study in a possible industrial application of phase-transfer catalysis," Chem. Eng. J., Vol. 82, (2001), pp. 43-56.
14. Rozie, H.J., Dsinter, M.L.C., Dakka J.B., Zoran A. and Sasson Y., "Process for the manufacture of benzaldehyde," (Patent # WO9520560, 1995).
15. Snia Viscosa, "Improved process for the oxidation of toluene and xylene," (Patent # GB1005315, 1965).
16. Poilane, G. and Bonnard, J., "Production of benzyl alcohol and benzaldehyde," (Patent # US3387036, 1968).
17. Sioli, G., Sabatini, A. and Sanchioni, S., "Improvements in the process of oxidation of toluene to benzoic acid," (Patent # GB1219453, 1971).
18. Dakka, J., Zoran, A. and Sasson Y., "Process for the production of benzaldehyde by the catalytic liquid phase air oxidation of toluene," (European Patent # EP0300921, 1989).
19. Bychkov, B.N., Churkin, V.N., Komarov, S.M., Pavlov, S.J.U., Surovtsev, A.A., Bespalov, V.P., Karpov, O.P., Surovtseva, E.H.A., Dobrovinskij, V.E., "Reactors for liquid-phase oxidation of hydrocarbons," (Patent # RU2202408, 2003).
20. Tenneco chemicals, "Improvements in or relating to the production of benzaldehyde," (Patent # GB1291342, 1972).
21. Sheldon, R.A. and Kochi, J.K., "Metal-Catalysed Oxidations of Organic Compounds" (Academic Press, 1981).
22. Chandalia, S.B., Oxidation of hydrocarbons (Bombay: Sevak Publications, 1977), pp. 59-61.
23. Tekie Z., "Mass transfer and modeling of the liquid-phase cyclohexane oxidation process in agitated reactors" (unpublished Ph.D. dissertation, School of Engineering, University of Pittsburgh, 1997).

24. van Dierendonck L., de Jong P., Von den Hoff J., and Vonken H., "Practical Model of the benzoic Acid Oxidation Step as a Means towards Optimization of the Phenol Process," Adv. Chem. Ser., Vol. 133, (1974), pp. 432-448.
25. Merck Handbook
26. Lachowicz, S.K., and Weale, K.E., "Prediction of gas solubility in non polar liquids," Ind. Eng. Chem. Data, Vol. 3, (1958), pp.162-166.
27. Prausnitz, J.M. and Benson, P.R., "Solubility of Liquids in Compressed Hydrogen, Nitrogen, and Carbon Dioxide," A.I.Ch.E. J., Vol. 5(2), (1959), pp. 161-164.
28. Stephen H. and Stephen, T., "Solubilities of Inorganic and Organic Compounds" (The MacMillan Company, New York: Pergamon Press Book, 1963), Vol. 1(1), pp.572-575.
29. Wilhem, E. and Battino, R., "Thermodynamic functions of the solubilities of gases in liquids at 25 °C," Chemical Reviews, Vol. 73(1), (1973), pp. 1-9.
30. Field, L.R., Wilhem, E. and Battino, R., "The solubility of gases in liquids," J. Chem. Therm., Vol. 6, (1974), pp. 237-243.
31. Battino, R., Clever, H.L., and Young, C.L., "The solubility of gases in liquid," IUPAC Solubility Data Series (Oxford: Pergamon, 1982), Vol. 7-10.
32. Battino, R., Rettich, T.R. and Tominaga, T., "Solubility of Nitrogen and Air in liquids," J. Phys.Chem. Ref. Data, Vol.13(2), (1984), pp. 579-580.
33. Liave, F.M. and Chung, T. H., " Vapor- liquid equilibria of nitrogen-hydrocarbon systems at elevated pressures," J. Chem. Eng. Data, Vol. 33, (1988), pp. 123-128.
34. Richon, D., Laugier, S., Renon, H., "High-Pressure Vapor-Liquid Equilibrium Data for Binary Mixtures Containing N₂, CO₂, H₂S, and an Aromatic Hydrocarbon or Propylcyclohexane in the Range 313-473 K," J. Chem. Eng. Data, Vol. 37, (1992), pp. 264-288.

35. Schlichting, H., Langhorst, R., Knapp, H., "Saturation of high pressure gases with low volatile solvents: Experiments and correlation," Fluid Phase Equilibria, Vol. 84, (1993), pp. 143-163.
36. Lin, H.-M., Lee, M.-J. and Lee, R.-J., "Phase equilibria of toluene in mixtures with helium or Nitrogen at high temperatures," J. Chem. Eng. Data, Vol. 40, (1995), pp. 653-656.
37. Ashcroft, S.J. and Ben Isa, M., "Effect of dissolved gases on the density of hydrocarbons," J. Chem. Eng. Data, Vol. 42, (1997), pp. 1244-1248.
38. Emmanuel, N.M., Zaikov, G.E. and Maizus Z.K., "Oxidation of Organic Compounds" (Pergamon Press Book, 1984).
39. Vasvari, G. and Gal, D., "Self-reaction of benzylperoxy radicals in the oxidation of toluene," Ber. Bunsenges. Phys. Chem., Vol. 97(1), (1993), pp. 22-28.
40. Quiroga, O.D., Gottifredi, J.C. and Capretto de Castillo M.E., "Liquid-phase Toluene Oxidation. Formulation of a Kinetic Model," Rev. am. J. chem. Appl. Chem., (1980), pp. 77-88.
41. Dewar, "Electronic Theory of Organic Chemistry," (Oxford Univ. Press, 1949), pp. 277.
42. Cavill, G.W.K. and Solomon, D.H., "Organic Oxidation Processes. Part II," J. Chem. Soc., (1954), pp. 3943-3946.
43. Bacon, R., G.R. and Doggart, J.R., "Oxidation by Persulphate Part II," J. Chem. Soc., (1960), pp. 1333-1338.
44. Howard, J.A. and Ingold, K.U., "Absolute rate constants for hydrocarbon autoxidation," Canadian J. Chem., Vol. 45, (1967), pp. 793-802.
45. Gadelle, C. and Clement, G., "Etude cinetique de l'oxydation radicalaire par l'oxygene des alcoylaromatiques en phase liquide," Bull. Soc. Chim. De France, Vol. 1, (1968), pp. 44-54.
46. Sakota K., Kamiya Y. and Ohta N., "The autoxidation of toluene catalyzed with cobalt monobromide in acetic acid," Bull. Chem. Soc. Jap., 41(3), (1968), pp. 641-6.

47. Scott, E.J. Y. and Chester, A.W., "Kinetics of the cobalt-catalysed autoxidation of toluene in acetic acid," J. Phys. Chem., Vol. 76(11), (1972), pp. 1520-1524.
48. Bhattacharya, D., Guha, D.K. and Roy, A.N., "Liquid-phase Air-Oxidation of Toluene to Benzoic Acid-Part II Kinetics and Mechanism," Chem. Age India, Vol. 24(2), (1973), pp. 87-90.
49. Ivanov, S.K., Kalitchin, ZH.D. and Hinkova, M.K., "Direct Oxidation of Toluene to Benzaldehyde in the presence of N-Bromosuccinimide," Oxidation Communications, Vol. 3(2), (1989), pp. 89-102.
50. Taqui-Khan, M.M., Prakash Rao, A. and Bhatt, S.D., "Oxygenation reactions of saturated and unsaturated substrates by molecular O₂ catalysed by the versatile catalyst K[Ru(EDTA-H)Cl] 2H₂O," J. Molecular Cat., Vol. 75, (1992), pp. 41-51.
51. Gardner, K.A. and Mayer, J.M., "Understanding C-H Bond Oxidations: H* and H⁻ Transfer in the Oxidation of Toluene by Permanganate," Science, Vol. 269, (1995), pp. 1849-1851.
52. Lee, A.-C. and Chou, T.-C., "The role of Ag(I)/Ag(II) mediators in the anodic oxidation of toluene," Chem. Eng. J., Vol. 56, (1995), pp. 1-9.
53. Fereydoon M.-N., Rahimizadeh M. and Mirshahi H. A., "Kinetic studies of the catalytic oxidation of toluene to benzoic acid in the liquid phase," Iranian J. of Chemis. & Chem. Eng., Vol. 16(1), (1997), pp. 8-9.
54. Bahranowski, K., Gasior, M., Kielski, A., Podobinski, J., Serwicka, E.M., Vartikian, L.A. and Wodnicka, K., "Copper-doped alumina-pillared montmorillonites as catalysts for oxidation of toluene and xylenes with hydrogen peroxide," Clay Minerals Vol. 34,, (1999), pp. 79-87.
55. Kantam M.L.; Sreekanth P., Rao K.K., Kumar T.P., Rao B.P.C., Choudary B.M., "An Improved Process for Selective Liquid-Phase Air Oxidation of Toluene," Catalysis Letters, Vol. 81(3-4), (2002), pp. 223-232.
56. Inga, J., "Scale Up and Scale Down of Slurry Reactors: A New Methodology" (unpublished Ph.D. dissertation, School of Engineering, University of Pittsburgh, 1997).
57. Tatterson, G.B., "Scaleup and Design of Industrial Mixing Processes," (McGraw-Hill Inc., 1994).

58. Lee, J.H. and Foster, N.R., "Measurement of Gas-Liquid Mass Transfer in Multi-Phase Reactors," Applied Catalysis, Vol. 63, (1990), pp. 1-36.
59. Chandrasekhar S., "hydrodynamic and Hydromagnetic Stability," (Oxford, UK, Clarendon Press, 1961).
60. Clark, M.W. and Vermeulen, T., "Incipient Vortex Formation in Baffled Agitated vessels," A.I.Ch.E. J., Vol. 10, (1964), pp. 420-422.
61. Muenz, K. and Marchello, J.M., "Technique for Measuring Amplitudes of Small Surface Waves," Review of Scientific Instruments, Vol. 35(8), (1964), pp. 953-957.
62. Muenz, K. and Marchello, J.M., "Surface Motion and Gas Absorption," A.I.Ch.E. J., Vol. 12(2), (1966), pp. 249-253.
63. Boerma, H. and Lankester, J.H., "The Occurrence of Minimum Stirring Rates in Gas-Liquid Reactors," Chem. Eng. Sci., Vol. 23, (1968), pp. 799-801.
64. Metha, V.D. and Sharma, M.M., "Mass Transfer in Mechanically agitated Gas-Liquid Contactors," Chem. Eng. Sci., Vol. 26, (1971), pp. 461-479.
65. van Dierendonck, L.L., Fortuin, J.M.H. and Venderbos, D., "The Specific Contact Area in Gas-Liquid Reactors," Proc. 4th Eur. Conf. on Chem. Eng. Brussels Sep. 9-11, (Pergamon Press, 1971).
66. Bossier, J.A., Farritor, R.E., Hughmark, G.A. and Kao, J.T.F., "Gas-Liquid Interfacial Area Determination for a Turbine Agitated Reactor," A.I.Ch.E. J., Vol. 19, (1973), 1065.
67. Albal, R.S.; Shah, Y.T.; Carr, N.L. and Bell A.T., "Mass Transfer Coefficients and Solubilities for Hydrogen and Carbon Monoxide under Fischer-Tropsch Conditions," Chem. Eng. Sci., Vol. 39, (1984), pp. 905-907.
68. Greaves, M. and Kobbacy, K.A.H., "Surface Aeration in Agitated reactors," I. Chem. E. Symposium Series No. 64, (Rugby, Warks, England: Fluid Mixing, 1981), H1-L1.

69. Sverak, S. and Hruby, M., "Gas entrainment from the liquid surface of vessels with mechanical agitators," Int. Chem. Eng., Vol. 21(3), (1981), pp. 519-526.
70. Joshi, J.B.; Pandit, A.B. and Sharma, M.M., "Mechanically Agitated Gas-Liquid Reactors," Chem. Eng. Sci., Vol. 37(6), (1982), pp. 813-844.
71. Matsumura, M., Sakuma, H., Yamagata, T. and Kobayashi, J., "Gas Entrainment in a New Gas Entraining Fermentor," J. Ferment. Technol., Vol. 60(5), (1982), pp. 457-467.
72. Matsumura, M., Sakuma, H., Yamagata, T. and Kobayashi, J., "Performance of Oxygen Transfer in a New Gas Entraining Fermentor," J. Ferment. Technol., Vol. 60(6), (1982), pp. 551-563.
73. Heywood, N.T., Madhvi, P. and McDonagh, M., "Design of Ungassed Baffled Mixing Vessels to Minimise Surface Aeration of Low Viscosity Liquids," Proc. 5th Eur. Conf. on Mixing, (Wurzburg, Germany, BHRA Fluid Eng., Cranfield, England, 1985), pp. 243-261.
74. Tanaka, M., Noda, S. and O'shima, E., "Effect of the location of a submerged impeller on the enfoldment of air bubbles from the free surface in a stirred vessel," Int. Chem. Eng., Vol. 26(2), (1986), pp. 314-318.
75. Ram Mohan, D., "Performance of Surface Aerators," (unpublished Ms. dissertation, School of Engineering, University of Mumbai, India, 1987).
76. Kolte, P.P., "Design of Surface Aerators," (unpublished Ms. dissertation, School of Engineering, University of Mumbai, India, 1988).
77. Tanaka, M. and Izumi, T., "Gas Entrainment in Stirred-Tank Reactors," Chem. Eng. Res. Des., Vol. 65, (1987), pp. 195-198.
78. Bittins, K. and Zehner, P., "Power and discharge numbers of radial-flow impellers. Fluid-dynamic interactions between impeller and baffles," Chem. Eng. Processing, Vol. 33, (1994), pp. 295-301.
79. Kamen, A.A., Garnier, A., Andre, G., Archambault, J. and Chavarie, C., "Determination of mass transfer parameters in surface aerated bioreactors with bubble entrainment," Chem. Eng. J., Vol. 59, (1995), pp. 187-193.

80. Wichterle, K., "Free Level Effect on the Impeller Power Input in Baffled Tanks," Collect. Czech. Chem. Commun., Vol. 60, (1995), pp. 1274-1280.
81. Wu, H., "An Issue on Applications of a Disk Turbine for Gas-Liquid Mass Transfer," Chem. Eng. Sci., Vol. 50(17), (1995), pp. 2801-2811.
82. Ciofalo, M., Brucato, A., Grisafi, F. and Torracca, N., "Turbulent Flow in Closed and Free-Surface Unbaffled Tanks Stirred by Radial Impellers," Chem. Eng. Sci., Vol. 51(14), (1996), pp. 3557-3573.
83. Wichterle, K. and Sverak, T., "Surface Aeration Threshold in Agitated Vessels," Collect. Czech. Chem. Commun., Vol. 61, (1996), pp. 681-690.
84. Patwardhan, A. and Joshi, J.B., "Design of Stirred Vessels with Gas Entrained from Free Liquid Surface," Canad. J. Chem. Eng., Vol. 76, (1998), pp. 339-364.
85. Roberts, R.M. and Chang, H.-C., "Wave-enhanced interfacial Transfer," Chem. Eng. Sci., Vol. 55, (2000), pp. 1127-1141.
86. Vazquez-Una, G., Chenlo-Romero, F., Sanchez-Barral, M. and Perez-Munuzuri, V., "Mass transfer enhancement due to surface wave formation at a horizontal gas-liquid interface," Chem. Eng. Sci., Vol. 55, (2000), pp. 5851-5856.
87. Zlokarnik M. and Judat H., "Rohr- und Scheibenrührer-Zwei leistungsfähige Rührer zur Flüssigkeitsbegasung," Chemie Ing.-Techn., Vol. 39, (1967), pp. 1163-1168.
88. Zlokarnik M., "Auslegung von Hohlrührern zur Flüssigkeitsbegasung," Chemie Ing.-Techn., Vol. 38, (1966), pp. 357-366.
89. Martin, G.Q., "Gas-Inducing Reactors," Ind. Eng. Chem. Process Des. Dev., Vol. 11(3), (1972), pp. 397-404.
90. Topiwala, H.H., and Hamer, G., "Mass Transfer and Dispersion Properties in a Fermenter with Gas-Inducing Impeller," Trans. Inst. Chem. Eng., Vol. 52, (1974), pp. 113-120.

91. White, D.A., and de Villiers, J.U., "Rates of Induced Aeration in Agitated Vessels," Chem. Eng. J., Vol. 14, (1977), pp. 113-118.
92. Joshi, J.B. and Sharma, M.M., "Mass Transfer and Hydrodynamic Characteristics of Gas Inducing Type of Agitated Contactors," Canad. J. Chem. Eng., Vol. 55, (1977), pp. 683-695.
93. Sawant, S.B. and Joshi, J.B., "Critical impeller speed for the onset of gas induction in gas-inducing types of agitated contactors," Chem. Eng. J., Vol. 18, (1979), pp. 87-91.
94. Zundeleovich, Y., "Power Consumption and Gas Capacity of Self-Inducing Turbo Aerators," A.I.Ch.E. J., Vol. 25, (1979), pp. 763-773.
95. Sawant, S.B., Joshi, J.B. and Pangarkar, V.G., "Mass Transfer and Hydrodynamic Characteristics of the Wemco Type of Flotation Cell," Ind. Chem. Eng., Vol. 22, (1980), pp. 89-96.
96. Sawant, S.B., Joshi, J.B., Pangarkar, V.G. and Mhaskar, R.D., "Mass Transfer and Hydrodynamic Characteristics of the Denver Type of Flotation Cells," Chem. Eng. J., Vol. 21, (1981), pp. 11-19.
97. Raidoo, A.D., Raghav Rao, K.S.M.S., Sawant, S.B. and Joshi, J.B., "Improvements in a Gas-Inducing Impeller Design," Chem. Eng. Commun., Vol. 54, (1987), pp. 241-264.
98. He, D.X, Chiang, S.H. and Klinzing, G.E., "Operating Characteristics of a Gas/Liquid Contactor using Gas-Inducing Turbine," J. of the Chinese Inst. of Chem. Eng., Vol. 22, (1991), pp. 321-328.
99. Rielly, C.D., Evans, G.M., Davidson, J.F. and Carpenter, K.J., "Effect of Vessel Scale-Up on the Hydrodynamics of a Self-Aerating Concave Blade Impeller," Chem. Eng. Sci., Vol. 47, (1992), pp. 3395-3402.
100. Aldrich, C. and van Deventer, J.S.J., "Observations on Induced Aeration in Agitated Slurries," Chem. Eng. J., Vol. 54, (1994), pp. 199-205.
101. Aldrich, C. and van Deventer, J.S.J., "Observations on the Effect of Medium Density and Viscosity on the Rate of Induced Aeration in Agitated Vessels," Metallurgica and Materials Trans. B., Vol. 25B, (1994), pp. 303-306.

102. Saravanan, K., Mundale, V.D. and Joshi, J.B., "Gas Inducing Type Mechanically Agitated Contactors," Ind. Eng. Chem. Res., Vol. 33, (1994), pp. 2226-2241.
103. Aldrich, C. and van Deventer, J.S.J., "Modelling of Induced Aeration in Turbine Aerators by Use of Radial Basis Function Neural Networks," Canad. J. Chem. Eng., Vol. 73, (1995), pp. 808-816.
104. Al Taweel, A.M. and Cheng, Y.H., "Effect of Surface Tension on Gas/Liquid Contacting in a Mechanically-Agitated Tank with Stator," Trans. I. Chem. E., Vol. 73(A), (1995), pp. 654-659.
105. Hsu, Y.C. and Huang, C.-J., "Characteristics of a New Gas-Induced reactor," A.I.Ch.E. J., Vol. 42(11), (1996), pp. 3883-3891.
106. Heim, A., Kraslawski, A., Ryzski, E. and Stelmach, J., "Aeration of Bioreactors by Self-Aspirating Impellers," Chem. Eng. J., Vol. 58, (1995), pp. 59-63.
107. Saravanan, K. and Joshi, J.B., "Fractional Gas Hold-up in Gas Inducing Type of Mechanically Agitated Contactors," Canad. J. Chem. Eng., Vol. 74, (1996), pp. 16-30.
108. Hsu, Y.C. and Huang, C.-J., "Effects of Geometrical Factors on aLiquid Mixing in a Gas-Induced Agitated Tank," J. Chem. Tech. Biotechnol., Vol. 68, (1997), pp. 222-228.
109. Hsu, Y.C., Peng, R.Y. and Huang, C.-J., "Onset of Gas Induction, Power Consumption, Gas Holdup and Mass Transfer in a new Gas-Induced Reactor," Chem. Eng. Sci., Vol. 52, (1997), pp. 3883-3891.
110. Patwardhan, A.W. and Joshi, J.B., "Hydrodynamics of a Stirred Vessel Equipped with a Gas-Inducing impeller," Ind. Eng. Chem. Res., Vol. 36, (1997), pp. 3904-3914.
111. Forrester, S.E., Rielly, C.D. and Carpenter, K.J., "Gas-inducing Impeller Design and performance characteristics," Chem. Eng. Sci., Vol. 53, (1998), pp. 603-615.
112. Hsu, Y.C., Huang, C.-J., Yen, W.-H. and Peng, R.Y., "Onset of Gas Induction and Power Consumption in an Agitated Tank having Shortened Narrower Baffles," J. Chem. Tech. Biotechnol., Vol. 71, (1998), pp. 187-196.

113. Patil, S.S. and Joshi, J.B., "Stability of Gas-Inducing Type Impeller," Canad. J. Chem. Eng., Vol. 77, (1999), pp. 793-803.
114. Patwardhan, A.W. and Joshi, J.B., "Design of Gas-Inducing Reactors," Ind. Eng. Chem. Res., Vol. 38, (1999), pp. 49-80.
115. Evans, G.M., Reilly, C.D., Davidson, J.F. and Carpenter, K.J.A., "Fundamental Study of Gas Inducing Impeller Design," In Fluid Mixing IV, Institution of Chemical Engineers Symposium Series 121, (Rugby, UK, 1990), pp. 137-152.
116. Evans, G.M., Reilly, C.D., Davidson, J.F. and Carpenter, K.J.A., "Hydrodynamic Characteristics of a Gas Inducing Impeller," Proceedings of the 7th European Conference on Mixing, (Kiav, Brugge, Sept. 18-20, Belgium, 1991), pp. 515-523.
117. Topiwala, H.H. and Hamer, G., 1st Symposium on Advances in Mucrobial Engineering, (Marianske Lazne, 1972).
118. Calderbank, P.H., "Physical Rate Processes in Industrial Fermentation. Part I: The Interfacial Area in Gas-Liquid Contacting with Mechanical Agitation," Transactions of Institute of Chem. Eng., Vol. 36, (1958), pp. 442-459.
119. Calderbank, P.H., "Physical Rate Processes in Industrial Fermentation. Part II: Mass transfer Coefficient in Gas-Liquid Contacting with and without Mechanical Agitation," Transactions of Institute of Chem. Eng., Vol. 37, (1959), pp. 173-185.
120. Westerterp, K.R; van Dierendonck, L.L. and De Kraa, J. A., "Interfacial Areas in Agitated Gas-Liquid Contactors," Chem. Eng. Sci., Vol. 18, (1963), pp. 157-176.
121. Westerterp, K.R; "Design of Agitators for Gas-Liquid Contacting," Chem. Eng. Sci., Vol. 18, (1963), pp. 495-502.
122. Rushton, J.H. and Bimbinet J-J., "Holdup and flooding in air liquid mixing," The Canadian Journal of Chemical Engineering, Vol. 46, (1968), pp. 16-21.

123. Lee, J.C. and Meyrick, D.L., "Gas-Liquid interfacial Area in Salt Solutions in an Agitated Tank," Trans. Instn. Chem. Engrs., Vol. 48, (1970), pp. T37.
124. Reith, T. and Beek W.J., "Bubble Coalescence Rates in a Stirred Tank Contactor," Trans. Instn. Chem. Engrs., Vol. 48, (1970), pp. T56-T68.
125. Fuchs, R., Ryu, D.D. and Humphrey, A.E., "Effect of Surface Aeration on Scale-Up Procedures for Fermentation Processes," Ind. Eng. Chem. Process Des. Dev., Vol. 10(2), (1971), pp. 190-196.
126. Miller, D.N., "Scale-Up of Agitated vessels gas-Liquid mass Transfer," A.I.Ch.E. J., Vol. 20(3), (1974), pp. 445-453.
127. Hassan, I.T.M. and Robinson, C.W., "Stirred-Tank Mechanical Power Requirement and Gas Holdup in Aerated Aqueous Phases," A.I.Ch.E. J., Vol. 23, (1977), pp. 48.
128. Loiseau, B., Midoux, N. and Charpentier, J.-C., "Some Hydrodynamics and Power Input data in Mechanically Agitated Gas-Liquid Contactors," A.I.Ch.E. J., Vol. 23, (1977), pp. 931.
129. Matsumura, M., Masunaga, H., Haraya, K. and Kobayashi, J., "Effect of Gas Entrainment on the Power Requirement and Gas Holdup in a Aerated Stirred Tank," J. Ferment. Technol., Vol. 56(2), (1978), pp. 128-138.
130. Lopes de Feigueiredo, M.M. and Calderbank, P.H., "The Scale-Up of Aerated Mixing Vessels for Specified oxygen Dissolution Rates," Chem. Eng. Sci., Vol. 34, (1979), pp. 1333-1338.
131. Nienow, A.W., Chapman, C.M. and Middleton, J.C., "Gas Recirculation Rate through Impeller Cavities and Surface Aeration in Sparged Agitated Vessels," Chem. Eng. J., Vol. 17, (1979), pp. 111-118.
132. Sridhar, T. and Potter, O.E., "Gas Holdup and Bubble Diameters in Pressurized Gas-Liquid Stirred Vessels," Ind. Eng. Chem. Fundam., Vol. 19, (1980), pp. 21-26.
133. Sridhar, T. Potter, O.E., "Interfacial Areas in Gas-Liquid Stirred Vessels," Chem. Eng. Sci., Vol. 35, (1980), pp. 683-695.

134. Hughmark, G.A., "Power Requirements and Interfacial Area in Gas-Liquid Turbine Agitated Systems", Industrial Engineering Chemistry Process Design and Development, Vol. 19, (1980), pp.638-641.
135. Chapman, C.M., Nienow, A.W., Cooke, M. and Middleton, J.-C., "particle-gas-liquid Mixing in Stirred Vessels Part II: Gas-Liquid Mixing," Chem. Eng. Res. Des., Vol. 61, (1983), pp. 82.
136. Warmoeskerken, M.M.C.G. and Smith, J.M., "Flooding of Disc Turbines in Gas-Liquid Dispersions: A New Description of the Phenomenon," Chem. Eng. Sci., Vol. 40(11), (1985), pp. 2063-2071.
137. Hudcova, V., Nienow, A.W., Haozhung, W. and Houxing, L., "Chem. Eng. Sci., Vol. 42, (1987), pp. 375.
138. Greaves, M. and Barigou, M., "Estimation of Gas Hold-Up and Impeller Power in a Stirred vessel Reactor," I. Chem. E. Symposium Series No. 108, (Fluid Mixing III, 1988), pp. 235.
139. Oyevaar M.H.; Zijl A. and Westerterp, K.R., "Interfacial Areas and Gas Holdups at Elevated Pressures in a Mechanically Agitated Gas-Liquid Reactor,". Chem. Eng. Tech., Vol. 11, (1988), pp. 1-10.
140. Lu, W.-M. and Ju, S.-J., "Cavity Configuration, Flooding and Pumping Capacity of Disc-Type Turbines in Aerated Stirred Tanks," Chem. Eng. Sci., Vol. 44, (1989), pp. 333.
141. Veljkovic, V.B. and Skala, D., "Effect of Number of Turbine Impellers on Surface Aeration in Laboratory Fermentor," Biotechnology and Bioengineering, Vol. 34, (1989), pp. 207-213.
142. Oyevaar, M.H., Bos, R. and Westerterp, K.R., "Interfacial Areas and Gas Hold-ups in Gas-Liquid Contactors at Elevated Pressures From 0.1 to 8.0 MPa," Chemical Engineering Science, Vol. 46, (1991), pp. 1217-1231.
143. Veljkovic, V.B., Bicok, K.M. and Simonovic, D.M., "Mechanism, Onset and Intensity of Surface Aeration in Geometrically-Similar, Sparged, Agitated Vessels," Canad. J. Chem. Eng., Vol. 69, (1991), pp. 916-926.
144. Barigou, M. and Greaves, M., "Bubble-Size Distributions in a Mechanically Agitated Gas-Liquid Contactor," Chem. Eng. Sci., Vol. 47, (1992), pp. 2009.

145. Takahashi, K. and Nienow, A.W., "Effect of Gas Density on Power Consumption in Aerated vessel Agitated by a Rushton Turbine," J. Chem. Eng. Japan, Vol. 25, (1992), pp. 432.
146. Parthasarathy, R. and Ahmed, N., "Sauter mean and Maximum Bubble Diameters in Agitated Stirred Vessels," Trans. Instn. Chem. Engrs., Vol. 72(A), (1994), pp. 565.
147. Khare, A.S. and Niranjana, K., "Impeller-Agitated Aerobic Reactor: The Influence of Tiny Bubbles on Gas Hold-Up and Mass Transfer in Highly Viscous Liquids," Chem. Eng. Sci., Vol. 50(7), (1995), pp. 1091-1105.
148. Roman, R.V. and Tudose, R.Z., "Studies on transfer processes in mixing vessels: hydrodynamic of the modified Rushton turbine agitators in gas-liquid dispersions," Chem. Eng. J., Vol. 61, (1996), pp. 83-93.
149. Murugesan, T., "Dispersed Phase Hold-Up in Mechanically Agitated Gas-Liquid Contactors," J. Chem. Technol. Biotechnol., Vol. 72, (1998), pp. 221-226.
150. van Dierendonck, J.J., *et al.*, Chem. Eng. React Symp., (1968), pp. 205.
151. Fillion, B., Lemoine, R., Heintz, Y. and Morsi, B.I., "Characterization of Gas-Inducing Impeller at Elevated Temperatures and Pressures," *In preparation*, (2002).
152. Whitaker, S. and Cassano, A., "Recent Advances in Slurry Reactors by Chaudhari R.V. and Shah Y.T.," Concepts and Design of Chemical Reactors (New York: Gordon and Breach Science Publishers, 1986), Chapter 6, pp. 243-298.
153. Oshinowo T and Charles ME., "Vertical Two-Phase Flow. Part I. Flow Pattern Correlations," The Canadian Journal of Chemical Engineering, Vol. 52, (1974), pp. 25-35.
154. Deckwer, W.D., Louisi, Y., Zaidi, A., and Ralek, M., "Hydrodynamic Properties of the Fischer-Tropsch Slurry Process," Ind. Eng. Chem. Process Des. Dev., Vol. 19, (1980), pp. 699-708.
155. Saxena SC. and Chen ZD., "Hydrodynamics and Heat Transfer of Baffled and Unbaffled Slurry bubble Column," Rev. Chem. Eng., Vol. 10, (1994), pp. 193.
156. Lee SY and Tsui YP., "Succeed at Gas/Liquid Contacting," Chem Eng. Proc., (1999), pp. 23.

157. Vermeer D and Krishna R., "Hydrodynamics and mass transfer in bubble columns in operating in the churn-turbulent regime," Ind. Eng. Chem. Process Des. Dev., Vol. 20(3), (1981), pp. 475-482.
158. Behkish A, Lemoine R, Oukaci R and Morsi BI., "Gas Holdup and Bubble Size Behavior in a Large-Scale Slurry Bubble Column Reactor Operating With an Organic Liquid under Elevated Pressures and Temperatures," Submitted to The Chemical Engineering Journal 2004.
159. Shah YT, Joseph S, Smith DN and Ruether JA., "Two-bubble class model for churn turbulent bubble-column reactor," Ind. Eng. Chem. Process Des. and Dev., Vol. 24(4), (1985), pp. 1096-104.
160. De Swart JWA and Krishna R., "Simulation of the transient and steady state behavior of a bubble column slurry reactor for Fisher-Tropsch synthesis," Chem. Eng. Process., Vol. 41, (2002), pp. 35-47.
161. Gupta P, Al-Dahhan MH, Dudukovic MP and Toseland BA., "Comparison of single- and two-bubble class gas-liquid recirculation models-application to pilot-plant radioactive tracer studies during methanol synthesis," Chem. Eng. Sci., Vol. 56, (2001), pp. 1117-1125.
162. Vial Ch, Laine R, Poncin S, Midoux N and Wild G., "Influence of gas distribution and regime transition on liquid velocity and turbulence in a 3-D bubble column," Chem. Eng. Sci., Vol. 56, (2001), pp. 1085-1093.
163. Anderson JL and Quinn JA., "The Transition to Slug Flow in Bubble Columns," Chem. Eng. Sci., Vol. 25, (1970), pp. 338-340.
164. Chen J, Kemoun A, Al-Dahhan MH, Dudukovic MP, Lee DJ and Fan L-S., "Comparative hydrodynamic study in a bubble column using CARPT, computed tomography and PIV," Chem. Eng. Sci., Vol. 54, (1999), pp. 2199-2207.
165. Nedeltchev S, Kumar SB and Dudukovic MP., "Flow Regime Identification in a Bubble Column Based on Both Kolmogorov Entropy and Quality of Mixedness from CARPT Data," Can. J. Chem. Eng., Vol. 81, (2003), pp. 367-374.
166. Chen RC, Reese J and Fan LS., "Flow structure in a 3-D bubble column and three-phase fluidized bed," AIChE Journal, Vol. 40, (1994), pp. 1093-1104.
167. Lee DJ, McLain BK, Cui Z and Fan LS., "Pressure effect on the flow fields and the Reynolds stresses in a bubble column," Ind. Eng. Chem. Res., Vol. 40, (2001), pp. 1442-1447.

168. Mudde RF, Groen JS and van den Akker HEA., "Liquid velocity field in a bubble column: LDA experiments," Chem. Eng. Sci., Vol. 52, (1997), pp. 4217-4224.
169. Argo, W.B. and Cova, D.R., "Longitudinal Mixing in Gas Sparged Tubular Vessels," Industrial Engineering Chemistry Process Design and Development, Vol. 4, (1965), pp. 352-359.
170. Akita, K. and Yoshida, F., "Gas Holdup and Volumetric Mass Transfer Coefficient in Bubble Columns," Ind. Eng. Chem. Process Des. Dev., Vol. 12, (1973), pp. 76.
171. Godbole, S.P., Schumpe, A., Shah, Y.T. and Carr, N.L., "Hydrodynamics and Mass Transfer in Non-Newtonian Solutions in a Bubble Column," AIChE J., Vol. 30, (1984), pp. 213.
172. Tarmy, B., Chang, M., Coualoglou, C. and Ponzi, P., "The Three Phase Hydrodynamic Characteristics of The EDS Coal Liquefaction Reactors: Their Development and Use in Reactor Scaleup," International Chemical Engineering Symposium Series, Vol. 87, (1984), pp. 303-317.
173. Molerus, O. and Kurtin, M., "Hydrodynamics of Bubble Columns in the Uniform Bubbling Regime," Chem. Eng. Sci., Vol. 40, (1985), pp. 647-652.
174. Daly, J.G., Patel, S.A. and Bukur, D.B., "Measurement of gas holdups and sauter mean diameters in bubble column reactors by dynamic gas disengagement method," Chem. Eng. Sci., Vol. 47, (1992), pp. 3647-3654.
175. Grund, G., Schumpe, A, Deckwer, W.-d., "Gas-Liquid Mass Transfer in a Bubble Column with Organic Liquids," Chemical Engineering Science, Vol. 47(13-14), (1992), pp. 3509-3516.
176. Wilkinson, P.M., Spek, A.P. and van Dierendonck, L.L., "Design Parameters Estimation for Scale-Up of High-Pressure Bubble Columns," AIChE J., Vol. 38, (1992), pp. 544-554.
177. Chabot, J. and de Lasa, H.I., "Gas Holdups and Bubble Characteristics in a Bubble column Operated at High Temperature," Ind. Eng. Chem. Res., Vol. 32, (1993), pp. 2595-2601.
178. Reilly, I.G., Scott, D.S., de Bruijn, T.J.W. and MacIntyre, D., "The Role of Gas Phase Momentum in Determining Gas Holdup and Hydrodynamic Flow Regimes in Bubble Column Operations," Canadian Journal of Chemical Engineering, Vol. 72, (1994), pp. 3.

179. De Swart, J.W.A., "Scale-up of a Fischer-Tropsch Slurry Reactor," (unpublished Ph.D. dissertation, University of Amsterdam, Holland, 1996).
180. Stegeman, D., Knop, P.A., Wijnands, A.J.G. and Westerterp, K.R., "Interfacial Area and Gas Holdup in a Bubble Column Reactor at Elevated Pressures," Ind. Eng. Chem Res., Vol. 35, (1996), pp. 3842-3847.
181. Laari, A., Kallas, J. and Palosaari, S., "Gas-liquid Mass Transfer in Bubble Columns with a T-Junction Nozzle for Gas Dispersion," Chem. Eng. Technol., Vol. 20, (1997), pp. 550-556.
182. Letzel, H.M., Schouten, J.C., van den Bleek, C.M. and Krishna, R., "Influence of Elevated Pressure on the Stability of Bubbly Flows," Chemical Engineering Science, Vol. 52, (1997a), pp. 3733.
183. Letzel, H.M., Schouten, J.C., Krishna, R. and van den Bleek, C.M., "Characterization of regimes and regime transitions in bubble columns by chaos analysis of pressure signals," Chem. Eng. Sci., Vol. 52, (1997b), pp. 4447-4459.
184. Letzel, H.M., Schouten, J.C., van den Bleek, C.M. and Krishna, R., "Effect of Gas Density on Large-Bubble Column Reactors," AIChE J., Vol. 44, (1998), pp. 2333-2336.
185. Kang, Y., Cho, Y.J., Woo, K.J. and Kim, S.D., "Diagnosis of Bubble Distribution and Mass Transfer in Pressurized Bubble Columns with Viscous Liquid Medium," Chem. Eng. Sci., Vol. 54, (1999), pp. 4887.
186. Sarrafi, A., Jamialahmadi, M., Muller-Steinhagen, H. and Smith, J.S., "Gas Holdup in Homogeneous and Heterogeneous gas-Liquid Bubble Column Reactors," The Canadian J. Chem. Eng., Vol. 77, (1999), pp. 11-21.
187. Pohorecki, R., Moniuk, W. and Zdrojowski, A., "Hydrodynamics of a Bubble Column Under Elevated Pressure," Chem. Eng. Sci., Vol. 54, (1999), pp. 5187.
188. Krishna, R., Urseanu, M.I., Dreher, A.J., "Gas holdup in bubble columns: influence of alcohol addition versus operation at elevated pressures", Chem. Eng. Process., Vol. 39, (2000), pp. 371-378.

189. Bouafi, M., Hebrard, G., Bastoul, D. and Roustan, M., "A comparative study of gas holdup, bubble size, interfacial area, and mass transfer coefficient in stirred gas-liquid reactors and bubble columns," Chem. Eng. and Process., Vol. 40, (2001), pp. 97-111.
190. Jordan, U. and Schumpe, A., "The gas density Effect on Mass Transfer in Bubble Columns with Organic Liquids," Chem. Eng. Sci., Vol. 56, (2001), pp. 6267-6272.
191. Jordan, U., Terasaka, K., Kundu, G., Schumpe, A., "Stoffubergang in Druckblasensaulen mit Organischen Flussigkeiten," Chemie Ingenieur Technik, Vol. 73-8, (2001), "Mass transfer in High-Pressure Bubble Columns with Organic Liquids," Chem. Eng. Technol., Vol. 25, (2002), pp. 262-265.
192. Kemoun, A., Ong, B.C., Gupta, P., Al-Dahhan, H. and Dudukovic, M.P., "Gas holdup in bubble columns at elevated pressure via computed tomography," Int. J. Multiphase Flow, Vol. 27, (2001), pp. 929-946.
193. Magaud, F., Souhar, M., Wild and G, Boisson, N., "Experimental study of bubble column hydrodynamics," Chem. Eng. Sci., Vol. 56, (2001), pp. 4597-4607.
194. Moustiri, S., Hebrard, G., Tharre, S.S. and Roustan, M., "A unified correlation for predicting liquid axial dispersion coefficient in bubble columns," Chem. Eng. Sci., Vol. 56, (2001), pp. 1041-1047.
195. Pohorecki, R., Moniuk, W., Zdrojkowski, A. and bielski, P., "Hydrodynamics of a Pilot Plant Bubble Column Under Elevated temperature and Pressure," Chemical Engineering Science, Vol. 56, (2001), pp. 1167-1174.
196. Pohorecki, R., Moniuk, W., bielski, P. and Zdrojkowski, A., "Modelling of Coalescence/Redispersion Processes in Bubble Columns," Chemical Engineering Science, Vol. 56, (2001), pp. 6157-6164.
197. Davies, R.M. and Taylor, G., "The Mechanics Of Large Bubbles Rising Through Extended Liquids And Through Liquid In Tubes," Proceedings of the Royal Society, (1950), pp. 375-390.
198. Guy, C., Carreau, P.J. and Paris, J., "Mixing Characteristics and Gas Holdup of a Bubble Column.," Canadian Journal of Chemical Engineering, Vol. 64, (1986), pp. 23.
199. Wilkinson, P.M. and van Dierendonck, L.L., "Pressure and Gas Density Effects on Bubble Break-up and Gas Holdup in Bubble Columns," Chemical Engineering Science, Vol. 8, (1990), pp. 2309.

200. Wilkinson M. P.; Haringa H. and van Dierendonck L. L. "Mass Transfer and Bubble Size in a Bubble column Under Pressure," Chem. Eng. Chem. Res., (1993), pp. 2595-2601.
201. Cheng H, Hills J.H. and Azzopardi B.J., "A Study of the Bubble-to-Slug Transition in vertical Gas-Liquid Flow in Columns of Different Diameter," Int. J. Multiphase Flow, Vol. 24, No. 3, (1998), pp. 431-452.
202. Neubauer, G., (unpublished Ph-D dissertation, TU Munich SFB 153, 1977)
203. Camarasa, E., Vial, C., Poncin, S., Wild, G., Midoux, N. and Bouillard, J., "Influence of Coalescence Behavior of the Liquid and Gas Sparging on Hydrodynamics and Bubble Characteristics in Bubble Column," Chem. Eng. Proced., Vol. 38, (1999), pp. 329-344.
204. Kasireddy, V.K. and Al Taweel, A.M., "An Improved Light Attenuation Technique for Measuring Large Interfacial Areas," Canad. J. Chem. Eng., Vol. 68, (1990), pp. 690-693.
205. Takahashi, K. and Nienow, A.W., "Bubble Sizes and Coalescence Rates in an Agitated vessel Agitated by a Rushton Turbine," J. Chem. Eng. Japan, Vol. 26, (1993), pp. 536-542.
206. Kawecki, W., Reith, T., van Heuven, J.W. and Beek, W.J., Chem. Eng. Sci., Vol. 22, (1967), pp. 1519.
207. Lin, T.J., Tsuchiya, K. and Fan, L.S., "Bubble Flow Characteristics in Bubble Columns at Elevated Pressure and Temperature," AIChE J., Vol. 44(3), (1998), pp. 545-560.
208. Calderbank, P.H. and Moo-Young, M.B., "The continuous phase heat and mass-transfer properties of dispersions," Chem. Eng. Sci., Vol. 16, (1961), pp. 39-54.
209. Chang, J.S. and Harvel, G.D., "Determination of Gas-Liquid Bubble Column Instantaneous Interfacial Area and Void Fraction by a Real-Time Neutron Radiography Method," Chem. Eng. Sci., Vol. 47, (1992), pp. 3639-3646.
210. Burgess, J.M. and Calderbank, P.H., "The Measurement of Bubble Parameters in Two-Phase Dispersion-I," Chem. Eng. Sci., Vol. 30, (1975), pp. 743-750.

211. Soong, Y., Harke, F.W., Gamwo, I.K., Schehl, R.R. and Zarochak, M.F., "Hydrodynamic study in a slurry-bubble-column reactor," Catalysis Today, Vol. 35, (1997), pp. 427-434.
212. Lu, W.-M., Hsu, R.C. and Chien, W.C., "Measurement of Local Bubble Diameter and Analysis of Gas Dispersion in an Aerated Vessel with Disc Turbine Impeller," J. Chem. Eng. Japan., Vol. 26, (1993), pp. 551-557.
213. Prandit, A.B., Valery, J., Thorpe, R.B. and Davidson, J.F., "The continuous phase heat and mass transfer properties of dispersion," Chem. Eng. Sci., Vol. 47, (1992), pp. 1079-1089.
214. Behkish, A., Lemoine, R., Sehabiague L., Oukaci R. and Morsi BI., "Prediction of the Gas Holdup in Industrial-Scale Bubble Columns and Slurry Bubble Column Reactors Using Back-Propagation Neural Networks," Submitted to Int. J. Chem. React. Eng. 2004.
215. Sriram, K., and Mann, R., "Dynamic Gas Disengagement: A New Technique for Assessing the Behavior of Bubble Columns," Chemical Engineering Science, Vol. 32, (1977), pp. 571-580.
216. Charpentier J. C., "Gas-Liquid Reactors" in D. Luss and V. W. Weekman (Editors), "Chemical Engineering Reviews", Am. Chem. Soc. Symp. Series, 72, (1978), (Washington, D.C.).
217. Krishna, R. and Ellenberger, J., "A Unified Approach to the scaleup of Fluidized Multiphase Reactors," Transactions of Institute of Chemical Engineers, Vol. 73-A, (1995), pp. 217-221.
218. Yoshida, F., Akita, K., "Performance of Gas Bubble Columns: Volumetric Liquid-Phase Mass Transfer Coefficient and Gas Holdup," A.I.Ch.E. J., (1965), Vol. 11, pp. 9.
219. Shah, Y.T., Kelkar, B.G., Godbole, S.P. and Deckwer, W.D., "Design Parameters Estimations for Bubble Column Reactors," AIChE, J., Vol. 28, (1982), pp. 353.
220. Pino, L.Z., Solari, R.B., Siquier, S., Antonio Estevez, L. and Yopez, M.M., "Effect of Operating Conditions on Gas Holdup in Slurry Bubble Columns with a Foaming Liquid," Chem. Eng. Communication, Vol. 117, (1992), pp. 367.

221. Yasunishi, A., Fukuma, M. and Muroyama, K., "Measurement of Behavior of Gas Bubbles and Gas Holdup in a Slurry Bubble Column by a Dual Electroresistivity Probe Method," Journal of Chem. Eng. of Japan, Vol. 19, (1986), pp. 444.
222. Clark, K.N., "The Effect of High Pressure and Temperature on Phase Distributions in a Bubble Column Reactors," Chem. Eng. Sci., Vol. 45, (1990), pp. 2301-2307.
223. Lin, T.J., Tsuchiya, K. and Fan, L.S., "On the Measurements of Regime Transition in High-Pressure Bubble Columns," The Canad. J. of Chem. Eng., Vol. 77, (1999), pp. 370.
224. Charpentier, J.C., "Mass Transfer Rates in Gas-Liquid Absorbers and Reactors, Advances in Chemical Engineering, (Academic Press, 1981), Vol. 11.
225. Yoshida, F. and Miura, Y., "Gas Absorption in Agitated Gas-Liquid Contactors," Ind. Eng. Proc. Des. Dev., Vol. 2, (1963), pp. 263-268.
226. Bukur, D.B., Daly, J.G. and Patel, S.A., "Application of γ -ray Attenuation for Measurement of Gas Holdups and Flow Regime Transition in Bubble Columns," Ind. Eng. Chem. Res., Vol. 35, (1996), pp.70-80.
227. Kocamustafaogullari, G. and Wang, Z., "An Experimental Study on Local Interfacial Parameters in a Horizontal Bubbly Two-Phase Flow," Multiphase Flow, Vol. 17, (1991), pp. 553-572.
228. Quicker G. and Deckwer W.D. "A Further Note on Mass Transfer Limitations in the Fischer-Tropsch Slurry Process," Chemical Engineering Science, Vol. 36, (1981), pp. 1577-1579.
229. Fan, L.S., Bavarian, F., Gorowara, R.L. and Kreischer, B.E., "Hydrodynamics of Gas-Liquid-Solid Under High Gas Holdup Conditions," Powder Technology, Vol. 53, (1987), pp. 285-293.
230. Fukuma, M., Muroyama, K. and Yasunishi, A., "Properties of Bubble Swarm in a Slurry Bubble Column," J. Chem. Eng. of Japan, Vol. 20, (1987), pp. 28.
231. Patel, S.A., Daly, J.G. and Bukur, D.B., "Holdup and Interfacial Area Measurements Using Dynamic Gas Disengagement," American Institute of Chemical Engineers Journal, Vol. 35(6), (1989), pp. 931-942.

232. Patel, S.A., Daly, J.G. and Bukur, D.B., "Bubble Size Distribution in Fischer Tropsch Derived Waxes in a Bubble Column," AIChE J., Vol. 36(1), (1990), pp. 93-105.
233. Solanki, M.K.S., Mukherjee, A.K., and Das T.R., "Bubble Formation at Closely Spaced Orifices in Aqueous Solutions," Chem. Eng. Journal, Vol. 49, (1992), pp. 65-71.
234. Hyndman, C.L. and Guy, C., "Gas phase hydrodynamics in Bubble columns," Inst. Chem. Eng., Vol. 73, (1995), pp. 302-307.
235. Jiang, P., Lin, T.J., Luo, X. and Fan, L.S. "Flow Visualization of High Pressure (21mpa) Bubble Column: Bubble Characteristics," Transaction of the Institute of Chemical Engineers, Vol. 73(A), (1995), pp. 269-274.
236. Kundakovic, L.J., and Vunjak-Novakovic, G., "A Fluid Dynamic Model of the Draft Tube Gas-Liquid-Solid Fluidized Bed," Chem. Eng. Sci., Vol. 50 (23), (1995), pp. 3763-3775.
237. Smith, G.B., Gamblin, B.R. and Newton, D., "X-Ray Imaging of Slurry Bubble Column Reactors: The Effects of System Pressure and Scale," Chem. Eng. Res. and Des., Vol. 73, (1995), pp. 632.
238. Krishna, R., Urseanu, M.I., van Baten, J.M.. and Ellenberg, J., "Rise velocity of a swarm of large gas bubbles in liquids," Chem. Eng. Sci., Vol. 54, (1999), pp. 171-183.
239. Large, P.L.C. and Esposito, R.O., "Experimental determination of bubble size distributions in bubble columns: Prediction of mean bubble diameter and gas holdup," Powder Technology, Vol. 101, (1999), pp. 142-150.
240. Panneerselvam, S., Subramanian, T.V., and Jagannadhaswamy, B., "Kinetics of Liquid Phase of Toluene to Benzoic Acid in a Packed Bed Reactor," Indian Journal of Technology, Vol. 17, (1979), pp. 469-471.
241. Bejan, D., Lozar J., Falgayrac, G. and Savall, A., "Electrochemical assistance of catalytic oxidation in liquid phase using molecular oxygen: oxidation of toluenes," Catalysis Today, Vol. 48, (1999), pp. 363-369.
242. Mohunta, D. M., Vaidyanathan, A. S., and Laddha, G. S., Indian Chem Engr, Vol. 11(3)(Trans), (1969), p. 73.

243. Ozturk, S.S., Schumpe, A., Deckwer, W.-D., "Organic Liquids in a Bubble Column: Holdups and Mass Transfer Coefficients," AICHE, Vol. 33(9), (1987), pp. 1473-1480.
244. Lockett, M.J. and Safekourdi. A.A., "Light transmission through bubble swarms," AICHE Journal, Vol. 23(3) (1977), pp. 395-398.
245. Sridhar, T. and Potted 0-E., "Interfacial area measurements in gas-liquid agitated vessels: Comparison of techniques," Chem. Eng. Sci., Vol. 33(10), (1978), pp. 1347-53.
246. Midoux, N. and Charpentier, J.C., "Mechanically Agitated Gas-Liquid Reactors. 2: Interfacial Area," Int. Chem. Eng., Vol. 24, (1984), pp. 452.
247. van't Riet K., "Review of measuring Methods and results in Non Viscous gas-Liquid Mass Transfer in Stirred Vessels," Ind. Eng. Chem. Process Des. Dev., Vol. 18, (1979), p. 357.
248. Mann R., Gas-Liquid Contacting in Mixing Vessels, ICHEME. (Industrial Research Fellowship Report, 1983).
249. Chang, M.-Y., "Mass Transfer Characteristics of Gases in Aqueous and Organic Liquids and Slurries at Elevated Pressures and Temperatures in Agitated Reactors" (unpublished Ph.D. dissertation, School of Engineering, University of Pittsburgh, 1991).
250. Chang, M.-Y. and Morsi, B.I., "Mass Transfer in a Three Phase Reactor Operating at Elevated Pressures and Temperatures," Chem. Eng. Sci., Vol. 47, (1991), pp. 1779-1790.
251. Chang, M.-Y. and Morsi, B. I., "Mass Transfer Characteristics of Gases in n-Decane at Elevated Pressures and Temperatures in Agitated Reactors," Chem. Eng. J., Vol. 47, (1991), pp. 33-45.
252. Chang, M.-Y., Morsi, B. I. and Eiras, J.G., "Mass transfer characteristics of gases in n-hexane at elevated pressures and temperatures in agitated reactors," Chem. Eng. Process., Vol. 29, (1991), pp. 49-60.
253. Danckwert, P.V., Gas-Liquid reactions (New York, NY: McGraw-Hill, 1970).
254. Behkish A., Men Z., Inga J.R., Morsi, B.I., "Mass transfer characteristics in a large-scale slurry bubble column reactor with organic liquid mixtures," Chem. Eng. Sci., Vol. 57(16), (2002), pp. 3307-3324.

255. Eldib, I.A. and Albright, L.F., "Operating Variables in Hydrogenating Cotton seed Oil," Ind. Eng. Chem., Vol. 49, (1957), pp. 825-831.
256. Albright, L.F., Wei, C.-H., and Woods, J.M., "Solvent Hydrogenation of Cotton seed Oil," J. Am. Oil Chem. Soc., Vol. 37, (1960), pp. 315-320.
257. Yoshida, F. and Arakawa, S.-I., "Pressure Dependency of Liquid Phase Mass Transfer Coefficients," A.I.Ch.E. J., (1968), Vol. 14, pp. 962-963.
258. Kataoka, H. and Miyauchi, T., "Effect of Physical Properties and of Turbulence on the Rate Coefficient of Mass Transfer at the Free Surface of Agitated Vessels in Turbulent Region," Kagaku Kougaku, Vol. 36, (1972), pp. 888.
259. Teramoto, M., Tai, S., Nishii, K. and Teranishi, H., "Effects of Pressure on Liquid-Phase Mass Transfer Coefficients," Chem. Eng. J., Vol. 8, (1974), pp. 223-226.
260. Farritor, R.E. and Hughmark, G.A., "Mass Transfer to the Free Interface in a Stirred Vessel," AIChE. J., Vol. 20, (1974), pp. 1027.
261. Zwicky, J.J. and Gut, G., "Kinetics, Poisoning and Mass Transfer Effects in Liquid-Phase Hydrogenations of Phenolic Compounds over a Palladium Catalyst," Chem. Eng. Sci., (1978), Vol. 33, pp. 1963-1969.
262. Takase, H., Unno, H. and Akehata, T., "Oxygen Transfer in Surface Aeration Tank with Square Cross Section," Kagaku Kougaku Ronbunshu, Vol. 9, (1983), pp. 25.
263. Hozawa, M., Yokohata, H., Imaishi, N. and Fujinawa, K., "Effect of Surface Tension on Liquid Phase mass Transfer Coefficient at a Turbulent Free Surface," Kagaku Kougaku Ronbunshu, Vol. 7, (1981), pp. 138.
264. Ledakowicz, S., Nettelhoff, H. and Deckwer, W.-D., "Gas-liquid Mass Transfer Data in a stirred Autoclave Reactor," Ind. Eng. Chem. Fundam., Vol. 23, (1984), pp. 510-512.
265. Deimling, A., Karandikar, B.M., Shah, Y.T. and Carr, N.L., "Solubility and Mass Transfer of CO and H₂ in Fischer-Tropsch Liquids and Slurries," Chem. Eng. J., Vol. 29, (1984), pp. 127-140.

266. Versteeg, G.F., Blauwhoff, P.M.M. and van Swaaij, W.P.M., "The effect of Diffusivity on Gas-Liquid Mass Transfer in Stirred Vessels. Experiments at Atmospheric and Elevated Pressures," Chem. Eng. Sci., Vol. 42, (1987), pp. 1103-1119.
267. Tekie, Z., Li, J., Morsi, B.I. and Chang, M-Y. "Gas-liquid mass transfer in cyclohexane oxidation process using gas-inducing and surface-aeration agitated reactors," Chem. Eng. Sci., Vol. 52(9), (1997), pp. 1541-1551.
268. Fillion, B. and Morsi, B.I., "Gas-Liquid Mass Transfer and Hydrodynamic Parameters in a Soybean Oil Hydrogenation Process under Industrial Conditions," Ind. Eng. Chem. Res., Vol. 39, (2001), pp. 2157-2168.
269. Woodrow, P.T.Jr. and Duke, S.R., "Laser-Induced Fluorescence Studies of Oxygen transfer Across Unsheared Flat and Wavy Air-Water Interfaces," Ind. Eng. Chem. Res., Vol. 40, (2001), pp. 1985-1995.
270. Pawlowski, J. and Kricsfalussy, Z., "Reaktionskinetische Untersuchungen in Drei Phasen Systemen," Chem. Ing. Tech., Vol. 53, (1981), pp. 652-654.
271. Kara, M., Sung, S., Klinzing, G.E. and Chiang, S.H., "Hydrogen Mass Transfer in Liquid Hydrocarbons at Elevated Pressures and Temperatures," Fuel, Vol. 62, (1983), pp. 1492-1498.
272. Karandikar, B.M., Morsi, B.I., Shah, Y. T. and Carr, N. L., "Effect of Water on the Solubility and Mass Transfer Coefficient of Gases in a Heavy Fraction of Fischer-Tropsch Products," Can. J. Chem. Eng., Vol. 65, (1987), pp. 973-981.
273. Eiras, J.G., "Mass Transfer in Polymerization Process," (unpublished Master's Thesis, University of Pittsburgh, 1990).
274. Lee, J.H. and Foster, N.R., "Mass Transfer and Solubility of O₂ and CH₄ in Silicone Fluids," Ind. Eng. Chem. Res., Vol. 29, (1990), pp. 691-696.
275. Zlokamik, M., "Sorption characteristics for gas-liquid contacting in mixing vessels," Advan. Biochem. Eng., Vol. 29, (1990), pp. 1962-1968.

276. Yoshida, F., Ikeda, A., Imakawa, S. and Miura, Y., "Oxygen Absorption Rates in Stirred Gas-Liquid Contactors," Ind.Eng. Chem., Vol. 52, (1960), pp. 435-466.
277. Wisnaik, J. and Albright, L. F., "Hydrogenating cotton seed oil at relatively high pressure," Ind. Eng. Chem., Vol. 53, (1961), pp. 375-380.
278. Brian, P.L.T., Hales, H.B. and Sherwood, T.K., "Transport of Heat and Mass Between Liquids and Spherical Particles in an Agitated Tank," A.I.Ch.E. J., Vol. 15(5), (1969), pp. 727-732.
279. Prasher, B.D. and Wills, G.B., "Mass transfer in an Agitated Vessel," Ind. Eng. Process Des. Develop., Vol. 12(3), (1973), pp. 351-354.
280. Perez, J.F. and Sandall, O.C., "Gas Absorption by Non-newtonian Fluids in Agitated Vessels," A.I.Ch.E. J., Vol. 20, (1974), pp. 770.
281. Robinson, C.W. and Wilke, C.R., "Simultaneous Measurement of Interfacial Area and Mass Transfer Coefficients for a Well-Mixed Gas Dispersion in Aqueous Electrolyte Solutions," A.I.Ch.E. J., Vol. 20(2), (1974), pp. 285-294.
282. Yagi, H. and Yoshida, F., "gas Absorption by Newtonian and Non-Newtonian Fluids in Sparged Agitated Vessels," Ind. Eng. Process Des. Develop., Vol. 14, (1975), pp. 488.
283. Bern, L., Lidefelt, J.O. and Schoon, N.-H., "Mass Transfer and Scale-up in Fat Hydrogenation," J. Am. Oil Chem. Soc., Vol. 53, (1976), pp. 463-466.
284. Marangozis, J., Keramidas, O.B. and Paparisvas, G., "Rate and Mechanism of Hydrogenation of Cotton seed Oil in Slurry Reactors," Ind. Eng. Chem. Process Des. Dev., Vol. 16, (1977), pp. 361-369.
285. Matsumura, M., Masunaga, H. and Kobayashi, J., "Gas Absorption in an Aerated Stirred Tank at High Power Input," J. Ferment. Technol., Vol. 57(2), (1979), pp. 107-116.
286. Meister, D., Post, T., Dunn, I.J. and Bourne, J.R., "Design and Characterization of a Multistage, Mechanically Stirred Column Absorber," Chem. Eng. Sci., Vol. 34, (1979), pp. 1367.

287. Nishikawa, M., Nakamura, M., Yagi, H. and Hashimoto, K., "gas Absorption in Aerated Mixing Vessels," J. Chem. Eng. Japan, Vol. 14, (1981), pp. 219.
288. Judat, H., "Gas/liquid Mass transfer in Stirred Vessels-A Critical review," Ger. Chem. Eng., Vol. 5, (1982), pp. 357.
289. Gibilaro, L.G., Davies, S.N., Cooke, M., Lynch, P.M. and Middleton, J.C., "Initial response Analysis of Mass Transfer in a Gas Sparged Stirred Vessel," Chem. Eng. Sci., Vol. 40, (1985), pp. 1811.
290. Reisener, J., Reuter, M.A. and Kruger, J., "Modelling of the Mass Transfer in Gas-Sparged Electrolysers with Neural Nets," Chem. Eng. Sci., Vol. 48(6), (1993), pp. 1089-1101.
291. Stegeman, D., Ket, P.J., Kolk, H.A.; Bolk, J.W., Knop, P.A. and Westerterp, K.R., "Interfacial Area and Gas Holdup in an Agitated Gas-Liquid Reactor under Pressure," Ind. Eng. Chem. Res., Vol. 34, (1995), pp. 59-71.
292. Yoshida, M., Kitamura, A., Yamagiwa, K. and Ohkawa, A., "Gas Hold-Up and Volumetric Oxygen Transfer Coefficient in an Aerated Agitated Vessel Without Baffles Having Forward-Reverse Rotating Impellers," Can. J. Chem. Eng., Vol. 74, (1996), pp. 31-39.
293. Yang, H., Fang, B.S. and Reuss, M., "kLa Correaltion Established on the basis of a Neural Network Model," Can. J. Chem. Eng., Vol. 77, (1999), pp. 838-843.
294. Hikita, H., Asai, S., Tanigawa, K., Segawa, K. and Kitao, M., "The Volumetric Liquid-Phase Mass Transfer Coefficient in Bubble Columns," Chem. Eng. Journal, Vol. 22, (1981), pp. 61-69.
295. Kawase, Y., Halard, B. and Moo-Young, M., "Theoretical Prediction of Volumetric Mass Transfer Coefficients in Bubble Columns for Newtonian and Non-Newtonian Fluids," Chem. Eng. Sci., Vol. 42, (1987), pp. 1609-1617.
296. Moo Young, M. and Kawase, Y., "Gas Holdup And Mass Transfer In A Bubble Column With Viscoelastic Fluids," Can. J. of Chem. Eng., Vol. 65(1), (1987), pp. 113-118.
297. Popovic, M. and Robinson, C.W., "Specific Interfacial Area In External Circulation Loop Airlifts And A Bubble Column- I Aqueous Sodium Sulphite Solution," Chem. Eng. Sci., Vol. 42(12), (1987), pp. 2811-2824.

298. Popovic, M. and Robinson, C.W., "Specific Interfacial Area In External Circulation Loop Airlifts And A Bubble Column- II Carboxymethyl Cellulose/Sulphite Solution," Chem. Eng. Sci., Vol. 42(12), (1987), pp. 2825-2832.
299. Cho, J.S. and Wakao, N., "Determination Of Liquid-Side And Gas-Side Volumetric Mass Transfer Coefficients In A Bubble Column," Journal of Chem. Eng. of Japan, Vol. 21(6), (1988), pp. 576-581.
300. Akita, A., "Effect Of The Electrolyte On The Mass Transfer Characteristics Of A Bubble Column," Inter. Chem. Eng., Vol. 29(1), (1989), pp.127-135.
301. Allen, D., Grant, R. and Campbell, W., "Hydrodynamics And Mass Transfer In *Aspergillus Niger* Fermentations In Bubble Column And Loop Bioreactors," Biotechnology and Bioengineering, Vol. 34(6), (1989), pp. 731-740.
302. Halard, B., Kawase, Y. and Moo-Young, M., "Mass Transfer In A Pilot Plant Scale Airlift Column With Non-Newtonian Fluids," Ind. and Eng. Chem. Res., Vol. 28(2), (1989), pp. 243-245.
303. Medic, L., Cehovin, A., Koloini, T. and Pavko, A., "Volumetric Gas-Liquid Mass Transfer Coefficients In A Rectangular Bubble Column With A Rubber Aeration Pad," Chem. Eng. J. and Biochem. Eng. J., (1989), Vol. 41(3), pp. B51-B54.
304. Popovic, M.K. and Robinson, C.W., "Mass Transfer Studies Of External-Loop Airlifts And A Bubble Column," AIChE J., Vol. 35(3), (1989), pp. 393-405.
305. Uchida, S., Tsuyutani, S. and Seno, T., "Flow Regimes And Mass Transfer In Counter-Current Bubble Columns," Can. J. Chem. Eng., Vol. 67(5), (1989), pp. 866-869.
306. Vatai, G.Y. and Tekic, M.N., "Gas Hold-Up And Mass Transfer In Bubble Columns With Pseudoplastic Liquids," Chem. Eng. Sci., Vol. 44(10), (1989), pp. 2402-2407.
307. Seno, T., Uchida, S. and Tsuyutani, S., "Mass Transfer In Countercurrent And Cocurrent Bubble Columns," Chem. Eng. Techn., (1990), Vol. 13(2), pp. 113-118.

308. Huynh, L.X., Briens, C.L., Large, J.F., Catros, A., Bernard, J. R. and Bergougnou, M.A., "Hydrodynamics And Mass Transfer In An Upward Venturi/Bubble Column Combination," Can. J. Chem. Eng., Vol. 69(3), (1991), pp. 711-722.
309. Kawase, Y. and Moo-Young, M., "Oxygen Transfer In Slurry Bioreactors," Biotechn. and Bioeng., Vol. 37(10), (1991), pp. 960-966.
310. Rodemerck, U. and Seidel, A., "Analysis Of Transient Mass Transfer Measurements In Bubble Columns," Chem. Eng. Sci., Vol. 46(3), (1991), pp. 908-912.
311. Suh, I.-S., Schumpe, A., Deckwer, W.-D. and Kulicke, W.-M., "Gas-Liquid Mass Transfer In The Bubble Column With Viscoelastic Liquid," Can. J. Chem. Eng., Vol. 69(2), (1991), pp. 506-512.
312. Terasaka, K. and Tsuge, H., "Mass Transfer In Highly Viscous Liquids In A Bubble Column With Constant-Flow Nozzles," J. Chem. Eng. of Japan, Vol. 24(4), (1991), pp. 424-429.
313. Goto, S. and Gaspillo, P.D., "Effect Of Static Mixer On Mass Transfer In Draft Tube Bubble Column And In External Loop Column," First International Conference on Gas-Liquid and Gas-Liquid-Solid Reactor Engineering, (Columbus, OH, USA, Sep 13-16, 1992), Chemical Engineering Science, Vol. 47(13-14), (1992), pp. 3533-3539.
314. Merchuk, J.C. and Ben-Zvi, S., "Novel Approach To The Correlation Of Mass Transfer Rates In Bubble Columns With Non-Newtonian Liquids," 1st Int. Conf. on Gas-Liquid and Gas-Liquid-Solid Reactor Engineering, (Columbus, OH, USA, Sep 13-16, 1992), Chem. Eng. Sci., Vol. 47(13-14), (1992), pp. 3517-3523.
315. Muller, F.L. and Davidson, J.F., "On The Contribution Of Small Bubbles To Mass Transfer In Bubble Columns Containing Highly Viscous Liquids," 1st Int. Conf. on Gas-Liquid and Gas-Liquid-Solid Reactor Engineering, (Columbus, OH, USA, Sep 13-16, 1992), Chem. Eng. Sci., Vol. 47(13-14), (1992), pp. 3525-3532.
316. Kawasaki, H., Yamamoto, T. and Tanaka, H., "Relationship Between Gas Holdup And Volumetric Mass Transfer Coefficient In A Bubble Column With Single Hole Orifice," J. of Chem. Eng. of Japan, Vol. 27(5), (1994), pp. 667-668.

317. Kawasaki, H., Hirano, H. and Tanaka, H., "Effect Of Multiple Draft Tubes With Perforated Plates On Gas Holdup And Volumetric Mass Transfer Coefficient In A Bubble Column," J. of Chem. Eng. of Japan, Vol. 27(5), (1994), pp. 669-670.
318. Wilkinson, P.M., Haringa, H. and van Dierendonck, L.L., "Mass Transfer and Bubble Size in a Bubble Column Under Pressure," Chem. Eng. Sci., Vol. 49, (1994), pp. 1417.
319. Zhao, M., Niranjana, K. and Davidson J.F., "Mass Transfer To Viscous Liquid In Bubble Column And Airlift Reactors: Influence Of Baffles," Chem. Eng. Sci., Vol. 49(14), (1994), pp. 2359-2369.
320. Eickenbusch, H., Brunn, P.-O. and Schumpe, A., "Mass transfer into viscous pseudoplastic liquid in large-diameter bubble columns," Chem. Eng. Process., Vol. 34, (1995), pp. 479-485.
321. Terasaka, K., Hullmann, D. and Schumpe, A., "Mass Transfer in Bubble Columns studied with an oxygen optode," Short communications Chem. Eng. Sci., Vol. 53(17), (1998), pp. 3181-3184.
322. Vazquez, G., Cancela, M.A., Riverol, C., Alvarez, E. and Navaza, J.M., "Application of the Danckwerts Method in a Bubble Column: Effects of surfactants on mass transfer coefficient and interfacial area," Chem. Eng. J., Vol. 78, (2000), pp. 13-19.
323. Vazquez, G., Cancela, M.A., Riverol, C., Alvarez, E. and Navaza, J.M., "Determination of the Interfacial Areas in a Bubble Column by Different Chemical Method," Ind. Eng. Chem. Res., Vol. 39, (2000), pp. 2541-2547.
324. Rose, L.M., "Chemical Reactor Design in Practice," (Amsterdam, The Netherlands: Elsevier Science Publishers B.V., 1981).
325. Dobbins, W.E., "Biological Treatment of Sewage and Industrial Wastes," (New York, Reinhold: M.L. McCable and W.W. Eckenfelder, 1956), Part 1-2.
326. Toor, H.L. and Marchello, A.I.Ch.E.J., Vol. 4, (1958), pp. 98.
327. Kishinevskii, M.K. and Serebrianskii, V.T., J. Appl. Chem. USSR, Vol. 29, (1956), pp. 29.

328. Reid, R.C., Prausnitz, J.M. and Poling, B.E., "The properties of gases and liquids," (New York: McGraw-Hill, 1987).
329. Lefrançois, B. and Bourgeois, Y., "Tension superficielle des Liquides en Presence de gaz sous pression," Chimie et Industrie-Genie Chimique, Vol. 105(15), (1972), pp. 989-992.
330. Broseta, D. and Ragil, K., "Parachors in Terms of Critical Temperature, Critical Pressure and Acentric Factor," Society of Petrol. Eng., SPE 30784, (1995), pp. 859-866.
331. Wilke, C.R. and Chang, P., "Correlations of Diffusion Coefficients in Dilute Solutions," AIChE J., Vol. 1, (1955), pp. 264-270.
332. Faber, T.E., "Fluid Dynamics for Physicists," (Cambridge: Cambridge University Press, 1995).
333. Goethals, M., Vanderstraeten, B., Berghmans, J., De Smedt, G., Vliegen, S. and Van't Oost, E., "Experimental study of the flammability limits of toluene-air mixtures at elevated pressure and temperature," J. of Hazard. Mat., Vol. A70, (1999), pp. 93-104.
334. Burgoyne, J.H., Tang, T.L. and Newitt, D.M., "The combustion of aromatic and alicyclic hydrocarbons .III Ignition and cool-flame characteristics," Proc. Roy. Soc. A, (1940), Vol. 174, pp. 379.
335. Norrish, R.G.W., Taylor, G.W. and Taylor, F.R.S., "Cool flames in the combustion of toluene and ethylbenzene," Proc. Roy. Soc. A, Vol. 239, (1956), pp. 143.
336. Rozlovskii, A.I. and Borisova, I.Yu., "Explosion-safe conditions for the liquid oxidation of toluene by air," Khim. Prom., Vol. 3, (1964), pp. 199-201.
337. Bodurtha, F. T., "Industrial Explosion Prevention and Protection," (New York: McGraw-Hill, 1980).
338. Panagiotopolous, A. and Reid, R., "A New Mixing Rule for Cubic Equations for Highly Polar, Asymmetric Systems," ACS Symposium on Equation of State -Theories and Applications, (Miami, FL: April 20-May 3, 1985).

339. Enick, R.M., Holder, G.D. and Mohamed R.S., "Four-phase flash equilibrium calculations using Peng-Robinson equation of state and a mixing rule for asymmetric systems," SPERE, (1987), 687-694.
340. Crane, "Flow of Fluids through valves, fittings and pipe," (New York: CRANE CO., Technical Paper No. 410, 1986).
341. Jamialahmadi, M., Branch, C., and Muller-Steinhagen, H., "Terminal Bubble Rise Velocity in Liquids," Trans. I.Chem.E., Vol. 72 (A), (1994), pp. 119-122.
342. Gharat, S.D. and Joshi, J.B., "Transport phenomena in bubble column reactors, II: pressure drop," The Chemical Engineering Journal, Vol. 48, (1992), pp. 153-166.
343. Boyer, C., Duquenne, A.-M., Wild, G., "Measuring techniques in gas-liquid and gas-liquid-solid reactors," Chemical Engineering Science, Vol. 57, (2002), pp. 3185-3215.
344. De Swart, J.W.A., Van Vliet, R.E. and Krishna, R., "Size, Structure and Dynamics of "Large" Bubbles in a Two-Dimensional Slurry Bubble Column," Chem. Eng. Sci., Vol. 51, (1996), pp. 4619.
345. Lee, Y.H. and Weinberger, C.B., "Analysis of Dispersion Structure of Fermentation Media by Dynamic Gas Disengagement Method," Biotechn. and Bioeng., Vol. 37, (1991), pp. 288-291.
346. Schumpe, A. and Grund, G., "The Gas Disengagement Technique for Studying Gas Holdup Structure in Bubble Columns," Can. J. Chem. Eng., Vol. 64, (1986), pp. 891-896.
347. Molerus, O. and Kurtin, M., "Hydrodynamics of Bubble Columns in the Liquid Circulation Regime," Chem. Eng. Sci., Vol. 41, (1986), pp. 2685-2692.
348. Li, J., Tekie, Z., Mohammed, A. and Morsi, B.I., "Statistical Assessment of Gas/Liquid Mass Transfer Slurry-Phase Propylene Polymerization Process," Canad. J. Chem. Eng., Vol. 74, (1996), pp. 77-83.
349. Fillion B., "Modeling of Soybean Oil Hydrogenation Process," (unpublished Ph.D. dissertation, School of Engineering, University of Pittsburgh, 2001).
350. Himmelblau, D. M., "Solubilities of Inert Gases in Water," J. Chem. Eng. Data, Vol. 5(1), (1960), pp. 10-15.

351. Schulze, G. and Prausnitz, J.M., "Solubilities of Gases in Water at High Temperature," Ind. Eng. Chem. Fundam., Vol. 20, 1981, pp. 175-177.
352. Carroll, J.J., Sluskey, J.D. and Mather, A., "The Solubility of Carbon Dioxide in Water at Low Pressure," J. Phys. Chem. Ref. Data, Vol. 20(6), 1991, pp. 1201-1209.
353. Sherwood, A.E. and Prausnitz, J.M., "The Heat of Solution of Gases at High Pressure," A.I.Ch.E. J., Vol. 8(4), (1962), pp. 519-521.
354. Krichevsky, I.R. and Kasarnovsky, J.S., "Thermodynamical Calculations of Solubilities of Nitrogen and Hydrogen in Water at High Pressure," J. Am. Chem. Soc., Vol. 57, (1935), pp. 2168-2171.
355. Wilhelm, E. and Battino, R., "The Solubility of Gases in Liquids, I: The Solubility of a Series of Fluorine-containing Gases in several Non-polar Solvents," J. Chem. Therm., Vol. 3, (1971), pp. 379-392.
356. Hildebrand, J.H., Prausnitz, J.M. and Scott, R.L., "Regular and Related Solutions," (New York: Van Nostrand Reinhold Company, 1970).
357. Fernandez-Prini, R. and Crovetto, R., "A critical Evaluation of the solubility of simple inorganic gases in water at high temperature," AIChE. J., Vol. 31(3), (1985), pp. 513-516.
358. Prausnitz, J.M. and Lichtenthaler, "Molecular theory of fluid phase equilibria," (New York: Prentice-Hall, Englewood Cliff, 1986).
359. Yaws, C.L., "Chemical properties handbook: physical, thermodynamic, environmental, transport, safety, and health related properties for organic and inorganic chemicals," (New York: McGraw-Hill, 1999).
360. Beutier, D. and Renon, H., "Gas Solubilities near the Solvent Critical Point," A.I.Ch.E. J., Vol. 24(6), (1978), pp. 1122-1125.
361. Doraiswamy, L.K. and Sharma, M.M., "Heterogeneous Reactions: Analysis, Examples and Reactor Design," (New York: John Wiley, 1984), Vol. 2.

362. Ganguli, K.L. and van den Berg, H.J., "Liquid-Side Mass transfer Coefficient for a Hydrogen Oil System in a Agitated Reactor," Chem. Eng. J., Vol. 19, (1980), pp. 11-14.
363. Linek, V., Kordac, M., Fujasova, M., Moucha, T., "Gas-liquid mass transfer coefficient in stirred tanks interpreted through models of idealized eddy structure of turbulence in the bubble vicinity," Chem. Eng. Process., Vol. 43, (2004), pp. 1511-1517.
364. Linek, V., Kordac, M., Moucha, T., "Mechanism of mass transfer from bubbles in dispersions Part II: Mass transfer coefficients in stirred gas-liquid reactor and bubble column," Chem. Eng. Process., Vol. 44, (2005), pp. 121-130.
365. van't Riet, K. and Smith, J.M., "the behavior of gas-liquid mixtures near Rushton turbines blades," Chem. Eng. Sci., Vol. 28, (1973), pp. 1031-1037.
366. Bruijn, W., van't Riet, K. and Smith, J.M., "Power Consumption with Aerated Rushton Turbines," Trans. Inst. Chem. Eng., Vol. 52, (1974), pp. 88-104.
367. Beenackers, A.A.C.M. and van Swaaij, W.P.M., "Mass Transfer in Gas-Liquid Slurry Reactors," Chem. Eng. Sci., Vol. 48, (1993), pp. 3109-3139.
368. Inga, J.R. and Morsi, B.I., "Effect of Operating Variables on the Gas Holdup in a Large-Scale Slurry Bubble Column Reactor Operating with an Organic Liquid Mixture," Ind. Eng. Chem. Res., Vol. 38, (1999), pp. 928.
369. Inga, J.R. and Morsi, B.I., "A novel approach for the assessment of the rate limiting step in Fischer-Tropsch slurry process," Energy & Fuels, Vol. 10, (1996), pp. 566.
370. Dewes, I., Kuksal, A. and Schumpe, A., "Gas Density Effect on Mass Transfer in Three-Phase Sparged Reactors," Chem. Eng. Res. Dev., Vol. 73, (1995), pp. 697.
371. Marrucci, G., "," Ind. Chem. Eng., Vol. 4, (1965), pp. 224.
372. Dewes, I., Kuksal, A. and Schumpe, A., "Gas Density Effect on Mass Transfer in Three-Phase Sparged Reactors," Chem. Eng. Res. Dev., Vol. 73, (1995), pp. 697.

373. Deckwer W-D and Schumpe A., "Improved Tools for Bubble Column Reactor Design and Scale-Up," Chem. Eng. Sci., Vol. 48(5), (1993), pp. 889-911.
374. Midoux N. and Charpentier J.-C., "Les Réacteurs gaz-liquide à cuve agitée mécaniquement Partie 1: Hydrodynamique," Entropie, Vol. 88, (1979), pp. 5-38.
375. Poncin S., Nguyen C., Midoux N. and Breyse J., "Hydrodynamics and volumetric gas-liquid mass transfer coefficient of a stirred vessel equipped with a gas-inducing impeller," Chem. Eng. Sci., Vol. 57, (2002), pp. 3299-3306.
376. Saravanan K., Patwardhan A.W., Mundale V.D. and Joshi J.B., "Power Consumption in Gas Inducing Type Mechanically Agitated Contactors," Ind. Eng. Chem. Res., Vol. 35, (1996), pp. 1583-1602.
377. Bouaifi M., Hebrard G., Bastoul D. and Roustan M., "A comparative study of gas hold-up, bubble size, interfacial area and mass transfer coefficients in stirred gas-liquid reactors and bubble columns," Chem. Eng. Process., Vol. 40, (2001), pp. 97-111.
378. Loiseau B., "Contribution à l'étude de l'hydrodynamique et du transfert de matière dans les réacteurs à cuve agitée mécaniquement," (Ph.D. dissertation, INPL Nancy, France, 1976).
379. Botton R., Cosserat D. and Charpentier J.C., "Operating zone and scale up of mechanically stirred gas-liquid reactors," Chem. Eng. Sci., Vol. 35, (1980), pp. 82-89.
380. Smith J.M., "Simple Performance Correlations for Agitated Vessels," Proc. 7th Euro. Congress on Mixing, Brugge, (1991), pp. 233-241.
381. Koneripalli N., "Mass Transfer Characteristics of Gases in Methanol and Ethanol Under Elevated Pressures and Temperatures in Agitated Reactors," (M.S. Dissertation, University of Pittsburgh, Pittsburgh, PA, USA, 1992).
382. Mizan T.I., "Characterization of Mass Transfer of Gases in Olefinic Polymerization Solvents and Slurries in Agitated Reactors," (MS. Dissertation, University of Pittsburgh, Pittsburgh, PA, USA, 1992).

383. Rewatkar V.B., Deshpande A.J., Pandit A.B. and Joshi J.B., "Gas hold-Up Behavior of Mechanically Agitated Gas-Liquid Reactors using Pitched Blade Downflow Turbines," Can. J. Chem. Eng., Vol. 71, (1993), pp. 226-237.
384. Nienow A.W., Hunt G. and Buckland B.C., "A fluid Dynamic Study of the Retrofitting of Large Agitated Bioreactors: Turbulent Flow," Biotechn. Bioeng., Vol. 44, (1994), pp. 1177-1185.
385. Li J., "Mass Transfer and Mathematical Modeling For Propylene Polymerization Process," (Ph.D. Dissertation, University of Pittsburgh, Pittsburgh, PA, USA, 1995).
386. Saravanan K. and Joshi J.B., "Gas-Inducing-Type Mechanically Agitated Contactors: Hydrodynamics Characteristics of Multiple Impeller," Ind. Eng. Chem. Res., Vol. 34, (1995), pp. 2499-2514.
387. Solomakha G.P. and Tarasova T.A., "Scale-up of Mass Transfer in Mechanically Agitated Gas-Liquid Contactors," Theor. Found. Chem. Eng., Vol. 32(5), (1998), pp. 456-461.
388. Vrabel P., van der Lans R.G.J.M., Luyben K.Ch.A.M., Boon L. and Nienow A.W., "Mixing in large-scale vessels stirred with multiple radial or radial and axial up-pumping impellers: modelling and measurements," Chem. Eng. Sci., Vol. 55, (2000), pp. 5881-5896.
389. Yawalkar A.A., Pangarkar V.G. and Beenackers A.A.C.M., "Gas Hold-Up in Stirred Tank Reactors," Can. J. Chem. Eng., Vol. 80, (2002), pp. 158-166.
390. Alves S.S., Maia C.I. and Vasconcelos J.M.T., "Gas-liquid mass transfer coefficient in stirred tanks interpreted through bubble contamination kinetics," Chem. Eng. Process., Vol. 43, (2004), pp. 823-830.
391. Lemoine R., Fillion A. and Morsi B.I., "Hydrodynamic and Mass Transfer Parameters in Agitated Reactors Part I: Critical Mixing Speed, Induced Gas Flow Rate, and Wavy Surface in SARs and GIRs," Int. J. Chem. Reac. Eng., Vol. 2, (2004), A29.
392. Heintz Y., Lemoine R., Soriano J.-P. and Morsi B.I., "Hydrodynamic and Mass Transfer Characteristics of Fluorocarbons in an Agitated Reactor," DOE report 2005.
393. Lemoine R. and Morsi B.I., "Hydrodynamic and Mass Transfer Parameters in Agitated Reactors, Part II: Gas-Holdup, Sauter Mean Bubble Diameters, Volumetric Mass Transfer Coefficients, Gas-Liquid Interfacial Areas, and Liquid-Side Mass Transfer Coefficients," submitted to IJCRE.

394. Soriano J.-P., "Mass Transfer Characteristics in an Agitated Slurry Reactor Operating under Fischer-Tropsch Conditions," (MS. Dissertation, University of Pittsburgh, Pittsburgh, PA, USA, 2005).
395. Behkish A., "Hydrodynamic and Mass Transfer Parameters in Large-Scale Slurry Bubble Column Reactors," (Unpublished PhD Thesis: University of Pittsburgh, 2004).
396. O'Dowd W., Smith DN., Ruether JA. and Saxena SC., "Gas and solids behavior in a baffled and unbaffled slurry bubble column," AIChE J., Vol. 33, (1987), pp. 1959-1970.
397. Saxena SC., Rao NS. and Thimmapuram PR., "Gas Phase Holdup in Slurry Bubble Column for Two- and Three-Phase Systems," Chem. Eng. J., Vol. 49, (1992), pp. 151-159.
398. Shah Y.T., Ratway C.A. and McIlvried H.G., "Back-Mixing Characteristics of a Bubble Column with vertically Suspended Tubes," Transactions of the Institution of Chemical Engineers, Vol. 56, (1978), pp. 107-112.
399. Joseph S., "Hydrodynamic and Mass Transfer Characteristics of a Bubble Column," (Unpublished PhD Thesis: University of Pittsburgh, 1985).
400. Yamashita F., "Effects of Vertical Pipe and Rod Internals on Gas Holdup in Bubble Columns," J. Chem. Eng. Japan, Vol. 20(2), (1987), pp. 204-206.
401. Chen J., Li F., Degaleesan S., Gupta P., Al-Dahhan M.H., Dudukovich M.P. and Toseland B.A., "Fluid dynamic parameters in bubble columns with internals," Chem. Eng. Sci., Vol. 54, (1999), pp. 2187-2197.
402. De S.K., Ghosh S., Parichha R.K. and De P., "Gas hold-up in two-phase system with internals," Indian Chemical Engineer, Vol. 41(2), (1999), pp. 112-116.
403. Forret A., Schweitzer J.-M., Gauthier T., Krishna R. and Schweich D., "Liquid dispersion in large diameter bubble columns, with and without internals," Canadian Journal of Chemical Engineering, Vol. 81(3-4), (2003), pp. 360-366.

404. Towell, G.D., Strand, C.P., Ackerman, G.H., "Mixing and Mass Transfer in Large-Diameter Bubble Columns," Proc. AIChE-Inst. Chem. Eng., Vol. 10 (1965), pp. 97-105.
405. Bhaga D., Pruden BB. and Weber ME., "Gas holdup in bubble column containing organic liquid mixtures," Can. J. Chem. Eng., vol. 49, (1971), pp. 417-420.
406. Botton R., Cosserat D. and Charpentier JC., "Influence of Column Diameter and High Gas Throughputs on the Operation of a Bubble Column," Chem. Eng. Journal, Vol. 16, (1978), pp. 107-115.
407. Jackson, M. L., Shen, C.C., "Aeration and Mixing in Deep Tank Fermentation Systems," AIChE Journal, Vol. 24, (1978), pp. 63-71.
408. Kataoka, H., Takeuchi, H., Nakao, K., Yagi, H., Tadaki, T., Otake, T., Miyauchi, T., Washimi, K., Watanabe, K., Yoshida, F., "Mass Transfer in a Large Bubble Column," Journal of Chemical Engineering of Japan, Vol. 12 (1979), pp. 105-110.
409. Kastanek F., Zahradnik J., Rylek M. and Kratochvil J., "Scaling-up of bubble Reactors on basis of laboratory Data," Chem. Eng. Sci., Vol. 35, (1980), pp. 456-462.
410. Godbole, S.P., "Study of Hydrodynamic and Mass Transfer Characteristics of Multiphase Bubble Column Reactor," (unpublished Ph.D. Dissertation, University of Pittsburgh, 1983).
411. Moujaes, S.F., Internal R&D Task Summary Report: Large-Scale Dissolver Cold-Flow Modeling, (DOE report # DOE/OR/03054-20, 1984).
412. Shah YT., Joseph S., Smith DN. and Ruether JA., "On the behavior of the gas phase in a bubble column with ethanol-water mixtures," Ind. Eng. Chem. Process Des. Dev., Vol. 24, (1985), pp. 1140-1148.
413. Grover GS., Rode CV. and Chaudhari RV., "Effect of temperature on flow regime and gas holdup in a bubble column," Can. J. Chem. Eng., Vol. 64, (1986), pp. 501-504.
414. Idogawa K., Ikeda K., Fukuda T. and Morooka S., "Behavior of bubbles of the air-water system in a column under high pressure," International Chemical Engineering, Vol. 26(3), (1986), pp. 468-474.

415. Wezorke, H., "Einfluss von Grössblasen in Blasensäulenreaktoren," (Ph.D. Dissertation, University of Dortmund, Germany, 1986).
416. Bukur, D.B., Daly, J.G., "Gas Hold-Up in Bubble Columns for Fischer-Tropsch Synthesis", Chemical Engineering Science, Vol. 42, (1987), pp. 2967-2969.
417. Idogawa K., Ikeda K., Fukuda T. and Morooka S., "Effect of gas and liquid properties on the behavior of bubbles in a column under pressure," International Chemical Engineering, Vol. 27(1), (1987), pp. 93-99.
418. O'Dowd W., Smith DN., Ruether JA. and Saxena SC., "Gas and solids behavior in a baffled and unbaffled slurry bubble column," AIChE J., Vol. 33, (1987), pp. 1959-1970.
419. Zou R., Jiang X., Li B., Zu Y. and Zhang L., "Studies on gas holdup in a bubble column operated at elevated temperature," Ind. Eng. Chem. Res., Vol. 27, (1988), pp. 1910-1916.
420. Halard, B., Kawase, Y., Moo-Young, M., "Mass Transfer in a Pilot Plant Scale Airlift Column with Non-Newtonian Fluids," Industrial and Engineering Chemistry Research, Vol. 28 (1989), pp. 243-245.
421. Pino, L.R.Z., Yopez, M.M., Saez, A.E., "Hydrodynamics of a Semibatch Slurry Bubble Column with a Foaming Liquid," AIChE Journal, Vol. 36 (1990), pp. 1758-1762.
422. Saxena SC., Rao NS. and Thimmapuram PR., "Gas Phase Holdup in Slurry Bubble Column for Two- and Three-Phase Systems," Chem. Eng. J., Vol. 49, (1992), pp. 151-159.
423. Ellenberger J. and Krishna R., "A unified approach to the scale-up of gas-solid fluidized bed and gas-liquid bubble column reactors," Chem. Eng. Sci., Vol. 49, (1994), pp. 5391-5411.
424. Choi, K.H., Chisti, Y., Moo-Young, M., "Comparative Evaluation of Hydrodynamic and Gas-Liquid Mass Transfer Characteristics in Bubble Column and Airlift Slurry Reactors," Chemical Engineering Journal, Vol 62 (1996), pp. 223-229.
425. Hyndman, C.L., Larachi, F., Guy, C., "Understanding Gas-Phase Hydrodynamics in Bubble Columns: A Convective Model Based on Kinetic Theory," Chemical Engineering Science, Vol. 52 (1997), pp. 63-77.

426. Krishna R., de Swart JWA., Ellenberg J., Martina GB. and Maretto C., "Gas Holdup in Slurry Bubble Columns: Effect of Column Diameter and Slurry Concentrations," AICHE J., Vol. 43, (1997), pp. 311-316.
427. Gandhi B., Prakash A. and Bergougnou MA., "Hydrodynamic behavior of slurry bubble column at high solids concentrations," Powd. Technol., Vol. 103, (1999), pp. 80.
428. Luo X., Lee DJ., Lau R., Yang G. and Fan LS., "Maximum Stable bubble size and gas holdup in high-pressure slurry bubble columns," AICHE J., Vol.45, (1999), pp. 665-680.
429. Krishna R., Urseanu MI. and Dreher AJ., "Gas holdup in bubble columns: influence of alcohol addition versus operation at elevated pressures," Chem. Eng. Process., Vol. 39, (2000), pp. 371-378.
430. Shimizu, K., Takada, S., Minekawa, K., Kawase, Y., "Phenomenological Model for Bubble Column Reactors: Prediction of Gas Hold-Ups and Volumetric Mass Transfer Coefficients," Chemical Engineering Science, Vol. 78, (2000), pp. 21-28.
431. Chen W., Hasegawa T., Tsutsumi A. and Otawara K., "Scale-up effects on the time-averaged and dynamic behavior in bubble column reactors," Chem. Eng. Sci., Vol. 56(21-22), (2001), pp. 6149-6155.
432. Jamialahmadi M., Zehtaban MR., Muller-Steinhagen H., Sarrafi A. and Smith JM., "Study of bubble formation under constant flow conditions," Trans IChemE, Vol. 79(A), (2001), pp. 523-532.
433. Kluytmans JHJ., van Wachem BGM., Kuster BFM. and Schouten JC., "Gas Holdup in a Slurry Bubble Column: Influence of Electrolyte and Carbon Particles," Ind. Eng. Chem. Res., Vol. 40, (2001), pp. 5326-5333.
434. Veera, U. P., Kataria, K.L., Joshi, J.B., "Gas Hold-Up in Foaming Liquids in Bubble Columns," Chemical Engineering Journal, Vol. 84 (2001), pp. 247-256.
435. Schäfer, R., Merten, C., Eigenberger, G., "Bubble Size Distributions in a Bubble Column Reactor Under Industrial Conditions," Experimental Thermal and Fluid Science, Vol. 26, (2002), pp. 595-604
436. Syeda, S. R., Afacan, A., Chuang, K.T., "Prediction of Gas Hold-Up in a Bubble Column Filled with Pure and Binary Liquids," The Canadian Journal of Chemical Engineering, Vol. 80 (2002), pp. 44-50.

437. Jordan U., Saxena AK. and Schumpe A., "Dynamic Gas Disengagement in a High-Pressure Bubble Column," Can. J. Chem. Eng., Vol. 81, (2003), pp. 491-498.
438. Li, H., Prakash, A., Margaritis, A., Bergougnou, M.A., "Effect of Micron-Sized Particles on Hydrodynamics and Local Heat Transfer in a Slurry Bubble Column," Powder Technology, Vol. 133 (2003), pp. 177-184.
439. Lau R., Peng W., Velazquez-Vargas G., Yang GQ. and Fan LS., "Gas-Liquid Mass Transfer in High-Pressure Bubble Columns," Ind. Eng. Chem. Res., Vol. 43, (2004), pp. 1302-1311.
440. Sehabiague, L., Behkish, A., Lemoine, R., Heintz, Y., Morsi, B.I., "Hydrodynamic and Mass Transfer Parameters of Slurry Bubble Column Reactors Operating Under Fischer-Tropsch Conditions," Presented at the Annual AIChE meeting, Austin, TX, Nov 7-12, (2004).
441. Vandu, C.O., Krishna, R., "Volumetric Mass Transfer Coefficients in Slurry Bubble Columns Operating in the Churn-Turbulent Flow Regime," Chemical and Engineering Processing, Vol. 43, (2004), pp. 987-995.
442. Lemoine R., Behkish A. and Morsi BI., "Hydrodynamic and Mass Transfer Characteristics in Organic Liquid Mixtures in a Large-Scale Bubble Column Reactor for the Toluene Oxidation Process," Ind. Eng. Chem. Res., Vol. 43(19), (2004), pp. 6195-6212.
443. Mills P.L., Turner J.R., Ramachandran P.A. and Dudukovic M.P., "The Fischer-Tropsch Synthesis in Slurry Bubble Column Reactors: Analysis of Reactor Performance Using the Axial Dispersion Model," Topics in Chemical Engineering, vol. 8 Gordon and Breach, London, 1996.
444. Rados N., Al-Dahhan M. H., Dudukovic M.P., "Modeling of the Fischer-Tropsch synthesis in slurry bubble column reactors," Catalysis Today, Vol. 79-80, (2003), pp. 211-218.
445. Dudukovic M.P., Devanathan N. and Holub R., "Multiphase reactors: Models and experimental verification," Revue de l'institut Francais de Petrole, Vol. 46, (1991), pp. 439-465.
446. Deckwer W.-D., "Bubble Column Reactors," Wiley and Sons, New York, 1992.
447. Abulnaga B.E., "Slurry System Handbook," McGraw-Hill, 2002.

448. Fernandez-Prini R. and Dooley R.B., "The International Association for the Properties of Water and Steam," Erlangen, Germany, 1997.
449. Mills P.L. and Chaudhari R.V., "Multiphase catalytic reactor engineering and design of pharmaceuticals and fine chemicals," Catalysis Today, Vol. 37, (1997), pp. 367-404.
450. Krishna R., van Baten J.M., "Design and Scale up of a bubble column slurry reactor for Fisher-Tropsch synthesis," Chem. Eng. Sci., Vol. 56, (2001), 537-545.
451. Krishna R. and van Baten J.M., "Scaling up bubble column reactors with the aid of CFD," Trans. IChemE, Vol. 79(A), (2001), pp. 283-308.
452. Karcz J., "Studies of Local heat transfer in a gas-liquid system agitated by double disc turbines in a slender vessel," Chem. Eng. J., Vol. 72, (1999), pp. 217-227.
453. Schluter S., Steiff A. and Weinspach P.M., "Heat Transfer in two- and three-phase bubble column reactors with internals," Chem. Eng. Processing, Vol. 34, (1995), pp. 157-172.
454. <http://www.alleghenytechnologies.com>.
455. <http://www.foamglasinsulation.com>.
456. Levenspiel O., "Chemical Reaction Engineering," Wiley and Sons, 2nd edition, New York, 1972.
457. Matsumura, M., Masunaga, H. and Kobayashi, J., "A Correlation for Flow Rate of Gas Entrained from Free Surface of Aerated Stirred Tank," J. Ferment. Technol., Vol. 55(4), (1977), pp. 388-400.
458. Vermeulen, T., Williams, G.M. and Langlois, G.E., Chem. Eng. Progr., Vol. 51, (1955), pp. 2(85F).
459. Parthasarathy, R., Jameson, G.J. and Ahmed, N., "Bubble Breakup in Stirred Vessels-Predicting the Sauter Mean Diameter," Trans. Instn. Chem. Engrs., Vol. 69(A), (1991), pp. 295.
460. Peebles, F.N., and Garber, H.J., "Studies on the Motion of Gas Bubbles in Liquids," Chemical Engineering Progress, Vol. 49, (1953), pp. 88-94.

461. Hinze, J.O., "Fundamental of the Hydrodynamics Mechanism of Splitting in Dispersion Processes," AICHE Journal, Vol. 1, (1955), pp. 289.
462. Akita, K. and Yoshida, F., "Bubble size, Interfacial Area, and Liquid-Phase Mass Transfer Coefficient in Bubble Columns," Ind. Eng. Chem. Process Des. Dev., Vol. 13, (1974), pp. 84.
463. Gaddis, E.S. and Vogelpohl, A., "Bubble formation in Quiescent Liquid Under Constant Flow Conditions," Chem. Eng. Sci., Vol. 41, (1986), pp. 97-105.
464. Pandit, A.B. and Davidson, J.F., "Bubble Breakup in Turbulent Liquid," (Cambridge, UK, Proceedings of the International Conference on Bioreactor Fluid Dynamics, 1986), pp. 109.
465. Wilkinson, P.M., "Physical Aspects and Scaleup of High Pressure Bubble Columns," (unpublished Ph.D. dissertation, School of Engineering, Rijksuniversiteit, Groningen, Holland, 1991).
466. Grevskott, S., Sannaes, B.H., Dudukovic, M.P., Hjarbo, K.W. and Swendsen, H.F., "Liquid Circulation, Bubble Size Distribution and Solids Movement in Two- and Three-Phase Bubble Columns," Chem. Eng. Sci., Vol. 51, (1996), pp. 1703.
467. Abou-El Hassan M.E., "A Generalized Rise Velocity Correlation," Chem. Eng. Communications, Vol. 22, (1983), pp. 243-250.
468. Fan, L.S. and Tsuchiya, K., "Bubble Wake Dynamics in Liquids and Liquid Solid Suspensions" (Ma Butterworth Heinemann Series in Chemical Engineering, 1990), Vol. 50.
469. De Swart, J.W.A. and Krishna, R., "Influence of Particles Concentration on the Hydrodynamic of Bubble Column Slurry Reactors," Chem. Eng. Res. Des., Vol. 73, (1995), pp. 308.
470. Hughmark, G.A., "Holdup and Mass Transfer in Bubble Columns," Ind. Eng. Chem. Process Design and Development, Vol. 6, (1967), pp. 218.
471. Kumar, A., Degaleesan, T.E., Laddha, G.S. and Hoelscher, H.E., "Bubble Swarm Characteristics in Bubble Columns," Can. J. Chem. Eng., Vol. 54, (1976), pp. 503.

472. Bach, H.F. and Pilhofer, T., "Variations of Gas Hold-up in Bubble Columns with Physical Properties of Liquids and Operating Parameters of Column," German Chemical Engineering, Vol. 1, (1978), pp. 270.
473. Mersmann, A., "Design and scale up of Bubble and Spray Columns," Ger. Chem. Eng., Vol. 1, (1978), pp. 1-11.
474. Hikita, H., Asai, S., Tanigawa, K., Segawa, K. and Kitao, M., "Gas Hold-up in Bubble Columns," Chem. Eng. J., Vol. 20, (1980), pp. 59.
475. Reilly, I.G., Scott, D.S., de Bruijn, T.J.W., Jain, A. and Piskorz, J., "A Correlation for Gas Holdup in Turbulent Coalescing Bubble Columns," Can. J. Chem. Eng., Vol. 64, (1986), pp. 705.
476. Sauer, T. and Hempel, D.C., "Fluid Dynamics and Mass Transfer in a Bubble Column with Suspended Particles," Chem. Eng. Techn., Vol. 10, (1987), pp. 180.
477. Renjun, Z., Xinzhen, J., Baozhang, L., Yong, Z. and Laiqi, Z., "Studies on Gas Holdup in a Bubble Column Operated at Elevated Temperatures," Ind. Eng. Chem. Res., Vol. 27, (1988), pp. 1910-1916.
478. Fan, L.S., Yang, G.Q., Lee, D.J., Tsuchiya, K. and Luo, X., "Some Aspects of High-Pressure Phenomena of Bubbles in Liquid and Liquid-Solid Suspensions," Chem. Eng. Sci., Vol. 54, (1999), pp. 4681.
479. Wu, Y., Cheng Ong, B. and Al-Dahhan, M.H., "Predictions of radial gas holdup profiles in bubble column reactors," Chem. Eng. Sci., Vol. 56, (2001), pp. 1207-1210.
480. Nagata, S., "Mixing: Principle and Applications," (New York, Wiley, 1975).
481. Smit, L. and During, J., "Vortex geometry in stirred vessels," Proc. of the 7th European Congress on Mixing, (Bruges, Belgium, 1991), Vol. 2, pp. 633-639.
482. Mizan T.I., Li J., Morsi B.I., Chang M.-Y., Maier E.E. and Singh C.P.P., "Solubilities and Mass Transfer Coefficients of Gases in Liquid Propylene in a Surface-Aeration Agitated Reactor," Chem. Eng. Sci., Vol. 49, (1994), pp. 821-830.

483. Tekie, Z., Li, J., and Morsi, B.I., "Mass Transfer Parameters of O₂ and N₂ in Cyclohexane under Elevated Pressures and Temperatures: A Statistical Approach," Ind. Eng. Chem. Res., Vol. 36, (1997), pp. 3879-3888.
484. Kara, M., "An Experimental Study of Hydrogen Mass Transfer Rate in Liquids Hydrocarbons at High Temperatures and Pressures," (unpublished Ph.D. dissertation, School of Engineering, University of Pittsburgh, 1981).
485. Hichri H., Accary A. and Andrieu J., "Kinetics and Slurry-Type Reactor Modeling during Catalytic Hydrogenation of o-Cresol on Ni/SiO₂," Chem. Eng. Process., Vol. 30, (1991), pp. 133-140.
486. Chang, M.-Y. and Morsi, B.I., "Solubilities and Mass Transfer Coefficients of Carbon Monoxide in a Gas-Inducing Reactor Operating with Organic Liquids under High Pressures and Temperatures," Chem. Eng. Sci., Vol. 47, (1992), pp. 3541-3548.
487. Dietrich, E. Mathieu, C., Delmas, H. and Jenck, j. "Raney-Nickel Catalysed Hydrogenations: Gas-Liquid Mass Transfer in Gas-Induced Stirred Slurry Reactors," Chem. Eng. Sci., Vol. 47, (1992), pp. 3597-3604.
488. Koneripalli, N., Tekie, Z., Morsi, B.I. and Chiang, M.-Y., "Mass Transfer Characteristics of Gases in Methanol and Ethanol under Elevated Pressure and Temperature," Chem. Eng. J., (1994), Vol. 54, pp. 63-77.
489. Fair, J.R., Lambright, A.J. and Anderson, J.W., Chem. Eng., Vol. 67(74), (1967), pp. 207-214.
490. Gestrich, W., Esenwein, H. and Krauss, W., "Liquid-side mass transfer coefficient in bubble layers," Int. Chem. Eng., Vol. 18(1), (1978), pp. 38-47.
491. Koide, K., Takazawa, A., Komura, M. and Matsunaga, H., "Gas Holdup and Volumetric Liquid-Phase Mass Transfer Coefficient in Solid-Suspended Bubble Columns," J. Chem. Eng. of Japan, Vol. 17, (1984), pp. 459.
492. Schumpe, A., Saxena, A.K. and Fang, L.K., "Gas/Liquid Mass Transfer in a Slurry Bubble Column," Chem. Eng. Sci., Vol. 42, (1987), pp. 1787.
493. Salvacion, J.L., Murayama, M., Ohtaguchi, K. and Koide, K., "Effects of Alcohols on Gas Holdup and Volumetric Liquid-Phase Mass Transfer Coefficient in Gel-Particle-Suspended Bubble Column," J. Chem. Eng. Jap., Vol. 28(4), (1995), pp. 434-441.

494. Dewes, I. and Schumpe, A., "Gas Density Effect on Mass Transfer in the Slurry Bubble Column," Chem. Eng. Sci., Vol. 52, (1997), pp. 4105-4109.
495. Kojima, H., Sawai, J. and Suzuki, H., "Effect of Pressure on Volumetric Mass Transfer Coefficient and Gas Holdup in Bubble Column," Chem. Eng. Sci., Vol. 52, (1997), pp. 4111.
496. Chen, C.M. and Leu, L.P., "Hydrodynamics and Mass Transfer in Three-Phase Magnetic Fluidized Beds," Powder Technology, Vol. 117, (2001), pp. 98-206.
497. Whitman, W.G., Chem. Met. Eng., Vol. 29, (1923), pp. 146.
498. Higbie, R., Trans. Am. Inst. Chem. Engrs., Vol. 31, (1935), pp. 365.
499. Danckwerts, P.V., Ind. Eng. Chem., Vol. 43, (1951), pp. 1460.
500. King, C.J., "Turbulent Liquid Phase Mass Transfer at a free Gas-Liquid Interface," I. & E.C. Fundamentals, Vol. 5(1), (1966), pp. 1-8.
501. Kuthan, K. and Broz, Z., "Mass Transfer in Liquid Films during Absorption Part III: Dependence of the Liquid-Side Mass Transfer Coefficient on the Molecular Diffusivity of Gases at High Values of the Schmidt Number," Chem. Eng. Process., Vol. 25, (1989), pp. 75-84.
502. Yoshimura, P.N., Nosoko, T. and Nagata, T., "Enhancement of Mass transfer into a Falling laminar Liquid Film by Two-Dimensional Surface Waves-Some Experimental Observations and Modelling," Chem. Eng. Sci., Vol. 51(8), (1996), pp. 1231-1240.
503. Roberts, R.M. and Chang, H.-C., "Wave-enhanced Mass Transfer," Chem. Eng. Sci., Vol. 55, (2000), pp. 1127-1141.
504. Fair, J.R., "Heat Transfer and Gas Holdup in a Sparged Contactor," Ind. Eng. Chem. Process Des. Dev., Vol. 1, (1962), pp. 33.

505. Lamont, J.C. and Scott, D.S., "An Eddy Cell Model of Mass Transfer into the Surface of a Turbulent Liquid," AIChE. J., Vol. 16(4), (1970), pp. 513-519.
506. Schumpe, A. and Deckwer, W.D., Ind. Eng. Chem. Process Des. Dev., Vol. 21, (1982), pp. 706-711.
507. Cockx, A., Roustan, M., Line, A. and Hebrard, G., "Modeling of Mass Transfer Coefficient k_L in Bubble Columns," Trans. I.Chem.E., Vol. 7(A), (1995), pp. 627-631.
508. Tsuchiya, K., Mikasa, H. and Saito, T., "Absorption dynamics of CO₂ bubbles in a pressurized liquid flowing downward and its simulation in seawater," Chem. Eng. Sci., Vol. 52, (1997), pp. 4119-4126.
509. Crane, "Flow of Fluids through valves, fittings and pipe," (New York: CRANE CO., Technical Paper No. 410, 1986)
510. Buckingham, E., "On Physical Similar Systems: Illustrations of the Use of Dimensional Equations," Physical Review, Vol. 4, (1914), pp. 345-376.
511. Midoux N. and Charpentier J.C., "Les reacteurs gaz-liquide a cuve agitee mecaniquement, Partie 1: Hydrodynamique," Entropie, Vol. 88, (1979), pp. 5-38.
512. Montgomery, D.C., "Design and Analysis of Experiments," (New York: Wiley, 1991).
513. Li, J., Tekie, Z., Mizan, T.I. and Morsi B.I., "Gas-Liquid Mass Transfer in a Slurry Reactor Operating Under Olefinic Polymerization Process Conditions," Chem. Eng. Sci., Vol. 51, (1996), pp. 549-559.
514. Kim, S.S., Morsi, B.I. and Chiang, S.H., "A Statistical Analysis of the Performance of a Selective Agglomeration Process Using n-Heptane as Agglomeration," Coal Preparation, Vol. 15, (1994), pp. 51.
515. Box, G.E.P. and Draper, N.R., "Empirical Model-Building and Surface Response," (New York: Wiley, 1987).
516. Lemoine, R., Fillion, B., Behkish, A., Smith, A., Morsi, B.I., "Prediction of the Gas-Liquid Volumetric Mass Transfer Coefficient in Surface Aeration and Gas Inducing Reactors using Neural Networks," Chem. Eng. Process., Vol. 42(8-9), (2003), pp. 621-643.

517. Fausset, L., "Fundamentals of Neural Networks: Architectures, Algorithms and Applications," (New Jersey: Prentice Hall inc., Englewood Cliffs, 1994).
518. Rumelhart, D.E., Hinton, G.E. and Williams, R.J., "Learning Internal Representations by Error Propagation," Parallel Distributed Processing: Explorations in the Microstructure of Cognition, (MA: The MIT Press, Foundations D.E. Rumelhart and J.L. McClelland eds., 1986), Vol. 1, pp. 318-362.
519. Funahashi, K., "On the Approximate Realization of Continuous Mappings by Neural Networks," Neural Networks, Vol. 2, (1989), pp. 183-192.
520. Hornik, K., Stinchcombe, M. and White, H., "Multilayer Feedforward Networks are Universal Approximators," Neural Networks, Vol. 2, (1989), pp. 359-366.
521. German, S., Bienenstock, E. and Doursat, R., "Neural Networks and the Bias/Variance Dilemma," Neural Computation, Vol. 4, (1992), pp. 1-58.
522. Twomey, J.M and Smith, A.E., "Bias and Variance of Validation Methods for Function Approximation Neural Networks Under Conditions of Sparse Data," IEEE Transactions on Systems, Man, and Cybernetics, Vol. 28(3) Part C, (1998), pp. 417-430.